DOCTORAL THESIS

An Observational Study of Molecular Dust Precursors in Circumstellar Envelopes

Author:
Sarah MASSALKHI

Supervised by:
Dr. Marcelino AGÚNDEZ CHICO
Prof. José CERNICHARO QUINTANILLA

Tutor:
Dr. Gwendolyn MEEUS

A thesis submitted in fulfillment of the requirements for the degree of Doctor of Philosophy in Astrophysics

in the

UNIVERSIDAD AUTÓNOMA DE MADRID
Facultad de Ciencias
Departamento de Física Teórica

and

CONSEJO SUPERIOR DE INVESTIGACIONES CIENTÍFICAS
Instituto de Física Fundamental
Grupo de Astrofísica Molecular

"what is essential is invisible to the eye"

Antoine de Saint-Exupéry, *The Little Prince*

Abstract

An Observational Study of Molecular Dust Precursors in Circumstellar Envelopes

by Sarah MASSALKHI

The asymptotic giant branch (AGB) phase is a late stage in the evolution of low- to intermediate mass stars. Towards the end of this phase, AGB stars lose copious amounts of material via dense and slow stellar winds which give rise to an extended circumstellar envelope (CSE) surrounding the central star. These envelopes are remarkable astrophysical environments because the physical and chemical conditions throughout the envelope change rapidly to allow for the formation of various types of molecules and dust grains, as evidenced by infrared, millimeter and sub-millimeter observations. This material is eventually blown away by the stellar outflow and will be the primary source of the enrichment of the interstellar medium (ISM), by that providing the main building blocks for a further generation of stars and planets.

One of the main ingredients of this material is dust, however questions regarding its formation processes remain a mystery. What the gas-phase building blocks of condensation nuclei are and how these particles evolve toward the micrometer-sized grains that populate the ISM are key questions that are not yet well understood. These questions are at the heart of NANOCOSMOS, the ERC Synergy project within which this thesis has been completed, that aims to better understand the physical and chemical processes that govern the formation and evolution of cosmic dust, both, observationally and experimentally.

The work presented in this thesis is based on obtaining and analyzing millimeter observations in order to study the molecular gas in the CSEs of AGB stars which is fundamental to understanding dust formation. The aim of the observations is to look for emission of possible candidates that could act as gas-phase precursors of dust around AGB stars and to investigate the importance of their role in the formation of dust. For this reason, we performed sensitive observations in the λ 2 mm band using the IRAM 30m telescope towards a large sample of AGB stars. The sample contained both, carbon- and oxygen-rich CSEs, and covered a wide range of mass-loss rates and circumstellar properties. We looked for emission of SiC_2, SiO, SiS, and CS in 25 carbon-rich CSEs, and SiO, SiS, CS, SO and SO_2 in 30 oxygen-rich CSEs. We modeled the observed lines by performing non-LTE excitation and radiative transfer calculations based on the large velocity gradient (LVG) method to derive the fractional abundance of these molecules in the objects.

For the carbon-rich CSEs, we find a clear trend where the denser the envelope, the less abundant SiC_2, SiO, and CS are. The trend is however only tentatively seen for SiS. The observed trend is interpreted as an evidence of efficient incorporation of these molecules onto dust grains suggesting that they contribute to the formation of dust around C-rich AGB stars. For the oxygen-rich CSEs, the abundance of SiO also decreases the denser the envelope is and a similar trend, albeit less clear than for SiO, is also observed for SO, indicating that SiO and possibly SO act as gas-phase precursors of dust in circumstellar envelopes around O-rich AGB stars. Comparing the fractional abundance of the molecules in both chemical types of stars, we find that CS and SiS show a marked differentiation between C-rich and O-rich sources, while the fractional abundance of SiO seems to be insensitive to the C/O ratio. Furthermore, we discuss the derived abundaces in detail and compare them to previous observational and theoretical studies.

For some circumstellar envelopes, molecular abundances are reported for the first time in this work. Moreover, the samples of C-rich and O-rich envelopes are some of the largest thusfar to have been studied consistently for several molecules.

Resumen

Estudio Observacional de Moléculas Precursoras de Polvo en Envolturas Circunestelares

de Sarah MASSALKHI

La fase de gigante roja conocida como AGB (*Asymptotic Giant Branch*) es una etapa tardía en la evolución de las estrellas de masa pequeña a intermedia. Hacia el final de esta fase, las estrellas pierden una importante cantidad de materia a través de vientos estelares densos y lentos que dan lugar a una envoltura circunestelar extendida que rodea a la estrella central. Estas envolturas son entornos astrofísicos notables porque las condiciones físicas y químicas en toda la envoltura cambian rápidamente para permitir la formación de varios tipos de moléculas y granos de polvo, como lo demuestran las observaciones infrarrojas, milimétricas y submilimétricas. Este material es finalmente arrastrado por el viento estelar constituyendo la principal fuente de enriquecimiento del medio interestelar y proporcionando los principales bloques de construcción de una nueva generación de estrellas y planetas.

Uno de los principales ingredientes de este material expulsado por estrellas moribundas es el polvo. Sin embargo, las preguntas sobre sus procesos de formación siguen siendo un misterio. Cuáles son los principales precursores gaseosos que darán lugar a los primeros núcleos de condensación y cómo estas partículas evolucionan hacia los granos de tamaño micrométrico que pueblan el medio interestelar son preguntas clave que aún no se comprenden bien. Estas preguntas están en el corazón de NANOCOSMOS, el proyecto ERC Synergy dentro del cual se ha completado esta tesis, que tiene como objetivo comprender mejor los procesos físicos y químicos que gobiernan la formación y evolución del polvo cósmico, utilizando tanto observaciones astronómicas como experimentos de laboratorio.

El trabajo que se presenta en esta tesis se basa en la obtención y análisis de observaciones en el rango de longitudes de onda milimétricas de amplias muestras de estrellas AGB, con el fin de estudiar el gas molecular en sus envolturas y arrojar luz sobre algunos aspectos de la formación de polvo. El objetivo de las observaciones es buscar la emisión de posibles candidatos que podrían actuar como precursores del polvo en fase gaseosa alrededor de las estrellas AGB e investigar la importancia de su papel en la formación de polvo. Por esta razón, realizamos observaciones sensibles en la banda λ 2 mm gran de una amplia muestra de estrellas AGB utilizando el telescopio de 30m de diámetro de IRAM. La muestra contiene envolturas ricas en carbono (C/O $>$ 1) y ricas en oxígeno (C/O $<$ 1), y cubre una amplio

rango de tasas de pérdida de masa y propiedades circunestelares. Buscamos la emisión de las moléculas SiC_2, SiO, SiS, y CS en 25 envolturas ricas en carbono, y de SiO, SiS, CS, SO, y SO_2 en 30 envolturas ricas en oxígeno. Modelamos las líneas observadas realizando cálculos de excitación fuera del equilibrio termodinámico y de transporte de radiación utitlizando el método de gran gradiente de velocidad, más comunmente conocido como LVG (*Large Velocity Gradient*) por sus iniciales en inglés para determinar las abundancias de estas moléculas en los objetos observados.

En el caso de las envolturas ricas en carbono, hemos encontrado una clara correlación que muestra que la abundancia de SiC_2, SiO, y CS disminuye conforme aumenta la densidad de la envoltura. En el caso de SiS, la correlación se aprecia sólo de forma tentativa. Interpretamos la tendencia observada como una indicación de que estas moléculas se incorporan de forma eficaz a los granos de polvo, lo que sugiere que estas especies gaseosas contribuyen a la formación de polvo en envolturas ricas en carbono. En el caso de envolturas ricas en oxígeno, la abundancia de SiO también muestra una disminución conforme aumenta la densidad de la envoltura, mientras que para SO la tendencia se observa, aunque de forma menos clara que para SiO. Esto indica que SiO y posiblemente SO actúan como precursores gaseosos de polvo en envolturas ricas en oxígeno. Al comparar las abundancias moleculares determinadas en los distintos tipos de envolturas, encontramos que la abundancia de CS y SiS muestra una clara diferencición entre envolturas ricas en carbono y ricas en oxígeno, mientras que la abundancia de SiO no parece depender de la relaci'on C/O. Las abundancias determinadas son puestas en contexto mediante la comparación con trabajos previos y con estudios teóricos.

Para algunas de las envolturas circunestelares estudiadas, hemos determinado por primera vez abundancias moleculares. Además, las muestras de envolturas estudiadas en este trabajo están entre las más grandes que se han estudiado hasta la fecha de forma sistemática y coherente para varias moléculas.

Acknowledgements

"*It would not be much of a universe if it wasn't home to the people you love.*", Stephen Hawking.

No man is an island, and no thesis is a solo accomplishment. Over the span of my PhD, I have been surrounded by a cluster of colleagues, friends and family members who have supported me in numerous ways. Any success I have had throughout this journey has been greatly due to my good fortune in meeting you all.

I dedicate this milestone to my family. To my mom and dad, the endless fountain of love and support, you have accompanied me through thick and thin and have been a constant encouragement in my undertakings. Thank you for instilling in me the courage to live a fulfilling life, and the drive to always seek more. To my brother, one of my very best friends, thank you for your unconditional and never-ending support through all walks of life. And to my loving and caring sister, I am thankful for you.

I extend my deepest gratitude to my supervisor, Dr. Marcelino Agúndez. You have taken the tremendous responsibility of starting me down the path of research in astronomy, devoting countless of hours as a mentor to help me acquire the knowledge, grit and resilience to become a young researcher. My work and accomplishments would not have been possible without your guidance, support, motivation and unwavering patience and kindness. Your contribution is immensely treasured and I consider myself to have been extraordinarily lucky.

I am grateful to my supervisor, Prof. Jóse Cernicharo for giving me the opportunity to be a part of his group at NANOCOSMOS. Thank you for supporting my travels to participate in conferences and summerschools to expand my knowledge and share my research. It has been a pleasure working for someone who has an inspiring knowledge and passion for many subjects and who pushes research ideas into bold directions.

Javier Goicoechea, a colleague and a dear friend, though you have a questionable taste in football teams, I must say, I owe you heaps of appreciation. There's a lot that I'm inspired by, from your enthusiasm when discussing research ideas to your ability not to take life too seriously. I have learned a great deal from you. Thank you for the crazy laughs, the thought-provoking conversations, the valuable advice, and the continous support during my uncertain times.

Many thanks to my colleagues at the Molecular Astrophysics group: Pablo Fonfría, Guillermo Quintana-Lacaci, Luis Vellila-Prieto, Natalia Ruiz Zelmanovich, Nuria Mareclino, Juan Ramón Pardo, Miriam Garcia and Sara Cuadrado. You have all contributed to

my success in different and unique ways. An additional thanks to Marcelo Castellanos for your timely help and support.

My thesis work would not exist without the great team of the IRAM institute, for building, maintaining, and constantly improving the superb 30 m radiotelescope. Thank you to the operators and astronomers on duty whom I have learned so much from, and to the staff members who always ensured I had a pleasant stay at Pico Veleta. I also acknowledge the OAN administration for giving me access to carry out observations remotely from the Royal Observatory of Madrid at the beautiful Retiro park.

Emeric Bron and Jason Champion, my cheese bringers right from the land of cheese, aka France, and my ultimate mountain buddies. We started hiking as officemates, and ended as friends. At times, it was physically tiring, painful and draining. At other times, it was mentally challenging; I, the less confident wanted to keep up with you, the more experienced. But you held my hand, and we pushed on, always emerging on the other side having seen the starriest skies, and the most gorgeous sunrises and sunsets. You have given me the best metaphor: hard work pays off. Thank you for the memorable experiences. My PhD would have been less fun without you.

Madi Subaiti, you have played many roles in my life over the past 4 years: a gym buddy, a fellow volunteer, but mostly importantly a true friend. I cherish our shared bond over experiencing life together in Spain. Thank you for the fun times − gathering our social group for dinner or a game board night on a weekend has been particularly refreshing after an exhausting work week.

Sarah Tannir, you deserve a special mention. Thank you for the homely feeling you have given me for the past many years I've been away from home. You are always there when I need it and when things get a bit discouraging.

To my friends and family in Lebanon, Denmark, and Spain, thank you.

Last but not least, there are scientists whose research over the past decades has given rise to the material out of which this thesis was written. Some of them are mentioned specifically, but many of them appear in the chapters through their discoveries and ideas, rather than their names. I thank them all.

Contents

List of Figures

List of Tables

List of Abbreviations

A/D	**A**nalog-to-**D**igital
AFGL	**A**ir **F**orce **G**eophysics **L**aboratory
AGB	**A**symptotic **G**iant **B**ranch
ALMA	**A**tacama **L**arge **M**illimeter **A**rray
CSE	**C**ircum**S**tellar **E**nvelope
CNRS	**C**entre **N**ational de la **R**echerche **S**cientifique
CMB	**C**osmic **M**irowave **B**ackground
DC	**D**irect-**C**oupled
E-AGB	**E**arly **A**symptotic **G**iant **B**ranch
EM	**E**lectro**M**agnetic
EMIR	**E**ight **MI**xer **R**eceiver
ERC	**E**uropean **R**esearch **C**ouncil
FWHM	**F**ull **W**idth at **H**alf **M**aximum
HB	**H**orizontal **B**ranch
HBB	**H**ot **B**ottom **B**urning
HIFI	**H**eterodyne **I**nstrument for the **F**ar-**I**nfrared
HR	**H**ertzsprung-**R**ussell
IF	**I**ntermediate **F**requency
IGN	**I**nstituto **G**eográfico **N**acional
IR	**I**nfra**R**ed
IRAM	**I**nstitute **R**adio **A**stronomie **M**illimétrique
IRC	**I**nfra**R**ed **C**atalog
ISM	**I**nter**S**tellar **M**edium
ISO	**I**nfrared **S**pace **O**bservatory
ISRF	**I**nter**S**tellar **R**adiation **F**ield
IRAS	**I**nfrared **A**stronomical **S**atellite
LTE	**L**ocal **T**hermodynamic **E**quilibrium
LO	**L**ocal **O**scillator

LPV	**L**ong-**P**eriod **V**ariable
LSR	**L**ocal **S**tandard of **R**est
LVG	**L**arge **V**elocity **G**radient
NOEMA	**NO**rthern **E**xtended **M**illimeter **A**rray
MASER	**M**icrowave **A**mplification by **S**timulated **E**mission of **R**adiation
MPG	**M**ax-**P**lanck-**G**esellschaft
OAN	**O**bservatorio **A**stronomico **N**acional
PN	**P**lanetary **N**ebulae
PSF	**P**oint **S**pread **F**unction
pwv	**P**recipitable **W**ater **V**apor
RF	**R**adio **F**requency
RGB	**R**ed **G**iant **B**ranch
rms	**R**oot **M**ean **S**quare
SED	**S**pectral **E**nergy **D**istribution
SOFIA	**S**tratospheric **O**bservatory **F**or **I**nfrared **A**stronomy
TE	**T**hermodynamical **E**quilibrium
TP-AGB	**T**hermally **P**ulsing **A**symptotic **G**iant **B**ranch
UV	**U**ltra**V**iolet
WD	**W**hite **D**warf

To my family

Outline

The thesis constitutes of three main parts. Here, the basic structure is laid out.

In Part I, we give a brief overview that provides the reader with the necessary background information relevant for this thesis. Chapter 1 briefly summarizes the stellar evolution of low-to-intermediate mass stars, Chapter 2 introduces the main aspects of AGB stars and their circumstellar envelopes, Chapter 3 presents fundamental concepts about single-dish radiotelescopes and Chapter 4 some relevant aspects relating to molecules. In Chapter 5, we describe the radiative transfer and the excitation of molecules and shed lights on the photon escape formalism and the Large Velocity Gradient approximation. By this, we introduce and contextualize the research carried out in this thesis.

Part II includes the bulk of the work carried out in this thesis that is based on three publications. We start off in Chapter 6 with a global introduction that presents the main subject, motivation and goal of this thesis. In Chapter 7, we present a study of the abundance of SiC_2 in C-rich AGB envelopes while in Chapter 8, we investigate the abundance of SiO, SiS, CS in C-rich AGB envelopes as well. In Chapter 9, we present a study of the abundance of SiO, CS, SiS, SO and SO_2 in O-rich envelopes. A copy of the publications are found in the Appendix. In each of Chapter 7, Chapter 8, and Chapter 9, we briefly introduce the relative topic, present the observations and the observational results, describe the analysis of the excitation and radiative transfer and the modeling results, and finally discuss the main results of each study and present our conclusions. In Chapter 10, we present a general summary, the main conclusions reached within this thesis, and highlight future prospects that complement and build on the findings in this thesis.

In Part III, we present the appendices that contain copies of the published articles.

Part I

Introduction

Chapter 1

Stellar Evolution

This Chapter is based on reviews by Chiosi et al., (1992), Habing et al., (2004), Herwig, (2005), and Karakas et al., (2014).

The exact evolution of stars is dependant on the stellar mass. Therefore, it is convenient to define mass ranges according to the evolutionary behaviour the stars will experience. According to Iben et al., (1983), the stars are classified as low-mass ($M < M_{HeF}$), intermediate-mass ($M_{HeF} < M < M_{w}$) and high-mass ($M > M_{w}$) stars, where M_{HeF} = 1.8 - 2.2 $M_{\odot}$ represents the maximum initial mass of the star experiencing helium flash (HeF) in the core, and M_{w} = 7 - 9 $M_{\odot}$ represents the maximum initial mass for which the final product of evolution is a white dwarf with a C-O core.

1.1 Evolution towards the AGB

All stars begin their nuclear-burning life on the *main sequence* (Fig. 1.1), where fusion converts H to He in the stellar core. The main sequence is the longest part of the life of a star and most stars are observed during this evolutionary phase, hence it is the most populated region of the HR diagram (Fig. 1.2). A main sequence star can be described as in a state of hydrostatic equilibrium, where the gravitational force (which causes the matter to collapse towards the center of the star) is balanced by the radiation pressure force (which pushes the matter outward). For stars with initial mass ≤ 1 $M_{\odot}$, the fusion of H to He in the core is powered through the proton-proton (*p*-*p*) chain reactions:

$$4\ {}^{1}\mathrm{H} \rightarrow 4\ \mathrm{He} + 2\nu_{e} + \gamma$$

More massive main sequence stars with > 1 $M_{\odot}$ burn hydrogen through catalytic nuclear reactions in the core in what is known as the *CNO chain* cycle which uses as catalysts carbon, nitrogen, and oxygen, all of which can undergo alpha capture to produce other elements.

The most notable by-products are ^{12}C and ^{14}N. The CNO-cycle has a strong dependance on the temperature, and so this type of fusion occurs only in regions with suitable conditions.

Eventually, a star will reach a point where all the hydrogen in the core is exhausted which marks the end of the main sequence phase of the stellar evolution. The star will then settle in a state where hydrogen is burning in a shell surrounding a helium core. When fusion ceases in the core and nuclear energy is no longer released, the hydrostatic equilibrium is disrupted where the force of gravity can no longer resist the force of radiation pressure, and the core starts to contract and heat up. The hydrogen fusion then shifts to a shell just outside the contracting core and there is no active nuclear burning in the core anymore, which is mainly made of the ashes of the former fusion cycle, namely helium. The hydrogen shell burning adds helium to the underlying core and increases the helium core mass gradually on a nuclear timescale. As a result, the core contracts and heats, which implies that the overlying layers have to decrease in pressure and density to counteract the core compression which is only achieved by expanding outwards. Consequently, the surface temperature of the stars becomes cooler, therefore appears redder, and it becomes larger, therefore is more luminous than on the main sequence. The star is then a *red giant* (Fig. 1.1) and climbs up the red giant branch (RGB) in the HR diagram (Fig. 1.2).

At this point, the hydrogen envelope is deep and highly convective which leads to mixing of the outer envelope with inner regions that are enriched by previous nuclear reactions. Hence, the products of H-burning, of the p-p chain and the CNO cycle, are brought up to the stellar surface, where a change in elementary composition becomes observable. This is known as the *first dredge-up* which particularly increases the helium (^{4}He) and nitrogen (^{14}N) abundance at the stellar surface. At this stage, the star is very big (up to $\sim$100 times its radius on the main sequence) but most of the mass in the core is within a small fraction of the total radius. As a consequence, the outer layers are loosely bound to the star and can be lost through an outflow of the stellar wind. The ejected mass forms a circumstellar envelope around the star that is tenuously held. Simultaneously, the temperature of the He core continues to increase to reach a point where the *triple-α* process begins to take place:

$$\begin{aligned} \mathrm{He} + {}^4\mathrm{He} &\rightarrow {}^8\mathrm{Be} + \gamma, \\ {}^8\mathrm{Be} + {}^4\mathrm{He} &\rightarrow {}^{12}\mathrm{C} + \gamma \end{aligned}$$

The main product from the triple-α process is ^{12}C. This reaction could also be expressed as ^{4}He(α,γ)^{8}Be(α,γ)^{12}C. Furthermore, an α-capture can form oxygen via ^{12}C(α,γ)^{16}O. When the helium core burning is not efficient anymore to counteract gravity, the core which now consists mainly of C and O, contracts and its density eventually becomes so high that the

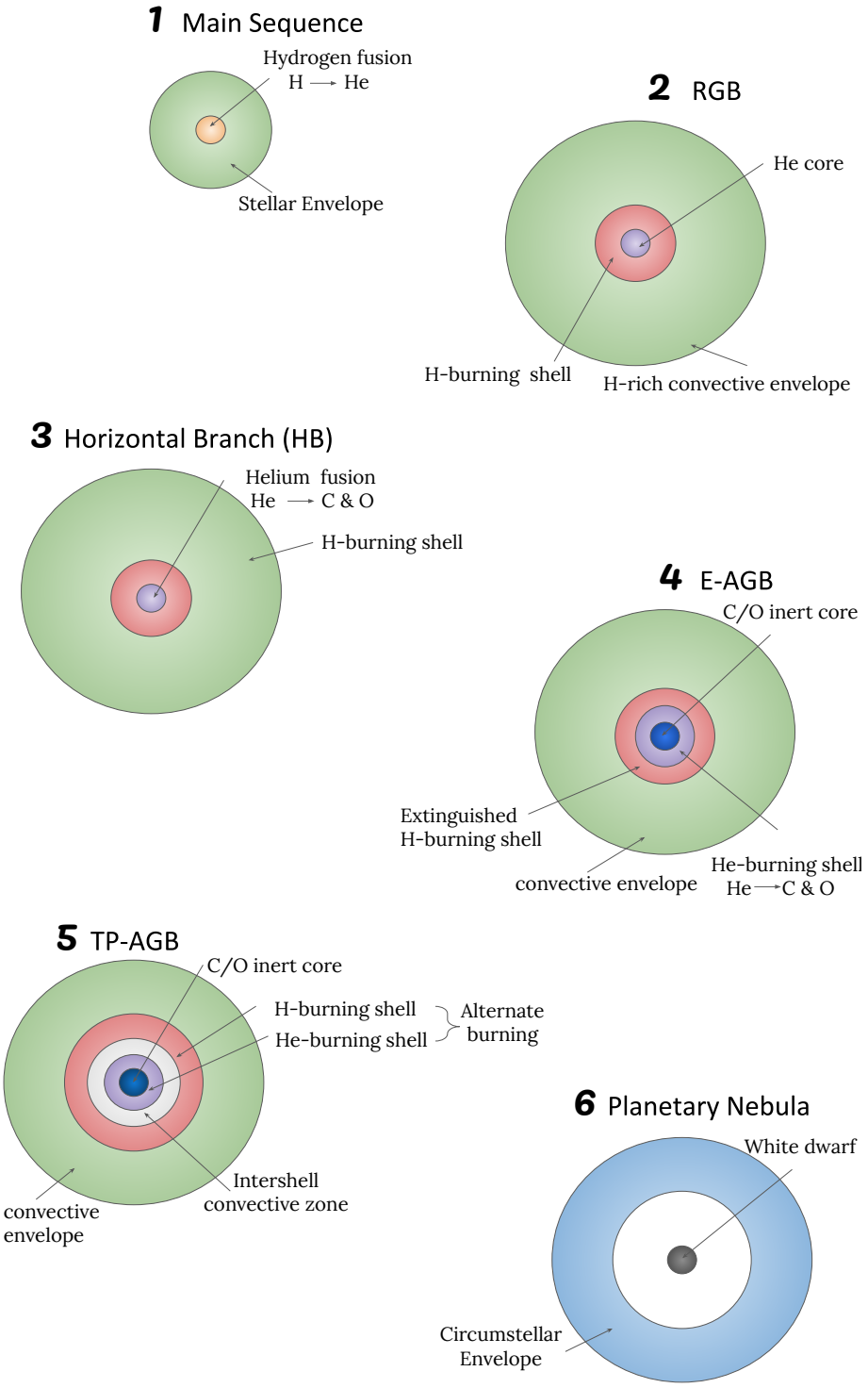

Figure 1.1: Structure of a star through the different phases of its evolution: 1) main sequence, 2) redgiant branch, 3) horizontal branch, 4) early aymptotic giant branch, 5) thermal pulse asymptotic giant branch, 6) planetary nebula.

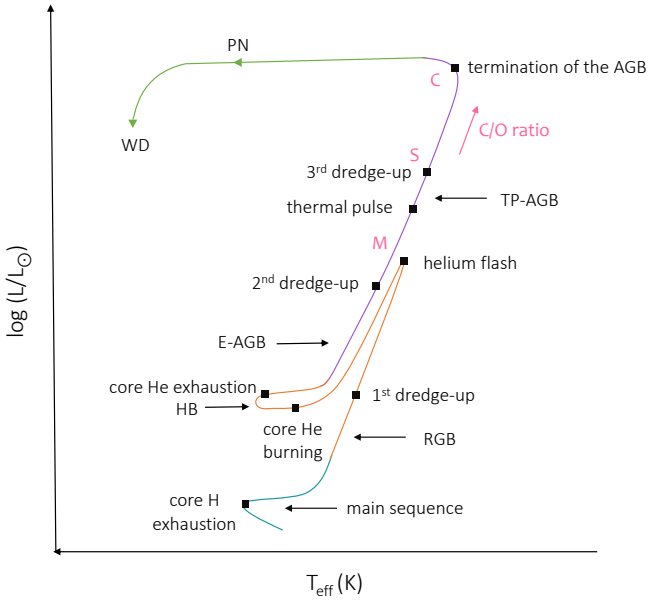

Figure 1.2: The evolution of the star in the HR diagram from the main sequence to the termination of the AGB. The main phases mentioned in the text are highlighted.

material will be *degenerate*, the conversion of helium to carbon and oxygen then occurs very quickly, or in an explosive manner. This sudden release of energy is called *helium flash*. This is the case for low-mass stars that ultimately develop a degenerate He-core. Intermediate-mass stars do not experience helium flash, but ignite He steadily in a non-violent manner and develop a non-degenerate He-core. For the low- and intermediate mass stars, the energy released is absorbed by the outer layers of the star, and the star settles into a new state, where helium is burning to carbon and oxygen. This is known as the Horizontal Branch (HB) (Fig. 1.2). Ultimately, all the helium in the core is converted into carbon and oxygen. This will leave behind an inert C-O core surrounded by a He-burning shell (which lies immediately above the C-O core) and a convective H-burning outer shell. On the HR diagram, low- and intermediate mass stars will now lie on what is known as the *asymptotic giant branch* (AGB) (Fig. 1.2).

1.2 The AGB Phase

The AGB star consists of a degenerate C-O core, surrounded by a He- and a H-shell, and a deep convective envelope (Fig. 1.1). AGB stars have effective temperatures $T_{\rm eff}$ between

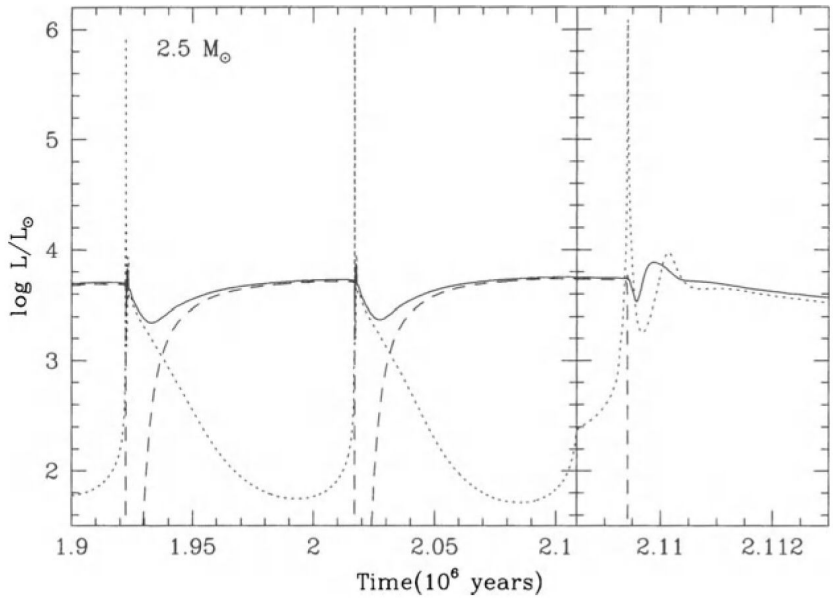

Figure 1.3: Luminosity variation during a thermal pulse: total luminosity (solid line), H-burning luminosity (dashed line), and He-burning luminosity (dotted line) from Habing et al., (2004).

2000 and 3500 K, their absolute bolometric magnitudes are confined to the range $-3.6 \lesssim M_{bol} \lesssim -7.1$ which corresponds to luminosities $2200 \lesssim L/L_{\odot} \lesssim 55\ 000$, and they have stellar radii $R_{\star}$ up to several 100 $R_{\odot}$. The asymptotic giant branch can be divided into two phases: the *early asymptotic giant branch* (E-AGB) phase where the star has not yet begun to pulsate, and the *thermally-pulsing asymptotic giant branch* (TP-AGB) phase where the star is pulsating. The AGB phase has total lifetime of the order of 10^6 years (depending on the initial mass and metallicity of the star, e.g. Vassiliadis et al. 1993).

During the E-AGB, the stellar envelope expands significantly and cools. The cooling in the outer layers causes the H-burning shell to be extinguished so that the underlying He-shell becomes the only source of stellar energy. In the HR diagram, the star will move towards lower effective temperature and higher luminosity (Fig. 1.2).

As a consequence to the extinguished H-burning shell, there is no radiative layer around the H-shell, the external convection can penetrate deeper into regions enriched by products of the CNO cycle and brings up freshly processed ^{4}He and ^{14}N for stars with $\gtrsim 4\ M_{\odot}$ (for solar composition) and the stars experience a *second dredge-up*. In contrast to the first dredge-up, the second dredge-up goes deeper because there is no thin radiative layer around the H-rich shell. Below this critical mass, i.e., $\sim 4\ M_{\odot}$, convection is not able to penetrate

below the H-shell, and second dredge-up does not occur. Eventually, the expansion of the envelop ceases due to its own cooling and the envelope retracts and the luminosity decreases. The matter that has been propelled outwards falls back inwards towards the base of the hydrogen envelope and heats which causes the H-burning shell to ignite again.

However, the configuration with two burning shells is unstable. For a small fraction of the time, the He-shell becomes subject to thermal instabilities and suffers fierce thermonuclear runaway process (Schwarzschild et al., 1965) causing the star to be severely out of thermal equilibrium. The nuclear burning in the shells will therefore not continue steadily, instead there will be an interplay between the He- and H-shell in the AGB star in which they alternate burning. This terminates the E-AGB phase and marks the beginning of the TP-AGB phase. The star will begin to pulsate which initiates a sudden release of energy causing the He-shell luminosity to reach up to 10^8 $L_\odot$ for a brief time (of the order of a year). The increase in luminosity is referred to as the *thermal pulse*. The change in surface luminosity over time due to several thermal pulses is shown in Fig 1.3. The surface luminosity depends essentially on the stellar core expressed by Paczyński, (1971) through the luminosity-mass core relation: $L = 5.2 \times 10^4 (M_{core} - 0.5)$, in other words, the luminosity increases linearly with the mass of the core.

The release of energy results in a convective intershell zone which extends from the He-shell up to almost the H-shell (Fig. 1.4). This mixes products, mainly carbon, of the underlying He-shell throughout the intershell convective zone. As the thermal pulse fades out, convection in the intershell pulls back in what is referred to as the power down phase. During the power down phase, the energy deposited in the intermediate shell goes into the expansion and the cooling of the layers, essentially extinguishing the H-burning shell. The outer convective envelope retracts and reaches to the now carbon-rich region in the intermediate shell and mixes carbon to the surface. This is called the *third dredge-up* during which the material processed, mainly carbon, is brought to the outer convective envelope and exposed to the surface. From the structural point of view, the third dredge-up is very similar to the second dredge-up; however, its occurrence is much faster and is expected to be more frequent (Busso et al., 1999). Following the third dredge up, the star contracts, so the material propelled outwards falls back reigniting the H-shell and goes into a phase of extended quiescent H-burning, known as the *interpulse* phase. This is the longest phase of the pulse cycle during which the star is powered by the H-shell that essentially provides all of its luminosity. Eventually, there will be another thermal pulse, and the cycle repeats. The timescale between pulses depends on the initial stellar mass; it is $\sim 10^4$ yrs for 4 $M_\odot$ stars and $\sim 10^6$ yrs for 1 $M_\odot$ stars (Wagenhuber et al., 1998).

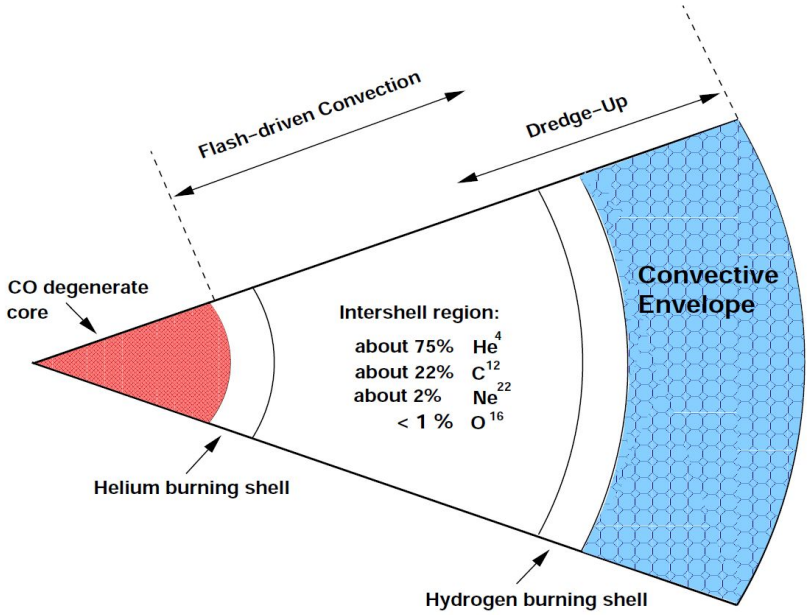

Figure 1.4: Schematic structure of an AGB star, showing the degenerate CO core surrounded by a He-burning shell above the core and a H-burning shell below the deep convective envelope from Karakas et al., (2002).

The TP-AGB phase will not only result in important changes in the structure of a star, but also in its chemistry. One of the transformations that occur to ^{12}C happens during the interpulse phase, when protons are captured by ^{12}C which in turn β-decays to ^{13}C, via ^{12}C(p,γ)^{13}N(β + ν)^{13}C, called the ^{13}C-pocket. ^{13}C reacts with the abundant α-particles which produces many neutrons via : ^{13}C(α,n)^{16}O and ^{22}Ne(α,n)^{25}Mg. The neutron density is $\sim 10^8$ cm^{-3} in the intershell-region. This neutron flux is in fact involved in one of the most important nucleosynthesis processes occuring in AGB stars, the slow neutron capture process, or *s-process*. This process is responsible for generating about 50% elements heavier than Fe (Busso et al., 2004). The nuclei can capture these neutrons to produce successively heavier isotopes. If the newly produced nucleus is not stable, it will $\beta-$decay to form a different stable element with the next higher atomic number. The rate of neutron-captures is much slower than the rate of the $\beta-$decay, hence the name, such that an unstable isotope decays before it captures another neutron. Some of the elements formed in this way are rubidium, strontium, technetium, and lead which are then mixed to the surface via the third dredge-up and can result in stars of C/O $\approx$ 1, barium stars, and technetium-rich stars (Wallerstein et al., 1998). A direct confirmation that the s-process nucleosynthesis occurs in AGB stars and that heavy elements are produced within this evolutionary phase was

provided by the detection of ^{99}Tc (the isotope of the element Tc) on the surface of AGB stars (Merrill, 1952). This is because the half-life of ^{99}Tc is of the order of $\sim 2 \times 10^5$ yrs, comparable to the lifetime of the TP-AGB phase of 1×10^6 yrs for a low mass star (e.g., Smith et al. 1988). Some of the heavy elements produced through the s-process are ^{16}O, ^{19}F, ^{22}Ne, ^{23}Na, ^{25}Mg, ^{26}Mg, ^{26}Al, and ^{27}Al and mixed to the surface. It is therefore during the TP-AGB stage that AGB stars produce a large fraction of the elements we find in the universe.

Yet perhaps the most obvious consequence of the pulses and dredge-up events, is the increase in the C content at the stellar surface which ultimately determines the spectral type of the star. Stars begin their lives with an atmosphere that is oxygen-rich, in the sense that the ratio of the abundance of carbon to oxygen C/O is less than unity. This is the default chemistry of an AGB star since oxygen is more abundant in the ISM than carbon is. The occurrence and repetition of the third dredge-up process mixes additional newly produced carbon to the surface and alters the ratio to become C/O > 1 hence becoming a carbon star, or carbon-rich (Fig. 2.1). This has important consequences on the appearance of the stars because the more abundant species will determine which molecules and dust, oxygen- or carbon-bearing, will later on form. Detailed models show that the likelihood of an AGB star becoming a carbon-rich star, instead of remaining an oxygen-rich star is in fact strongly dependent on stellar mass. It is believed that stars with $\lesssim 1.5$ M$_\odot$ remain oxygen-rich stars because they do not undergo a third dredge up nor hot bottom burning (HBB, see below). Stars with $\sim 1.5 - 4$ M$_\odot$ will transition into carbon-rich stars due to the third dredge up, while the highest mass AGB stars, i.e., > 5 M$_\odot$ do not end their lives as carbon stars due to HBB (Karakas et al. 2014, and references therein).

Another mechanism that is just as important for the chemistry of an AGB star and that can cause a drastic change in the chemical composition at the stellar surface is a process called *hot bottom burning* (HBB). For stars with initial mass $\gtrsim 4 - 5$ M$_\odot$, the radiative layer between the H-shell and the convective envelope is absent so that the bottom of the convective envelope is situated near the top of the H-burning shell. The temperature at the base of the convective envelope is high enough (exceeds 5×10^7 K) that in addition to the CNO cycle, the Ne-Na and the Mg-Al chains are activated as well. The effect is to convert carbon and oxygen to nitrogen, neon to sodium, and magnesium to aluminium which are directly mixed to the surface via convection. This prevents the formation of carbon-rich atmospheres by turning the stars into efficient producers of nitrogen and other elements, unless the third dredge-up continues after HBB ceases (Fishlock et al. 2014; Herwig 2004; Lugaro et al. 2012).

What determines how much enriched material reaches the surface depends on the efficiency of the third dredge-up, λ, as:

$$\lambda = \frac{\Delta M_{dredge}}{\Delta M_{core}} \tag{1.1}$$

where ΔM_{dredge} is the mass dredged up after a thermal pulse, and ΔM_{core} is the amount of growth by which the core increased over the preceeding interpulse phase. λ increases with increasing stellar mass and with decreasing metallicity, yet how exactly is still unclear (Lattanzio, 1989).

At the same time of the thermal pulses, the envelope mass is being reduced by mass loss. The exact mechanisms and the details of mass loss on the AGB are not fully known, but the three processes of pulsations, third dredge-up, and mass loss all influence each other. Various observational methods indicate that AGB stars can experience mass loss rates in the range of $10^{-9} - 10^{-5}$ $M_\odot$ yr^{-1}, but values as high as 10^{-4} $M_\odot$ yr^{-1} have been found for more extreme objects that develop the so-called *superwind* phase in the upper part of the AGB due to continously increasing mass loss, such as luminous long-period variables including OH/IR stars and Miras (Iben et al., 1983). Once an AGB star enters this superwind phase, the mass loss experienced in this phase reduces the envelope mass dramatically.

1.3 Termination of the AGB

When the mass of the envelope becomes very small, $\sim 10^{-2} - 10^{-3}$ $M_\odot$, as a consequence of nuclear burning and mass loss during the AGB phase, the star can no longer maintain its large size and begins to shrink. This terminates the AGB phase. The H-shell surrounding the C-O core is essentially still active and dominates the luminosity. The stellar radius decreases and the star now evolves at almost constant luminosity to higher temperatures (Fig. 1.2). At temperatures of $\sim$ 30,000 K and higher, the released energetic radiation can ionize and dissociate the circumstellar material that was previously shed from the star and create a planetary nebula (PN) that often have complex shapes, morphologies and compositions (Balick, 2015). The transition time from the AGB phase to the PN phase can take between $10^2 - 10^4$ years. When the envelope mass is further reduced and becomes very thin (10^{-5} $M_\odot$), the H-shell is finally extinguished and nuclear burning stops. The luminosity decreases abruptly, leaving behind a cool C-O remnant of the former AGB star, known as a *white dwarf* (WD).

Chapter 2

AGB Stars and Their Circumstellar Envelopes

This Chapter is based off of the review book Asymptotic Giant Branch Stars by Habing et al., (2004).

Here, we briefly describe some of the observational characteristics of AGB stars that are linked to their evolution and internal properties. We then describe the physical and chemical properties of circumstellar envelopes and the tools to study them.

2.1 Observational Character of an AGB star

2.1.1 Spectral Classification

As mentioned in the previous chapter, nuclear burning and dredge-up of processed material during the TP-AGB influence the C/O ratio at the surface of the star. The ratio gradually changes from an initial C/O < 1 to above unity at which point the star becomes a carbon star. This is easily distinguished from the stellar spectra that reflect the chemical composition of the star. The C/O ratio has a profound impact on the chemistry of the outer layer of the star as it determines the nature of the condensation products which are crucial to dust formation.

At high densities and temperatures at the stellar photosphere, thermodynamic equilibrium (TE) is ensured which implies that molecules with high dissociation energy, i.e., strong bond, are preferentially formed. Carbon monoxide CO has a very large binding energy, which means that all the available C and O will be consumed by the formation of the CO molecule. It follows as shown in Fig. 2.1:

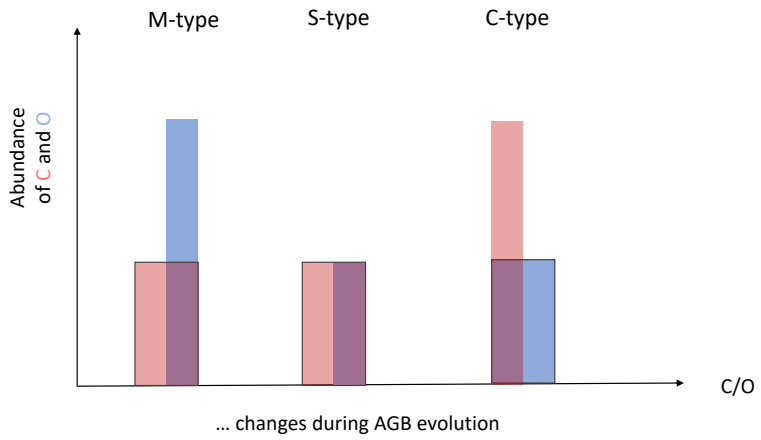

Figure 2.1: Schematic picture of the atmospheric chemistry in AGB stars: the relative abundances of C and O lead to three different cases. The high bond energy of CO ensures that all the available C and O will combine to form CO (shaded area), the excess O (M-type) or C (C-type) is available for other molecules and dust grains.

– M-type : C/O < 1, all carbon is bound in CO. The leftover oxygen is available for the formation of oxygen-bearing molecules and dust. The optical spectra of M-type stars shows the presence of TiO molecular bands (e.g., Joyce et al. 1998). Their CSEs are dominated by an O-rich chemistry (e.g., Velilla Prieto et al. 2017).

– C-type : C/O > 1, all oxygen is bound in CO, the leftover carbon is available for the formation of other carbon-bearing molecules and dust. The optical spectra of C-type stars shows strong bands of C_2, CN, and SiC_2 (e.g., Bakker et al. 1997; Sarre et al. 2000). Their CSEs are dominated by a C-rich chemistry (e.g., Cernicharo et al. 2000).

– S-type : C/O ≈ 1, nearly all carbon and oxygen atoms are bound in CO. These stars are believed to represent a brief transitional phase between M- and C-type. The non-availability of sufficient quantities of either C or O leads to vastly different condensates. The optical spectra of S-type stars shows absorption bands of ZrO and LaO (e.g., Keenan 1954). Their CSEs show features of both O-rich and C-rich chemistry (e.g., Smolders et al. 2012).

2.1.2 Pulsation and Variability

Observations show that AGB stars are variable, that is, they experience periodic changes in their luminosity, a sinusoidal light curve with typical periods of $\sim$ 100–1000 days. As such, they belong to the long-period variables (LPVs) class of pulsating stars. The pulsations are first observed with small amplitudes, short periods, and low luminosities, then the pulsations grow to bigger amplitudes, longer periods and higher luminosities. According to the characterisitics of the variability, that is, the periodicity and amplitude of the light variation, AGB stars can be divided into three main classes:

(1) *Regulars (M):* also called Mira variables (or simply "Miras"). They have regular variations and are charactarized by large amplitude $>$ 2.5 mag in the V-band.

(2) *Semiregular (SR):* are further distinguished into two subclasses, *SRa* are of regular variability with smaller amplitude than the Miras $<$ 2.5 mag in the V-band and *SRb* are charactarized by poor regularity with $<$ 2.5 mag in the V-band.

(3) *Irregular (L):* show irregular variations of low amplitude.

The exact cause behind this variability is unclear. The luminosity variations are thought to be driven by thermal pulses in the interior of the star, however, these occur on much greater timescales ($\sim 10^5$ yrs) than the typical periods of the pulsations. Another explanation suggests a link to the rapid structural changes that take place during the stellar evolution that can cause large convective cells on the stellar surface leading to instabilities in the convective envelope (e.g., Freytag et al. 2008; Lebzelter et al. 2000; Wood 2010). Regardless of the exact cause, the pulsations lead to the expansion and contraction of the surface of the star, where longer pulsation periods occur for larger radii leading to an increase in luminosity. Hence, a relation between the pulsation period and the luminosity of the star can be established. This feature of AGB stars has led to the derivation of some of the most useful empirical relations between periods and luminosities (Fig. 2.2), especially for objects in the Small and Large Magellanic Cloud, for which the distances are (relatively) well known (e.g., Gerasimovic 1928; Groenewegen et al. 1996a; Van Leeuwen et al. 1997). These empirical relations can be utilized to predict distance estimates for AGB stars in our own Galaxy where distance determinations are more challenging.

The pulsations trigger propagating shock waves in the thin layers of the stellar photosphere that periodically deposit mechanical energy into the outer regions of the atmosphere which are loosely bound to the star. This leads to a dynamical levitation of the material in the outer atmosphere. With each pulsation cycle, the outward blown material follows a

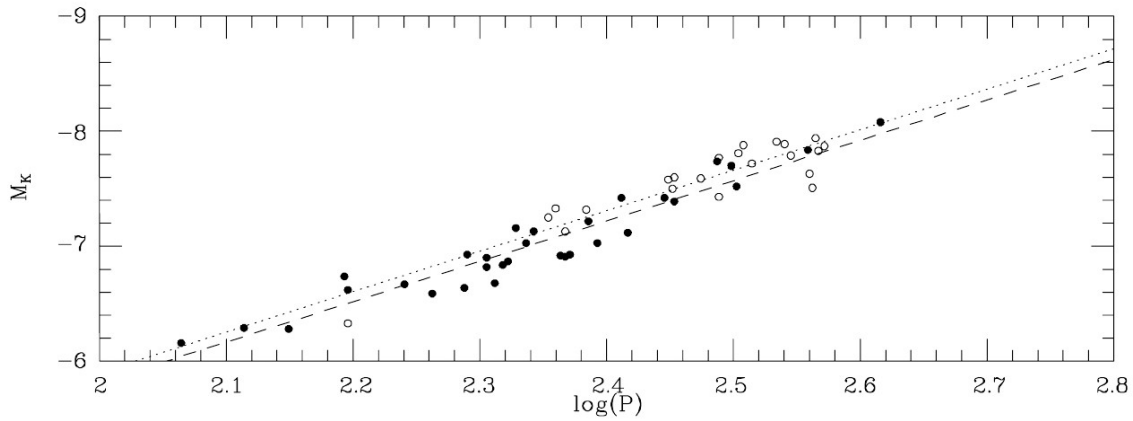

Figure 2.2: Period-luminosity relationship for Mira variables in the LMC. Solid symbols are M-type AGB stars, open symbols are C-type AGB stars. The dashed line is a fit to the M-type stars, while the dotted line is a fit to the C-type stars, from Whitelock et al., (2008).

ballistic trajectory, until it encounters the material expelled in the next shock. The pattern is then repeated. Fig. 2.3 shows the results of a model in which the atmosphere is affected by pulsations. The pulsations cause the material to reach periodically significant heights above the photosphere, however, it then falls back to the original location. As a result, the density is enhanced of several orders of magnitude at certain heights away from the star (a few stellar radii away) where the conditions are favourable to allow for the formation of molecules and dust grains. Observational studies of variability and evidence supporting the shock-induced pulsations are ample, most notably using photometric monitoring and high-resolution spectroscopy of line-profile variations (e.g., Hinkle 1978; Hinkle et al. 1982; Nowotny et al. 2005; Willson 1976). More direct methods like interferometric monitoring have made it possible to reveal temporal changes of the stellar radii due to the pulsations (Burns et al. 1998; Pardo et al. 2018; Woodruff et al. 2008).

2.1.3 Mass Loss

Mass loss from AGB stars is carried out through continous outflow of gas and dust in the form of a, more or less, steady and isotropic *stellar wind*. Several mechanisms responsible for driving the stellar wind have been proposed. These include: i) *pressure-driven winds* where the driving force is attributed to dissipation of energy provided by shock waves, convection zones, and stellar pulsations, ii) *radiation-driven winds* where the acceleration of material is caused by the momentum of absorbed photons by either spectral lines of atoms

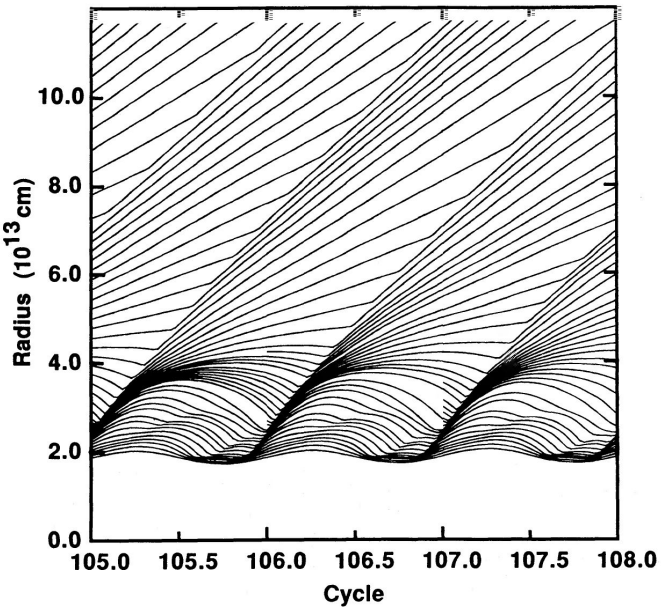

Figure 2.3: Radius as a function of time for a pulsating atmosphere of a variable Mira variable. The figure corresponds to a model in which the atmosphere is affected by pulsation, from Bowen, (1988).

(hot stars), or by molecules and dust particles (cool stars), and iii) *wave-driven winds* e.g., acoustic and/or Alfvén waves. For a detailed description of these mechanisms we refer to the review by Willson, (2000), Höfner et al., (2018) and the comprehensive book by Lamers et al., (1999). A most important class of radiation-driven winds constitutes the *dust-driven wind*. This mechanism is currently the most widely accepted scenario in driving the stellar wind and the corresponding mass loss in AGB stars.

The pulsations of a star play presumably a major key role in driving the extensive mass loss in AGB stars. As mentioned in the previous section, the pulsation-induced shock waves lift the gas above the stellar surface creating dense, cool layers above the stellar surface where the high enough densities and low enough temperatures create favourable conditions for dust formation. Dust is very efficient in absorbing and scattering starlight, much more than molecules and atoms do. Subsequently, newly formed dust grains absorb optical photons from the strong stellar radiation, re-emitting the photons isotropically at IR wavelenghths. When the dust grains absorb photons, they gain both momentum and energy. As a consequence, the dust grains acquire considerable radiation pressure against the gravitational pull of the star and accelerate away. As they move away, the dust grains collide with

the surrounding gas, transferring momentum to the molecules, and dragging them along away from the star. This is often referred to as momentum-coupling to the gas through grain-gas collisions (Gilman, 1972). So, it is the series of events of i) the shock waves due to stellar pulsation and (ii) the radiation pressure on the dust grains that leads to the observed mass loss rates of up to 10^{-4} $M_{\odot}$ yr^{-1}. At high mass loss rates, the central star is completely obscured at optical and near IR-wavelengths as it is enshrouded by the dusty circumstellar envelope.

Estimating mass loss rates is one of the most important tasks in the study of AGB stars, specially pertaining to their evolution. The reason is because the mass loss will eventually go at a rate much faster than that at which matter is added to the core, which is a significant factor in determining the lifetime of the AGB. Determining mass loss rates can be done using several methods. It can based on molecular lines observed at mm/sub-mm wavelengths (e.g., Knapp et al. 1985) which thus far is the most reliable method. For example, using the circumstellar CO rotational line emission. The CO molecule plays a special role for several reasons. Its high abundance in both chemical environments, C-rich and O-rich, makes it useful to determine the mass loss rate estimates in both chemistries. In addition, its high dissociation energy (11.1 eV) allows it to be a tracer of gas density over a wide radial range. For example, the CO ($J = 1 - 0$) emission at 3 mm wavelength traces the outermost coldest molecular gas ($3 - 10$ K), while the higher-excitation transitions ($J > 7 - 6$) trace the dense warm ($500 - 2000$ K) gas close to the star. Moreover, the CO molecule has strong line profiles that give information on the gas expansion velocity, optical depth, and extent of the gas emitting region. A major uncertainty in this method is the distance to the object. Another method pertaining to molecular lines is using the OH maser emission, however an obvious disadvantage to this method is its inability to provide mass loss rates for C-rich CSEs. An alternative method for estimating the mass loss rates is one that is based on dust emission. This method is less useful for several reasons. The properties of the dust grains are poorly known as it is ambiguous to identify the carrier of the dust features. Furthermore, our knowledge of the dust composition, grain size, and shapes is limited which can result in major uncertanities when accounting for the physics/chemistry of the CSE. A safer approach is using the spectral energy distribution (SED) when accompanied with detailed radiative transfer modeling that can take into consideration the complexities of the dust properties and morphology of the CSE (Groenewegen et al. 2007; Gullieuszik et al. 2012; Jura 1986).

It is intuitive that the mass loss of an AGB star is dependant on other stellar parameters, like for example, the effective temperature which is expected to influence the dust condensation and as a result the mass loss (Wachter et al., 2002), yet observational studies show no apparent dependence of the mass loss rate on the effective temperature (e.g., Olofsson et al. 2002; Schöier et al. 2001). Another dependance is on the luminosity parameter, expressed by Reimers, (1975) as $\dot{M} \propto Lr/M$, where L is the luminosity, r is the radius, and M is the mass of the star. The most considerable effect caused by the variation of the luminosity on the mass loss rate is the creation of very thin and spherical, detached shells associated with the thermal-pulse cycle (Olofsson et al., 1988). Metallicity has also been investigated but no strong dependence of gas and/or dust mass loss rates on metallicity is expected (e.g., Sloan et al. 2008).

2.2 Circumstellar Envelopes of AGB stars

In this section, we briefly mention some of the CSE's observational properties and describe their basic anatomy. We then describe the physics and chemistry of the CSE from the stellar surface to the interstellar medium. The following section is mainly based on reviews by Zuckerman, (1980), Glassgold, (1996) and Habing et al., (2004).

2.2.1 Observing Circumstellar Envelopes

During the mass loss process, the AGB star forms a dusty envelope around it. The solid dust particles absorb a large fraction of the stellar radiation and re-emit it at longer wavelengths. According to Wien's displacement law for a blackbody, $\lambda_{\max} \approx 2898/T_{\rm eff}$, AGB stars with an optically thin or no envelope emit the peak of their radiation at $\sim 1-2\,\mu$m which corresponds to the near-IR domain. Both the stellar and circumstellar characteristics can then be studied from the SED simultaneously. As the mass loss increases, the SED will shift to longer wavelengths due to thermal emission from the dusty envelope and the peak is between 10 and 20 μm. At high mass loss, the stellar radiation can be completely absorbed by the dust, and the central star will be obscured at visible wavelengths. The only available information then will be from the CSE.

From an observational point of view, there are several ways to study CSEs, yet the most frequent ones are through (i) the measurement of the IR continuum emission produced by the vibrationally excited molecules and microscopic solid dust particles in the outflow.

Table 2.1: Circumstellar molecules detected in IRC +10216 based on Cernicharo et al., (2000) and updates from more recent literature.

CO	c-C_3H	HC_4N	SiC_2	HCl
H_2O	CH_3C_2H	HC_5N	SiC_4	AlCl
OH	H_2CO	HC_7N	Si_2C	NaCN
C_3O	H_2C_4	HC_9N	SiH_4	NaCl
HCO^+	H_2C_6	CH_2CN	CH_3SiH_3	AlF
C_2H_2	C_4H^-	CH_3CN	SiO	HF
l-C_3H	C_6H^-	C_2H_3CN	SiN	NH_3
CH_4	C_8H^-	HNC	SiS	AlNC
C_2	CN	HNCCC	SiCN	MgCN
C_3	C_3N	HCCNC	SiNC	KCl
C_5	C_5N	CS	c-SiC_3	KCN
C_4H	CN^-	C_2S	CP	FeCN
C_5H	C_3N^-	C_3S	C_2P	PN
C_6H	C_5N^-	C_5S	HCP	MgNC
C_7H	HCN	H_2CS	CaNC	MgC_2H
C_8H	HC_2N	H_2S	HMgNC	MgC_4H
c-C_3H_2	HC_3N	SiC	PH_3	MgC_3N

Because dust with different properties (e.g., composition and size) emit at different wavelengths, the IR observations of AGB stars allowed for the identifcation of the dust components around these stars (Speck et al. 2000; Zijlstra et al. 2006). Some of the most useful IR catalogues have been produced thanks to the *Infrared Space Observatory* (ISO) that operated at wavelengths $3-240\,\mu$m and the *Infrared Astronomical Satellite* (IRAS) missions that observed the sky in the 12, 25, 60, and $100\,\mu$m wavelengths (Kessler et al. 1996; Neugebauer et al. 1984). Other infrared catalogues include the IRC (Neugebauer et al., 1969), and the AFGL (Price et al., 1976) catalogues. A comprehensive database of Mira variables have also been provided by the General Catalog of Variable Stars (Kholopov et al., 1985).

The other used method to study CSEs is through the (ii) measurement of emission lines of rotational transitions of various molecules at (sub-)millimeter wavelengths which can trace the gaseous molecules in the envelopes. One of the most extensive catalogues was compiled by Loup et al., (1993) and contained measurements of excited CO and HCN emission lines in more than 300 circumstellar envelopes. This has allowed us to determine parameters such as the mass loss rate and expansion velocity improving our understanding of the kinematics of these envelopes. Moreover, this method allows for the identification of many molecules in the envelope (e.g., Table 2.1) which has provided us with a wealth of information on the chemical composition in the CSEs (Cernicharo et al., 2000).

2.2.2 Regions of an AGB Circumstellar Envelope

The CSE can basically be described as consisting of three main parts (Fig. 2.4):

- *Inner CSE:* This region is located just outside the stellar surface and extends to a few stellar radii, $\sim 3-5$ $R_{\odot}$. Pulsation-driven shocks propagate outwards through the atmosphere, accelerating the gas above the stellar surface. It is charactarized by high densities $\sim 10^{15}$ cm^{-3} and temperatures $\sim 3000-1500$ K where fairly simple molecular species form under thermodynamic equilibrium (TE) conditions close to the stellar photosphere. Non-LTE effects also play a role (e.g., Cherchneff 2006; Willacy et al. 1998) as evidenced by the detection of molecules within this region that are not expected to form under TE (Bujarrabal et al., 1994; Decin et al., 2010a).

- *Intermediate CSE:* This region lies between $\sim 5-100$ $R_{\odot}$. The temperature is sufficiently low $\sim 1500-500$ K and the density is sufficiently high $\sim 10^{8}$ cm^{-3} to provide favorable conditions for dust condensation. Molecules adsorb onto dust grains, and grain surface reactions can occur. The material is accelerated by radiation pressure on dust grains and the density drops by r^{-2}.

- *Outer CSE:* In this region, the wind has reached the terminal expansion velocity, v_{∞}, and is now expanding at a steady outflow velocity of $\sim 5-30$ km s^{-1} with temperatures $\sim 500-10$ K. The density has decreased considerably $< 10^{5}$ cm^{-3} to a point where the region is now dominated by penetration of UV photons and cosmic rays which photodissociate and ionize the molecules. These processes can in turn lead to the formation of new molecules through neutral-neutral and ion-molecule reactions, and photochemistry. At ~ 20000 $R_{\odot}$, bow shocks form the interface between the outer CSE and the ISM (Cox et al., 2012).

2.3 The Physical Structure of a CSE

To describe a CSE around an AGB star, astrophysicists refer to the *standard CSE model*. In this section we will describe some of its main physical properties. It assumes a spherical envelope of smoothly distributed gas particles and dust grains that is formed by a constant mass loss rate and is expanding with a constant velocity (outside the region where the material is accelerated).

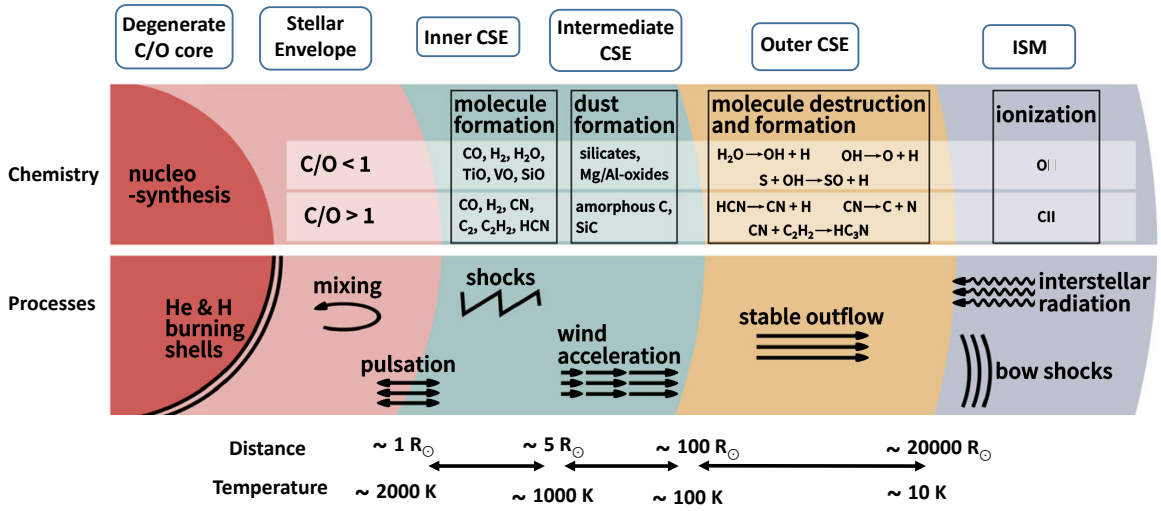

Figure 2.4: A schematic figure of an AGB star and its circumstellar environment, including regions and processes relevant to this PhD. Adapted from Höfner et al., (2018).

2.3.1 Density Distribution

The gas density distribution $n(r)$ in the CSE is linked to the expansion velocity $v_{\rm exp}(r)$ of the outflow at a distance r and a mass loss rate $\dot{M}$ by the continuity equation that describes the principle of mass conservation :

$$n(r) = \frac{\dot{M}}{4\pi r^2 \, \overline{m}_g \, v_{\rm exp}(r)} \tag{2.1}$$

where $\overline{m}_g$ is the average mass of the gas particles, expressed as:

$$\overline{m}_g = \frac{\sum_i m_i x_i}{\sum_i x_i} \tag{2.2}$$

where m_i and x_i are the mass and abundance of every particle respectively. The gaseous CSE is primarily made of H_2 and the abundant species He and CO. Then, for He with a solar elemental abundance, and CO with an abundance of $\sim 10^{-3}$ relative to H_2, this results in $\overline{m}_g = 2.3$ amu.

The high abundance of H_2, in addition to it being self-shielding, makes its spatial distribution be of the largest extent. Because of this, the gas density in CSEs is often described

in terms of the H_2 particle density. The density distribution of other molecules is often expressed in terms of their *fractional abundance* with respect to H_2:

$$f_x(r) = \frac{n_x(r)}{n_{H_2}(r)} \tag{2.3}$$

From Eq. 2.1, the densities decrease with distance as r^{-2}. This implies a significant range in particle densities within a single CSE. For example, for a typical CSE expanding at $v_{\rm exp}$ = 15 km s^{-1} and $\dot{M} = 10^{-5}$ $M_\odot$ yr^{-1}, n(10^{14} cm) $\approx 10^9$ cm^{-3}, and n(10^{18} cm) $\approx 10^2$ cm^{-3}. Eq. 2.1 mainly describes regions where there is a steady outflow, that is, the mass loss rate is constant and the expansion velocity is unchanging. This normally corresponds to the outer regions of the CSE. However, in the inner CSE the situation is more complicated. Near the stellar photosphere, the pulsations "levitate" the material in the atmosphere causing density enhancements at certain heights above the photosphere. The density structure in the inner CSE still decreases with radius but it is strongly affected by the presence of these shocks and the density distribution experiences complex and variable alterations that are difficult to account for. Despite this, attempts have been made over the years to derive analytical expressions decribing the density structure in the shocked zone. An example is the expression proposed by Cherchneff et al., (1992):

$$n(r) = n(r_0)\exp\left\{-\frac{r_0(1-\gamma^2)}{H_0(r_0)(1-\alpha)}\left[1-\left(\frac{r}{r_0}\right)^{(\alpha-1)}\right]\right\} \tag{2.4}$$

where r_0 is the radius where shocks are formed, H is the height scale, α is the exponent of the temperature law (see below), and γ is a dimensionless factor that relates the instantaneous velocity of the flow when a shock forms, v, to the local escape velocity, $v_{\rm e}$, as $v = \gamma\, v_{\rm e}$.

So, the density in the CSE drops as the radius increases, however, how steeply it does depends on the region in the envelope. The density in the inner CSE drops more steeply than in the outer CSE as given by the r^{-2} law, yet less steepily than at the stellar atmosphere where the gas is in hydrostatic equilibrium.

2.3.2 Velocity Profile

The gas that escapes the outer layers of the AGB star is accelerated outwards from a small velocity ($v \leq 1$ km s^{-1}) at a distance r_0 up to some high velocity at a very large distance r from the star. In principle, once the dust grains start to form and grow, they experience a

very large radiative force and the material is quickly accelerated to supersonic speeds. The velocity gradient then decreases due to the interaction of the dust grains with the energetic gas molecules, the acceleration then ceases and the gas expands at a terminal velocity. Hence, in principle, the velocity structure in a CSE comprises of two different regions: i) the inner region where the outflow is accelerated by radiation pressure on dust grains that form at a distance from the star, and ii) the outer region where the outflow reaches a constant velocity for large distances from the star.

For a stationary outflow, the time-independant momentum equation is given by:

$$v(r)\frac{dv}{dr} = \frac{GM_\star}{r^2}(\Gamma - 1) \tag{2.5}$$

where $M_\star$ is the stellar mass. In Eq. 2.5, the gas pressure gradient is ignored, since the outflow is supersonic. The only forces acting on the gas are the gravitational attraction and the momentum transfer by collision from the dust to the gas. Γ is the ratio between the radiation pressure force onto the dust and the gravitational force on the gas:

$$\Gamma = \frac{\kappa_{rp}\, L_\star}{4\pi\, c\, G\, n(r) M_\star} \tag{2.6}$$

where, κ_{rp} is radiation pressure mean opacity of the dust grains (cm^2 g^{-1}), c is the speed of light, $L_\star$ is the stellar luminosity and G is the gravitational constant (Lamers et al., 1999). Γ>1 implies that the acceleration of a gas molecule due to radiation pressure by collision with a dust grain overcomes the gravitational attraction that decelerates the molecules, and the material flows outward.

The solution to the momentum equation, Eq. 2.5, gives the velocity profile which can be expressed in terms of β-law:

$$v(r) = v_0 + (v_\infty - v_0)(1 - \frac{r_0}{r})^\beta \tag{2.7}$$

where r_0 is the initial point at which the acceleration starts (often taken to be the dust condensation radius). The terminal velocity v_∞ is also referred to as the expansion velocity of the CSE. Typical expansion velocities of AGB winds range between $\sim 5 - 30$ km s^{-1}.

2.3.3 Temperature Profile

The temperature structure of the material in a CSE is mainly determined by heating and cooling processes. There are several mechanism that contribute to the heating in a CSE,

these include heat exchange due the photoelectric effect by the interstellar UV photons, photodissociation of molecules, and cosmic ray ionization. These processes may dominate in specific parts of the CSE. However, the dominant heating process in a circumstellar envelope is due to collision of the gas with the dust grains while the dominant cooling process is due to the adiabatic expansion of the envelope. There is also considerable contribution from radiative line cooling, i.e., rotational excitation of mainly CO and HCN in C-rich CSEs, and CO and H_2O in O-rich CSEs. Therefore, the temperature profile of the gas is determined by a balance between those two processes through an energy balance equation (e.g., Goldreich et al. 1976):

$$\frac{dT}{dr} = (2-2\gamma)\frac{T}{r} + \frac{\gamma-1}{n_{H_2} k v_\infty}(H-C) \tag{2.8}$$

where is γ is the adiabatic index considered to be $\gamma = 5/3$, k is the Boltzmann constant, H is the total heating rate per unit volume, and C is the total cooling rate per unit volume. The solution of the energy balance equation is then obtained by solving for the heating and cooling terms. An analytical expression is often used as an approximation to the solution of the energy balance equation and describes the gas kinetic distribution by a power law:

$$T_k(r) = T_\star(r)\left(\frac{r}{R_\star}\right)^{-\alpha} \tag{2.9}$$

where $R_\star$ is the stellar radius, $T_\star$ is the stellar effective temperature and α lies in the range $\approx 0.6-1.2$ (De Beck et al. 2010; Maercker et al. 2016; Teyssier et al. 2006). As an example, for a typical AGB star, the gas kinetic temperature in the CSE ranges between $\sim$600 K in the inner regions at 10^{14} cm and $\sim$10 K in the outer regions at 10^{17} cm. Generally, it is not possible to assign a simple power law to the radial behaviour of the gas temperature throughout the entire CSE since different cooling and/or heating processes might dominate in different parts of the envelope and might raise/lower the temperature. Moreover, the kinetic temperature of the gas is strongly dependant on the mass loss rate, $\dot{M}$, (Kwan et al., 1982) through the heating of the gas by the dust that streams through the envelope. It is expected that high mass loss rate CSEs to have lower kinetic temperatures and low mass loss rate CSEs to have higher temperatures (Jura et al., 1988). This is because the higher the mass loss (i.e., the higher the density), the more dust will absorb stellar radiation and emit at long wavelengths, the cooler the dust envelope will be which will in turn affect the gas kinetic temperature.

Similarly, the dust temperature profile can be approximated by :

$$T_d(r) = T_d(r_c)\left(\frac{r}{R_\star}\right)^{-\delta_d} \tag{2.10}$$

where r_c is the condensation radius, and δ_d is for the dusty component of the envelope.

2.3.4 Envelope Size

The size of the molecular envelope is mainly determined by two factors: i) mass loss rate and ii) the rate of the photodissociation by the interstellar UV photons which is responsible for how deep the UV photons penetrate into the CSE.

The photodissociation of molecules in CSEs is caused by the energetic UV photons of the ambient interstellar radiation field (ISRF). The photodissociation by the photons emitted by AGB stars is unimportant. AGB stars are too cool to produce UV photons; they emit most of their radiation in the infrared part of the electromagnetic spectrum*. When a molecule is exposed to interstellar UV radiation, the molecule is dissociated (and/or ionized). The photodissociation rate κ can be expressed as :

$$\kappa = \int \sigma(\lambda) I(\lambda) d\lambda \tag{2.11}$$

where $\sigma(\lambda)$ is the photodissociation cross-section in cm^2 and $I(\lambda)$ is the mean intensity of the photons in cm^{-2} s^{-1} Å. In reality, the CSEs can be inhomogeneous and clumpy (e.g., Agúndez et al. 2017; Khouri et al. 2016), that is, any region within the CSE may have some lines of sight with high optical depth while others with low optical depth, so the UV photons can penetrate in certain regions much deeper than others. The photodissociation rates for many species are poorly known, however typical values are $\sim 10^{-9} - 10^{-10}$ s^{-1}.

On the other hand, the dust plays an important role when it comes to photodissociation and therefore determining the emission extent. The dust grains interact effectively with UV photons and prevent them from reaching the molecules by absorbing and scattering them. The dust will therefore attentuate the UV photons and cause radiation extinction, thus Eq. 2.11 can be modified and expressed in terms of the visual extinction, A_v:

$$\kappa = \alpha \exp(-\gamma A_v) \tag{2.12}$$

*Stellar emission can be approximated by blackbody radiation, which follows the Wien's displacement law: $\lambda_{max} \propto 1/T$, where λ_{max} is the wavelength at which the maximum of the intensity per unit wavelength is emitted. For typical AGB temperatures $\sim 2000-3000$ K, λ_{max} falls in the IR wavelength range.

where α is the unshieleded photodissociation rate and γ takes into account the increased extinction at ultraviolet wavelengths compared to the visible. A_v is given by:

$$A_v = \frac{N_H}{1.87 \times 10^{21}} \tag{2.13}$$

where N_H is the hydrogen column density in cm^{-2} (Bohlin et al., 1978). This amount of shielding provided by the dust is responsible for protecting the molecules from being destroyed by photodissociation which will ultimately affect the radial extent of the molecules.

When the CSE expands and dilutes, the UV photons eventually break down most of the molecules depending on their respective binding energy, thus limiting their spatial extent but the stronger the molecular bond is, the better it survives photodisociation and can therefore be found at larger radii. For example, CO has a high binding energy and dissociates by line absorption. The line transitions become optically thick due to its high abundance and CO is therefore regarded as *self-shielding* (Morris et al., 1983). This phenomena leads to a decreased photodissociation rate. Cernicharo et al., (2015b) found CO to be present at r $\sim 10^{17} - 10^{18}$ cm in IRC +10216. H_2 is another important example of self-shielding but is more difficult to detect due to it being non-polar.

The envelope size can be constrained in two main methods: directly from interferometeric observations or from modelling a wide range of high-resolution J lines.

2.4 Basic Chemical Scenario of a CSE

The CSE of an AGB star is divided into four distinct regions of different dominating chemistry (Fig. 2.5), which are described in this section.

2.4.1 Gas Composition

The gas in the universe mainly consists of hydrogen and helium. The ability of the gas then to form molecules with other elements such as carbon, oxygen, nitrogen, and sulfur depends on the relative abundance of the element to that of hydrogen, i.e., the elemental abundance. These values have been derived for the Sun's photosphere (Asplund et al., 2005), and some of the abundances are given in Table 2.2. Generally, gas with these relative elemental abundances is said to have solar *metallicity*. Even though the metallicity in different environments vary, it is often assumed that the relative elemental abundance

follow solar values. However, this is not the case everywhere. For example, the dredge-up processes that occur in AGB stars lead to differences in the elemental abundances in their atmospheres and envelopes, most notably in the C/O ratio that was roughly solar in the main-sequence stage, where the increase in the abundance of carbon which may end up being greater than that of oxygen.

Table 2.2: Approximate solar elemental abundances relative to the total number of hydrogen nuclei (Asplund et al., 2005). The values correspond to the number density of an element X to that of Hydrogen.

Element	Abundance	Element	Abundance
H	1	Si	3.2×10^{-5}
He	0.085	Mg	3.4×10^{-5}
O	4.6×10^{-4}	Fe	2.8×10^{-5}
C	2.4×10^{-4}	S	1.4×10^{-5}
N	6.0×10^{-5}	Na	1.5×10^{-6}

2.4.2 Molecule Formation

Close to the stellar photosphere, the temperatures and densities ($T \sim 3000 - 2000$ K, $n \sim 10^{13} - 10^{15}$ cm^{-3}, $r \leq 10^{14}$ cm, Fig 2.5) are relatively high that the gas is dominated by energetic collisions and molecules, known as the *parent molecules*, are formed under local thermodynamic equilibrium (LTE) conditions. LTE preferentially forms molecules with high stability. In addition to H_2, CO becomes the most abundant species in CSEs due to its high binding energy which prevents the less abundant element from forming other molecules. The picture follows as: the CO formation consumes all the available oxygen and carbon, and the remaining free oxygen or carbon atoms determine the molecules and solids formed (Millar, T.J, in Habing et al. 2004). As a result, AGB stars provide mainly three chemically different environments, those that are O-rich (C/O $<$ 1) and those that are C-rich (C/O $>$ 1), and those that are in between, S-type (C/O $\approx$ 1). The molecular setup is markedly distinct in O-rich and C-rich environments as shown by chemical equilibrium calculations (Tsuji, 1973) and by observations (Cernicharo et al. 2000; Velilla Prieto et al. 2017). In O-rich environments, the excess oxygen ends up in O-bearing species such as H_2O, SiO, OH and metal oxides such as TiO, TiO_2, and AlOH. In C-rich environments, the excess carbon forms C-bearing molecules and C_2H_2, HCN, and CS are some of the most abundant molecules. The environments of C-rich CSEs are chemically more varied and rich due to the unique bonding properties of carbon atoms where we find more complex molecules, such as long carbon chains: cyanopolyynes (HC_nN), hydrocarbons C_nH (Cernicharo et al., 1996), and

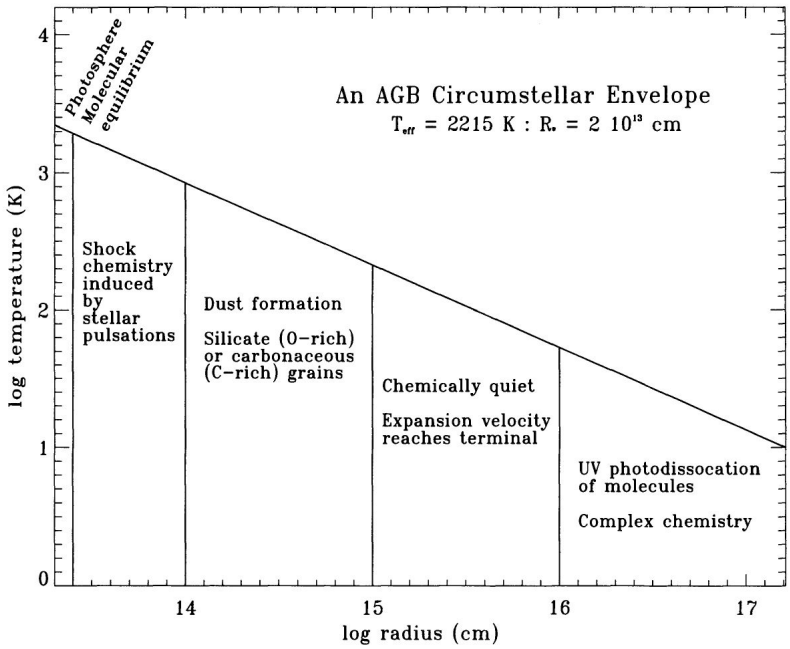

Figure 2.5: Scheme of the structure in an AGB circumstellar envelope showing the dominating chemistry in each region of the AGB circumstellar envelope where the y-axis is the ambient temperature and the x-axis is the radial distance from the central star, from Millar in Habing, (1996).

carbenes H_2C_n (Cernicharo et al., 1991). Nitrogen–carbon chains C_nN (Guélin et al., 1998), silicon–carbon chains C_nSi (Ohishi et al., 1989a) and simple ring molecules(e.g., SiC_3) have been detected as well (Apponi et al., 1999a). The CSEs of S-type stars show features of both, C-rich and O-rich environments (Danilovich et al. 2014; Schöier et al. 2011).

However, the picture is not as simple. When the material flows out, the gas encounters processes that alter the densities and temperatures removing the gas from LTE conditions and perturbing the LTE abundances. Chemical models investigated the effects that shocks can have on altering the chemistry in the inner regions of the envelope (Agúndez et al. 2006; Cherchneff 2006; Gobrecht et al. 2016; Willacy et al. 1998). The models have shown that in O-rich CSEs the abundance of species like HCN or CS is increased by the effect of shock waves, where otherwise their abundance in chemical equilibrium is very low. Similarly, in C-rich CSEs, Decin et al., (2010b) found warm water in the atmosphere of IRC +10216, which is otherwise unexpected to be present. It is thought that fast shocks can destroy CO by collisional dissociation to release atomic oxygen to the gas where these atoms quickly react with H_2 to form OH and H_2O. Agúndez et al., (2010) investigated another alternative formation mechanism in the outer CSE that involved a scenario of photon-driven chemistry following deep penetration of the interstellar photons through a clumpy envelope.

In general, for molecules to form, the chemical timescale, $\tau_{\rm chem}$, has to be shorter than the dynamical timescale, $\tau_{\rm dyn}$. For a chemical reaction where species X_1 destroys species X_2 with rate coefficient κ_{12}, the timescale for the destruction of the less abundant species X_1 is $\tau_{\rm chem} \approx 1/(\kappa_{12} n\, x_2)$, where n is the density of the particles, and x_2 is the fractional abundance of the more abundant species X_2. The chemical timescale is specific to the reaction and species in question. The dynamical timescale describes the expansion of the circumstellar material as $\tau_{\rm dyn} = r/v_{\rm exp}$, where r is the radial distance of the star to the region considered, and $v_{\rm exp}$ the expansion velocity in that region. When $\tau_{\rm chem} < \tau_{\rm dyn}$, the chemical kinetics are fast enough to adapt to the changes in the physical conditions (densities and temperatures) which is the case in the inner CSE where shocks take place. If on the other hand, $\tau_{\rm chem} > \tau_{\rm dyn}$, which occurs as the material flows out, the speed of the chemical reaction is not fast enough to adapt to the changes induced by the dynamics, in other words, the chemical composition does not vary with the variations in the physical conditions, the molecular abundances will experience a *freeze-out* at the values prior to the dynamic disturbance. The freeze-out will happen at a radius called the *quench radius*, $r_{\rm qu}$. The abundances then will be injected to the rest of the CSE and the frozen-out values will be constant with radius except for possible effects of dust formation and eventually photodissociation.

2.4.3 Dust Formation

As the gas continues to be pushed away from the star, the temperature decreases to a point to allow for the condensation of small solid particles made of refractory elements. This region is known as the dust formation zone ($T \sim 1500$ K, $n \sim 10^8$ cm^{-3}, $r \leq 10^{15}$ cm, Fig 2.5). AGB stars have long been regarded as the main providers of dust in the Galaxy (Gehrz, 1989). The presence of dust around AGB stars is evidenced by the excess of thermal emission seen at mid- and far-infrared (IR) wavelengths ($2.5 - 100\,\mu$m) where warm dust mostly emits.

Dust condensation, which is mainly the transition from the gas phase molecules to the solid phase particles, is given in a two-step process (Gail et al., 2014):

1 *Nucleation:* Gas-phase precursors condense to form a *seed nuclei*. This process happens on a molecular level and the molecular species involved typically consist of 10 to several hundred atoms.

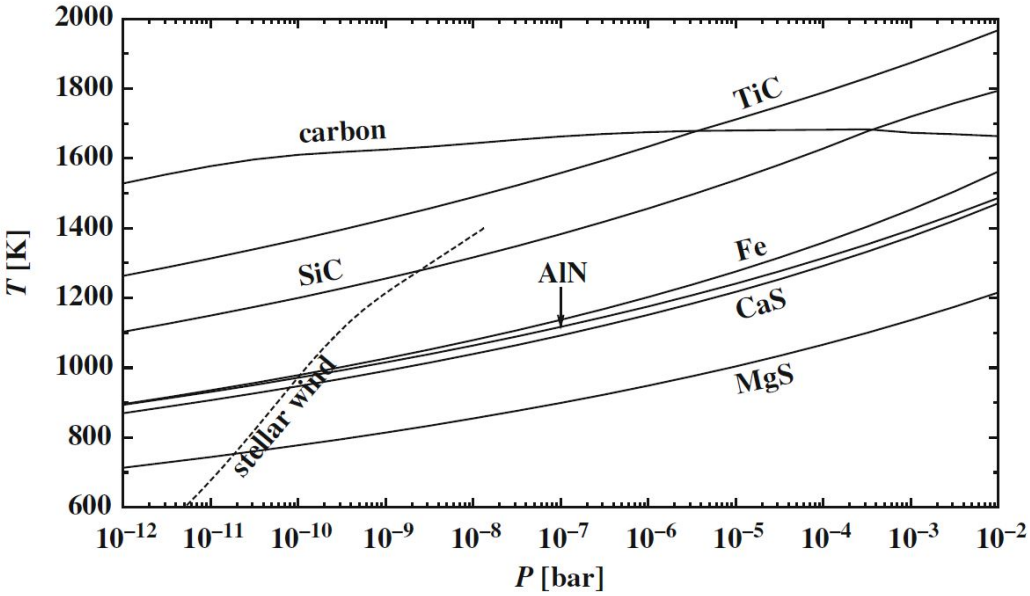

Figure 2.6: Condensation temperature of major elements plotted as a function of total pressure for a C-rich AGB star. The dashed line shows the variation of temperature and pressure for a stellar outflow of $\dot{M} = 10^{-5}$ $M_\odot$ yr^{-1}, from H.-P. Gail in Henning, (2010).

2 *Growth:* The seed nuclei forms a condensate unto which gas molecules gently collide and stick to form a growing layer. By this, the seed particle will grow to a microscopically sized dust grain. This process is called *adsorption*. If the dust grain survives, it can continue to grow once ejected to the ISM through accretion and coagulation processes.

The formation of dust occurs at the expense of the gas in the envelope, and the chemical composition of dust will reflect the C/O nature of the gas. Which type of condensate will form depends on the condensation temperature T_c of a species, above which the material cannot undergo the phase change from gas to solid. T_c will thus indicate in which order different types of condensates form as a result of the falling ambient temperatures as the gas is moving away from the stellar surface. The material that will condense will depend on the temperature, pressure, as well as the densities and element abundances which will primarily affect the nucleation and growth. Fig. 2.6 shows the most abundant solids in C-rich AGB stars as predicted by chemical equilibrium models. Of those, SiC and MgS dust are observed through their infrared emission at 11.3 µm and 30 µm respectively. TiC is not thought to be abundant due to the low Ti abundance, but is detected in presolar carbon grains. Fe is found as inclusions in the latter as well (Croat et al., 2005). AlN is believed

to be formed heterogeneously with SiC dust and not independently as a dust component (Stroud et al., 2005). In O-rich AGB stars, the dust grains are composed of refractory silicates (mainly amorphous with a smaller population that is crystalline) such as olivine- ($Mg_{2x}Fe_{2(1-x)}SiO_4$, with $0 \leq x \leq 1$) and proxene- ($Mg_xFe_{(1-x)}SiO_3$) type materials, and oxides such as aluminum (Al_2O_3) and titanium oxides (TiO_2). S-type stars, with C/O$\approx$1, represent the transition between O-rich and C-rich chemistry. Since all the oxygen is locked with carbon, there is little C or O left for the formation of abundant molecules. Observational studies have pointed to the presence of MgS dust in this class of objects, and with less certainity, to the presence of amorphous silicate, alumina (Al_2O_3), diopside ($MgCaSi_2O_6$) and gehlenite ($Ca_2Al_2SiO_7$) (Hony et al. 2009; Smolders et al. 2012). Theoretically, FeSi and metallic iron dust are predicted to form, but this still lacks observational confirmation (Ferrarotti et al., 2002). Dust grains can play an important role for the catalysis of molecules on the grain surfaces. Some of the molecules formed are hydrides such as: NH_3 and SiH_4. The molecules might also evaporate from the dust surface depending on the temperature and properties of the dust grain.

With the expansion of the envelope, the density and temperatures become so low that dust formation is no longer efficient. Once dust formation has ceased, the dust and gas expand at constant velocity and the outflow reaches its terminal velocity. The chemistry becomes rather "quiet", and unless something happens, there would be no further chemical evolution (Fig.2.5).

2.4.4 Circumstellar Photochemistry

At r $\geq 10^{16}$ cm, the envelope dilutes to a point where the material becomes exposed to UV photons of the ISRF (Fig 2.5). When the density in the outer CSE has decreased to $n \sim 10^5$ cm^{-3}, the ISRF UV photons can penetrate the envelope and interact with the gas and dust. Dust grains are heated by the radiation field and reradiate the energy at longer wavelengths, while the molecules become subject to processes like photodissociation and photoionization which alter their chemical state. These processes become the dominant chemical processes in the outer CSE (Fig.2.5).

The photodissociation breaks down the parent molecules into atoms that are rapidly photoionized to form ions[†]. The photodissociation of molecules also gives rise to radicals that are known as the *daughter species* of the parent molecules. Before being completely

[†]Only atoms with an ionization potential lower than that of H (13.6 eV) will be ionized. The reason is that photons with energies > 13.6 eV are all used in the ISM to ionize H and will no longer be available to cause further ionization in the CSEs.

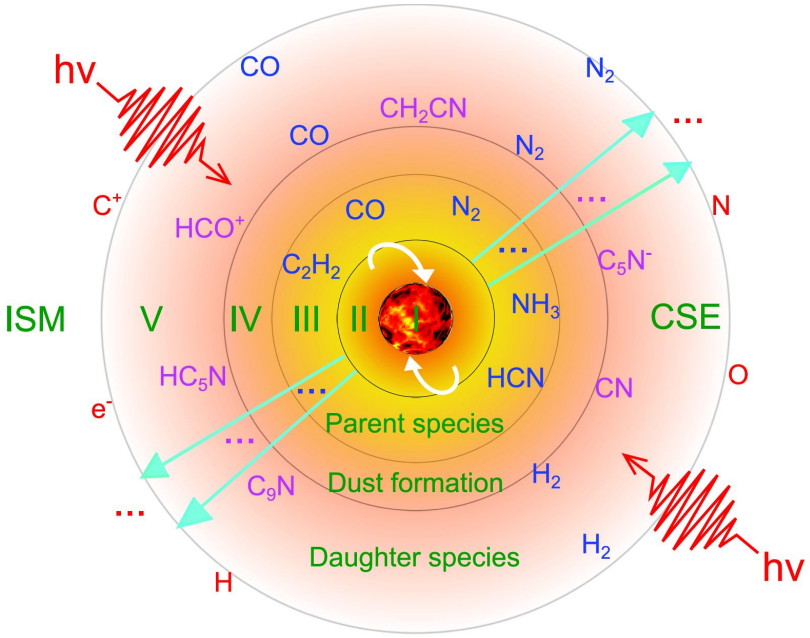

Figure 2.7: Schematic structure of the a CSE for an C-rich AGB star. (I): a degenerate C/O core and He/H burning shell; (II): a convective atmosphere; (III): a shocked inner wind where parent species are formed; (IV): an intermediate expanding envelope where dust grains are formed; (V): an outer CSE where daughter species are formed by photodissociation and ionization; (VI): the ISM, from Li et al., (2014).

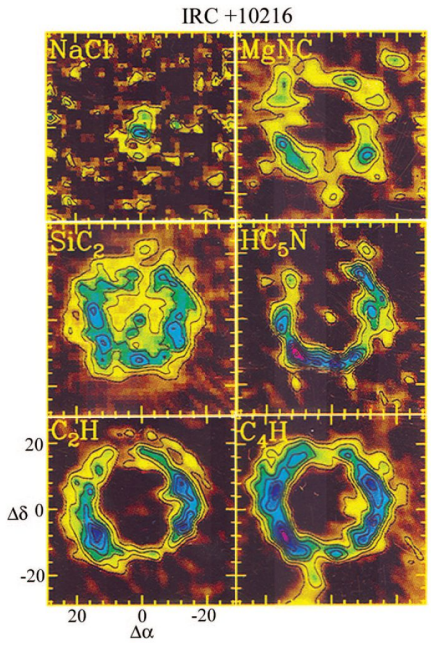

Figure 2.8: Interferometric maps showing the molecular distribution of different species in in the envelope of IRC +10216, from Ziurys, (2006).

destroyed by photodissociation, the radicals produced by photodissociation of the molecules react to form new and possibly complex species thereby enriching the chemical composition of the envelope. For example, in M-type stars, the photodissociation of H_2O produces the radical OH, which rapidly reacts with O to form oxygen (O_2) molecules which is challenging to observe since it has no permanent electric dipole. In C-rich CSEs, the photodissociation of HCN molecules produces CN radicals that react rapidly with C_2H_2 to produce HC_3N molecules. Fig 2.8 shows other various radicals such as C_3H and C_4H in the envelope of IRC +10216. All the molecules will be finally photodissociated and will be incorporated into the interstellar medium as neutral or ionized atoms. The only entities that survive are the dust grains that are dense enough not to be affected by photodissociation. In fact, and as mentioned in Sec. 2.3, dust grains act as a "shield" by absorbing and scattering the UV photons thus cutting down the UV photon flux so that more molecules further inside can survive.

In addition to photodissociation by UV photons in the outer CSE, cosmic rays, the highly energetic [$\sim$GeV] charged particles (protons), can penetrate through and provide a source of ionization, creating free electrons and positively charged molecules:

$$\text{Cosmic ray} + A \rightarrow A^+ + e$$

The electrons produced are also energetic and can cause heating of the gas by electronic excitation (Prasad et al., 1983) leading to secondary ionizations. For example, in the CSE, a cosmic ray particle can react with a H_2 to produce H_2^+, which can rapidly react with another H_2 to produce H_3^+, which in turn will react with various atoms and molecules in the gas, like O, N, and CO, to produce OH^+, NH_2^+, and HCO^+ respectively.

In general, the reactions relevant to the formation and destruction of molecules and that contribute to the photochemistry in the CSE (Glassgold, 1996):

$$1\cdot\ \text{Neutral} - \text{Neutral} : A + B \rightarrow C + D$$

$$2\cdot\ \text{Ion} - \text{Molecule} : A^+ + B \rightarrow C^+ + D$$

$$3\cdot\ \text{Dissociative recombination: } A^+ + e \rightarrow B + C$$

$$4\cdot\ \text{Radiative association: } A + B \rightarrow AB + h\nu$$

$$5\cdot\ \text{Photodissociation: } AB + h\nu \rightarrow A + B$$

To summarize the chemical scenario in a CSE, the gas molecules are affected by a sequence of processes in the different regions of the envelope that goes as such: first, in the inner regions, the high density and high temperature activate LTE chemistry at the stellar photosphere which produces the parent molecules (region (III) in Fig. 2.7). The result of this is highly dependant on the C/O ratio at the stellar photosphere. These molecules will then be expelled outwards. Second, the shocks will activate a non-LTE chemistry on the outflowing gas. Third, the formation of dust grains will take place at the expense of the existing molecules through grain adsorption and grain surface chemistry which will decrease the abundance of some of the molecular species (region (IV) in Fig. 2.7). Fourth, as the CSE expands and dilutes, the interstellar UV photons penetrate and destroy the molecules giving rise to new molecules that can in turn undergo photo-induced chemistry via photons and cosmic rays to form new species (region (V) in Fig. 2.7.)

Chapter 3

Radioastronomy

In the following, important concepts of radio astronomy are introduced. The text is largely based on Klein, (2006) and Marr et al., (2015).

3.1 The Radio Window

Different sources, like stars, dust, or gases, emit photons with different wavelengths depending on their properties (e.g. composition, density, temperature) so that almost everything that we know about astronomical objects has been acquired by gathering and studying the light they emit and reflect. The dramatic improvement in our observing capabilities and the opening up of different parts of the electromagnetic spectrum in the past decades have allowed astronomers to piece together a coherent picture about how the universe works. Radioastronomy has the ability to study a wide range of astrophysical phenomena, but the the mm and submm wavelength range in particular has been essential to the understanding of the molecular universe. The chemical richness of the circumstellar envelopes has only recently been realized, with the development of radioastronomy in the 1960s which enabled the measurement of the rotational spectra of molecules.

The first radio detection of a molecule in a CSE of an evolved star was by Wilson et al., (1968) when they observed strong OH emission towards four stars at a wavelength of 18 cm. Shortly afterwards, H_2O was discovered in VY Canis Majoris (Knowles et al., 1969) at 1 cm. Both of these molecules were attributed to circumstellar masers. But the first detected molecule in a CSE at millimeter wavelengths was CO toward IRC +10216 (Solomon et al., 1971) which proved to be the most usefully studied molecule. This was soon followed by the detection of CS, CN and ^{13}CO (Wilson et al., 1971). It was then realized that envelopes around evolved stars could be rich in molecular species.

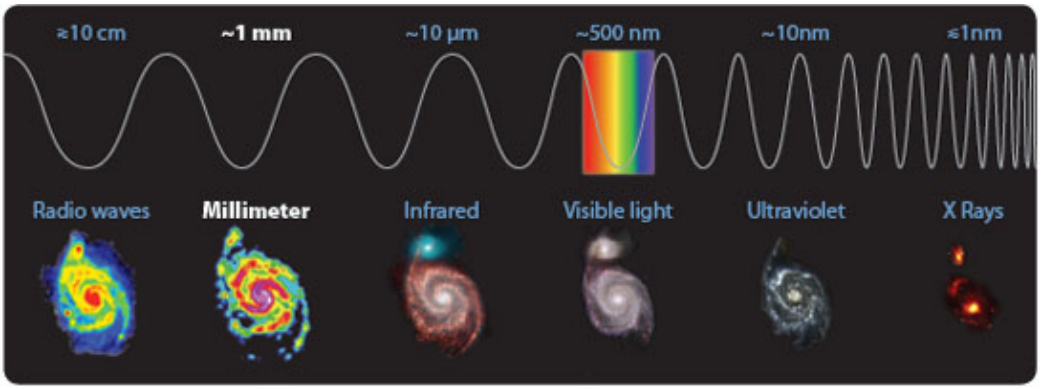

Figure 3.1: The illustration above shows the M51 galaxy viewed at different wavelengths. Radio waves mainly probe the coldest matter, millimeter wavelengths mainly probe molecules, infrared wavelengths mostly probe dust grains and planets, the visible regime probes mainly starlight and ionized gas, the UV wavelengths probe the hottest stars, and X-rays probe plasma. By combining data from across the spectrum astronomers can form a comprehensive understanding about astronomical objects. Credit: IRAM*

The radio domain covers a wide range of frequencies, of about five decades, between 10 MHz $\lesssim \nu \lesssim$ 1 THz which corresponds to wavelengths 0.3 mm $\lesssim \lambda \lesssim$ 30 m. A major problem in observations at radio wavelengths is the Earth's atmosphere. The atmosphere is totally opaque at some wavelengths and partially transparent at other wavelengths. As the radiation from the astronomical radio object traverses the atmosphere, it interacts with the molecules present in the atmosophere. These molecules can absorb photons of certain wavelengths while allowing photons with differing wavelengths to pass through. In the radio domain, two molecules are mostly responsible for this: water vapor and O_2. Water vapor has lines at ν = 22.2 GHz (λ = 1.35 cm) and 183 GHz (1.63 mm), while O_2 has a considerably strong line at 60 GHz (5 mm). The absorption of electromagnetic radiation by other abundant molecules in Earth's atmosphere, N_2 and CO_2, occurs at frequencies above 300 GHz. The water content is quantified as the total column water vapor (or Total Precipitable Water; pwv) which is the total gaseous water contained in a vertical column of atmosphere. It is measured by radiometers and with atmospheric models on the observatory site. The wavelengths at which observations are possible from the ground are called *atmospheric windows*. To cancel the effects of the atmosphere, observatories are placed at higher altitudes (with > 3000 m), where the air is dry (with pwv < 4 mm) to avoid the absorption and attenuation of the signal. This suggests deserts like the *ALMA* telescope, or mountains like the *IRAM 30m* telescope. For some observatories in other wavelength ranges like the infrared or submillimeter, even minimal atmosphere causes problems, so observations from space are carried out such as the *Herschel Space Observatory* or the airborne facility SOFIA.

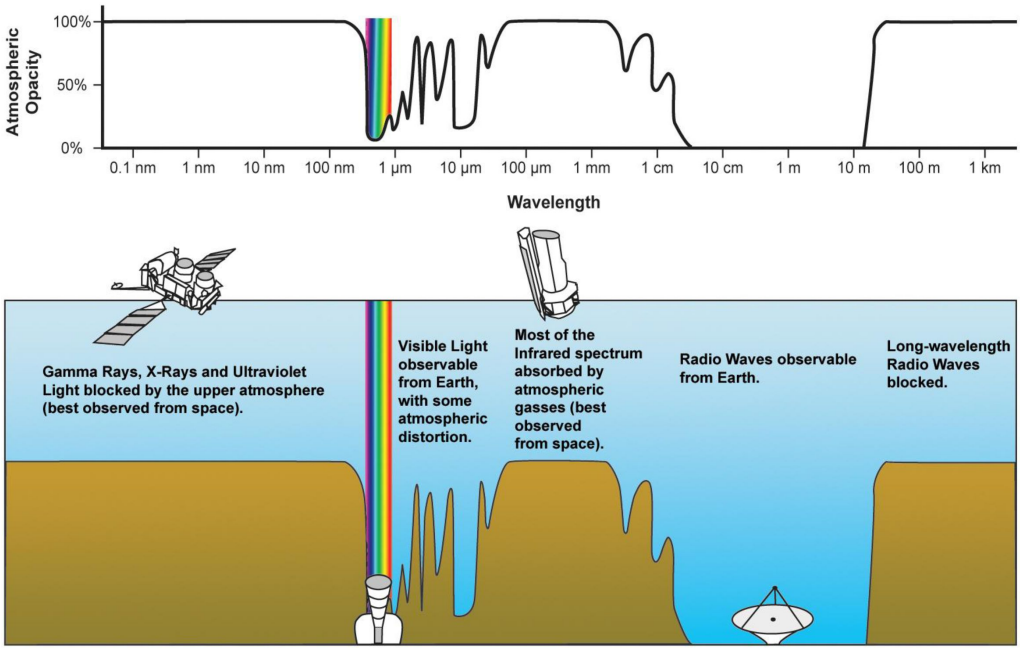

Figure 3.2: The electromagnetic windows through Earth's atmosphere. Source: NASA public domain, acquired from Wikimedia Commons

3.2 Single-dish Radio Telescope

There are two main methods for performing radio astronomy observations: single-dish observations that utilize only one telescope, and observations made with multiple telescopes that are combined together using interferometric techniques. Here, we focus on the single-dish radio telescope since it repesents the IRAM 30m telescope which was utilized to carry out the observations in this thesis (Sec. 3.5).

The main structure of a typical radio telescope consists of a primary *parabolic reflector* (or *dish*, also referred to as *antenna*), a *second reflector*, a *feed* and a *receiver system* (Fig. 3.3). The two most common types of receivers in radio astronomy are *heterodyne* receivers and *bolometer* receivers. Here, we will mention only the heterodyne receivers as the observations performed in this thesis were based on them.

The incoming radiation strikes the primary reflector with a certain number of photons per unit area per second. The parabola is a very useful mathematical shape as it forces the incoming photons to bounce up to a point above it, called the *focal plane*. Most radio telescopes are of a Cassegrain design, which means that a second reflector (or mirror, also called *subreflector*) is placed before the focal plane of the primary reflector to redirect the

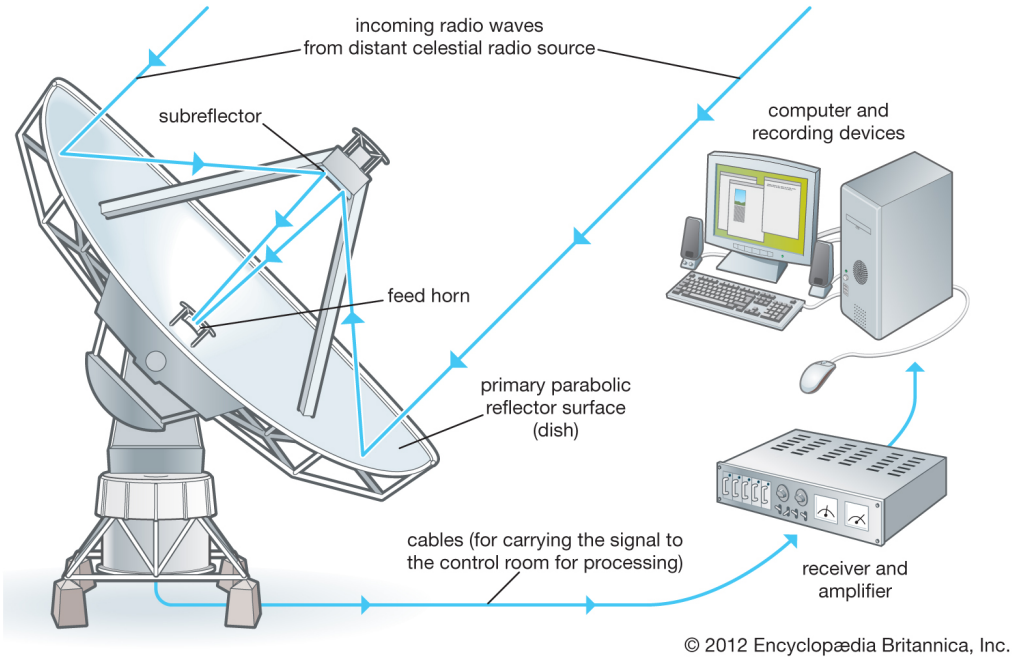

Figure 3.3: Sketch of a radio telescope along with the ray path. The basic function of a radio telescope is to collect weak radio waves, bring it to a focus, amplify it and make it ready for analysis.

waves to another focus. At the focus of the telescope are feed-horns. These feeds are horn-shaped antennas typically with a size comparable to the wavelength being observed. The EM radiation enters the feed-horn through a finite-size opening into a type of transmission line called a *waveguide* (a metal tube or a cable) which sends the signal along its length to the receiver system (Fig. 3.3). Transmission lines are needed throughout the entire journey made by the EM radiation from the feed to the detector. The radio signals are generally very weak, so in order for them to be measured, the signals must be amplified and processed in the receiver system.

3.3 Receiver System

The receiver system of a radio telescope consists of different components that are connected through transmission lines to allow the journey of the EM radiation towards the detector. The main purpose of the receiver system is to amplify the incoming signal from the feed, filter the signal and "down-convert" it to a lower frequency where it can be more easily sampled or detected. The receiver system is made of two parts: i) the front-end, located near the feed, that provides the amplification and the frequency conversion, and ii) the back-end,

located at the observatory control room, that provides the detection and the measurement of the signal (Fig. 3.4).

Usually, the first function of the receiver is to increase the amplitude of the input radio signal, hence the first component in the receiver system is typically an amplifier. However, the amplifier not only increases the amplitude of the radio wave, it also introduces unwanted noise, characterized by the *gain*, $G = P_{\text{out}}/P_{\text{in}}$, defined in terms of power P. If not handled properly, the gain might conceal the weak radio signals that are aimed to be measured.

After the amplification, it is usually essential to convert the signal to a different and much lower frequency. This is done for a couple of reasons. First, it is technologically more challenging and more costly to build components for very high frequencies. Second, there is a chance that very high frequency signals experience greater loss in power while passing in the transmission line and might produce strong feedback effects. This conversion to another frequency is done by a device called the *mixer*, where another signal of slightly different frequency, created by the local oscillator (LO), is used to shift the input signal. The output signal of the mixer at a lower frequency is called the *intermediate frequency* (IF). Therefore, the mixer combines the *radio frequency* (RF) from the source being observed and a LO signal to produce an IF signal that carries the same information as the RF signal, but at a different frequency. This principle is called *heterodyne* which relates to the idea of combining/mixing two different signals together to accomplish a conversion in frequency. So, the IF signal has all of the spectral information that was in the RF signal, just shifted to a lower frequency range. The output IF frequency is then simply the difference between the LO frequency and the RF as:

$$\nu_{\text{IF}} = \nu_{\text{RF}} \pm \nu_{\text{LO}} \tag{3.1}$$

where, "$+$" refers to the upper sideband, and the "$-$" refers to the lower sideband.

For the signal to be eventually detected, there needs to be more amplification. This is done at the IF signal. The mixer is followed by an IF amplifier which is different from the RF amplifier in that it is designed to amplify the lower IF frequency.

The detection is carried out by measuring the amount of power the EM waves contain. In order to do that, a *band pass* filter is needed that allows radio waves of a well-defined frequency range to pass and rejects all waves outside these frequencies. This is important to prevent unwanted signals that might be present to be included in the power measurement. The detection of the signal power is done by a device called a *square-law detector*, which

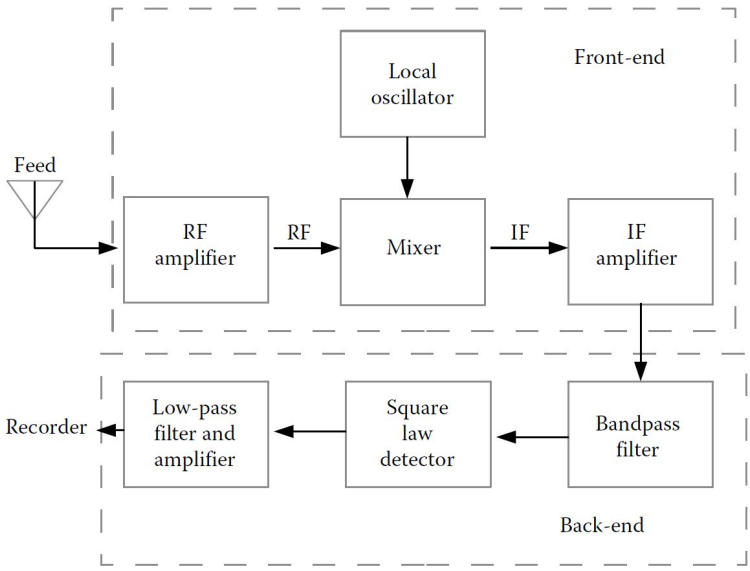

Figure 3.4: Schematic diagram showing the component's of a radio telescope's receiver, the front-end and the back-end (Marr et al., 2015)

is usually made up of either a crystal diode or a semiconductor diode. The diodes produce a current that is proportional to the square of the electric field of the input EM wave. The current then passes through a resistor and is converted to a voltage that is proportional to the power of the incoming radio wave. The voltage varies on very short timescales, so the signal fluctuates. Therefore, the output of the detector is then sent into a *low-pass* filter, which removes the high-frequency variations while preserving the DC signal. Following the low-pass filter, a DC amplifier is used to boost the voltage so that it can be readily digitized by an A/D (analog to digital) converter and recorded by a computer.

3.4 Basic measurements with a single-dish telescope

3.4.1 Flux Density and Brightness Temperature

The flux density of the source, F_ν in Jy, is related to the power the telescope receives, P in W, which depends on the effective collecting area of the telescope, A_{eff} in m^2, and the frequency bandwidth, $\Delta\nu$ in Hz, as:

$$F_\nu = 2\frac{P}{A_{\text{eff}}\,\Delta\nu} \tag{3.2}$$

The brightness temperature of the source, T_b, is given by the Rayleigh-Jeans approximation ($h\nu << kT$), as:

$$B_\nu(T_b) = \left(\frac{2\nu^2 k}{c^2}\right) T_b \qquad [\mathrm{W\,m^{-2}\,Hz^{-1}}] \tag{3.3}$$

3.4.2 Pattern, Antenna Beam, Beam Efficiency

The *beam pattern*, $P_n(\theta)$, measures the response of the telescope to incoming radio signals as a function of angle on the sky, also known as the *power pattern* or the *point-spread function* (PSF).

$$P_n(\theta) \propto sin^2(\theta) \tag{3.4}$$

The value of $P_n(\theta)$ is unity when $\theta = 0$ and decreases for increasing angle θ. Ideally, each feed in the telescope collects radio signals from only one position in the sky so that the power detected through each feed corresponds to the radiation coming from only the observed source. However, this is not the case due to diffraction of light. The telescope's beam pattern can then resemble that in Fig. 3.5. The pattern is characterized by a central peak when the source is on the pointing axis, called *main beam*, and off-axis responses called *sidelobes* which are undesirable since they can add confusion to the observations.

However, in principle, the beam pattern is a function of angular position in a two-dimensional geometry (azimuth and elevation angles), so we will denote the normalized beam power pattern as, $P_n(\theta, \Phi)$. The integration of the beam power pattern over all angles in the sky (4π, which includes the main beam and the sidelobes), gives the *beam solid angle* or the *antenna solid angle*, Ω_A:

$$\Omega_\mathrm{A} = \iint_{4\pi} P_n(\theta, \Phi)\, d\Omega \tag{3.5}$$

where $\mathrm{d}\Omega = \sin\theta\ \mathrm{d}\theta\ \mathrm{d}\Phi$. For example, an antenna that responds fully to radiation from all directions with the same intensity, would have $\Omega_\mathrm{A} = 4\pi$ sr. A simple expression of the antenna solid angle can be given by :

$$\Omega_\mathrm{A} = \frac{\lambda^2}{A_\mathrm{eff}} \tag{3.6}$$

The antenna solid angle refers to the angular area that the telescope is sensitive to.

The main beam pattern is often approximated as a Gaussian function of the form:

$$P_{\text{main}}(\theta) = exp\left[-4\,ln2\left(\frac{\theta}{\theta_{\text{FWHM}}}\right)^2\right] \tag{3.7}$$

Integrating Eq. 3.7 over the main lobe angle gives the solid angle of the main beam :

$$\Omega_{\text{main}} = \frac{\pi}{4\,ln2}\theta^2_{\text{FWHM}} \tag{3.8}$$

The full width at half maximum (FWHM) of the main beam of the telescope where the received power of the incoming radiation falls to one-half defines the angular resolution of the telescope, such that $\theta_{\text{FWHM}} = 1.02\lambda/D$, where θ_{FWHM} is in radians, λ is the wavelength of the observations, and D is the diameter of the primary reflector.

The main beam efficiency B_{eff}, denoted as η_{mb}, is the ratio of the main-beam solid angle to the antenna solid angle as :

$$B_{\text{eff}} = \eta_{\text{mb}} = \frac{\Omega_{\text{main}}}{\Omega_A} \tag{3.9}$$

There are a few factors that affect B_{eff} in Eq. 3.9. Ω_A comprises radiation from the side lobes which are unwanted features of the beam coming from other parts in the sky that will eventually contribute to the power detected. For that reason, one wants the response in the sidelobes to be as small as possible, since the bigger Ω_A the lower B_{eff} is. Moreover, from Eq. 3.6, the bigger the effective collecting area of the telescope A_{eff}, the smaller Ω_{A}, hence the smaller the region in the sky the telescope will see, therefore the better the sensitivity, that's why the bigger the A_{eff}, the better B_{eff} is. On the other hand, irregularities on the surface of the reflector dilute A_{eff} of the telescope due to scattering. Due to these reasons and other effects, $\text{B}_{\text{eff}} \leqslant 1$. Ideally, one would want the difference between the antenna solid angle and main beam solid angle to be as small as possible.

F_{eff} refers to the fraction of the collected power that comes from the forward part of the beam and it is given by:

$$F_{\text{eff}} = \frac{\iint_{2\pi} P_n(\theta,\Phi)\,d\Omega}{\Omega_{\text{A}}} \tag{3.10}$$

Another important efficiency parameter is the *aperture efficiency* which describes the ratio of the telescope's effective area to its geometrical area A_{geom} as :

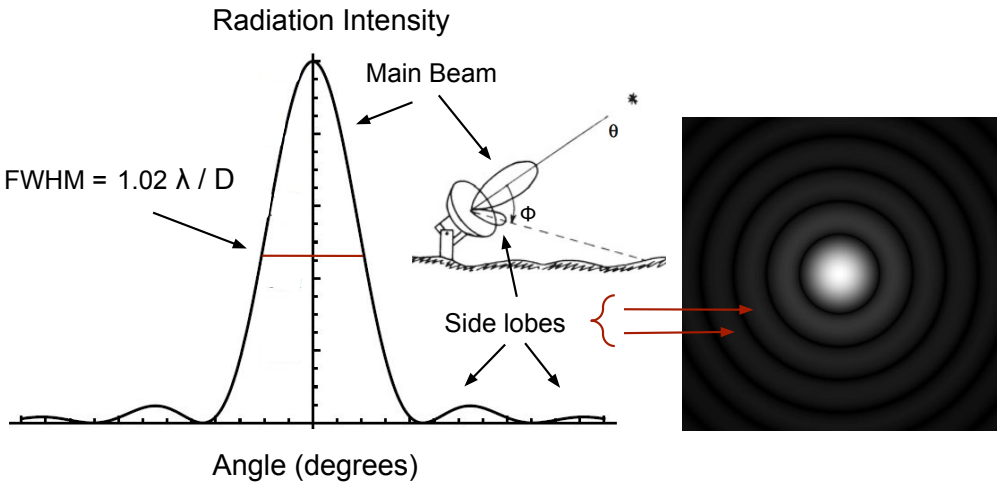

Figure 3.5: *(left)* Typical profile of a beam pattern of a radio telescope as a function of angle relative to the telescope's central axis. The beam pattern shown has a main maxima which peaks in the pointing direction of the telescope. The pattern then decreases to zeron, then oscillates to ever-decreasing values. *(Reft)* Airy disc showing the diffraction patten.

$$\eta_{\mathrm{A}} = \frac{A_{\mathrm{eff}}}{A_{\mathrm{geom}}} \tag{3.11}$$

3.4.3 Noise, Noise Temperature, and Antenna Temperature

The power of the radiation that travels through the feed to the receiver system and is finally measured at the detector is not only due to the astronomical source, but also due to many independent random contributions that are unavoidable and undesired as they interfere with our ability to measure the power strictly due to the astronomical radio source. The signals from these contributions are referred to as *noise* and can be characterized by their own temperature according to the Nyquist theorem:

$$T = \frac{P}{k\Delta\nu} \tag{3.12}$$

where P is the power of the radiation, k is Boltzmann's constant and $\Delta\nu$ is the frequency bandwidth.

The temperature of the power that the antenna delivers to the transmission line, is called the *antenna temperature*, T_{A}. In other words, T_{A} is strictly a measure of the power detected

due to the astronomical source.

However, one of the main contributors to the noise which, in fact, accounts for the majority of the power measured at the detector is: the receiver system. The components of the receiver can generate their own electrical signals which produce thermal noise and can be described by the *receiver temperature*, T_{rec}. Each component of the receiver system has its own temperature T_i and gain factor G_i where G > 1 for amplification and G < 1 for loss. The total T_{rec} is then :

$$T_{\text{rec}} = T_1 + \frac{T_2}{G_1} + \frac{T_3}{G_1 G_2} + \cdots + \frac{T_N}{G_1 G_2 \cdots G_{N-1}} \tag{3.13}$$

In order to minimize the noise due to the receiver system, it is important to cool down the receiver of the radio telescope since the receiver noise is largely thermal. This is typically achieved using cryogenic refrigerators.

There are additional noise sources that contribute to the final output power, like, noise contribution from microwave and galactic backgrounds, T_{bg}, contribution from atmospheric emission, T_{atm}, contribution due to the spillover, T_{spill}, contribution due to the scattered radiation from the ground, T_{g} etc, such that *system temperature* represents all of the added noise of the system as:

$$T_{\text{sys}} = T_{\text{rec}} + T_{\text{bg}} + T_{\text{atm}} + T_{\text{spill}} + T_{\text{g}} + \cdots$$

so the total output temperature, T_{tot}, and correpondingly the total output power, P_{tot}:

$$T_{\text{tot}} = T_{\text{A}} + T_{\text{sys}} \implies P_{\text{tot}} = P_{\text{A}} + P_{\text{sys}}$$

The nature of the noise power is that it is random and it fluctuates. For example, these flucuations could be due to the behavior of the receiver electronics, or due to the fluctuations of the water vapor in the atmosphere. The former can occur on timescales of seconds, while the latter typically on timescales of minutes to hours. In any case, it is these flucuations that limit the ability to detect a weak astronomical signal. The amount of variance due to random fluctuations in the noise is given by the *radiometer equation*:

$$\sigma_{\text{rms}} = \frac{T_{\text{sys}}}{\eta_{spec}\sqrt{t\Delta\nu}} \tag{3.14}$$

where σ_{rms} is called the rms noise obtained by integration during time t in s, in a frequency resolution $\Delta\nu$ in Hz and with a spectrometer that has an efficinecy η_{spec}. Eq. 3.14 shows that to decrease σ_{rms}, that is, to improve the sensitivity or the signal-to-noise ratio

by a factor of 2, the observation time has to be increased by a factor of 4. Typically, any measure of $T_A < 3 - 5\,\sigma_{\rm rms}$ is considered a non-detection. The type of observations carried out in Part II are called ON-OFF observations (Sec 3.4.5), so Eq. 3.14 can be written as :

$$\sigma_{\rm rms} = \sqrt{\sigma_{on}^2 + \sigma_{off}^2} = \frac{T_{\rm sys}}{\eta_{spec}\sqrt{t_{sig}\Delta\nu}} \tag{3.15}$$

where t_{sig} is the total integration time given by:

$$t_{sig} = \frac{t_{\rm on} t_{\rm off}}{t_{\rm on} + t_{\rm off}} \tag{3.16}$$

3.4.4 Detected Power from Resolved and Unresolved Sources

From Eq. 3.2, the power detected by the telescope due to radiation from an astronomical source can be described by:

$$P = \frac{1}{2}\, F_\nu\, A_{\rm eff}\, \Delta\nu \tag{3.17}$$

The factor $\frac{1}{2}$ refers to the fact that there are two polarizations, and $\mathrm{F}_\nu = \mathrm{I}_\nu\, d\Omega$, where Ω is the solid angle of the source.

However, this equation needs modifying as it assumes that the response of the telescope is equally sensitive to the flux of the source. Suppose we have an extended source with an angular diameter much larger than the angular diameter of the main beam, so that the radiation of the source not only comes from the beam center, but also from other positions away from the beam center and contributes to the detected power. If we consider that the radiation of a source comes from a direction (θ, ϕ) and has an intensity $\mathrm{I}(\theta, \phi)$, then the amount of the total power detected would be :

$$P = \frac{1}{2} A_{\rm eff} \Delta\nu \int I_\nu(\theta,\phi)\, P_n(\theta,\phi) d\Omega \tag{3.18}$$

To express Eq. 3.18 in terms of antenna temperature, using Eq. 3.12:

$$T_A = \frac{A_{\rm eff}}{2k} \int I_\nu(\theta,\phi)\, P_n(\theta,\phi) d\Omega \tag{3.19}$$

For an *unresolved* source, also called a *point* source, with the solid angle of the source, $\Omega_{\rm s}$, much smaller than the main beam solid angle $\Omega_{\rm main}$, such that $\Omega_{\rm s} < \Omega_{\rm main}$, so from Eq. 3.19 the integral of the normalized beam pattern over the solid angle of the source,

$P_n(\theta,\phi)$, can be considered equal to 1, then the antenna temperature for an unresolved source is :

$$T_A = \frac{A_{\text{eff}}}{2k}\int I_\nu(\theta,\phi)d\Omega\,, \implies T_A = \frac{A_{\text{eff}}}{2k}F_\nu \tag{3.20}$$

which means that if the source is a point source, then the antenna temperature directly measures the flux density of the source. The quantity $2k/A_{\text{eff}}$ is the calibration factor that converts antenna temperature to flux density for a point source. The inverse of this factor, $A_{\text{eff}}/2k$, is used in the calibration of the telescope to determine the conversion factor between the antenna temperature and the flux density in K Jy^{-1}.

For a *resolved* source, also called an *extended* source where $\Omega_s > \Omega_{\text{main}}$, some of the flux density of the source does not get detected because of the reduced sensitivity at angles offset from the central pointing direction, then the integral of $P_n(\theta,\phi)$ over the solid angle of the source is not unity. The antenna temperature would then be:

$$T_A = \frac{A_{\text{eff}}}{2k}I_\nu\Omega_{\text{main}} \tag{3.21}$$

where Ω_{main} is given by Eq. 3.8.

3.4.5 Observing Modes

As mentioned previously, the amount of power measured at the detector is not only due to the astronomical radio source, but also due to noise arising from electrical components, spillover from the antenna and background radiation. Therefore, the total detected power is in reality a poor measure of the power emitted by the astronomical object. To avoid this, the power received by all these unwanted contributions must be subtracted from the power due to the target source only, this is why a fundamental strategy adopted by single-dish radio observations requires the subtraction of these noise signals from the signal of the astronomical source. This is done by a process called *switching*. There are three main modes of switching, *position-*, *wobbler-* or *frequency*-switching. In position-switching, observations are carried out on the astronomical source, called the "*ON*" observation, then the entire telescope is moved to a nearby blank patch of sky that does not contain the target source, to measure the "*OFF*" observation, which is then subtracted from the ON-observation. The wobbler-switching is similar to the position-switching, but differs in that the primary reflector stays fixed and the only component that is slightly moved is the subreflector. Because the secondary reflector is smaller and lighter than the entire telescope, it can be moved

more quickly and with less disturbance to the telescope. Determining the OFF position depends on factors such as the beam size, the source size, and the presence of other sources, however, it should be as near to the ON position as possible to avoid large atmospheric variations. These two methods are quite efficient with wobbler-switching (useful for compact sources) producing flatter baselines than position-switching (useful for extended sources). The frequency-switching method is best used when the sources have a low density of spectral lines and when the lines are very narrow. It involves slightly shifting the frequency of the observation on and off the spectral line. This method is considered to be very rapid and to be more sensitive than the other modes by a factor of $\sqrt{2}$, however it typically results in not as good baselines as with position- or wobbler- switching. In all of these modes, it is assumed that signal of interest is the only thing that changes during the ON and OFF measurements, and the signal from all the other contributions hardly differ, so both can be easily distinguished, and thus the final spectrum is proportional to the difference of these two measurements.

3.4.6 Calibration

In the mm/sub-mm range, there are two main parameters that can have a large effect on the final T_A: the stability of the receiver system and the variations in Earth's atmosphere, therefore some corrections are needed to obtain well calibrated data. First, the receiver temperature, T_{rec} is determined and subtracted from the T_{sys} to determine $T_A = T_{sys} - T_{rec}$.

The calibration process used in the mm/sub-mm domain is referred to as the *chopper wheel* method (Penzias et al., 1973). This method consists of measuring the receiver output at two known temperatures, first on a cold load, often the blank sky, alternatively, it can be on liquid nitrogen $\sim$ 77 K, and then on a hot load that measures the ambient temperature $\sim$ 300 K. This is the so-called *hot-cold* calibration process. If we denote, *h* for "hot" and *c* for "cold" then the receiver output power is:

$$P_h = G(T_{rec} + T_h) \qquad P_c = G(T_{rec} + T_c) \tag{3.22}$$

where G is the total receiver gain. Then, the receiver noise temperature is determined by the ratio of P_h and P_c that gets rid of the gain, G:

$$\frac{P_h}{P_c} = \frac{T_{rec} + T_h}{T_{rec} + T_c} = Y \implies T_{rec} = \frac{T_h - Y\,T_c}{Y - 1} \tag{3.23}$$

T_{rec} is then subtracted from the total system temperature T_{sys} to determine the temperature of the source.

Concerning the atmospheric effects at mm/sub-mm wavelengths, the signal suffers attenuation by O_2 and H_2O molecules in the atmosphere which needs to be accounted for. The atmospheric effects at a given frequency ν can be described by the brightness temperature T_b of the source as :

$$T_b = T_s\, e^{-\tau_\nu} + T_{\text{atm}}(1 - e^{-\tau_\nu}) \tag{3.24}$$

where τ is the atmospheric opacity. The first term in the right-hand side of Eq. 3.24 decribes the attenuation of the source temperature T_s, while the second term describes the thermal emission and molecular absorption effects in the sky. T_s is also referred to T'_A, the antenna temperature in the absence of any atmospheric attenuation.

We can express the antenna temperature as :

$$T_A = T_s + T_{\text{sky}} + T_{\text{g}}$$

Using the *forward efficiency* of the telescope, the sky temperature can then be expressed as:

$$T_{sky} = F_{\text{eff}} T_{atm}(1 - e^{-\tau_\nu}) \tag{3.25}$$

The telescope also detects a fraction of the radiation from the ambient temperature, also called *ground* temperature, T_{gr}:

$$T_{gr} = (1 - F_{\text{eff}}) T_{\text{amb}} \tag{3.26}$$

Performing, the hot-cold calibration, the output voltages of the hot load and the sky:

$$V_{\text{load}} = G(T_{\text{amb}} + T_{\text{rec}}) \tag{3.27}$$

$$V_{\text{sky}} = G(T_{\text{sky}} + T_g + T_{\text{rec}}) \tag{3.28}$$

which implies:

$$V_{\text{sky}} = G[F_{\text{eff}} T_{\text{atm}}(1 - e^{-\tau_\nu}) + (1 - F_{\text{eff}}) T_{\text{amb}} + T_{\text{rec}}] \tag{3.29}$$

The temperature of the atmosphere is assumed to be very similar to the ambient temperature ($T_{amb} \approx T_{atm}$). By subtracting V_{load} from V_{sky}, one obtains a calibration signal with a voltage V_{cal}:

$$V_{cal} = G\, F_{eff}\, T_{amb}\, e^{-\tau_\nu} \tag{3.30}$$

Likewise, observing the source with the ON-OFF technique, the voltage of the observed source, V_s is given by:

$$V_s = G\, T'_A e^{-\tau_\nu} \tag{3.31}$$

Now that we determined V_{cal} and V_s from the hot-cold calibration method, we can combine these two quantities and estimate their ratio in order to determine the corrected antenna temperature :

$$\frac{V_s}{V_{cal}} = \frac{T'_A}{F_{eff}\, T_{amb}} \tag{3.32}$$

It is common to write :

$$T^*_A = \frac{V_s}{V_{cal}} T_{amb} = \frac{T'_A}{F_{eff}} \tag{3.33}$$

T^*_A is the corrected antenna temperature. It contains the amplitude from the target source corrected for the receiver and atmospheric effects.

3.4.7 Main Beam Brightness Temperature

The main beam brightness temperature T_{mb} of the source is related to T^*_A as:

$$T_{mb} = \frac{T'_A}{B_{eff}} = \frac{F_{eff}}{B_{eff}} T^*_A \tag{3.34}$$

3.5 IRAM 30m Telescope

The *Institut de Radio Astronomie Millimétrique* or *IRAM* is a French-German-Spanish collaboration that was founded by the French CNRS (Centre National de la Recherche Scientifique), the German MPG (Max-Planck-Gesellschaft) and the Spanish IGN (Instituto Geográfico Nacional). It operates two observatories in the (sub-)millimeter wavelength range: a 30-meter single dish telescope on Pico Veleta, Granada, Spain, and NOEMA, an interferometer of currently ten 15 m antennas on the Pic de Bure in the French Alps.

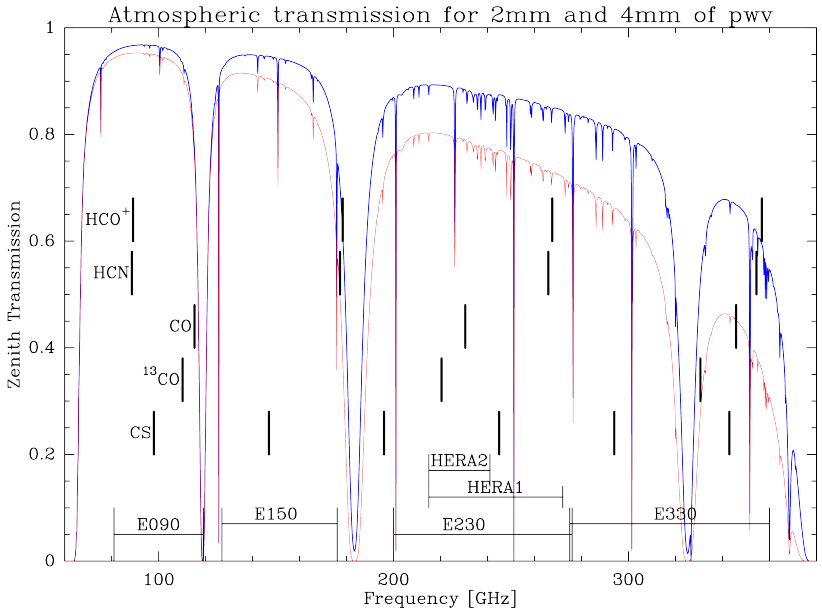

Figure 3.6: Atmospheric transmission at the IRAM 30m site between 60 and 400 GHz for 2 and 4 mm of precipitable water vapor, derived from the ATM model (Cernicharo, 1985; Pardo et al., 2001). The EMIR bands relevant for this PhD thesis are indicated, from `http://www.iram.es/IRAMES/mainWiki/EmirforAstronomers`.

The 30 m single dish of IRAM is the telescope used to collect the observational data in Part II. It was built in four years (1980 to 1984) and is located near 2900 m altitude on Pico Veleta, the third highest mountain of the Iberian peninsula, in Sierra Nevada, Granada, Spain. The large surface of the parabolic antenna, 30 m in diameter, makes it one of today's largest and most sensitive (sub-)millimeter telescopes in the world. The telescope is equipped with various heterodyne receivers and continuum cameras operating at 3, 2, 1, and 0.9 millimeters (covering frequencies between 70 and 375 GHz). When the IRAM 30m telescope observes at 0.9 mm, the angular resolution[†], θ, is 7.5 $''$.

The IRAM 30m telescope provides a powerful tool to study evolved stars since the frequency range contains the spectral lines of many circumstellar (and interstellar) molecules and offers a good atmospheric transparency (Fig. 3.6).

[†]The angular resolution of a telescope, θ, in radians is determined by the ratio of the wavelength of the radiation being collected, λ, to the diameter of the collecting dish, D, as $\theta = 1.22\frac{\lambda}{D}$.

Figure 3.7: Carrying out observations with the IRAM 30m telescope on-site. Photos by Sarah Massalkhi.

Table 3.1: Overview of the heterodyne receiver, EMIR, of the IRAM 30m telescope.

Telescope	EMIR	Frequency (GHz)	IF width (GHz)	HPWB (″)	Mixer Type
IRAM 30m	E0	73−117	8	34−21	2SB
	E1	125−184	8	20−13	2SB
	E2	202−274	8	12−9	2SB
	E3	277−350(375)	8	9−7(6)	2SB

Chapter 4

Molecules

4.1 Molecular Line Transitions

Molecules are typically identified in different astronomical environments by directly observing their spectra with telescopes. Molecules have discrete electronic, vibrational and rotational energy states according to quantum mechanics. Each electronic state of a molecule contains numerous vibrational levels, and each of those vibrational levels has a ladder of rotational levels corresponding to it. Spectral lines arise as a result of transitions between these discrete energy levels. Excitation to higher levels can occur via absorbing energy by collisions, mainly with H_2 (collisional excitation) or by photons (radiative excitation). Likewise, deexcitation to lower levels can occur via collision (collisional deexcitation) or by photon emission (radiative deexcitation). If a molecule goes from a higher energy state to a lower energy state, the emitted photon has an energy equal to the energy difference between both states:

$$\Delta E_{ul} = \frac{hc}{\lambda} = h\nu \tag{4.1}$$

where $\Delta E_{ul} = \mathrm{E}_u - \mathrm{E}_l$ is the energy difference between the levels u and l ($u > l$). Every transition of each molecular species corresponds to a particular frequency by which it can be identified in the observed spectra, as $h\nu = \Delta E_{ul}$ and the photons released or absorbed have a wavelength corresponding to $\lambda = hc/\Delta E_{ul}$.

Transitions in a molecule can be put into three different categories:

a) Electronic transitions occur due to the absorption or emission of energy which causes the electrons to jump to a different orbital. The transitions correspond to the visible and UV regions of the spectrum.

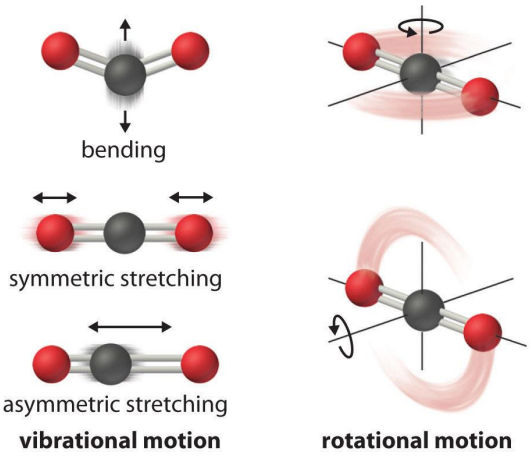

Figure 4.1: Vibrational and rotational motion of a carbon dioxide molecule. Adapted from Mike Blaber (Florida State University) ©.

b) Vibrational transitions are caused by oscillations of the relative positions of nuclei with respect to their equilibrium positions. Vibrations can take place in a "stretching" or a "bending" mode.

c) Rotational transitions are caused by the rotation of the nuclei around an axis that causes a change in the net dipole moment. These typically lie in the mm/sub-mm range. The transitions can occur between specific rotational levels of different vibrational states, called ro-vibrational transitions, or between rotational levels of the same vibrational state, called pure rotational transitions.

By far most of the molecular detections in circumstellar envelopes have been made in the mm wavelengths range which corresponds to pure rotational transitions owing to the relatively cool temperatures of the CSE. Vibrational transitions are also possible. IR photons arising from warm dust, and photons from the central star can be absorbed by the molecule to induce a vibrational excitation which can be re-emitted leaving the molecule in a rotationally excited state in the ground vibrational level. Rotational transitions at $v > 0$ can also occur as seen from SiO maser emission in CSEs (e.g., Bujarrabal et al. 1987; Cernicharo et al. 1992).

Molecules that undergo rotational transitions can be diatomic or polyatomic. Polyatomic molecules can be further divided into three different categories: linear molecules like HCN, symmetric tops like NH_3, and asymmetric tops like H_2O. Transitions between rotational levels can only occur if the molecule has a permanent dipole moment, μ (in cgs-unit Debye), i.e., the atoms in a molecule have substantially different electronegativity, thus the molecule

must be polar. Homonuclear diatomic molecules like H_2, N_2 and or O_2 do not possess permanent electric dipole moments and therefore cannot undergo allowed transitions. This is one reason why it is challenging to detect these species.

4.2 Rotational Spectra

In quantum chemistry and molecular physics, the rotational energy levels for a rotating molecule can be obtained by solving the time-independent Schrödinger equation:

$$H\Psi = -\frac{\hbar^2}{2\mu}\nabla^2\Psi = E\Psi \tag{4.2}$$

where H is the Hamiltonian of the system, Ψ is the wave function of the system, $\hbar$ is the reduced Planck constant and μ is the reduced mass. Using the *Born-Oppenheimer approximation*, which allows us to treat the motions of the electrons and the nuclei separately, one can separate the wavefunction for the motions of electrons Ψ_{electr} from the wavefunction for the motions of the nuclei Ψ_{nucl} (vibrational + rotational) as :

$$\Psi = \Psi_{\text{electr}}\Psi_{\text{rot}}\Psi_{\text{vib}} \tag{4.3}$$

$$E = E_{\text{electr}} + E_{\text{rot}} + E_{\text{vib}} \tag{4.4}$$

where $\mathrm{E}_{\text{electr}} \gg \mathrm{E}_{\text{rot}} \gg \mathrm{E}_{\text{vib}}$.

Diatomic and polyatomic linear molecules have one rotational axis, thus for both cases, the solution to the Schrödinger equation for molecular rotation of a rigid rotor gives the rotational energy levels by:

$$E_J = \frac{\hbar}{2I}J(J+1) \tag{4.5}$$

where J is the rotational quantum number or the total angular momentum (used to specify the rotational level of a molecule), and I is the moment of intertia which for a diatomic rigid rotor of nuclei A and B is given by:

$$I = \mu\, r^2 = \frac{m_A m_B}{m_A + m_B}r^2 \tag{4.6}$$

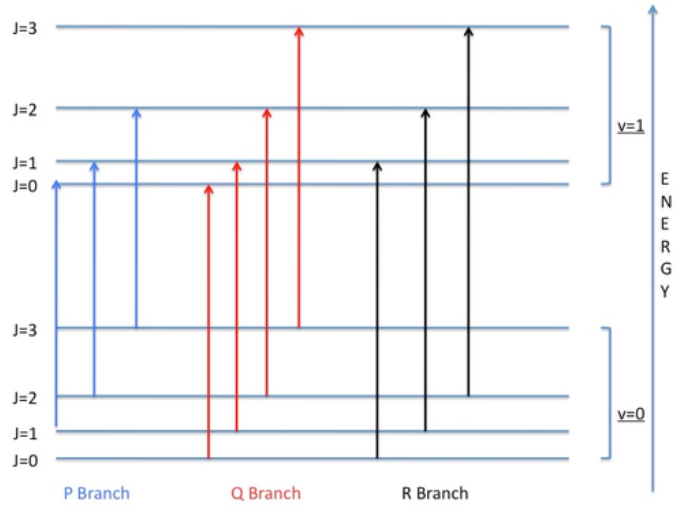

Figure 4.2: Schematic diagram of the P, Q, and R rotational transitions for two vibrational states. Photo credit: Chun-Yi Lin & Zhou Lu (University of California, Davis).

where r is the internuclear distance. The selection rules for linear molecules are $\Delta J = J(upper) - J(lower) = \pm 1$. For ro-vibrational transitions, the selection rule $\Delta J = -1$ gives rise to a *P-branch*, $\Delta J = +1$ to an *R-branch* and $\Delta J = 0$ to a *Q-branch* (Fig. 4.2).

With the rotational constant B in cm^{-1}:

$$B = \frac{\hbar^2}{2I} \tag{4.7}$$

Eq. 4.5 can be written as : $\mathrm{E}_J = \mathrm{B\,J(J+1)}$. The spacing between peaks in a rotational spectrum is related to the constant B. According to the equations above, B decreases as the mass of the nuclei increases, so the rotational energy levels will tend to be closer (and hence the wavelength is larger) for heavier molecules. What that means is, for example in the millimeter and submillimeter domain, for heavy species, several transitions are found close together.

Polyatomic nonlinear molecules are vastly different than linear molecules and require different considerations. Nonlinear molecules rotate about three principal axes and have moments of inertia, I_A, I_B, I_C, where A, B, and C are the orthogonal axes*. Symmetric tops have two rotational axes of the same inertia and one unique rotational axis with a different inertia. Symmetric tops can be classified into two categories: oblate where $\mathrm{I}_A = \mathrm{I}_B < \mathrm{I}_C$ and

*Linear molecules have $\mathrm{I}_A = \mathrm{I}_B$, and I_C=0. Rotation about the principal axis would result in I=0 since all the atoms lie along the axis, hence no angular momentum will be present in the direction of the principal axis.

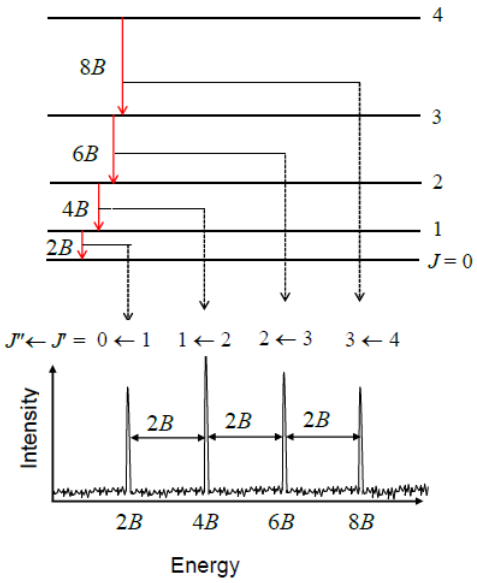

Figure 4.3: Illustration showing the rotational energy levels of linear molecules with the rotational constant B and the corresponding rotational spectrum obtained by lab experiments, `https://www.wikiwand.com/en/Rotational_spectroscopy`.

prolate where $I_A < I_B = I_C$. The rotational states of nonlinear molecules may then involve rotation about any molecular axis in space, i.e., the angular momentum may be oriented in any given direction in space. Therefore, there needs to be an additional quantum number, K, to describe the rotational states.

The rotational energies of symmetric tops are given by :

$$E(J,K) = \frac{\hbar^2}{2I_A} J(J+1) + \frac{\hbar^2}{2}\left(\frac{1}{I_A} - \frac{1}{I_B}\right) K^2 \tag{4.8}$$

where K is the quantum number that represents the projection of J on the principal axis of the molecule. The selection rules for symmetric top molecules are $\Delta K = 0$ and $\Delta J = 0, \pm 1$.

Asymmetric tops, have $I_A \neq I_B \neq I_C$. The energy levels are associated with quantum numbers J_{K_A,K_c}, where K_A and K_C are the projections of J on the A and C principal axes, respectively. The selection rules for asymmetric tops depend on the components of the permanent dipole moment, μ, along the A, B, and C axes. An example, when $\mu_A \neq 0$, $\Delta K_A = 0, \pm 2, \pm 4 \ldots$, $\Delta K_C = \pm 1, \pm 3 \ldots$; when $\mu_B \neq 0$, $\Delta K_A = \pm 1, \pm 3 \ldots$, $\Delta K_C = \pm 1, \pm 3 \ldots$; when $\mu_C \neq 0$, $\Delta K_A = \pm 1, \pm 3 \ldots$, $\Delta K_C = \pm 2, \pm 4, \ldots$.

Part II of this PhD thesis focuses on the analysis of rotational emission lines of various molecules in the intermediate parts of CSEs.

4.3 The spectral line of a molecular transition

When a molecule undergoes a transition from a higher energy level u to a lower energy level l, it emits a photon and produces a spectral line. The spectral line has a *natural line width* defined by the time the particle spends in the upper energy level before spontaneously decaying, also known as the *natural lifetime*. Since all transitions have this quantum mechanical characteristic, all spectral lines have a natural linewidth. In the absence of other effects, the shape of the line, or *line profile* is Lorentzian.

In astrophysical environments, there are additional mechanisms that widen the line beyond its natural width. The two main ones are *pressure broadening*, also known as *collision broadening*, and *doppler broadening*. The former is related to the physical state of the gas and becomes important in high densities such as dense stellar atmospheres. The latter is due to the collective motions of the gas molecules emitting the spectral line, these are local microscopic motions, such as *thermal* motions which characterize any gas at temperature T with particles in a Maxwellian velocity distribution, and *microturbulent* motions caused by the small-scale movement of the gas molecules. Each component (microturbulent and thermal) will produce a different Doppler shift, and the net result will be a superposition of all Doppler shifted lines that will yield a broadened line that has a *Guassian* line shape:

$$\phi(\nu) = \frac{1}{\Delta\nu\sqrt{\pi}}\, exp\left[-\left(\frac{\nu-\nu_0}{\Delta\nu}\right)^2\right] \tag{4.9}$$

where ν_0 is the rest frequency of the line, and $\Delta\nu$ is the linewidth related to the FWHM as :

$$\Delta\nu = \frac{\mathrm{FWHM}}{2\sqrt{\ln 2}} \tag{4.10}$$

The local linewidth is mainly determined by the microscopic motions, and those are the thermal and microtubulent components, having linewidths Δv_{kin} and Δv_{tur}, respectively. The local linewidth is expressed as :

$$\Delta\nu = \frac{\nu_0}{c}\sqrt{\Delta v_{kin}^2 + \Delta v_{tur}^2} \tag{4.11}$$

The thermal velocity component, Δv_{kin}, is determined from the gas kinetic temperature structure in the envelope as:

$$\Delta v_{kin} = \sqrt{\frac{2kT}{m}} \tag{4.12}$$

where T is the gas kinetic temperature, and m is the mass of molecule.

In circumstellar envelopes, the object of interest in this thesis, the spectral line broadening is dominated by the macroscopic expansion of the gas with a velocity, V_{exp}. The spectral line should then have a profile whose width reflects the maximum velocities of both sides, the advancing and receding sides of the envelope. The expansion velocity is then half of the line width, given by:

$$V_{\rm exp} = \frac{\Delta v}{2} \tag{4.13}$$

The velocity due to microturbulence, $\Delta v_{\rm tur}$, in CSEs is usually $\Delta v_{\rm tur} << V_{\rm exp}$ with typical values ranging between $0.65 - 1.5$ km s^{-1}, derived for the C-rich envelope IRC +10216 (De Beck et al. 2012; Skinner et al. 1999). This parameter has higher values and could have a higher contribution to the line broadening in the innermost regions of the envelope where the ejections of the matter from the stellar photosphere increase the velocity of the microturbulent motions and where the expansion velocity of the gas is still relatively low (Fonfría et al. 2008; Keady et al. 1988).

4.4 What does circumstellar molecular spectra tell us?

It's been said that the most satisfying and eloquent evidence is spectroscopic. Astronomers do not learn most about an object from its flux, but rather from its spectrum, the way in which the electromagnetic radiation is distributed with wavelength. Measuring the flux or brightness is like taking a glimpse at the cover of a book about the object, while measuring its spectrum is like opening the book and reading chapters that may explain the object's chemical composition and physical properties. Thus, by studying the spectrum, one can understand more about the nature of the object.

In what concerns CSEs, the CO molecule remains the primary probe of the main properties of circumstellar envelopes around AGB stars. Analysis of the CO line emission (e.g., half-width and strength of the CO lines) enables estimates of the physical properties of the CSE such as the gas expansion velocity, mass loss rate, density and temperature structure,

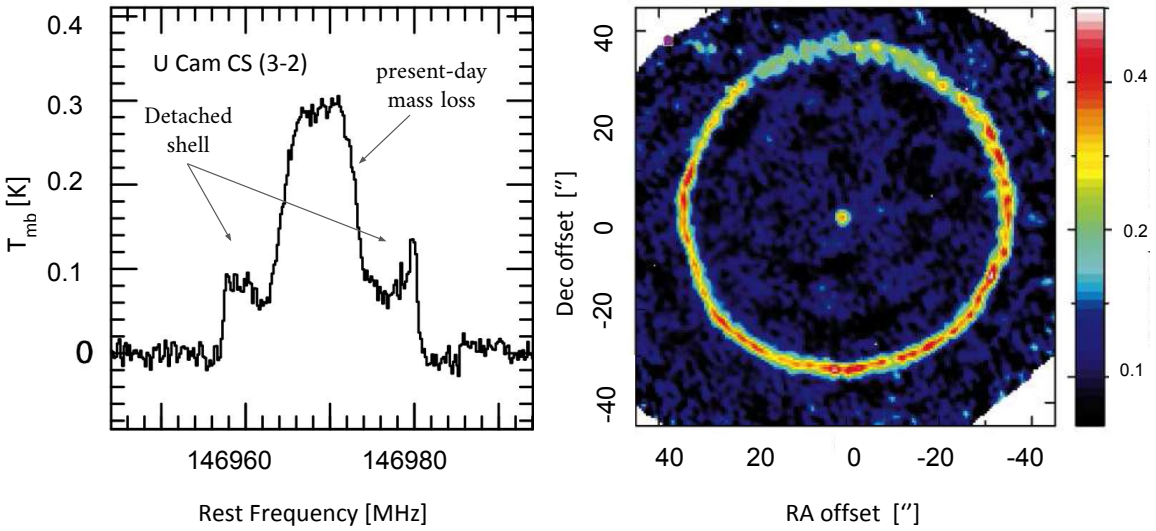

Figure 4.4: *left:* the CS $J = 3 - 2$ emission of U Cam obtained with the IRAM telescope (Massalkhi et al., 2019), *right:* CO $J = 1 - 0$ brightness map of the detached shell around TT Cyg obtained with the IRAM interferometer (Olofsson et al., 2000).

and the size of the envelope, in other words, the photodissociation radius, beyond which the interstellar UV photons destroy the CO molecules.

The CO spectral emission also provides information on the kinematics, dynamics and morphology of the CSE. For example, in the left panel of Fig. 4.4, CS emission towards the C-rich U Cam indicates a two-component line profile, one originating from the present-day wind, and one originating from a detached shell, suggesting episodic mass loss caused by a He-shell flash (i.e., a thermal pulse) (Olofsson et al. 1988, 1996; Schöier et al. 2005) and in the right panel, the CO line emission shows remarkable circular symmetry of the detached shell of the semiregular C-rich TT Cyg. Other examples include stars with high-velocity bipolar outflows, such as V Hya (Hirano et al., 2004; Knapp et al., 1997; Sahai et al., 2019). High signal-to-noise CO $J = 3 - 2$ and $J = 2 - 1$ line profiles reveal outflows at more than one velocity component indicating the presence of a very fast molecular outflow and a slow expanding one (Fig. 4.5).

The molecular spectra of CSEs do not only provide us with a wealth of information on the physical properties of CSEs, but also on the chemistry in these objects. Observations at mm/sub-mm wavelengths have allowed the measurement of pure rotational transitions of

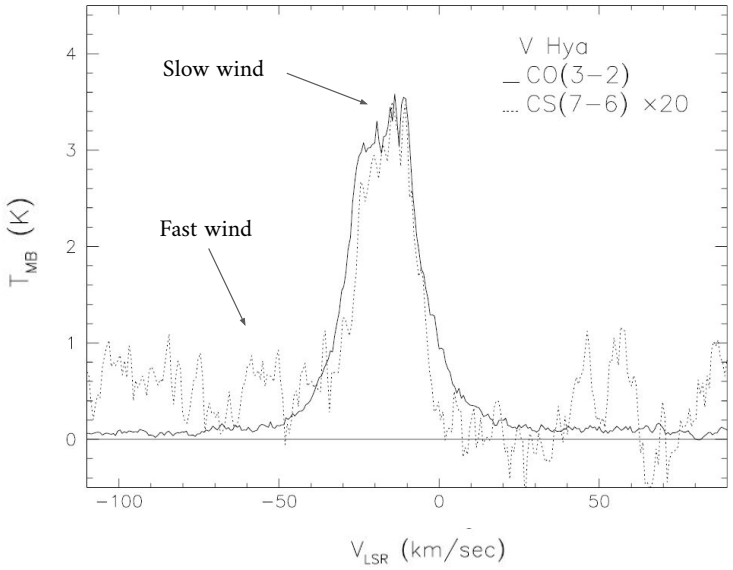

Figure 4.5: The CO $J = 3 - 2$ line profile of V Hya obtained with the CSO telescope revealing a very fast molecular wind, seen as weak emission extending to about $\pm$ 165 km s^{-1} and a slow wind seen at $\pm$ 15 km s^{-1} (Knapp et al., 1997).

numerous circumstellar molecules, giving insight about the chemical composition of CSEs in C-rich, O-rich and S-type CSEs (Chapter 2). There remains many unidentified features arising from unidentified species in the mm spectra (e.g., McCarthy et al. 2019; Ziurys et al. 2002). In addition, mid- (and far-) IR spectroscopy allowed for the discovery and measurement of many dust features such as SiC and MgS at 11.3 and 26-35 µm respectively and many molecular bands such as CO at 4.6 µm and C_3 at 5.2 µm. It has also made possible to identify species with no permanent dipole moment such as CH_4 and SiH_4. These observations have also allowed the direct link of molecular features to the dust content in AGB stars (e.g., Sloan et al. 2003).

The shape of the line profile can also tell us about the observed emission. In principle, the line profile is mainly determined by two factors: (i) the angular size of the emitting source relative to the size of the telescope beam and (ii) the opacity of the molecular line (e.g., Olofsson et al. 1982).

If the emitting source is unresolved by the beam of the telescope and the emission is optically thin, then the line profile is flat-topped (Fig. 4.6). This is because for an optically thin emission, the telescope beam is sensitive to emission coming from everywhere within

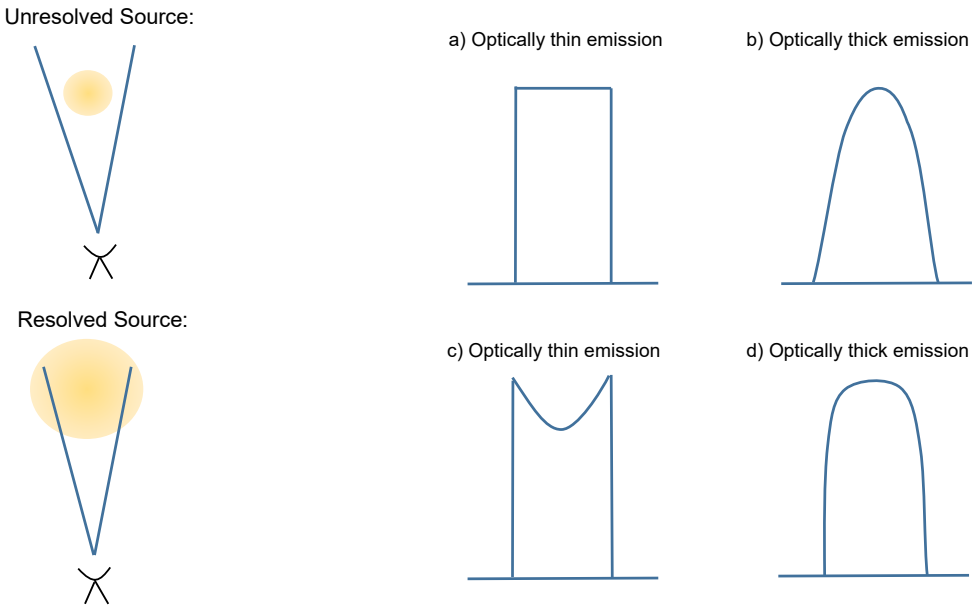

Figure 4.6: Illustration of the line profile shapes of molecular emission at mm wavelenths.

the source, and the line intensity would be proportional to the emission along the line of sight, so the antenna detects similar flux densities from all velocity components in the envelope, therefore, for geometrical reasons the line produced is flat-topped in shape. However, if the emitting source is unresolved by the beam of the telescope and the emission is optically thick, the line intensity is not proportional to the total emission along the line of sight, and the antenna does not detect emission from all the line of sight, then the line profile is parabolic.

On the other hand, if the *source is resolved* by the beam of the telescope, the line profile is double-peaked for an optically thin emission. This is due to the fact that the telescope is not sensitive to the most extended emission and it is this emission that contributes to the center of the line profile. And in the case where the emission is optically thick, the line profile is less parabolic than the unresolved optically thick case.

Chapter 5

Radiative Transfer and Molecular Excitation

5.1 Radiative Transfer

When we observe the circumstellar molecular line emission, we are basically detecting the emitted photons that have travelled throughout the circumstellar envelope before being collected by the telescope. As these photons propagate the CSE, they interact with the matter inside the envelope, undergoing processes such as absorption and emission. The general concepts of the interactions of the radiation with matter are described thoroughly by Mihalas, (1978) and Rybicki et al., (2008). These interactions are described mathematically by the radiative transfer equation for radiation of frequency ν:

$$\frac{dI_\nu}{ds} = -\alpha_\nu I_\nu + j_\nu \tag{5.1}$$

where I_ν is the specific intensity (in erg s^{-1} cm^{-2} Hz^{-1} sr^{-1}), s is the path length (in cm), α_ν is the absorption coefficient (in cm^{-1}), and j_ν is the emission coefficient (in erg s^{-1} cm^{-3} Hz^{-1} sr^{-1}). In the right-hand side of Eq. 5.1, the first term describes the removal of energy due to absorption, and the second term describes the input of energy due to emission. The scattering effects by dust grains are not included in Eq. 5.1.

α_ν and j_ν can be combined into the source function, S_ν, as:

$$S_\nu = \frac{j_\nu}{\alpha_\nu} \tag{5.2}$$

By defining the optical depth, τ_ν, as the measure of how transparent or opaque the emitting material along the line of sight is for a certain transition:

$$d\tau_\nu = \alpha_\nu \, ds \tag{5.3}$$

Eq. 5.1 can be re-written as:

$$\frac{dI_\nu}{d\tau_\nu} = -I_\nu + S_\nu \tag{5.4}$$

The formal solution of the radiative transfer equation is given by:

$$I_\nu(\tau) = I_\nu(0)\, e^{-\tau_\nu} + \int_0^{\tau_\nu} S_\nu(\tau') e^{-(\tau_\nu - \tau'_\nu)} d\tau'_\nu \tag{5.5}$$

where I_ν is the radiation emerging from the medium and $I_\nu(0)$ is the "background" radiation entering the medium. If the source function S_ν is constant in the region of interest, then Eq. 5.5 becomes:

$$I_\nu(\tau) = I_\nu(0)\, e^{-\tau_\nu} + S_\nu(1 - e^{-\tau_\nu}) \tag{5.6}$$

In the optically thin case ($\tau_\nu \to 0$), $I_\nu(\tau) = I_\nu(0) + [S_\nu - I_\nu(0)]\tau_\nu$. In the optically thick case ($\tau_\nu \to \infty$), $I_\nu(\tau) = S_\nu$.

5.2 Einstein Coefficients and Radiative Excitation

In Eq. 5.4, the properties of the matter are described using the absorption coefficient, α_ν, and the emission coefficient, j_ν, that are both macroscopic parameters and tend to be meaningless when considering line radiation of gas molecules. In this case, the Einstein coefficients provide a more convenient description to the interaction of the photons with the surrounding medium, that is, to microscopic systems.

For a molecular transtion between two states l (for "lower") and u (for "upper") where $E_u > E_l$, there are three radiative processes that affect I_ν: spontaneous emission, stimulated emission and absorption. The photon emitted or absorbed during a transition between the upper and lower energy levels will have an $h\nu = E_u - E_l$. Each of the radiative processes is associated with an Einstein coefficient which is a measure of the probability that a transition due to that particular process will take place:

1) A_{ul}: probability of a transition from u to l by spontaneous emission (in s^{-1}) defined by the Einstein A coefficient. This probability does not depend on any external condition such temperature, or the radiation field, but only on the nature of the transition. In

particular, it is related to the inverse of the time a particle spends in an excited state before dropping to a lower energy level.

2) $4\pi\bar{J}B_{ul}$: probability of a transition from u to l by stimulated emission (s^{-1}). It is determined by the product of the Einstein coefficient for stimulated emission, B_{ul}, and the existence of a suitable photon. If the molecule is in an isotropic radiation field, this photon may come from any direction, thus we describe the probability with $\bar{J}$, the intensity of the radiation field averaged over all directions. The incident photon essentially provides a stimulus that induces the molecule to drop down to the lower energy level immediately, emitting a photon. In reality, the emitted photons are not all precisely at the same frequency due to the number of effects that cause line broadening (Section 4.3). In fact, they are spread over a small range of frequencies characterized by the line profile function, $\phi(\nu)$, which describes the probability that a photon will be emitted at a particular frequency ν. The line profile function, ϕ (in Hz^{-1}), integrated over all frequencies is normalized according to $\int_0^\infty \phi(\nu)d\nu = 1$. Hence,

$$\bar{J} = \frac{1}{4\pi}\int_0^{4\pi} d\Omega \int_0^\infty I_\nu \, \phi(\nu)d\nu \tag{5.7}$$

$\bar{J}$ is called the profile-weighted mean intensity of the radiation field averaged over all angles and all frequencies.

3) $4\pi\bar{J}B_{lu}$: probability of a transition from l to u by absorption of a photon (s^{-1}). This definition is analogous to the previous one.

5.3 Relations between the Einstein coefficients

If we consider a molecule in thermodynamic equilibrium with the surrounding and n_u and n_l are the number densities of particles in energy levels u and l respectively, then we expect the number of radiative transitions to the energy level u are equal to the radiative transitions out of it. This is the principle of *detailed balancing*:

$$n_u A_{ul} + n_u B_{ul}\bar{J} = n_l B_{lu}\bar{J} \tag{5.8}$$

In thermodynamic equilibrium, the energy levels are populated according to the Boltzmann distribution as:

$$\frac{n_u}{n_l} = \frac{g_u}{g_l}\exp\left[-\frac{E_u - E_l}{kT}\right] = \frac{g_u}{g_l}\exp\left(-\frac{h\nu}{kT}\right) \tag{5.9}$$

where g_u and g_l are the statistical weights of energy levels u and l, respectively, and the energy distribution of the radiation field is given by the Planck function. Solving Eq. 5.8 for a certain $\bar{J}$, we notice then that the Einstein coefficients are not independent of each other, in fact they are coupled as:

$$B_{lu} = \frac{g_u}{g_l} B_{ul} \qquad A_{ul} = \frac{8\pi h\nu^3}{c^3} B_{ul} \tag{5.10}$$

We can now re-express α_ν and j_ν in terms of the Einstein coefficients in Eq. 5.10 and the line profile function $\phi(\nu)$. For the case of spontaneous emission, A_{ul} is the rate coefficient of how many photons of hν get emitted per particle in state u. So, the total rate per volume is then $A_{ul}n_u$ and that the energy, dE, per unit volume, dV, per unit time, dt, per unit solid angle, $d\Omega$, is:

$$\frac{dE}{dV\,dt\,d\Omega} = \frac{\Delta E_{ul} A_{ul} n_u}{4\pi} \tag{5.11}$$

The spontaneous emission is distributed over a frequency range following $\phi(\nu)$, then:

$$j_\nu = \frac{dE}{dV\,dt\,d\Omega\,d\nu} = \frac{h\nu}{4\pi} A_{ul}\, n_u\, \phi(\nu) \tag{5.12}$$

Similarly, for the case of absorption, the rate of photon absorption is given by $n_l B_{lu} I_\nu$. Therefore the rate of energy absorbed, dE, per unit volume, per unit time, per unit solid angle, per unit frequency, is:

$$\frac{dE}{dV\,dt\,d\Omega\,d\nu} = -\frac{h\nu}{4\pi} n_l B_{lu} I_\nu \phi(\nu) \tag{5.13}$$

Following the same line of reason for absorption, we can write for stimulated emission:

$$\frac{dE}{dV\,dt\,d\Omega\,d\nu} = \frac{h\nu}{4\pi} n_u B_{ul} I_\nu \phi(\nu) \tag{5.14}$$

We can view stimulated emission as negative absorption where the stimulated emission is a process that adds to the intensity of the radiation field, whereas absorption removes intensity from the radiation field, thus if we combine those two processes:

$$\frac{dE}{dV\,dt\,d\Omega\,d\nu} = -\frac{h\nu}{4\pi} \left[n_l B_{lu} - n_u B_{ul}\right] I_\nu \phi(\nu) \tag{5.15}$$

With $dV = dA\,ds$ and $dI_\nu = -I_\nu\,\alpha_\nu\,ds$, then we can write the absorption coefficient in terms of the Einstein A and B coefficients as:

$$\alpha_\nu = \frac{h\nu}{4\pi}(n_l B_{lu} - n_u B_{ul})\phi(\nu) = \frac{c^2 A_{ul} g_u}{8\pi\nu^2}\left(\frac{n_l}{g_l} - \frac{n_u}{g_u}\right)\phi(\nu) \tag{5.16}$$

We can re-express the source function, S_ν:

$$S_\nu = \frac{j_\nu}{\alpha_\nu} = \frac{2h\nu^3}{c^2}\left(\frac{g_u}{g_l}\frac{n_l}{n_u} - 1\right)^{-1} \tag{5.17}$$

In general, the level populations in two energy states u and l can be described by the *excitation temperature*, T_{ex}, as :

$$\frac{n_u}{n_l} = \frac{g_u}{g_l}\exp\left(-\frac{\Delta E_{ul}}{kT_{ex}}\right) \tag{5.18}$$

where $\Delta E_{ul} = E_u - E_l = h\nu$, that is, the excitation temperature is the temperature at which we would expect to find a system with a ratio of level populations according to the Boltzmann distribution. In other words, T_{ex} is not a real temperature; it is rather a measure of the ratio of n_u and n_l. In LTE conditions, T_{ex} is equal to the kinetic temperature of the gas, T_{kin}, such that $T_{ex} = T_{kin}$ and the populations are said to be *thermalized*. For $T = T_{ex} = T_{kin}$, that is when LTE holds and the level populations are described by the Boltzmann distribution (Eq. 5.18), the source function S_ν equals the Planck function B_ν (blackbody):

$$S_\nu = \frac{2h\nu^3}{c^2}\frac{1}{e^{h\nu/kT_{ex}} - 1} = B_\nu(T_{ex}) \tag{5.19}$$

In non-LTE conditions, the level populations can still be found through Eq. 5.18, however, T_{ex} will be different for every pair of levels. A system with $T_{ex} < T_{kin}$ is said to be *subthermally* excited, and a system with $T_{ex} > T_{kin}$ is said to be *suprathermally* excited.

The normal state of the system is when the lower energy state is more populated than the higher energy state ($n_l < n_u$). However, it is possible also that the higher energy state is overpopulated ($n_l > n_u$), which is called *inverted populations*. In this case, we have a negative excitation temperature, which leads to negative absorption coefficient α_ν (Eq. 5.16), so rather than a decrease along a ray, the intensity actually increases. Such a system is called a *maser*.

5.4 Collisional Excitation

The level population of molecules can also be changed by inelastic collisions with other abundant species, mainly H_2 and sometimes with He as another collision partner in CSEs, where kinetic energy is exchanged during the process. The transition probabilites or the rate collisions are given by:

4) C_{lu}: probability of a transition from l to u (s^{-1}), called collisional excitation

5) C_{ul}: probability of a transition from u to l (s^{-1}), called collisional de-excitation.

These collision rates are defined by:

$$C_{ul} = \gamma_{ul}\, n_{col}, \qquad C_{lu} = \gamma_{lu}\, n_{col} \tag{5.20}$$

where γ_{ul} and γ_{lu} are the downward and upward collisional rate coefficients in $cm^3\ s^{-1}$ and n_{col} is the number density of the collision partner in cm^{-3}, so that the collision rates are proportional to the density of colliders n_{col}, so by defining the γ-coefficients we are simply factoring out this dependence. In thermodynamic equilibrium we must again have detailed balancing for the collisional processes:

$$n_l C_{lu} = n_u C_{ul} \tag{5.21}$$

So,

$$C_{lu} = \frac{n_u}{n_l} C_{ul} = \frac{g_u}{g_l} C_{ul}\, e^{-h\nu/kT} \tag{5.22}$$

We can write:

$$\frac{\gamma_{lu}}{\gamma_{ul}} = \frac{g_u}{g_l}\, e^{-h\nu/kT} \tag{5.23}$$

In principle, the rate coefficient is the collision cross section, σ, averaged over the Maxwellian velocity distribution for a temperature T as:

$$\gamma_{ul} = \left(\frac{8kT}{\pi\mu}\right)^{-1/2} \left(\frac{1}{kT}\right)^2 \int_0^\infty \sigma E e^{-E/kT} dE \tag{5.24}$$

where k is the Boltzmann constant, μ is the reduced mass of the system, and E is the collision energy. The upward rates can then be obtained through Eq. 5.23.

These collisional rate coefficients are mainly determined theoretically by *ab initio* quantum mechanical calculations of molecule encounters and sometimes through experimental methods although the latter is more difficult. In some cases the rate coefficients are not available for collisions between the molecule of interest "X" and H_2 (the most abundant molecule in AGB CSEs), and for example are only available for He as a collision partner, in this case, the rate coefficients can be scaled to estimate those with H_2 as:

$$\gamma_{X-H_2} = \gamma_{X-He}\sqrt{\frac{\mu_{X-He}}{\mu_{X-H_2}}} \tag{5.25}$$

where μ is the reduced mass of the colliding system and γ_{X-H_2} and γ_{X-He} are the collision rates for H_2 and He respectively.

If we now consider all collisional and radiative processes for a two-level system, Eq. 5.8 can be modified into:

$$n_u(A_{ul} + B_{ul}\bar{J} + C_{ul}) = n_l(B_{lu}\bar{J} + C_{lu}) \tag{5.26}$$

In the absence of a radiation field, $\bar{J} = 0$, Eq. 5.26 simplifies to :

$$\frac{n_u}{n_l} = \frac{C_{lu}}{A_{ul} + C_{ul}} \tag{5.27}$$

If n_{col} is sufficiently high that collisional de-excitation happens much faster than spontaneous emission ($C_{ul} >> A_{ul}$), we can neglect the Einstein A coefficient, and this equation becomes the Boltzmann equation (Eq. 5.22). Hence, in high densities collisions dominate and the level populations are in LTE.

5.5 Statistical Equilibrium

Generally, the population of an energy level is determined by including all processes that populate and de-populate the level which include all de-excitations from higher levels and all excitations from lower levels by collisional (excitation and de-excitation), as well as radiative processes (spontaneous emission, absorption, and stimulated emission).

In a steady state, the molecular level populations do not change with respect to time ($\frac{dn_i}{dt} = 0$). In circumstellar envelopes, this is the case, because the typical transition rates are much faster than the typical evolution times of the physical conditions of the envelope, that is, the excitation timescales are shorter than the dynamical timescales. In a steady

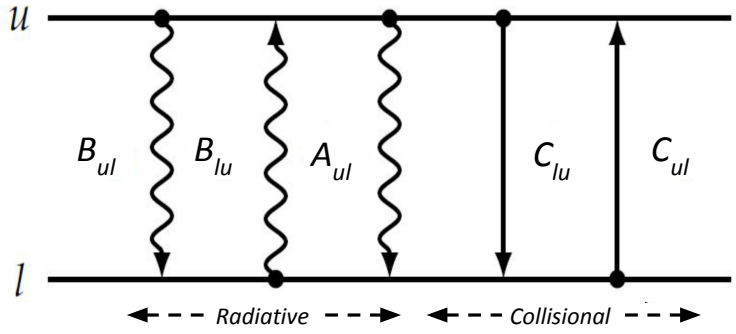

Figure 5.1: Schematic diagram showing the radiative and collisional processes and their respective transition probabilities between two energy levels, u and l, where $E_u > E_l$.

state, the transition rate into any level must be equal to the transition rate out of that level. This is the principle of *statistical equilibrium*. For a transition $i \rightarrow j$:

$$n_i \left[\sum_{j<i} A_{ij} + \sum_{j \neq i} (B_{ij}\bar{J} + C_{ij}) \right] = \sum_{j>i} n_j A_{ji} + \sum_{j \neq i} n_j (B_{ji}\bar{J} + C_{ji}) \tag{5.28}$$

The left-hand side of Eq. 5.28 represents the total number of transitions *out* of level i, ie., de-populating it and the right-hand side corresponds to the total transitions *into* level i from all other levels, i.e., populating it. So, to determine the level populations, statistical equilibrium equations are set up for each level which depend on the density of the particles n in each level, the radiation field $\bar{J}$, and the coefficients that describe the collisional and radiative transition probabilities (Eq. 5.28). The equations are then solved to determine the level populations, however, this is a complex problem not always easy to solve. The key problem lies in the determination of $\bar{J}$ which cannot be computed unless the source function (that is, the level populations) is known. On the one hand, solving the radiative transfer equation requires knowledge of the absorption coefficient, α_ν, and the source function, S_ν, which depend on the level populations according to Eq. 5.16 and Eq. 5.17 respectively, so I_ν (and hence $\bar{J}$ everywhere) depends on the level populations. On the other hand, the level populations depends on the radiation field $\bar{J}$ through the radiative transition probabilities, B_{ij} and B_{ji}, that determine how the levels are populated as seen in Eq. 5.28. Therefore, the statistical equilibrium equations are coupled to the radiative transfer equation along all frequencies ν. This results in a complex set of coupled equations that need to be solved

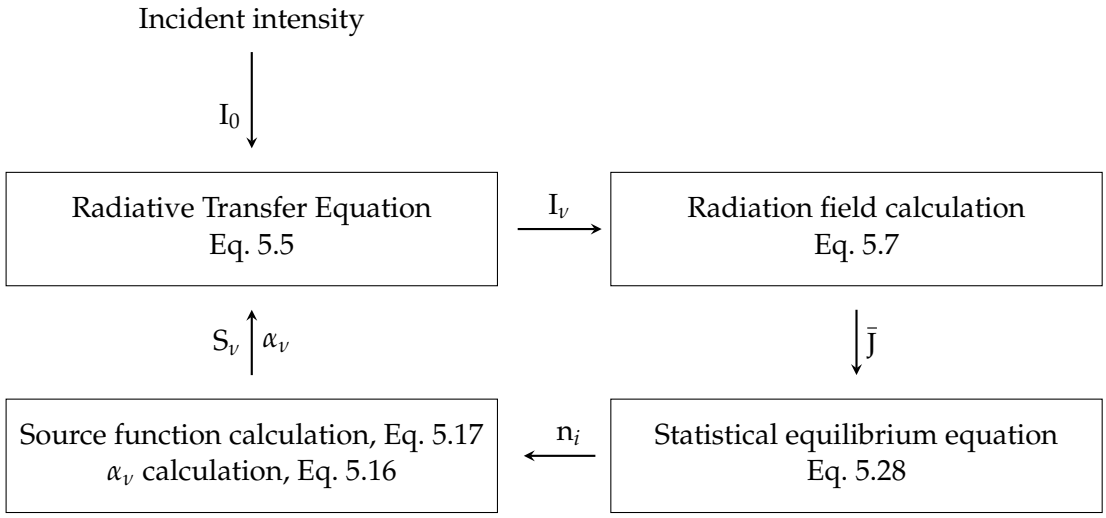

Figure 5.2: Flow diagram of the molecular line radiative transfer problem. Redrawn and adapted from Van Zadelhoff et al., (2002).

simultaneously in order to determine the level populations and radiation field for every frequency at every point of the medium. So the basic formulation of the problem is that the equation of the radiative transfer cannot be fully determined unless the source function and the absorption coefficient are determined. But these quantities depend on the level populations which cannot be determined unless the radiation field is known. Numerically, this can be solved by an iterative process as shown in Fig. 5.2 to evaluate all the quantities. To solve this problem, an initial level population has to be assumed. With these level populations, the radiative transfer is solved for I_ν and $\bar{J}$, which is inserted in Eq. 5.28 to calculate the new level populations. The steps are repeated until a convergence criterium is achieved.

Under certain assumptions the radiative transfer problem can be simplified. One is by assuming the gas is in thermodynamic equilibrium in which case the level populations are given directly by the Boltzmann equation (Eq. 5.18). Another is given by the concept of an escape probability where the photons produced locally can only be absorbed locally. Such a situation can be found in CSEs and will be described in the following section.

5.6 The LVG or Sobolev approximation

One of the commonly used direct methods of solving the radiative transfer problem and estimating the molecular excitation, i.e., the level populations, is the Large Velocity Gradient (LVG) approximation. It was first introduced by V. Sobolev and known as the *Sobolev*

approximation (Sobolev, 1957; Sobolev, 1960) and applied to the emission of atomic lines in circumstellar envelopes by Castor, (1970). It is also known as the *escape probability* approximation. The basic definition of the escape probability of photons is the probability that a photon emitted at a given point will escape the cloud and reach the observer without suffering absorption or scattering on its way. The escape of photons is greatly enhanced by the presence of macroscopic velocity fields – large velocity gradients, so that two distant regions are then radiatively decoupled from each other. This method is not only widely used in circumstellar envelopes of AGB stars but also in other astronomical environments such as molecular clouds.

When a molecule is excited by a radiative or a collisional event, a photon is then emitted at position r_1 in a specific direction with a frequency that corresponds to the transition between the two energy levels. Upon its flight, this photon can encounter another molecule of the same species at position r_2 and be absorbed and re-emitted with a different frequency in a different direction. This effect complicates the radiative transfer problem since it is non-local, that is, it can influence the level population at other positions. A simplified way to address this is the LVG approximation. LVG assumes that a sufficiently high velocity gradient exists between positions r_1 and r_2 (due to the outflow of the gas) compared to the width of the velocity distribution at either r_1 or r_2 (due to microturbulent and thermal motion of the gas) so that due to the Doppler effect that causes a shift in resonance frequencies, the photon emitted at r_1 will unlikely be absorbed at r_2*, this means that there is no radiative interaction between r_1 and r_2 and the two positions are radiatively decoupled. It is also assumed that where the points are radiatively coupled, for example at r_1, the physical conditions of the gas (e.g., gas kinetic temperature, gas density, etc) are the same, that is to say, the gas is in a steady state, so the level populations do not vary. With these two simplifications, $\bar{\mathrm{J}}$ and the level populations can be approximated locally, i.e., at each position, and the radiative transfer problem becomes a local one. In this Section, we briefly mention the formalism of the LVG approximation.

By defining an escape probability, β, that a photon emitted during a transition from a position r will escape the local region in any direction without being absorbed, and similarly β_c, that a photon escapes from the local region without being absorbed and strikes the stellar core, then $\bar{\mathrm{J}}$ (now local) can be written in terms of the source function as (Castor, 1970):

$$\bar{\mathrm{J}} = (1 - \beta)\, S_\nu + \beta_c I_{\nu,c} \tag{5.29}$$

*If the frequency shift is larger than the line width, then the photon is 'shifted out of the line' and can escape

where r is the radial distance from the center and $I_{\nu,c}$ is the specific intensity of the background radiation (i.e., continuum intensity). In the right term of Eq. 5.29, the left-hand side represents the contribution to $\bar{J}$ from the photons that did not escape the local region, whereas the right-hand side represents the contribution to $\bar{J}$ from the continuum photons that penetrated to that part of the envelope. In the case where no photons escape, $\beta = \beta_c = 0$, then $\bar{J} = S_\nu$. The escape probabilities, β and β_c, are expressed by:

$$\beta = \int_0^1 \frac{1 - e^{-\tau(r)}}{\tau(r)} d\mu\,, \qquad \beta_c = \frac{1}{2} \int_{[(1-(r_c/r)^2]^{1/2}}^1 \frac{1 - e^{-\tau(r)}}{\tau(r)} d\mu \tag{5.30}$$

where μ is the cosine of the angle between the ray and the outward radial direction and $\tau(r)$ is the optical depth along the path of the impact parameter $p = \sqrt{1-\mu^2}$ from $z = -\infty$ to $z = \sqrt{r^2 - p^2}$, and depends on the logarithmic velocity gradient $\frac{d\,lnv(r)}{d\,lnr}$ as:

$$\tau(r) = \frac{\tau_0(r)}{1 + \mu^2 \left(\frac{d\,lnv(r)}{d\,lnr} - 1 \right)}\,, \qquad \tau_0(r) = \frac{c^2 A_{ul} g_u}{8\pi\nu^2} \left(\frac{n_l}{g_l} - \frac{n_u}{g_u} \right) \frac{c\,r}{\nu\,v(r)} \tag{5.31}$$

where $\tau_0(r)$ is the optical depth along the path of the impact parameter from $z = -\infty$ to $z = +\infty$.

This shows that if β and β_c are known, then with Eq. 5.29 $\bar{J}$ can be estimated without actually solving the radiative transfer equation.

β and β_c are related to each other through the *geometric dilution factor*, $W(r, r_c)$, as $\beta_c = W(r, r_c)\,\beta$, where $W(r, r_c)$ is given by:

$$W(r, r_c) = \frac{1}{2} \left[1 - \left(1 - \frac{r_c^2}{r^2} \right)^{\frac{1}{2}} \right] \tag{5.32}$$

In LVG approximations, the velocity gradient is usually assumed to simply be $\frac{d\,lnv(r)}{d\,lnr} = 1$, so from Eq. 5.30:

$$\beta = \frac{1 - e^{-\tau}}{\tau} \tag{5.33}$$

where $\beta \sim 1$ in the optically thin case, and $\beta \sim 1/\tau$ in the optically thick case.

The LVG formalism is widely used to solve the radiative transfer problem in environments with large velocity gradients, those include circumstellar envelopes where the expansion velocity increases monotonically in the inner regions with a gradient steep enough to

ensure that the points are decoupled radiatively. This approach is known to provide good results even when the approximations of the method are only marginally satisfied, for example, where the velocity gradient is low (Bujarrabal et al., 2013). On the other hand, the LVG approach starts to fail at very high opacities ($\tau > 1$) where other approaches are then necessary to treat strong radiative coupling. An example of these is the Monte Carlo method, developed by Bernes, (1979) and described in Schöier et al., (2001) and Schöier et al., (2002). This method uses model photons that represent the photons of the transitions under study to simulate their absorptions and emissions through the medium. However, a disadvantage to the Monte Carlo method is that it is computationally expensive. Another approach is the Lambda Iteration and its more practical scheme, the Accelerated Lambda Iteration, developed by Rybicki et al., (1991, 1992) which uses a "Lambda Operator", Λ , to compute the mean radiation field $\bar{J}$. For a review on this method, see Van Zadelhoff et al., (2002).

5.7 Applying the LVG to a multishell circumstellar envelope

In this thesis, we used a code that was written by Dr. M. Agúndez to solve the radiative transfer problem in circumstellar envelopes using the LVG formalism. The ultimate goal of using the code is to analyze the molecular line observations in the circumstellar envelopes. This Section is dedicated to describing the application of the LVG method in CSEs and is largely based on Agúndez, (2009).

To solve the radiative transfer and molecular line excitation in CSEs, the envelope is divided radially into multiple concentric shells, where it is assumed that the physical and chemical conditions within each shell do not vary. The radiative transfer is then solved independently in each shell, starting from the inner shell to the outer one. The objective of this method is to determine the level populations and obtain a line profile to be compared with the observations.

To determine the level populations, the statistical equilibrium equation should be solved, which in turn requires the knowledge of the radiation field, $\bar{J}$:

$$\bar{J} = (1-\beta)\, S_\nu + \beta_c I_{\nu,c} \tag{5.34}$$

Both, gas and dust, will contribute to the absorption and emission coefficients:

$$j_\nu = j_{\nu,g} + j_{\nu,d} \qquad \alpha_\nu = \alpha_{\nu,g} + \alpha_{\nu,d} \tag{5.35}$$

where the subscript "g" refers to "gas" and the subscript "d" refers to "dust". The source function, S_ν, can then be expressed as:

$$S_\nu = \frac{j_{\nu,g} + j_{\nu,d}}{\alpha_{\nu,g} + \alpha_{\nu,d}} \tag{5.36}$$

where the gas emission and absorption coefficients, $j_{\nu,g}$ and $\alpha_{\nu,g}$, can be written as:

$$j_{\nu,g} = \frac{hc}{4\pi^{3/2}} \frac{n_u}{\Delta\nu} \qquad \alpha_{\nu,g} = \frac{c^3 A_{ul} g_u}{8\pi^{3/2}\nu^3 \Delta v} \left(\frac{n_l}{g_l} - \frac{n_u}{g_u} \right) \tag{5.37}$$

where Δv is the width of the local line profile expressed in velocity, i.e. $\Delta v = c\Delta\nu/\nu$. Whereas the dust emission and absorption coefficients, $j_{\nu,d}$ and $\alpha_{\nu,d}$, can be written as:

$$j_{\nu,d} = \alpha_{\nu,d}\, B_\nu(T_d) \qquad \alpha_{\nu,d} = \kappa_d \frac{\langle m_g \rangle n}{\rho_g/\rho_d} \tag{5.38}$$

where $B_\nu(T_d)$ is the Planck function at a temperature equal to the dust temperature, T_d, κ_d is the opacity of the dust (in cm^2 g^{-1}), m_g is the average mass of the gas particles, n is the number density of the gas particles, and ρ_g/ρ_d is gas-to-dust density ratio.

To evaluate the escape probability, β (Eq. 5.33), τ_ν, should be determined, which comprises the sum of both the gas and dust contributions, as:

$$\tau_\nu = \frac{c^3 A_{ul} g_u}{8\pi^{3/2}\nu^3 \Delta v} N_{mol} \left(\frac{x_l}{x_l} - \frac{x_u}{x_u} \right) + \kappa_d \frac{\langle m_g \rangle n}{\rho_g/\rho_d} N \tag{5.39}$$

where in the right-hand side of the Eq. 5.39, the first term represents the contribution to the optical depth from the gas, and the second terms represents the contribution to the optical depth from the dust, x_l and x_u are the level populations of the lower and upper level, respectively, N_{mol} is the column density of the molecules under consideration, and N is the total number of gas particles.

The specific intensity of the background radiation, $I_{\nu,c}$, is composed of three contributions within the shells, the cosmic microwave background, the radiation from the central star, and the thermal emission from the surrounding dust:

$$I_{\nu,c} = B_\nu(T_{cmb}) + I_\nu^* + I_\nu^d \tag{5.40}$$

where $B_\nu(T_{cmb})$ corresponds to the cosmic microwave background with T_{cmb} = 2.725 K, while I_ν^* corresponds to the radiation from the central star diluted geometrically and

attenuated by the material between the star and the shell in question, plus emission from the material present in the shells, and so we obtain an expression as the following:

$$I_\nu^* = \Big[\Big[B_\nu(T_\star)W(r,R_\star)e^{-\tau_{\nu,1}} + W(r,r_1)S_{\nu,1}(1-e^{-\tau_{\nu,1}})e^{-\tau_{\nu,,2}}\Big] + W(r,r_2)S_{\nu,2}(1-e^{-\tau_{\nu,2}})\Big] + ... \tag{5.41}$$

where $T_\star$ and $R_\star$ are the effective temperature and radius of the central star, W (r_i, r_j) is the geometric dilution factor (Eq. 5.32), and the subscripts 1, 2, ... refer to the number of the shell. Finally, I_ν^d corresponds to the background radiation emanated from the dust from the immediate external shell of the shell in question. The expression of I_ν^d is then similar to that of Eq. 5.41 except that there is no $B_\nu(T_\star)$ and the subscripts 1, 2, ... are replaced with N_s, (N_s being the number of shells), $N_s - 1$, ... until the shell that is lying directly above the shell in question, where then only τ_ν and S_ν contribute.

With all the equations and approximations described above that allowed for the determination of the source function, S_ν (Eq. 5.36), the escape probability, β (Eq. 5.33), and the specific intensity, $I_{\nu,c}$ (Eq. 5.40), it is now possible to determine the radiation field, $\bar{J}$ (Eq. 5.34). However, as described earlier, S_ν (through α_ν) and τ_ν, are dependeant on the level populations, as seen from Eq. 5.37 and Eq. 5.39, respectively. So, in order to proceed, we assume an initial level populations (e.g., Boltzmann distribution) from which we can evaluate S_ν and τ_ν, and then it would be possible to determine $\bar{J}$, which we use to solve the statistical equilibrium equations (Eq.5.28), which in turn will yield new level populations, that we can use to re-evaluate the value of $\bar{J}$. This iterative process is done in all of the shells from the innermost to the outer one until convergence is achieved.

It is then possible to calculate the emergent line profile from a technique called *ray-tracing technique* (see Fig. 5.3) where it is given as a function of the impact parameter, p, going from $z = -\infty$ to $z = +\infty$ (towards the observer), and the velocity, v :

$$\Phi(p,v,z) = \frac{c}{\sqrt{\pi}\nu_0\Delta v}\, exp\left[-\left(\frac{v + \frac{z}{(z^2+p^2)^{1/2}}v_{exp}}{\Delta v}\right)^2\right] \tag{5.42}$$

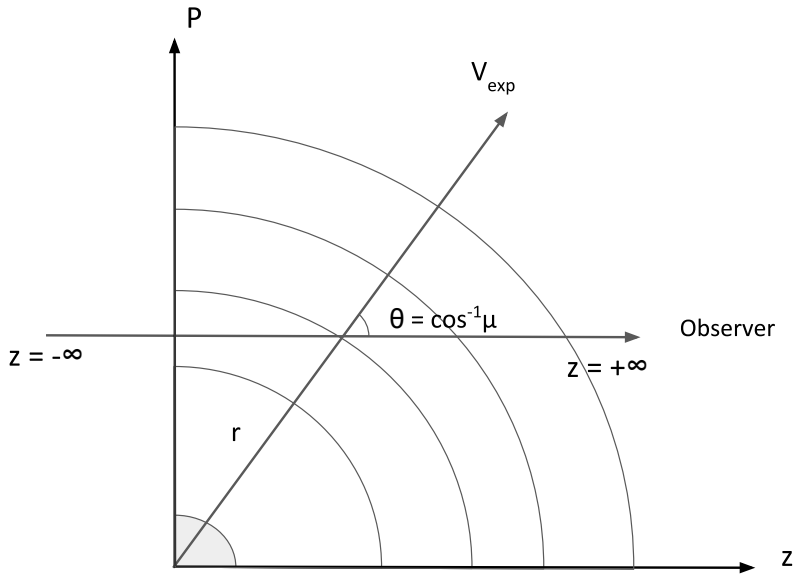

Figure 5.3: Schematic diagram of the ray tracing multishell CSE.

Part II

Estimating Molecular Abundances in the Envelopes of AGB Stars: Based on observations carried out with the IRAM 30 m Telescope

Chapter 6

Setting the Scene

6.1 Introduction (English)

6.1.1 Molecular and dusty circumstellar envelopes

Circumstellar envelopes (CSEs) around AGB stars are made of gas, primarily in the form of molecules, and dust. At the stellar photosphere, CO formation consumes all the carbon or oxygen due to its high stability and will be abundant. The remaining carbon or oxygen atoms will determine the type of molecular species and dust that will form, and will therefore give rise to either a carbon-rich or oxygen-rich environment. As such, parent molecules are produced in the inner regions of the envelope according to LTE chemistry. Non-LTE effects, such as shocks due to pulsations, can change the chemical composition by producing molecular species that are otherwise unexpected to be present. As the envelope expands, formation of dust will take place at the expense of molecules in a way that some molecular abundances will experience a decline because of adsorption onto dust, and hence grain growth. New molecules may be formed via grain-surface chemistry. The interstellar UV photons eventually destroy the molecules whereas the dust may survive and incorporate into the interstellar medium.

6.1.2 What makes circumstellar envelopes interesting to study?

The CSEs are the astronomical objects at the core of this thesis. Low and intermediate mass stars (< 8 $M_\odot$) that are on the asymptotic giant branch experience extensive mass loss up to rates of $\sim 10^{-4}$ $M_\odot$ yr^{-1} that gives rise to an expanding circumstellar envelope surrounding the central star. AGB stars are considered to be the main providers of dust to the galaxy through their strong stellar winds. The CSEs are characterized by a relatively simple geometry and kinematics which allow for a radially outward trajectory. As a consequence, these objects exhibit a range of physical conditions. Near the stellar photosphere, the material in

the envelope is gaseous, dense and warm with typical temperatures $\sim$ 2000 K, and densities $\sim 10^8$ cm^{-3}. As the matter flows away from the star, it expands and cools, and the physical conditions of the external parts of the envelope become similar to those of the interstellar medium, with temperatures $\sim$ 30 K and densities of a few particles per cm^{-3}. Therefore, the physical conditions in the very outer regions of the envelope are very different from those in the inner regions near the photosphere.

As a consequence of the density and temperature distribution of the particles decreasing considerably with distance from the star in the envelope, the circumstellar material undergoes changes in favor for the formation of various molecular species and dust grains, which makes them amongst the most remarkable chemical laboratories in the universe. It is thus fortunate that significant observational efforts over a broad range of wavelengths, have been put, both currently and during the past decades, to allow for the detailed study of these environments.

6.1.3 The motivating factor

Despite the important role of dust in various areas of astronomy, key aspects regarding its formation processes remain a mystery. Dust formation is a two-step process where (i) condensation nuclei of nanometer size are formed from some gas-phase precursors of highly refractory character near the surroundings of the stellar photosphere and (ii) the condensation nuclei grow to micrometer sizes as a consequence of accretion and coagulation processes. However, this picture remains poorly constrained from an observational point of view. It is not well understood how the transition between gas-phase molecules and solid phases occurs and what the gas-phase building blocks of dust grains are in CSEs, questions that serve as the driving motivation behind this thesis. We know that the formation of the first condensation nuclei must necessarily occur from gas-phase species present in the inner parts of the envelope, and the bulk of dust must be formed at the expense of gaseous species during the phase of grain growth. Since the gas around AGB stars is largely molecular, molecules are good candidates to serve as precursors of dust.

6.1.4 Knowledge prior to this thesis

Many have studied circumstellar envelopes of AGB stars. IRC +10216 in particular has been an important target to derive knowledge about circumstellar chemistry from an observational perspective due to it being one of the closest high-mass losing carbon-rich AGB

star. However, this situation is far from perfect, because in order to draw more general conclusions, it is necessary for studies to be done on larger samples. Efforts to derive molecular abundances in large samples have been done (e.g., Bujarrabal et al. 1994; Olofsson et al. 1993b), however they are based on simple modelling methods. More sophisticated methods that use detailed radiative transfer modelling have been carried out during the past years and these studies have provided hints as to which molecules could act as precursors of dust in the circumstellar envelopes of evolved stars. One of the first major studies of abundances in a large sample of AGB stars was performed by González Delgado et al., (2003), who investigated SiO in $\sim$ 40 M-type AGB star envelopes. Later on, Schöier et al., (2006) studied SiO in a sample of 19 C-rich AGB stars and similarly Ramstedt et al., (2009) in 26 S-type AGB stars. The SiO abundance estimates for all three chemical types are given as a function of the envelope density proxy, $\dot{M}/V_{\rm exp}$, (upper panel, Fig 6.1). Those studies found a trend of decreasing SiO abundance with increasing wind density, which is thought to be due to an increased depletion of SiO onto dust grains, a process more efficient at high densities owing to the enhanced collision rate between particles and the acceleration of accretion and coagulation processes. On the other hand, when Schöier et al., (2007) investigated SiS in a reduced sample of C-rich and M-type stars, they did not find a strong correlation of the circumstellar SiS with the density of the CSE (lower left panel, Fig 6.1), which could imply that SiS is less likely to be adsorbed onto dust grains than SiO in AGB envelopes. Similarly, the HCN fractional abundance shows no dependence on $\dot{M}/V_{\rm exp}$ (lower right panel, Fig 6.1) as investigated by Schöier et al., (2013) in a sample of 25 carbon star, 25 M-type AGB stars and 19 S-type AGB stars, which suggests that HCN, like SiS, is not affected by grain formation and/or evolution. However, there is a clear dependence of the circumstellar HCN and SiS abundance on the C/O-ratio of the star, in contrast to the circumstellar abundance of SiO that does not depend on the C/O ratio at the stellar surface.

6.1.5 Goal

Prior to this thesis, not much was known about molecular abundances in large samples of AGB stars apart from the studies done on SiO, SiS and HCN. How the molecular abundances behave from one AGB star to another, whether they show a differentiation based on the chemical type of the star or not, and how different parameters like the mass loss rate affect them, are questions that remain largely unanswered. Motivated by these, and by the question that is, *what are the main gas-phase precursors of dust around evolved stars and how important is their role in the dust formation process?*, we aim to investigate the possible candidates that could act as seed nuclei of dust in a large sample of AGB star envelopes.

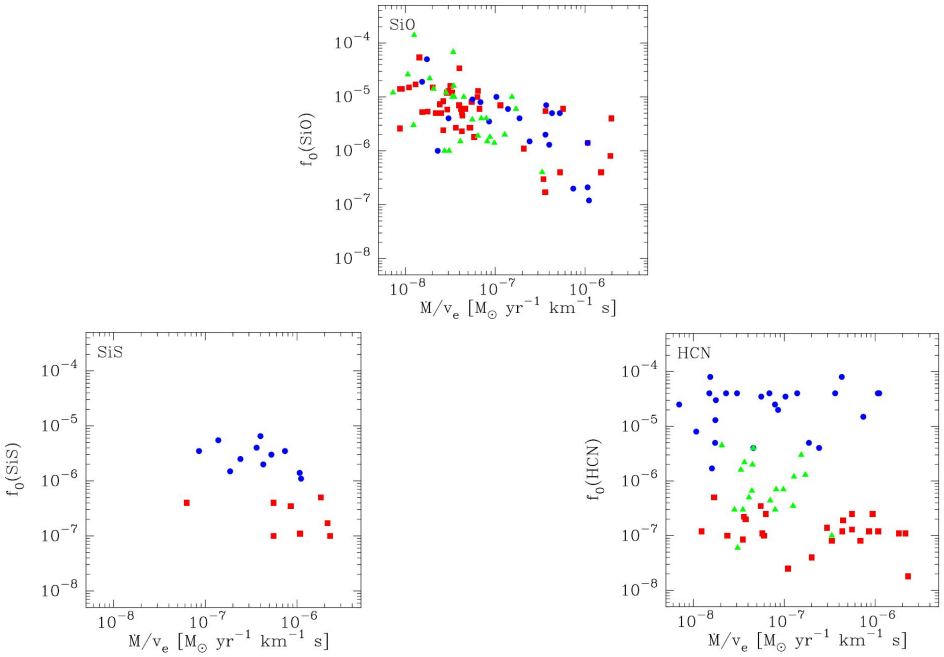

Figure 6.1: *Upper:* Fractional abundance of SiO, f_0(SiO), as a function of $\dot{M}/V_{\rm exp}$, for carbon stars (blue circles) from Schöier et al., (2006) M-type AGBs (red squares) from González Delgado et al., (2003), S-type (green triangles) from Ramstedt et al., (2009). *Lower left:* Fractional abundance of SiS, f_0(SiS), as a function of $\dot{M}/V_{\rm exp}$, for carbon stars (blue circles) and M-type AGB stars (red squares) from Schöier et al., (2007). *Lower right:* Fractional abundance of HCN, f_0(HCN), as a function of circumstellar density measure, $\dot{M}/V_{\rm exp}$, for carbon stars (blue squares), M-type AGB stars (red sqaures), and S-type AGB stars (green triangles) from Schöier et al., (2013).

Studies done on large samples allow for more meaningful conclusions to be drawn on the general behavior of circumstellar chemistry.

The molecular composition of C-rich envelopes is known to host a variety of abundant species, such as HCN, CO, C_2H_2, SiS, CS, SiO, and SiC_2 (Agúndez et al. 2012; Cernicharo et al. 2000), whereas in O-rich CSEs, some of the abundant molecules are CO, H_2O, SiS, SiO, SO and SO_2 (Justtanont et al. 2012; Velilla Prieto et al. 2017). We focus on the most likely molecular species that could act as seeds of dust around C-rich and O-rich envelopes. Our ultimate goal from these studies is to be able to derive abundances in a statistically meaningful sample and have an overall view of the behavior of the most abundant species. We aim at exploring how the abundances vary with parameters such as the chemical type and the mass loss rate. The latter is particularly interesting as circumstellar chemistry is expected to show variations depending on mass-loss rates which is one of the parameters that controls dust formation. Specifically, adsorption of gas molecules into dust grains is a process more efficient at high mass-loss rates since collisions between particles and coagulation processes become faster. Therefore, our goal is to survey a large sample of AGB stars in lines of abundant molecules, perform excitation and radiative transfer calculations to derive their abundances, and provide an overall view on the abundance and behavior of these molecules in the envelopes of AGB stars. Due to the large number of sources surveyed and limitations in the amount of telescope time that can be reasonably used, we could only observe a small number of lines for each molecule. All observations were carried out with the IRAM 30 m telescope in the λ 2 mm band.

6.1.6 Personal contribution

Apart from the observations performed in Chapter 7, all other observations were carried out by myself with the IRAM 30m telescope on-site at Pico Veleta, Granada and remotely at the Spanish National Observatory (OAN) in Madrid, Spain. I carried out the data reduction, and line identification in the spectra.

I modelled the molecular line emission using a radiative transfer code that was written by Dr. Marcelino Agúndez. The discussion of the results was done by me with regular consultation with my supervisor, Dr. Marcelino Agúndez. The thermochemical equilibrium calculations and the discussion of their results were done by Dr. Marcelino Agúndez.

6.2 Introduccíon (Español)

6.2.1 Envolturas circunestelares de gas molecular y polvo

Las envolturas circunestelares en torno a estrellas AGB están hechas de gas, principalmente en forma de moléculas y polvo. En la fotosfera estelar, la formación de CO consume todo el carbono u oxígeno (dependiendo de cuál sea menos abundante) debido a su elevada estabilidad. Los átomos de carbono u oxígeno restantes determinarán el tipo de moléculas y polvo que se formarán y, por lo tanto, darán lugar a un entorno rico en carbono o rico en oxígeno. Moléculas pequeñas y estables se forman en las regiones más internas de la envoltura en condiciones de equilibrio químico. Los efectos fuera del equilibrio, como los inducidos por choques debidos a las pulsaciones, pueden alterar la composición química produciendo moléculas que, de otro modo, serían muy poco abundantes. A medida que la envoltura se expande, la formación de polvo tendrá lugar a expensas de las moléculas gaseosas de forma que algunas moléculas disminuirán su abundancia debido a la adsorción sobre granos de polvo y, por lo tanto, al crecimiento de estos granos. Se pueden formar nuevas moléculas mediante la química en la superficie de los granos. En las regiones más externas de la envoltura, los fotones ultravioleta interestelares eventualmente destruyen las moléculas, mientras que el polvo puede sobrevivir e incorporarse al medio interestelar.

6.2.2 ¿Qué hace interesante el estudio de envolturas circunestelares?

Las envolturas circunestelares son los objetos astronómicos que forman el corazón de esta tesis. Las estrellas de masa pequeña e intermedia (< 8 $M_\odot$) que se encuentran en la fase AGB experimentan una importante pérdida de masa con tasas que pueden llegar hasta $\sim 10^{-4}$ $M_\odot$ yr^{-1}. Esta pérdida de masa da lugar a una envoltura circunestelar en expansión que rodea a la estrella central. Se considera que las estrellas AGB son las principales proveedoras de polvo a la galaxia a través de sus fuertes vientos estelares. Las envolturas circunestelares se caracterizan por una geometría y una cinemática relativamente simples en que la materia se mueve radialmente hacia afuera. Las condiciones físicas varían enormemente dependiendo de la región de la envoltura en que nos encontremos. Cerca de la fotosfera estelar, el material es gaseoso, denso, y caliente, con temperaturas típicas de ~ 2000 K y densidades de $\sim 10^8$ cm $^{-3}$. A medida que la materia se aleja de la estrella, se diluye y se enfría, y las condiciones físicas de las partes externas de la envoltura se vuelven similares a las del medio interestelar, con temperaturas ~ 30 K y densidades de unas pocas partículas por cm^{-3}. Por lo tanto, las condiciones físicas en las regiones más externas de la envoltura son muy diferentes a las de las regiones internas cercanas a la fotosfera.

Como consecuencia de que la densidad y la temperatura disminuyen considerablemente con la distancia a la estrella, el material circunestelar sufre transformaciones químicas con la formación de nuevas moléculas y de granos de polvo, lo que los sitúa entre los laboratorios químicos más interesantes en el Universo. Es por tanto una suerte que se hayan realizado importantes esfuerzos de observación en una amplia gama de longitudes de onda, tanto en la actualidad como durante las últimas décadas, para permitir el estudio detallado de estos entornos.

6.2.3 El factor de motivación

A pesar del importante papel del polvo en diversas áreas de la astronomía, existen numerosos aspectos clave de su formación que siguen siendo un misterio. La formación de polvo es un proceso de dos pasos donde (i) se forman núcleos de condensación de tamaño nanométrico a partir de algunos precursores en fase gaseosa de carácter altamente refractario en las inmediaciones de la estrella y (ii) los núcleos de condensación crecen a tamaños micrométricos como consecuencia de los procesos de acreción y coagulación. Sin embargo, este escenario está pobremente caracterizado desde un punto de vista observacional. No se comprende bien cómo se produce la transición entre las moléculas en fase gaseosa y las fases sólidas y cuáles son las especies precursoras de los granos de polvo, lo cual sirve como motivación para esta tesis. Sabemos que la formación de los primeros núcleos de condensación debe ocurrir necesariamente a partir de especies en fase gaseosa presentes en las partes internas de la envoltura, y la mayor parte del polvo debe formarse a expensas de las especies gaseosas durante la fase de crecimiento del grano. Dado que el gas alrededor de las estrellas AGB es en gran parte molecular, las moléculas son buenos candidatos para servir como precursores del polvo.

6.2.4 Conocimientos previos a esta tesis

Muchos han estudiado las envolturas circunestelares de estrellas AGB. IRC +10216 en particular ha sido un objeto importante para profundizar en el conocimiento de la química circunestelar desde una perspectiva observacional debido a que es una de las estrellas AGB rica en carbono con elevada pérdida de masa más cercana a nosotros. Sin embargo, esta situación está lejos de ser perfecta, ya que para sacar conclusiones más generales es necesario que los estudios se realicen en muestras más amplias. Se han realizado esfuerzos para derivar abundancias moleculares en muestras grandes (e.g., Bujarrabal et al. 1994; Olofsson et al. 1993b), sin embargo, se basan en métodos de modelado simples. Durante los últimos años se han llevado a cabo métodos más sofisticados que utilizan modelos detallados

de transporte de radiación y estos estudios han proporcionado pistas sobre qué moléculas podrían actuar como precursoras del polvo en las envolturas circunestelares de las estrellas evolucionadas. Uno de los primeros estudios importantes de abundancias en una gran muestra de estrellas AGB fue realizado por González Delgado et al., (2003), quien estudió SiO en una muestra de 40 envolturas de estrellas AGB ricas en oxígeno. Más tarde, Schöier et al., (2006) estudió SiO en una muestra de 19 estrellas AGB ricas en C y de manera similar Ramstedt et al., (2009) estudió SiO en 26 estrellas AGB de tipo S. En el panel central superior de la Fig 6.2 se muestran las abundancias de SiO derivadas para los tres tipos químicos en función del parámetro $\dot{M}/V_{\rm exp}$, que es una medida de la densidad de la envoltura. Estos estudios encontraron una tendencia en que la abundancia de SiO disminuye al aumentar la densidad de la envoltura, que se interpreta en términos de la desaparición de SiO de la fase gas para incorporarse a los granos de polvo, proceso que resulta más eficiente a altas densidades debido a un mayor ritmo de colisiones entre partículas y una aceleración de los procesos de acreción y coagulación. Por otro lado, cuando Schöier et al., (2007) investigó SiS en una muestra reducida de estrellas ricas en C y ricas en O, no encontraron una correlación clara entre la abundancia de SiS y la densidad de la envoltura (panel inferior izquierdo, Fig. 6.2), lo que podría implicar que es menos probable que SiS se deposite en granos de polvo que SiO. De manera similar, la abundancia de HCN no muestra dependencia con $\dot{M}/V_{\rm exp}$ (abajo a la derecha, Fig 6.2) según el estudio de Schöier et al., (2013) de una muestra de 25 estrellas ricas en C, 25 estrellas ricas en O, y 19 estrellas AGB de tipo S, lo que sugiere que el HCN, como el SiS, no se ve afectado por la formación y/o evolución de granos. Sin embargo, existe una clara dependencia de la abundancia de HCN y SiS con la relación C/O de la estrella, en contraste con la abundancia de SiO, que no depende de la relación C/O.

6.2.5 Objetivo

Antes de esta tesis no se sabía mucho sobre abundancias moleculares en grandes muestras de estrellas AGB, aparte de los estudios realizados sobre SiO, SiS y HCN. Cómo se comportan las abundancias moleculares de una estrella AGB a otra, si muestran una diferenciación basada en el tipo químico de la estrella y cómo los diferentes parámetros como la tasa de pérdida de masa les afectan son preguntas para las que no teníamos respuesta. Motivados por estas cuestiones, y por la pregunta *¿cuáles son los principales precursores del polvo en fase gaseosa alrededor de las estrellas evolucionadas y cuán importante es su papel en el proceso de formación de polvo?*, nuestro objetivo ha sido el de investigar los posibles candidatos que podrían actuar como precursores para la formaci'on de polvo en una amplia muestra de

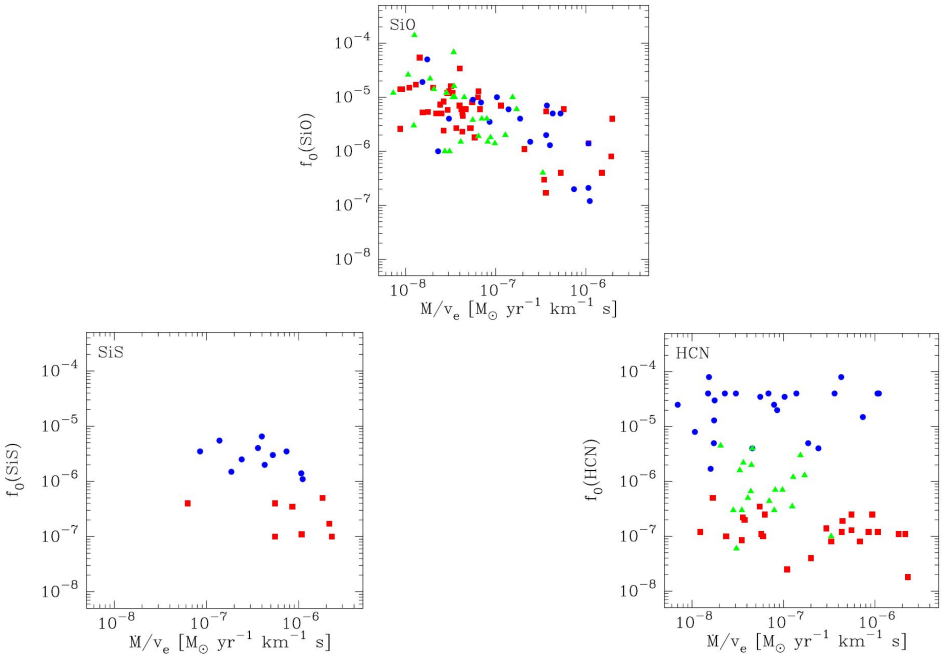

Figure 6.2: *Arriba:* Abundancia relativa a H_2 de SiO, f_0(SiO), en función de la medida de la densidad circunestelar, $\dot{M}/V_{\rm exp}$, para estrellas ricas en C (círculos azules; Schöier et al. 2006), estrellas ricas en O (cuadrados rojos; González Delgado et al. 2003), y estrellas de tipo S (triángulos verdes; Ramstedt et al. 2009). *Abajo a la izquierda:* Abundancia relativa a H_2 de SiS, f_0(SiS), en función de $\dot{M}/V_{rmexp}$, para estrellas ricas en C (círculos azules) y estrellas ricas en O (cuadrados rojos), según Schöier et al., (2007). *Abajo a la derecha:* Abundancia relativa a H_2 de HCN, f_0(HCN), en función de $\dot{M}/V_{\rm exp}$, para estrellas ricas en C (cuadrados azules), estrellas ricas en O (cuadrados rojos) y estrellas AGB de tipo S (triángulos verdes), según Schöier et al., (2013).

envolturas de estrellas AGB. Los estudios realizados en muestras grandes permiten extraer conclusiones estadśticamente significativas sobre cómo funciona la química circunestelar.

Se sabe que la composición molecular de las envolturas ricas en C alberga una variedad de especies abundantes, como HCN, CO, C_2H_2, SiS, CS, SiO, y SiC_2 (Agúndez et al. 2012; Cernicharo et al. 2000), mientras que en las envolturas ricas en O, algunas de las moléculas abundantes son CO, H_2O, SiS, SiO, SO and SO_2 (Justtanont et al. 2012; Velilla Prieto et al. 2017). En esta tesis nos hemos centrado en las moléculas abundantes que más probablemente podrían actuar como precursoras en la formación del polovo, tanto en envolturas ricas en C como en aquellas ricas en O. Pretendemos derivar abundancias en una muestra estadísticamente significativa y tener una visión general del comportamiento de las especies más abundantes. Nuestro objetivo es explorar cómo varían las abundancias dependiendo de parámetros como el tipo químico y la tasa de pérdida de masa. Esto último es particularmente interesante ya que se espera que la química circunestelar muestre variaciones dependiendo de la tasa de pérdida de masa, que es uno de los parámetros que controla la formación de polvo. Específicamente, la adsorción de moléculas de gas en granos de polvo es un proceso más eficiente a altas tasas de pérdida de masa, ya que las colisiones entre partículas y los procesos de coagulación se vuelven más rápidos. Para responder a estas cuestiones hemos estudiado una amplia muestra de estrellas AGB en líneas de moléculas abundantes, hemos realizado cálculos de excitación y transporte de radiación para determinar sus abundancias y proporcionar una visión general de la abundancia y el comportamiento de estas moléculas en envolturas de estrellas AGB. Debido a la gran cantidad de estrellas en nuestra muestra y las limitaciones en la cantidad de tiempo del telescopio que se puede usar razonablemente, hemos restringido las observaciones a un pequeño número de líneas para cada molécula. Todas las observaciones se realizaron con el telescopio IRAM 30 m en la banda λ 2 mm.

6.2.6 Contribución personal

Todas las observaciones presentadas en esta tesis han sido llevadas a cabo por mḿisma, a excepción de las observaciones de SiC_2 presentadas en el Capítulo 7. Las observaciones se llevaron a cabo con el telescopio IRAM 30-m in situ en Pico Veleta (Granada) y de forma remota en el Observatorio Astron'omico Nacional (OAN) en Madrid. Yo misma llevé a cabo la reducción de los datos y la identificación de las líneas en los espectros.

Además, he llevado a cabo el modelado de las línea moleculares observadas usando un código deexcitación y transporte de radiación que fue escrito por el Dr. Marcelino Agúndez.

La discusión de los resultados fue realizada por mí, en consulta regular con mi supervisor, el Dr. Marcelino Agúndez, quien realizó los cálculos de equilibrio termoquímico.

Chapter 7

Abundance of SiC_2 in carbon star envelopes

This chapter is based on the publication:

Abundance of SiC_2 in carbon star envelopes*:
Evidence that SiC_2 is a gas-phase precursor of SiC dust

S. Massalkhi, M. Agúndez, J. Cernicharo, L. Velilla Prieto, J. R. Goicoechea, G. Quintana-Lacaci, J. P. Fonfría, J. Alcolea, and V. Bujarrabal

ASTRONOMY & ASTROPHYSICS, A&A, 611, A29 (2018)

*Based on observations carried out with the IRAM 30m Telescope. IRAM is supported by INSU/CNRS (France), MPG (Germany), and IGN (Spain).

ABSTRACT

Context: Silicon carbide dust is ubiquitous in circumstellar envelopes around C-rich asymptotic giant branch (AGB) stars. However, the main gas-phase precursors leading to the formation of SiC dust have not yet been identified. The most obvious candidates among the molecules containing an Si–C bond detected in C-rich AGB stars are SiC_2, SiC, and Si_2C. To date, the ring molecule SiC_2 has been observed in a handful of evolved stars, while SiC and Si_2C have only been detected in the C-star envelope IRC +10216.

Aims: We aim to study how widespread and abundant SiC_2, SiC, and Si_2C are in envelopes around C-rich AGB stars, and whether or not these species play an active

role as gas-phase precursors of silicon carbide dust in the ejecta of carbon stars.

Method: We carried out sensitive observations with the IRAM 30m telescope of a sample of 25 C-rich AGB stars to search for emission lines of SiC_2, SiC, and Si_2C in the λ 2 mm band. We performed non-LTE excitation and radiative transfer calculations based on the LVG method to model the observed lines of SiC_2 and to derive SiC_2 fractional abundances in the observed envelopes.

Results: We detect SiC_2 in most of the sources, SiC in about half of them, and do not detect Si_2C in any source except IRC +10216. Most of these detections are reported for the first time in this work. We find a positive correlation between the SiC and SiC_2 line emission, which suggests that both species are chemically linked; the SiC radical is probably the photodissociation product of SiC_2 in the external layer of the envelope. We find a clear trend where the denser the envelope, the less abundant SiC_2 is. The observed trend is interpreted as evidence of efficient incorporation of SiC_2 onto dust grains, a process that is favored at high densities owing to the higher rate at which collisions between particles take place.

Conclusion: The observed behavior of a decline in the SiC_2 abundance with increasing density strongly suggests that SiC_2 is an important gas-phase precursor of SiC dust in envelopes around carbon stars.

7.1 Introduction

In this Chapter, we perform an observational study to constrain the main gas-phase precursors of silicon carbide (SiC) dust in C-rich AGB stars. The presence of SiC dust in circumstellar envelopes around C-rich AGB stars was established through the observation of a solid-state emission band at $\sim$11.3 μm (Hackwell, 1972; Treffers et al., 1974). The 11.3 μm feature has been observed toward a large number of C-rich AGB stars with the *IRAS* and *ISO* satellites (e.g., Chan et al. 1990; Little-Marenin 1986; Yang et al. 2004). However, what the gas-phase precursors of SiC dust are is still a pending question.

Various molecules containing an Si−C bond have been observed in envelopes around C-rich AGB stars and are potential gas-phase precursors of SiC dust. The ring molecule SiC_2 has long been observed in the atmospheres of optically visible carbon stars through the Merrill–Sanford electronic bands (see, e.g., Sarre et al. 2000). Thaddeus et al., (1984) reported the first observation of the rotational spectrum of SiC_2 toward the highly reddened envelope IRC +10216; since then observations of this molecule have been reported in only

a few other C-rich AGB or post-AGB objects: IRAS 15194−5115 (Nyman et al., 1993), CRL 2688 (Bachiller et al., 1997), CIT 6 (Zhang et al., 2009c), and CRL 3068 (Zhang et al., 2009b). The diatomic molecule SiC was found by Cernicharo et al., (1989) in IRC +10216, and more recently Cernicharo et al., (2015a) have reported on the discovery of Si_2C toward the same source. IRC +10216 is the only source where SiC_2 has been thoroughly studied across the mm and sub-mm ranges (Cernicharo et al., 2010; Fonfría et al., 2014; Lucas et al., 1995; Müller et al., 2012; Patel et al., 2011; Velilla Prieto et al., 2015) and where SiC and Si_2C detections have been reported. The scenario emerged from the studies of IRC +10216 is that only SiC_2 and Si_2C are present in the innermost regions, while SiC is probably a photodissociation product of these two triatomic molecules and it is thus present in the outer envelope. The U-shaped line profiles of SiC (Cernicharo et al., 2000) and the upper limits derived to its abundance in the inner envelope (Velilla Prieto et al., 2015) support this idea. Moreover, chemical equilibrium calculations predict abundant SiC_2 and Si_2C but little SiC in the hot and dense surroundings of the AGB star (Cernicharo et al., 2015b; Tejero et al., 1991; Yasuda et al., 2012). It therefore seems that the gas-phase molecule SiC is not an important building block of SiC dust, while SiC_2 and Si_2C are probably the main gas-phase precursors. In addition to these species, other molecules containing an Si−C bond detected in IRC +10216 are SiC_3 (Apponi et al., 1999b), SiC_4 (Ohishi et al., 1989b), SiCN (Guélin et al., 2000), SiH_3CN, and CH_3SiH_3 (Agúndez et al., 2014; Cernicharo et al., 2017), but their abundances are low and the observed line profiles suggest that they are formed in the external layers of the envelope.

Most of our knowledge about the role of the SiC_2, SiC, and Si_2C molecules as gas-phase precursors of silicon carbide dust comes from the study of IRC +10216, but little is known about how widespread these molecules are in other carbon stars, what their relative abundances are, and what their role in the formation of SiC dust is. Here we present the results of a systematic survey carried out with the IRAM 30m telescope to observe these three molecules in a sample of 25 C-rich AGB stars. We report the detection of SiC_2 in most of the sources and of the radical SiC in about half of them. The sample of stars and observational details are presented in Section 7.2 and the main results obtained from the observations in Section 7.3. In Section 7.4 we describe the model and the excitation and radiative transfer calculations, and discuss the results from these calculations in Section 7.5. Finally, we discuss the implications of the derived SiC_2 abundances in Section 7.6, and present our conclusions in Section 7.7.

Table 7.1: Sample of carbon stars

Name	R.A. J2000.0	Dec. J2000.0	$V_{\rm LSR}$ (km s^{-1})	D (pc)	$T_\star$ (K)	$L_\star$ ($L_\odot$)	$\dot{M}$ ($M_\odot$ yr^{-1})	$V_{\rm exp}$ (km s^{-1})	$T_{\rm d}(r_c)$ (K)	r_c (cm)	Ψ
IRC +10216	09:47:57.45	+13:16:43.9	−26.5	130 [a]	2330 [a]	8750 [a]	2.0×10^{-5} [a]	14.5	800 [a]	2.0×10^{14} [a]	300 [a]
CIT 6	10:16:02.27	+30:34:18.6	−1	440 [g]	1800 [g]	10000 [g]	6.0×10^{-6} [g]	17	1000 [g]	2.1×10^{14} [g]	141 [d]
CRL 3068	23:19:12.24	+17:11:33.4	−31.5	1300 [g]	1800 [g]	10900 [g]	2.5×10^{-5} [g]	14.5	1500 [g]	2.0×10^{14} [g]	174 [d]
S Cep	21:35:12.83	+78:37:28.2	−15.3	380 [k]	2200 [k]	7300 [k]	1.2×10^{-6} [k]	22.5	1400 [k]	5.8×10^{13} [k]	360 [d]
IRC +30374	19:34:09.87	+28:04:06.3	−12.5	1200 [j]	2000 [j]	9800 [j]	1.0×10^{-5} [j]	25	1000 [j]	2.2×10^{14} [j]	1008 [d]
Y CVn	12:45:07.83	+45:26:24.9	+22	220 [k]	2200 [k]	4400 [k]	1.5×10^{-7} [k]	7	1500 [k]	8.7×10^{13} [k]	500 [h]
LP And	23:34:27.53	+43:33:01.2	−17	630 [g]	1900 [g]	9600 [g]	7.0×10^{-6} [g]	14.5	1100 [g]	1.8×10^{14} [g]	288 [d]
V Cyg	20:41:18.27	+48:08:28.8	+13.5	366 [g]	2300 [g]	6000 [g]	1.6×10^{-6} [g]	12	1400 [g]	9.4×10^{13} [g]	364 [d]
UU Aur	06:36:32.84	+38:26:43.8	+6.7	260 [k]	2800 [k]	6900 [k]	2.4×10^{-7} [k]	10.6	1500 [k]	6.3×10^{13} [k]	11111 [b]
V384 Per	03:26:29.51	+47:31:48.6	−16.8	560 [k]	2000 [k]	8100 [k]	2.3×10^{-6} [b]	15.5	1300 [k]	1.0×10^{14} [k]	584 [d]
IRC +60144	04:35:17.54	+62:16:23.8	−48.8	1030 [b]	2000 [b]	7800 [b]	3.7×10^{-6} [b]	19.5	1200 [n]	2.0×10^{14} [b]	11 [b]
U Cam	03:41:48.17	+62:38:54.4	+6	430 [i]	2695 [i]	7000 [i]	2.0×10^{-7} [i]	13	1500 [j]	4.4×10^{13} [j]	833 [i]
V636 Mon	06:25:01.43	−09:07:15.9	+10	880 [f]	2500 [n]	8472 [e]	5.8×10^{-6} [f]	20	1200 [n]	1.7×10^{14} [n]	300 [n]
IRC +20370	18:41:54.39	+17:41:08.5	−0.8	600 [k]	2200 [k]	7900 [k]	3.0×10^{-6} [b]	14	1500 [k]	8.1×10^{13} [k]	266 [d]
R Lep	04:59:36.35	−14:48:22.5	+11.5	432 [b]	2200 [b]	5500 [b]	8.7×10^{-7} [b]	17.5	1000 [g]	1.8×10^{14} [b]	2000 [b]
W Ori	05:05:23.72	+01:10:39.5	−1	220 [k]	2600 [k]	3500 [k]	7.0×10^{-8} [k]	11	1500 [k]	4.3×10^{13} [k]	333 [h]
CRL 67	00:27:41.10	+69:38:51.5	−27.5	1410 [d]	2500 [n]	9817 [d]	1.1×10^{-5} [d]	16	1200 [n]	1.8×10^{14} [n]	495 [d]
CRL 190	01:17:51.62	+67:13:55.4	−39.5	2790 [d]	2500 [c]	16750 [d]	6.4×10^{-5} [d]	17	1000 [c]	4.7×10^{14} [c]	424 [d]
S Aur	05:27:07.45	+34:08:58.6	−17	300 [k]	3000 [k]	8900 [k]	4.0×10^{-7} [k]	24.5	1500 [k]	7.3×10^{13} [k]	500 [h]
V Aql	19:04:24.15	−05:41:05.4	+53.5	330 [k]	2800 [k]	6500 [k]	1.4×10^{-7} [k]	8	1500 [k]	6.1×10^{13} [k]	500 [h]
CRL 2513	20:09:14.25	+31:25:44.9	+17.5	1760 [d]	2500 [c]	8300 [c]	2.0×10^{-5} [d]	25.5	1200 [c]	1.6×10^{14} [c]	453 [d]
CRL 2477	19:56:48.43	+30:43:59.9	+5	3380 [m]	3000 [m]	13200 [m]	1.1×10^{-4} [m]	20	1800 [m]	2.8×10^{14} [m]	532 [d]
CRL 2494	20:01:08.51	+40:55:40.2	+29	1480 [b]	2400 [b]	10200 [b]	7.5×10^{-6} [b]	20	1200 [n]	2.3×10^{14} [b]	436 [d]
RV Aqr	21:05:51.74	−00:12:42.0	+0.5	670 [k]	2200 [k]	6800 [k]	2.3×10^{-6} [b]	15	1300 [k]	7.6×10^{13} [k]	200 [h]
ST Cam	04:51:13.35	+68:10:07.6	-13.6	360 [k]	2800 [k]	4400 [k]	1.3×10^{-7} [k]	8.9	1500 [k]	5.0×10^{13} [k]	500 [h]

References: [a] Agúndez et al. (2012), [b] Danilovich et al. (2015), [c] Groenewegen et al. (1998), [d] Groenewegen et al. (2002), [e] Guandalini et al. (2013), [f] Guandalini et al. (2006) [g] Ramstedt et al. (2014), [h] Schöier & Olofsson et al. (2001), [i] Parameters of the present-day wind of U Cam from Schöier et al. (2005), [j] Schöier et al. (2006), [k] Schöier et al. (2013), [m] Speck et al. (2009), [n] Assumed value for the stellar effective temperature $T_\star$ is 2500 K, for the condensation radius r_c is 5 $R_\star$, for the dust temperature at the condensation radius $T_{\rm d}(r_{\rm c})$ is 1200 K, and for the gas-to-dust mass ratio Ψ is 300.

7.2 Observations

The observations were carried out in February and May 2016 with the IRAM 30m telescope, located at Pico Veleta (Spain). We selected a sample of 25 C-rich AGB stars with intense molecular emission, mainly based on the intensity of the HCN $J = 1 - 0$ line (Bujarrabal et al., 1994; Loup et al., 1993; Schöier et al., 2013). The list of sources and their parameters are given in Table 7.1. The coordinates and LSR systemic velocities were taken from the literature (Cernicharo et al., 2000; Groenewegen et al., 1996b, 2002; Olofsson et al., 1993a; Sánchez Contreras et al., 2012) and checked using the SIMBAD astronomical database* (Wenger et al., 2000). For some sources, systemic velocities were not accurately known and thus we determined them from intense lines observed in this study (see below).

We used the E150 receiver in dual side band, with image rejections >10 dB, and observed the frequency ranges 138.5-146.3 GHz and 154.1-161.9 GHz (in the lower and upper side bands, respectively). This spectral setup was chosen to include several strong lines of SiC_2, various lines of Si_2C, and the $J = 4 - 3$ rotational transition of the radical SiC in its $^3\Pi_2$ state. The strongest lines of these three species covered in the observed frequency range are listed in Table 7.2. In the IRC +10216 spectrum, the line intensity ratios of the three species are typically SiC_2:Si_2C:SiC $\sim$ 100:1:10 (Cernicharo et al., 2000, 2015a), and thus we expect that in the rest of the sources of the sample, SiC_2 will be the most easily detectable molecule, while Si_2C will display the weakest lines and thus will be the most difficult to detect. The adopted spectral range also covers lines which are typically intense in carbon-rich circumstellar envelopes, such as HC_3N $J = 16 - 15$ and $J = 17 - 16$, C_4H $N = 15 - 14$ and $N = 17 - 16$, and SiS $J = 8 - 7$.

The beam size of the telescope at these frequencies is in the range 15.0-17.5″. We used the wobbler-switching technique, with the secondary mirror nutating by 3′ at a rate of 0.5 Hz. The focus was regularly checked on Venus and Uranus and the pointing of the telescope was systematically checked on a nearby quasar before observing each AGB star. The error in the pointing is estimated to be 2-3″. The E150 receiver was connected to a fast Fourier transform spectrometer providing a spectral resolution of 200 kHz. The weather was good and stable during most of the observations, with typical amounts of precipitable water vapor of 1-3 mm and system temperatures ranging from 80 K to 150 K. The intensity scale, calibrated using two absorbers at different temperatures and the atmospheric transmission model (ATM) (Cernicharo, 1985; Pardo et al., 2001), is expressed in terms of T_A^*, the antenna temperature corrected for atmospheric absorption and for antenna ohmic and

*http://simbad.u-strasbg.fr/Simbad

Table 7.2: Covered rotational transitions of SiC_2, Si_2C, and SiC

Transition	Frequency (MHz)	A_{ul} (s^{-1})	E_u (K)
	SiC_2		
$6_{2,5} - 5_{2,4}$	140920.171	7.65×10^{-5}	31.5
$6_{4,3} - 5_{4,2}$	141751.492	4.87×10^{-5}	55.0
$6_{4,2} - 5_{4,1}$	141755.360	4.87×10^{-5}	55.0
$6_{2,4} - 5_{2,3}$	145325.875	8.39×10^{-5}	32.0
$7_{0,7} - 6_{0,6}$	158499.228	1.23×10^{-4}	31.0
	Si_2C		
$11_{1,11} - 10_{0,10}$	144033.475	9.57×10^{-6}	29.3
$22_{2,20} - 22_{1,21}$	155600.100	1.54×10^{-5}	115.0
$13_{1,13} - 12_{0,12}$	157768.156	1.28×10^{-5}	39.3
$20_{2,18} - 20_{1,19}$	157959.754	1.54×10^{-5}	97.4
$18_{2,16} - 18_{1,17}$	160644.790	1.55×10^{-5}	81.4
	SiC		
$^3\Pi_2$ $J = 4 - 3$	157494.101	3.98×10^{-5}	13.2

spillover losses. To convert to main beam antenna temperature, T_A^* has to be divided by 0.78 (the ratio of the main beam efficiency to the forward efficiency of the IRAM 30m telescope at the observed frequencies[†]. For each source, we averaged the spectra corresponding to the horizontal and vertical polarizations, subtracted a baseline consisting of a first-order polynomial, and smoothed the resulting spectrum to a spectral resolution of 1 MHz, which is good enough to spectrally resolve the lines whose widths in most sources are typically in the range 15-50 km s^{-1} (7.5-25 MHz at the observed frequencies). Typical on-source integration times, after averaging horizontal and vertical polarizations, were $\sim$1 h for each source, resulting in T_A^* rms noise levels per 1 MHz channel of 2-5 mK.

7.3 Results from observations

The observations resulted in the detection of SiC_2 in 22 out of the 25 targeted sources, i.e., all sources except UU Aur, R Lep, and ST Cam. The five rotational transitions of SiC_2 listed in Table 7.2, which have upper level energies in the range 31-55 K, were clearly detected in most of the 22 sources where SiC_2 was identified. The lines corresponding to

[†]http://www.iram.es/IRAMES/mainWiki/Iram30mEfficiencies). The error in the intensities due to calibration is estimated to be $\sim$20 %.

The data were reduced using the software CLASS within the package GILDAS[‡]

the rotational transitions $6_{4,3} - 5_{4,2}$ and $6_{4,2} - 5_{4,1}$ appear blended together because line widths are larger than the frequency separation of the two transitions, although in most sources each of these lines could be fitted individually. The observed line profiles of SiC_2 are shown in Fig. 7.1 and the parameters derived from line fits using the `shell` method of CLASS[‖] are given in Table 7.5. We note that in U Cam, the line profiles of SiC_2 are consistent with emission arising exclusively from the present-day wind, rather than from the detached envelope (compare line profiles in Fig. 7.1 with those of CO in Schöier et al. 2005).

We also report the detection of SiC in 12 of the 25 targeted C-rich AGB envelopes (see Fig. 7.2). We note that prior to this study, this radical had been detected only in the C-star envelope IRC +10216 (Cernicharo et al., 1989). The SiC emission line is relatively strong in IRC +10216, CIT 6, CRL 3068, and LP And, while it is marginally detected in IRC +30374, V Cyg, V384 Per, IRC +60144, IRC +20370, CRL 67, CRL 2477, and CRL 2494. In Fig. 7.3 we compare the velocity-integrated intensity of the SiC $^3\Pi_2$ $J = 4 - 3$ line with that of the SiC_2 $7_{0,7} - 6_{0,6}$ line. We note that the SiC lines are brighter in the sources where SiC_2 is more intense, which suggests that the abundances of both species are correlated, as is expected if the radical SiC is a photodissociation product of SiC_2. This suggests that the nondetection of SiC in some of the sources is probably due to a lack of sensitivity and not due to a low fractional abundance of the radical. The related molecule Si_2C was not detected in any of the targeted sources, with the exception of IRC +10216, which at present is the only source in which this molecule has been identified (Cernicharo et al., 2015a). In IRC +10216, the lines of Si_2C are typically 100 times less intense than those of SiC_2. This difference in intensity is not due to a significant difference in abundance, but it is related to the larger partition function of Si_2C and its lower dipole moment, as discussed in detail by Cernicharo et al., (2015a). If the same relative intensities between SiC_2 and Si_2C holds for the rest of C-star envelopes, the nondetection of disilicon carbide is very likely due to an insufficient sensitivity.

In addition to the lines of SiC_2 and SiC, we also detected within the frequency range covered 138.5-146.3 GHz and 154.1-161.9 GHz, emission lines of other species typically present in the spectra of carbon-rich AGB envelopes. For example, the J = 16-15 and J = 17-16 lines of HC_3N and the J = 3-2 line of some isotopologues of carbon monosulfide, mainly $C^{34}S$ and ^{13}CS, are intense and prevalent among most of the sources. The J = 8-7 line of SiS is observed in many of the envelopes as one of the most intense lines, but it is not even detected in some of the other sources. The N = 15-14 and N = 17-16 lines of C_4H and the N = 14-13 and N = 16-15 of C_3N are also intense in some of the envelopes, although in many of them the lines of these two radicals are below the detection limit. In those sources

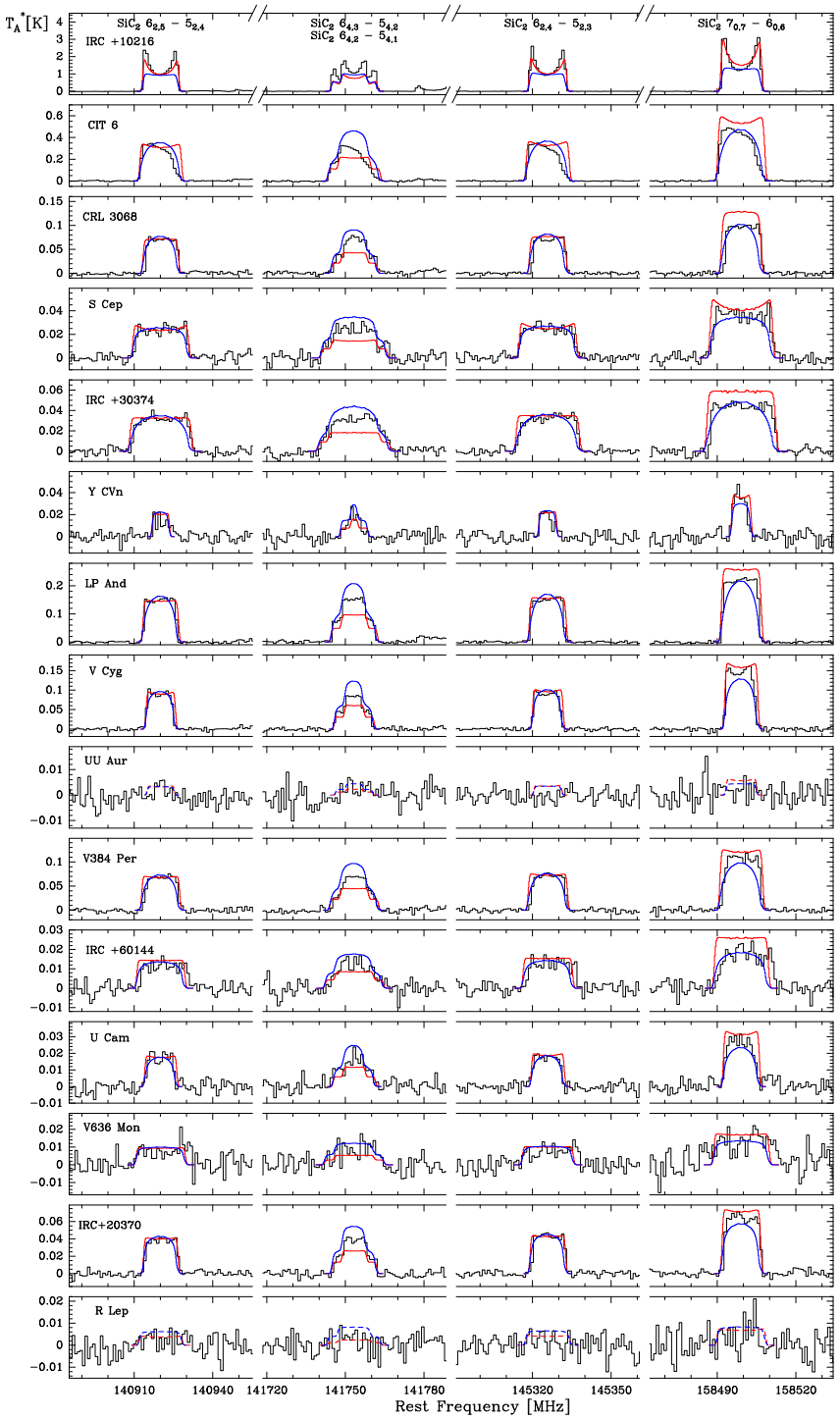

Figure 7.1: Rotational lines of SiC_2 observed with the IRAM 30m telescope in the 25 target sources (black histograms). The spectral resolution of the observed lines is 1 MHz. The blue lines are the calculated emerging line profiles from the best-fit model using the LVG method. The red lines are the predicted line profiles assuming LTE excitation. Dashed lines correspond to calculated lines profiles for those sources where SiC_2 was not detected.

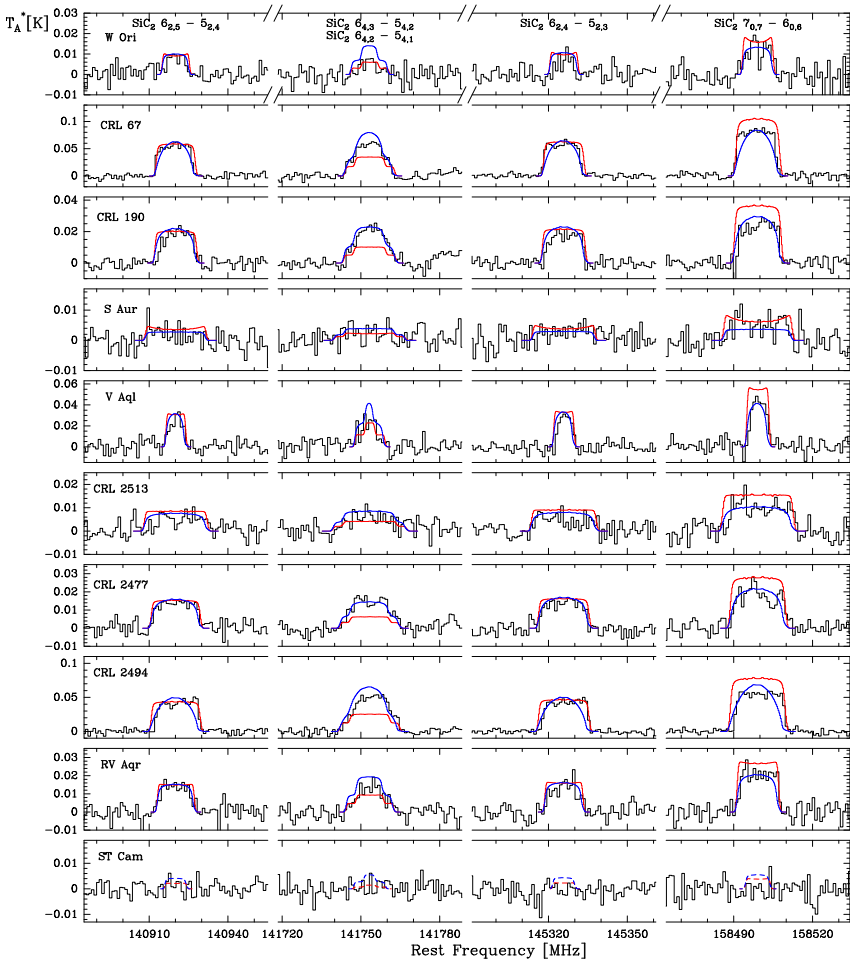

Figure 7.1 (cont.)

where molecular emission is most intense, such as CIT 6, CRL 3068, and LP And, lines of other molecules such as *l*-C_3H, *c*-C_3H_2, C_2S, HC_5N, and rare isotopologues of CS, SiS, SiC_2, and HC_3N are detected. In a couple of sources, UU Aur and ST Cam, no molecular emission was observed above a detection threshold of a few mK in the covered frequency range.

The availability of strong lines of molecules such as HC_3N, SiS, C_4H, $C^{34}S$, and SiC_2 in our data allows us to derive accurate values of the velocity of the source $V_{\rm LSR}$ and of the terminal expansion velocity of the envelope $V_{\rm exp}$ in most of the sources. These two parameters are reported in the literature mainly from CO J = 1-0 and J = 2-1 lines (Groenewegen et al., 1996b, 2002; Loup et al., 1993; Olofsson et al., 1993a) with varying degrees of accuracy. We carried out a critical evaluation of the values of $V_{\rm LSR}$ and $V_{\rm exp}$ derived from our data and those in the literature. In cases where our lines have a well-defined shape, the values from

Table 7.3: Observed parameters of the SiC $^3\Pi_2$ $J = 4 - 3$ line

Source	ν_{calc} (MHz)	ν_{obs} (MHz)	V_e (km s^{-1})	$\int T_A^* dv$ (K km s^{-1})
IRC +10216	157494.101	157494.1(1)	15.4(8)	5.86(6)
CIT 6	157494.101	157493.2(10)	15.4(8)	0.96(9)
CRL 3068	157494.101	157494.2(5)	15.7(5)	0.29(6)
IRC +30374	157494.101	157495.5(10)	25.1(10)	0.18(3)[a]
LP And	157494.101	157493.8(5)	14.4(4)	0.56(6)
V Cyg	157494.101	157496.3(10)	11.3(10)	0.11(2)[a]
V384 Per	157494.101	157493.7(10)	15.2(10)	0.17(3)[a]
IRC +60144	157494.101	157492.8(10)	20.2(10)	0.12(6)[a]
IRC +20370	157494.101	157494.3(10)	15.8(10)	0.13(2)[a]
CRL 67	157494.101	157494.8(10)	16.6(10)	0.28(6)[a]
CRL 2477	157494.101	157493.7(10)	18.7(10)	0.10(2)[a]
CRL 2494	157494.101	157493.5(10)	21.8(10)	0.23(4)[a]

Notes. Numbers in parentheses are 1σ uncertainties in units of the last digits.
[a] Marginal detection.

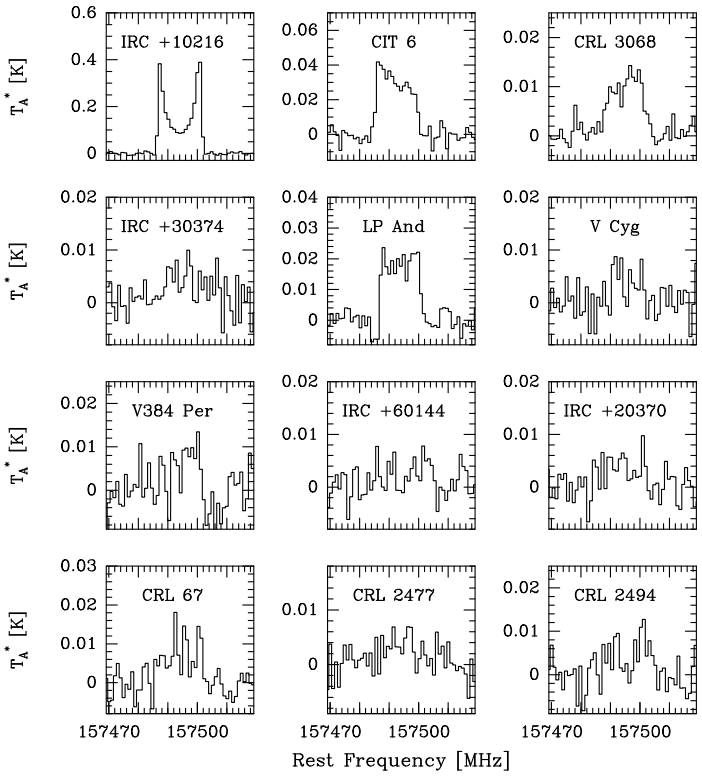

Figure 7.2: SiC $^3\Pi_2$ $J = 4 - 3$ line observed in 12 out of the 25 sources in our sample. The spectral resolution is 1 MHz.

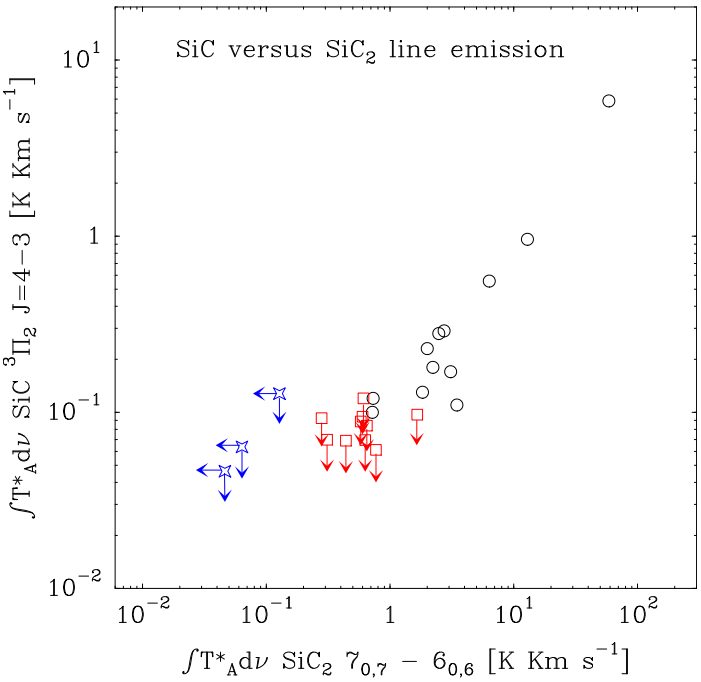

Figure 7.3: Velocity-integrated intensity of the SiC $^3\Pi_2$ J = 4-3 line versus the velocity-integrated intensity of the SiC_2 $7_{0,7} - 6_{0,6}$ line. Black circles correspond to sources where both SiC_2 and SiC are detected, red squares to envelopes where SiC_2 is detected but not SiC, and blue stars to sources where neither SiC nor SiC_2 is detected.

our dataset were preferred, whereas when lines show a less clear shape, the values from literature were favored. The final values of $V_{\rm LSR}$ and $V_{\rm exp}$ adopted in this work are given in Table 7.1.

In this Chapter we focus on the analysis of SiC_2 and leave the interpretation of other molecules for future studies. Silicon dicarbide was detected in most of the targeted sources and we aim to model its emission and determine its abundance in each source to provide a global view of how abundant this molecule is in circumstellar envelopes around C-rich AGB stars.

7.4 SiC_2 radiative transfer modeling

7.4.1 Envelope model

We adopted a common physical scenario to model all sources consisting of a spherically symmetric envelope of gas and dust expanding with a constant velocity and mass-loss rate

around a central AGB star. The parameters of the star and envelope adopted for the different sources are detailed in Table 7.1.

The central AGB star is characterized by an effective temperature T_* and a luminosity L_*. The stellar radius R_* is then determined by T_* and L_* using the Stefan–Boltzmann law. Effective temperatures for the photosphere of AGB stars, typically in the range 2000-3000 K, are difficult to estimate accurately. For most of the stars in our sample, we adopted the values of T_* from studies where T_* is derived by modeling the spectral energy distribution (SED) of each star (Agúndez et al. 2012; Danilovich et al. 2015; Ramstedt et al. 2014; Schöier et al. 2005, 2013). In some cases, the adopted values of T_* are taken from studies where the effective temperature was chosen to be a round number that fitted the SED reasonably well (Groenewegen et al. 1998; Speck et al. 2009). For those objects for which T_* was not available from the literature, we assumed a typical value for AGB stars of 2500 K. Regarding the stellar luminosities L_*, we adopted values from the literature (see references in Table 7.1) in which they were mostly derived using the period-luminosity relation for Mira variables.

The spherical envelope is described by the radial profile of various physical quantities, such as the gas density, the temperature of gas and dust, the expansion velocity, and the microturbulence velocity. The gas density as a function of the distance r from the star is determined by the law of conservation of mass as

$$n_g = \frac{\dot{M}}{\overline{m}_g \, 4\pi \, r^2 \, V_e}, \tag{7.1}$$

where n_g is the number of gas particles per unit volume, $\overline{m}_g$ is the average mass of gas particles, $\dot{M}$ is the mass-loss rate, and V_e is the expansion velocity of the envelope. We assume that V_e is equal to the terminal expansion velocity of the envelope $V_{\rm exp}$ across the entire envelope. This is certainly not true inside the acceleration region, but these inner layers contribute little to the emission of the SiC_2 lines observed here. We adopt $\overline{m}_g$= 2.3 amu, adequate for a gas composed mainly of H_2, He with a solar elemental abundance, and CO with an abundance of $\sim 10^{-3}$ relative to H_2. Mass-loss rates were taken from the literature where $\dot{M}$ was determined by modeling observations of multiple CO lines (see references in Table 7.1).

The radial structure of the gas kinetic temperature T_k is described by a power law of the type

$$T_k = T_\star \left(\frac{r}{R_\star} \right)^{-\delta}, \tag{7.2}$$

where R_* is the stellar radius. In reality, the gas kinetic temperature is determined by a balance between the different heating and cooling processes at work, and cannot be accurately described by a single power law across the entire envelope. We do not aim to derive the gas kinetic temperature radial profile for each individual source, and thus for simplicity we adopt a uniform value of $\delta = 0.7$, which is in line with findings from previous studies of circumstellar envelopes around AGB stars (e.g., De Beck et al. 2010; Guélin et al. 2018; Schöier et al. 2001).

The microturbulence velocity is assumed to be $1\,\mathrm{km\,s^{-1}}$ throughout the envelope, which is within the range of values 0.65 - $1.5\,\mathrm{km\,s^{-1}}$, derived in the literature for the C-rich envelope IRC +10216 (De Beck et al., 2012; Skinner et al., 1999); however, this parameter has a limited impact when modeling the SiC_2 lines because it is well below the terminal expansion velocity of the wind for all sources.

We also consider the dusty component of the envelope, although, as will be discussed below, in our models dust plays a minor role in the excitation of the rotational lines of SiC_2 observed. We consider spherical grains of amorphous carbon with a radius of $0.1\,\mu\mathrm{m}$, a mass density of 2 g $\mathrm{cm^{-3}}$, and optical properties from Suh, (2000). Dust grains are assumed to be present from the dust condensation radius r_c with a constant gas-to-dust mass ratio Ψ. The radial structure of the dust temperature T_d is assumed to be given by the power-law expression

$$T_d = T_d(r_c)\left(\frac{r}{r_c}\right)^{-\delta_d}, \tag{7.3}$$

where we assume $\delta_d = 0.4$ based on theoretical expectations for carbonaceous grains (e.g., Kerschbaum et al. 2007). This value is also close to that derived for IRC +10216 (Agúndez et al., 2012). The values of Ψ, r_c, $T_d(r_c)$ were taken from the literature where they are typically derived by modeling the SED using photometric data, such as IRAS and 2MASS fluxes and in some cases submillimeter data (Danilovich et al. 2015; Ramstedt et al. 2014; Schöier et al. 2006, 2013). In cases where those parameters were not available in the literature, we assumed a typical value of 5 $R_\star$ for r_c, 1200 K for $T_\mathrm{d}(r_\mathrm{c})$, and 300 for the gas-to-dust mass ratio Ψ.

The adopted distances to the AGB stars were taken from the literature (see references in Table 7.1). The data include measurements from Hipparcos parallaxes and estimations based on bolometric magnitudes using the period-luminosity relation for Mira variables. When nothing else was available, the distances were estimated assuming $L_* = 10^4\ \mathrm{L_\odot}$.

7.4.2 Excitation and radiative transfer calculations

We performed excitation and radiative transfer calculations to model the line emission of SiC_2 based on the multi-shell large velocity gradient (LVG) method. The circumstellar envelope is divided into a number of concentric shells, each of which has a characteristic set of physical properties and SiC_2 abundance, and statistical equilibrium equations are solved in each of them. In each shell, the contribution of the background radiation field (cosmic microwave background, stellar radiation, and thermal emission from surrounding dust) is included (see Agúndez et al. 2012 for further details). For the current study, the LVG method provides a good compromise between the assumption of local thermal equilibrium (LTE) and more computationally expensive nonlocal methods. Rate coefficients for the rotational excitation of SiC_2 through collisions have been computed theoretically (Chandra et al., 2000), which makes it worth using more advanced methods than LTE. Our calculations indicate that the emission from the SiC_2 lines observed here arises from intermediate regions in the envelope where the rotational levels are not fully thermalized (see Section 7.5). Moreover, the observed lines of SiC_2 are optically thin in most sources, which implies that the LVG method should be accurate enough.

In the excitation calculations, we consider rotational levels up to $J = 39$ and $K_a = 20$ within the ground vibrational state of SiC_2 (i.e., a total number of 620 energy levels). Level energies and transition frequencies were calculated from the rotational constants reported by Müller et al., (2012), and line strengths for rotational transitions were computed from the dipole moment, 2.393$\pm$0.006 D, measured by Suenram et al., (1989). The rate coefficients for excitation through inelastic collisions with H_2 and He were taken from Chandra et al., (2000), who calculated rate coefficients for transitions between the first 40 rotational levels in the temperature range 25-125 K. At temperatures higher than 125 K, we adopted the theoretical rate coefficients calculated at 125 K and did not perform an extrapolation in temperature. This could introduce uncertainties in the excitation calculations. To evaluate the impact of this assumption, we carried out calculations in which we implemented a linear extrapolation in temperature of the rate coefficients at $T_k > 125$ K and verified that the calculated line profiles of the SiC_2 transitions observed were not sensitive to the particular choice of the collision rate coefficients at temperatures higher than 125 K. The reason is that, as is discussed in Section 7.5, most of the SiC_2 emission detected with the IRAM 30m telescope arise from intermediate regions of the envelope, where gas kinetic temperatures are in the range $\sim$ 50-300 K, i.e., not excessively far from the 25-125 K temperature range. Since the calculations of Chandra et al., (2000) only include the first 40 rotational levels, for transitions involving higher levels, the de-excitation rate coefficients were approximated

using the expression

$$\log \gamma = -10 - 0.25\,(J' - J'') - 0.45\,|K'_a - K''_a|, \tag{7.4}$$

where γ is the rate coefficient in units of $cm^3\ s^{-1}$, and $'$ and $''$ denote the upper and lower level, respectively. Equation (7.4) provides a first-order approximation for asymmetric rotors, based on theoretical calculations carried out for the molecules SiC_2 (Chandra et al., 2000), SO_2 (Green, 1995), and HCO_2^+ (Hammami et al., 2007).

7.4.3 The SiC_2 radial abundance profile

We consider that SiC_2 is formed close to the star with a given fractional abundance that remains constant throughout the envelope up to the outer regions of the envelope, where it is photodissociated by the ambient ultraviolet radiation field of the local interstellar medium. To compute the falloff of abundance due to photodissociation, we assume that the photodissociation rate of SiC_2 is given by the expression $\alpha \exp(-\beta A_V)$, where A_V is the visual extinction. We adopt an unattenuated rate of $\alpha = 10^{-10}\ s^{-1}$ and a dust shielding factor of $\beta = 1.7$, values which are merely educated guesses (MacKay et al., 1999) because the photodissociation cross section of SiC_2 is not well known. The radial variation of the SiC_2 abundance in the expanding envelope is then given by the differential equation (Huggins et al., 1982; Jura et al., 1981)

$$\frac{df}{dr} = -\frac{\alpha}{V_{\rm exp}} \exp\left[-\left(\frac{r_d}{r}\right)\right] f, \tag{7.5}$$

where f is the fractional abundance of SiC_2 relative to H_2 and r_d is a parameter that can be considered as a photodissociation radius and which is given by

$$r_d = \frac{\beta\,\dot{M}}{4\pi\,V_{\rm exp}\,\overline{m}_g\,1.87\times 10^{21}}, \tag{7.6}$$

where the numerical value is the canonical $N_{\rm H}/A_V$ ratio given by Bohlin et al., (1978) for the local interstellar medium. The solution to Eq. (7.5) can be expressed as

$$\begin{aligned} \ln\frac{f}{f_0} = -\frac{\alpha}{V_{\rm exp}} \Bigg\{ & \left[r_d\,E_i\left(-\frac{r_d}{r}\right) + r\,e^{(-r_d/r)}\right] \\ & - \left[r_d\,E_i\left(-\frac{r_d}{R_*}\right) + R_*\,e^{(-r_d/R_*)}\right] \Bigg\}, \end{aligned} \tag{7.7}$$

where E_i is the exponential integral. This approach provides a simple and accurate way to take into account the abundance falloff due to photodissociation. Once the physical structure of the envelope is set and a given initial abundance f_0 is chosen, the abundance profile $f(r)$ becomes fully described by Eq. (7.7). We note that it is likely that SiC_2 can experience an abundance decline around the dust formation zone. The adopted abundance profile, however, does not include such a feature since we are tracing a specific region of the envelope, more specifically the intermediate one (see Section 7.5), and thus it is not possible to accurately derive the radial abundance profile from the very inner regions out to the outer envelope. In this work we thus determine the mean abundance of SiC_2 in the intermediate regions of the envelope of the studied sources.

In summary, to model the emission lines of SiC_2 and determine its abundance in the observed sources we constructed a model of the envelope for each source, as described in Section 7.4.1, with the parameters given in Table 7.1. We then performed excitation and radiative transfer calculations, as explained in Section 7.4.2, using the abundance profile described in Section 7.4.3. We varied the initial fractional abundance of SiC_2 relative to H_2, f_0 in Eq. (7.7), until the calculated line profiles matched the observed ones. We choose as the best-fit model the one that results in the best overall agreement between calculated and observed line profiles for the entire set of SiC_2 lines observed. In those cases where no lines of SiC_2 are detected, we derive upper limits to the abundance of SiC_2 by choosing the maximum abundance that results in line intensities compatible with the noise level of the observations.

7.5 Results from SiC_2 radiative transfer modeling

In most sources (see Fig. 7.1), the shapes of the SiC_2 lines observed are nearly flat-topped, which is indicative of optically thin emission not resolved by the 15.0-17.5″ beam of the IRAM 30m telescope. One notable exception is IRC +10216, whose close proximity (130 pc) means that the emission is spatially resolved by the telescope beam, and the line profiles show a marked double-peaked character. The calculated line profiles resulting from our best-fit LVG model for each of the sources are shown in blue in Fig. 7.1, where they are compared with the observed line profiles. The agreement between calculated and observed line shapes is good in most sources, except in IRC +10216, for which the LVG model produces a less marked U-shape than observed, and a few sources like LP And, for which the calculated lines are more curved than flat-topped; in other words, in some sources the

LVG model seems to result in lines that are more optically thick than indicated by the observed line shapes. To investigate this, we also ran models where we assumed LTE excitation for SiC_2. These models tend to produce line shapes that are in better agreement with the observed ones in sources like IRC +10216, where calculated line profiles have a clearer U-shaped character, and LP And, where line shapes are more flat-topped (see red lines in Fig. 7.1). This suggests that the LVG model lacks sufficient excitation for the levels involved in the observed SiC_2 transitions. There are various possible causes of the suspected lack of excitation, which we discuss below.

According to the LVG model, the excitation of the rotational levels of SiC_2 in the envelopes studied is dominated by inelastic collisions with H_2 and He. Even though thermal emission from dust is included in the model, it has little impact on the excitation of the observed SiC_2 rotational lines. The five lines of SiC_2 observed here involve upper levels with relatively low energies (31-55 K), and thus are preferentially excited in intermediate layers of the envelope where gas kinetic temperatures are of this order. In Fig. 7.4 we show the contribution to the velocity-integrated intensity of the five SiC_2 lines observed as a function of the impact parameter relative to the position of the star for two sources in our sample, U Cam and IRC +30374. These two envelopes are representative of very different mass-loss rates. While U Cam lies in the lower range, with $\dot{M} = 2 \times 10^{-7}$ $M_\odot$ yr^{-1}, IRC +30374 lies at the higher end, with $\dot{M} = 10^{-5}$ $M_\odot$ yr^{-1}. In U Cam, the maximum contribution to the line emission comes from regions at $\sim 10^{15}$ cm, while in the case of IRC +30374 the regions around $\sim 10^{16}$ cm contribute the most to the observed emission; i.e., in envelopes with low mass-loss rates the SiC_2 rotational levels involved in the five observed transitions are only efficiently excited by collisions in the inner regions (and thus most of the emission detected in these lines comes from such regions), while in envelopes with high mass-loss rates the densities are still high enough in the outer regions to excite the SiC_2 rotational levels and thus most emission comes from these outer regions. Among the studied sources, the LVG models indicate that emission from the five SiC_2 observed lines arises typically from intermediate regions of the envelope, at radial distances in the range 10^{15}-10^{16} cm.

It is interesting to have a look at the excitation of SiC_2 predicted by the LVG model in the studied envelopes, in particular to the extent to which the rotational levels involved in the five observed transitions are close to or far from thermalization. In Fig. 7.5 we show the calculated ratio of excitation to gas kinetic temperature ($T_{\rm ex}/T_k$) for the five SiC_2 transitions as a function of radius for the envelopes U Cam and IRC +30374, which lie at low and high ranges, respectively, of mass-loss rates. We see that for most transitions $T_{\rm ex}/T_k = 1$, i.e., rotational levels are thermalized, in the hot and dense inner regions, and that as

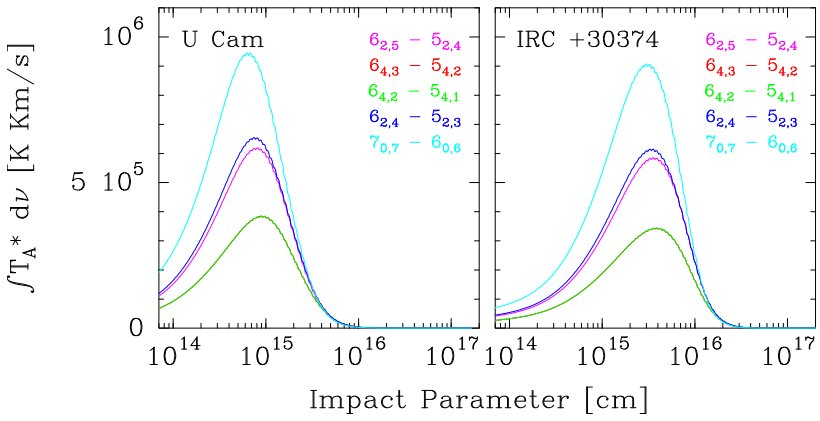

Figure 7.4: Velocity-integrated intensity plotted as a function of impact parameter for the five observed SiC_2 lines in U Cam and IRC +30374. The transitions $6_{4,3} - 5_{4,2}$ and $6_{4,2} - 5_{4,1}$ have overlapping curves. For visualization reasons, the intensities of U Cam are multipled by a factor of 2.75.

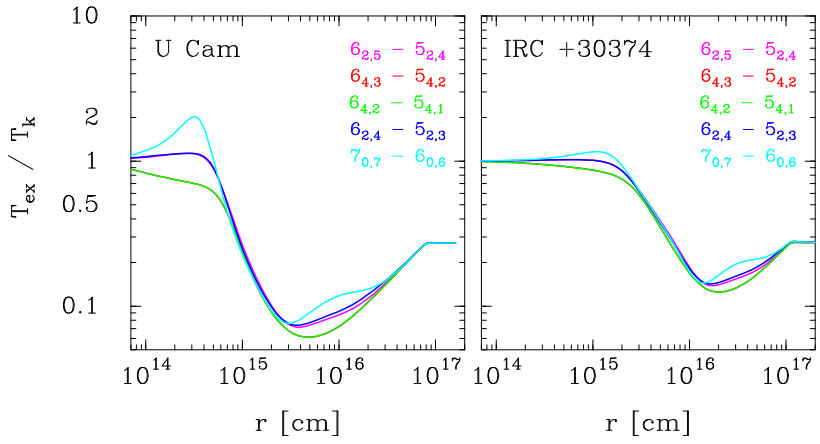

Figure 7.5: Calculated ratio of excitation temperature to kinetic temperature (T_{ex}/T_k) as a function of radius for the five observed rotational transitions of SiC_2 in U Cam and IRC +30374. The transitions $6_{4,3} - 5_{4,2}$ and $6_{4,2} - 5_{4,1}$ have overlapping curves.

the radius increases and the gas density decreases, the rotational levels become increasingly subthermally excited, as indicated by the fact that the ratio $T_{\rm ex}/T_k$ falls below unity. The much lower mass-loss rate of U Cam compared to IRC +30374 implies substantially lower densities in the envelope and thus in U Cam rotational populations start to deviate from thermalization at shorter radii than in IRC +30374. We note that in the intermediate region of the envelope from where most emission comes from, $\sim 10^{15}$ cm in U Cam and $\sim 10^{16}$ cm in IRC +30374 (see Fig. 7.4), the SiC_2 rotational levels are mostly subthermally excited.

As commented above, for some of the sources, the LVG model could lack sufficient excitation for the levels involved in the observed transitions of SiC_2. One possible missing source of excitation could be related to the existence of shells with an enhanced density with respect to the surrounding media (Agúndez et al., 2017; Cernicharo et al., 2015b; Cordiner et al., 2009; Guélin et al., 2018; Mauron et al., 2000). From models of IRC +10216 and LP And we notice that density enhancements above a factor of 10 are needed to start to reproduce adequately the observed line shapes. In IRC +10216, the shell–intershell density contrast is just 3 (Guélin et al., 2018). It is currently unknown whether episodic mass loss in other stars could be abrupt enough to result in shell–intershell density contrasts above 10. We also note that uncertainties in the rate coefficients of SiC_2 excitation through inelastic collisions may also be at the origin of the suspected lack of excitation of SiC_2 in IRC +10216. In this sense, it would be interesting to revisit the collisional rate coefficients calculated by Chandra et al., (2000). Another possible missing source of excitation in the LVG model could be infrared (IR) pumping, i.e., absorption of IR photons and pumping to excited vibrational states followed by spontaneous radiative decay to rotational levels in the ground vibrational state. This effect is not included in the model for SiC_2 (mainly because there is a complete lack of information about infrared intensities), although it is an important excitation mechanism of some molecules in IRC +10216 (e.g., Agúndez et al. 2006) where the infrared flux is large (Cernicharo et al., 1999). However, vibrationally excited SiC_2 seems to be restricted to the inner layers, as indicated by the narrow lines from the vibrational states $\nu_3 = 1, 2$ detected with ALMA (Cernicharo et al., 2013). Moreover, if IR pumping was playing an important role for SiC_2 we could expect to see the time variation of the line intensities found by Cernicharo et al., (2014) for other molecules, but the lines of SiC_2 show a rather constant intensity along the stellar period of CW Leo, which suggests that IR pumping is not important for this molecule (Cernicharo et al., 2014).

The differences between calculated and observed line shapes for some of the sources suggests that the LVG model may lack excitation for SiC_2, and that this could happen for other sources as well. We have thus run models assuming LTE excitation for all sources. The

calculated line profiles are shown in red in Fig. 7.1. Assuming LTE excitation throughout the whole envelope increases the excitation to outer radii, which leads to an increase in the emission size. Therefore, in general, the line opacities and fractional abundance of SiC_2 required to reproduce the observed intensities are lower when assuming LTE than when using the LVG method. Since it is unlikely that the rotational levels of SiC_2 are populated in LTE out to the outermost low-density regions of the envelope, the abundance of SiC_2 in the envelope of the observed sources is most likely between the values given by the LVG and the LTE models, which typically differ by a factor of $\sim$3 (see Table 7.4).

7.6 Discussion

The fractional abundances of SiC_2 derived in the 25 studied envelopes are given in Table 7.4. We give the abundances derived using the LVG method, while those obtained assuming LTE excitation are given in the last column. The fractional abundances obtained using the LVG method range between 3.7×10^{-7} and 3.7×10^{-5} relative to H_2. Assuming that silicon has a solar elemental abundance in AGB stars (Asplund et al., 2009), the maximum possible abundance of SiC_2 relative to H_2 is 6.5×10^{-5}. Therefore, the high fractional abundances of SiC_2 of a few times 10^{-5} derived in some of the envelopes imply that gaseous SiC_2 locks an important fraction of the available silicon, possibly making it a major reservoir of this element. We note, however, that if the abundances are closer to the values derived under LTE, the maximum abundances derived for SiC_2 are $\sim 7 \times 10^{-6}$ relative to H_2, which would imply that SiC_2 locks at most $\sim 10\%$ of the available silicon.

In most of the carbon-rich AGB envelopes in our sample, SiC_2 abundances are reported for the first time in this work. The only source where SiC_2 has been previously studied in detail is IRC +10216, which in fact has the lowest fractional abundance of SiC_2 among all the sources in our sample (3.7×10^{-7} relative to H_2) (see Table 7.4). Cernicharo et al., (2010) observed 55 rotational transitions of SiC_2 in IRC +10216 using the HIFI spectrometer on board *Herschel*. These authors derive an abundance of 2×10^{-7} relative to H_2 in the inner regions of the envelope using an LTE radiative transfer analysis. Based on mm-wave interferometric observations, Lucas et al., (1995) derive an abundance relative to H_2 of 5×10^{-7} for the inner regions, and more recently Fonfría et al., (2014) inferred an abundance relative to H_2 of 8×10^{-7} at the stellar surface decreasing down to 8×10^{-8} at 20 R_*. The SiC_2 abundance derived in this work for IRC +10216 (3.7×10^{-7}) is in good agreement with the values reported in these articles.

Table 7.4: Derived fractional abundances of SiC_2

Name	$\dot{M}$ ($M_\odot$ yr^{-1})	V_{exp} (km s^{-1})	$f_0(SiC_2)_{LVG}$	$f_0(SiC_2)_{LTE}$
IRC +10216	2.0×10^{-5}	14.5	3.7×10^{-7}	3.7×10^{-7}
CIT 6	6.0×10^{-6}	17	1.1×10^{-5}	3.4×10^{-6}
CRL 3068	2.5×10^{-5}	14.5	1.9×10^{-6}	7.2×10^{-7}
S Cep	1.2×10^{-6}	22.5	1.0×10^{-5}	2.0×10^{-6}
IRC +30374	1.0×10^{-5}	25	9.7×10^{-6}	2.3×10^{-6}
Y CVn	1.5×10^{-7}	7	4.0×10^{-6}	1.7×10^{-6}
LP And	7.0×10^{-6}	14.5	6.8×10^{-6}	2.2×10^{-6}
V Cyg	1.6×10^{-6}	12	6.6×10^{-6}	2.3×10^{-6}
UU Aur	2.4×10^{-7}	10.6	$< 1.0 \times 10^{-6}$	$< 3.5 \times 10^{-7}$
V384 Per	2.3×10^{-6}	15.5	1.3×10^{-5}	3.6×10^{-6}
IRC +60144	3.7×10^{-6}	19.5	6.0×10^{-6}	1.8×10^{-6}
U Cam	2.0×10^{-7}	13	3.7×10^{-5}	6.7×10^{-6}
V636 Mon	5.8×10^{-6}	20	1.7×10^{-6}	5.1×10^{-7}
IRC +20370	3.0×10^{-6}	14	4.2×10^{-6}	1.5×10^{-6}
R Lep	8.7×10^{-7}	17.5	$< 2.7 \times 10^{-6}$	$< 4.1 \times 10^{-7}$
W Ori	7.0×10^{-8}	11	1.4×10^{-5}	2.4×10^{-6}
CRL 67	1.1×10^{-5}	16	1.0×10^{-5}	2.6×10^{-6}
CRL 190	6.4×10^{-5}	17	8.8×10^{-7}	2.9×10^{-7}
S Aur	4.0×10^{-7}	24.5	3.6×10^{-6}	7.3×10^{-7}
V Aql	1.4×10^{-7}	8	2.0×10^{-5}	7.3×10^{-6}
CRL 2513	2.0×10^{-5}	25.5	1.6×10^{-6}	5.3×10^{-7}
CRL 2477	1.1×10^{-4}	20	6.0×10^{-7}	1.9×10^{-7}
CRL 2494	7.5×10^{-6}	20	2.7×10^{-5}	4.9×10^{-6}
RV Aqr	2.3×10^{-6}	15	3.0×10^{-6}	1.0×10^{-6}
ST Cam	1.3×10^{-7}	8.9	$< 4.0 \times 10^{-6}$	$< 6.0 \times 10^{-7}$

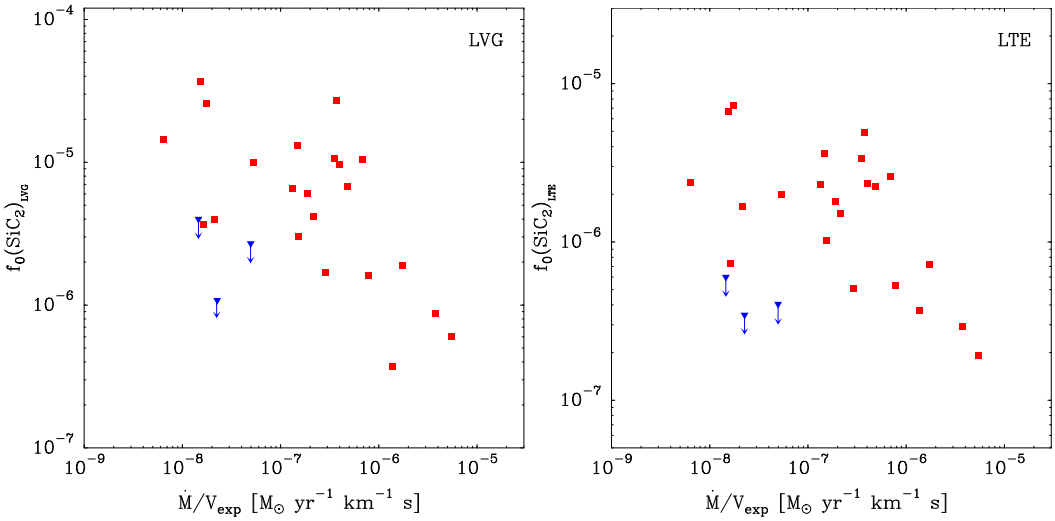

Figure 7.6: Plot of the fractional abundances of SiC_2 (f_0) derived with the LVG method (left panel) and assuming LTE excitation (right panel) versus the envelope density proxy $\dot{M}/V_{exp}$ for the 25 C-rich envelopes studied here. Blue downward triangles represent upper limits for f_0.

The fractional abundance of SiC_2 shows an interesting trend with either the mass-loss rate $\dot{M}$ or the density in the envelope, evaluated through the quantity $\dot{M}/V_{exp}$. As shown in Fig. 7.6, SiC_2 becomes less abundant as the density in the envelope increases. This trend is also present when the abundances derived assuming LTE are used. At this point, it is worth noting that the SiC_2 abundances derived in this work correspond to intermediate regions of the envelope. In a standard scenario describing the chemistry of an expanding envelope around an AGB star, the abundance with which a molecule is injected into the intermediate and outer envelope is set by the processes occurring in the inner regions. In this sense, the abundance of SiC_2 in the intermediate regions of the envelope is set by thermochemical equilibrium (TE) at the stellar surface and is possibly modified, i.e., driven out of thermochemical equilibrium, later on during the expansion by processes such as the formation of dust grains, shocks driven by the stellar pulsation, or even photochemical processes (e.g., Agúndez et al. 2010; Cherchneff 2012). The observational finding of a decrease in the SiC_2 abundance with increasing gas density can therefore be interpreted in different ways.

The observational trend could simply be a consequence of the way in which the TE abundance of SiC_2 depends on the density. To evaluate whether this could be a plausible explanation, we carried out thermochemical equilibrium calculations using the radial profiles of density and temperature of IRC +10216 (Agúndez et al. 2012; see downward revision on the density profile by Cernicharo et al. 2013) and scaling the density profile down or up

depending on the mass-loss rate. In Fig. 7.7 we show the resulting TE abundance of SiC_2 within the first 10 R_* around the star for mass-loss rates between 10^{-7} and 10^{-4} $M_\odot$ yr^{-1}. In the region where SiC_2 reaches its maximum TE abundance, between 2 and 5 R_*, the abundance of SiC_2 is not very sensitive to the density. Outside this region the abundance of SiC_2 shows a marked dependence on density. At radii < 2 R_*, SiC_2 becomes more abundant with increasing density (contrary to the observational trend), while beyond 5 R_* the SiC_2 abundance increases with decreasing density (as observed). At radii larger than 5 R_*, however, the TE abundance of SiC_2 experiences a drastic decline to values well below those observed, and thus it is unlikely that such regions set the abundance that is injected into the expanding envelope. Although it is difficult to precisely locate the region where molecular abundances, in general, and that of SiC_2 in particular, quench to the TE value, such a region should be located around 2-3 R_* (Agúndez et al., 2006, 2012), i.e., near the region where SiC_2 abundance is maximum and nearly insensitive to the density. We thus conclude that it is unlikely that the observational trend shown in Fig. 7.6 is caused by thermochemical equilibrium.

It therefore seems that the observational finding of a decline in the SiC_2 abundance with increasing density is caused by some nonequilibrium process that takes place beyond the region where thermochemical equilibrium holds. The most natural explanation is that SiC_2 molecules deplete from the gas phase to incorporate into solid dust grains, a process that is favored at higher densities owing to the higher rate at which collisions between particles occur. We stress that since the SiC_2 abundances derived here correspond to intermediate regions of the envelope where dust formation has already taken place, they have to be considered as post-condensation abundances. Further support for this scenario comes from mm-wave interferometric observations of SiC_2 in the C-star envelope IRC +10216 (Fonfría et al., 2014; Lucas et al., 1995; Velilla Prieto et al., 2015), which shows that SiC_2 is present in regions close to the star, then experiences a marked abundance decline at 10-20 R_* (very likely due to condensation onto dust grains), and appears again in the outer envelope (probably as a result of the interaction between the UV radiation field and the envelope).

In order to further evaluate the hypothesis that the decline in the abundance of SiC_2 with increasing envelope density is caused by a more efficient incorporation of SiC_2 on silicon carbide dust, we collected information on infrared IRAS and ISO data for the sources in our sample that exhibit the SiC dust emission feature at 11.3 µm. Among the 25 sources in our sample, for 15 of them Sloan et al., (1998) have analyzed the IRAS LRS spectra and for 9 of them Yang et al., (2004) have studied the ISO SWS spectra. These authors determine the relative flux of SiC dust as the ratio of the integrated flux of the 11.3 µm emission feature

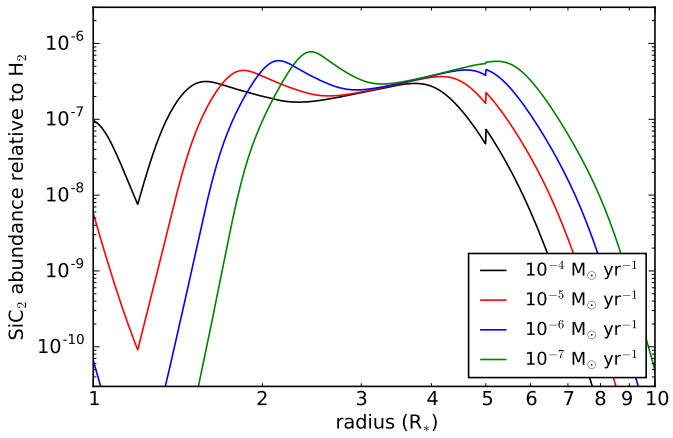

Figure 7.7: Calculated fractional abundance of SiC_2 at thermochemical equilibrium as a function of distance to the star for various radial density profiles corresponding to mass-loss rates in the range 10^{-7}-10^{-4} $M_\odot$ yr^{-1}.

(after continuum substraction) divided by the integrated flux of the continuum[§]. In Fig. 7.8 we plot the relative integrated flux of SiC dust versus the fractional abundance of SiC_2 for the sources in our sample which have IRAS or ISO data. If the relative flux of SiC dust is a good proxy of the amount of silicon carbide dust, and if the hypothesis that SiC_2 is a gas-phase precursor of SiC dust is correct, one would expect to see a trend where the relative flux of SiC dust increases as the gas-phase abundance of SiC_2 decreases. This trend is not visible in Fig. 7.8. We note, however, that the relative flux of the 11.3 µm SiC band is an observable quantity that may not necessarily be a good proxy of the mass of silicon carbide dust in the envelope, the derivation of which requires a detailed radiative transfer analysis that includes a thorough description of the chemical composition and temperature of dust throughout the envelope. At this point, it therefore remains inconclusive whether or not there is a clear observational relation between the abundances of SiC_2 gas and SiC dust in C-rich envelopes. We plan to address this issue in a future study.

The question of identifying the main gas-phase precursors of dust grains in the ejecta of AGB stars has been, and continues to be, an exciting scientific topic. The problem has been addressed from different perspectives, mainly in the context of oxygen-rich AGB stars. For example, in a series of studies the abundance of SiO has been investigated in detail in a wide sample of envelopes around M stars (González Delgado et al., 2003), C stars (Schöier

[§]The main difference between the two studies lies in the integration range, which is 7.67-14.03 µm for the IRAS spectra and 9-13.6 µm for the ISO data. For the sources that were observed with both telescopes, the main causes of the differences between the IRAS and ISO relative fluxes of SiC dust are the different integration ranges and the specific error in the spectra taken by each telescope.

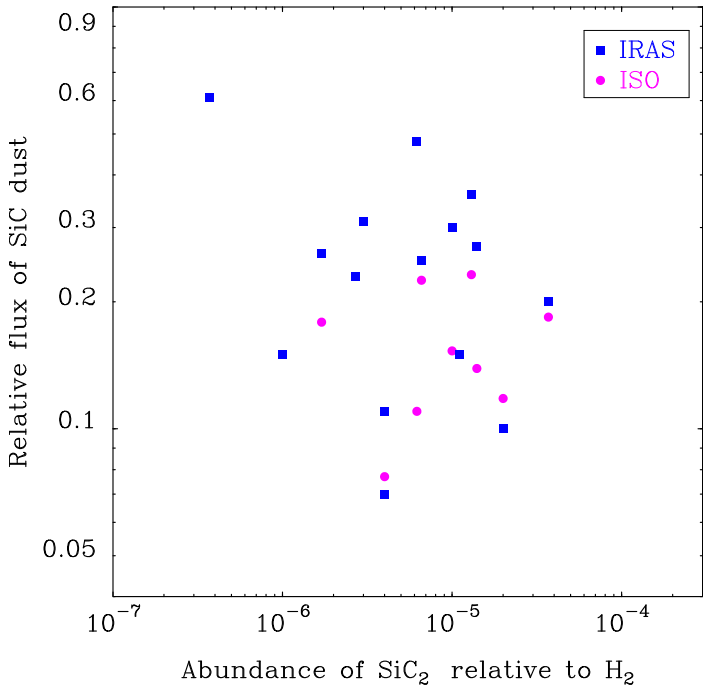

Figure 7.8: Relative integrated flux of the SiC dust feature at 11.3 µm taken from the literature versus the fractional abundance of SiC_2 derived in this work.

et al., 2006), and stars of S type (Ramstedt et al., 2009). Results from these studies show a clear trend of SiO becoming less abundant as the density of the envelope increases, a similar behavior to that found in this work for SiC_2 in C-rich envelopes. The observed trend for SiO has been also interpreted in terms of a more efficient adsorption of SiO onto dust grains for high envelope densities. It has been noted, however, that in the case of S stars, the trend is not as clear as in M and C stars, although this may be due to the low number of high mass-loss S stars observed (see Ramstedt et al. 2009). A similar study carried out on the abundance of SiS in envelopes around O- and C-rich stars (Schöier et al., 2007) did not find a clear correlation between the fractional abundance of SiS and the density of the envelope, suggesting that this molecule is not affected as much as SiO by freeze-out onto dust grains. The conclusions regarding SiS, however, are limited by the low number of O- and C-rich stars studied.

In a recent study, Liu et al., (2017) investigated the relation between the intensities of SiO maser and silicate dust emission in a sample of O-rich AGB and post-AGB stars in an attempt to relate the abundance of SiO, a highly plausible gas-phase precursor of silicates, with the amount of silicate dust. These authors find a positive correlation between the velocity-integrated intensity of SiO maser and the emission power of silicate dust, which

is not against the hypothesis that SiO is a gas-phase precursor of silicate dust. It is important to note that in envelopes around O-rich AGB stars, SiO masers probe inner regions to where dust forms (Danchi et al., 1994; Reid et al., 1997), and thus the more abundant the precursor SiO in the maser formation region is, the higher the amount of silicate dust can later be formed. In any case, given the peculiar nature of maser emission (e.g., Gray et al. 2009) and the fact that the observables are not a straightforward proxy of abundances, it is not clear whether the observed trend can be interpreted in terms of a higher fractional abundance of SiO in envelopes with a higher amount of silicate dust.

Various studies carried out in recent years have used ALMA to investigate the potential role of titanium and aluminum oxides as gas-phase precursors of inorganic dust in oxygen-rich evolved stars. In M stars, TiO_2 and Al_2O_3 are predicted to be among the first solid compounds to condense out of the gas phase (Gail et al., 1998) and thus are ideal candidates to initiate the dust formation process. De Beck et al., (2015) and more recently Kamiński et al., (2017) have observed TiO and TiO_2 in the surroundings of the evolved stars VY Canis Majoris and Mira and found that these molecules extend out to several stellar radii from the star, and thus are unlikely to act as gas-phase precursors of TiO_2 dust. In a similar study, Kamiński et al., (2016) observed AlO around the star Mira, although they could not quantitatively assess the role of AlO as a gas-phase precursor of Al_2O_3 dust. ALMA is indeed a very promising tool for identifying gas-phase precursors of dust in evolved stars, but results are still not conclusive.

7.7 Conclusions

In this Chapter we used the IRAM 30m telescope to survey a sample of 25 C-rich circumstellar envelopes and search for rotational emission from the molecules SiC_2, SiC, and Si_2C. We detected SiC_2 in most of the sources and SiC in about half of them, while Si_2C was not detected in any of the sources with the exception of IRC +10216. We carried out excitation and radiative transfer calculations to derive SiC_2 fractional abundances. We found a clear trend in which SiC_2 becomes less abundant as the envelope density increases. We interpret this result as evidence of efficient incorporation of SiC_2 onto dust grains, a process that is more efficient at high densities because collisions between particles and coagulation processes become faster. The ring molecule SiC_2 thus emerges as a very likely gas-phase precursor in the process of formation of SiC dust in envelopes around C-rich AGB stars; therefore, SiC_2 seems to behave similarly to SiO, which has been found to deplete from the gas phase as the density in the envelope increases.

Table 7.5: Observed line parameters of SiC_2

Line	ν_{calc} (MHz)	ν_{obs} (MHz)	V_e (km s^{-1})	$\int T_A^* dv$ (K km s^{-1})
		IRC +10216		
$6_{2,5} - 5_{2,4}$	140920.171	140920.1(1)	13.8(1)	41.2(4)
$6_{4,3} - 5_{4,2}$	141751.492	141751.3(1)	13.8(1)	21.5(2)[a]
$6_{4,2} - 5_{4,1}$	141755.360	141755.2(1)	13.8(1)	22.2(2)[a]
$6_{2,4} - 5_{2,3}$	145325.875	145325.8(1)	14.3(1)	42.4(4)
$7_{0,7} - 6_{0,6}$	158499.228	158499.1(1)	15.3(1)	58.7(5)
		CIT 6		
$6_{2,5} - 5_{2,4}$	140920.171	140920.5(10)	16.2(8)	8.2(8)
$6_{4,3} - 5_{4,2}$	141751.492	141751.1(2)	15.4(8)	5.4(5)[a]
$6_{4,2} - 5_{4,1}$	141755.360	141754.9(3)	14.0(8)	2.7(3)[a]
$6_{2,4} - 5_{2,3}$	145325.875	145325.0(10)	13.8(10)	8.0(8)
$7_{0,7} - 6_{0,6}$	158499.228	158498.5(10)	15.1(8)	12.9(13)
		CRL 3068		
$6_{2,5} - 5_{2,4}$	140920.171	140920.5(1)	12.8(8)	1.78(2)
$6_{4,3} - 5_{4,2}$	141751.492	141751.3(1)	12.8(4)	1.07(1)[a]
$6_{4,2} - 5_{4,1}$	141755.360	141755.3(1)	12.8(4)	1.02(1)[a]
$6_{2,4} - 5_{2,3}$	145325.875	145325.7(1)	13.2(6)	1.84(2)
$7_{0,7} - 6_{0,6}$	158499.228	158499.2(2)	14.5(8)	2.73(3)
		S Cep		
$6_{2,5} - 5_{2,4}$	140920.171	140920.3(5)	20.5(4)	0.94(9)
$6_{4,3} - 5_{4,2}$	141751.492	141751.3(5)	21.8(1)	0.63(6)[a]
$6_{4,2} - 5_{4,1}$	141755.360	141755.9(5)	22.4(1)	0.49(5)[a]
$6_{2,4} - 5_{2,3}$	145325.875	145325.5(5)	21.7(8)	1.06(10)
$7_{0,7} - 6_{0,6}$	158499.228	158499.9(2)	23.0(5)	1.66(16)
		IRC +30374		
$6_{2,5} - 5_{2,4}$	140920.171	140920.4(1)	23.0(8)	1.43(14)
$6_{4,3} - 5_{4,2}$	141751.492	141751.8(3)	22.8(4)	0.84(8)[a]
$6_{4,2} - 5_{4,1}$	141755.360	141755.5(3)	22.9(4)	0.62(6)[a]
$6_{2,4} - 5_{2,3}$	145325.875	145325.9(1)	23.4(4)	1.50(4)
$7_{0,7} - 6_{0,6}$	158499.228	158499.4(1)	25.5(8)	2.22(2)
		Y CVn		
$6_{2,5} - 5_{2,4}$	140920.171	140921.7(10)	8.6(10)	0.23(4)

Table 7.5: Continued.

Line	ν_{calc} (MHz)	ν_{obs} (MHz)	V_e (km s^{-1})	$\int T_A^* dv$ (K km s^{-1})
$6_{4,3} - 5_{4,2}$	141751.492	141751.7(2)	7.3(8)	0.16(2)[a]
$6_{4,2} - 5_{4,1}$	141755.360	141755.7(2)	7.5(6)	0.12(2)[a]
$6_{2,4} - 5_{2,3}$	145325.875	145326.3(10)	7.1(10)	0.26(5)
$7_{0,7} - 6_{0,6}$	158499.228	158499.1(5)	6.6(5)	0.44(9)
		LP And		
$6_{2,5} - 5_{2,4}$	140920.171	140920.3(1)	13.0(8)	3.86(4)
$6_{4,3} - 5_{4,2}$	141751.492	141751.6(2)	13.1(8)	1.93(2)[a]
$6_{4,2} - 5_{4,1}$	141755.360	141755.4(2)	13.2(8)	2.06(2)[a]
$6_{2,4} - 5_{2,3}$	145325.875	145325.9(1)	13.4(8)	3.99(4)
$7_{0,7} - 6_{0,6}$	158499.228	158499.3(1)	14.6(8)	6.34(6)
		V Cyg		
$6_{2,5} - 5_{2,4}$	140920.171	140920.3(1)	10.4(8)	1.87(2)
$6_{4,3} - 5_{4,2}$	141751.492	141751.7(2)	10.8(4)	0.91(2)[a]
$6_{4,2} - 5_{4,1}$	141755.360	141755.4(2)	10.6(4)	0.91(2)[a]
$6_{2,4} - 5_{2,3}$	145325.875	145326.1(3)	11.0(8)	1.95(2)
$7_{0,7} - 6_{0,6}$	158499.228	158499.4(1)	11.8(8)	3.47(3)
		V384 Per		
$6_{2,5} - 5_{2,4}$	140920.171	140920.2(1)	13.5(4)	1.80(2)
$6_{4,3} - 5_{4,2}$	141751.492	141751.4(1)	13.9(2)	0.80(1)[a]
$6_{4,2} - 5_{4,1}$	141755.360	141755.1(1)	13.8(2)	1.04(2)[a]
$6_{2,4} - 5_{2,3}$	145325.875	145326.0(1)	13.6(8)	1.88(2)
$7_{0,7} - 6_{0,6}$	158499.228	158499.3(1)	15.1(1)	3.09(3)
		IRC +60144		
$6_{2,5} - 5_{2,4}$	140920.171	140920.4(5)	19.1(8)	0.55(5)
$6_{4,3} - 5_{4,2}$	141751.492	141751.3(1)	18.5(2)	0.37(4)[a]
$6_{4,2} - 5_{4,1}$	141755.360	141755.4(4)	19.9(3)	0.25(2)[a]
$6_{2,4} - 5_{2,3}$	145325.875	145325.9(2)	19.7(1)	0.25(2)
$7_{0,7} - 6_{0,6}$	158499.228	158499.4(2)	21.5(4)	0.73(7)
		U Cam		
$6_{2,5} - 5_{2,4}$	140920.171	140920.8(5)	11.2(5)	0.39(4)
$6_{4,3} - 5_{4,2}$	141751.492	141751.9(10)	14.0(8)	0.21(2)[a]
$6_{4,2} - 5_{4,1}$	141755.360	141755.5(10)	13.1(8)	0.19(2)[a]

Table 7.5: Continued.

Line	ν_{calc} (MHz)	ν_{obs} (MHz)	V_e (km s^{-1})	$\int T_A^* dv$ (K km s^{-1})
$6_{2,4} - 5_{2,3}$	145325.875	145326.3(10)	11.9(8)	0.41(4)
$7_{0,7} - 6_{0,6}$	158499.228	158499.6(5)	12.6(5)	0.63(6)
		V636 Mon		
$6_{2,5} - 5_{2,4}$	140920.171	140921.2(10)	21.3(10)	0.35(7)
$6_{4,3} - 5_{4,2}$	141751.492	141751.8(4)	20.3(8)	0.17(3)[a]
$6_{4,2} - 5_{4,1}$	141755.360	141754.4(3)	19.7(6)	0.23(5)[a]
$6_{2,4} - 5_{2,3}$	145325.875	145326.5(10)	23.3(10)	0.37(1)
$7_{0,7} - 6_{0,6}$	158499.228	158499.9(10)	21.8(10)	0.61(2)
		IRC +20370		
$6_{2,5} - 5_{2,4}$	140920.171	140920.2(1)	13.0(2)	0.98(9)
$6_{4,3} - 5_{4,2}$	141751.492	141751.6(5)	13.2(5)	0.53(5)[a]
$6_{4,2} - 5_{4,1}$	141755.360	141755.3(5)	13.4(5)	0.51(5)[a]
$6_{2,4} - 5_{2,3}$	145325.875	145325.9(3)	13.2(5)	1.12(11)
$7_{0,7} - 6_{0,6}$	158499.228	158499.3(2)	14.6(1)	1.83(18)
		W Ori		
$6_{2,5} - 5_{2,4}$	140920.171	140920.2(10)	9.4(10)	0.12(5)[c]
$6_{4,3} - 5_{4,2}$	141751.492	141751.5(10)	10.5(10)	0.06(1)[c]
$6_{4,2} - 5_{4,1}$	141755.360	141754.6(10)	10.9(10)	0.06(3)[c]
$6_{2,4} - 5_{2,3}$	145325.875	145325.2(10)	8.2(10)	0.11(2)[c]
$7_{0,7} - 6_{0,6}$	158499.228	158499.9(5)	12.1(10)	0.31(6)
		CRL 67		
$6_{2,5} - 5_{2,4}$	140920.171	140920.3(1)	14.6(1)	1.57(1)
$6_{4,3} - 5_{4,2}$	141751.492	141751.5(5)	15.6(5)	0.72(7)[a]
$6_{4,2} - 5_{4,1}$	141755.360	141755.2(5)	14.9(5)	0.96(9)[a]
$6_{2,4} - 5_{2,3}$	145325.875	145325.9(2)	14.6(4)	1.61(2)
$7_{0,7} - 6_{0,6}$	158499.228	158499.3(3)	15.8(4)	2.47(2)
		CRL 190		
$6_{2,5} - 5_{2,4}$	140920.171	140920.6(1)	16.4(1)	1.08(10)
$6_{4,3} - 5_{4,2}$	141751.492	141751.6(3)	16.3(5)	0.29(3)[a]
$6_{4,2} - 5_{4,1}$	141755.360	141755.1(2)	15.2(5)	0.37(4)[a]
$6_{2,4} - 5_{2,3}$	145325.875	145325.9(1)	15.4(1)	0.12(1)

Table 7.5: Continued.

Line	ν_{calc} (MHz)	ν_{obs} (MHz)	V_e (km s^{-1})	$\int T_A^* dv$ (K km s^{-1})
$7_{0,7} - 6_{0,6}$	158499.228	158499.6(1)	16.8(4)	0.77(7)
		S Aur		
$6_{2,5} - 5_{2,4}$	140920.171	140920.3(10)	23.7(10)	0.11(2)[c]
$6_{4,3} - 5_{4,2}$	141751.492	141753.1(10)	22.2(14)	0.13(3)[b,c]
$6_{4,2} - 5_{4,1}$	141755.360	-	-	-
$6_{2,4} - 5_{2,3}$	145325.875	145324.9(10)	25.7(15)	0.15(3)[c]
$7_{0,7} - 6_{0,6}$	158499.228	158499.1(5)	24.4(8)	0.28(6)
		V Aql		
$6_{2,5} - 5_{2,4}$	140920.171	140920.1(5)	6.7(4)	0.31(6)
$6_{4,3} - 5_{4,2}$	141751.492	141751.7(10)	8.0(10)	0.26(5)[b]
$6_{4,2} - 5_{4,1}$	141755.360	141755.3(10)	9.7(10)	0.12(2)[b]
$6_{2,4} - 5_{2,3}$	145325.875	145326.1(5)	8.1(6)	0.38(7)
$7_{0,7} - 6_{0,6}$	158499.228	158499.2(5)	8.0(5)	0.60(12)
		CRL 2513		
$6_{2,5} - 5_{2,4}$	140920.171	140922.1(10)	20.3(10)	0.22(4)
$6_{4,3} - 5_{4,2}$	141751.492	141751.7(10)	20.6(10)	0.23(4)[b]
$6_{4,2} - 5_{4,1}$	141755.360	-	-	-
$6_{2,4} - 5_{2,3}$	145325.875	145326.3(10)	25.6(10)	0.29(6)[c]
$7_{0,7} - 6_{0,6}$	158499.228	158499.8(5)	26.9(4)	0.58(11)
		CRL 2477		
$6_{2,5} - 5_{2,4}$	140920.171	140920.1(1)	18.5(10)	0.46(4)
$6_{4,3} - 5_{4,2}$	141751.492	141751.5(2)	18.2(4)	0.28(6)[a]
$6_{4,2} - 5_{4,1}$	141755.360	141755.2(2)	19.9(4)	0.30(6)[a]
$6_{2,4} - 5_{2,3}$	145325.875	145325.7(5)	19.3(5)	0.51(1)
$7_{0,7} - 6_{0,6}$	158499.228	158499.5(5)	20.0(5)	0.72(14)
		CRL 2494		
$6_{2,5} - 5_{2,4}$	140920.171	140920.2(5)	17.4(8)	1.41(1)
$6_{4,3} - 5_{4,2}$	141751.492	141751.8(5)	18.1(5)	0.81(1)[a]
$6_{4,2} - 5_{4,1}$	141755.360	141755.3(5)	18.1(5)	0.91(1)[a]
$6_{2,4} - 5_{2,3}$	145325.875	145326.7(5)	18.3(8)	1.53(1)
$7_{0,7} - 6_{0,6}$	158499.228	158499.5(3)	19.5(4)	2.10(2)

Table 7.5: Continued.

Line	ν_{calc} (MHz)	ν_{obs} (MHz)	V_e (km s^{-1})	$\int T_A^* dv$ (K km s^{-1})
		RV Aqr		
$6_{2,5} - 5_{2,4}$	140920.171	140920.7(10)	14.3(10)	0.37(7)
$6_{4,3} - 5_{4,2}$	141751.492	141751.4(5)	14.7(10)	0.18(3)[a]
$6_{4,2} - 5_{4,1}$	141755.360	141755.3(5)	14.2(10)	0.18(3)[a]
$6_{2,4} - 5_{2,3}$	145325.875	145325.9(10)	15.6(10)	0.39(8)
$7_{0,7} - 6_{0,6}$	158499.228	158499.6(5)	15.5(5)	0.65(10)

Notes. Numbers in parentheses are 1σ uncertainties in units of the last digits.

[a] Blend of two lines, each of which could be fitted individually.

[b] Blend of two lines which could not be fitted individually. Only one component was fitted.

[c] Marginal detection.

Chapter 8

Study of CS, SiO, and SiS abundances in carbon star envelopes

This chapter is based on the publication:

Study of CS, SiO, and SiS abundances in carbon star envelopes*: assessing their role as gas-phase precursors of dust

S. Massalkhi, M. Agúndez, and J. Cernicharo

ASTRONOMY & ASTROPHYSICS, A&A, 628, A62 (2019)

*Based on observations carried out with the IRAM 30m Telescope. IRAM is supported by INSU/CNRS (France), MPG (Germany), and IGN (Spain).

ABSTRACT

Aims: We aim to determine the abundances of CS, SiO, and SiS in a large sample of carbon star envelopes covering a wide range of mass loss rates to investigate the potential role that these molecules could play in the formation of dust in the surroundings of the central AGB star.

Method: We surveyed a sample of 25 carbon-rich AGB stars in the λ 2 mm band, more concretely in the $J = 3 - 2$ line of CS and SiO, and in the $J = 7 - 6$ and $J = 8 - 7$ lines of SiS, using the IRAM 30 m telescope. We performed excitation and radiative transfer calculations based on the large velocity gradient (LVG) method to model the

observed lines of the molecules and to derive their fractional abundances in the observed envelopes. We also assessed the effect of infrared pumping in the excitation of the molecules.

Results: We detected CS in all 25 targeted envelopes, SiO in 24 of them, and SiS in 17 sources. Remarkably, SiS is not detected in any envelope with a mass loss rate below 10^{-6} $M_{\odot}$ yr^{-1} while it is detected in all envelopes with mass loss rates above that threshold. We found that CS and SiS have similar abundances in carbon star envelopes, while SiO is present with a lower abundance. We also found a strong correlation in which the denser the envelope, the less abundant are CS and SiO. The trend is however only tentatively seen for SiS in the range of high mass loss rates. Furthermore, we found a relation in which the integrated flux of the MgS dust feature at 30 μm increases as the fractional abundance of CS decreases.

Conclusion: The decline in the fractional abundance of CS with increasing density could be due to gas-phase chemistry in the inner envelope or to adsorption onto dust grains. The latter possibility is favored by a correlation between the CS fractional abundance and the 30 μm feature, which suggests that CS is efficiently incorporated onto MgS dust around C-rich AGB stars. In the case of SiO, the observed abundance depletion with increasing density is most likely caused by an efficient incorporation onto dust grains. We conclude that CS, SiO (very likely), and SiS (tentatively) are good candidates to act as gas-phase precursors of dust in C-rich AGB envelopes.

8.1 Introduction

In this Chapter, we follow up on our study in Chapter 7 to investigate the abundance of CS, SiO, and SiS in the envelopes of carbon stars and to understand their potential role as gas-phase precursors of dust grains. We present observations of SiO ($J = 3-2$), SiS ($J = 7-6$ and $J = 8-7$), and CS ($J = 3-2$) in a sample of 25 carbon stars with diverse mass loss rates. We carried out a detailed non-local thermodynamic equilibrium (non-LTE) radiative transfer analysis to derive molecular abundances in the CSEs. The sample of stars and observational details are presented in Sec. 8.2 and the main results obtained from the observations in Sec. 8.3. In Sec. 8.4 we describe the model and the excitation and radiative transfer calculations and discuss the most interesting features from these calculations in Sec. 8.5. Finally, we discuss the main implications of our study in Sec. 8.6 and present our conclusions in Sec. 8.7.

Table 8.1: Sample of carbon stars

Name	R.A. J2000.0	Dec. J2000.0	$V_{\rm LSR}$ (km s^{-1})	D (pc)	$T_\star$ (K)	$L_\star$ (L$_\odot$)	$\dot{M}$ (M$_\odot$ yr^{-1})	$V_{\rm exp}$ (km s^{-1})	$T_{\rm d}(r_c)$ (K)	r_c (cm)	Ψ
IRC +10216	09:47:57.45	+13:16:43.9	−26.5	130	2330	8750	2.0×10^{-5}	14.5	800	2.0×10^{14}	300
CIT 6	10:16:02.27	+30:34:18.6	−1	400	1800	10000	6.0×10^{-6}	17	1000	2.1×10^{14}	141
CRL 3068	23:19:12.24	+17:11:33.4	−31.5	1300	1800	10900	2.5×10^{-5}	14.5	1500	2.0×10^{14}	174
S Cep	21:35:12.83	+78:37:28.2	−15.3	380	2200	7300	1.2×10^{-6}	22.5	1400	5.8×10^{13}	360
IRC +30374	19:34:09.87	+28:04:06.3	−12.5	1200	2000	9800	1.0×10^{-5}	25	1000	2.2×10^{14}	1008
Y CVn	12:45:07.83	+45:26:24.9	+22	220	2200	4400	1.5×10^{-7}	7	1500	8.7×10^{13}	500
LP And	23:34:27.53	+43:33:01.2	−17	630	1900	9600	7.0×10^{-6}	14.5	1100	1.8×10^{14}	288
V Cyg	20:41:18.27	+48:08:28.8	+13.5	366	2300	6000	1.6×10^{-6}	12	1400	9.4×10^{13}	364
UU Aur	06:36:32.84	+38:26:43.8	+6.7	260	2800	6900	2.4×10^{-7}	10.6	1500	6.3×10^{13}	1000
V384 Per	03:26:29.51	+47:31:48.6	−16.8	560	2000	8100	2.3×10^{-6}	15.5	1300	1.0×10^{14}	584
IRC +60144	04:35:17.54	+62:16:23.8	−48.8	1030	2000	7800	3.7×10^{-6}	19.5	1200	2.0×10^{14}	1014
U Cam	03:41:48.17	+62:38:54.4	+6	430	2695	7000	2.0×10^{-7}	13	1500	4.4×10^{13}	833
V636 Mon	06:25:01.43	−09:07:15.9	+10	880	2500	8472	5.8×10^{-6}	20	1200	1.7×10^{14}	300
IRC +20370	18:41:54.39	+17:41:08.5	−0.8	600	2200	7900	3.0×10^{-6}	14	1500	8.1×10^{13}	266
R Lep	04:59:36.35	−14:48:22.5	+11.5	432	2200	5500	8.7×10^{-7}	17.5	1000	1.8×10^{14}	500
W Ori	05:05:23.72	+01:10:39.5	−1	220	2600	3500	7.0×10^{-8}	11	1500	4.3×10^{13}	333
CRL 67	00:27:41.10	+69:38:51.5	−27.5	1410	2500	9817	1.1×10^{-5}	16	1200	1.8×10^{14}	495
CRL 190	01:17:51.62	+67:13:55.4	−39.5	2790	2500	16750	6.4×10^{-5}	17	1000	4.7×10^{14}	424
S Aur	05:27:07.45	+34:08:58.6	−17	300	3000	8900	4.0×10^{-7}	24.5	1500	7.3×10^{13}	500
V Aql	19:04:24.15	−05:41:05.4	+53.5	330	2800	6500	1.4×10^{-7}	8	1500	6.1×10^{13}	500
CRL 2513	20:09:14.25	+31:25:44.9	+17.5	1760	2500	8300	2.0×10^{-5}	25.5	1200	1.6×10^{14}	453
CRL 2477	19:56:48.43	+30:43:59.9	+5	3380	3000	13200	1.1×10^{-4}	20	1800	2.8×10^{14}	532
CRL 2494	20:01:08.51	+40:55:40.2	+29	1480	2400	10200	7.5×10^{-6}	20	1200	2.3×10^{14}	436
RV Aqr	21:05:51.74	−00:12:42.0	+0.5	670	2200	6800	2.3×10^{-6}	15	1300	7.6×10^{13}	200
ST Cam	04:51:13.35	+68:10:07.6	−13.6	360	2800	4400	1.3×10^{-7}	8.9	1500	5.0×10^{13}	500

Notes. The adopted parameters are discussed in Massalkhi et al., (2018) (see Chapter 6). See references therein. Ψ for UU Aur and R Lep is from Schöier et al., (2001) and for IRC +60144 from Groenewegen et al., (2002)

8.2 Observations

The observations were carried out in September 2017 with the IRAM 30 m telescope, located at Pico Veleta, Spain. The sample of 25 C-rich AGB stars observed is the same used in our previous study of SiC_2 (Massalkhi et al., 2018) and was selected according to intense molecular emission, mainly based on the intensity of the HCN $J = 1 - 0$ line (Bujarrabal et al., 1994; Loup et al., 1993; Schöier et al., 2013). The observed sources and their parameters are listed in Table 8.1. In this study, we focused on the emission of CS, SiO, and SiS and therefore the spectral setup used was slightly shifted from that employed in Massalkhi et al., (2018) and accommodated in a way to include the lines CS $J = 3 - 2$, SiO $J = 3 - 2$ and SiS $J = 7 - 6$ and $J = 8 - 7$ (see line parameters in Table 8.2).

We used the E150 receiver in dual side band, with image rejections >10 dB, and observed the frequency ranges $125.7 - 133.5$ GHz and $141.4 - 149.2$ GHz in the lower and upper side bands, respectively. The beam size of the telescope at these frequencies is in the range 16.7-19.3″. We used the wobbler-switching technique. This technique consists of a symmetric position switching with the OFF position (atmosphere) at 180″ in azimuth from the ON position (source + atmosphere). Spectra at the OFF and ON positions are taken by nutating the secondary mirror at a rate of 0.5 Hz, and the OFF is subtracted from the ON to remove the contribution of the atmosphere to the signal. The focus was regularly checked on Venus and the pointing of the telescope was systematically checked on a nearby quasar before observing each AGB star. The error in the pointing is estimated to be 2-3″. The E150 receiver was connected to a fast Fourier transform spectrometer providing a spectral resolution of 0.2 MHz. The weather was good and stable during most of the observations, with typical amounts of precipitable water vapor of 1-3 mm and average system temperatures of 115 K. The intensity scale, calibrated using two absorbers at different temperatures and the atmospheric transmission model (ATM) (Cernicharo, 1985; Pardo et al., 2001), is expressed in terms of $T_{\rm mb}$, the main beam brightness temperature. The error in the intensities due to calibration is estimated to be ∼20 %.

The data were reduced using the CLASS* within the package GILDAS†. For each source, we averaged the spectra corresponding to the horizontal and vertical polarizations and subtracted a baseline consisting of a first order polynomial. When the lines were not very strong, the spectra were smoothed to a spectral resolution of 1 MHz to increase the signal-to-noise ratio. This corresponds to a velocity resolution of 2-2.4 km s^{-1}. Typical on source

*Continuum and Line Analysis Single-dish Software

†http://www.iram.fr/IRAMFR/GILDAS

Table 8.2: Covered rotational transitions of CS, SiO, and SiS

Transition	Frequency (MHz)	A_{ul} (s^{-1})	E_u (K)	θ_{mb} ($''$)
CS $J = 3-2$	146969.025	6.07×10^{-5}	14.1	16.7
SiO $J = 3-2$	130268.665	1.06×10^{-4}	12.5	18.8
SiS $J = 7-6$	127076.178	3.36×10^{-5}	24.4	19.3
SiS $J = 8-7$	145227.052	5.05×10^{-5}	31.4	16.9

integration times, after averaging horizontal and vertical polarizations, were $\sim$1 h for each source, resulting in $T_{\rm mb}$ rms noise levels per 1 MHz channel of 2-6 mK.

8.3 Observational results

The spectra obtained are shown in Fig. 8.1 (CS $J = 3-2$), Fig. 8.2 (SiO $J = 3-2$), and Figs. 8.3 and 8.4 (SiS $J = 7-6$ and $J = 8-7$, respectively). The observed lines exhibit profiles typical of expanding circumstellar shells, i.e., either double-peaked, flat-topped, or parabolic, which can be reasonably well fit by the `shell` method of CLASS. The method fits the function

$$f(\nu) = \frac{A}{\Delta\nu}\frac{1+4H[(\nu-\nu_0)/\Delta\nu]^2}{1+H/3}, \tag{8.1}$$

where A is the area under the profile in K MHz, ν_0 is the middle frequency in MHz, $\Delta\nu$ is the full width at zero intensity level in MHz, and H is the horn-to-center ratio, which is dimensionless. The expansion velocity $V_{\rm exp}$ can then be obtained by the following expression:

$$V_{\rm exp} = c\frac{\Delta\nu/2}{\nu_0}, \tag{8.2}$$

where c is the speed of light.

By performing the fit, we aim to derive for the target lines in every source the centroid frequency, expansion velocity, and line area, i.e., the velocity-integrated intensity. Most of the observed lines show profiles that match one of the types mentioned above, apart from the two sources U Cam (see line profile of CS emission in Fig. 8.1) and CIT 6 (see line profile of SiO in Fig. 8.2), which have profiles that deviate from the expected line profile of a spherical expanding shell. The CS emission of U Cam is interpreted below as having two components, which we faced no difficulty considering separately. CIT 6 shows a rather

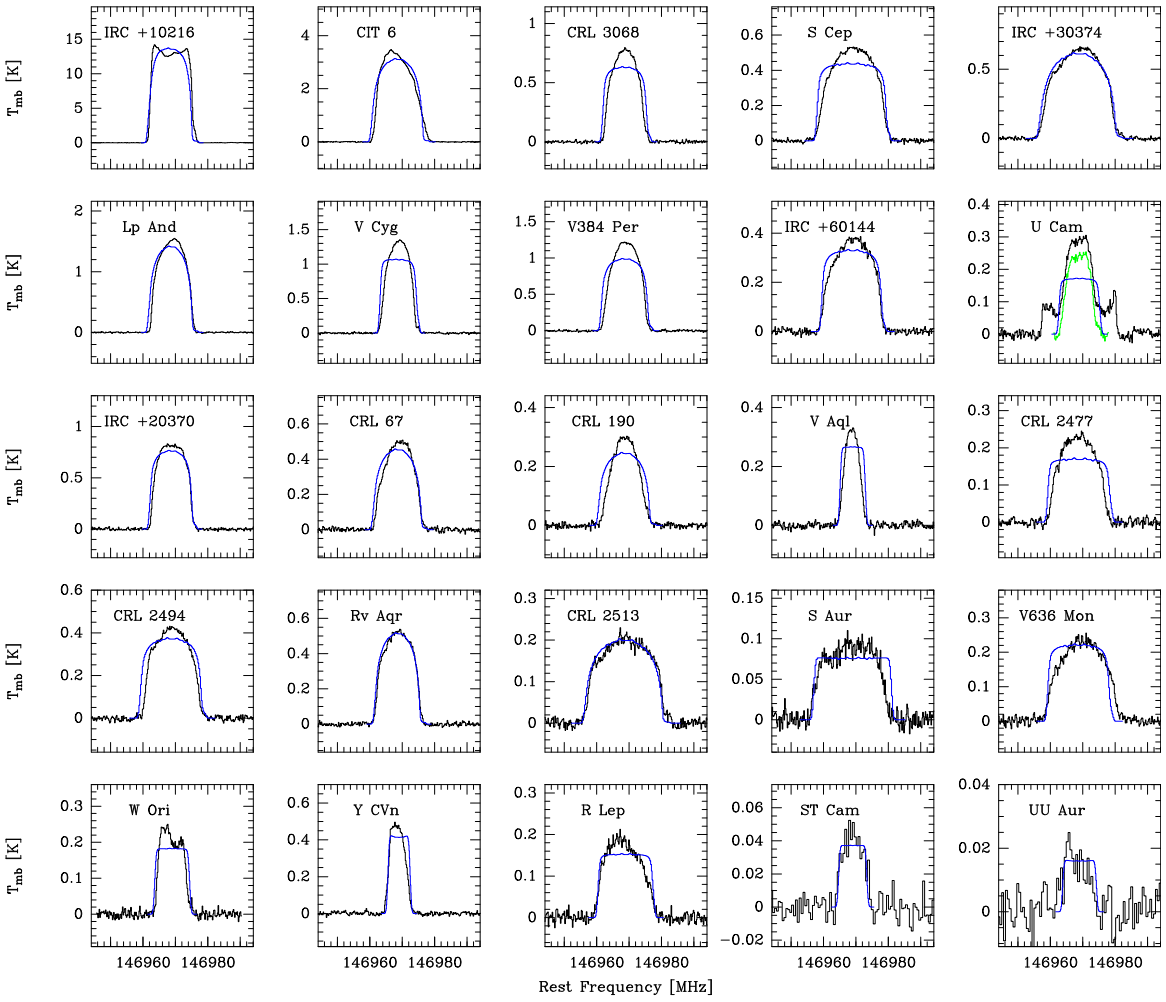

Figure 8.1: CS $J = 3 - 2$ line observed with the IRAM 30 m telescope in the 25 carbon stars (black histograms). U Cam shows emission contribution from the present day wind and the detached envelope. The green histogram corresponds to the observed line profile in which a fit to the detached envelope contribution (the wider one) has been subtracted. The blue lines indicate the calculated line profiles from the best-fit LVG model.

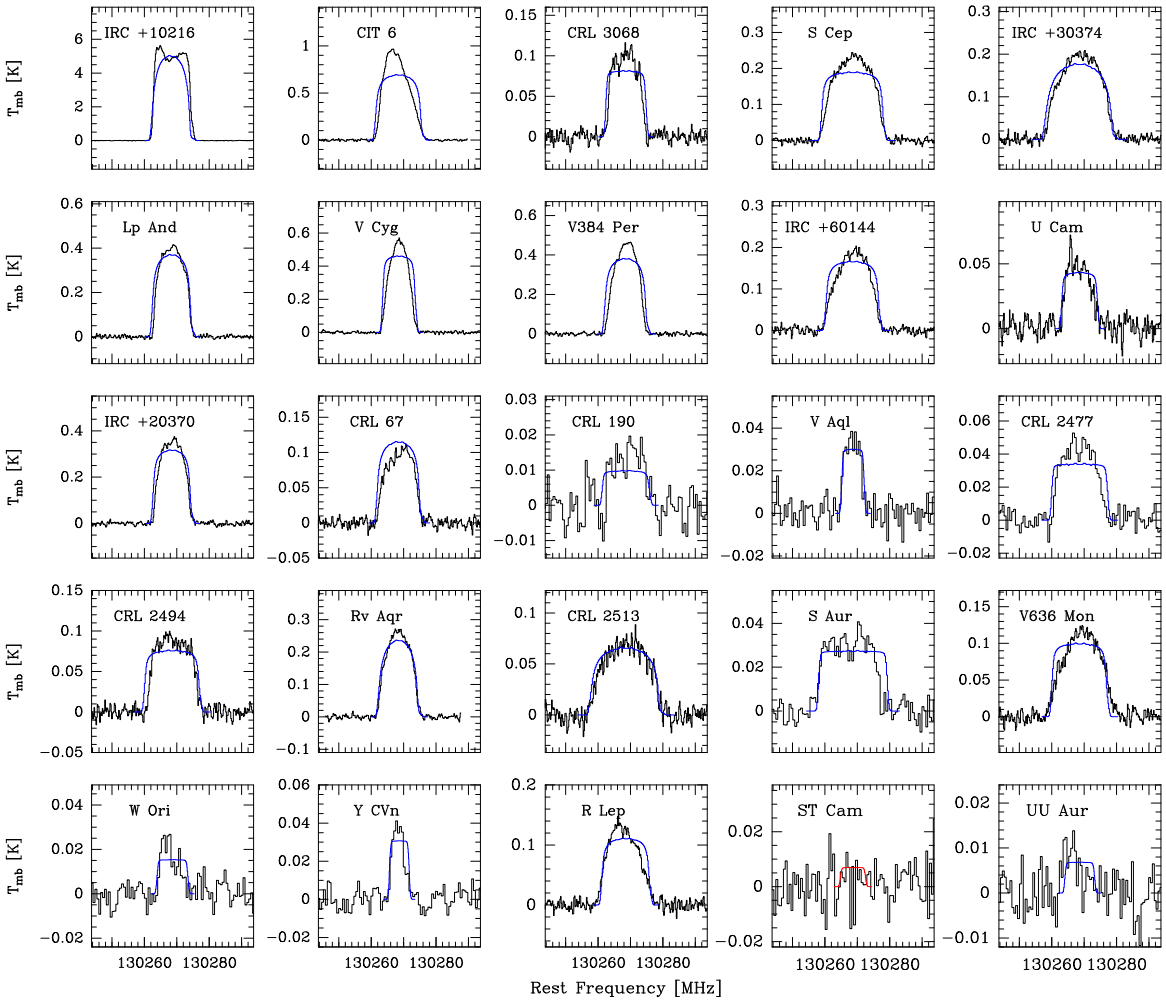

Figure 8.2: SiO $J = 3 - 2$ line observed with the IRAM 30 m telescope in the 25 carbon stars (black histograms). The blue lines indicate the calculated line profiles from the best-fit LVG model. The SiO line is not detected in ST Cam; the red line corresponds to the calculated line profile with the maximum intensity compatible with the non-detection.

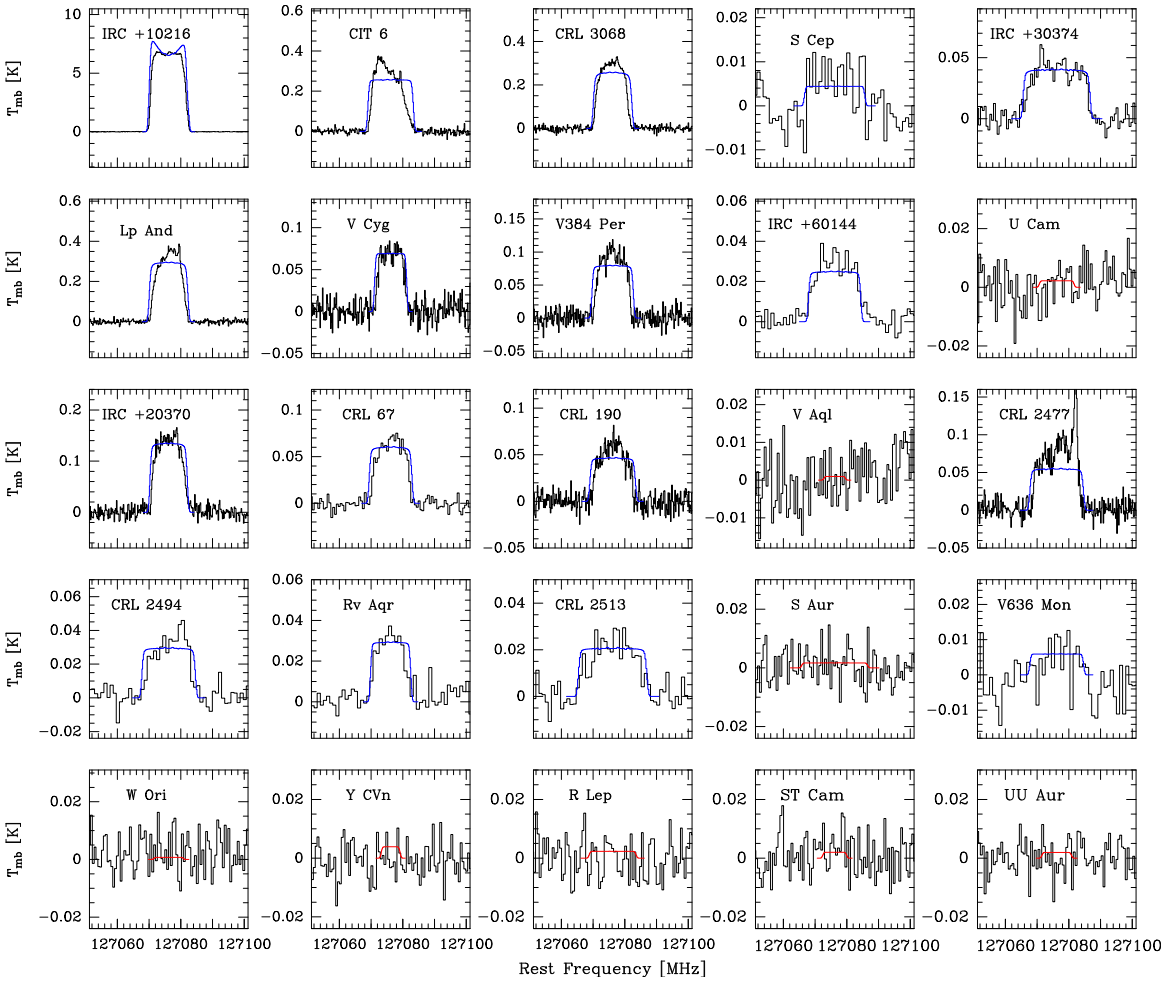

Figure 8.3: SiS $J = 7 - 6$ line observed with the IRAM 30 m telescope in the 25 carbon stars (black histograms). The blue lines indicate the calculated line profiles from the best-fit LVG model. The SiS line is not detected in various sources, for which we plot in red the calculated line profiles with the maximum intensity compatible with the non-detection.

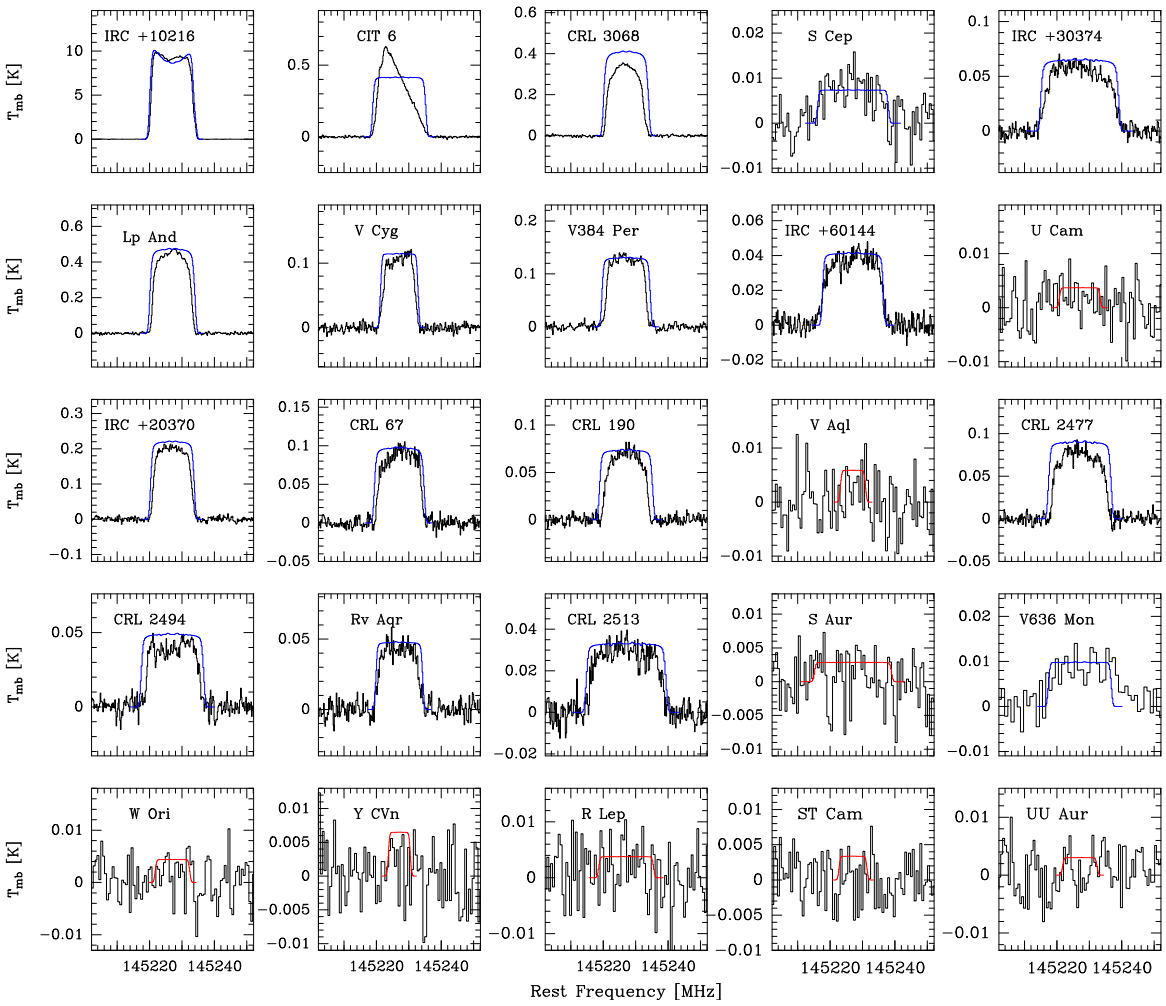

Figure 8.4: Same as in Fig. 8.3 but for SiS $J = 8 - 7$.

asymmetrical profile in the SiO $J = 3-2$, SiS $J = 7-6$ and $J = 8-7$ lines. In any case, the two most interesting parameters, the line area and the expansion velocity, are reasonably well fitted. The derived parameters of the observed line profiles are shown in Table 8.6.

The observations resulted in the clear detection of CS $J = 3-2$ in all targeted sources. In the case of SiO, we detected the $J = 3-2$ line in all target sources with the exception of ST Cam. As previously mentioned, the case of U Cam deserves particular attention because this source exhibits emission arising from a present-day wind and from a geometrically thin detached shell surrounding the central star (Schöier et al., 2005). The detached shell is probably the result of episodic mass loss driven by helium shell flashes, i.e., thermal pulses (Olofsson et al., 1990). According to the observed line profiles, CS emission in U Cam arises from both the present-day wind and the detached envelope, while SiO emission arises exclusively from the present-day wind; compare line profiles of CS and SiO in Figs. 8.1 and 8.2, respectively, with that of CO $J = 1-0$ in Fig. 6 of Schöier et al., (2005). To disentangle the contribution from each component in the emission line of CS, we fitted the observed line with two components of different line widths; the narrow line width corresponds to the present-day wind and the wide to the detached envelope. The green line in Fig. 8.1 corresponds to the emission from the present-day wind, which we are ultimately interested in modeling. In the case of SiS, the $J = 7-6$ and $J = 8-7$ lines were detected in 17 out of 25 sources, that is, in all sources except U Cam, V Aql, S Aur, W Ori, Y CVn, R Lep, ST Cam, and UU Aur.

The lines profile shapes usually give information about the emission being observed. When the emission is optically thick and unresolved by the beam of the telescope, the line profiles can be described as parabolic. We see that in most sources, the observed line shapes of CS and SiO exhibit such profile. If the emission is optically thin and unresolved, a flat-topped profile is seen. This kind of profile is seen in the observed lines of SiS. One notable exception for the three molecules is IRC +10216, whose close proximity and high mass loss rate result in an extended envelope whose molecular emission is spatially resolved by the telescope beam, and the line profiles show a more or less marked double-peak character.

8.4 Excitation and radiative transfer modeling

We aim at deriving molecular abundances of CS, SiO, and SiS in each source of our sample to provide a global view of how abundant these molecules are in envelopes around carbon stars. For this purpose, we performed excitation and radiative transfer calculations. The rotational lines of CS, SiO, and SiS studied in this work have upper level energies in the range

12.5 - 31.4 K. As shown in Sec. 8.5, the emission from these lines does not arise from the inner parts of the envelope but from the intermediate and outer regions, where gas densities are not high enough to thermalize the rotational levels. Therefore, level populations cannot be described by local thermodynamic equilibrium (LTE), and detailed non-LTE excitation and radiative transfer calculations have to be carried out taking into account the specific parameters for each envelope (see Table 8.1) to derive accurate molecular abundances.

We consider an envelope model consisting of a central AGB star surrounded by a spherically symmetric envelope of gas and dust expanding at constant velocity $V_{\rm exp}$ and with a mass loss rate $\dot{M}$, so that the radial density distribution follows an r^{-2} law. The adopted physical properties of the stars and associated CSEs are presented in Table 8.1. The various physical quantities describing the envelope, such as the radial profiles of the gas density, gas temperature, and dust temperature, as well as the properties of the dust grains, are described in Massalkhi et al., (2018).

We performed excitation and radiative transfer calculations to model the line emission of the studied molecules based on the multishell large velocity gradient (LVG) method. The LVG formalism is described in Sobolev, (1960) and Castor, (1970), whereas the implementation of the multishell method for CSEs is described in more detail in Agúndez, (2009) and Agúndez et al., (2012). The LVG method deals well with optically thin lines and lines with moderate optical thickness (Castor 1970). This method is a good compromise with respect to other methodologies such as Monte Carlo, which are more computationally expensive and exhibit problems of convergence when including a high number of energy levels. Briefly, the circumstellar envelope is divided into a number of concentric shells, each of which has a characteristic set of physical properties. The excitation and radiative transfer is solved locally in each shell through statistical equilibrium equations, where collisional and radiative processes determine the level populations. In each shell, the contribution of the background radiation field is included and is composed of the cosmic microwave background, stellar radiation, and thermal emission from dust. We also include infrared (IR) pumping, that is, absorption of IR photons and pumping to excited vibrational states followed by spontaneous radiative decay to rotational levels in the ground vibrational state. This process has been found to play an important role in the excitation of some molecules in IRC +10216 (e.g., Agúndez et al. 2006). For the three molecules studied here (CS, SiO, and SiS), we only considered IR pumping to the first vibrationally excited state ($v = 1$). We did verify that adding upper vibrational states had no effect on the calculated line intensities, i.e., including up to $v = 1$ changed the line intensities for the three molecules in all the stars, but including up to $v = 3$ did not cause further changes.

8.4.1 Molecular data

A major prerequisite for a successful radiative transfer code is the availability of accurate spectroscopic and collisional excitation data. We discuss below the spectroscopic and collisional excitation data of the three molecules that were input into our calculations. We considered enough rotational states to include levels with energies higher than 2000 K to better deal with the inner hot regions of the envelopes.

In the excitation analysis of CS we considered the first 50 rotational levels within the $v = 0$ and $v = 1$ vibrational states (i.e., a total number of 100 energy levels). The level energies and transition frequencies were calculated from the Dunham coefficients given by Müller et al., (2005b). The line strengths of pure rotational transitions were computed from the dipole moments for each vibrational state, $\mu_{v=0}$ =1.958 D and $\mu_{v=1}$ = 1.936 D (Winnewisser et al., 1968), while for ro-vibrational transitions we used the Einstein coefficient of 15.8 s^{-1} given for the $v = 1 \rightarrow 0$ P(1) transition by Chandra et al., (1995). We adopted the collision rate coefficients recently calculated by Denis-Alpizar et al., (2018) for pure rotational transitions and up to temperatures of 300 K. At higher temperatures and for ro-vibrational transitions we used the rate coefficients calculated by Lique et al., (2007) multiplying the original values computed for He as collider by the squared ratio of the reduced masses of the H_2 and He colliding systems.

In the case of SiO, we considered the first 50 rotational levels of the ground and first excited vibrational states. To calculate the line frequencies and strengths, we used the Dunham coefficients given by Sanz et al., (2003), the dipole moments for pure rotational transitions within the $v = 0$ and $v = 1$ vibrational states of 3.0982 D and 3.1178 D, respectively, from Raymonda et al., (1970) and an Einstein coefficient for the ro-vibrational transition $v = 1 \rightarrow 0$ P(1) of 6.61 s^{-1} from Drira et al., (1997). As collisional rate coefficients we adopted those calculated by Dayou et al., (2006) for pure rotational transitions and for temperatures up to 300 K, while at higher temperatures and for ro-vibrational transitions we used the values computed by Balança et al., (2017) scaling from He to H_2 as collider as in the case of CS.

For SiS, we include the first 70 rotational levels within the $v = 0$ and $v = 1$ vibrational states. Level energies were computed from the Dunham coefficients given by Müller et al., (2007). Line strengths were computed from the dipole moments $\mu_{v=0}$ =1.735 D, $\mu_{v=1}$ = 1.770 D, and $\mu_{v=1\rightarrow0}$ = 0.13 D (Müller et al., 2007; Piñeiro et al., 1987). The collisional rate coefficients have been taken from the calculations of Kłos et al., (2008), while for

temperatures higher than 300 K and for ro-vibrational transitions we adopted the collisional rate coefficients computed by Toboła et al., (2008) scaled from He to H_2 as with CS and SiO.

8.4.2 Abundance distributions

We consider that CS, SiO, and SiS are formed close to the star with a given fractional abundance that remains constant throughout the envelope up to some region in the envelope where the abundance drops. This abundance falloff can be driven by at least two different processes: (1) condensation onto grains around the dust formation zone, and (2) photodissociation by the ambient UV radiation field in the outer envelope. While these molecules can certainly deplete in the dust formation region owing to condensation onto dust grains, in this work we are not sensitive to such potential abundance decline since the observed lines mostly probe intermediate and outer regions of the envelopes, that is, post-condensation regions (see Sec. 8.5). It is interesting to note that in IRC +10216, the emission from CS, SiO, and SiS vanishes at relatively outer radii, where photodissociation takes place (Bieging et al. 1989; Lucas et al. 1992, 1995; Velilla-Prieto et al. 2019). Various studies have reported on the abundance depletion in the inner regions of IRC +10216. These studies show different degrees of depletion for the molecules, and in some cases the studies even have contradictory findings (Agúndez et al. 2012; Boyle et al. 1994; Decin et al. 2010b; Keady et al. 1993; Schöier et al. 2006.) Regardless of whether these molecules may experience a first abundance decline in the dust formation region or not, what is clear is that they maintain a significant abundance in the gas phase out to the outer envelope, where photodissociation is probably driving the disappearance of these molecules from the gas phase.

The above considerations suggest that a constant fractional abundance from the star and an abundance falloff driven by photodissociation in the outer envelope is a reasonable abundance distribution to model the lines observed in this work. In this scenario, the radial extent of each molecule would be entirely controlled by its corresponding photodissociation rate under the ambient UV radiation field and by the way in which circumstellar dust attenuates UV photons as they penetrate into the envelope. See Massalkhi et al., (2018) for more details on how the radial distributions were calculated using the photodissociation model. We however noticed that by using photodissociation rates from the literature when available (Heays et al. 2017 for SiO and Pattillo et al. 2018 for CS; see Sec. 8.6.4 for more details) and adopting the canonical interstellar $N_{\rm H}/A_V$ ratio for the local ISM (Bohlin et al., 1978), where $N_{\rm H}$ is the hydrogen column density in cm^{-2} and A_V is the visual extinction measured in magnitudes, the radial extent of these molecules is very likely underestimated, at least for some of the envelopes. This suspicion was based on the fact that the abundances derived for

CS, SiO, and/or SiS were anomalously high in some sources, as they exceeded the elemental abundances of sulfur and/or silicon, which a priori are expected to be similar to those in the Sun (Asplund et al., 2009). Given the small number of observed lines (one for CS and SiO and two for SiS), the fact that they are sensitive to both the fractional abundance and the radial extent[‡] and the fact that the radial extent is very likely not well described by a simple photodissociation model, we thus decided to fix the radial extent using an empirical correlation from the literature (see below) and leave as a free parameter the fractional abundance so that it can be derived by modeling the observed lines. Therefore, following the work by González Delgado et al., (2003) and Schöier et al., (2006, 2007), in this study we adopted a simple abundance distribution given by a Gaussian

$$f(r) = f_0 \exp\Big(-(r/r_e)^2\Big), \tag{8.3}$$

where f is the fractional abundance relative to H_2, f_0 is the initial abundance, and r_e is the e-folding radius at which the abundance has dropped by a factor e. From a multiline study of SiO in M-type stars, González Delgado et al., (2003) found the following empirical correlation between the e-folding radius and the envelope density evaluated through the quantity $\dot{M}/V_{\rm exp}$,

$$\log r_e({\rm SiO}) = 19.2 + 0.48 \log\left(\frac{\dot{M}}{V_{\rm exp}}\right), \tag{8.4}$$

where r_e is given in cm, the mass loss rate $\dot{M}$ in $M_\odot$ yr^{-1}, and $V_{\rm exp}$ in km s^{-1}. Although the scaling law in Eq. (8.4) was derived for SiO in oxygen-rich stars, we adopted this law for SiO and SiS in our sample of carbon stars. Schöier et al., (2006, 2007) made the same assumption in the lack of better constraints for C-type stars. Concerning the assumption of similar radial extents for SiO and SiS, it is worth noting that although the photodissociation rate of SiS is unknown[§], there are arguments that to a first order SiO and SiS should behave similarly with respect to photodissociation (Van Dishoeck, 1988; Wirsich, 1994). Interferometric observations of these two molecules in IRC +10216 show that they have similar emission sizes, where the SiO emission is slightly more extended than that of SiS (Velilla-Prieto et al., 2019). In the case of CS, we found it necessary to adopt a larger radial extent than for SiO and SiS because using Eq. (8.4) resulted in anomalously high CS abundances for some sources. We therefore adopted the following relation between e-folding radius and

[‡]The emission arises from intermediate and outer regions of the envelopes and such regions are not resolved by the IRAM 30 m beam in most sources, with the notable exception of IRC +10216.

[§]Prasad et al., (1980) reported a photodissociation rate of 1.0×10^{-10} s^{-1} for SiS. Although it is difficult to trace the exact origin of this number, we suspect that it was most likely assumed to be equal to that of SiO.

density in the envelope:

$$\log r_e(\mathrm{CS}) = 19.65 + 0.48 \log \left(\frac{\dot{M}}{V_{\mathrm{exp}}} \right), \tag{8.5}$$

which was derived by starting from Eq. (8.4) and increasing the first term in small steps so that the amount of sulfur locked in CS and SiS does not exceed the solar elemental abundance of sulfur (i.e., $f_0(\mathrm{CS}) + f_0(\mathrm{SiS}) \leq 2.6 \times 10^{-5}$; Asplund et al. 2009) in any envelope of our sample. Such a larger radial extent for CS, compared with SiO and SiS, is consistent with the lower photodissociation rate calculated for CS compared to that computed for SiO (Heays et al. 2017; Pattillo et al. 2018; see Sec. 8.6.4) and with the larger emission size observed for CS with respect to SiO and SiS in IRC +10216 (Velilla-Prieto et al., 2019).

In a recent study, Danilovich et al., (2018) derived empirical relations between r_e and $\dot{M}/V_{\mathrm{exp}}$ for SiS and CS from a limited sample of M-, C-, and S-type stars. We noticed that implementing their empirical relations in our model calculations resulted in anomalously high abundances for CS and SiS for some low mass loss rate envelopes, for example, for W Ori $f_0(\mathrm{CS}) = 3.2 \times 10^{-5}$ and $f_0(\mathrm{SiS}) = 8.8 \times 10^{-5}$, which imply a sulfur abundance well above the solar value. The main lesson from these calculations is that the empirical relations derived by Danilovich et al., (2018) cannot be safely extrapolated outside the relatively narrow range of $\dot{M}/V_{\mathrm{exp}}$ over which they were derived. We therefore decided not to adopt the CS and SiS scaling laws of these authors. It is worth noting that Danilovich et al., (2018) derived larger e-folding radii for CS than for SiS, which again points to CS being more extended than SiS in agreement with the above arguments. Meanwhile, their SiS extent is smaller than that of SiO derived by González Delgado et al., (2003), which could point to SiS being photodissociated faster than SiO.

In summary, to model the emission lines of CS, SiO, and SiS and determine their abundance in the observed sources, we constructed a model of the envelope for each source with the parameters given in Table 8.1 and adopting the abundance distribution given by Eq. (8.3), using Eq. (8.4) and Eq. (8.5) accordingly, and performed excitation and radiative transfer calculations by varying the initial fractional abundance relative to H_2, f_0 in Eq. (8.3), until the calculated line profiles matched the observed profiles. We chose the model that results in the best overall agreement between calculated and observed line profiles as the best-fit model. More specifically, our criterion was to match the line area of the calculated profile and the observed profile, and so we scaled the derived abundance until

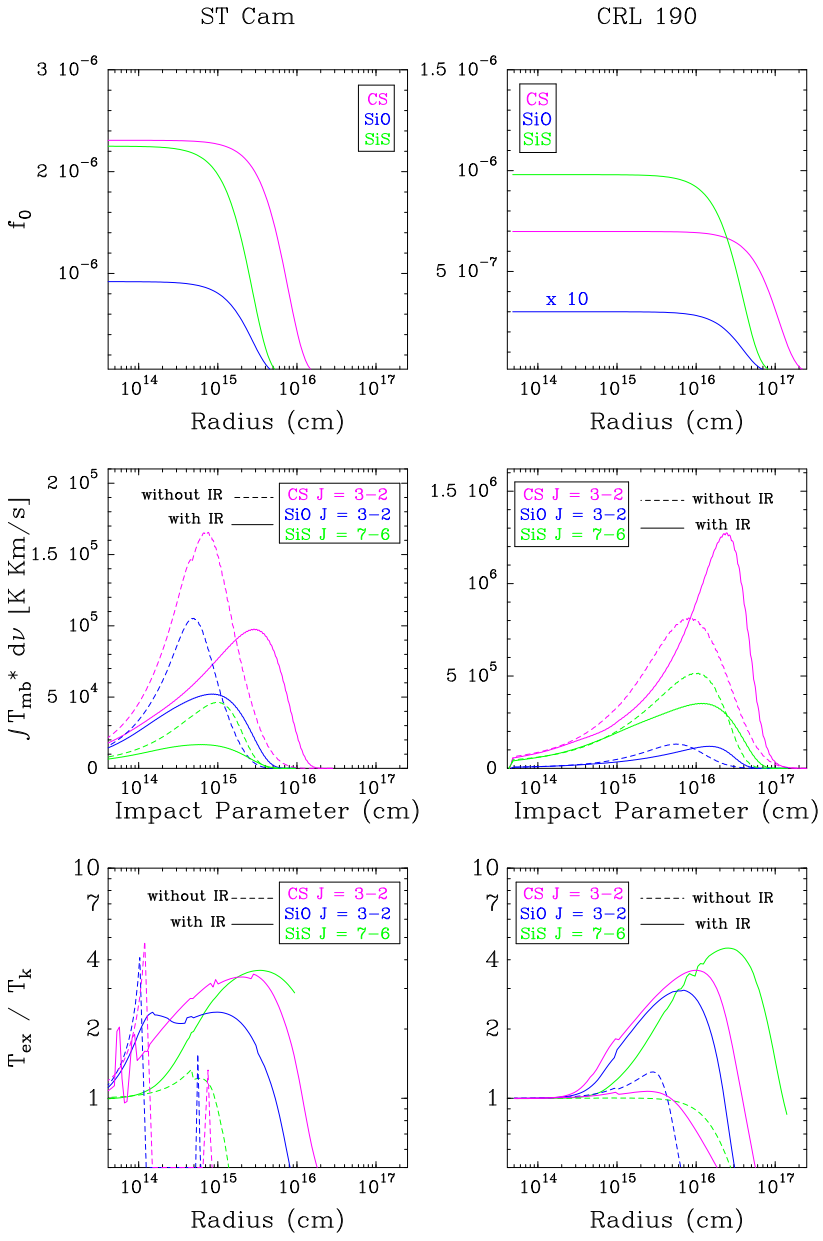

Figure 8.5: Various features from the excitation and radiative transfer models for a low mass loss rate object (ST Cam) and a high mass loss rate object (CRL 190). *Top panels:* radial abundance profiles of CS, SiO, and SiS. *Middle panels:* calculated velocity-integrated intensities for the observed lines of CS, SiO, and SiS as functions of the impact parameter. *Bottom panels:* calculated ratio of excitation temperature to kinetic temperature (T_{ex}/T_k) as a function of radius for observed lines of CS, SiO, and SiS. Solid lines correspond to the model in which IR pumping is included, whereas dashed lines correspond to the model excluding IR pumping. The SiS abundance in ST Cam corresponds to an upper limit.

the line area is reproduced. In those cases where no line is detected, we derive upper limits to the corresponding molecular abundance by choosing the maximum abundance that results in line intensities compatible with the noise level of the observations.

8.5 Results from line modeling

The calculated line profiles resulting from our best-fit LVG model for each of the sources are shown in blue in Fig. 8.1 for CS, Fig. 8.2 for SiO, and Figs. 8.3 and 8.4 for SiS, where they are compared with the observed line profiles (black histograms). We note that the overall agreement of the model is good given that our criterion of matching the line areas is fulfilled as described in the previous section. Concerning the line shapes, globally, the agreement is good as well. To facilitate the differentiation between line detections and non-detections, the calculated line profiles of the latter are plotted in red. In the case of CS in U Cam, the contribution from the present-day wind, which is that we are interested in modeling, is shown in green.

In Fig. 8.5 we show some salient features of the excitation and radiative transfer calculations for two envelopes, ST Cam and CRL 190, which are representative of very different envelope densities. While ST Cam lies in the lower range, with $\dot{M}/V_{\rm exp} = 1.5 \times 10^{-8}$ M$_\odot$ yr^{-1} km^{-1} s, CRL 190 lies at the higher end, with $\dot{M}/V_{\rm exp} = 3.7 \times 10^{-6}$ M$_\odot$ yr^{-1} km^{-1} s. The bottom panels of Fig. 8.5 show the calculated ratio of excitation temperature to gas kinetic temperature ($T_{\rm ex}/T_k$) for the observed lines of CS and SiO and that of the observed lines of SiS as a function of radius. We see that the rotational levels involved in the targeted transitions of the three molecules are thermalized ($T_{\rm ex}/T_k = 1$) in the hot and dense inner regions, while as the radial distance from the star increases and the gas density decreases, the rotational levels deviate from thermalization. Concretely, lines become increasingly suprathermally excited ($T_{\rm ex}/T_k > 1$) with increasing radius, an effect that is largely caused by IR pumping. Therefore, IR pumping plays an important role in the excitation of the rotational transitions of these molecules. The much lower mass loss rate of ST Cam compared to CRL 190 implies substantially lower densities in the envelope and thus in ST Cam rotational populations start to deviate from thermalization at shorter radii than in CRL 190. The fact that the observed lines are not thermalized throughout most of the envelope, especially at low mass loss rates, stresses the need for non-LTE excitation calculations. For the low-mass loss rate ST Cam, the models without IR pumping for SiO and CS display a peculiar behavior caused by the excitation temperature becoming negative from intermediate regions of the envelope. Including IR pumping makes this behavior disappear. We note the SiS lines seem

to end so abruptly because of the choice of the envelope outer edge in our model, where we chose the envelope to end at a radius at which the fractional abundance has dropped by a factor of 10^5.

The middle panels of Fig. 8.5 show the velocity-integrated intensity of the observed lines as a function of the impact parameter (solid lines). We see that in ST Cam the maximum contribution to the line emission comes from regions at a few 10^{15} cm from the star, while in the case of CRL 190 the regions located at radii of a few 10^{16} cm contribute the most to the observed emission. Therefore, most of the emission of the observed lines arises from intermediate and outer regions of the envelope, rather than from inner regions. Moreover, the λ 2 mm lines studied in this work probe regions where the abundance falloff has already started, which is especially marked in objects with low mass loss rates such as ST Cam (compare middle and top panels in Fig. 8.5). This fact explains why the observed lines are sensitive to both the fractional abundance and the radial extent, and why adopting a more compact (extended) distribution would require a higher (lower) fractional abundance to reproduce the observed lines.

Infrared pumping not only plays an important role in regulating the excitation of the observed lines but also in determining their emission distribution. The bottom panels in Fig. 8.5 show that the emission is more compact if IR pumping is not included (dashed lines) than if it is taken into account (solid lines). Therefore, IR pumping results in a more extended emission distribution with an impact on the emerging line intensity. In fact, neglecting IR pumping results in a systematic decrease in the integrated line intensities of CS $J = 3-2$ and SiO $J = 3-2$ of $\sim$ 60% and $\sim$ 50%, respectively, on average. In the case of SiS $J = 7-6$ and $J = 8-7$ the effect of excluding IR pumping is not as systematic as with CS and SiO as it leads to a decrease of the line intensities in some sources and an increase in other sources. If higher J lines of SiS were targeted (above $J = 10-9$) the effect of excluding IR pumping would be a systematic decrease in the integrated line intensities.

8.6 Discussion

8.6.1 Fractional abundances

The abundances derived for CS, SiO, and SiS in the 25 carbon-rich envelopes studied are summarized in Table 8.4. For some of these sources, abundances have been previously reported. For example, in IRC +10216 the abundances of CS, SiO, and SiS were derived by Agúndez et al., (2012) from a multiline study including lines from vibrationally excited

Table 8.4: Fractional abundances of CS, SiO, and SiS derived

Name	$\dot{M}$ ($M_\odot$ yr^{-1})	V_{exp} (km s^{-1})	f_0(CS)	f_0(SiO)	f_0(SiS)
IRC +10216	2.0×10^{-5}	14.5	1.1×10^{-6}	2.6×10^{-7}	1.3×10^{-6}
CIT 6	6.0×10^{-6}	17	6.4×10^{-6}	1.5×10^{-6}	4.8×10^{-6}
CRL 3068	2.5×10^{-5}	14.5	7.4×10^{-7}	1.4×10^{-7}	3.8×10^{-6}
S Cep	1.2×10^{-6}	22.5	9.9×10^{-6}	9.4×10^{-6}	1.9×10^{-6}
IRC +30374	1.0×10^{-5}	25	1.0×10^{-5}	5.0×10^{-6}	7.2×10^{-6}
Y CVn	1.5×10^{-7}	7	5.7×10^{-6}	8.1×10^{-7}	$<8.0 \times 10^{-7}$
LP And	7.0×10^{-6}	14.5	3.6×10^{-6}	1.0×10^{-6}	7.0×10^{-6}
V Cyg	1.6×10^{-6}	12	3.3×10^{-6}	2.9×10^{-6}	4.0×10^{-6}
UU Aur	2.4×10^{-7}	10.6	3.0×10^{-7}	2.5×10^{-7}	$<6.1 \times 10^{-7}$
V384 Per	2.3×10^{-6}	15.5	8.4×10^{-6}	6.4×10^{-6}	1.0×10^{-5}
IRC +60144	3.7×10^{-6}	19.5	7.3×10^{-6}	9.5×10^{-6}	1.0×10^{-5}
U Cam[a]	2.0×10^{-7}	13	1.9×10^{-5}	1.0×10^{-5}	$<4.1 \times 10^{-6}$
V636 Mon	5.8×10^{-6}	20	2.0×10^{-6}	1.7×10^{-6}	9.6×10^{-7}
IRC +20370	3.0×10^{-6}	14	4.1×10^{-6}	3.0×10^{-6}	1.1×10^{-5}
R Lep	8.7×10^{-7}	17.5	3.6×10^{-6}	5.7×10^{-6}	$<1.1 \times 10^{-6}$
W Ori	7.0×10^{-8}	11	2.1×10^{-5}	3.6×10^{-6}	$<4.9 \times 10^{-6}$
CRL 67	1.1×10^{-5}	16	3.5×10^{-6}	1.1×10^{-6}	4.6×10^{-6}
CRL 190	6.4×10^{-5}	17	7.0×10^{-7}	3.0×10^{-8}	9.8×10^{-7}
S Aur	4.0×10^{-7}	24.5	9.3×10^{-6}	6.9×10^{-6}	$<3.3 \times 10^{-6}$
V Aql	1.4×10^{-7}	8	1.0×10^{-5}	2.5×10^{-6}	$<2.3 \times 10^{-6}$
CRL 2513	2.0×10^{-5}	25.5	3.1×10^{-6}	1.3×10^{-6}	2.8×10^{-6}
CRL 2477	1.1×10^{-4}	20	2.7×10^{-7}	1.0×10^{-7}	1.7×10^{-6}
CRL 2494	7.5×10^{-6}	20	7.0×10^{-6}	2.9×10^{-6}	1.1×10^{-5}
RV Aqr	2.3×10^{-6}	15	7.7×10^{-6}	5.5×10^{-6}	4.6×10^{-6}
ST Cam	1.3×10^{-7}	8.9	2.3×10^{-6}	$<9.2 \times 10^{-7}$	$<2.2 \times 10^{-6}$

Notes [a] U Cam has a present-day wind and a detached shell expanding away from the central star (for further details see Schöier et al. 2005). The values of f_0 given in this table correspond to the present-day wind.

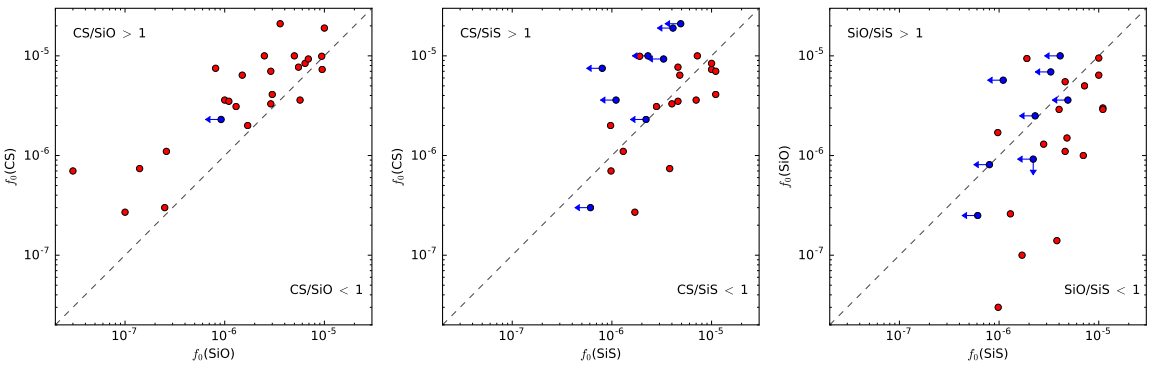

Figure 8.6: Comparison of abundances between different pairs of molecules. The plots show the derived fractional abundances relative to H_2 of CS vs. SiO (left panel), CS vs. SiS (middle panel), and SiO vs. SiS (right panel). Those sources with non-detections are denoted with blue arrows. Diagonal dashed lines indicate where the abundances of the two molecules become equal.

states. These authors found abundances relative to H_2 of 7×10^{-7} for CS, 1.8×10^{-7} for SiO, and 1.3×10^{-6} for SiS, which are in very good agreement with the abundances derived in this work.

Olofsson et al., (1993a) looked for CS $J = 2 - 1$ emission in a large sample of carbon stars, 12 of which are in our sample. However, in about half of these stars the line was not detected and only loose abundance upper limits could be derived. These authors used a relatively simple method for estimating the molecular abundances, which is based on an analytical expression and where they assumed a constant excitation temperature for simplicity. In those sources where CS was detected, the abundances derived were very high, often greater than the maximum amount obtainable for solar abundance of sulfur. They suggested that these anomalously high abundances probably originate from uncertainties in the envelope model. In another study, Bujarrabal et al., (1994) surveyed a large sample of evolved stars in lines of several molecules including CS, SiO, and SiS. Their sample contains 16 C-rich AGB stars, 12 of which are also in our sample. These authors derived the abundances using an analytical expression that estimated only a lower limit if the line was optically thick. In general, their CS, SiO, and SiS abundances are lower than ours by a factor of a few and not higher than a factor of 10, apart from U Cam, where our derived CS and SiO abundances are one and two orders of magnitude, respectively, higher than theirs. Bujarrabal et al., (1994) remarked that their abundances may be underestimated owing to optical depth effects.

More recently, Schöier et al., (2006) surveyed a sample of 19 C-rich AGB stars and

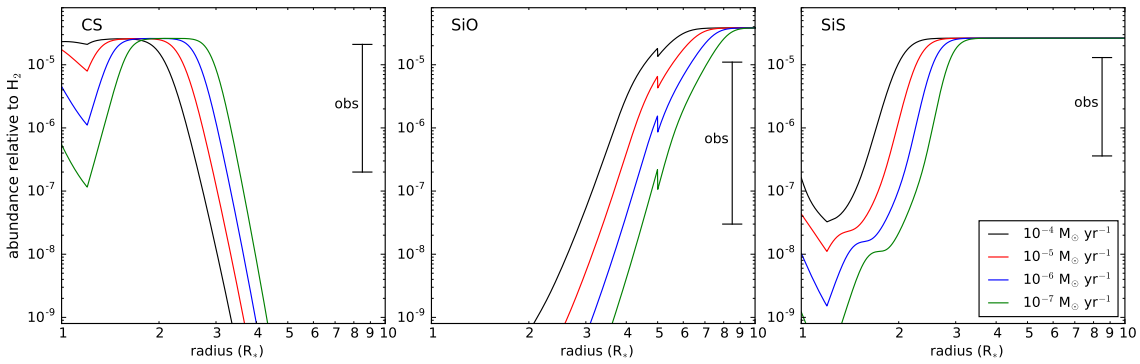

Figure 8.7: Calculated fractional abundances of CS (left panel), SiO (middle panel), and SiS (right panel) under TE as a function of distance to the AGB star for various mass loss rates. The range of observed abundances is indicated.

detected SiO line emission in all of these objects. They performed radiative transfer calculations to derive abundances adopting, similar to us, an abundance distribution based on the scaling law established by González Delgado et al., (2003) for SiO in M-type stars. We share 13 sources with the former. Our SiO abundances are in good agreement with theirs for some sources, while for others there are significant differences. In LP And, for example, our derived SiO abundance is higher than theirs by almost a factor of ten, but on the other hand, our derived value in UU Aur is one order of magnitude lower than theirs, probably owing to differences in both the observations and the model. Later on, Schöier et al., (2007) reported on the detection of SiS line emission in 14 carbon stars, most of which are included in our sample. In general, the SiS abundances derived by us are similar to theirs, except for LP And, where we derive a SiS abundance higher than theirs by a factor of $\sim$6.

In this work, the fractional abundances relative to H_2 derived range between 2.7×10^{-7} and 2.1×10^{-5} for CS, 3×10^{-8} and 1×10^{-5} for SiO, and $< 6.1 \times 10^{-7}$ and 1.1×10^{-5} for SiS. Silicon monoxide is the molecule experiencing the largest variations (more than two decades) from source to source, while CS abundances span over two decades, and SiS shows the most uniform abundances across sources (with variations of less than two decades). We find that CS is systematically more abundant than SiO in most of the sources (see left panel of Fig. 8.6, where it is seen that most sources fall in the region of CS/SiO > 1). We also note that SiO tends to be less abundant than SiS; the right panel of Fig. 8.6 shows that for most sources SiO/SiS $\lesssim 1$, while only in a few SiO/SiS is greater than one. Therefore, SiS seems to be a more efficient gas-phase reservoir of silicon than SiO in most carbon star envelopes. When comparing between CS and SiS, the two major gas-phase molecular reservoirs of sulfur in C-rich envelopes (see, Danilovich et al. 2018 and, e.g., the case of IRC +10216; Agúndez et al. 2012), we notice that in some sources such as IRC +30374 and U Cam, CS

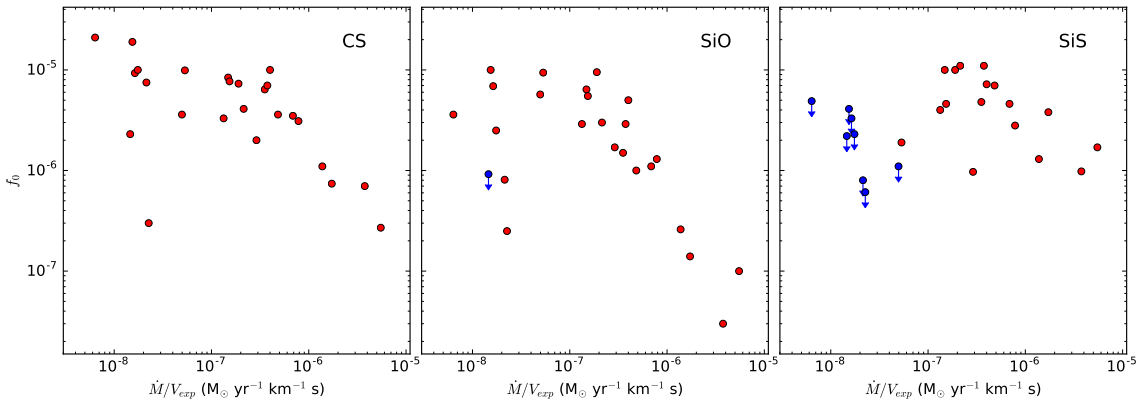

Figure 8.8: Fractional abundances f_0 derived for CS (left panel), SiO (middle panel), and SiS (right panel) are plotted as a function of the envelope density proxy $\dot{M}/V_{\rm exp}$ for the 25 C-rich envelopes studied here. Blue downward arrows represent upper limits to f_0.

is more abundant than SiS, while in others (e.g., CRL 3068 and CRL 2494) the contrary is found. Overall, the data points in the middle panel of Fig. 8.6 fall along the line defined by f_0(CS) = f_0(SiS), with no clear preference for either the CS/SiS > 1 or the CS/SiS < 1 sides.

We can therefore extract as statistically meaningful conclusions that in carbon star envelopes CS and SiS have abundances of the same order, and that SiO is in general less abundant than CS and SiS. This is most likely a chemical feature related to C-rich AGB envelopes. Danilovich et al., (2018) determined the CS and SiS abundances in a sample of AGB stars, and likewise found comparable CS and SiS abundances in C-rich AGB stars, while in their O-rich sample, SiS was found to be systematically higher than CS. S stars were also found to have similar abundances. In this line, it is interesting to see what TE predicts for these molecules in C-rich AGB atmospheres. In Fig. 8.7 we show the calculated fractional abundances of CS, SiO, and SiS as a function of radial distance from the star for various mass loss rates. The underlying physical scenario adopted for the TE calculations is the same as adopted in Massalkhi et al., (2018), where we used the radial profiles of density and temperature of IRC +10216 (Agúndez et al. 2012; see downward revision on the density profile by Cernicharo et al. 2013) and scaled the density profile up or down depending on the mass loss rate, that is in the range of 10^{-7}-10^{-4} $M_\odot$ yr^{-1}. Therefore, the TE calculations adopt different density profiles to account for low and high mass loss rates. We see that CS is predicted to have a high abundance (locking most of the available sulfur) in the close surroundings of the AGB star (at 1-3 R_*), while at farther distances its TE abundance vanishes to very low levels. On the other hand, SiS has almost the opposite behavior,

with low abundance levels close to the star and a very high abundance beyond 2-3 R_*. The fact that CS and SiS are observed with similar abundances in our sample of envelopes is consistent with the abundances of these molecules being quenched to their TE values at radii of 2-3 R_*, which agrees with findings from the study of IRC +10216 (Agúndez et al., 2006, 2012). The process of abundance quenching is expected because as the gas expands the temperature and density drop and chemical reactions become slower and eventually too slow to proceed efficiently so that abundances are not further modified. Silicon monoxide shows a calculated radial TE abundance profile similar to that of SiS but shifted to larger radii. That is, SiO has a vanishingly small TE abundance close to the star, although calculations predict that this will reach a very high abundance (trapping most of the available silicon) beyond 5-8 R_*. The fact that the TE abundance of SiO is only high at a relatively large distance from the star is probably at the origin of the lower observed abundance of SiO compared to CS and SiS. In any case, given the range of SiO abundances derived from observations, SiO must quench its abundance to the TE value at somewhat larger radii than for CS and SiS. Predictions from a chemical kinetics model of the inner wind of AGB stars, including shocks driven by the pulsation of the star (Cherchneff, 2006), indicate that for a C-rich object with a C/O elemental abundance ratio of 1.1, the abundances of CS, SiO, and SiS injected into the expanding envelope would be similar within a factor of ~ 1.5, where CS is slightly more abundant than SiO and SiS. Given the scatter in the relative abundances of CS, SiO, and SiS derived by us and the very concrete physical scenario of AGB wind adopted by Cherchneff, (2006), it is difficult to establish meaningful conclusions regarding whether the relative abundances we derive may be ultimately driven by shock-induced chemistry in the inner wind.

It is interesting to note that regardless of which pair of molecules is chosen, the plots in Fig. 8.6 show a trend in which the higher the abundance of one molecule the more abundant the other is. That is, the abundances of CS, SiO, and SiS seem to scale with each other, so that there are envelopes in which the three molecules are abundant, while in others the three molecules maintain low abundance levels. This conclusion seems robust when considering CS and SiO, although it may not be completely true concerning SiS because in some of the sources where SiS is not detected, SiS may have a low abundance while CS and SiO do not. This point is discussed in more detail below. We note that a correlation of this type was found by Danilovich et al., (2018) for CS and SiS in a sample including C-, M-, and S-type stars, although in that study the trend is considered tentative because of the small number of sources included.

In Fig. 8.8 we plot the fractional abundances f_0 derived for CS, SiO, and SiS as a function

of the density in the envelope, evaluated through the quantity $\dot{M}/V_{\rm exp}$. In the case of CS, the data strongly suggest a negative correlation between CS abundance and envelope density. The same behavior is even more evident for SiO. That is, as the density in the envelope increases the abundances of CS and SiO decrease. This behavior was already found for SiO in both M-type stars by González Delgado et al., (2003) and carbon stars by Schöier et al., (2006) and was interpreted as an evidence of enhanced SiO adsorption onto dust grains (and thus depletion from the gas phase) with increasing density. Using a larger sample of carbon stars, we thus confirm the result found by Schöier et al., (2006) for SiO. The same trend of decreasing abundance with increasing density was also found recently for SiC_2, pointing to this molecule as a gas-phase precursor of silicon carbide dust around carbon stars (Massalkhi et al., 2018). We note that in the recent study by Danilovich et al., (2018), the abundances of CS derived in C-type AGB envelopes do not show the anticorrelation with envelope density found by us. The reason is that their sample of carbon stars, with just seven objects, is small and the range of $\dot{M}/V_{\rm exp}$ covered does not include high density envelopes, of which those in our sample give better evidence of the trend of decreasing abundance with increasing density.

It is worth looking at the predictions of TE to investigate whether the anticorrelation between abundance and envelope density observed for CS and SiO could be caused by an effect of the density on the TE abundance of these molecules. As shown in Fig. 8.7, the main effect of an increase in the mass loss rate, and thus on the envelope density, on the abundances of CS and SiO is that the curves shift slightly to inner radii. If the radius at which the CS abundance is quenched to its TE value is the same for different mass loss rates, then the quenched abundance of CS would be lower for higher mass loss rates, in agreement with the observed behavior. It is however unlikely that the radius of abundance quenching is the same for different mass loss rates because higher densities would make the region of abundance quenching occur at larger radii. The reason is that higher densities imply shorter chemical timescales and a larger region in which TE prevails. This would result in an even more pronounced decrease of the quenched CS abundance with increasing density. Although qualitatively this scenario would be in agreement with the observed trend of decreasing abundance of CS with increasing density, a detailed chemical kinetics model is needed to obtain quantitative estimates. In the case of SiO, a similar reasoning implies that the quenched abundance would be higher for higher densities (see Agúndez et al. 2006) contrary to what observations indicate. It is therefore very unlikely that the observed decrease in the abundance of SiO with increasing density is caused by gas-phase chemistry. The most likely explanation is that SiO incorporates into dust grains and depletes from the

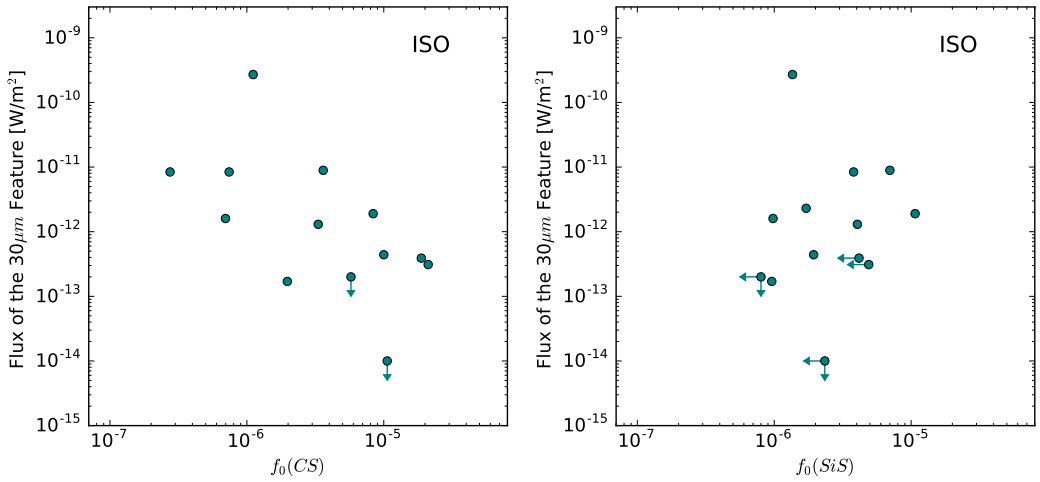

Figure 8.9: Flux of the MgS dust feature at 30 µm observed by ISO (Hony et al., 2002) vs. the fractional abundance of CS (left panel) and SiS (right panel) derived in this work.

gas phase with increasing density in the envelope.

The case of SiS deserves special attention. It is remarkable that SiS is not detected in envelopes with low mass loss rates below 10^{-6} $M_\odot$ yr^{-1}, while it is detected in all sources with mass loss rates above that threshold. This fact, which has been noticed to some extent in previous observational studies (Bujarrabal et al., 1994; Danilovich et al., 2018; Schöier et al., 2007), is shown in this work in a robust way (see Table 8.4 and right panel of Fig. 8.8). The reason behind this behavior is not clear. The non-detection of SiS in these envelopes might either be due to a lack of sensitivity or a low fractional abundance of the molecule. Looking at the predictions of TE (right panel in Fig. 8.7), we note that for low mass loss rates the predicted abundance of SiS is indeed lower. This fact is even more marked if we take into account that the radius at which the abundance quenches to the TE value is expected to be shifted to inner radii for lower mass loss rates. A scenario of TE chemistry plus abundance quenching would be in agreement with objects with low mass loss rates having lower SiS abundances. If that is the underlying cause, it is however strange that the observed SiS abundances do not show a smooth variation with density but an abrupt differentiation between sources with and without SiS detection at 10^{-6} $M_\odot$ yr^{-1}, and show no evidence of increasing SiS abundance with increasing density for those sources where SiS is detected. We suspect that the lack of SiS detections in objects with low mass loss rates could be caused by a lack of its constituent elements, which would be largely trapped in SiO and SiC_2 (in the case of silicon) and CS (regarding sulfur). As shown in this work and in Massalkhi et al., (2018), the molecules SiO, CS, and SiC_2 (probably also Si_2C; Cernicharo et al. 2015a)

become very abundant in C-rich objects with low mass loss rates. This suspicion however would need to be corroborated with a detailed chemical kinetics model of the inner wind of envelopes with different mass loss rates. Apart from the upper limits to the abundance of SiS in objects with low mass loss rates, the SiS abundances derived through positive detections show hints of decreasing SiS abundance with increasing density (right panel in Fig. 8.8). This has to be seen as tentative, however, and in any case it is not as evident as in the cases of CS and SiO. Therefore, if the tentative decrease in the abundance of SiS with increasing envelope density is interpreted in terms of adsorption onto dust grains, we can conclude that SiS is not incorporated into dust grains to an extent as important as that of SiO.

Schöier et al., (2007) found that the SiS abundance does not show any particular correlation with the envelope density for C-rich envelopes. However, they found a slightly better fit to their observations for the case of IRC +10216 by including a compact SiS component with a fractional abundance 1.7×10^{-5} out to a radius of 5×10^{14} cm, which could imply an SiS abundance gradient in line with the results found by Agúndez et al., (2012). Introducing an inner high-abundance SiS component also produced a better fit for the oxygen-rich IK Tau implying SiS depletion. This result is similar to that found by Decin et al., (2010a) when modeling low- and high-excitation lines, however a recent study by Danilovich et al., (2019), using sensitive ALMA observations to determine the SiS distribution in the envelope of IK Tau, does not reveal a compact inner region as previously found. Regardless, we do maintain that the evidence of SiS depletion in C-rich envelopes is weak.

In any case, in this work we investigated SiS in a larger sample of carbon stars covering a broader range of envelope densities than previously studied, which permitted us to clearly see a systematic non-detection of SiS at low mass loss rates and a tentative negative correlation between SiS abundance and envelope density seen at high mass loss rates.

8.6.2 MgS dust: Possible gas-phase precursors

A common characteristic that is seen in C-rich evolved stars is the presence of a prominent IR emission band that is centered around 30 µm. The feature was discovered by Forrest et al., (1981) in dusty carbon-rich environments; Goebel et al., (1985) first suggested that magnesium sulfide (MgS) dust may be responsible for this spectral feature and this suggestion has been widely accepted since then. However, the carrier is still argued upon. One of the major concerns is regarding the sulfur abundance that is required to explain the observed emission. Zhang et al., (2009a) argued that the amount of MgS required to explain the power emitted by the 330 µm feature in the post-AGB, HD 56126, would require ten

times more atomic sulfur than available in the ejected envelope. Zhukovska et al., (2008) found the only way MgS dust can form for C-rich AGB stars is by precipitation on preexisting silicon carbide grains. Lombaert et al., (2012) then discussed that if the grains were of a heterogeneous composite nature, meaning if MgS dust forms in a layer coated around an amorphous carbon/SiC core grain, then there would not be an abundance constraint. Investigating the formation mechanism of MgS dust is out of the scope of this Chapter. However, we can investigate if there is a connection between the sulfur bearing molecules studied in this work and the 30 µm feature attributed to MgS dust. This way we could identify if any of these S-bearing molecules could act as precursors of MgS dust in the ejecta of AGB stars. More specifically, we aim to investigate whether there is a relation between the derived fractional abundances of CS and SiS and the strength of the 30 µm feature.

Hony et al., (2002) carried out an observational study of the 30 µm feature of a large number of C-rich sources observed with the Infrared Space Observatory (ISO). There are 13 sources in common between their sample and ours. In the left panel of Fig. 8.9 we plot the flux of MgS dust versus the fractional abundance of CS for these 13 sources. We clearly see a trend in which the flux of MgS dust increases as the gas-phase abundance of CS decreases. If the flux of the 30 µm feature is a good proxy of the amount of MgS dust and if the hypothesis that CS is a gas-phase precursor of dust in C-rich AGB stars is correct, then this result supports the idea that the decline in the abundance of CS with increasing envelope density is caused by a more efficient incorporation of CS on MgS dust. In the case of SiS there is no obvious correlation between the fractional abundance and the flux of the 30 µm feature (see right panel of Fig. 8.9). The lack of correlation suggests that SiS does likely not play a role in the formation of MgS dust in these stars, although we note that the range of SiS abundances covered is limited. Smolders et al., (2012) carried out an observational study on a large sample of S-type stars and found that many stars that show the MgS emission feature also show emission peaks at 6.6 µm and 13.5 µm due to molecular SiS. This fact led these authors to suggest that MgS dust could be formed as a consequence of a reaction between Mg and SiS in S-type stars in contrast with our conclusion that CS, rather than SiS, is a precursor of MgS dust in C-rich AGB stars.

8.6.3 SiO and SiS as possible precursors of SiC dust

Since both SiO and SiS are important Si-carriers (Agúndez et al. 2012; Lucas et al. 1995; Olofsson et al. 1982), in this section we assess if there could be a relation between these molecules and the formation of SiC dust around AGB stars. We collected information on the Infrared Astronomical Satellite (IRAS) and the ISO data for the sources in our sample that

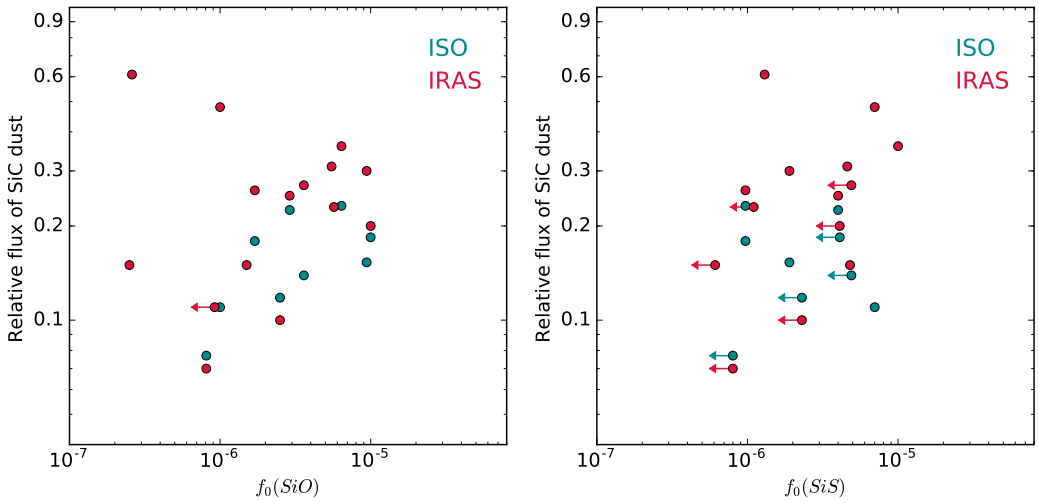

Figure 8.10: Relative integrated flux of the SiC dust feature at 11.3 µm taken from Sloan et al., (1998) and Yang et al., (2004) vs. the fractional abundance of SiO and SiS derived in this work.

exhibit the SiC dust emission feature at 11.3 µm. Sloan et al., (1998) analyzed the IRAS spectra of carbon stars with which we share 15 sources, and Yang et al., (2004) studied the ISO spectra of C-rich AGB stars with 9 sources in common with our sample. These authors determined the relative flux of SiC dust as the ratio of the integrated flux of the 11.3 µm emission feature (after continuum substraction) divided by the integrated flux of the continuum. In Fig. 8.10 we plot the relative integrated flux of SiC dust versus the fractional abundance of SiO (left) and SiS (right) for the sources in our sample that have IRAS or ISO data. With the same reasoning as in the previous section, if the relative flux of SiC dust is a direct indicator of the amount of silicon carbide dust and the hypothesis that SiO and/or SiS contribute to the formation of SiC dust is correct, we would expect to see a trend in which the relative flux of SiC dust increases as the gas-phase abundance of SiO and/or SiS decreases. However, Fig. 8.10 does not show any clear trend indicating this; the same result was found between the gas-phase SiC_2 and SiC dust by Massalkhi et al., (2018). Regardless, it is important to note that the relative flux of the 11.3 µm SiC band is an observable quantity that may not be a direct indicator of the mass of silicon carbide dust in the envelope. The derivation of the amount of SiC dust in the envelope requires a radiative transfer analysis that involves a meticulous description of the chemical composition, size, and temperature of dust throughout the envelope.

Table 8.5: Photodissociation parameters

Molecule	α	β	Ref.	α'	$\langle$Dev.$\rangle$
CS	3.7×10^{-10}	2.32	a	1.5×10^{-10}	35%
SiO	1.6×10^{-9}	2.66	b	7×10^{-10}	31%
SiS	1.6×10^{-9}	2.66	c	8×10^{-10}	47%

Notes The values of α and β are taken from the literature. References are (a) Pattillo et al., (2018), (b) Heays et al., (2017), (c) assumed the same as SiO. The parameter α' are the values that best reproduce the empirical relations between r_e and $\dot{M}/V_{\rm exp}$ adopted in this study. The mean deviations $\langle$Dev.$\rangle$ are also given (see text).

8.6.4 Radial extent: Photodissociation versus empirical relations

As discussed in Sec. 8.4.2, the radial extent of CS, SiO, and SiS in carbon star envelopes is probably controlled by photodissociation from the ambient interstellar UV radiation field. However, given the aforementioned difficulties to account properly for the abundance falloff using photodissociation rates from the literature (in which case the radial extent is very likely underestimated), in this work we adopted a simple radial abundance distribution given by a Gaussian function with *e*-folding radii derived from empirical relations between r_e and the wind density. These relations were ultimately based on a scaling law between r_e and $\dot{M}/V_{\rm exp}$ derived from a multiline study of SiO in M-type stars (González Delgado et al., 2003). In this work we adopted the same relation for SiO, based on the assumption that SiO behaves similarly in envelopes around M- and C-type stars; for SiS we adopted the same relation, based on the assumption that SiS and SiO have similar emission sizes as mentioned previously; and for CS we adopted a modified version, based on arguments to avoid requiring a sulfur abundance higher than the solar abundance. If we consider as good the adopted empirical relations and we assume that the abundance falloff is entirely controlled by photodissociation, then it is possible to extract some useful conclusions about the photodissociation of these molecules. More specifically, we aim to find the unattenuated photodissociation rates that best reproduce the abundance falloff given by the adopted empirical laws for r_e.

The photodissociation model used for this exercise is the same employed in Massalkhi et al., (2018). Briefly, the radial variation of the fractional abundance can be expressed as (Huggins et al., 1982; Jura et al., 1981)

$$\frac{df}{dr} = -\frac{\alpha}{V_{\rm exp}} \exp\left[-\left(\frac{r_d}{r}\right)\right] f, \tag{8.6}$$

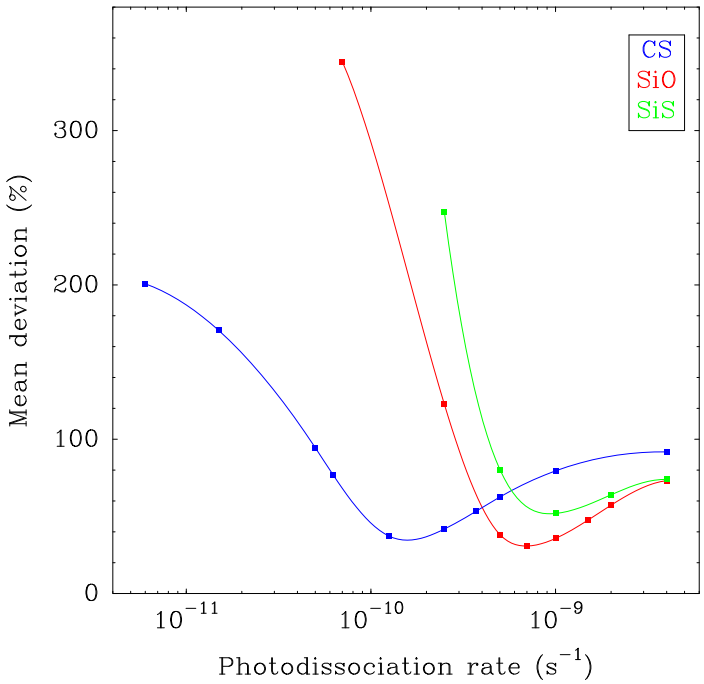

Figure 8.11: The mean deviation between the calculated line areas with the photodissociation model and the model using empirical laws is plotted as a function of the unattenuated photodissociation rate adopted in the photodissociation model for CS, SiO, and SiS.

where α is the unattenuated photodissociation rate in s^{-1} and the photodissociation radius r_d is given by

$$r_d = \frac{\beta \dot{M}}{4\pi V_{\rm exp} \overline{m}_g 1.87 \times 10^{21}}, \tag{8.7}$$

where β is the dust shielding factor, $\overline{m}_g$ is the average mass of gas particles in grams, and the numerical value is the canonical $N_{\rm H}/A_V$ ratio for the local ISM (Bohlin et al., 1978). In Table 8.5 we list the unattenuated photodissociation rates α and dust shielding factors β collected from the literature for CS, SiO, and SiS, which were used as starting values. For each of the three molecules, we then varied the unattenuated photodissociation rate in small steps, computed the associated abundance radial profile for each envelope in the sample, and calculated the corresponding line profiles. To decide which photodissociation rate agrees best with the empirical abundance falloff, we computed for each envelope the difference between the velocity-integrated line intensity calculated with the photodissociation model and that calculated with the empirical falloff model and then estimated the mean difference.

The mean deviations found are plotted as a function of the photodissociation rate in

Fig. 8.11. The optimal photodissociation rate α' for which the lowest mean deviation is found is given in the right side of Table 8.5 for each of the three molecules, together with the associated mean deviation. In the case of CS, we found that the lowest mean deviation (35 %) occurs for $\alpha' = 1.5 \times 10^{-10}$ s^{-1}, while for SiO and SiS the lowest deviation (31 and 47 %, respectively) is found for photodissociation rates of 7×10^{-10} and 8×10^{-10} s^{-1}, respectively. There are two interesting aspects to comment on. First, the optimal photodissociation rates found for SiO and SiS are very similar, while that of CS is significantly lower. These results merely reflect the adopted empirical abundance falloffs, which were the same for SiO and SiS, while for CS we adopted an empirical scaling law implying an outer abundance falloff. And second, the optimal photodissociation rates α' are significantly lower than the literature values α. This illustrates in a different way our initial suspicion that literature photodissociation rates underestimate the radial extent of CS, SiO, and SiS. Whether, this finding implies that real photodissociation rates are indeed lower than the literature values or whether this points to a different $N_{\rm H}/A_V$ ratio than the canonical interstellar value of Bohlin et al., (1978) is not yet clear.

8.7 Conclusions

In this work we used the IRAM 30 m telescope to survey a sample of 25 C-rich CSEs in the $J = 3-2$ line of CS and SiO and in the $J = 7-6$ and $J = 8-7$ lines of SiS. We carried out excitation and radiative transfer calculations based on the LVG method to derive fractional abundances relative to H_2. We found that the abundances of the three molecules are positively correlated with each other (especially those of CS and SiO) and that while CS and SiS have similar abundances, SiO is present at a lower abundance level.

We also found a clear trend in which SiO and CS become less abundant as the envelope density increases. The depletion of CS with increasing density can be due to gas-phase chemistry in the inner wind or to incorporation onto dust grains. The latter scenario is favored by the fact that we find a negative correlation between the fractional abundance of CS and the 30 μm feature attributed to MgS dust, which suggests that CS is a likely precursor of MgS dust grains in C-rich AGB envelopes. In the case of SiO, the most likely explanation of the negative correlation between fractional abundance and envelope density is that SiO incorporates more efficiently onto dust grains at increasing density owing to the enhanced collision rate between particles and the acceleration of accretion and coagulation processes. Thus, both CS and SiO are probable candidates to act as gas-phase precursor of dust grains.

We find that SiS is systematically not detected in envelopes with mass loss rates below 10^{-6} $M_\odot$ yr^{-1}, probably because of the increasing importance of other molecules that lock most silicon and sulfur (SiO, SiC_2, and CS) or because of a lack of sensitivity. The SiS abundances derived in the sources in which the molecule is detected suggest a tentative trend of decreasing abundance with increasing density. This trend indicates that SiS could also be incorporated into dust grains, although the non-detections clearly undermine this tentative trend. Nevertheless, this conclusion is not as robust as that of CS and SiO.

Table 8.6: Observed line parameters of CS $J = 3-2$, SiO $J = 3-2$, and the $J = 7-6$ and $J = 8-7$ lines of SiS

Line	ν_{calc} (MHz)	ν_{obs} (MHz)	$V_{\rm exp}$ (km s^{-1})	$\int T_{\rm mb} dv$ (K km s^{-1})
		IRC +10216		
SiO $J = 3-2$	130268.665	130268.4(1)	13.1(1)	130.7(13)
SiS $J = 7-6$	127076.180	127076.0(1)	12.7(1)	162.9(16)
SiS $J = 8-7$	145227.054	145227.0(1)	14.7(1)	270.5(27)
CS $J = 3-2$	146969.025	146968.7(1)	14.7(1)	379.3(37)
		CIT 6		
SiO $J = 3-2$	130268.665	130267.8(5)	16.2(5)	19.8(19)
SiS $J = 7-6$	127076.180	127075.3(5)	16.4(5)	7.55(7)
SiS $J = 8-7$	145227.054	145225.4(10)	17.5(10)	12.5(19)
CS $J = 3-2$	146969.025	146968.6(5)	16.4(5)	89.0(89)
		CRL 3068		
SiO $J = 3-2$	130268.665	130268.4(1)	12.3(1)	2.18(2)
SiS $J = 7-6$	127076.180	127075.9(1)	12.2(1)	6.36(5)
SiS $J = 8-7$	145227.054	145226.7(1)	13.8(1)	9.24(9)
CS $J = 3-2$	146969.025	146968.6(1)	14.2(1)	17.2(10)
		S Cep		
SiO $J = 3-2$	130268.665	130268.6(1)	23.3(1)	7.80(7)
SiS $J = 7-6$	127076.180	127076.5(10)	21.0(5)	0.30(6) [a]
SiS $J = 8-7$	145227.054	145227.2(10)	20.8(10)	0.34(7) [a]
CS $J = 3-2$	146969.025	146968.9(1)	23.8(1)	19.8(2)
		IRC +30374		
SiO $J = 3-2$	130268.665	130268.7(1)	25.1(2)	7.07(7)
SiS $J = 7-6$	127076.180	127076.3(1)	22.6(4)	1.73(2)
SiS $J = 8-7$	145227.054	145227.2(1)	25.2(2)	2.99(3)

Table 8.6: Continued.

Line	ν_{calc} (MHz)	ν_{obs} (MHz)	$V_{\rm exp}$ (km s^{-1})	$\int T_{\rm mb} dv$ (K km s^{-1})
CS $J = 3 - 2$	146969.025	146968.6(1)	25.8(2)	26.7(26)
		LP And		
SiO $J = 3 - 2$	130268.665	130268.5(1)	12.9(2)	8.56(8)
SiS $J = 7 - 6$	127076.180	127076.1(1)	12.1(2)	7.01(7)
SiS $J = 8 - 7$	145227.054	145226.9(1)	13.8(1)	12.3(1)
CS $J = 3 - 2$	146969.025	146969.0(1)	14.7(1)	35.6(35)
		V Cyg		
SiO $J = 3 - 2$	130268.665	130268.5(1)	12.2(1)	9.03(9)
SiS $J = 7 - 6$	127076.180	127076.4(1)	12.9(1)	1.41(1)
SiS $J = 8 - 7$	145227.054	145227.2(1)	12.3(1)	2.45(2)
CS $J = 3 - 2$	146969.025	146968.8(1)	12.1(1)	25.2(25)
		V384 Per		
SiO $J = 3 - 2$	130268.665	130268.6(1)	14.8(1)	9.29(9)
SiS $J = 7 - 6$	127076.180	127076.1(1)	12.7(1)	2.15(2)
SiS $J = 8 - 7$	145227.054	145227.0(1)	14.1(1)	4.02(4)
CS $J = 3 - 2$	146969.025	146968.8(1)	15.6(1)	28.7(29)
		IRC +60144		
SiO $J = 3 - 2$	130268.665	130268.6(1)	20.8(1)	5.34(5)
SiS $J = 7 - 6$	127076.180	127076.2(10)	19.4(10)	0.9(2) [a]
SiS $J = 8 - 7$	145227.054	145226.9(1)	20.9(1)	1.65(1)
CS $J = 3 - 2$	146969.025	146968.7(1)	20.9(1)	12.5(12)
		U Cam		
SiO $J = 3 - 2$	130268.665	130268.2(1)	11.6(1)	0.96(1)
SiS $J = 7 - 6$	127076.180	-	-	-
SiS $J = 8 - 7$	145227.054	-	-	-
CS $J = 3 - 2$	146969.025	146968.8(1)	13.5(1)	4.7(5)
		IRC +20370		
SiO $J = 3 - 2$	130268.665	130268.5(1)	13.1(1)	7.25(7)
SiS $J = 7 - 6$	127076.180	127076.1(1)	12.7(1)	3.10(2)
SiS $J = 8 - 7$	145227.054	145227.1(5)	13.8(4)	5.64(5)
CS $J = 3 - 2$	146969.025	146968.9(5)	13.2(8)	19.9(20)

Table 8.6: Continued.

Line	ν_{calc} (MHz)	ν_{obs} (MHz)	$V_{\rm exp}$ (km s^{-1})	$\int T_{\rm mb} dv$ (K km s^{-1})
		CRL 67		
SiO $J = 3 - 2$	130268.665	130268.6(1)	14.5(1)	2.88(3)
SiS $J = 7 - 6$	127076.180	127076.4(1)	13.6(1)	1.62(1)
SiS $J = 8 - 7$	145227.054	145226.9(1)	15.4(2)	2.83(2)
CS $J = 3 - 2$	146969.025	146968.9(1)	16.1(2)	12.3(12)
		CRL 190		
SiO $J = 3 - 2$	130268.665	130269.5(5)	16.3(5)	0.39(4)
SiS $J = 7 - 6$	127076.180	127076.2(1)	16.6(1)	1.45(1)
SiS $J = 8 - 7$	145227.054	145227.0(1)	16.2(1)	1.93(2)
CS $J = 3 - 2$	146969.025	146968.7(1)	16.9(2)	6.76(7)
		V Aql		
SiO $J = 3 - 2$	130268.665	130268.4(1)	7.2(1)	0.44(4)
SiS $J = 7 - 6$	127076.180	-	-	-
SiS $J = 8 - 7$	145227.054	-	-	-
CS $J = 3 - 2$	146969.025	146968.8(1)	9.2(1)	4.30(4)
		CRL 2477		
SiO $J = 3 - 2$	130268.665	130268.1(1)	16.7(1)	1.28(1)
SiS $J = 7 - 6$	127076.180	127076.2(1)	16.5(1)	2.64(2)
SiS $J = 8 - 7$	145227.054	145226.8(1)	19.2(2)	2.93(3)
CS $J = 3 - 2$	146969.025	146968.6(1)	20.1(1)	7.17(7)
		CRL 2494		
SiO $J = 3 - 2$	130268.665	130268.8(1)	16.4(2)	2.64(3)
SiS $J = 7 - 6$	127076.180	127077.0(10)	20.4(10)	1.04(20)
SiS $J = 8 - 7$	145227.054	145227.4(2)	19.0(6)	1.57(15)
CS $J = 3 - 2$	146969.025	146968.9(1)	19.6(1)	13.2(13)
		Rv Aqr		
SiO $J = 3 - 2$	130268.665	130268.3(1)	14.0(2)	5.58(5)
SiS $J = 7 - 6$	127076.180	127076.1(5)	13.3(5)	0.71(7)
SiS $J = 8 - 7$	145227.054	145226.9(1)	14.6(2)	1.34(1)
CS $J = 3 - 2$	146969.025	146968.6(1)	15.4(2)	13.3(13)
		CRL 2513		
SiO $J = 3 - 2$	130268.665	130268.5(1)	25.7(1)	2.58(2)

Table 8.6: Continued.

Line	ν_{calc} (MHz)	ν_{obs} (MHz)	$V_{\rm exp}$ (km s^{-1})	$\int T_{\rm mb} dv$ (K km s^{-1})
SiS $J = 7-6$	127076.180	127076.0(5)	24.2(6)	0.84(8)
SiS $J = 8-7$	145227.054	145226.7(5)	24.9(4)	1.66(16)
CS $J = 3-2$	146969.025	146968.7(1)	26.5(2)	8.92(9)
		S Aur		
SiO $J = 3-2$	130268.665	130267.5(1)	21.8(2)	1.25(1)
SiS $J = 7-6$	127076.180	-	-	-
SiS $J = 8-7$	145227.054	-	-	-
CS $J = 3-2$	146969.025	146968.1(1)	26.5(1)	4.05(4)
		V636 Mon		
SiO $J = 3-2$	130268.665	130269.3(1)	24.3(1)	3.74(4)
SiS $J = 7-6$	127076.180	127076.2(5)	24.1(5)	0.60 [a]
SiS $J = 8-7$	145227.054	145227.9(5)	26.5(5)	0.50(5) [a]
CS $J = 3-2$	146969.025	146969.8(1)	25.8(1)	8.85(9)
		W Ori		
SiO $J = 3-2$	130268.665	130268.1(5)	8.5(4)	0.29(3)
SiS $J = 7-6$	127076.180	-	-	-
SiS $J = 8-7$	145227.054	-	-	-
CS $J = 3-2$	146969.025	146968.8(5)	10.5(8)	4.2(4)
		Y CVn		
SiO $J = 3-2$	130268.665	130268.3(1)	7.3(1)	0.38(4)
SiS $J = 7-6$	127076.180	-	-	-
SiS $J = 8-7$	145227.054	-	-	-
CS $J = 3-2$	146969.025	146968.5(1)	9.4(1)	7.58(7)
		R Lep		
SiO $J = 3-2$	130268.665	130267.9(1)	19.8(2)	3.45(3)
SiS $J = 7-6$	127076.180	-	-	-
SiS $J = 8-7$	145227.054	-	-	
CS $J = 3-2$	146969.025	146968.3(1)	20.9(2)	5.78(6)
		ST Cam		
SiO $J = 3-2$	130268.665	-	-	-
SiS $J = 7-6$	127076.180	-	-	-
SiS $J = 8-7$	145227.054	-	-	-

Table 8.6: Continued.

Line	ν_{calc} (MHz)	ν_{obs} (MHz)	$V_{\rm exp}$ (km s^{-1})	$\int T_{\rm mb} dv$ (K km s^{-1})
CS $J = 3 - 2$	146969.025	146969.2(1)	11.5(1)	0.82(8)
		UU Aur		
SiO $J = 3 - 2$	130268.665	130266.2(10)	6.7(10)	0.09(2)
SiS $J = 7 - 6$	127076.180	-	-	-
SiS $J = 8 - 7$	145227.054	-	-	-
CS $J = 3 - 2$	146969.025	146968.6(10)	11.0(1)	0.30(3)

Notes. Numbers in parentheses are 1σ uncertainties in units of the last digits.

[a] Marginal detection.

Chapter 9

The abundance of S- and Si-bearing molecules in O-rich circumstellar envelopes of AGB stars

This chapter is based on the publication:

The abundance of S- and Si-bearing molecules in O-rich circumstellar envelopes of AGB stars*: SiO, CS, SiS, SO, and SO_2 abundances in oxygen star envelopes

S. Massalkhi, M. Agúndez, J. Cernicharo and L. Velilla-Prieto

ASTRONOMY & ASTROPHYSICS, A&A, 641, A57 (2020)

*Based on observations carried out with the IRAM 30m Telescope. IRAM is supported by INSU/CNRS (France), MPG (Germany), and IGN (Spain).

ABSTRACT

Aims: We aim to determine the abundances of SiO, CS, SiS, SO, and SO_2 in a large sample of oxygen-rich asymptotic giant branch (AGB) envelopes covering a wide range of mass loss rates to investigate the potential role that these molecules could play in the formation of dust in these environments.

Method: We surveyed a sample of 30 oxygen-rich AGB stars in the λ 2 mm band

using the IRAM 30m telescope. We performed excitation and radiative transfer calculations based on the large velocity gradient (LVG) method to model the observed lines of the molecules and to derive their fractional abundances in the observed envelopes.

Results: We detected SiO in all 30 targeted envelopes, as well as CS, SiS, SO, and SO_2 in 18, 13, 26, and 19 sources, respectively. Remarkably, SiS is not detected in any envelope with a mass loss rate below 10^{-6} $M_\odot$ yr^{-1}, whereas it is detected in all envelopes with mass loss rates above that threshold. From a comparison with a previous, similar study on C-rich sources, it becomes evident that the fractional abundances of CS and SiS show a marked differentiation between C-rich and O-rich sources, being two orders of magnitude and one order of magnitude more abundant in C-rich sources, respectively, while the fractional abundance of SiO turns out to be insensitive to the C/O ratio. The abundance of SiO in O-rich envelopes behaves similarly to C-rich sources, that is, the denser the envelope the lower its abundance. A similar trend, albeit less clear than for SiO, is observed for SO in O-rich sources.

Conclusion: The marked dependence of CS and SiS abundances on the C/O ratio indicates that these two molecules form more efficiently in C- than O-rich envelopes. The decline in the abundance of SiO with increasing envelope density and the tentative one for SO indicate that SiO and possibly SO act as gas-phase precursors of dust in circumstellar envelopes around O-rich AGB stars.

9.1 Introduction

In this Chapter, we focus on potential gas-phase precursors of dust in O-rich AGB stars. Some metal oxides recently detected have been suggested to act as precursors of seed nuclei, for example, TiO and TiO_2 (Gail et al., 1998) and AlO (Gobrecht et al., 2016). However, observational constraints are still not conclusive (Banerjee et al., 2012; De Beck et al., 2017; Decin et al., 2017; Kamiński et al., 2013, 2016, 2017). Previous observational studies done on large samples of O-rich AGB stars to investigate potential precursors of dust are meagre. To investigate which gas-phase molecules could play a role in the formation of dust around O-rich AGB stars, we carry out a study of the abundance of five molecules, SiO, CS, SiS, SO, and SO_2, in 30 oxygen-rich AGB stars. In Sec. 9.2, we outline the sample. In Sec. 9.3 we describe the observations carried out and in Sec. 9.4 we present the main results from the observations. In Sec. 9.5, we describe the radiative transfer model, the molecular data, and the procedure adopted for the derivation of the molecular abundances. In Sec. 9.6 we describe the results from the radiative transfer model and comment on a few peculiar cases

that stood out during the modeling. Finally, in Sec. 9.7 we discuss the main results of our study and present our conclusions in Sec. 9.8.

9.2 The sample

The sample contains 30 O-rich AGB stars, among which there are Mira variables (M), characterized by regular variations with a large amplitude ($>$ 2.5 mag in the V band), and semiregular variables (SR), characterized by a small amplitude ($<$ 2.5 mag in the V band). We selected sources from samples in the literature (e.g., Danilovich et al. 2015; Ramstedt et al. 2014; Schöier et al. 2013) mainly based on strong line emission of molecules like CO, SiO, and SO. The sample was also chosen to cover a wide range of mass loss rates ($10^{-8} - 10^{-5}$ M$_\odot$ yr^{-1}). The list of AGB stars are presented in Tables 9.1 and 9.2 for regular and peculiar sources respectively along with their coordinates, systemic velocity with respect to the Local Standard of Rest ($V_{\rm LSR}$), distance (D), effective temperature of the star (T_*), stellar luminosity (L_*), mass loss rate ($\dot{M}$), terminal expansion velocity of the envelope ($V_{\rm exp}$), dust condensation radius (r_c), dust temperature at the condensation radius ($T_{\rm d}(r_{\rm c})$), gas-to-dust mass ratio (Ψ), and the corresponding references for each parameter.

Coordinates were taken from the literature and checked using the SIMBAD astronomical database*. The parameters $V_{\rm LSR}$ and $V_{\rm exp}$ are determined from various strong molecular lines available in this study. These two parameters are reported in the literature mainly from CO and SiO lines with varying degrees of accuracy (e.g., González Delgado et al. 2003; Groenewegen et al. 1999; Teyssier et al. 2006). We carried out an evaluation of the values of $V_{\rm LSR}$ and $V_{\rm exp}$ derived from our data and compared with those in the literature. In cases where our lines have a well-defined shape, the values from our dataset were preferred, whereas when lines show a less clear shape, the values from literature were favored (as denoted in Table 9.1 where the lack of reference means that the values are derived from this work). The final values of $V_{\rm LSR}$ and $V_{\rm exp}$ adopted in this work are given in Tables 9.1 and 9.2. We adopted the values of T_* from studies where this parameter is derived by modeling the SED of each star. Stellar luminosities were adopted from the literature, where they are mostly estimated using the period-luminosity relation for Mira variables. Mass loss rates were taken from the literature, where they are determined by modeling observations of multiple CO lines. Distances were adopted from Gaia† for the stars that have available Gaia data. Although Gaia distances are known to be problematic for AGB stars due to the

*http://simbad.u-strasbg.fr/Simbad

†https://gea.esac.esa.int/archive/

Table 9.1: Sample of oxygen stars

Name	R.A. J2000.0	Decl. J2000.0	$V_{\rm LSR}$ (km s^{-1})	D (pc)	$T_\star$ (K)	$L_\star$ ($L_\odot$)	$\dot{M}$ ($M_\odot$ yr^{-1})	$V_{\rm exp}$ (km s^{-1})	$T_{\rm d}(r_c)$ (K)	r_c (cm)	Ψ
IK Tau	03:53:28.87	+11:24:21.7	+34.5 [e]	285 [a]	2100 [b]	9250 [b*]	2.4×10^{-5} [b*]	17.5 [e]	1000 [b]	1.8×10^{14} [b]	435 [i]
KU And	00:06:52.94	+43:05:00.0	−22	680 [c]	2000 [c]	11800 [c]	9.4×10^{-6} [d]	19.5	1100 [c]	1.5×10^{14} [c]	200 [m]
RX Boo	14:24:11.63	+25:42:13.4	+1.5	128 [a]	1800 [c]	4550 [c*]	6.1×10^{-7} [b*]	7.5	900 [c]	1.5×10^{14} [c]	144 [x]
RT Vir	13:02:37.98	+05:11:08.4	+18.5	226 [l]	2000 [b]	4500 [b]	4.5×10^{-7} [b]	7	1000 [b]	1.6×10^{14} [b]	2000 [q]
R Leo	09:47:33.49	+11:25:43.7	+0.1	71 [a]	2000 [b]	2500 [b]	1.0×10^{-7} [b]	5	1200 [b]	1.3×10^{14} [b]	167 [m]
WX Psc	01:06:25.98	+12:35:53.1	+9.5	700 [b]	1800 [b]	10300 [b]	4.0×10^{-5} [b]	19	800 [b]	3.2×10^{14} [b]	250 [m]
GX Mon	06:52:46.91	+08:25:19.0	−9.5	416 [a]	2600 [c]	4700 [c*]	4.9×10^{-6} [d*]	18	900 [c]	1.1×10^{14} [c]	200 [m]
NV Aur	05:11:19.44	+52:52:33.2	+3	1200 [c]	2000 [c]	9800 [c]	2.5×10^{-5} [d]	17.5	1100 [c]	1.7×10^{14} [c]	1000 [m]
V1111 Oph	18:37:19.26	+10:25:42.2	−31	357 [a]	1800 [b]	2300 [b*]	2.7×10^{-6} [d*]	15.5	800 [b]	2.7×10^{14} [b]	200 [m]
RR Aql	19:57:36.06	−01:53:11.3	+28	318 [a]	2000 [c]	2800 [c*]	8.6×10^{-7} [d*]	8.5	1500 [c]	5.9×10^{13} [c]	185 [t]
R LMi	09:45:34.28	+34:30:42.8	+0.9	330 [d]	2400 [d]	5500 [d]	2.6×10^{-7} [d]	5.5	1000 [d]	1.7×10^{14} [d]	115 [t]
BX Cam	05:46:44.10	+69:58:25.2	−1	244 [a]	2800 [c]	1800 [c*]	1.0×10^{-6} [d*]	17	1500 [c]	7.1×10^{13} [c]	300 [z]
V1300 Aql	20:10:27.87	−06:16:13.6	−17.5	620 [c]	2000 [c]	10600 [c]	1.0×10^{-5} [d]	15	1100 [c]	1.8×10^{14} [c]	1000 [m]
R Cas	23:58:24.87	+51:23:19.7	+26.5	188 [a]	1800 [e]	10400 [e*]	9.5×10^{-7} [e*]	7.5	1050 [e]	2.5×10^{14} [e]	91 [m]
IRC −30398	18:59:13.85	−29:50:20.4	−7.5	390 [m]	2000 [m]	8700 [m]	6.0×10^{-6} [m]	14.5	800 [b]	2.6×10^{14} [b]	200 [m]
TX Cam	05:00:50.40	+56:10:52.6	+11.5	334 [a]	2600 [c]	6600 [c*]	7.7×10^{-6} [c*]	17.5	1300 [c]	1.0×10^{14} [c]	500 [x]
S CrB	15:21:23.96	+31:22:02.6	+1.5	431 [a]	2400 [d]	6300 [d*]	2.7×10^{-7} [d*]	5	1000 [d]	1.7×10^{14} [d]	300 [z]
IRC +60169	06:34:34.88	+60:56:33.2	−22	510 [a]	2200 [c]	5900 [c*]	9.6×10^{-6} [c*]	15	1000 [c]	1.1×10^{14} [c]	300 [z]
R Hya	13:29:42.78	−23:16:52.8	−10 [o]	224 [a]	2600 [c]	17200 [c*]	4.7×10^{-7} [c*]	5 [o]	1500 [c]	6.1×10^{13} [c]	200 [m]
R Crt	11:00:33.85	-18:19:29.6	+11.5	236 [a]	2800 [c]	7700 [c*]	1.0×10^{-6} [c*]	11	600 [c]	3.5×10^{14} [c]	333 [q]
o Ceti	02:19:20.79	−02:58:39.5	+47	107 [f]	3000 [g]	9000 [g]	2.0×10^{-7} [h]	3	1000 [z]	9.7×10^{13} [y]	195 [t]
W Hya	13:49:02.00	−28:22:03.5	+40.5	164 [a]	2600 [b]	16800 [b*]	4.2×10^{-7} [b*]	6	1200 [b]	6.3×10^{13} [b]	500 [v]
T Cep	21:09:31.78	+68:29:27.2	−2.5	176 [a]	2400 [d]	4900 [d*]	7.8×10^{-8} [d*]	4	1000 [d]	1.8×10^{14} [d]	300 [z]
V1943 Sgr	20:06:55.24	−27:13:29.8	−14.5	666 [a]	2200 [d]	55400 [d*]	1.0×10^{-6} [d*]	4.5	1000 [d]	1.6×10^{14} [d]	300 [z]
SW Vir	13:14:04.39	−02:48:25.2	−10.5	300 [a]	2400 [b]	17600 [b*]	2.2×10^{-6} [b*]	7.5	800 [b]	2.9×10^{14} [b]	1000 [q]
AFGL 292	02:02:38.63	+07:40:36.5	+23.7	253 [a]	2200 [d]	6000 [d]	1.3×10^{-7} [d*]	7	1000 [d]	1.8×10^{14} [d]	300 [z]
BK Vir	12:30:21.01	+04:24:59.2	+17.5	234 [a]	3000 [n]	4500 [n*]	2.3×10^{-7} [m*]	4	1000 [z]	8.6×10^{13} [z]	2000 [q]

References and notes: The coordinates of the O-rich stars are taken from the literature. An asterisk in the value of the luminosity ($L_\star$) or mass loss rate ($\dot{M}$) indicates that the value has been scaled according to the updated value of the distance. [a] Gaia Collaboration et al., (2018), [b] Ramstedt et al., (2014), [c] Schöier et al., (2013), [d] Danilovich et al., (2015), [e] Maercker et al., (2016), [f] Knapp et al., (2003), [g] Woodruff et al., (2004),[h] Ryde et al., (2001), [i] Gobrecht et al., (2016), [k] Justtanont et al., (1996), [l] Zhang et al., (2017), [m] González Delgado et al., (2003), [n] Ohnaka et al., (2011), [o] Knapp et al., (1998), [p] De Beck et al., (2010), [q] Olofsson et al., (2002), [r] Dyck et al., (1996), [s] Winters et al., (2007), [t] Groenewegen et al., (1999), [v] Khouri et al., (2014), [x] Dharmawardena et al., (2018), [w] Gardan et al., (2006) , [y] Kamiński et al., (2016) [z] Assumed value for the condensation radius r_c is 5 $R_\star$, for the dust temperature at the condensation radius $T_{\rm d}(r_{\rm c})$ is 1000 K, and for the gas-to-dust mass ratio Ψ is 300.

Table 9.2: Peculiar sources

Name	R.A. J2000.0	Decl. J2000.0	comp.	$V_{\rm LSR}$ (km s^{-1})	D (pc)	$T_\star$ (K)	$L_\star$ (L$_\odot$)	$\dot{M}$ (M$_\odot$ yr^{-1})	$V_{\rm exp}$ (km s^{-1})	$T_{\rm d}(r_c)$ (K)	r_c (cm)	Ψ
Ep Aqr	21:46:31.85	−02:12:45.9	Narrow	−33.5	124 [a]	3200 [s]	4100[s*]	1.7×10^{-8} [s*]	1 [q]	1000 [z]	7.2×10^{13} [z]	860 [x]
			Broad					5.0×10^{-7} [s*]	9.2 [q]			
X Her	16:02:39.17	+47:14:25.3	Narrow	−73	145 [a]	3300 [r]	5100 [w*]	4.3×10^{-8} [m*]	2.2 [m]	1000 [z]	6.7×10^{13} [z]	500 [q]
			Broad					1.6×10^{-7} [m*]	6.5 [m]			
OH 26.5+0.6	18:37:32.51	−05:23:59.2	AGB wind	+27	1370 [k]	2200 [k]	14000 [k]	1.0×10^{-6} [k]	15.4 [k]	1000 [k]	4.5×10^{14} [k]	278 [k]
			Superwind					5.5×10^{-4} [k]				

References in Table 9.1

variability of the photocenter position (which may introduce an error of up to 20 % in the parallax; Chiavassa et al. 2018), here we decided to favor distances from Gaia over those from Hipparcos or from the period-luminosity relation (see, e.g., Díaz-Luis et al. 2019; McDonald et al. 2018). Mass loss rates and luminosities are two quantities that follow the inverse-square law as $\propto D^2$, so we consistently scaled them taking into account the newly adopted Gaia distance and mark the new values in Table 9.1 with an asterisk. Note however that empirical mass loss rates derived from CO lines may scale with distance in a slightly different way according to Appendix A of Ramstedt et al., (2008), where scaling laws of the type $\propto D^{1.4-1.9}$ are found, depending on the CO line used. In any case, we evaluated the impact of adopting a scaling law $\propto D^{1.4}$ instead of $\propto D^2$ would have on the scaled mass loss rates and it is at most a factor of two.

9.3 The observations

The observations were carried out in the period February to October 2018 with the IRAM 30m telescope, located at Pico Veleta (Spain). Table 9.3 includes some basic information about the targeted lines: the rest frequency, the Einstein coefficient, A_{ul}, the upper level energy, E_u, and the beam size of the telescope, θ_{mb}. We used the E150 receiver in dual side-band mode, with image rejections >10 dB, and observed the frequency ranges $128.5-136.2$ GHz and $144.1-151.9$ GHz (in the lower and upper side bands, respectively). The beam size of the telescope at these frequencies is in the range 16.2-19.0″. The observations were done in the wobbler-switching mode with a throw of 180″ in azimuth. This technique implies that the target source is measured (ON), followed by a measurement of the sky (OFF) with similar atmospheric conditions. The OFF measurement is then subtracted from the ON measurement to obtain a spectra of the source from which the contribution of the atmosphere to the signal has been removed. The focus was regularly checked on a planet and the pointing of the telescope was systematically checked on a nearby quasar before the observation of each AGB star. The error in the pointing is estimated to be 2-3″. The E150 receiver was connected to a fast Fourier transform spectrometer providing a spectral resolution of 0.2 MHz which corresponds to velocity resolutions 0.46 km s^{-1} at 129 GHz and 0.39 km s^{-1} at 151 GHz. The weather was good and stable during most of the observations, with typical amounts of precipitable water vapor of 2-4 mm and average system temperatures of 115 K. The observations were calibrated by observing the sky and two absorbers at different temperatures, a hot (ambient) and a cold (liquid nitrogen) load using the atmospheric transmission model ATM (Cernicharo, 1985; Pardo et al., 2001) adopted by the IRAM 30m

Table 9.3: Targeted molecular lines

Transition	Frequency (MHz)	A_{ul} (s^{-1})	E_u (K)	θ_{mb} ($''$)
SiO $J = 3-2$	130268.665	1.06×10^{-4}	12.5	18.8
CS $J = 3-2$	146969.025	6.07×10^{-5}	14.1	16.7
SiS $J = 8-7$	145227.052	5.05×10^{-5}	31.4	16.9
SO $3_3 - 2_2$	129138.983	2.21×10^{-5}	25.5	19.0
SO_2 $8_{2-6} - 8_{1-7}$	134004.811	2.50×10^{-5}	43.1	18.3
SO_2 $5_{1-5} - 4_{0,4}$	135696.016	2.21×10^{-5}	15.7	18.1
SO_2 $4_{2-2} - 4_{1,3}$	146605.519	2.47×10^{-5}	19.0	16.7
SO_2 $2_{2-0} - 2_{1,1}$	151378.662	1.88×10^{-5}	12.6	16.2

telescope. The intensity scale of the output spectra obtained from the antenna is calibrated in antenna temperature (T_A^*). To express the latter in terms of the main beam brightness temperature (T_{mb}), we used the recommended values of B_{eff} and F_{eff} for EMIR[‡] at the frequencies of the observed lines[§], where $B_{eff} = 0.863 \exp[-(\nu(GHz)/361)^2]$ and $F_{eff} = 0.93$. The error in the intensities due to calibration is estimated to be $\sim$20 %. Typical on source integration times, after averaging horizontal and vertical polarizations, were $\sim$1-2 hrs for each source, resulting in T_{mb} rms noise levels per 0.2 MHz channel of 3-7 mK.

The data were reduced using the software CLASS[¶] within the package GILDAS[||]. To obtain the final spectra for each source, we followed the standard procedure of data reduction that consists of removal of bad channels and low-quality scans, averaging the spectra corresponding to the horizontal and vertical polarizations, and subtracting a baseline of a first order polynomial. In the case of weak lines, the spectra were smoothed to a spectral resolution of 0.4 MHz to increase the signal-to-noise ratio. This corresponds to a velocity resolution of 0.8-1 km s^{-1}. When a line was undetected, we smoothed the spectrum to a spectral resolution of 0.8 MHz, corresponding to 1.6-1.9 km s^{-1}.

9.4 Observational results

A total of 30 O-rich CSEs were observed. The spectra obtained is shown in Fig. 9.1. We clearly detected SiO $J = 3-2$ in all the 30 sources, CS $J = 3-2$ in 18 sources, SiS $J = 8-7$

[‡]Eight MIxer Receiver

[§]http://www.iram.es/IRAMES/mainWiki/Iram30mEfficiencies

[¶]Continuum and Line Analysis Single-dish Software

[||]GILDAS is a software to reduce and analyze mainly (sub-)mm observations from single-dish and interferometric telescopes. See http://www.iram.fr/IRAMFR/GILDAS

in 13 sources, SO $3_3 - 2_2$ in 26 sources, while SO_2 was detected in at least one of the targeted lines in 19 sources. The detection rates are therefore 100 % for SiO, 60 % for CS, 43 % for SiS, 86 % for SO, and 63 % for SO_2.

The lines were fit using the `shell` method of CLASS as described in Massalkhi et al., (2019). By performing the fit, we aim to derive for each target lines in every source the centroid frequency in MHz, the expansion velocity in km s^{-1}, and the line area, that is, the velocity-integrated intensity in K km s^{-1}. These line parameters are given in Table 9.5.

The shapes of the emission lines arising from spherically expanding envelopes are essentially determined by the angular size of the emitting source relative to the size of the telescope beam and the line opacity. Most of the line shapes observed here are typical of spherically expanding envelopes, that is, parabolic (optically thick spatially unresolved emission; e.g., SiO $J = 3 - 2$ in KU And), flat-topped (optically thin spatially unresolved emission; e.g., CS $J = 3 - 2$ in V1111 Oph), or double-peaked (optically thin spatially resolved emission; e.g., SO_2 lines in V1300 Aql). However, there is a number of lines that show profiles with varying kinds of asymmetries. The triangular profile shown in SiO $J = 3 - 2$ in R Leo and RR Aql is said to indicate that the emission is mainly originating from a region close to the star where the gas is still accelerating. Some striking lines show one side of the profile brighter than the other, sometimes in the blue-shifted side and sometimes in the red-shifted side. An example of these are the SO_2 lines in IK Tau (blue-shifted emission) and GX Mon (red-shifted emission). This indicates an asymmetry in the distribution of the gas emission. Another explanation could be due to self absorption in the line of sight, however, this effect is rather unlikely because the lines are optically thin. Regardless, the `shell` method of CLASS cannot deal with these kind of asymmetries, but we nevertheless use it on the account that the line area and the expansion velocity resulting from the fit should be trustworthy.

9.5 Excitation and radiative transfer modeling

We aim to derive the abundances of SiO, CS, SiS, SO, and SO_2 in each source of our sample to provide a statistically meaningful view of how abundant these molecules are in envelopes around O-rich stars. The five molecules studied here are not excited according to local thermodynamic equilibrium (LTE) in the regions of the envelope which contribute mostly to the observed emission (see Sec. 9.6). Determining the level populations then requires detailed knowledge of collisional excitation data. In Section 9.5.1 we describe the spectroscopic and collisional excitation data of the five molecules that were input into our calculations and in

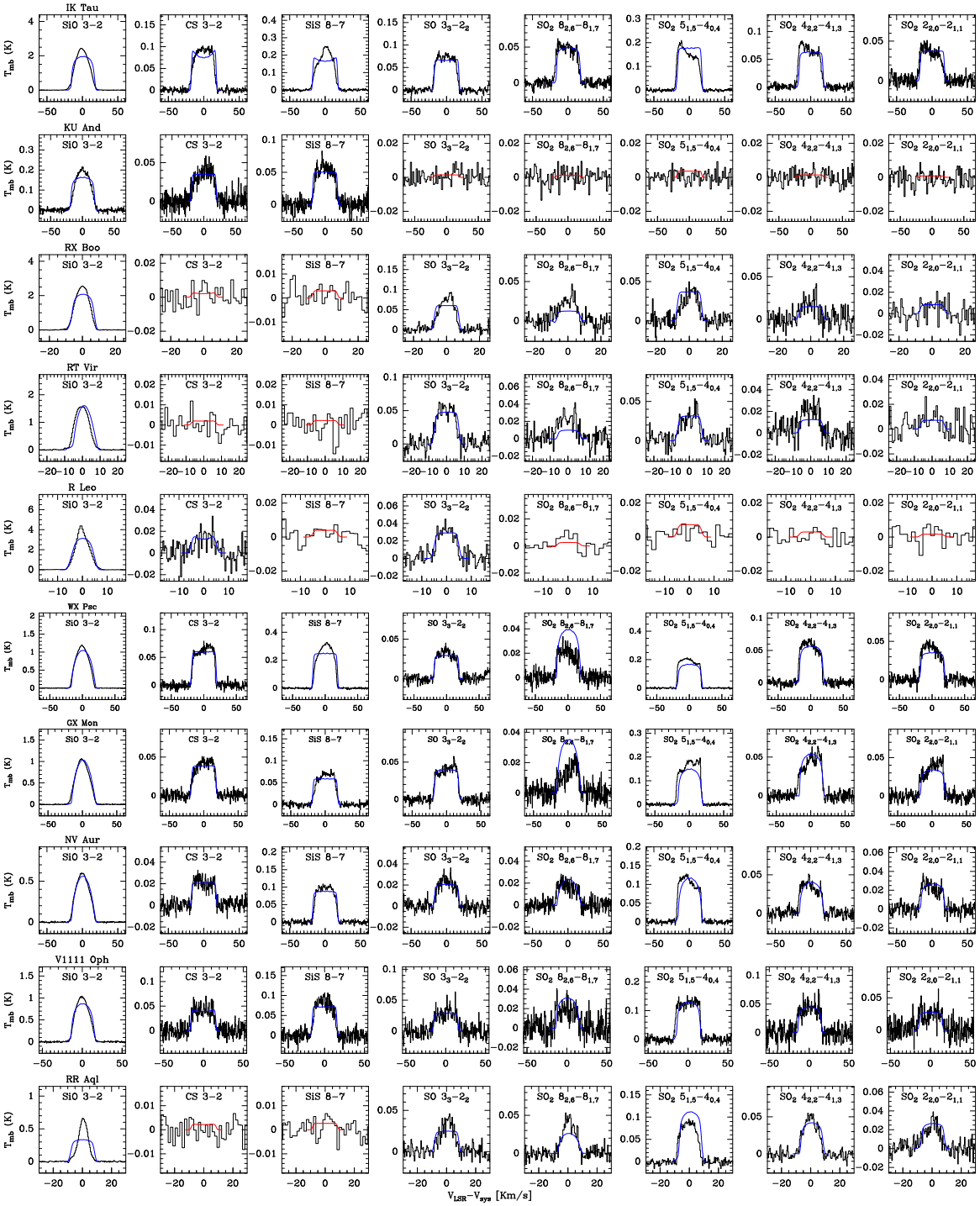

Figure 9.1: Rotational lines observed with the IRAM 30m telescope in the 30 O-rich CSEs (black histograms). The blue lines indicate the calculated line profiles from the best-fit LVG model. The red lines correspond to the calculated line profiles with the maximum intensity compatible with the nondetection.

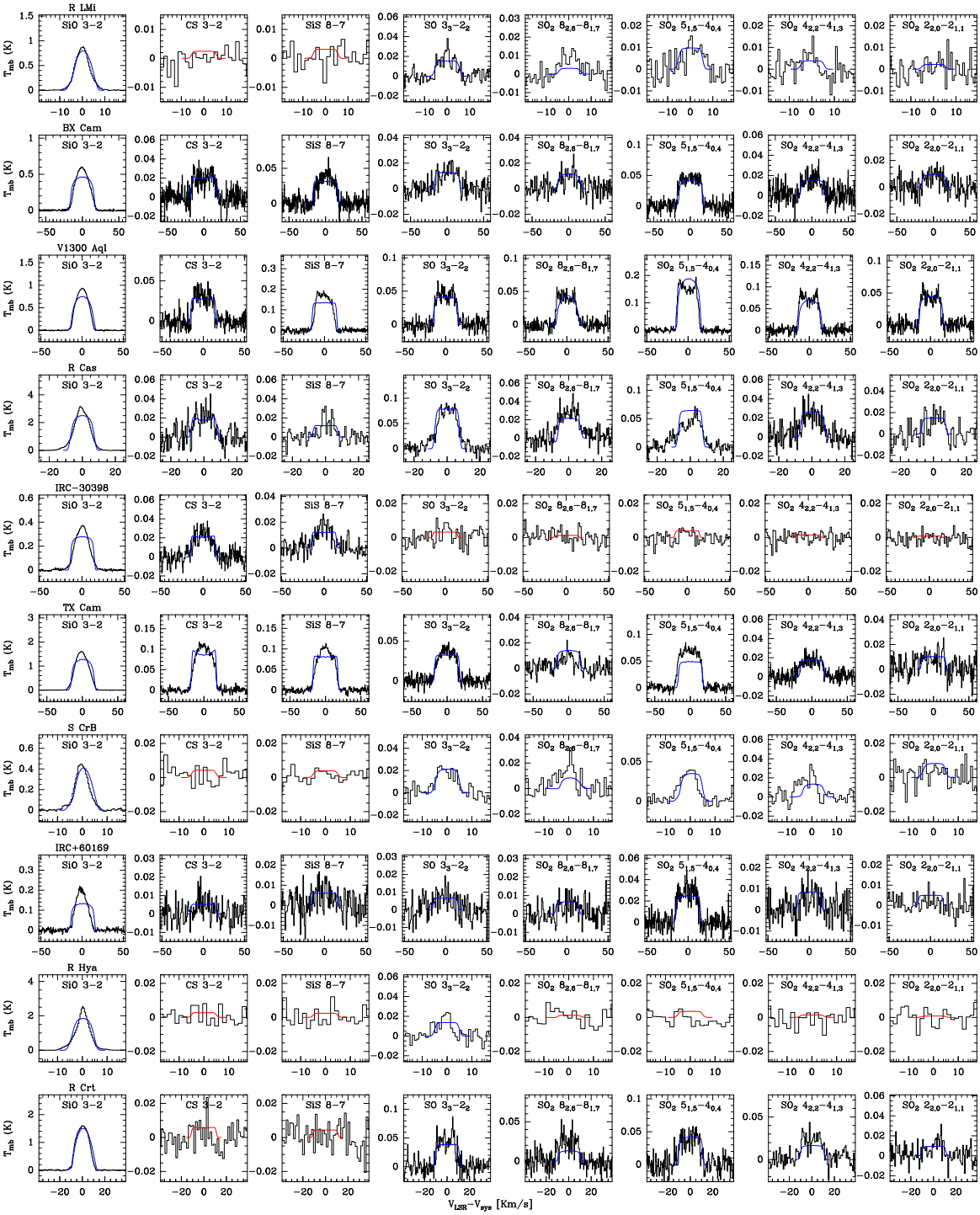

Figure 9.1 (cont.)

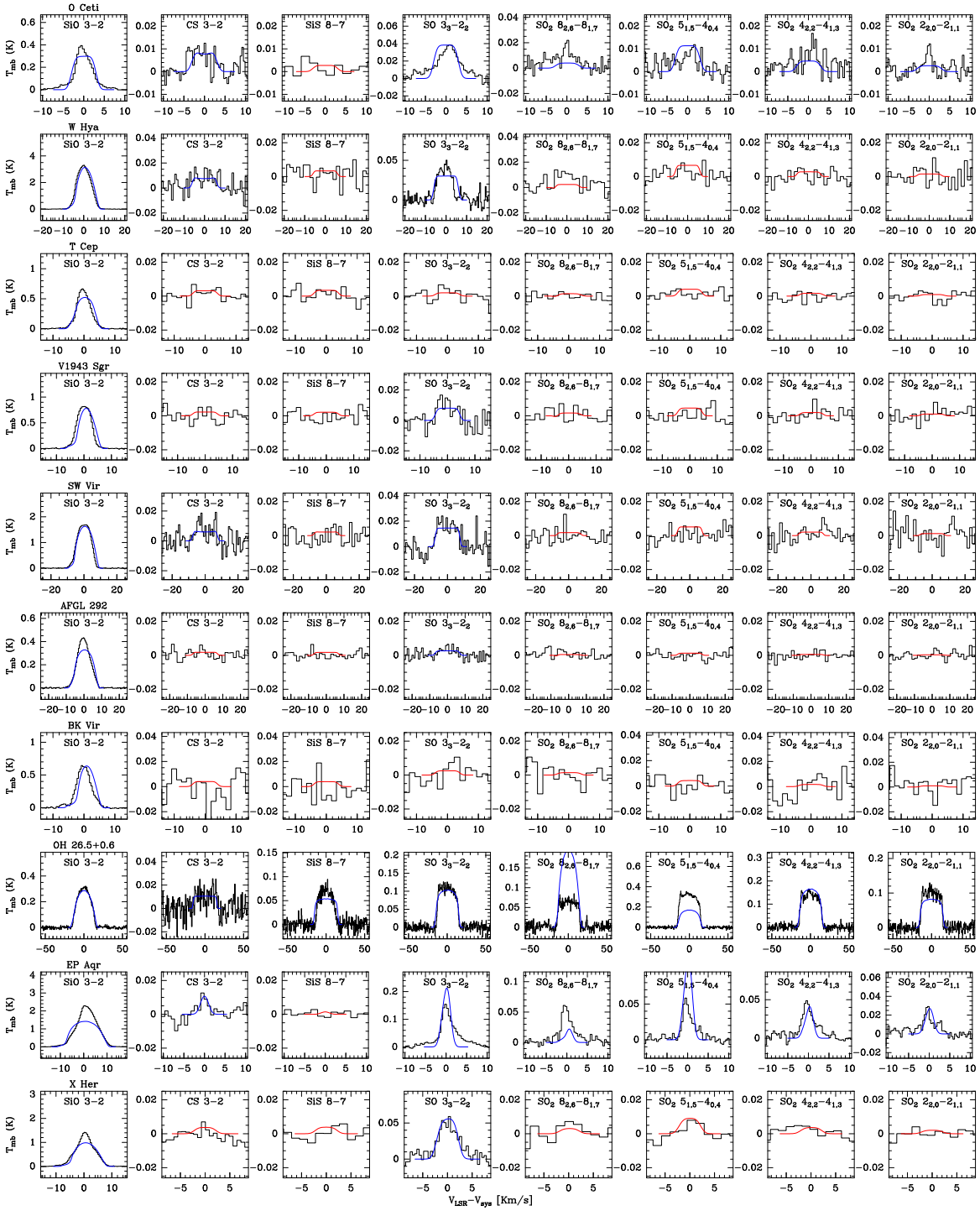

Figure 9.1 (cont.)

Section 9.5.2 we briefly describe the CSE model and how information on the abundances can be derived from the observed lines using non-LTE radiative transfer modeling.

9.5.1 Molecular data

In the excitation analysis of SiO, we considered the first 50 rotational levels within the $v = 0$ and $v = 1$ vibrational states (i.e., a total number of 100 energy levels). The level energies and transition frequencies were calculated from the Dunham coefficients given by Sanz et al., (2003). The dipole moments for pure rotational transitions within the $v = 0$ and $v = 1$ vibrational states, 3.0982 D and 3.1178 D, respectively, were taken from Raymonda et al., (1970) and the Einstein coefficient for the ro-vibrational transition $\nu = 1 \rightarrow 0$ P(1) of 6.61 s^{-1} from Drira et al., (1997). As collisional rate coefficients for pure rotational transitions we adopted those calculated by Balança et al., (2018) for H_2 as collider and by Dayou et al., (2006) for He as collider, while for ro-vibrational transitions we used the values computed by Balança et al., (2017) scaling from He to H_2 as collider (by multiplying by the squared ratio of the reduced masses of the SiO-H_2 and SiO-He colliding systems) when needed.

For CS, we included the first 50 rotational levels within the $v = 0$ and $v = 1$ vibrational states (i.e., a total number of 100 energy levels). The level energies and transition frequencies were calculated from the Dunham coefficients given by Müller et al., (2005b). The line strengths of pure rotational transitions were computed from the dipole moments for each vibrational state, $\mu_{v=0}$ =1.958 D and $\mu_{v=1}$ = 1.936 D (Winnewisser et al., 1968), while for ro-vibrational transitions we used the Einstein coefficient of 15.8 s^{-1} given for the $v = 1 \rightarrow 0$ P(1) transition by Chandra et al., (1995). We adopted the H_2 collision rate coefficients recently calculated by Denis-Alpizar et al., (2018) for pure rotational transitions and up to temperatures of 300 K. At higher temperatures and for ro-vibrational transitions we used the rate coefficients calculated by Lique et al., (2007) scaling from He to H_2 as collider. Rate coefficients for collisions with He were taken from Lique et al., (2006) and Lique et al., (2007).

For SiS, we considered the first 70 rotational levels within the $v = 0$ and $v = 1$ vibrational states (i.e., a total number of 140 energy levels). Level energies were computed from the Dunham coefficients given by Müller et al., (2007). Line strengths were computed from the dipole moments $\mu_{v=0}$ =1.735 D, $\mu_{v=1}$ = 1.770 D, and $\mu_{v=1\rightarrow0}$ = 0.13 D (Müller et al., 2007; Piñeiro et al., 1987). The rate coefficients for inelastic collisions with H_2 were taken from the calculations of Kłos et al., (2008), while for temperatures higher than 300 K and for ro-vibrational transitions we adopted the rate coefficients computed by Toboła et al.,

(2008) scaled from He to H_2. Rate coefficients for He as collider were taken from Toboła et al., (2008).

For SO, we considered rotational levels up to $J = 30$ within the ground vibrational state $v = 0$ (i.e., a total number of 91 energy levels). Level energies and transition frequencies were calculated from the rotational constants reported by Bogey et al., (1997), and line strengths for rotational transitions were computed from the dipole moment, 1.52±0.02 D, measured by Lovas et al., (1992). The rate coefficients for excitation through inelastic collisions were taken from Lique et al., (2005) for temperatures up to 50 K and from Lique et al., (2006) for higher temperatures, scaling from He to H_2 when needed.

For SO_2, we included the first 31 energy levels within the ground vibrational state. We used the rotational constants reported by Müller et al., (2005a). Line strengths for rotational transitions were computed from the dipole moment measured by Patel et al., (1979). The rate coefficients for excitation through inelastic collisions with H_2 were taken from Cernicharo et al., (2011) for temperatures up to 30 K, and from Balança et al., (2016) for higher temperatures, while for collisions with He rate coefficients were taken from Green, (1995).

9.5.2 Modeling procedure

Here, we give a brief description of the model used to perform the non-LTE excitation and radiative transfer calculations (for details see Massalkhi et al. 2018). To derive accurate molecular abundances in each object, we take into account the specific physical properties for each envelope and source presented in Table 9.1 and Table 9.2.

The main assumption in the model is that the CSE that surrounds the central AGB star has a smooth and spherically symmetric geometry that is produced by an isotropic mass loss with a constant mass loss rate $\dot{M}$ and a constant expansion velocity $V_{\rm exp}$. We assume that the hydrogen in the CSE is molecular and its density structure (as a function of a distance r from the star) follows an r^{-2} law. The various physical quantities relating to the envelope such as the radial profiles of the gas density, gas temperature, and dust temperature, as well as the properties of the dust grains are described in Massalkhi et al., (2018). The only difference in this study is that we consider spherical grains of silicate with a radius of 0.1 µm, a mass density of 3.3 g cm^{-3}, and optical properties for warm silicate from Suh, (1999).

We chose to model the molecular line emission using the multishell large velocity gradient (LVG) method explained in more detail in Agúndez, (2009) and Agúndez et al., (2012).

The LVG formalism, first developed by Sobolev, (1960), has been widely used to solve the molecular excitation and radiative transfer problem in environments with large velocity gradients. This approach is valid for molecular lines in circumstellar envelopes as long as they are not too optically thick. Bujarrabal et al., (2013) showed that this formalism yields quite accurate excitation conditions even when the approximations of the method are marginally satisfied. These authors investigated the validity of the LVG formalism by studying the CO molecular excitation for different conditions and conclude that although the LVG approximation still produces good behavior in cases where the velocity gradient is low, the behavior is not as accurate for the very outer regions with high opacities. The LVG method provides a good compromise with respect to other methodologies such as Monte Carlo, which are more computationally expensive and exhibit problems of convergence when including a high number of energy levels.

Briefly, the CSE is divided into several concentric shells. The statistical equilibrium equations are then solved in each shell to determine the level populations. The radiation field which is needed to solve the statistical equilibrium equations is evaluated solving the radiative transfer under the LVG approximation. We assume that the molecules are excited by collisions with H_2 molecules and He atoms and through radiation from three sources: the cosmic microwave background, the stellar radiation, and the thermal emission from dust. We also include infrared (IR) pumping to excited vibrational states for SiO, CS, and SiS. In the cases of SO and SO_2, we only consider rotational levels within the ground vibrational state for simplicity and because of the less reliable collisional rate coefficients for ro-vibrational transitions.

9.5.3 Adopted abundance distribution

The abundance distribution is important in the radiative transfer modeling. For parent molecules that are injected from the inner parts of the envelope, the abundance may vary with radius due to two processes: condensation onto grains and photodissociation by ultraviolet (UV) photons. In reality, the abundance is expected to decrease from the thermochemical equilibrium (TE) value at the stellar surface in the dust formation region. The molecules are further depleted by the ambient radiation field which eventually determines the size of the emission envelope. Relating to this scenario, a few studies have reported on an abundance distribution to be consisting of two components, a compact high abundance in the inner regions of the CSE, and a lower abundance in the extended outer regions of the CSE (e.g., Decin et al. 2010a; Schöier et al. 2007). For example, Schöier et al., (2004) modeled the SiO emission of the $J = 6 - 5$, $J = 5 - 4$, $J = 3 - 2$, and $J = 2 - 1$ lines in the CSE

of the M-type star R Dor and found the need for a two-component abundance distribution which was characterized by a high abundance of 4×10^{-5} up to 1.2×10^{15} cm and a lower abundance of 3×10^{-6} at larger radii. This initial high abundance followed by a decrease was interpreted as adsorption of SiO onto dust. However, when Van de Sande et al., (2018) modeled the SiO emission with several low- and high-J transitions (up to $J = 38 - 37$) in the same object, R Dor, they found no indication of a two-component abundance distribution. Similarly, in the case of SiS, Schöier et al., (2007) modeled the emission in IK Tau and found a better fit to their observations when they included an inner component out to 1×10^{15} cm with a high SiS abundance of 2×10^{-5}. However, Danilovich et al., (2019) performed sensitive ALMA observations with an angular resolution of $\sim$ 150 mas that correponds to $\sim 6 \times 10^{14}$ cm and did not find evidence for such a jump in the abundance of SiS in the same source. Other studies reported on the molecular abundance distribution in CSEs as well. Agúndez et al., (2012) modeled lines of CS in the $v = 0 - 3$ states in addition to several transitions of the isotopologues ^{13}CS, C^{34}S, and C^{33}S in IRC +10216 and derived an abundance of 4×10^{-6} in the inner regions that decreased to 7×10^{-7} in the mid envelope at a radius of 2×10^{15} cm. Their result is in good agreement with that derived by Velilla-Prieto et al., (2019) that modeled the $J = 2 - 1$ lines of CS, and ^{13}CS, C^{34}S, and C^{33}S using ALMA which also showed a decline in the abundance toward the intermediate envelope of IRC +10216 supporting a depletion scenario. However, no such abundance distribution is reported for the sulfur oxides thusfar that evidence any depletion (e.g., Danilovich et al. 2016, 2020).

Regardless whether or not these molecules experience a first abundance depletion due to dust condensation, they maintain a significant abundance in the extended outer envelope where photodissociation further removes the molecules from the gas phase. The lines observed in this study probe intermediate/outer regions of the envelope (see Sec. 9.6). That is, we are not sensitive to abundance gradients occurring in the inner envelope and the abundances derived are valid for the post-condensation region. We therefore adopt a simple scenario in which the fractional abundance remains constant throughout the envelope up to some region where it drops due to photodissociation. The adopted abundance radial distribution $f(r)$ is described by a Gaussian as:

$$f(r) = f_0 \exp\Big(- (r/r_e)^2 \Big), \tag{9.1}$$

where f is the fractional abundance of the molecule relative to H_2, f_0 is the initial abundance, and r_e is the e-folding radius at which the abundance has dropped by a factor

e. Danilovich et al., (2016) observed SO and SO_2 emission in a sample of five stars O-rich CSEs, and found that SO_2 has a Gaussian abundance distribution, whereas the SO abundance distribution differs between Gaussian for high mass-loss rate envelopes, and shell-like for low mass-loss rate envelopes where the abundance peaks at a distance from the central star. In their recent study on these two molecules using ALMA in two CSEs R Dor and IK Tau, Danilovich et al., (2020) found that SO and SO_2 in R Dor have Gaussian distribution, while in IK Tau, SO and probably SO_2 have a shell-like abundance distribution. Here, we adopt a Gaussian abundance distribution for all the molecules.

In their study on M-type stars, González Delgado et al., (2003) estimated the SiO emission size by using a scaling law that correlated r_e and the envelope density evaluated through the quantity $\dot{M}/V_{\rm exp}$,

$$\log r_e({\rm SiO}) = 19.2 + 0.48 \log \left(\frac{\dot{M}}{V_{\rm exp}} \right), \tag{9.2}$$

where r_e is given in cm, $\dot{M}$ in $M_\odot$ yr^{-1}, and $V_{\rm exp}$ in km s^{-1}. We use Eq. (9.2) to determine the emission size of SiO, SiS, SO, and SO_2 in our sample. The assumption of similar radial extents for SiO and SiS is discussed in our previous study of these molecules in C-rich CSEs in Massalkhi et al., (2019). Danilovich et al., (2018) derived empirical relations between r_e and $\dot{M}/V_{\rm exp}$ for SiS and CS from a limited sample of M-, C-, and S-type stars which we noticed are unreliable outside the relatively narrow range of $\dot{M}/V_{\rm exp}$ over which they were derived (for details see Massalkhi et al. 2019). In their recent study using ALMA data, Danilovich et al., (2020) found that SO and SO_2 are colocated around the O-rich R Dor, with SO being slightly more extended than SO_2. However, statistically robust empirical relations for the emission size of SO and SO_2 have not been derived. Since the photodissociation rates of SO and SO_2 under the interstellar radiation field are of the same order of that of SiO, a few times 10^{-9} s^{-1} (Agúndez et al., 2018; Heays et al., 2017), in the lack of better constraints on the emission size, we adopt the same radial extent for SiO, SiS, SO, and SO_2. For CS, which has a significantly lower photodissociation rate than SiO, SO, and SO_2, a few times 10^{-10} s^{-1} (Pattillo et al., 2018), we use a larger emission size as suggested by Massalkhi et al., (2019) for C-rich AGB stars and described by the following empirical relation:

$$\log r_e({\rm CS}) = 19.65 + 0.48 \log \left(\frac{\dot{M}}{V_{\rm exp}} \right), \tag{9.3}$$

Briefly, we construct a physical model of the envelope for each source with the parameters given in Table 9.1 and 9.2. Adopting the fractional abundance distributions given in the previous section, we perform excitation and radiative transfer calculations by varying the initial fractional abundance, f_0, until the calculated line profiles match the observed ones. The criteria we adopted to determine how well the model fits the data is by matching the area of the calculated line to the observed one. The agreement between observed and calculated line area was better than 3% for the molecules for which we have only one line, SiO, CS, SiS, and SO, and better than 30% for SO_2 because for this molecule we have four observed lines. When the line is undetected, we derive upper limits of the fractional abundance by choosing the maximum abundance that results in line intensities compatible with the noise level of the observations.

In our sample there are three sources which deserve to be considered separately, EP Aqr, X Her, and OH 26.5+0.6. We discuss the reasons and the procedure adopted for the line modeling of these sources in Sec. 9.5.4.

9.5.4 Peculiar sources

Some AGB stars are known to exhibit a double-component profile in some molecular lines like CO, with a narrow spectral feature centered on a much broader plateau, with both components having the same LSR velocity (Kahane et al., 1996; Kerschbaum et al., 1999; Knapp et al., 1998; Olofsson et al., 2002). The origin of these double-component profiles is still not clear. Knapp et al., (1998) suggested that it is an effect of episodic mass loss with highly varying gas expansion velocities that produces multiple shells where each shell has a different expansion velocity and different mass loss rate. Other studies argued that complicated geometries and kinematics play a role in the rise of the effect (Castro-Carrizo et al., 2010; Homan et al., 2015; Kim et al., 2012, 2019; Nakashima, 2005; Neri et al., 1998). Two of the sources that are known to exhibit this type of profile, X Her and Ep Aqr (Homan et al., 2018), are in our sample and their spectra are shown in Fig.9.1. The two stars are M-type semiregular variable AGBs. From the rotational transitions observed here there is no sign of the superimposition of the narrow profile on the broader one in both sources. However, based on the observed line widths and expansion velocities it appears that the SiO line emission of X Her and EP Aqr are coming from the broad component, while the CS, SO and SO_2 line emissions arise from the narrow component. The SiS rotational line is not detected in any of the sources, but in deriving abundance upper limits we assume that it behaves as CS, SO, and SO_2 and arises from the narrow component. We then consider two different winds for the narrow and the broad component each with different values of the

expansion velocity and the mass loss rate, as given in Table 9.2, and perform the radiative transfer and excitation analysis independently.

Another source we encountered problems modeling is the extreme OH/IR AGB star OH 26.5+0.6. This star is thought to have gone through a superwind phase characterized by a dramatic increase of the mass loss rate (by a factor of ten at least) toward the end of the AGB (Iben et al., 1983) which ejects most of the remaining envelope and the initial mass of the star allowing the latter to evolve toward the planetary nebula phase. Justtanont et al., (1996) show evidence of two mass loss regimes: a higher density superwind that started recently (<200 yr), and a lower density AGB wind that started earlier. From Justtanont et al., (1996), the reported gas mass loss rate for the superwind is $\dot{M} = 5.5 \times 10^{-4}$ $M_{\odot}$ yr^{-1} at $r < 8.0 \times 10^{15}$ cm and for the outer AGB wind is $\dot{M} = 1 \times 10^{-6}$ $M_{\odot}$ yr^{-1} at greater radii. Moreover, we adopt the gas kinetic temperature profile for the object reported by the authors as well (solid line in Fig. 7b of Justtanont et al. 1996). After setting the density and temperature structure in the envelope, we model the rotational line emission of the molecules.

9.6 Results from line modeling

The calculated line profiles from our best-fit LVG model for each of the sources are shown in blue in Fig. 9.1, where they are compared with the observed line profiles (black histograms). In those cases in which the lines are not detected, the calculated line profile is plotted in red instead.

In general, the calculated line shapes agree well with the observed ones. However, there are profiles that exhibit complexities which our model is not able to reproduce, for example, the SO_2 emission in IK Tau. This is probably due to the simplicity of our approximated physical model which assumes smooth and spherically symmetric envelopes and does not take into consideration any deviations from that. In the case of the SiO $J = 3 - 2$ line, the observed profiles are mostly parabolic or triangular, although for some sources, such as RR Aql, the model produces flat-topped shapes. The assumption of a constant expansion velocity in our model could be playing a factor in the discrepency between the calculated and the observed line profile since as mentioned previously triangular line profiles probably indicate emission from accelerating regions close to the star. Another explanation could be related to the line opacity τ. In these cases, the line opacity is probably around one, with the modeled line having τ slightly below one and the observed line having τ slightly above

one. In any case, the overall agreement between calculated and observed line profiles is good.

The excitation and radiative transfer calculations give us information about the excitation and emission region of the molecules in the envelope. In regards to the emission region, the model indicates that most of the contribution to the line emission of the five molecules is coming from regions $10^{15} - 10^{16}$ cm from the star, i.e, most of the emission arises from intermediate and outer regions of the envelope, rather than from the inner regions. To evaluate the role of IR pumping to vibrationally excited states for SiO, CS, and SiS, we ran models excluding IR pumping. Our calculations indicate that in the absence of IR pumping, the emission is more compact than when IR pumping is included. The calculations also show that IR pumping has an effect on the intensities of the observed lines of SiO, CS and SiS. Neglecting IR pumping results in a systematic decrease in the integrated line intensities of $\sim 40\%$ for SiO $J = 3 - 2$, $\sim 50\%$ for CS $J = 3 - 2$, and $\sim 35\%$ for SiS $J = 8 - 7$.

In regards to the excitation of the rotational levels, the model indicates that the rotational levels of the five studied molecules are thermalized in the warm and dense inner layers of the envelopes. However, as the radial distance from the star increases and the gas density decreases, the rotational levels become suprathermally populated (with the ratio of the excitation temperature, T_{ex}, to the kinetic temperature, T_k, greater than unity, $T_{ex}/T_k > 1$) for SiS, CS, SO and SO_2 in the regions where most of the emission is coming from. For SiO, the population of rotational levels vary. Mostly, they are subthermally populated ($T_{ex}/T_k < 1$), however for a few envelopes (e.g., RR Aql, NV Aur, WX PSc), the levels are suprathermally populated . The behavior for SiO, CS, and SiS, is largely caused by IR pumping. In comparison, in C-rich CSEs, IR pumping causes the rotational transitions of these molecules to be all suprathermally excited (Massalkhi et al., 2019). We can conclude that IR pumping plays an important role in the excitation of the rotational emission of SiO, CS, and SiS whether in C-rich or O-rich envelopes.

9.7 Discussion

The fractional abundances relative to H_2, f_0, derived for SiO, CS, SiS, SO, and SO_2 in the 30 O-rich envelopes are presented in Table 9.4 and are shown as a function of the envelope density proxy, $\dot{M}/V_{\rm exp}$, in blue in Fig. 9.2. In the panels of SiO, CS, and SiS we also include (plotted in red) the fractional abundances derived in a sample of 25 C-rich envelopes by Massalkhi et al., (2019).

Table 9.4: Fractional abundances of SiO, CS, SiS, SO, and SO_2 derived

Name	Star Var.	$\dot{M}$ ($M_\odot$ yr^{-1})	V_{exp} (km s^{-1})	f_0(SiO)	f_0(CS)	f_0(SiS)	f_0(SO)	f_0(SO_2)
IK Tau	M	2.4×10^{-5}	17.5	3.1×10^{-7}	1.0×10^{-8}	1.0×10^{-7}	1.7×10^{-7}	3.2×10^{-7}
KU And	M	9.4×10^{-6}	19.5	6.2×10^{-7}	8.2×10^{-8}	9.9×10^{-7}	$< 9.8 \times 10^{-8}$	$< 1.8 \times 10^{-7}$
RX Boo	SRb	6.1×10^{-7}	7.5	1.7×10^{-6}	$< 1.0 \times 10^{-9}$	$< 1.2 \times 10^{-8}$	8.3×10^{-7}	3.5×10^{-7}
RT Vir	SRb	4.5×10^{-7}	7	4.5×10^{-5}	$< 3.0 \times 10^{-9}$	$< 2.5 \times 10^{-8}$	2.7×10^{-6}	1.2×10^{-6}
R Leo	M	1.0×10^{-7}	5	5.7×10^{-6}	1.2×10^{-8}	$< 3.0 \times 10^{-8}$	6.6×10^{-7}	$< 1.1 \times 10^{-7}$
WX Psc	M	4.0×10^{-5}	19	8.9×10^{-7}	2.7×10^{-8}	4.5×10^{-7}	2.5×10^{-7}	1.0×10^{-6}
GX Mon	M	4.8×10^{-6}	18	1.0×10^{-5}	8.9×10^{-8}	7.6×10^{-7}	2.5×10^{-6}	7.4×10^{-6}
NV Aur	M	2.5×10^{-5}	17.5	2.9×10^{-6}	2.8×10^{-8}	7.8×10^{-7}	8.5×10^{-7}	4.1×10^{-6}
V1111 Oph	M	2.7×10^{-6}	15.5	5.8×10^{-6}	7.7×10^{-8}	1.3×10^{-6}	2.0×10^{-6}	7.8×10^{-6}
RR Aql	M	8.6×10^{-7}	8.5	1.3×10^{-6}	$< 4.5 \times 10^{-9}$	$< 6.3 \times 10^{-8}$	1.7×10^{-6}	6.5×10^{-6}
R LMi	M	2.6×10^{-7}	5.5	2.6×10^{-5}	$< 1.0 \times 10^{-8}$	$< 1.5 \times 10^{-7}$	2.3×10^{-6}	9.8×10^{-7}
BX Cam	M	1.0×10^{-6}	17	5.5×10^{-6}	1.1×10^{-7}	1.9×10^{-6}	2.3×10^{-6}	5.8×10^{-6}
V1300 Aql	M	1.0×10^{-5}	15	1.5×10^{-6}	2.2×10^{-8}	9.3×10^{-7}	1.2×10^{-6}	4.5×10^{-6}
R Cas	M	9.5×10^{-7}	7.5	3.1×10^{-6}	1.2×10^{-8}	7.4×10^{-8}	1.2×10^{-6}	6.8×10^{-7}
IRC -30398	M	6.0×10^{-6}	14.5	2.9×10^{-7}	1.5×10^{-8}	6.5×10^{-8}	$< 6.8 \times 10^{-8}$	$< 6.0 \times 10^{-8}$
TX Cam	M	7.7×10^{-6}	17.5	1.4×10^{-6}	5.1×10^{-8}	3.9×10^{-7}	5.8×10^{-7}	6.3×10^{-7}
S CrB	M	2.7×10^{-7}	5	1.8×10^{-5}	$< 2.0 \times 10^{-8}$	$< 2.0 \times 10^{-7}$	4.2×10^{-6}	4.9×10^{-6}
IRC +60169	M	9.6×10^{-6}	15	1.5×10^{-7}	5.0×10^{-9}	2.6×10^{-8}	1.3×10^{-7}	3.5×10^{-7}
R Crt	SRb	1.0×10^{-6}	11	2.3×10^{-5}	$< 1.0 \times 10^{-8}$	$< 5.0 \times 10^{-8}$	2.3×10^{-6}	1.7×10^{-6}
R Hya	M	4.7×10^{-7}	5	3.3×10^{-6}	$< 2.0 \times 10^{-9}$	$< 2.0 \times 10^{-8}$	3.1×10^{-7}	$< 5.2 \times 10^{-8}$
o Ceti	M	2.0×10^{-7}	3	7.0×10^{-8}	1.4×10^{-9}	$< 4.0 \times 10^{-9}$	2.0×10^{-7}	4.0×10^{-8}
W Hya	SRa	4.2×10^{-7}	6	1.4×10^{-5}	5.0×10^{-9}	$< 2.0 \times 10^{-8}$	6.9×10^{-7}	$< 9.8 \times 10^{-8}$
T Cep	M	7.8×10^{-8}	4	4.4×10^{-6}	$< 9.0 \times 10^{-9}$	$< 1.0 \times 10^{-7}$	$< 2.2 \times 10^{-7}$	$< 3.0 \times 10^{-7}$
V1943 Sgr	SRb	1.0×10^{-6}	4.5	1.5×10^{-5}	$< 3.0 \times 10^{-9}$	$< 3.0 \times 10^{-8}$	4.1×10^{-7}	$< 1.5 \times 10^{-7}$
SW Vir	SRb	2.2×10^{-6}	7.5	2.0×10^{-6}	2.1×10^{-9}	$< 5.0 \times 10^{-9}$	1.6×10^{-7}	$< 3.9 \times 10^{-8}$
AFGL 292	...	1.3×10^{-7}	7	1.2×10^{-5}	$< 2.0 \times 10^{-8}$	$< 2.0 \times 10^{-7}$	1.2×10^{-6}	$< 3.6 \times 10^{-7}$
BK Vir	SRb	2.3×10^{-7}	4	7.0×10^{-6}	$< 5.0 \times 10^{-9}$	$< 3.0 \times 10^{-8}$	$< 1.0 \times 10^{-7}$	$< 1.2 \times 10^{-7}$
OH 26.5+0.6	M	1.0×10^{-6}	15.4	2.2×10^{-6}	3.1×10^{-8}	5.2×10^{-7}	6.0×10^{-6}	2.1×10^{-6}
Ep Aqr	SRb	1.7×10^{-8}	1	-	6.0×10^{-9}	$< 6.0 \times 10^{-9}$	5.4×10^{-6}	1.9×10^{-6}
		5.0×10^{-7}	9.2	3.6×10^{-6}	-	-	-	-
X Her	SRb	4.3×10^{-8}	2.2	-	$< 4.2 \times 10^{-9}$	$< 3.6 \times 10^{-8}$	2.5×10^{-6}	$< 2.5 \times 10^{-7}$
		1.6×10^{-7}	6.5	1.4×10^{-5}	-	-	-	-

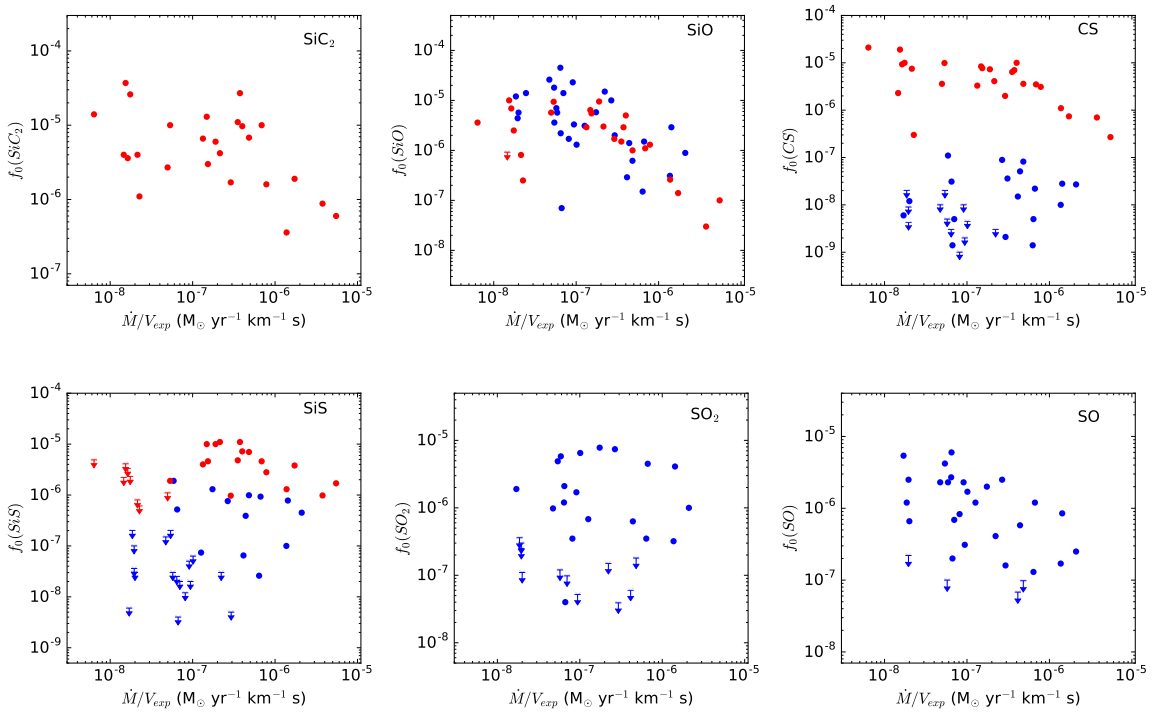

Figure 9.2: Results for the radiative transfer and excitation analysis toward the sample of AGB stars. Fractional abundance f_0 derived for SiC_2 obtained by Massalkhi et al., (2018) for C-rich AGB stars (*upper left*), fractional abundance for SiO (*upper middle*), fractional abundance for CS (*upper right*), and fractional abundance for SiS (*lower left*) as a function of density measure $\dot{M}/V_{\rm exp}$ for oxygen stars (blue) and carbon stars (red) (Massalkhi et al. 2019). Fractional abundance for SO (*lower middle*) and for SO_2 (*lower right*) in O-rich envelopes as a function of density measure $\dot{M}/V_{\rm exp}$. Downward arrows represent upper limits to f_0.

9.7.1 Fractional abundances derived

9.7.1.1 SiO

The SiO fractional abundances f_0(SiO) derived in this study for the 30 O-rich AGB stars are presented in blue in the upper middle panel of Fig. 9.2. We overplot in red the SiO abundances derived by Massalkhi et al., (2019) for 25 C-rich AGB stars.

One of the first comprehensive studies of molecular abundances in circumstellar envelopes was done by González Delgado et al., (2003), who focused on SiO in a large sample of about 40 O-rich CSEs. They used multiline data to determine the size of the emitting region and the SiO abundance simultaneously. We share 21 objects with these authors. In general, our derived SiO abundances are very similar to theirs.

From Fig. 9.2, we notice from the SiO fractional abundances we are not able to distinguish the chemical type, either O-rich (in blue) or C-rich (in red). Schöier et al., (2006) found the same result when comparing the distribution of their derived SiO abundances in C-rich stars to the distribution of SiO abundances in M-type stars derived by González Delgado et al., (2003). That is, observations indicate that the SiO abundance does not depend on the C/O ratio at the stellar surface. The mean fractional abundance of SiO we obtain is similar in both types of CSEs, with log f_0(SiO) = -5.5 $\pm$ 0.7 in O-rich CSEs and log f_0(SiO) = -5.8 $\pm$ 0.6 in C-rich CSEs**.

The fact that the SiO abundance injected into the expanding wind is not sensitive to the C/O ratio is in line with theoretical expectations. Thermochemical equilibrium calculations predict that SiO maintains a uniform and high fractional abundance of several 10^{-5} from the photosphere out to 10 $R_\star$ in O-rich CSEs, while in C-rich CSEs the predicted fractional abundance from 5 $R_\star$ is also on the order of 10^{-5}. The main difference occurs in the innermost region, from the photosphere to around 5 $R_\star$, where SiO has a low abundance in C-rich conditions while it maintains a high abundance in O-rich CSEs (Agúndez et al., 2006, 2020). In a scenario of chemical equilibrium, it seems that the low SiO abundance within 5 $R_\star$ in C-rich CSEs does not have an influence on the final SiO abundance that is injected into the expanding wind, and that chemical equilibrium holds for SiO in the high abundance region located beyond 5 $R_\star$. The low SiO abundance predicted by chemical equilibrium in the innermost envelope has been inferred by modeling multiwavelength observations of the carbon star IRC +10216 by Schöier et al., (2006). The nonequilibrium scenario of shocks induced by the stellar pulsation of Cherchneff, (2006) also predicts a low sensitivity of the

**We consider upper limits as abundances to compute mean abundances and standard deviations. The same approach is adopted for the rest of molecules: CS, SiS, SO and SO_2.

SiO abundance on the photospheric C/O ratio. In the model of Cherchneff, (2006), for C/O < 1 shocks have a very limited effect on the SiO fractional abundance in the inner part of the wind as it stays around $\sim 10^{-5}$ from the photosphere out to 5 $R_\star$. For C/O > 1, the authors find that the low chemical equilibrium abundance of $\sim 10^{-8}$ is enhanced rapidly to values around 10^{-5} in the 1-5 $R_\star$ region. Therefore, the SiO abundances calculated at 5 $R_\star$, which are supposed to be the ones injected into the expanding wind, are of the same order in O-rich and C-rich stars. In summary, theoretical studies show that the SiO abundance has no apparent dependence on the C/O ratio in the outer wind which is in agreement with the findings from our observational study. The different behavior of the SiO abundance in the inner wind as predicted by theoretical studies probably explains why strong SiO maser emission is detected toward O-rich stars and not toward carbon stars (e.g., Cotton et al. 2004; Pardo et al. 2004). In view of the high SiO abundance observed in C-rich stars, this could suggest that the SiO molecules are formed further out in the wind in C-rich envelopes where the physical conditions are not likely to allow the pumping by IR photons, and thus the inversion of SiO level populations.

The fractional abundance of SiO in the O-rich sample varies substantially from as low as 7.0×10^{-8} up to 4.5×10^{-5}. This variation in the SiO abundance as illustrated in Fig. 9.2, whether C-rich or O-rich, shows a clear trend in which SiO becomes less abundant as the density in the wind, $\dot{M}/V_{\rm exp}$, increases. Schöier et al., (2006) and Massalkhi et al., (2019) presented analysis of circumstellar SiO abundances for carbon stars, and González Delgado et al., (2003) for M-type stars and likewise they find a similar behavior of a strong anticorrelation between the abundance and the wind density which was interpreted as an effect of increased adsorption of SiO onto dust grains at high densities. Here, we confirm the results found for O-rich stars by González Delgado et al., (2003). We found a similar trend when we investigated SiC_2 in a sample of 25 carbon-rich AGB stars (see upper left panel in Fig. 9.2 for comparison), which was interpreted as that SiC_2 is being efficiently incorporated into dust grains and playing an important role in the formation of silicon carbide dust in C-rich envelopes (Massalkhi et al., 2018). Adsorption of SiO onto dust grains in O-rich envelopes is predicted theoretically by chemical kinetics models (Van de Sande et al., 2019). We note that the median fractional abundance of SiO of the Mira-type variables, 2.5×10^{-6}, is lower by a factor of 6 with respect to the median value of the semiregular variables, 1.5×10^{-5}, which may be related to the mass loss rate rather than the stellar variability type. González Delgado et al., (2003) found a similar result where the high mass-loss rate Miras in their sample have a median abundance that is more than six times lower than that of the irregular and semiregular variables.

Silicates are known to be one of the most important types of dust in oxygen-rich envelopes and SiO has long been discussed to be the gas-phase precursor of silicate dust, mainly because of its high abundance in O-rich envelopes. The trend that we see here between the fractional abundance and the wind density supports this hypothesis.

9.7.1.2 CS

The fractional abundances derived for CS in the O-rich envelopes are shown in blue as a function of $\dot{M}/V_{\rm exp}$ in the upper right panel of Fig. 9.2. We also show in red the CS fractional abundances derived for the 25 C-rich AGB stars studied in Massalkhi et al., (2019).

Bujarrabal et al., (1994) searched for CS $J = 3-2$ and $J = 5-4$ transitions in a large sample of evolved stars. Their sample contains 17 O-rich stars, 10 of which are in our sample. These authors derived abundances using a simple analytical expression based on the integrated intensities of the observed lines and assumes a constant fractional abundance inside a given radius. In general, their CS abundances are higher than ours with varying degrees, for example, ranging from a factor of two for some sources, like V1300 Aql, to one order of magnitude for other sources, like IK Tau, to a highest factor of 47 for RX Boo, where our value is an upper limit. These authors remark that their approach holds for optically thin lines and estimated only a lower limit if the line was optically thick. Danilovich et al., (2018) surveyed a diverse sample of AGB stars. They detected CS in only the highest mass loss rate O-rich stars and derived CS abundances in agreement with ours for some sources, such as GX Mon and V1300 Aql, while for other sources their derived values were approximately an order of magnitude higher than ours, such as IK Tau and RR Aql, the latter being an upper limit in both studies.

Comparing the values of f_0(CS) in oxygen-rich and carbon-rich envelopes in Fig. 9.2, the derived abundances show substantial variations between the two chemical types where the mean fractional abundance for O-rich CSEs is $\log f_0$(CS) = -8.0 $\pm$ 0.6, more than two orders of magnitude lower than for C-rich CSEs, $\log f_0$(CS) = -5.4 $\pm$ 0.5. It is clear that the formation of CS is dependent on the photospheric C/O ratio of the star. We also notice that CS is mostly detected in O-rich CSEs with high mass-loss rates, while in C-rich CSEs, CS is detected in all the sources of the sample, regardless of the mass loss rate. Carbon monosulfide forms more readily in C-rich environments since there is available carbon, that is, not trapped by CO, to form C-bearing molecules. On the other hand, the formation of CS in O-rich CSEs is more surprising as all the available carbon is expected to be locked up in CO.

Chemical equilibrium calculations predict negligible abundances for CS in O-rich CSEs, more than 3-4 orders of magnitude below the observed values (Agúndez et al., 2020). It is clear that some nonequilibrium process is enhancing the abundance of CS in O-rich envelopes. A possible explanation for the synthesis of this molecule could be related to photochemistry in a clumpy CSE, as investigated by Agúndez et al., (2010). In this scenario, interstellar UV photons penetrate into the inner regions of the envelope, break the CO bond and induce changes in the chemical composition which ultimately allow for the formation of CS and other C-bearing molecules. Their calculations predict abundances of $\sim 10^{-9} - 10^{-8}$ for mass-loss rates in the $10^{-7} - 10^{-5}$ $M_{\odot}$ yr^{-1}, in agreement with the abundances we find here. Similar models by Van de Sande et al. (2018) examined the effects that clumping and porosity have on the chemistry in the AGB outflow and found slightly higher peak abundances of $\sim 10^{-7}$. However, in their recently published corrigendum these authors no longer find this peak, instead the fractional abundance of CS drop to $\sim 10^{-10}$ (Van de Sande et al., 2020). Another explanation for the formation of CS in O-rich environments could be related to the variable nature of AGB stars. Periodic shock waves caused by stellar pulsations propagate through the photosphere and alter the gas chemistry where the collisional destruction of CO in the shocks could release free atomic carbon and trigger the formation of CS in O-rich environments (Cherchneff, 2006; Duari et al., 1999; Gobrecht et al., 2016). The shock-induced chemistry model of Cherchneff, (2006) predicts that CS reaches abundances of a few times 10^{-6} in envelopes with C/O < 1, that is to say, significantly above the mean abundance derived here from observations.

To investigate the reason for the nondetection of CS in the low mass loss rate objects, we consider the variability type (Mira variable and semiregular variable, see Table 9.4) of the O-rich stars. The type of variability is generally attributed to the pulsation of the star and therefore could influence the shock conditions and provide an explanation of the abundance differentiation between high- and low-mass loss rate O-rich stars. However, we see no indication of a dependence between the abundance of CS and the variability type. On one hand, the nondetection of CS in these envelopes could be due to a low fractional abundance of the molecule, on the other hand, it could be due to a lack of sensitivity.

The CS fractional abundance in the O-rich sample varies by about two orders of magnitude, ranging from as low as 1×10^{-9} to as high as 1.1×10^{-7}, yet unlike the case of SiO, this variation shows no apparent trend that the CS abundance decreases as the density in the wind ($\dot{M}/V_{\rm exp}$) increases for O-rich envelopes. Such a trend is however evident for carbon-rich envelopes. This suggests that CS molecules are more likely to adsorb onto dust grains in C-rich CSEs than in O-rich ones. While CS is thought to play a role in the formation

of MgS dust in C-rich envelopes (Massalkhi et al., 2019), in the case of O-rich envelopes CS does not seem to be affected by adsorption onto dust grains and to be playing a role in the formation of dust.

9.7.1.3 SiS

In the lower left panel of Fig. 9.2 we show as a function of $\dot{M}/V_{\rm exp}$ the fractional abundances of SiS derived in the 30 O-rich envelopes studied here (in blue) and in the 25 C-rich envelopes studied by Massalkhi et al., (2019) (in red).

Schöier et al., (2007) reported on the detection of SiS line emission in 8 oxygen-rich envelopes, all of which are included in our sample. They performed radiative transfer calculations to derive abundances adopting, similarly to us, an abundance distribution based on the scaling law established by González Delgado et al., (2003) for SiO in M-type stars. Our SiS abundances are in good agreement with theirs for all of the sources.

By looking to the fractional abundances f_0(SiS) derived in the O-rich sample (see Table 9.4) we notice that they vary considerably among different sources, between $< 4.0 \times 10^{-9}$ and 1.9×10^{-6}. The mean fractional abundance in the O-rich sample is $\log f_0$(SiS) = -7.0 $\pm$ 0.7, while in C-rich AGB stars is $\log f_0$(SiS) = -5.5 $\pm$ 0.4, that is, an order of magnitude higher than in O-rich envelopes. Similarly, in their study of SiS in a small sample of oxygen- and carbon-rich envelopes, Schöier et al., (2007) found SiS abundances in carbon-rich envelopes about an order of magnitude higher than in oxygen-rich envelopes. This indicates that SiS has a marked chemical differentiation based on the photospheric C/O ratio, being more preferentially formed in C-rich environments than in O-rich ones.

According to chemical equilibrium, in C-rich envelopes SiS reaches a high fractional abundance of about 10^{-5} from 2 $R_\star$, while in O-rich envelopes the abundance of SiS is low in the very inner regions but rises to values slightly below 10^{-5} from 2 $R_\star$ beyond 5 $R_\star$ (Agúndez et al., 2020). That is, the differentiation between C-rich and O-rich is restricted to the very inner regions, but beyond 5 $R_\star$ SiS is predicted to reach high abundances, on the order of 10^{-5}, in both C- and O-rich envelopes. The low SiS abundances observed here in some O-rich envelopes are thus not expected according to chemical equilibrium. On the other hand, nonequilibrium chemical models based on shocks induced by the stellar pulsation predict a dependence of the SiS abundance on the C/O ratio, with abundances on the order of 10^{-5} and 10^{-8} at 5 $R_\star$ in the inner regions of C- and O-rich, respectively, envelopes (Cherchneff, 2006). The SiS abundances derived from observations here agree with the predictions of these models in terms of differentiation based on the C/O ratio, although

there is a discrepancy because some of our observed abundances are significantly above those predicted by the model. For example, Cherchneff, (2006) predicts an SiS fractional abundance for TX Cam of $\sim 10^{-8}$ at 5 $R_\star$, while for this source we derive an abundance of 3.9×10^{-7}. Therefore, chemical equilibrium overestimates the SiS abundances in O-rich envelopes while nonequilibrium models underestimate them.

Strikingly, we noticed that SiS is not detected in envelopes with low mass loss rates $< 10^{-6}$, while it is detected in all sources above this threshold. This fact has been reported by some previous observational studies (Bujarrabal et al., 1994; Danilovich et al., 2015, 2018; Massalkhi et al., 2019). Massalkhi et al., (2019) surveyed a sample of 25 C-rich AGB stars in SiS $J = 8-7$ and $J = 7-6$ emission and did not detect emission below the same threshold as well. They speculated that the nondetection of SiS in the low mass-loss rate C-rich envelopes could be either caused by a lack of the constituent elements, which would be trapped in other S- and Si-bearing molecules like SiO, SiC_2, and CS, or could be due to sensitivity which might be the case here as well. Danilovich et al., (2019) discussed based on previous studies that SiS does not form readily in low-mass loss rate semi-regular variables, where the molecule otherwise reaches higher abundunces in Mira variable type CSEs. However, these authors detect faint SiS $J = 19-18$ emission toward the low mass-loss rate semiregular variable, R Dor, using ALMA and derive an abundance of 1.5×10^{-8} which indicates that the nondetection of SiS in low mass loss rate semiregular variables could be due to low sensitivity. In this study, we do not detect SiS in low-mass loss rate objects of both, semiregular and Mira variables, that is to say, we do not see a dependence of the SiS fractional abundance on the variability type, similar to the case of CS.

While SiS shows a tentative trend of a decreasing abundance with increasing envelope density for C-rich CSEs (Massalkhi et al., 2019), which was interpreted in terms of adsorption onto dust grains, here we do not see any similar trend, implying that SiS is probably not an important gas-phase precursor of dust in O-rich CSEs. However, chemical kinetics models by Van de Sande et al., (2019) predict adsorption of SiS onto dust grains in O-rich outflows.

9.7.1.4 SO

The resulting SO fractional abundances are shown as a function of $\dot{M}/V_{\rm exp}$ in the lower middle panel of Fig. 9.2. Systematic studies of the abundance of SO on large samples of AGB stars are scarce. In fact, for some of the sources in our sample, SO abundances are reported for the first time. One of those studies was made by Bujarrabal et al., (1994), who surveyed a large sample of evolved stars in several molecular lines, including SO 6_5-5_4.

Their sample contains 18 O-rich objects, 11 of which are in our sample. For some sources, our derived abundances are higher than theirs, and for other sources, the opposite is found. But in general the difference is within a factor of a few. The modeling performed by these authors is based on a somewhat simple method as mentioned previously, in which an analytical expression is used to derive the abundance of the molecules. A more complex abundance derivation based on radiative transfer modeling was done by Danilovich et al., (2016) using high- and low-E_u lines of SO (and SO_2; see below) in a small sample of five M-type AGB stars, four of which are in our sample. The authors find that the spatial distribution of SO differs between the low mass loss rate objects (R Dor, and W Hya) and the high mass loss rate ones (IK Tau, R Cas, and TX Cam), where the former were best reproduced by a Gaussian disribution whereas the latter by a shell-like one. For the four sources we have in common, their derived abundances are higher than ours by a factor of a few. In their recent study of two O-rich envelopes using ALMA, Danilovich et al., (2020) confirmed their previous findings in that the SO abundance distribution in IK Tau is shell-like with a constant inner abundance of 4.1×10^{-7}, not very different from the value derived in this study (1.7×10^{-7}), that increases to 2.2×10^{-6} at 5×10^{15} cm followed by a decline at $e-$folding radius 1.3×10^{16} cm. Velilla Prieto et al., (2017) also surveyed IK Tau and derived f_0(SO) $\geq 8 \times 10^{-6}$, which is significantly higher than the value derived here (1.7×10^{-7}). These authors discuss that their derived SO abundance for this source may be overestimated since it is higher than previous observational studies and higher than abundances predicted by chemical equilibrium models, and that the reason behind this discrepancy is the uncertainty in the adopted SO emitting region.

The values of f_0(SO) range between $< 6.8 \times 10^{-8}$ and 6×10^{-6} and have a mean fractional abundance of $\log f_0$(SO) = -6.1 $\pm$ 0.6. Chemical equilibrium calculations predict a peak SO abundance in the 1-10 $R_\star$ region of $\sim 10^{-7}$ (Agúndez et al., 2020), while nonequilibrium chemical models considering shocks induced by the pulsation of the star predict similar abundances at 5 $R_\star$ (Cherchneff, 2006). Therefore, on average, our observed SO abundances are higher than theoretical predictions of the inner wind. For SO, we see no dependence of the fractional abundance on the stellar variability type.

The distribution of the fractional abundances derived in the O-rich sample show hints of decreasing SO abundance with increasing density. This is however tentative as it is not as evident as in the case of SiO. Danilovich et al., (2016) found a similar trend of SO being less abundant with wind density, although this result was based on a reduced sample of only 3 objects (TX Cam, IK Tau, and R Cas) with a limited range of mass loss rates. If the tentative decrease in the abundance of SO with increasing envelope density that we see here

is interpreted in terms of adsorption onto dust grains, SO could emerge as a candidate to gas-phase precursor of dust. To date, no sulfur-containing condensate has been identified in the spectra of O-rich envelopes, although CaS and FeS are expected to be important solid carriers of sulfur in these environments (Agúndez et al., 2020; Lodders et al., 1999).

9.7.1.5 SO_2

The fractional abundances derived for SO_2 are shown as a function of $\dot{M}/V_{\rm exp}$ in the lower right panel of Fig. 9.2. For some of the sources in our sample, SO_2 abundances are reported for the first time.

Infrared observations, in particular, the ISO/SWS detection of the 7.3 µm ν_3 band in a few AGB stars by Yamamura et al., (1999) and observations of high energy rotational lines by, e.g., Danilovich et al., (2016) and Velilla Prieto et al., (2017) indicate that SO_2 is formed in the inner layers of the CSE. Omont et al., (1993) surveyed a diverse sample of evolved stars in sulfur-bearing molecules and derived SO_2 abundances for 7 of the objects in our sample. For some sources, the abundances derived by these authors are similar to the values derived in this work. While for other sources, the derived abundances are different, like RX Boo, their value is 50 times higher than ours. These authors used a relatively simple method for estimating the molecular abundances, which is based on an analytical expression in which they assumed a constant excitation temperature for simplicity. A study was conducted by Danilovich et al., (2016) to investigate the SO_2 rotational lines observed with Herschel/HIFI in addition to further archival data toward a small sample M-type AGB stars. They performed radiative transfer modeling and derived SO_2 abundance toward three of the objects that are in our sample, IK Tau, W Hya, and R Cas. They find SO_2 fractional abundance in IK Tau similar to ours assuming a Gaussian distribution. They note that their SO_2 model for IK Tau is uncertain due to the difficulty of determining an abundance distribution. In fact, in their recent study using ALMA, these authors suspect that the SO_2 abundance in IK Tau is consistent with a shell-like distribution and not a Gaussian distribution (Danilovich et al., 2020). For W Hya and R Cas, their derived abundances are higher than ours, by a factor of 50 (with ours being an upper limit) and an order of magnitude, respectively. They also note that their SO_2 model for R Cas is very uncertain due to the fact that they had only two detected lines toward that source. The mean fractional abundance of SO_2 in the 30 O-rich envelopes studied here is $\log f_0(SO_2)$ = -6.2 $\pm$ 0.7, that is, very similar to that of SO.

Sulfur dioxide is predicted to have low abundances ($< 10^{-10}$), well below the observed values, in the inner regions of O-rich envelopes according to chemical equilibrium (Agúndez

et al., 2020). There must be a nonequilibrium process that enhances the formation of SO_2 in the inner envelope. The shock-induced chemistry scenario of Cherchneff, (2006) also predicts very low abundances (10^{-13}-10^{-12}) for SO_2 in the inner winds of O-rich AGB stars. Clearly, observations and theory maintain a severe discrepancy with respect to the abundance of SO_2 in the inner envelope of M-type stars. Similar to SO, we see no dependence of the SO_2 fractional abundance on the stellar variability type.

In their study on sulfur molecules in M-type AGB stars, Danilovich et al., (2016) reported that SO and SO_2 are the main reservoirs of sulfur in the inner regions of the CSE of W Hya and R Cas, with more uncertainties for the latter. For W Hya, they derived a combined fractional abundance of SO and SO_2 of $\sim 10^{-5}$ within the inner layers of the wind, thus accounting for most of the sulfur. Here in this work, the combined fractional abundance of CS, SiS, SO, and SO_2 in the intermediate regions of the W Hya envelope is just $\sim 8 \times 10^{-7}$, well below the elemental abundance of S. This could point to depletion of sulfur through dust condensation in this object. A large fraction of the sulfur could also be trapped as gaseous H_2S, which is abundant in O-rich CSEs (Danilovich et al., 2017). In any case, for SO_2 we do not see any clear trend of decreasing $f_0(SO_2)$ with increasing envelope density that could point to this molecule as a gas-phase precursor of dust in O-rich envelopes.

9.7.2 Correlations between abundances of different molecules

In Fig. 9.3 we plot the derived fractional abundance of CS against that of SiS (upper panel) and the fractional abundance of SO against that of SO_2 (lower panel). We find that SiS is systematically more abundant than CS in the 30 O-rich envelopes studied, as indicated by the fact that all sources lie in the region of SiS/CS > 1, apart from EP Aqr that falls on the dashed line representing equal amounts of SiS and CS. Similarly, Danilovich et al., (2018) determined the CS and SiS abundances in a sample of AGB stars, and found SiS to be systematically more abundant than CS in their O-rich sample. Therefore, SiS seems to be a more abundant gas-phase reservoir of sulfur than CS in oxygen star envelopes. The behavior is thus different to that of C-rich envelopes, where CS and SiS have comparable abundances (Massalkhi et al., 2019). Moving on to the lower panel in Fig. 9.3, the comparison of SO and SO_2 shows that in some sources SO is more abundant, like in R LMi and BK Vir, while in other sources SO_2 is more abundant, like in NV Aur and V1111 Oph. In general, the data points fall along the line defined by $f_0(SO) = f_0(SO_2)$ and there is no clear preference for either the SO/$SO_2 > 1$ or the SO/$SO_2 < 1$ sides. By looking to those sources where both SO and SO_2 are detected, it seems that in oxygen-rich envelopes, SO and SO_2 have abundances of the same order, carrying similar amounts of sulfur.

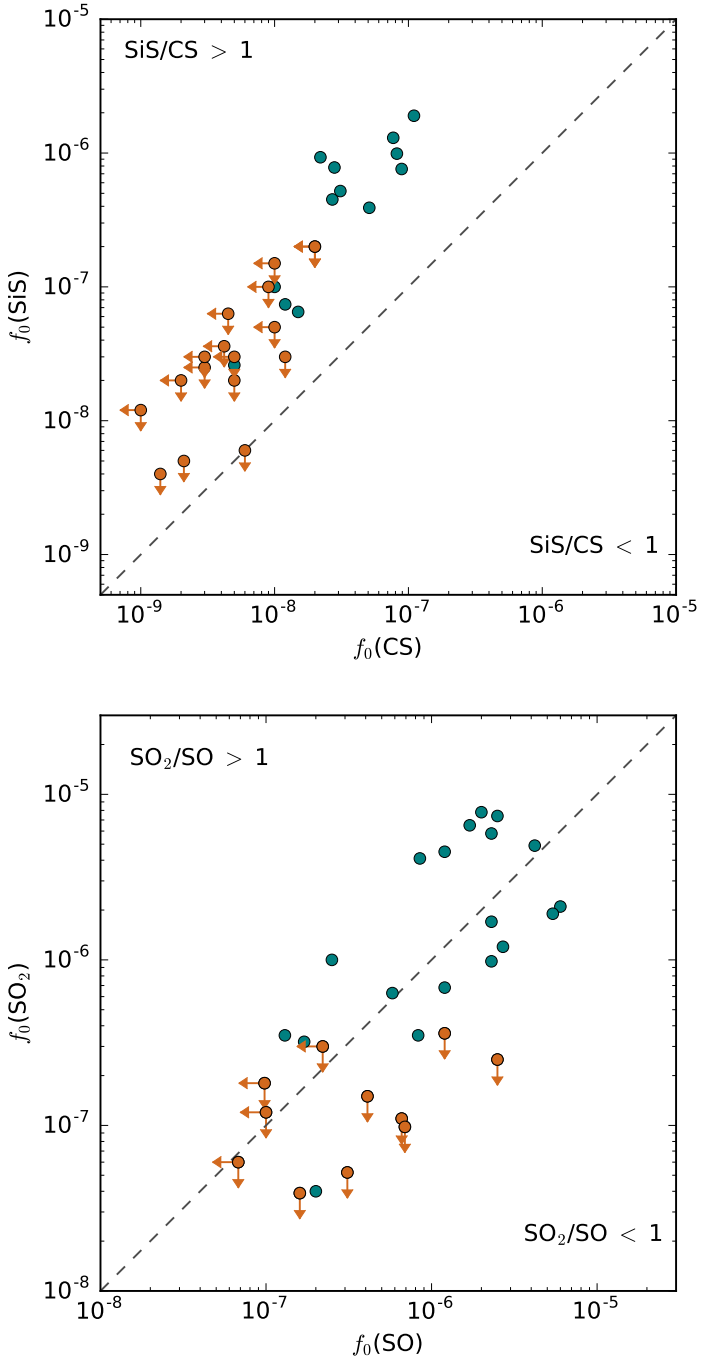

Figure 9.3: Comparison of abundances between different pairs of molecules. The derived fractional abundances relative to H_2 of CS vs SiS (*upper panel*) and SO vs. SO_2 (*lower panel*). Those sources with nondetections are denoted with arrows. The diagonal dashed lines indicate where the abundances of the two molecules become equal.The orange circles indicate fractional abundances with an upper limit.

Regardless of which pair of molecules from those shown in Fig. 9.3, in both cases there is a trend in which the higher the abundance of one molecule the more abundant the other is, ie., the abundances of SO and SO_2, and of SiS and CS, seem to scale with each other which suggests a chemical connection between the members of each couple of molecules. Danilovich et al., (2018) found this type of correlation for CS and SiS in a sample including C-, M-, and S-type stars, although in that study the trend is considered tentative because of the small number of sources included. Massalkhi et al., (2019) also found a similar correlation between the three molecules CS, SiO, and SiS in their large sample of C-rich CSEs. We remark, however, that the trends in Fig. 9.3 become less robust given the upper limits on some of the fractional abundances in the sources where these molecules are not detected.

9.8 Conclusion

In this study we observed SiO, CS, SiS, SO, and SO_2 using the IRAM 30m telescope in a statistically meaningful sample of 30 O-rich AGB stars covering a wide range of mass-loss rates and circumstellar properties. We performed an extensive radiative transfer and excitation analysis based on the LVG method to derive the fractional abundance of these molecules in the circumstellar envelopes.

We found that the derived circumstellar abundances of SiS and CS have a clear dependence on the photospheric C/O ratio of the star, while SiO is not sensitive to it. Moreover, the fractional abundance of CS and SiS in carbon-rich CSEs are about two and one orders of magnitude, respectively, higher than in oxygen-rich envelopes, whereas the fractional abundance of SiO in both chemical types is of the same order of magnitude. Chemical equilibrium correctly predicts that SiO is abundant and that SiS and SO can reach high abundances in O-rich stars. However, the observed abundances of CS and SO_2 are higher than predicted by several orders of magnitude. Nonequilibrium chemical models succeed to different extents in reproducing the observed abundances. A scenario of photochemistry in a clumpy envelope accounts for the abundance enhancement of CS. On the other hand, a scenario of shocks induced by the stellar pulsation results in abundances that are 1-3 orders of magnitude too high for CS, somewhat lower than observed for SiS and SO, and well below the observed values for SO_2.

We find that the abundances of SiS and CS, on one hand, and SO and SO_2, on the other, are positively correlated which suggests a chemical connection between the members of each couple. Moreover, as already found for C-rich envelopes, we find a clear trend

of decreasing SiO abundance with increasing envelope density in O-rich envelopes, which points to adsorption of SiO onto dust grains. A similar trend is observed for SO, although not as clear as for SiO. Therefore, SiO and SO are likely candidates to act as gas-phase precursors of dust in O-rich envelopes. In the cases of CS, SiS, and SO_2, abundances span over 2-3 orders of magnitude with no obvious correlation with the envelope density. These three molecules are thus less attractive candidates to be precursors of dust.

Table 9.5: Observed line parameters.

Line		ν_{calc} (MHz)	ν_{obs} (MHz)	V_e (km s^{-1})	$\int T_{\rm mb}\, dv$ (K km s^{-1})
			IK Tau		
SiO	$3-2$	130268.665	130268.7(1)	17.7(2)	55.6(55)
SiS	$8-7$	145227.054	145226.9(5)	19.5(5)	6.1(6)
CS	$3-2$	146969.025	146969.4(5)	17.3(8)	3.11(3)
SO	3_3-2_2	129138.983	129139.5(5)	16.8(6)	2.29(2)
SO_2	$8_{2-6}-8_{1-7}$	134004.811	134005.3(5)	16.6(5)	3.80(4)
SO_2	$5_{1-5}-4_{0,4}$	135696.016	135696.7(5)	16.8(8)	5.20(5)
SO_2	$4_{2-2}-4_{1,3}$	146605.519	146606.3(6)	16.6(6)	2.19(2)
SO_2	$2_{2-0}-2_{1,1}$	151378.662	151379.4(5)	17.0(6)	1.21(1)
			KU And		
SiO	$3-2$	130268.665	130268.3(1)	20.7(1)	5.62(6)
SiS	$8-7$	145227.054	145227.1(1)	19.0(1)	1.88(2)
CS	$3-2$	146969.025	146968.5(1)	19.4(1)	1.4(4)
SO	3_3-2_2	129138.983	-	-	-
SO_2	$8_{2-6}-8_{1-7}$	134004.811	-	-	-
SO_2	$5_{1-5}-4_{0,4}$	135696.016	-	-	-
SO_2	$4_{2-2}-4_{1,3}$	146605.519			
SO_2	$2_{2-0}-2_{1,1}$	151378.662	-	-	-
			RX Boo		
SiO	$3-2$	130268.665	130268.7(1)	7.8(1)	26.0(26)
SiS	$8-7$	145227.054	-	-	-
CS	$3-2$	146969.025	-	-	-
SO	3_3-2_2	129138.983	129138.9(1)	7.8(1)	0.88(1)
SO_2	$8_{2-6}-8_{1-7}$	134004.811	134005.0(5)	7.9(5)	0.83(8)
SO_2	$5_{1-5}-4_{0,4}$	135696.016	135695.9(1)	6.5(1)	0.37(4)

Table 9.5: Continued.

Line		ν_{calc} (MHz)	ν_{obs} (MHz)	V_e (km s^{-1})	$\int T_A^* dv$ (K km s^{-1})
SO_2	$4_{2-2} - 4_{1,3}$	146605.519	146606.4(5)	6.3(4)	0.23(5)[a]
SO_2	$2_{2-0} - 2_{1,1}$	151378.662	151377.8(10)	9.0(10)	0.12(2)[a]
			RT Vir		
SiO	$3 - 2$	130268.665	130268.7(1)	7.1(1)	6.56(6)
SiS	$8 - 7$	145227.054	-	-	-
CS	$3 - 2$	146969.025	-	-	-
SO	$3_3 - 2_2$	129138.983	129139.2(1)	6.9(1)	0.64(1)
SO_2	$8_{2-6} - 8_{1-7}$	134004.811	134004.9(5)	6.0(4)	0.67(3)
SO_2	$5_{1-5} - 4_{0,4}$	135696.016	135696.0(5)	5.8(6)	0.35(3)
SO_2	$4_{2-2} - 4_{1,3}$	146605.519	146605.5(5)	5.5(6)	0.24(2)
SO_2	$2_{2-0} - 2_{1,1}$	151378.662	151379.3(10)	4.5(10)	0.09(2)[a]
			R Leo		
SiO	$3 - 2$	130268.665	130268.6(5)	5.1(5)	15.09(15)
SiS	$8 - 7$	145227.054	-	-	-
CS	$3 - 2$	146969.025	146968.5(5)	4.8(5)	0.10(1)[a]
SO	$3_3 - 2_2$	129138.983	129138.9(1)	4.5(3)	0.27(3)
SO_2	$8_{2-6} - 8_{1-7}$	134004.811	-	-	-
SO_2	$5_{1-5} - 4_{0,4}$	135696.016	-	-	-
SO_2	$4_{2-2} - 4_{1,3}$	146605.519	-	-	-
SO_2	$2_{2-0} - 2_{1,1}$	151378.662	-	-	-
			WX Psc		
SiO	$3 - 2$	130268.665	130268.7(1)	18.8(4)	29.0(30)
SiS	$8 - 7$	145227.054	145227.0(1)	19.4(4)	26.2(26)
CS	$3 - 2$	146969.025	146969.0(1)	17.8(6)	2.41(2)
SO	$3_3 - 2_2$	129138.983	129139.2(1)	18.5(3)	1.11(1)
SO_2	$8_{2-6} - 8_{1-7}$	134004.811	134005.2(5)	17.7(5)	1.7(2)
SO_2	$5_{1-5} - 4_{0,4}$	135696.016	135696.2(1)	18.3(4)	6.81(7)
SO_2	$4_{2-2} - 4_{1,3}$	146605.519	146605.8(1)	18.4(2)	2.02(2)
SO_2	$2_{2-0} - 2_{1,1}$	151378.662	151378.8(1)	18.0(6)	1.40(1)
			GX Mon		
SiO	$3 - 2$	130268.665	130268.6(1)	18.4(1)	25.0(25)
SiS	$8 - 7$	145227.054	145226.8(4)	18.2(6)	2.10(20)

Table 9.5: Continued.

Line		ν_{calc} (MHz)	ν_{obs} (MHz)	V_e (km s^{-1})	$\int T_A^* dv$ (K km s^{-1})
CS	$3-2$	146969.025	146968.9(5)	17.4(8)	1.51(1)
SO	3_3-2_2	129138.983	129138.9(1)	17.6(6)	1.39(1)
SO_2	$8_{2-6}-8_{1-7}$	134004.811	134005.2(5)	16.6(6)	1.2(1)
SO_2	$5_{1-5}-4_{0,4}$	135696.016	135696.2(5)	18.1(5)	5.79(8)
SO_2	$4_{2-2}-4_{1,3}$	146605.519	146605.4(5)	18.5(6)	1.54(1)
SO_2	$2_{2-0}-2_{1,1}$	151378.662	151379.1(5)	18.0(4)	1.28(1)
		NV Aur			
SiO	$3-2$	130268.665	130268.5(1)	17.7(1)	13.7(14)
SiS	$8-7$	145227.054	145226.9(5)	17.1(4)	2.98(3)
CS	$3-2$	146969.025	146968.5(5)	16.3(4)	0.77(8)
SO	3_3-2_2	129138.983	129138.7(5)	16.4(4)	0.67(7)
SO_2	$8_{2-6}-8_{1-7}$	134004.811	134004.9(5)	17.0(4)	1.4(1)
SO_2	$5_{1-5}-4_{0,4}$	135696.016	135696.1(1)	17.1(1)	3.57(3)
SO_2	$4_{2-2}-4_{1,3}$	146605.519	146605.6(5)	17.0(8)	1.14(1)
SO_2	$2_{2-0}-2_{1,1}$	151378.662	151379.0(6)	17.3(5)	0.76(7)
		V1111 Oph			
SiO	$3-2$	130268.665	130268.6(6)	15.7(1)	21.0(20)
SiS	$8-7$	145227.054	145227.2(5)	14.2(7)	2.17(2)
CS	$3-2$	146969.025	146969.4(1)	14.2(1)	1.18(1)
SO	3_3-2_2	129138.983	129138.9(5)	15.2(3)	0.87(8)
SO_2	$8_{2-6}-8_{1-7}$	134004.811	134005.0(1)	14.5(1)	1.2(3)
SO_2	$5_{1-5}-4_{0,4}$	135696.016	135696.1(5)	15.9(5)	3.89(4)
SO_2	$4_{2-2}-4_{1,3}$	146605.519	146605.4(5)	15.5(6)	1.27(1)
SO_2	$2_{2-0}-2_{1,1}$	151378.662	151378.7(5)	15.3(5)	0.77(7)
		RR Aql			
SiO	$3-2$	130268.665	130268.4(1)	6.0(10)	4.86(5)
SiS	$8-7$	145227.054	-	-	-
CS	$3-2$	146969.025	-	-	-
SO	3_3-2_2	129138.983	129138.9(5)	8.5(6)	0.40(4)
SO_2	$8_{2-6}-8_{1-7}$	134004.811	134004.3(1)	7.8(1)	0.36(3)
SO_2	$5_{1-5}-4_{0,4}$	135696.016	135696.2(1)	8.0(1)	1.17(1)
SO_2	$4_{2-2}-4_{1,3}$	146605.519	146605.5(1)	8.0(1)	0.58(1)

Table 9.5: Continued.

Line		ν_{calc} (MHz)	ν_{obs} (MHz)	V_e (km s^{-1})	$\int T_A^* dv$ (K km s^{-1})
SO_2	$2_{2-0} - 2_{1,1}$	151378.662	151379.0(5)	7.5(4)	0.31(3)
			R LMi		
SiO	$3 - 2$	130268.665	130268.6(5)	5.8(5)	6.23(6)
SiS	$8 - 7$	145227.054	-	-	-
CS	$3 - 2$	146969.025	-	-	-
SO	$3_3 - 2_2$	129138.983	129139.1(5)	5.5(5)	0.18(2)
SO_2	$8_{2-6} - 8_{1-7}$	134004.811	134004.9(5)	4.8(5)	0.21(2)
SO_2	$5_{1-5} - 4_{0,4}$	135696.016	135694.6(10)	4.6(10)	0.09(2)[a]
SO_2	$4_{2-2} - 4_{1,3}$	146605.519	146606.1(5)	5.2(5)	0.05(1)[a]
SO_2	$2_{2-0} - 2_{1,1}$	151378.662	-	-	-
			BX Cam		
SiO	$3 - 2$	130268.665	130268.6(1)	17.3(1)	13.2(13)
SiS	$8 - 7$	145227.054	145226.7(5)	15.4(6)	1.06(3)
CS	$3 - 2$	146969.025	146969.0(5)	17.6(5)	0.74(7)
SO	$3_3 - 2_2$	129138.983	129138.7(5)	15.4(5)	0.84(17)[a]
SO_2	$8_{2-6} - 8_{1-7}$	134004.811	134004.5(5)	14.9(8)	0.72(14)[a]
SO_2	$5_{1-5} - 4_{0,4}$	135696.016	135696.3(1)	17.0(1)	1.47(1)
SO_2	$4_{2-2} - 4_{1,3}$	146605.519	146606.0(1)	14.9(1)	0.49(5)[a]
SO_2	$2_{2-0} - 2_{1,1}$	151378.662	151378.9(10)	14.8(10)	0.25(5)[a]
			V1300 Aql		
SiO	$3 - 2$	130268.665	130268.5(1)	14.1(1)	7.51(7)
SiS	$8 - 7$	145227.054	145227.3(1)	14.7(5)	10.9(11)
CS	$3 - 2$	146969.025	146969.3(5)	14.0(5)	0.91(18)
SO	$3_3 - 2_2$	129138.983	129138.9(4)	13.6(4)	1.19(1)
SO_2	$8_{2-6} - 8_{1-7}$	134004.811	134004.8(6)	13.0(5)	1.16(11)
SO_2	$5_{1-5} - 4_{0,4}$	135696.016	135696.1(2)	13.7(5)	4.02(4)
SO_2	$4_{2-2} - 4_{1,3}$	146605.519	146605.6(5)	13.1(8)	1.91(2)
SO_2	$2_{2-0} - 2_{1,1}$	151378.662	151378.9(5)	13.2(5)	1.14(1)
			R Cas		
SiO	$3 - 2$	130268.665	130268.7(5)	8.3(5)	31.9(32)
SiS	$8 - 7$	145227.054	145226.2(10)	6.4(10)	0.18(4)[a]
CS	$3 - 2$	146969.025	146969.2(5)	6.8(5)	0.32(6)

Table 9.5: Continued.

Line		ν_{calc} (MHz)	ν_{obs} (MHz)	V_e (km s^{-1})	$\int T_A^* dv$ (K km s^{-1})
SO	$3_3 - 2_2$	129138.983	129138.8(1)	7.0(1)	0.98(1)
SO_2	$8_{2-6} - 8_{1-7}$	134004.811	134004.9(5)	6.8(5)	0.87(9)
SO_2	$5_{1-5} - 4_{0,4}$	135696.016	135696.1(6)	8.2(8)	0.67(7)
SO_2	$4_{2-2} - 4_{1,3}$	146605.519	146606.0(5)	7.3(5)	0.30(3)
SO_2	$2_{2-0} - 2_{1,1}$	151378.662	151378.0(10)	6.7(10)	0.18(4)[a]
			IRC -30398		
SiO	$3 - 2$	130268.665	130268.6(1)	14.8(5)	6.90(7)
SiS	$8 - 7$	145227.054	145227.2(5)	13.7(5)	0.34(7)
CS	$3 - 2$	146969.025	146969.1(5)	14.0(5)	0.59(6)
SO	$3_3 - 2_2$	129138.983	-	-	-
SO_2	$8_{2-6} - 8_{1-7}$	134004.811	-	-	-
SO_2	$5_{1-5} - 4_{0,4}$	135696.016	-	-	-
SO_2	$4_{2-2} - 4_{1,3}$	146605.519	-	-	-
SO_2	$2_{2-0} - 2_{1,1}$	151378.662	-	-	-
			TX Cam		
SiO	$3 - 2$	130268.665	130268.8(5)	17.7(7)	36.4(36)
SiS	$8 - 7$	145227.054	145226.7(1)	17.1(1)	7.6(7)
CS	$3 - 2$	146969.025	146968.9(1)	19.4 (1)	8.8(9)
SO	$3_3 - 2_2$	129138.983	129139.5(1)	16.7(1)	1.09(1)
SO_2	$8_{2-6} - 8_{1-7}$	134004.811	134005.5(10)	18.6(10)	0.60(12) [a]
SO_2	$5_{1-5} - 4_{0,4}$	135696.016	135696.5(5)	17.9(5)	2.29(2)
SO_2	$4_{2-2} - 4_{1,3}$	146605.519	146606.6(5)	19.5(5)	0.60(6)
SO_2	$2_{2-0} - 2_{1,1}$	151378.662	151379.1(10)	19.2(10)	0.39(8)[a]
			S CrB		
SiO	$3 - 2$	130268.665	130268.7(1)	4.9(1)	2.74(30)
SiS	$8 - 7$	145227.054	-	-	-
CS	$3 - 2$	146969.025	-	-	-
SO	$3_3 - 2_2$	129138.983	129139.0(5)	4.5(5)	0.17(4)[a]
SO_2	$8_{2-6} - 8_{1-7}$	134004.811	134005.6(5)	4.4(5)	0.30(3)[a]
SO_2	$5_{1-5} - 4_{0,4}$	135696.016	135696.4(5)	5.4(7)	0.31(3)[a]
SO_2	$4_{2-2} - 4_{1,3}$	146605.519	146606.7(5)	4.7(5)	0.18(2)[a]
SO_2	$2_{2-0} - 2_{1,1}$	151378.662	151378.5(10)	4.2(10)	0.02(1)[a]

Table 9.5: Continued.

Line		ν_{calc} (MHz)	ν_{obs} (MHz)	V_e (km s^{-1})	$\int T_A^* dv$ (K km s^{-1})
			IRC +60169		
SiO	$3-2$	130268.665	130268.8(1)	13.2(1)	3.43(3)
SiS	$8-7$	145227.054	145227.8(10)	15.6(10)	0.15(3)[a]
CS	$3-2$	146969.025	146969.5(10)	11.3(10)	0.11(2)[a]
SO	3_3-2_2	129138.983	129138.5(10)	15.3(10)	0.17(3)[a]
SO_2	$8_{2-6}-8_{1-7}$	134004.811	134004.2(10)	15.0(10)	0.10(2)[a]
SO_2	$5_{1-5}-4_{0,4}$	135696.016	135696.7(5)	15.1(1)	0.77(7)
SO_2	$4_{2-2}-4_{1,3}$	146605.519	146604.5(10)	15.0(10)	0.18(21)[a]
SO_2	$2_{2-0}-2_{1,1}$	151378.662	151378.5(10)	15.3(10)	0.20(4)[a]
			R Hya		
SiO	$3-2$	130268.665	130268.5(5)	4.9(5)	14.0(14)
SiS	$8-7$	145227.054	-	-	-
CS	$3-2$	146969.025	-	-	
SO	3_3-2_2	129138.983	129140.0(10)	3.9(10)	0.11(2)[a]
SO_2	$8_{2-6}-8_{1-7}$	134004.811	-	-	-
SO_2	$5_{1-5}-4_{0,4}$	135696.016	-	-	-
SO_2	$4_{2-2}-4_{1,3}$	146605.519	-	-	-
SO_2	$2_{2-0}-2_{1,1}$	151378.662	-	-	-
			R CrT		
SiO	$3-2$	130268.665	130268.5(1)	10.4(1)	22.3(20)
SiS	$8-7$	145227.054	-	-	-
CS	$3-2$	146969.025?	-	-	-
SO	3_3-2_2	129138.983	129139.5(5)	8.5(4)	0.82(1)
SO_2	$8_{2-6}-8_{1-7}$	134004.811	134004.5(5)	10.6(6)	1.3(1)
SO_2	$5_{1-5}-4_{0,4}$	135696.016	135696.4(1)	9.6(3)	0.73(7)
SO_2	$4_{2-2}-4_{1,3}$	146605.519	146605.2(5)	10.4(6)	0.49(9)[a]
SO_2	$2_{2-0}-2_{1,1}$	151378.662	151379.0(5)	10.3(5)	0.20(4)[a]
			O Ceti		
SiO	$3-2$	130268.665	130268.6(5)	3.4(10)	1.62(16)
SiS	$8-7$	145227.054	-	-	-
CS	$3-2$	146969.025	146969.4(5)	5.3	0.17(3)[a]
SO	3_3-2_2	129138.983	129138.7(5)	5.1(4)	0.22(2)

Table 9.5: Continued.

Line		ν_{calc} (MHz)	ν_{obs} (MHz)	V_e (km s^{-1})	$\int T_A^* dv$ (K km s^{-1})
SO_2	$8_{2-6} - 8_{1-7}$	134004.811	134005.3(10)	4.7(10)	0.21(4) [a]
SO_2	$5_{1-5} - 4_{0,4}$	135696.016	135696.6(5)	2.7(5)	0.04(1)[a]
SO_2	$4_{2-2} - 4_{1,3}$	146605.519	146605.6(5)	3.7(7)	0.05(1)[a]
SO_2	$2_{2-0} - 2_{1,1}$	151378.662	151378.7(10)	1.5(10)	0.020(4)[a]
			W Hya		
SiO	$3-2$	130268.665	130268.6(1)	6.3(1)	26.6(26)
SiS	$8-7$	145227.054	-	-	-
CS	$3-2$	146969.025	146969.7(10)	6.1(10)	0.31(6)[a]
SO	$3_3 - 2_2$	129138.983	129139.3(5)	4.7(1)	0.33(3)
SO_2	$8_{2-6} - 8_{1-7}$	134004.811	-	-	-
SO_2	$5_{1-5} - 4_{0,4}$	135696.016	-	-	-
SO_2	$4_{2-2} - 4_{1,3}$	146605.519	-	-	-
SO_2	$2_{2-0} - 2_{1,1}$	151378.662	-	-	-
			T Cep		
SiO	$3-2$	130268.665	130268.7(1)	3.8(1)	3.20(3)
SiS	$8-7$	145227.054	-	-	-
CS	$3-2$	146969.025	-	-	-
SO	$3_3 - 2_2$	129138.983	-	-	-
SO_2	$8_{2-6} - 8_{1-7}$	134004.811	-	-	-
SO_2	$5_{1-5} - 4_{0,4}$	135696.016	-	-	-
SO_2	$4_{2-2} - 4_{1,3}$	146605.519			
SO_2	$2_{2-0} - 2_{1,1}$	151378.662	-	-	-
			V1943 Sgr		
SiO	$3-2$	130268.665	130268.6(1)	4.5(5)	5.07(5)
SiS	$8-7$	145227.054	-	-	-
CS	$3-2$	146969.025	-	-	-
SO	$3_3 - 2_2$	129138.983	129138.9(10)	4.2(10)	0.20(4)
SO_2	$8_{2-6} - 8_{1-7}$	134004.811	-	-	-
SO_2	$5_{1-5} - 4_{0,4}$	135696.016	-	-	-
SO_2	$4_{2-2} - 4_{1,3}$	146605.519	-	-	
SO_2	$2_{2-0} - 2_{1,1}$	151378.662	-	-	-
			SW Vir		

Table 9.5: Continued.

Line		ν_{calc} (MHz)	ν_{obs} (MHz)	V_e (km s^{-1})	$\int T_A^* dv$ (K km s^{-1})
SiO	$3-2$	130268.665	130268.6(1)	7.5(1)	17.4(17)
SiS	$8-7$	145227.054	-	-	-
CS	$3-2$	146969.025	146969.0(10)	7.5(8)	0.33(6)[a]
SO	3_3-2_2	129138.983	129139.0(5)	7.1(6)	0.57(11)
SO_2	$8_{2-6}-8_{1-7}$	134004.811	-	-	-
SO_2	$5_{1-5}-4_{0,4}$	135696.016	-	-	-
SO_2	$4_{2-2}-4_{1,3}$	146605.519	-	-	-
SO_2	$2_{2-0}-2_{1,1}$	151378.662	-	-	-
			AFGL 292		
SiO	$3-2$	130268.665	130268.6(1)	6.9(6)	3.69(4)
SiS	$8-7$	145227.054	-	-	-
CS	$3-2$	146969.025	-	-	-
SO	3_3-2_2	129138.983	129138.7(10)	5.5(7)	0.09(2)[a]
SO_2	$8_{2-6}-8_{1-7}$	134004.811	-	-	-
SO_2	$5_{1-5}-4_{0,4}$	135696.016	-	-	-
SO_2	$4_{2-2}-4_{1,3}$	146605.519	-	-	-
SO_2	$2_{2-0}-2_{1,1}$	151378.662	-	-	-
			BK Vir		
SiO	$3-2$	130268.665	130268.6(1)	4.2(8)	3.3(3)
SiS	$8-7$	145227.054	-	-	-
CS	$3-2$	146969.025	-	-	-
SO	3_3-2_2	129138.983	-	-	-
SO_2	$8_{2-6}-8_{1-7}$	134004.811	-	-	-
SO_2	$5_{1-5}-4_{0,4}$	135696.016	-	-	-
SO_2	$4_{2-2}-4_{1,3}$	146605.519	-	-	-
SO_2	$2_{2-0}-2_{1,1}$	151378.662	-	-	-
			OH 26.5+0.6		
SiO	$3-2$	130268.665	130268.6(1)	14.2(1)	6.55(6)
SiS	$8-7$	145227.054	145227.0(1)	12.6(1)	1.54(1)
CS	$3-2$	146969.025	146968.5(5)	15.6(5)	0.96(9)
SO	3_3-2_2	129138.983	129138.6(1)	13.1(3)	6.29(3)
SO_2	$8_{2-6}-8_{1-7}$	134004.811	134005.5(1)	14.2(1)	4.15(4)

Table 9.5: Continued.

Line		ν_{calc} (MHz)	ν_{obs} (MHz)	V_e (km s^{-1})	$\int T_A^* dv$ (K km s^{-1})
SO_2	$5_{1-5} - 4_{0,4}$	135696.016	135696.1(1)	14.3(4)	8.53(8)
SO_2	$4_{2-2} - 4_{1,3}$	146605.519	146605.4(4)	14.4(7)	3.79(4)
SO_2	$2_{2-0} - 2_{1,1}$	151378.662	151378.6(5)	14.1(4)	2.71(3)
			Ep Aqr		
SiO	$3 - 2$	130268.665	130268.0(5)	8.1(10)	22.5(22)
SiS	$8 - 7$	145227.054	-	-	-
CS	$3 - 2$	146969.025	146969.0(10)	0.9(5)	0.030(6)[a]
SO	$3_3 - 2_2$	129138.983	129138.8(5)	3.0(10)	1.16(23)
SO_2	$8_{2-6} - 8_{1-7}$	134004.811	134004.8(5)	2.2(10)	0.38(8)
SO_2	$5_{1-5} - 4_{0,4}$	135696.016	135696.0(5)	2.3(10)	0.13(1)
SO_2	$4_{2-2} - 4_{1,3}$	146605.519	146605.4(5)	3.2(10)	0.15(2)
SO_2	$2_{2-0} - 2_{1,1}$	151378.662	151378.6(5)	3.7(10)	0.08(2)
			X Her		
SiO	$3 - 2$	130268.665	130268.4(5)	6.5(5)	10.2(10)
SiS	$8 - 7$	145227.054	-	-	-
CS	$3 - 2$	146969.025	-	-	-
SO	$3_3 - 2_2$	129138.983	129138.8(5)	2.8(5)	0.52(5)
SO_2	$8_{2-6} - 8_{1-7}$	134004.811	-	-	-
SO_2	$5_{1-5} - 4_{0,4}$	135696.016	-	-	-
SO_2	$4_{2-2} - 4_{1,3}$	146605.519	-	-	-
SO_2	$2_{2-0} - 2_{1,1}$	151378.662	-	-	-

Notes. Numbers in parentheses are 1σ uncertainties in units of the last digits.

[a] Marginal detection.

Chapter 10

Conclusion

10.1 Summary, Conclusions, and Prospects (English)

10.1.1 General Summary and Conclusions

In this thesis, we have presented a detailed study of molecular abundances in large samples of AGB circumstellar envelopes. The ultimate goal is to gain better insight on the process of dust formation in these objects by identifying what molecules act as gas-phase precursors of dust in the envelopes, thereby the understanding of the dust formation around AGB stars will improve. AGB stars are known to be the main producers of dust in the Galaxy (along with supernovae), and so the dust ejected from their envelopes can go on to play an important role in the formation and evolution of many astronomical objects (e.g., new stars, planets, galaxies, etc.), therefore, the work carried out in this thesis has the ability to benefit many areas of astronomical research.

We looked for emission of the most likely candidates of gas-phase precursors of dust in two large samples, each of a different chemical character. We carried out sensitive observations in the λ 2mm with the IRAM 30 m telescope to search for emission lines of SiC_2 ($6_{2,5}-5_{2,4}$, $6_{4,3}-5_{4,2}$, $6_{4,2}-5_{4,1}$, $6_{2,4}-5_{2,3}$, $7_{0,7}-6_{0,6}$), SiO ($J=3-2$), SiS ($J=7-6$ and $J=8-7$) and CS ($J=3-2$) in 25 C-rich CSEs, and SiO ($J=3-2$), SiS ($J=8-7$), CS ($J=3-2$), SO (3_3-2_2) and SO_2 ($8_{2-6}-8_{1-7}$, $5_{1-5}-4_{0,4}$, $4_{2-2}-4_{1,3}$, $2_{2-0}-2_{1,1}$) in 30 O-rich CSEs where both samples are characterized by a wide range of mass-loss rates ($10^{-8}-10^{-5}$ $M_\odot$ yr^{-1}). These molecules are known to be abundant and could act as possible candidates for seed nuclei of dust within their respective chemical environments. By deriving their fractional abundance, and exploring any potential trend of the abundance with parameters such as the chemical type and the mass loss rate, we are able to extract information about which of these molecules act as main gas-phase precursors of dust and

have an overall idea about the behavior and occurrence of these molecules in circumstellar envelopes of AGB stars.

We performed detailed (non-LTE) excitation and radiative transfer calculations based on the large velocity gradient (LVG) method to model the observed lines of the molecules and to derive their fractional abundances in the observed envelopes. To derive accurate abundances in each CSE, we took into account the specific parameters of each envelope (e.g., D, $T_\star$, $L_\star$, V_{exp}, $\dot{M}$, etc). The rotational lines observed probe the intermediate and outer regions of the envelope, so the abundance derived in this work correspond to postcondensation regions where dust formation has already started. These results are compared to previous observational studies and to models of equilibrium and nonequilibrium chemistry.

The main conclusions of the thesis are represented by Fig. 10.1. The figure shows the fractional abundances relative to H_2, f_0, derived for SiC_2 for 25 C-rich envelopes (red, Chapter 7), and SiO, CS, SiS, SO, and SO_2 in the 30 O-rich CSEs (blue, Chapter 9) as a function of the envelope density proxy, $\dot{M}/V_{\rm exp}$. We also include in the panels of SiO, CS, and SiS the fractional abundances of these molecules derived in the sample of 25 C-rich envelopes (red, Chapter 8).

The conclusions can be summarized in two-folds: that which corresponds to the behaviour of the fractional abundance with the chemical type of the CSE (for the molecules that we observed in an O-rich and C-rich sample, i.e., SiO, SiS and CS) and that which corresponds to the behavior with the density proxy of the envelope, $\dot{M}/V_{\rm exp}$ (for all of the molecules). We summarize our conclusions here.

- **SiC_2 in C-rich CSEs**

We estimate the abundance of SiC_2 in 25 C-rich envelopes. For most of the sources in the sample, this is the first time the circumstellar SiC_2 abundance is reported. The fractional abundnace of SiC_2 in the C-rich sample shows a trend where SiC_2 becomes less abundant as the density in the envelope increases (SiC_2 panel in Fig. 10.1). We interpret this as that the SiC_2 molecules deplete from the gas phase to incorporate into solid dust grains which strongly suggests that SiC_2 is an important gas-phase precursor of SiC dust in envelopes around carbon stars.

- **SiO in C-rich and O-rich CSEs**

We estimate the abundance of SiO in 25 C- and 30 O-rich CSEs. The derived SiO fractional abundance in both samples does not differ significantly in both samples, that is to say, any difference in SiO circumstellar abudances between C-rich and O-rich CSEs is not

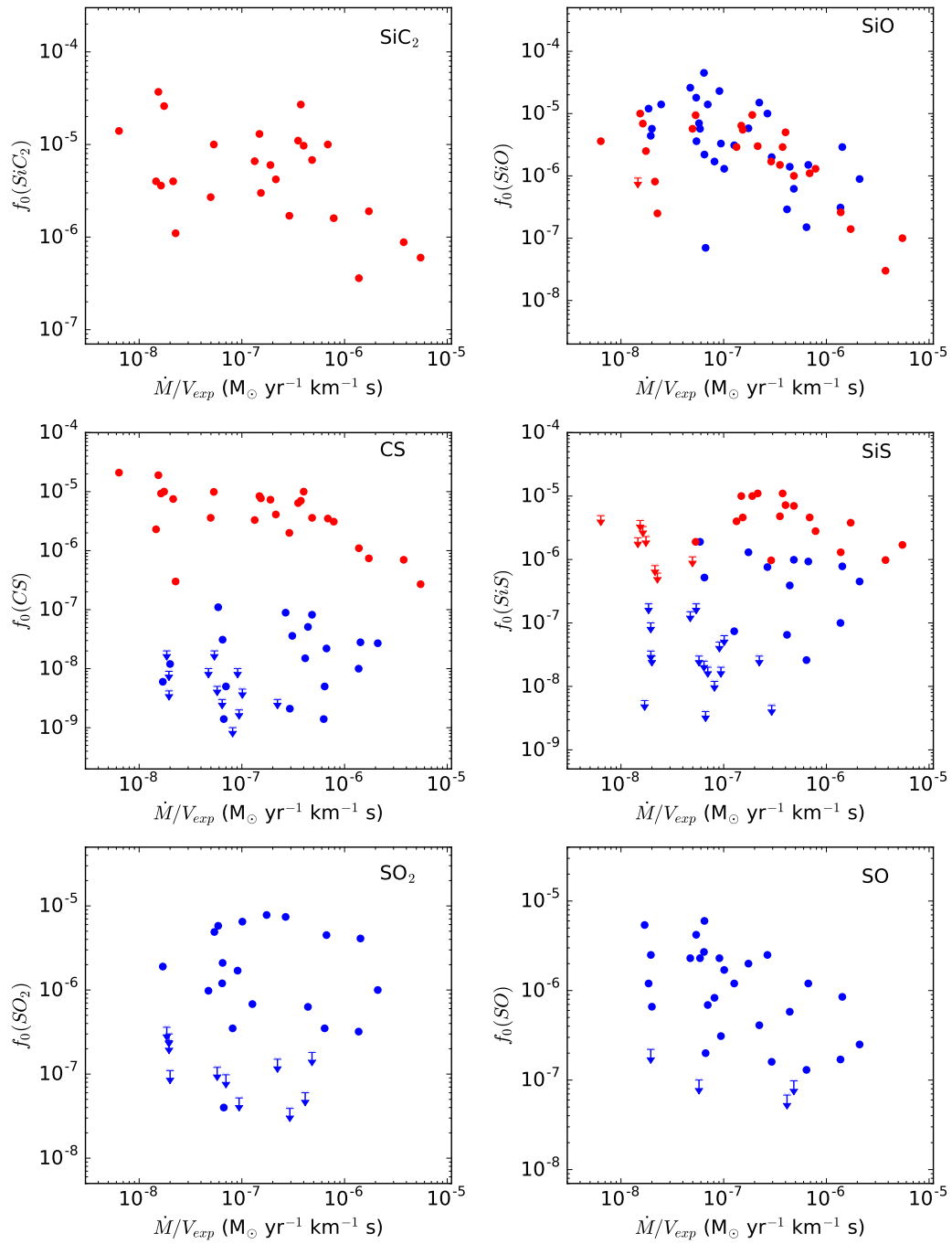

Figure 10.1: Fractional abundances, f_0, derived in this thesis for SiC_2, SiO, SiS, CS, SO, and SO_2 are shown as a function of the density proxy $\dot{M}/V_{\rm exp}$ for oxygen-rich stars (blue) and carbon-rich stars (red). Downward arrows represent upper limits to f_0.

present (SiO panel in Fig. 10.1). The results from our observations indicate that the SiO abundance does not depend on the photospheric C/O ratio. Chemical equilibrium models predict that SiO maintains a uniform and high abundance ($\sim 10^{-5}$) in O-rich envelopes whereas in C-rich envelopes SiO is predicted to have a low abundance at the stellar surface, although reaching a high abundance ($\sim 10^{-5}$) at a few stellar radii from the star. That is, according to chemical equilibrium we could expect some differentiation in the SiO abundance between stars of different chemical type. Nonequilibrium models which are based on calculations that take into account that abundances may be altered in the upper atmosphere due to shock effects triggered by stellar pulsation suggest that SiO abundance has no apparent dependence on the C/O ratio. Our observed results for the SiO abundances agree well with predictions from chemical equilibrium at a few stellar radii and with nonequilibrium models.

In addition, there is a trend of decreasing abundance with increasing density of the CSE, probably due to more efficient adsorption of SiO onto grains with increasing circumstellar density. This indicates that SiO is very likely a gas-phase precursor of dust around C- and O-rich CSEs.

♌ SiS in C-rich and O-rich CSEs

We estimate the abundance of SiS in 25 C- and 30 O-rich CSEs. Our results show that the circumstellar SiS abundances depend strongly on the C/O ratio (SiS panel in Fig. 10.1). The C-rich sample has a mean fractional abundance one order of magnitude higher than in O-rich AGB stars indicating that the molecule is favourably formed in C-rich environments than in O-rich ones. Chemical equilibrium predicts a differentiation in the SiS abundance between C-rich and O-rich stars in the very inner regions, while at a few stellar radii the abundance of SiS is expected to be similar in both environments. Nonequilibrium chemical models predict a dependence on the C/O ratio, which is in line with our observational findings.

A striking result concerning SiS, is the fact that it is not detected in low mass loss rate envelopes ($< 10^{-6}$ $M_{\odot}$ yr^{-1}) of both chemical types. The reason is not exactly known but could be due to either a lack of the constituent elements, which would be trapped in other S- and Si-bearing molecules, or could be due to a sensitivity issue within our observations.

In contrast to SiO, there is no strong correlation of the circumstellar SiS abundance with density of the CSE in either chemical types, as would be expected if adsorption onto dust grains were important for this molecule.

♌ CS in C-rich and O-rich CSEs

We estimate the abundance of CS in 25 C- and 30 O-rich CSEs. The differentiation in the circumstellar abundance between the C- and O-rich envelopes is even more pronounced for CS than for SiS, where the mean fractional abundance for O-rich CSEs is more than two orders of magnitude lower than for C-rich CSEs (CS panel in Fig. 10.1). It is evident that the formation of CS is dependent on the photospheric C/O ratio of the star and the molecule forms more readily in C-rich environments. The differentiation between C-rich and O-rich environments is in accordance with predictions by chemical equilibrium models. However, those models expect lower abundance (by about 3-4 orders of magnitude) for CS in O-rich environments than what is observed here. Nonequilibrium models show that effects such as shocks and photochemistry can trigger the formation of CS in O-rich environments and can thus explain the enhancement of the abudnance.

While there is no apparent trend that the CS abundance decreases as the density in the wind increases for O-rich envelopes, it is clearly evident for carbon-rich envelopes which indicates that the CS molecules are more likely to adsorb onto dust grains in C-rich environments than in O-rich ones. In fact, we find a negative correlation between the fractional abundance of CS and the 30 µm feature, attributed to MgS dust, which suggests that CS is a likely precursor of MgS dust grains in C-rich AGB envelopes.

♌ SO in O-rich CSEs

We estimate the abundance of SO in 30 O-rich CSEs. For some sources SO abundances are reported for the first time in this thesis. Theoretical studies predict this molecule to be abundant in O-rich environments, which is shown in the observed abundances here as well.

The SO fractional abundance show hints of decreasing abundance with increasing $\dot{M}/V_{\rm exp}$ (SO panel in Fig. 10.1). However, this is only tentative since the trend is not so evident. SO could emerge as a candidate to gas-phase precursors of dust in O-rich envelopes, however no sulfur-containing condensate has been identified in the spectra of O-rich envelopes yet.

♌ SO_2 in O-rich CSEs

We estimate the abundance of SO_2 in 30 O-rich CSEs. For some of the sources in our sample SO_2 abundances are reported for the first time. The observed values are well above the abundances predicted by chemical equilibrium ($< 10^{-10}$) in the inner regions of O-rich envelopes which suggests the non-LTE processes are enhancing the SO_2 abundance. However, nonequilibrium models of shock chemistry also predict negligible SO_2 abundances ($< 10^{-13}$). There remains a huge discrepancy between observational and theoretical studies for this molecule in the inner envelope of O-rich stars which cannot be currently explained.

For this molecule, we do not see any obvious trend of the fractional abundance with respect to the CSE density that could indicate that SO_2 is a gas-phase precursor of dust in O-rich envelopes (SO_2 panel in Fig. 10.1).

Our conclusions on the role of these molecules as gas-phase precursors of dust are based on low energy rotational lines, which probe post-condensation regions. More observations, in particular high-J lines and interferometric observations probing the inner regions of the envelopes, are needed to affirm the conclusions obtained in this study (see Sec. 10.1.2 for the future prospects).

10.1.2 Prospects for future research

The search for the gas-phase building blocks of dust grains in both carbon- and oxygen-rich AGB stars is a challenging scientific objective, in which astronomical observations still have to provide many answers. While the work carried out in this thesis provides us with clues about the role of certain molecules in the formation of dust and the behavior of the abundance with parameters like the C/O ratio, and the mass loss rate, it opens up several new research questions and opportunities to be explored.

The derivation of the fractional abundance of the molecules in this thesis is based on a limited number of rotational lines for every species, that is to say, we did not have access to many molecular lines for every species. During the analysis of our results, we noticed that the derived fractional abundances are sensitive to the adopted emission size of the molecules. That is, a change in the outer boundary of the abundance distribution has important effects on the derived abundance. Therefore, follow-up observations of more *J* lines would better constrain the extent of the emission size. The emission from high-J lines probe warm inner regions of the envelope, while low-J lines probe the outer regions of the envelope. By having access to multiple transitions spanning a wide range of upper level energies, we can better constrain both the molecular abundance and the emission size. In fact, we have already embarked on this follow-up by observing more J lines across the λ 0.8 mm, λ 1 mm and λ 3mm bands with the IRAM 30m telescope of a sample of 12 sources of C- and O-rich envelopes. Along with the λ 2 mm data we already have, we will be able to derive more precise abundances and thereby more precise trends.

In what concerns the chemical type of the CSEs, the detection of molecules which are otherwise unexpected to form according to thermochemical equilibrium, like CS, SO_2 (Fig. 10.1) and HCN (Fig. 6.1) in O-rich environments, indicates that nonequilibrium processes must be occuring in the inner regions of AGB circumstellar envelopes to form these

molecules and enhance their abundance over the expectations from chemical equilibrium. However, we still lack a satisfactory observational scenario that explains these peculiarities within the inner parts of the envelopes. In particular, we do not know what the radius of formation of these molecules is and which nonequilibrium processes (e.g., shocks or photochemistry) are taking place that are causing the enhacement of abundances. ALMA maps, with their very high angular resolution, have the ability to probe these innermost regions and constrain the region of formation of these molecules.

In what concerns the mass loss rate of the CSEs, if the trend of a decreasing abundance with increasing mass loss rate indicates more efficient adsorption of gas molecules onto dust, then the high-J lines of ALMA can be an important tool to probe the inner regions of CSEs of different mass loss rates in order to investigate how the fractional abundance of a likely gas-phase precursor behaves in the inner parts of the envelope. We expect that the fractional abundance of a molecule, like SiO, would experience a more substantial decline for high mass loss rate CSEs than for low mass loss rate ones.

10.2 Resumen, conclusiones, y perspectivas (Español)

10.2.1 Resumen general y conclusiones

En esta tesis hemos presentado un estudio detallado de abundancias moleculares en una amplia muestra de envolturas circunestelares en torno a estrellas AGB. El objetivo final es obtener una mejor comprensión del proceso de formación de polvo en estos objetos mediante la identificación de qué moléculas en fase gaseosa actúan como precursoras de polvo en las envolturas. Se sabe que las estrellas AGB son las principales productoras de polvo en la Galaxia (junto con las supernovas), por lo que el polvo expulsado por sus envolturas juega un papel importante en la formación y evolución de muchos objetos astronómicos (por ejemplo, nuevas estrellas, planetas, galaxias, etc.), por lo que el trabajo desarrollado en esta tesis tiene la capacidad de beneficiar a muchas áreas de investigación astronómica.

Hemos buscado la emisión de los candidatos más probables a precursores del polvo en dos muestras grandes de estrellas, cada una de ellas con un carácter químico diferente. Para ello hemos realizado observaciones en la banda de λ 2 mm con el telescopio IRAM 30-m para buscar líneas de emisión de SiC_2 ($6_{2,5}-5_{2,4}$, $6_{4,3}-5_{4,2}$, $6_{4,2}-5_{4,1}$, $6_{2,4}-5_{2,3}$, $7_{0,7}-6_{0,6}$), SiO ($J=3-2$), SiS ($J=7-6$ and $J=8-7$) y CS ($J=3-2$) en 25 envolturas ricas en C, y SiO ($J=3-2$), SiS ($J=8-7$), CS ($J=3-2$), SO (3_3-2_2) y SO_2 ($8_{2-6}-8_{1-7}$, $5_{1-5}-4_{0,4}$, $4_{2-2}-4_{1,3}$, $2_{2-0}-2_{1,1}$) en 30 envolturas ricas en O. Ambas muestras cubren una amplia gama de tasas de pérdida de masa ($10^{-8}-10^{-5}$ $M_\odot$ yr^{-1}). Se sabe que estas moléculas son abundantes y podrían actuar como posibles precursoras de granos de polvo en sus respectivos entornos químicos. Mediante la determinación de su abundancia y la exploración de posibles dependencias con parámetros como el tipo químico y la tasa de pérdida de masa, podemos extraer información sobre cuáles de estas moléculas actúan como precursoras del polvo y tener una idea general sobre la abundancia y comportamiento de estas moléculas en envolturas circunestelares de estrellas AGB.

Hemos llevado a cabo cálculos de excitación y transporte de radiación basados en el método LVG para modelar las líneas observadas de las distintas moléculas y derivar sus abundancias. Para determinar abundancias precisas en cada envoltura, hemos adoptado los parámetros específicos de cada una (e.g., distancia, temperatura y luminosidad de la estrella, velocidad de expansión, tasa de pérdida de masa, etc.). Las líneas de rotación observadas sondean las regiones intermedia y externa de la envoltura, por lo que la abundancia derivada en este trabajo corresponde a regiones en que la formación del polvo ya ha tenido lugar. Estos resultados se comparan con estudios observacionales previos y con modelos de química en equilibrio y fuera del equilibrio.

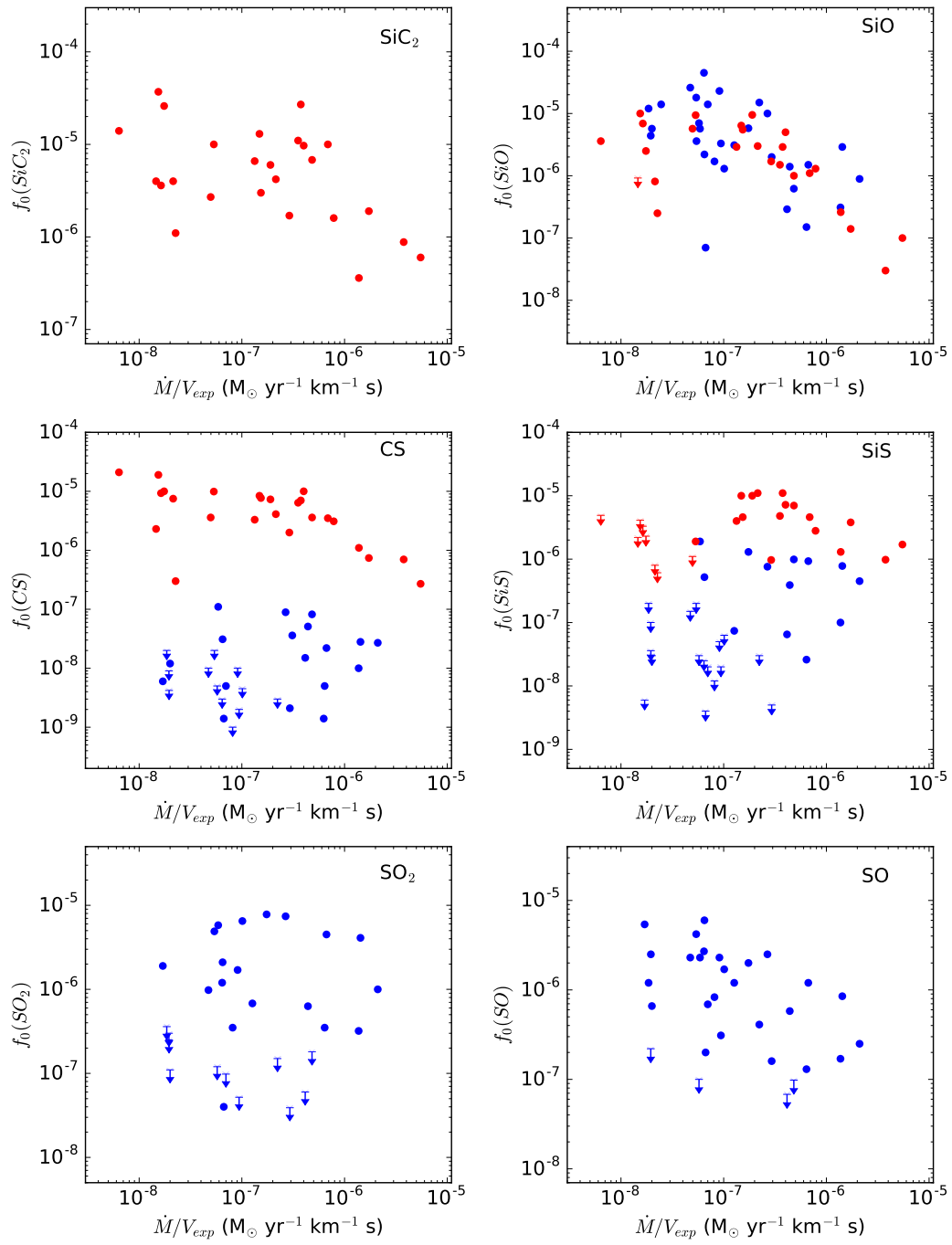

Figure 10.2: Las abundancias relativas a H_2 f_0 determinadas en esta tesis para SiC_2, SiO, SiS, CS, SO, y SO_2 se muestran en función de $\dot{M}/V_{\rm exp}$ para estrellas ricas en O (azul) y estrellas ricas en C (rojo). Las flechas hacia abajo representan límites superiores de f_0.

Las principales conclusiones de la tesis están representadas en la Fig. 10.2. La figura muestra las abundancias relativas a H_2 determinadas para SiC_2 en 25 estrellas ricas en C (rojo, Capítulo 7), y para SiO, CS, SiS, SO, y SO_2 en 30 estrellas ricas en O (azul, Capítulo 9) en función de $\dot{M}/V_{\rm exp}$. También incluimos en los paneles de SiO, CS, y SiS las abundancias determinadas en la muestra de 25 estrellas ricas en C (rojo, Capítulo 8).

Las conclusiones se pueden resumir en dos partes: la que corresponde al comportamiento de la abundancia según el tipo químico de la envoltura (para aquellas moléculas observadas en los dos tipos de envolturas, es decir, SiO, SiS y CS) y el que corresponde al comportamiento de la abundancia con la densidad de la envoltura (para todas las moléculas). Resumimos aquí nuestras conclusiones.

- **SiC_2 en envolturas ricas en C**

Hemos determinado la abundancia de SiC_2 en 25 envolturas circunestelares ricas en C. Para la mayoría de las fuentes de la muestra, esta es la primera vez que se determina la abundancia de SiC_2. La abundancia de SiC_2 muestra una tendencia en la que SiC_2 se vuelve menos abundante a medida que aumenta la densidad de la envoltura (panel SiC_2 en Fig. 10.2). Interpretamos esto como que las moléculas de SiC_2 desaparecen de la fase gaseosa para incorporarse a los granos de polvo sólido conforme aumenta la densidad del medio, lo que sugiere que SiC_2 es un precursor importante en la formación de polvo de SiC en envolturas de estrellas AGB ricas en carbono.

- **SiO en envolturas ricas en C y ricas en O**

Para el moóxido de silicio, hemos determinado su abundancia en 25 envolturas ricas en C y en 30 envolturas ricas en O. La abundancia de SiO no muestra una dependencia con el tipo químico de la envoltura, rico en C o rico en O (panel de SiO en la Fig. 10.2). Esto es, la abundancia de SiO no depende de la relación C/O en la superficie de la estrella AGB. Los modelos de equilibrio químico predicen que SiO mantiene una abundancia elevada y uniforme ($\sim 10^{-5}$ relativo a H_2) en atmósferas ricas en O, mientras que en ambientes ricos en C se predice que SiO tiene una abundancia baja en la superficie estelar, aunque alcanza una elevada abundancia ($\sim 10^{-5}$ relativo a H_2) a distancias de unos pocos radios estelares de la estrella. Es decir, de acuerdo con el equilibrio químico, podríamos esperar alguna diferenciación en la abundancia de SiO entre estrellas de diferente tipo químico. Modelos de química fuera del equilibrio que consideran los efectos de choques provocados por la pulsación estelar sugieren que la abundancia de SiO no tiene una dependencia aparente con la relación C/O. Nuestros resultados están de acuerdo con las predicciones del equilibrio

químico a distancias de unos pocos radios estelares y con modelos de química fuera del equilibrio.

Además, existe una tendencia a la disminución de la abundancia de SiO con el aumento de la densidad de la envoltura, probablemente debido a una adsorción más eficiente de SiO en los granos con una densidad circunestelar creciente. Esto indica que SiO es muy probablemente un precursor del polvo tanto en envolturas ricas en C como ricas en O.

♌ SiS en envolturas ricas en C y ricas en O

La abundancia de SiS se ha determinado en 25 envolturas ricas en C y 30 envolturas ricas en O. Nuestros resultados muestran que la abundancia de SiS depende en gran medida de la relación C/O (panel de SiS en la Fig. 10.2). La moécula SiS tiene una abundancia de media un orden de magnitud superior en la muestra rica en c comparado con la muestra rica en O, lo que indica que SiS se forma más favorablemente en entornos ricos en C que en los ricos en O. El equilibrio químico predice una diferenciación en la abundancia de SiS entre estrellas ricas en C y ricas en O en las regiones más internas, mientras que a distancias de unos pocos radios estelares se espera que la abundancia de SiS sea similar en ambos ambientes. Los modelos de química fuera del equilibrio predicen una dependencia de la relación C/O, que está en línea con nuestros hallazgos observacionales.

Un resultado sorprendente con respecto a SiS, es el hecho de que no se detecta en envolturas con poca pérdida de masa ($<10^{-6}$ $M_{\odot}$ yr^{-1}) independientemente del tipo químico de la envoltura. La razón no se conoce con exactitud, pero podría deberse a una falta de los elementos constituyentes, que quedarían atrapados en otras moléculas portadoras de Si o S, o podría deberse a un problema de sensibilidad en nuestras observaciones.

A diferencia de SiO, para SiS no existe una correlación clara de su abundancia con la densidad de la envoltura en ninguno de los dos tipos químicos. Esto significa que no existe una indicación clara de que SiS sea adsorbido sobre los granos de polvo.

♌ CS en envolturas ricas en C y ricas en O

Hemos determinado la abundancia de CS en 25 envolturas ricas en c y en 30 envolturas ricas en O. Para CS existe una diferenciación aún más clara que para SiS en lo que respecta a su abundancia en envolturas ricas en C y envolturas ricas en O. La abundancia de CS en ambientes ricos en C es en término medio más de dos órdenes de magnitud mayor que en envolturas ricas en O (panel de CS en la Fig. 10.2). Es evidente que la formación de CS depende de la relación C/O fotosférica de la estrella y que la molécula se forma más fácilmente en entornos ricos en C. La diferenciación entre entornos ricos en C y ricos en O está de acuerdo con las predicciones de los modelos de equilibrio químico. Sin embargo,

esos modelos predicen una abundancia mucho menor que la observada (por 3-4 órdenes de magnitud) para CS en ambientes ricos en O. Los modelos de química fuera del equilibrio muestran que efectos como los choques y la fotoquímica pueden promover la formación de CS en entornos ricos en O, lo que explicaría el aumento de abundancia observado con respecto a las predicciones del equilibrio químico.

Si bien no existe una tendencia aparente de que la abundancia de CS disminuya a medida que aumenta la densidad en el viento para las envolturas ricas en O, este comportamiento sí se observa claramente en objetos ricos en C, lo que indica que las moléculas de CS se adsorben sobre los granos de polvo más facilmente en ambientes ricos en C que en entornos ricos en O. De hecho, encontramos una correlación negativa entre la abundancia de CS y la intensidad de la banda situada a 30 µm, atribuida a polvo de MgS, lo que sugiere que CS es un probable precursor de los granos de polvo de MgS en envolturas ricas en C.

- **SO en envolturas ricas en O**

Para SO hemos determinado su abundancia en la muestra de 30 objetos ricos en O. Para algunas fuentes, esta es la primera vez que se determina la abundancia de SO. Los estudios teóricos predicen que esta molécula es abundante en ambientes ricos en O, lo que está de acuerdo con las abundancias observadas aquí.

La abundancia de SO muestra indicios de una tendencia a la disminución conforme aumenta $\dot{M}/V_{\rm exp}$ (panel SO en la Fig. 10.2). Sin embargo, esto debe ser considerado como tentativo por el momento. La molécula de SO podría ser un candidato a precursor de polvo en envolturas ricas en O. Sin embargo, aún no se ha identificado ningún condensado que contenga azufre en los espectros infrarrojos de envolturas ricas en O.

- **SO_2 en envolturas ricas en O**

Hemos determinado la abundancia de SO_2 en la muestra de de 30 envolturas ricas en O. Para algunas de las fuentes, esta es la primera vez que se determina la abundancia de esta molécula. Los valores observados están muy por encima de las abundancias predichas por el equilibrio químico ($<10^{-10}$ con respecto a H_2) en las regiones internas de envolturas ricas en O, lo que sugiere que lo procesos químicos fuera del equilibrio están aumentando la abundancia de SO_2. Sin embargo modelos de química fuera del equilibrio en que se considera el efecto de los choques inducidos por mla pulsación estelar también predicen abundancias insignificantes para SO_2 ($<10^{-13}$). Por lo tanto, sigue existiendo una fuerte discrepancia entre los estudios teóricos y observacionales con respecto a la abundancia de SO_2 en envolturas ricas en O.

Para esta molécula, no vemos ninguna tendencia obvia de su abundancia con respecto a la densidad de la envoltura que pudiera indicar que SO_2 es un precursor de polvo (panel SO_2 en la Fig. 10.2).

Nuestras conclusiones sobre el papel de las moléculas estudiadas en esta tesis como precursoras en la formación de polvo se basan en líneas de rotación de baja energía, que sondean las regiones de las envolturas en que la condensación de granos de polvo ya ha tenido lugar. Se necesitan más observaciones, en particular de líneas de alta energía así como observaciones interferométricas que sondeen regiones más internas de las envolturas, para dar mayor solidez a las conclusiones obtenidas en este estudio (ver Sec. 10.2.2 para las perspectivas futuras).

10.2.2 Perspectivas para investigaciones futuras

La búsqueda de los precursores básicos que desencadenan la formación de los granos de polvo en estrellas AGB es un desafío científico en el que las observaciones astronómicas aún tienen que proporcionar muchas respuestas. El trabajo realizado en esta tesis nos proporciona pistas sobre el papel de determinadas moléculas en la formación de polvo y el comportamiento de su abundancia con respecto a parámetros como la relación C/O y la tasa de pérdida de masa, pero también crea nuevas preguntas y abre la puerta a nuevas investigaciones.

La determinación de la abundancia de las moléculas llevada a cabo en esta tesis se basa en un número limitado de líneas rotacionales para cada especie. Durante el análisis de nuestros datos hemos notamos que las abundancias determinadas son sensibles al tamaño de emisión adoptado. Es decir, un cambio en el límite exterior de la distribución de abundancia tiene efectos importantes sobre la abundancia derivada. Por lo tanto, la observación de más líneas rotacionales permitiría restringir mejor el tamaño de la emisión. La emisión de líneas rotacionales con número cuántico J elevado sondea regiones de las envolturas internas y calientes, mientras que las líneas de bajo J sondean regiones más externas. Teniendo acceso a múltiples transiciones que cubran una amplia gama de energías podemos restringir mejor tanto la abundancia molecular como el tamaño de la emisión. De hecho, ya nos hemos embarcado en un estudio para observar más líneas rotacionales en las bandas λ 0.8 mm, λ 1 mm y λ 3 mm con el telescopio IRAM 30m. Junto con los datos de λ 2 mm que ya tenemos, podremos derivar abundancias más precisas y, por lo tanto, tendencias más precisas.

En lo que concierne al tipo químico de las envolturas, la detección de moléculas que de otro modo serían inesperadas según el equilibrio termoquímico, como CS, SO_2 (Fig. 10.2) y

HCN (Fig. 6.2) en ambientes ricos en O, indica que deben ocurrir procesos químicos fuera del equilibrio en las regiones internas de las envolturas que favorezcan la formación de estas moléculas. Sin embargo, aún no disponemos de un escenario satisfactorio que explique estas peculiaridades dentro de las partes internas de las envolturas. En particular, no sabemos exactamente cuál es la distancia de la estrella a la que se forman estas moléculas ni qué procesos químicos fuera del equilibrio (por ejemplo, inducidos por choques o por fotoquímica) están teniendo lugar para producir estas moléculas. Mapas obtenidos con ALMA, gracias a su elevada resolución angular, tienen la capacidad de sondear estas regiones más internas y restringir la región de formación de estas moléculas.

En lo que respecta al comportamiento de las abundancias con la tasa de pérdida de masa, si la tendencia de una abundancia decreciente con una tasa de pérdida de masa en aumento indica una adsorción más eficiente de moléculas sobre el polvo, entonces esperamos que la abundancia de una molécula como SiO experimente una disminución progresiva al alejarse de la estrella. Observaciones de líneas de alta energía con ALMA puede ayudar a caracterizar este gradiente radial de abundancia. Esto proporcionaría una evidencia adicional de que ciertas moléculas efectivamente desaparecen de la fase gas para tomar parte en el proceso de formación del polvo.

Bibliography

Agúndez, M. (2009). PhD thesis. Departamento de Astrofisica, Centro de Astrobiologia, CSIC-INTA.

Agúndez, M. and J. Cernicharo (2006). ApJ 650, pp. 374–393.

Agúndez, M., J. Cernicharo, and M. Guélin (2010). ApJ 724, pp. L133–L136.

Agúndez, M. et al. (2012). A&A 543, A48, A48.

Agúndez, M., J. Cernicharo, and M. Guélin (2014). A&A 570, A45, A45.

Agúndez, M. et al. (2017). A&A 601, A4, A4.

Agúndez, M. et al. (2018). A&A 616, A19, A19.

Agúndez, M. et al. (2020). A&A 637, A59, A59.

Apponi, A. J. et al. (1999a). ApJ 516.2, pp. L103–L106.

Apponi, A. J. et al. (1999b). ApJ 516, pp. L103–L106.

Asplund, M., N. Grevesse, and A. J. Sauval (2005). Astronomical Society of the Pacific Conference Series 336. Ed. by III Barnes Thomas G. and Frank N. Bash, p. 25.

Asplund, M. et al. (2009). ARA&A 47, pp. 481–522.

Bachiller, R. et al. (1997). A&A 324, pp. 1123–1134.

Bakker, E. J. et al. (1997). A&A 323, pp. 469–487.

Balança, C., A. Spielfiedel, and N. Feautrier (2016). MNRAS 460.4, pp. 3766–3771.

Balança, C. and F. Dayou (2017). MNRAS 469.2, pp. 1673–1681.

Balança, C. et al. (2018). MNRAS 479.2, pp. 2692–2701.

Balick, B. (2015). *American Astronomical Society Meeting Abstracts #225*. Vol. 225. American Astronomical Society Meeting Abstracts, p. 400.01.

Banerjee, D. P. K. et al. (2012). ApJ 753.1, L20, p. L20.

Bernes, C. (1979). A&A 73, pp. 67–73.

Bieging, J. H. and Nguyen-Quang-Rieu (1989). ApJ 343, pp. L25–L28.

Bogey, M et al. (1997). *Journal of Molecular Spectroscopy* 182.1, pp. 85–97.

Bohlin, R. C., B. D. Savage, and J. F. Drake (1978). ApJ 224, pp. 132–142.

Bowen, G. H. (1988). ApJ 329, p. 299.

Boyle, R. J. et al. (1994). ApJ 420, pp. 863–868.

Bujarrabal, V., P. Planesas, and A. del Romero (1987). A&A 175, pp. 164–172.

Bujarrabal, V., A. Fuente, and A. Omont (1994). A&A 285, pp. 247–271.

Bujarrabal, V. and J. Alcolea (2013). A&A 552, A116, A116.

Burns, D. et al. (1998). MNRAS 297.2, pp. 462–466.

Busso, M., R. Gallino, and G. J. Wasserburg (1999). ARA&A 37, pp. 239–309.

Busso, M. et al. (2004). *Origin and Evolution of the Elements*. Ed. by Andrew McWilliam and Michael Rauch, p. 67.

Castor, J. I. (1970). MNRAS 149, pp. 111–127.

Castro-Carrizo, A. et al. (2010). A&A 523, A59, A59.

Cernicharo, J (1985). *IRAM Internal Report 52*.

Cernicharo, J. et al. (1989). ApJ 341, pp. L25–L28.
Cernicharo, J. et al. (1991). ApJ 368, p. L39.
Cernicharo, J. and V. Bujarrabal (1992). ApJ 401, p. L109.
Cernicharo, J. and M. Guelin (1996). A&A 309, pp. L27–L30.
Cernicharo, J. et al. (1999). ApJ 526, pp. L41–L44.
Cernicharo, J., M. Guélin, and C. Kahane (2000). A&AS 142, pp. 181–215.
Cernicharo, J. et al. (2010). A&A 521, L8, p. L8.
Cernicharo, J. et al. (2011). A&A 531, A103, A103.
Cernicharo, J. et al. (2013). ApJ 778, L25, p. L25.
Cernicharo, J. et al. (2014). ApJ 796, L21, p. L21.
Cernicharo, J. et al. (2015a). ApJ 806, L3, p. L3.
Cernicharo, J. et al. (2015b). A&A 575, A91, A91.
Cernicharo, J. et al. (2017). A&A 606, L5, p. L5.
Chan, S. J. and S. Kwok (1990). A&A 237, pp. 354–368.
Chandra, S. et al. (1995). A&AS 114, p. 175.
Chandra, S. and W. H. Kegel (2000). A&AS 142, pp. 113–118.
Cherchneff, I. (2006). A&A 456.3, pp. 1001–1012.
Cherchneff, I., J. R. Barker, and A. G. G. M. Tielens (1992). ApJ 401, p. 269.
Cherchneff, I. (2012). A&A 545, A12, A12.
Chiavassa, A., B. Freytag, and M. Schultheis (2018). A&A 617, L1, p. L1.
Chiosi, C., G. Bertelli, and A. Bressan (1992). ARA&A 30, pp. 235–285.
Cordiner, M. A. and T. J. Millar (2009). ApJ 697, pp. 68–78.
Cotton, W. D. et al. (2004). A&A 414, pp. 275–288.
Cox, N. L. J. et al. (2012). A&A 537, A35, A35.
Croat, T. K., F. J. Stadermann, and T. J. Bernatowicz (2005). ApJ 631.2, pp. 976–987.
Danchi, WC et al. (1994). *The Astronomical Journal* 107, pp. 1469–1513.
Danilovich, T. et al. (2014). A&A 569, A76, A76.
Danilovich, T. et al. (2015). A&A 581, A60, A60.
Danilovich, T. et al. (2016). A&A 588, A119, A119.
Danilovich, T. et al. (2017). A&A 602, A14, A14.
Danilovich, T. et al. (2018). A&A 617, A132, A132.
Danilovich, T. et al. (2019). MNRAS 484, pp. 494–509.
Danilovich, T. et al. (2020). MNRAS 494.1, pp. 1323–1347.
Dayou, F. and C. Balança (2006). A&A 459, pp. 297–305.
De Beck, E. et al. (2010). A&A 523, A18, A18.
De Beck, E. et al. (2012). A&A 539, A108, A108.
De Beck, E. et al. (2015). A&A 580, A36, A36.
De Beck, E. et al. (2017). A&A 598, A53, A53.
Decin, L. et al. (2010a). A&A 516, A69, A69.
Decin, L. et al. (2010b). Nature 467.7311, pp. 64–67.
Decin, L. et al. (2017). A&A 608, A55, A55.
Denis-Alpizar, O. et al. (2018). MNRAS 478, pp. 1811–1817.
Dharmawardena, T. E. et al. (2018). MNRAS 479.1, pp. 536–552.
Díaz-Luis, J. J. et al. (2019). A&A 629, A94, A94.

Drira, I. et al. (1997). A&A 319, pp. 720–724.
Duari, D., I. Cherchneff, and K. Willacy (1999). A&A 341, pp. L47–L50.
Dyck, H. M. et al. (1996). AJ 111, p. 1705.
Ferrarotti, A. S. and H. P. Gail (2002). A&A 382, pp. 256–281.
Fishlock, C.K. et al. (2014). ApJ 797.1, 44, p. 44.
Fonfría, J. P. et al. (2008). ApJ 673.1, pp. 445–469.
Fonfría, J. P. et al. (2014). MNRAS 445, pp. 3289–3308.
Forrest, W. J., J. R. Houck, and J. F. McCarthy (1981). ApJ 248, pp. 195–200.
Freytag, B. and S. H ofner (2008). A&A 483.2, pp. 571–583.
Gaia Collaboration et al. (2018). A&A 616, A1, A1.
Gail, H. P. and E. Sedlmayr (1998). *Faraday Discussions* 109, p. 303.
Gail, H. P. and E. Sedlmayr (2014). *Physics and chemistry of circumstellar dust shells*. Vol. 52. Cambridge University Press.
Gardan, E., E. Gérard, and T. Le Bertre (2006). MNRAS 365.1, pp. 245–254.
Gehrz, R. (1989). *Interstellar Dust*. Ed. by L. J. Allamandola and A. G. G. M. Tielens. Vol. 135. IAU Symposium, p. 445.
Gerasimovic, B. P. (1928). *Proceedings of the National Academy of Science* 14.12, pp. 963–968.
Gilman, Robert C. (1972). ApJ 178, pp. 423–426.
Glassgold, A. E. (1996). ARA&A 34, pp. 241–278.
Gobrecht, D. et al. (2016). A&A 585, A6, A6.
Goebel, J. H. and S. H. Moseley (1985). ApJ 290, pp. L35–L39.
Goldreich, P. and N. Scoville (1976). ApJ 205, pp. 144–154.
González Delgado, D. et al. (2003). A&A 411, pp. 123–147.
Gray, MD et al. (2009). *Monthly Notices of the Royal Astronomical Society* 394.1, pp. 51–66.
Green, S. (1995). ApJS 100, p. 213.
Groenewegen, M. A. T. and P. A. Whitelock (1996a). MNRAS 281.4, pp. 1347–1351.
Groenewegen, M. A. T. et al. (1996b). A&A 306, p. 241.
Groenewegen, M. A. T. et al. (1998). MNRAS 293, p. 18.
Groenewegen, M. A. T. et al. (1999). A&AS 140, pp. 197–224.
Groenewegen, M. A. T. et al. (2002). A&A 390, pp. 511–522.
Groenewegen, M. A. T. et al. (2007). MNRAS 376.1, pp. 313–337.
Guélin, M., N. Neininger, and J. Cernicharo (1998). A&A 335, pp. L1–L4.
Guélin, M. et al. (2000). A&A 363, pp. L9–L12.
Guélin, M. et al. (2018). A&A 610, A4, A4.
Gullieuszik, M. et al. (2012). A&A 537, A105, A105.
Habing, H. J. (1996). A&A Rev. 7.2, pp. 97–207.
Habing, H. J. and H. Olofsson (2004). *Asymptotic Giant Branch Stars*. Springer Science & Business Media.
Hackwell, J. A. (1972). A&A 21, pp. 239–248.
Hammami, K. et al. (2007). A&A 462, pp. 789–794.
Heays, A. N., A. D. Bosman, and E. F. van Dishoeck (2017). A&A 602, A105, A105.
Henning, T. (2010). *Astromineralogy*. Vol. 815. Springer Science & Business Media.
Herwig, F. (2004). ApJ 605.1, pp. 425–435.
Herwig, F. (2005). ARA&A 43.1, pp. 435–479.
Hinkle, K. H. (1978). ApJ 220, pp. 210–228.
Hinkle, K. H., D. N. B. Hall, and S. T. Ridgway (1982). ApJ 252, pp. 697–714.
Hirano, N. et al. (2004). ApJ 616.1, pp. L43–L46.

Höfner, S. and H. Olofsson (2018). A&A Rev. 26.1, 1, p. 1.
Homan, W. et al. (2015). A&A 579, A118, A118.
Homan, W. et al. (2018). A&A 616, A34, A34.
Hony, S., L. B. F. M. Waters, and A. G. G. M. Tielens (2002). A&A 390, pp. 533–553.
Hony, S. et al. (2009). A&A 501.2, pp. 609–617.
Huggins, P. J. and A. E. Glassgold (1982). ApJ 252, pp. 201–207.
Iben I., Jr. and A. Renzini (1983). ARA&A 21, pp. 271–342.
Joyce, R. R. et al. (1998). AJ 116.5, pp. 2520–2529.
Jura, M. (1986). ApJ 303, p. 327.
Jura, M. and M. Morris (1981). ApJ 251, pp. 181–189.
Jura, M., C. Kahane, and A. Omont (1988). A&A 201, pp. 80–88.
Justtanont, K. et al. (1996). ApJ 456, p. 337.
Justtanont, K. et al. (2012). A&A 537, A144, A144.
Kahane, C. and M. Jura (1996). A&A 310, pp. 952–960.
Kamiński, T. et al. (2013). A&A 551, A113, A113.
Kamiński, T. et al. (2016). A&A 592, A42, A42.
Kamiński, T. et al. (2017). A&A 599, A59, A59.
Karakas, A. I., J. C. Lattanzio, and O. R. Pols (2002). PASA 19.4, pp. 515–526.
Karakas, Amanda I. and John C. Lattanzio (2014). PASA 31, e030, e030.
Keady, J. J., Donald N. B. Hall, and S. T. Ridgway (1988). ApJ 326, p. 832.
Keady, J. J. and S. T. Ridgway (1993). ApJ 406, pp. 199–214.
Keenan, Philip C. (1954). ApJ 120, p. 484.
Kerschbaum, F. and H. Olofsson (1999). A&AS 138, pp. 299–322.
Kerschbaum, F., C. Charbonnel, and R. F. Wing, eds. (2007). Vol. 378. Astronomical Society of the Pacific Conference Series.
Kessler, M. F. et al. (1996). A&A 500, pp. 493–497.
Kholopov, P. N. et al. (1985). *Information Bulletin on Variable Stars* 2681, p. 1.
Khouri, T. et al. (2014). A&A 561, A5, A5.
Khouri, T. et al. (2016). A&A 591, A70, A70.
Kim, H. and R. E. Taam (2012). ApJ 759.1, 59, p. 59.
Kim, H., S.-Y. Liu, and Ronald E. Taam (2019). ApJS 243.2, 35, p. 35.
Klein, U. (2006). *Radio astronomy: tools, applications and impacts*. University of Bonn.
Kłos, J. and F. Lique (2008). MNRAS 390, pp. 239–244.
Knapp, G. R. and M. Morris (1985). ApJ 292, p. 640.
Knapp, G. R., A. Jorissen, and K. Young (1997). A&A 326, pp. 318–328.
Knapp, G. R. et al. (1998). ApJS 117.1, pp. 209–231.
Knapp, G. R. et al. (2003). A&A 403, pp. 993–1002.
Knowles, S. H. et al. (1969). BAAS. Vol. 1, p. 249.
Kwan, J. and R. A. Linke (1982). ApJ 254, pp. 587–593.
Lamers, H. and J. Cassinelli (1999). *Introduction to Stellar Winds*. Cambridge University Press.
Lattanzio, John C. (1989). ApJ 344, p. L25.
Lebzelter, T., L. L. Kiss, and K. H. Hinkle (2000). A&A 361, pp. 167–174.
Li, X. et al. (2014). A&A 568, A111, A111.
Lique, F et al. (2005). *The Journal of chemical physics* 123.13, p. 134316.
Lique, F., A. Spielfiedel, and J. Cernicharo (2006). A&A 451.3, pp. 1125–1132.

Lique, F et al. (2006). *Astronomy & Astrophysics* 450.1, pp. 399–405.
Lique, F. and A. Spielfiedel (2007). A&A 462, pp. 1179–1185.
Little-Marenin, I. R. (1986). ApJ 307, pp. L15–L19.
Liu, J. and B. Jiang (2017). *The Astronomical Journal* 153.4, p. 176.
Lodders, K. and Jr. Fegley B. (1999). *Asymptotic Giant Branch Stars*. Ed. by T. Le Bertre, A. Lebre, and C. Waelkens. Vol. 191. IAU Symposium, p. 279.
Lombaert, R. et al. (2012). A&A 544, L18, p. L18.
Loup, C. et al. (1993). A&AS 99, pp. 291–377.
Lovas, F. J. et al. (1992). *The Astrophysical Journal* 399, pp. 325–329.
Lucas, R. et al. (1992). A&A 262, pp. 491–500.
Lucas, R. et al. (1995). Ap&SS 224, pp. 293–296.
Lugaro, M. et al. (2012). ApJ 747.1, 2, p. 2.
MacKay, D. D. S. and S. B. Charnley (1999). MNRAS 302, pp. 793–800.
Maercker, M. et al. (2016). A&A 591, A44, A44.
Marr, J. M., R. L. Snell, and S. E. Kurtz (2015). *Fundamentals of Radio Astronomy: Observational Methods*. Vol. 13. CRC Press.
Massalkhi, S. et al. (2018). A&A 611, A29, A29.
Massalkhi, S., M. Agúndez, and J. Cernicharo (2019). A&A 628, A62, A62.
Massalkhi, S. et al. (2020). *arXiv e-prints*, arXiv:2007.00572.
Mauron, N. and P. J. Huggins (2000). A&A 359, pp. 707–715.
McCarthy, M. C., C. A. Gottlieb, and J. Cernicharo (2019). *Journal of Molecular Spectroscopy* 356, pp. 7–20.
McDonald, I. et al. (2018). MNRAS 481.4, pp. 4984–4999.
Merrill, Paul W. (1952). ApJ 116, p. 21.
Mihalas, D. (1978). *Stellar atmospheres*. W. H. Freeman.
Morris, M. and M. Jura (1983). ApJ 264, pp. 546–553.
Müller, Holger S. P. and S. Brünken (2005a). *Journal of Molecular Spectroscopy* 232.2, pp. 213–222.
Müller, Holger S. P. et al. (2005b). *Journal of Molecular Structure* 742.1-3, pp. 215–227.
Müller, Holger S. P. et al. (2007). *Physical Chemistry Chemical Physics* 9.13, pp. 1579–1586.
Müller, Holger S. P. et al. (2012). *Journal of Molecular Spectroscopy* 271, pp. 50–55.
Nakashima, Jun-ichi (2005). ApJ 620.2, pp. 943–947.
Neri, R. et al. (1998). A&AS 130, pp. 1–64.
Neugebauer, G. and R. B. Leighton (1969). *Two-micron sky survey. A preliminary catalogue*.
Neugebauer, G. et al. (1984). ApJ 278, pp. L1–L6.
Nowotny, W. et al. (2005). A&A 437.1, pp. 285–296.
Nyman, L.-A. et al. (1993). A&A 269, pp. 377–389.
Ohishi, M. et al. (1989a). ApJ 345, p. L83.
Ohishi, M. et al. (1989b). ApJ 345, pp. L83–L86.
Ohnaka, K. et al. (2011). A&A 529, A163, A163.
Olofsson, H. et al. (1982). A&A 107, pp. 128–144.
Olofsson, H., K. Eriksson, and B. Gustafsson (1988). A&A 196, pp. L1–L4.
Olofsson, H. et al. (1990). A&A 230, pp. L13–L16.
Olofsson, H. et al. (1993a). ApJS 87, pp. 267–304.
Olofsson, H. et al. (1993b). ApJS 87, p. 305.
Olofsson, H. et al. (1996). A&A 311, pp. 587–615.
Olofsson, H. et al. (2000). A&A 353, pp. 583–597.

Olofsson, H. et al. (2002). A&A 391, pp. 1053–1067.
Omont, A. et al. (1993). A&A 267, pp. 490–514.
Paczyński, B. (1971). Acta Astron. 21, p. 417.
Pardo, J. R., J. Cernicharo, and E. Serabyn (2001). *IEEE Transactions on Antennas and Propagation* 49.12, pp. 1683–1694.
Pardo, J. R. et al. (2004). A&A 424, pp. 145–156.
Pardo, J. R. et al. (2018). A&A 615, L4, p. L4.
Patel, D, D Margolese, and TR Dykea) (1979). *The Journal of Chemical Physics* 70.6, pp. 2740–2747.
Patel, N. A. et al. (2011). ApJS 193, 17, p. 17.
Pattillo, R. J. et al. (2018). ApJ 858, 10, p. 10.
Penzias, A. A. and C. A. Burrus (1973). ARA&A 11, p. 51.
Piñeiro, A. L., R. H. Tipping, and C. Chackerian (1987). *Journal of Molecular Spectroscopy* 125, pp. 184–187.
Prasad, S. S. and W. T. Huntress Jr. (1980). ApJS 43, pp. 1–35.
Prasad, S. S. and S. P. Tarafdar (1983). ApJ 267, pp. 603–609.
Price, S. D. and R. G. Walker (1976). Interim Report Air Force Geophysics Lab.
Ramstedt, S. et al. (2008). A&A 487.2, pp. 645–657.
Ramstedt, S., F. L. Schöier, and H. Olofsson (2009). *Astronomy & Astrophysics* 499.2, pp. 515–527.
Ramstedt, S. and H. Olofsson (2014). A&A 566, A145, A145.
Raymonda, J. W., J. S. Muenter, and W. A. Klemperer (1970). *The Journal of Chemical Physics* 52.7, pp. 3458–3461.
Reid, M. J. and K. M. Menten (1997). *The Astrophysical Journal* 476.1, p. 327.
Reimers, D. (1975). *Memoires of the Societe Royale des Sciences de Liege* 8, pp. 369–382.
Rybicki, G. B. and D. G. Hummer (1991). A&A 245, pp. 171–181.
Rybicki, G. B. and D. G. Hummer (1992). A&A 262, pp. 209–215.
Rybicki, G. B. and A. P. Lightman (2008). *Radiative processes in astrophysics*. John Wiley & Sons.
Ryde, N. and F. L. Schöier (2001). ApJ 547.1, pp. 384–392.
Sahai, R. et al. (2019). *IAU Symposium*. Ed. by Franz Kerschbaum, Martin Groenewegen, and Hans Olofsson. Vol. 343. IAU Symposium, pp. 495–497.
Sánchez Contreras, C. and R. Sahai (2012). ApJS 203, 16, p. 16.
Sanz, M. E., M. C McCarthy, and P. Thaddeus (2003). *The Journal of chemical physics* 119.22, pp. 11715–11727.
Sarre, P. J., M. E. Hurst, and T. Lloyd Evans (2000). MNRAS 319, pp. 103–110.
Schöier, F. L. and H. Olofsson (2001). A&A 368, pp. 969–993.
Schöier, F. L., N. Ryde, and H. Olofsson (2002). A&A 391, pp. 577–586.
Schöier, F. L. et al. (2004). A&A 422, pp. 651–663.
Schöier, F. L., M. Lindqvist, and H. Olofsson (2005). A&A 436, pp. 633–646.
Schöier, F. L., H. Olofsson, and A. A. Lundgren (2006). A&A 454, pp. 247–255.
Schöier, F. L. et al. (2006). ApJ 649.2, pp. 965–972.
Schöier, F. L. et al. (2007). A&A 473, pp. 871–882.
Schöier, F. L. et al. (2011). A&A 530, A83, A83.
Schöier, F. L. et al. (2013). A&A 550, A78, A78.
Schwarzschild, M. and R. H arm (1965). ApJ 142, p. 855.
Skinner, C. J. et al. (1999). MNRAS 302, pp. 293–304.
Sloan, G. C., I. R. Little-Marenin, and S. D. Price (1998). AJ 115, p. 809.
Sloan, G. C. et al. (2003). ApJ 594.1, pp. 483–495.
Sloan, G. C. et al. (2008). ApJ 686.2, pp. 1056–1081.
Smith, V. V. and D. L. Lambert (1988). ApJ 333, p. 219.

Smolders, K. et al. (2012). A&A 540, A72, A72.

Sobolev, V. V. (1957). Soviet Ast. 1, p. 678.

Sobolev, V. V. (1960). *Moving envelopes of stars*. Harvard University Press.

Solomon, P. et al. (1971). ApJ 163, p. L53.

Speck, A. K. et al. (2000). A&AS 146, pp. 437–464.

Speck, A. K. et al. (2009). ApJ 691, pp. 1202–1221.

Stroud, R. M. and T. J. Bernatowicz (2005). *36th Annual Lunar and Planetary Science Conference*. Ed. by Stephen Mackwell and Eileen Stansbery. Lunar and Planetary Science Conference, p. 2010.

Suenram, R. D., F. J. Lovas, and K. Matsumura (1989). ApJ 342, pp. L103–L105.

Suh, K. W. (1999). MNRAS 304.2, pp. 389–405.

Suh, K. W. (2000). MNRAS 315, pp. 740–750.

Tejero, J. and J. Cernicharo (1991). *Modelos de Equilibrio Termodinámico Aplicados a Envolturas Circunestelares de Estrellas Evolucionadas (Madrid: IGN)*.

Teyssier, D. et al. (2006). A&A 450.1, pp. 167–179.

Thaddeus, P., S. E. Cummins, and R. A. Linke (1984). ApJ 283, pp. L45–L48.

Toboła, R. et al. (2008). *Journal of Physics B Atomic Molecular Physics* 41.15, 155702, p. 155702.

Treffers, R. and M. Cohen (1974). ApJ 188, pp. 545–552.

Tsuji, T. (1973). A&A 23, p. 411.

Van de Sande, M. et al. (2018). A&A 616, A106, A106.

Van de Sande, M. et al. (2019). MNRAS 490.2, pp. 2023–2041.

Van de Sande, M. et al. (2020). A&A 634, C1, p. C1.

Van Dishoeck, E. F. (1988). *Rate Coefficients in Astrochemistry*. Ed. by T. J. Millar and D. A. Williams. Vol. 146. Astrophysics and Space Science Library, pp. 49–72.

Van Leeuwen, F. et al. (1997). MNRAS 287.4, pp. 955–960.

Van Zadelhoff, G. J. et al. (2002). A&A 395, pp. 373–384.

Vassiliadis, E. and P. R. Wood (1993). ApJ 413, p. 641.

Velilla Prieto, L. et al. (2015). ApJ 805, L13, p. L13.

Velilla Prieto, L. et al. (2017). A&A 597, A25, A25.

Velilla-Prieto, L. et al. (2019). A&A 629, A146, A146.

Wachter, A. et al. (2002). A&A 384, pp. 452–459.

Wagenhuber, J. and M. A. T. Groenewegen (1998). A&A 340, pp. 183–195.

Wallerstein, G. and G. R. Knapp (1998). ARA&A 36, pp. 369–434.

Wenger, M. et al. (2000). A&AS 143, pp. 9–22.

Whitelock, Patricia A., Michael W. Feast, and Floor Van Leeuwen (2008). MNRAS 386.1, pp. 313–323.

Willacy, Karen and Isabelle Cherchneff (1998). A&A 330, pp. 676–684.

Willson, L. A. (1976). ApJ 205, pp. 172–181.

Willson, L. A. (2000). ARA&A 38, pp. 573–611.

Wilson, R. W. et al. (1971). ApJ 169, p. L35.

Wilson, W. J. and A. H. Barrett (1968). *Science* 161.3843, pp. 778–779.

Winnewisser, G. and R. L. Cook (1968). *Journal of Molecular Spectroscopy* 28.2, pp. 266–268.

Winters, J. M. et al. (2007). A&A 475.2, pp. 559–568.

Wirsich, J. (1994). ApJ 424, pp. 370–375.

Wood, P. R. (2010). Mem. Soc. Astron. Italiana 81, p. 883.

Woodruff, H. C. et al. (2004). A&A 421, pp. 703–714.

Woodruff, H. C. et al. (2008). ApJ 673.1, pp. 418–433.
Yamamura, I. et al. (1999). A&A 341, pp. L9–L12.
Yang, X., P. Chen, and J. He (2004). A&A 414, pp. 1049–1063.
Yasuda, Y. and T. Kozasa (2012). ApJ 745, 159, p. 159.
Zhang, Bo et al. (2017). ApJ 849.2, 99, p. 99.
Zhang, K., B. W. Jiang, and A. Li (2009a). ApJ 702, pp. 680–685.
Zhang, Y., S. Kwok, and J.-i. Nakashima (2009b). ApJ 700, pp. 1262–1281.
Zhang, Y., S. Kwok, and Dinh-V-Trung (2009c). ApJ 691, pp. 1660–1677.
Zhukovska, S. and H.-P. Gail (2008). A&A 486, pp. 229–237.
Zijlstra, Albert A. et al. (2006). MNRAS 370.4, pp. 1961–1978.
Ziurys, L. M. (2006). *Proceedings of the National Academy of Science* 103.33, pp. 12274–12279.
Ziurys, L. M. et al. (2002). ApJ 564.1, pp. L45–L48.
Zuckerman, B. (1980). ARA&A 18, pp. 263–288.

Part III

Appendix

A&A 611, A29 (2018)
DOI: 10.1051/0004-6361/201732038

Astronomy & Astrophysics

Abundance of SiC_2 in carbon star envelopes*

Evidence that SiC_2 is a gas-phase precursor of SiC dust

S. Massalkhi[1], M. Agúndez[1], J. Cernicharo[1], L. Velilla Prieto[1], J. R. Goicoechea[1], G. Quintana-Lacaci[1], J. P. Fonfría[1], J. Alcolea[2], and V. Bujarrabal[3]

[1] Grupo de Astrofísica Molecular, Instituto de Ciencia de Materiales de Madrid, CSIC, C/ Sor Juana Inés de la Cruz 3, 28049 Cantoblanco, Spain
e-mail: sarah.massalkhi@csic.es
[2] Observatorio Astronómico Nacional (IGN), C/ Alfonso XII 3, 28014 Madrid, Spain
[3] Observatorio Astronómico Nacional (IGN), Apartado de Correos 112, 28803 Alcalá de Henares, Madrid, Spain

Received 4 October 2017 / Accepted 27 October 2017

ABSTRACT

Context. Silicon carbide dust is ubiquitous in circumstellar envelopes around C-rich asymptotic giant branch (AGB) stars. However, the main gas-phase precursors leading to the formation of SiC dust have not yet been identified. The most obvious candidates among the molecules containing an Si–C bond detected in C-rich AGB stars are SiC_2, SiC, and Si_2C. To date, the ring molecule SiC_2 has been observed in a handful of evolved stars, while SiC and Si_2C have only been detected in the C-star envelope IRC +10216.
Aims. We aim to study how widespread and abundant SiC_2, SiC, and Si_2C are in envelopes around C-rich AGB stars, and whether or not these species play an active role as gas-phase precursors of silicon carbide dust in the ejecta of carbon stars.
Methods. We carried out sensitive observations with the IRAM 30 m telescope of a sample of 25 C-rich AGB stars to search for emission lines of SiC_2, SiC, and Si_2C in the λ 2 mm band. We performed non-LTE excitation and radiative transfer calculations based on the LVG method to model the observed lines of SiC_2 and to derive SiC_2 fractional abundances in the observed envelopes.
Results. We detect SiC_2 in most of the sources, SiC in about half of them, and do not detect Si_2C in any source except IRC +10216. Most of these detections are reported for the first time in this work. We find a positive correlation between the SiC and SiC_2 line emission, which suggests that both species are chemically linked; the SiC radical is probably the photodissociation product of SiC_2 in the external layer of the envelope. We find a clear trend where the denser the envelope, the less abundant SiC_2 is. The observed trend is interpreted as evidence of efficient incorporation of SiC_2 onto dust grains, a process that is favored at high densities owing to the higher rate at which collisions between particles take place.
Conclusions. The observed behavior of a decline in the SiC_2 abundance with increasing density strongly suggests that SiC_2 is an important gas-phase precursor of SiC dust in envelopes around carbon stars.

Key words. astrochemistry – molecular processes – stars: abundances – stars: AGB and post-AGB – stars: carbon – circumstellar matter

1. Introduction

Low- and intermediate-mass stars, with initial masses <8 $M_\odot$, experience in their late stages of evolution known as the asymptotic giant branch (AGB), intense mass-loss processes which result in circumstellar envelopes (CSEs) made up of molecules and dust grains. AGB stars are the main sources of interstellar dust in the Galaxy (Gehrz 1989). The chemical nature of the synthesized dust is determined by the C/O elemental abundance ratio at the surface of the AGB star. Dust is mainly composed of silicates in envelopes around oxygen-rich stars (C/O < 1), while carbonaceous and silicon carbide dust is formed around carbon-rich stars (C/O > 1; e.g., Swamy 2005). The dust formation process involves a first step in which condensation nuclei of nanometer size are formed from some gas-phase precursors of highly refractory character, a process that takes place in the surroundings of the stellar atmosphere. The second step involves the growth of the nuclei to micrometer sizes by accretion and coagulation as the material is pushed out by the stellar wind (Gail et al. 1984). What the gas-phase building blocks of condensation nuclei are and how these particles evolve toward the micrometer-sized grains that populate the interstellar medium are key questions that are not yet well understood.

In this article we perform an observational study to constrain the main gas-phase precursors of silicon carbide (SiC) dust in C-rich AGB stars. The presence of SiC dust in circumstellar envelopes C-rich AGB stars was established through the observation of a solid-state emission band at ~11.3 μm (Hackwell 1972; Treffers & Cohen 1974). The 11.3 μm feature has been observed toward a large number of C-rich AGB stars with the IRAS and ISO satellites (e.g., Little-Marenin 1986; Chan & Kwok 1990; Yang et al. 2004). However, what the gas-phase precursors of SiC dust are is still a pending question.

Various molecules containing an Si−C bond have been observed in envelopes around C-rich AGB stars and are potential gas-phase precursors of SiC dust. The ring molecule SiC_2 has long been observed in the atmospheres of optically visible carbon stars through the Merrill-Sanford electronic bands (see, e.g., Sarre et al. 2000). Thaddeus et al. (1984) reported the first observation of the rotational spectrum of SiC_2 toward the highly reddened envelope IRC +10216; since then observations of this

* Based on observations carried out with the IRAM 30 m Telescope. IRAM is supported by INSU/CNRS (France), MPG (Germany), and IGN (Spain).

Table 1. Sample of carbon stars.

Name	RA J2000.0	Dec J2000.0	V_{LSR} (km s^{-1})	D (pc)	$T_\star$ (K)	$L_\star$ ($L_\odot$)	$\dot{M}$ ($M_\odot$ yr^{-1})	V_{exp} (km s^{-1})	$T_d(r_c)$ (K)	r_c (cm)	Ψ
IRC +10216	09:47:57.45	+13:16:43.9	−26.5	130 [a]	2330 [a]	8750 [a]	2.0×10^{-5} [a]	14.5	800 [a]	2.0×10^{14} [a]	300 [a]
CIT 6	10:16:02.27	+30:34:18.6	−1	440 [g]	1800 [g]	10000 [g]	6.0×10^{-6} [g]	17	1000 [g]	2.1×10^{14} [g]	141 [d]
CRL 3068	23:19:12.24	+17:11:33.4	−31.5	1300 [g]	1800 [g]	10900 [g]	2.5×10^{-5} [g]	14.5	1500 [g]	2.0×10^{14} [g]	174 [d]
S Cep	21:35:12.83	+78:37:28.2	−15.3	380 [k]	2200 [k]	7300 [k]	1.2×10^{-6} [k]	22.5	1400 [k]	5.8×10^{13} [k]	360 [d]
IRC +30374	19:34:09.87	+28:04:06.3	−12.5	1200 [j]	2000 [j]	9800 [j]	1.0×10^{-5} [j]	25	1000 [j]	2.2×10^{14} [j]	1008 [d]
Y CVn	12:45:07.83	+45:26:24.9	+22	220 [k]	2200 [k]	4400 [k]	1.5×10^{-7} [k]	7	1500 [k]	8.7×10^{13} [k]	500 [h]
LP And	23:34:27.53	+43:33:01.2	−17	630 [g]	1900 [g]	9600 [g]	7.0×10^{-6} [g]	14.5	1100 [g]	1.8×10^{14} [g]	288 [d]
V Cyg	20:41:18.27	+48:08:28.8	+13.5	366 [g]	2300 [g]	6000 [g]	1.6×10^{-6} [g]	12	1400 [g]	9.4×10^{13} [g]	364 [d]
UU Aur	06:36:32.84	+38:26:43.8	+6.7	260 [k]	2800 [k]	6900 [k]	2.4×10^{-7} [k]	10.6	1500 [k]	6.3×10^{13} [k]	11111 [b]
V384 Per	03:26:29.51	+47:31:48.6	−16.8	560 [k]	2000 [k]	8100 [k]	2.3×10^{-6} [b]	15.5	1300 [k]	1.0×10^{14} [k]	584 [d]
IRC +60144	04:35:17.54	+62:16:23.8	−48.8	1030 [b]	2000 [b]	7800 [b]	3.7×10^{-6} [b]	19.5	1200 [n]	2.0×10^{14} [b]	11 [b]
U Cam	03:41:48.17	+62:38:54.4	+6	430 [i]	2695 [i]	7000 [i]	2.0×10^{-7} [i]	13	1500 [j]	4.4×10^{13} [j]	833 [i]
V636 Mon	06:25:01.43	−09:07:15.9	+10	880 [f]	2500 [n]	8472 [e]	5.8×10^{-6} [f]	20	1200 [n]	1.7×10^{14} [n]	300 [n]
IRC +20370	18:41:54.39	+17:41:08.5	−0.8	600 [k]	2200 [k]	7900 [k]	3.0×10^{-6} [b]	14	1500 [k]	8.1×10^{13} [k]	266 [d]
R Lep	04:59:36.35	−14:48:22.5	+11.5	432 [b]	2200 [b]	5500 [b]	8.7×10^{-7} [b]	17.5	1000 [g]	1.8×10^{14} [b]	2000 [b]
W Ori	05:05:23.72	+01:10:39.5	−1	220 [k]	2600 [k]	3500 [k]	7.0×10^{-8} [k]	11	1500 [k]	4.3×10^{13} [k]	333 [h]
CRL 67	00:27:41.10	+69:38:51.5	−27.5	1410 [d]	2500 [n]	9817 [d]	1.1×10^{-5} [d]	16	1200 [n]	1.8×10^{14} [n]	495 [d]
CRL 190	01:17:51.62	+67:13:55.4	−39.5	2790 [d]	2500 [c]	16750 [d]	6.4×10^{-5} [d]	17	1000 [c]	4.7×10^{14} [c]	424 [d]
S Aur	05:27:07.45	+34:08:58.6	−17	300 [k]	3000 [k]	8900 [k]	4.0×10^{-7} [k]	24.5	1500 [k]	7.3×10^{13} [k]	500 [h]
V Aql	19:04:24.15	−05:41:05.4	+53.5	330 [k]	2800 [k]	6500 [k]	1.4×10^{-7} [k]	8	1500 [k]	6.1×10^{13} [k]	500 [h]
CRL 2513	20:09:14.25	+31:25:44.9	+17.5	1760 [d]	2500 [c]	8300 [c]	2.0×10^{-5} [d]	25.5	1200 [c]	1.6×10^{14} [c]	453 [d]
CRL 2477	19:56:48.43	+30:43:59.9	+5	3380 [m]	3000 [m]	13200 [m]	1.1×10^{-4} [m]	20	1800 [m]	2.8×10^{14} [m]	532 [d]
CRL 2494	20:01:08.51	+40:55:40.2	+29	1480 [b]	2400 [b]	10200 [b]	7.5×10^{-6} [b]	20	1200 [n]	2.3×10^{14} [b]	436 [d]
RV Aqr	21:05:51.74	−00:12:42.0	+0.5	670 [k]	2200 [k]	6800 [k]	2.3×10^{-6} [b]	15	1300 [k]	7.6×10^{13} [k]	200 [h]
ST Cam	04:51:13.35	+68:10:07.6	−13.6	360 [k]	2800 [k]	4400 [k]	1.3×10^{-7} [k]	8.9	1500 [k]	5.0×10^{13} [k]	500 [h]

References. [a] Agúndez et al. (2012), [b] Danilovich et al. (2015), [c] Groenewegen et al. (1998), [d] Groenewegen et al. (2002), [e] Guandalini & Cristallo (2013), [f] Guandalini et al. (2006), [g] Ramstedt et al. (2014), [h] Schöier & Olofsson et al. (2001), [i] parameters of the present-day wind of U Cam from Schöier et al. (2005), [j] Schöier et al. (2006), [k] Schöier et al. (2013), [m] Speck et al. (2009), [n] assumed value for the stellar effective temperature $T_\star$ is 2500 K, for the condensation radius r_c is 5 $R_\star$, for the dust temperature at the condensation radius $T_d(r_c)$ is 1200 K, and for the gas-to-dust mass ratio Ψ is 300.

molecule have been reported in only a few other C-rich AGB or post-AGB objects: IRAS 15194−5115 (Nyman et al. 1993), CRL 2688 (Bachiller et al. 1997), CIT 6 (Zhang et al. 2009a), and CRL 3068 (Zhang et al. 2009b). The diatomic molecule SiC was found by Cernicharo et al. (1989) in IRC +10216, and more recently Cernicharo et al. (2015b) have reported on the discovery of Si_2C toward the same source. IRC +10216 is the only source where SiC_2 has been thoroughly studied across the mm and sub-mm ranges (Lucas et al. 1995; Cernicharo et al. 2010; Patel et al. 2011; Müller et al. 2012; Fonfría et al. 2014; Velilla Prieto et al. 2015) and where SiC and Si_2C detections have been reported. The scenario emerged from the studies of IRC +10216 is that only SiC_2 and Si_2C are present in the innermost regions, while SiC is probably a photodissociation product of these two triatomic molecules and it is thus present in the outer envelope. The U-shaped line profiles of SiC (Cernicharo et al. 2000) and the upper limits derived to its abundance in the inner envelope (Velilla Prieto et al. 2015) support this idea. Moreover, chemical equilibrium calculations predict abundant SiC_2 and Si_2C but little SiC in the hot and dense surroundings of the AGB star (Tejero & Cernicharo 1991; Yasuda & Kozasa 2012; Cernicharo et al. 2015b). It therefore seems that the gas-phase molecule SiC is not an important building block of SiC dust, while SiC_2 and Si_2C are probably the main gas-phase precursors. In addition to these species, other molecules containing an Si−C bond detected in IRC +10216 are SiC_3 (Apponi et al. 1999), SiC_4 (Ohishi et al. 1989), SiCN (Guélin et al. 2000), SiH_3CN, and CH_3SiH_3 (Agúndez et al. 2014; Cernicharo et al. 2017), but their abundances are low and the observed line profiles suggest that they are formed in the external layers of the envelope.

Most of our knowledge about the role of the SiC_2, SiC, and Si_2C molecules as gas-phase precursors of silicon carbide dust comes from the study of IRC +10216, but little is known about how widespread these molecules are in other carbon stars, what their relative abundances are, and what their role in the formation of SiC dust is. Here we present the results of a systematic survey carried out with the IRAM 30 m telescope to observe these three molecules in a sample of 25 C-rich AGB stars. We report the detection of SiC_2 in most of the sources and of the radical SiC in about half of them. The sample of stars and observational details are presented in Sect. 2 and the main results obtained from the observations in Sect. 3. In Sect. 4 we describe the model and the excitation and radiative transfer calculations, and discuss the results from these calculations in Sect. 5. Finally, we discuss the implications of the derived SiC_2 abundances in Sect. 6, and present our conclusions in Sect. 7.

2. Observations

The observations were carried out in February and May 2016 with the IRAM 30 m telescope, located at Pico Veleta (Spain). We selected a sample of 25 C-rich AGB stars with intense molecular emission, mainly based on the intensity of the HCN J = 1−0 line (Loup et al. 1993; Bujarrabal et al. 1994; Schöier et al. 2013). The list of sources and their parameters are given in Table 1. The coordinates and LSR systemic velocities were taken from the literature (Olofsson et al. 1993; Groenewegen et al. 1996, 2002; Cernicharo et al. 2000; Sánchez Contreras & Sahai 2012) and checked using the SIMBAD astronomical database[1]

[1] http://simbad.u-strasbg.fr/Simbad

(Wenger et al. 2000). For some sources, systemic velocities were not accurately known and thus we determined them from intense lines observed in this study (see below).

We used the E150 receiver in dual side band, with image rejections >10 dB, and observed the frequency ranges 138.5−146.3 GHz and 154.1−161.9 GHz (in the lower and upper side bands, respectively). This spectral setup was chosen to include several strong lines of SiC_2, various lines of Si_2C, and the $J = 4-3$ rotational transition of the radical SiC in its $^3\Pi_2$ state. The strongest lines of these three species covered in the observed frequency range are listed in Table 2. In the IRC +10216 spectrum, the line intensity ratios of the three species are typically SiC_2:Si_2C:SiC ∼ 100:1:10 (Cernicharo et al. 2000, 2015b), and thus we expect that in the rest of the sources of the sample, SiC_2 will be the most easily detectable molecule, while Si_2C will display the weakest lines and thus will be the most difficult to detect. The adopted spectral range also covers lines which are typically intense in carbon-rich circumstellar envelopes, such as HC_3N $J = 16-15$ and $J = 17-16$, C_4H $N = 15-14$ and $N = 17-16$, and SiS $J = 8-7$.

The beam size of the telescope at these frequencies is in the range 15.0−17.5″. We used the wobbler-switching technique, with the secondary mirror nutating by 3′ at a rate of 0.5 Hz. The focus was regularly checked on Venus and Uranus and the pointing of the telescope was systematically checked on a nearby quasar before observing each AGB star. The error in the pointing is estimated to be 2−3″. The E150 receiver was connected to a fast Fourier transform spectrometer providing a spectral resolution of 200 kHz. The weather was good and stable during most of the observations, with typical amounts of precipitable water vapor of 1−3 mm and system temperatures ranging from 80 K to 150 K. The intensity scale, calibrated using two absorbers at different temperatures and the atmospheric transmission model (ATM; Cernicharo 1985; Pardo et al. 2001), is expressed in terms of T_A^*, the antenna temperature corrected for atmospheric absorption and for antenna ohmic and spillover losses. To convert to main beam antenna temperature, T_A^* has to be divided by 0.78 (the ratio of the main beam efficiency to the forward efficiency of the IRAM 30 m telescope at the observed frequencies[2]). The error in the intensities due to calibration is estimated to be ∼20%.

The data were reduced using the software CLASS within the package GILDAS[3]. For each source, we averaged the spectra corresponding to the horizontal and vertical polarizations, subtracted a baseline consisting of a first-order polynomial, and smoothed the resulting spectrum to a spectral resolution of 1 MHz, which is good enough to spectrally resolve the lines whose widths in most sources are typically in the range 15−50 km s^{-1} (7.5−25 MHz at the observed frequencies). Typical on-source integration times, after averaging horizontal and vertical polarizations, were ∼1 h for each source, resulting in T_A^* rms noise levels per 1 MHz channel of 2−5 mK.

3. Results from observations

The observations resulted in the detection of SiC_2 in 22 out of the 25 targeted sources, i.e., all sources except UU Aur, R Lep, and ST Cam. The five rotational transitions of SiC_2 listed in Table 2, which have upper level energies in the range 31−55 K, were clearly detected in most of the 22 sources where SiC_2 was identified. The lines corresponding to the rotational transitions $6_{4,3}-5_{4,2}$ and $6_{4,2}-5_{4,1}$ appear blended together because line widths are larger than the frequency separation of the two transitions, although in most sources each of these lines could be fitted individually. The observed line profiles of SiC_2 are shown in Fig. 1 and the parameters derived from line fits using the `shell` method of CLASS[3] are given in Table A.1. We note that in U Cam, the line profiles of SiC_2 are consistent with emission arising exclusively from the present-day wind, rather than from the detached envelope (compare line profiles in Fig. 1 with those of CO in Schöier et al. 2005).

Table 2. Covered rotational transitions of SiC_2, Si_2C, and SiC.

Transition	Frequency (MHz)	A_{ul} (s^{-1})	E_u (K)
	SiC_2		
$6_{2,5}-5_{2,4}$	140920.171	7.65×10^{-5}	31.5
$6_{4,3}-5_{4,2}$	141751.492	4.87×10^{-5}	55.0
$6_{4,2}-5_{4,1}$	141755.360	4.87×10^{-5}	55.0
$6_{2,4}-5_{2,3}$	145325.875	8.39×10^{-5}	32.0
$7_{0,7}-6_{0,6}$	158499.228	1.23×10^{-4}	31.0
	Si_2C		
$11_{1,11}-10_{0,10}$	144033.475	9.57×10^{-6}	29.3
$22_{2,20}-22_{1,21}$	155600.100	1.54×10^{-5}	115.0
$13_{1,13}-12_{0,12}$	157768.156	1.28×10^{-5}	39.3
$20_{2,18}-20_{1,19}$	157959.754	1.54×10^{-5}	97.4
$18_{2,16}-18_{1,17}$	160644.790	1.55×10^{-5}	81.4
	SiC		
$^3\Pi_2$ $J = 4-3$	157494.101	3.98×10^{-5}	13.2

We also report the detection of SiC in 12 of the 25 targeted C-rich AGB envelopes (see Fig. 2). We note that prior to this study, this radical had been detected only in the C-star envelope IRC +10216 (Cernicharo et al. 1989). The SiC emission line is relatively strong in IRC +10216, CIT 6, CRL 3068, and LP And, while it is marginally detected in IRC +30374, V Cyg, V384 Per, IRC +60144, IRC +20370, CRL 67, CRL 2477, and CRL 2494. In Fig. 3 we compare the velocity-integrated intensity of the SiC $^3\Pi_2$ $J = 4-3$ line with that of the SiC_2 $7_{0,7}-6_{0,6}$ line. We note that the SiC lines are brighter in the sources where SiC_2 is more intense, which suggests that the abundances of both species are correlated, as is expected if the radical SiC is a photodissociation product of SiC_2. This suggests that the nondetection of SiC in some of the sources is probably due to a lack of sensitivity and not due to a low fractional abundance of the radical. The related molecule Si_2C was not detected in any of the targeted sources, with the exception of IRC +10216, which at present is the only source in which this molecule has been identified (Cernicharo et al. 2015b). In IRC +10216, the lines of Si_2C are typically 100 times less intense than those of SiC_2. This difference in intensity is not due to a significant difference in abundance, but it is related to the larger partition function of Si_2C and its lower dipole moment, as discussed in detail by Cernicharo et al. (2015b). If the same relative intensities between SiC_2 and Si_2C holds for the rest of C-star envelopes, the nondetection of disilicon carbide is very likely due to an insufficient sensitivity.

In addition to the lines of SiC_2 and SiC, we also detected within the frequency range covered 138.5−146.3 GHz and 154.1−161.9 GHz, emission lines of other species typically present in the spectra of carbon-rich AGB envelopes. For example, the $J = 16-15$ and $J = 17-16$ lines of HC_3N and the

[2] http://www.iram.es/IRAMES/mainWiki/Iram30mEfficiencies
[3] http://www.iram.fr/IRAMFR/GILDAS

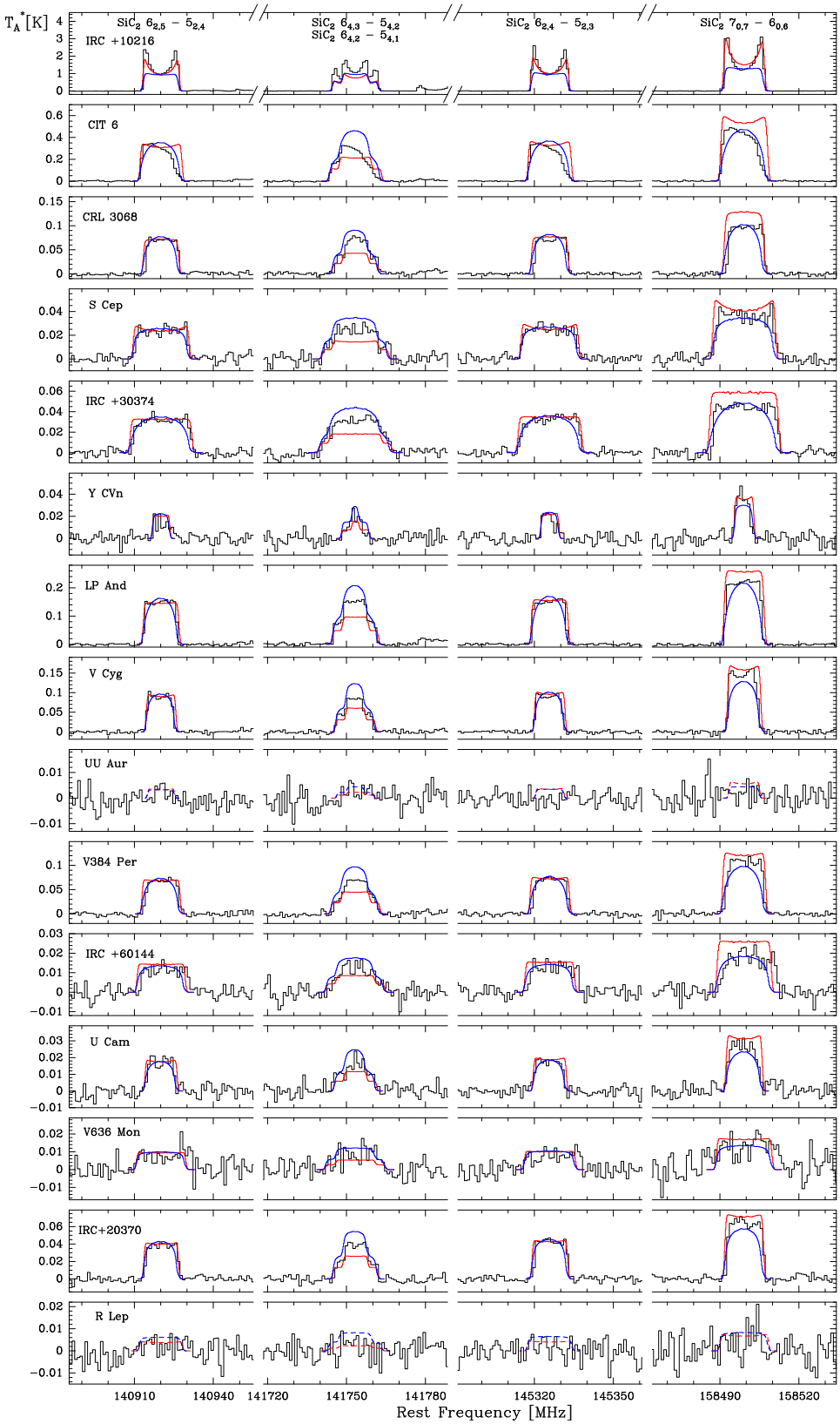

Fig. 1. Rotational lines of SiC_2 observed with the IRAM 30 m telescope in the 25 target sources (black histograms). The spectral resolution of the observed lines is 1 MHz. The blue lines are the calculated emerging line profiles from the best-fit model using the LVG method. The red lines are the predicted line profiles assuming LTE excitation. Dashed lines correspond to calculated lines profiles for those sources where SiC_2 was not detected.

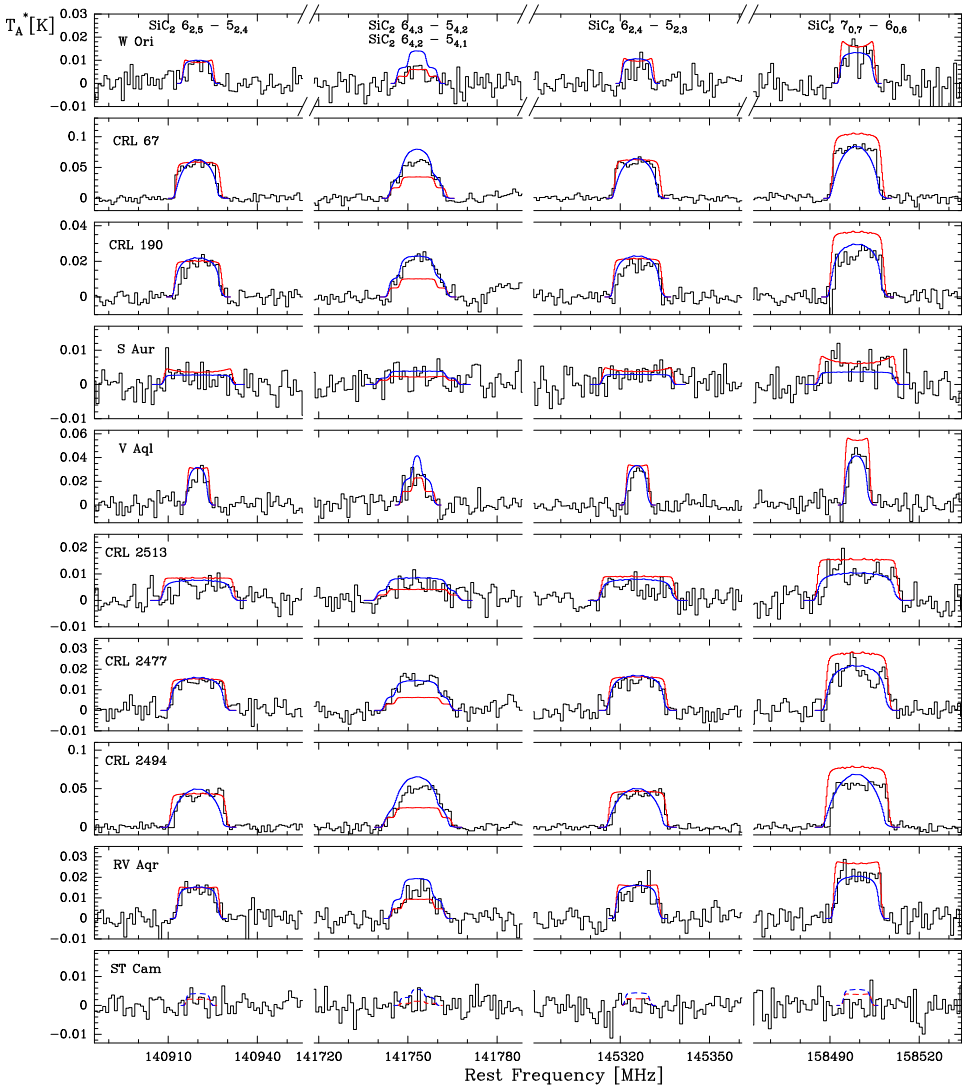

Fig. 1. continued.

J = 3–2 line of some isotopologues of carbon monosulfide, mainly $C^{34}S$ and ^{13}CS, are intense and prevalent among most of the sources. The J = 8–7 line of SiS is observed in many of the envelopes as one of the most intense lines, but it is not even detected in some of the other sources. The N = 15–14 and N = 17–16 lines of C_4H and the N = 14–13 and N = 16–15 of C_3N are also intense in some of the envelopes, although in many of them the lines of these two radicals are below the detection limit. In those sources where molecular emission is most intense, such as CIT 6, CRL 3068, and LP And, lines of other molecules such as l-C_3H, c-C_3H_2, C_2S, HC_5N, and rare isotopologues of CS, SiS, SiC_2, and HC_3N are detected. In a couple of sources, UU Aur and ST Cam, no molecular emission was observed above a detection threshold of a few mK in the covered frequency range.

The availability of strong lines of molecules such as HC_3N, SiS, C_4H, $C^{34}S$, and SiC_2 in our data allows us to derive accurate values of the velocity of the source V_{LSR} and of the terminal expansion velocity of the envelope V_{exp} in most of the sources. These two parameters are reported in the literature mainly from CO J = 1–0 and J = 2–1 lines (Loup et al. 1993; Olofsson et al. 1993; Groenewegen et al. 1996, 2002 with varying degrees of accuracy. We carried out a critical evaluation of the values of V_{LSR} and V_{exp} derived from our data and those in the literature. In cases where our lines have a well-defined shape, the values from our dataset were preferred, whereas when lines show a less clear shape, the values from literature were favored. The final values of V_{LSR} and V_{exp} adopted in this work are given in Table 1.

In this article we focus on the analysis of SiC_2 and leave the interpretation of other molecules for future studies. Silicon dicarbide was detected in most of the targeted sources and we aim to model its emission and determine its abundance in each source to provide a global view of how abundant this molecule is in circumstellar envelopes around C-rich AGB stars.

4. SiC_2 radiative transfer modeling

4.1. Envelope model

We adopted a common physical scenario to model all sources consisting of a spherically symmetric envelope of gas and dust expanding with a constant velocity and mass-loss rate around

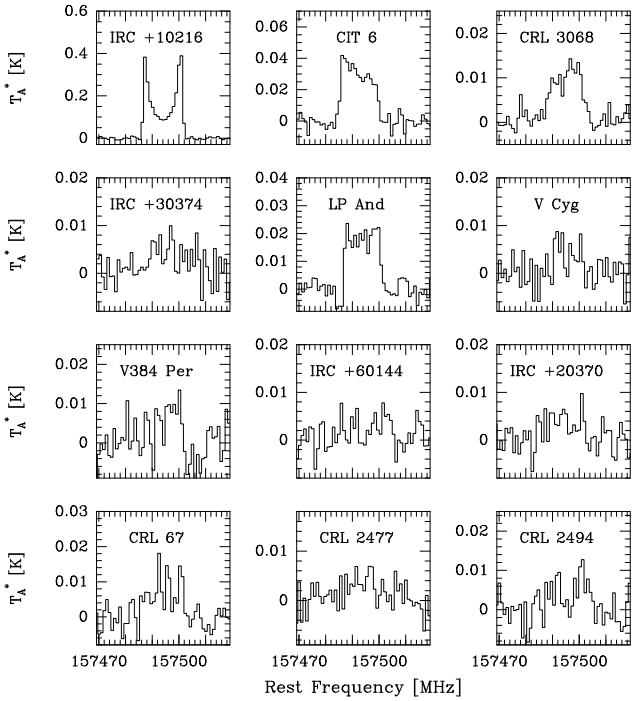

Fig. 2. SiC $^3\Pi_2$ $J = 4{-}3$ line observed in 12 out of the 25 sources in our sample. The spectral resolution is 1 MHz.

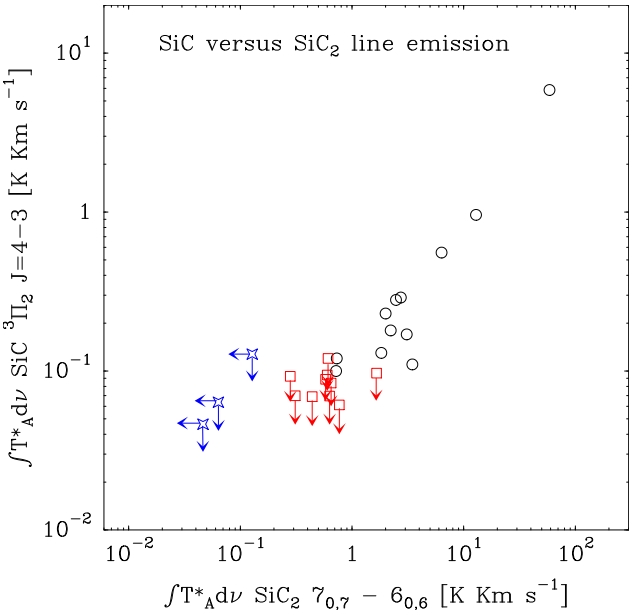

Fig. 3. Velocity-integrated intensity of the SiC $^3\Pi_2$ $J = 4{-}3$ line vs. the velocity-integrated intensity of the SiC_2 $7_{0,7}{-}6_{0,6}$ line. Black circles correspond to sources where both SiC_2 and SiC are detected, red squares to envelopes where SiC_2 is detected but not SiC, and blue stars to sources where neither SiC nor SiC_2 is detected.

a central AGB star. The parameters of the star and envelope adopted for the different sources are detailed in Table 1.

The central AGB star is characterized by an effective temperature T_* and a luminosity L_*. The stellar radius R_* is then determined by T_* and L_* using the Stefan-Boltzmann law. Effective temperatures for the photosphere of AGB stars, typically in the range 2000−3000 K, are difficult to estimate accurately. For most of the stars in our sample, we adopted the values of T_* from studies where T_* is derived by modeling the spectral energy distribution (SED) of each star (Schöier et al. 2005, 2013; Agúndez et al. 2012; Ramstedt & Olofsson 2014; Danilovich et al. 2015). In some cases, the adopted values of T_* are taken from studies where the effective temperature was chosen to be a round number that fitted the SED reasonably well (Groenewegen et al. 1998; Speck et al. 2009). For those objects for which T_* was not available from the literature, we assumed a typical value for AGB stars of 2500 K. Regarding the stellar luminosities L_*, we adopted values from the literature (see references in Table 1) in which they were mostly derived using the period-luminosity relation for Mira variables.

The spherical envelope is described by the radial profile of various physical quantities, such as the gas density, the temperature of gas and dust, the expansion velocity, and the microturbulence velocity. The gas density as a function of the distance r from the star is determined by the law of conservation of mass as

$$n_{\rm g} = \frac{\dot{M}}{\overline{m}_{\rm g}\, 4\pi\, r^2\, V_{\rm e}}, \tag{1}$$

where $n_{\rm g}$ is the number of gas particles per unit volume, $\overline{m}_{\rm g}$ is the average mass of gas particles, $\dot{M}$ is the mass-loss rate, and $V_{\rm e}$ is the expansion velocity of the envelope. We assume that $V_{\rm e}$ is equal to the terminal expansion velocity of the envelope $V_{\rm exp}$ across the entire envelope. This is certainly not true inside the acceleration region, but these inner layers contribute little to the emission of the SiC_2 lines observed here. We adopt $\overline{m}_{\rm g} = 2.3$ amu, adequate for a gas composed mainly of H_2, He with a solar elemental abundance, and CO with an abundance of $\sim 10^{-3}$ relative to H_2. Mass-loss rates were taken from the literature where $\dot{M}$ was determined by modeling observations of multiple CO lines (see references in Table 1).

The radial structure of the gas kinetic temperature $T_{\rm k}$ is described by a power law of the type

$$T_{\rm k} = T_\star \left(\frac{r}{R_\star}\right)^{-\delta}, \tag{2}$$

where R_* is the stellar radius. In reality, the gas kinetic temperature is determined by a balance between the different heating and cooling processes at work, and cannot be accurately described by a single power law across the entire envelope. We do not aim to derive the gas kinetic temperature radial profile for each individual source, and thus for simplicity we adopt a uniform value of $\delta = 0.7$, which is in line with findings from previous studies of circumstellar envelopes around AGB stars (e.g., Schöier & Olofsson 2001; De Beck et al. 2010; Guélin et al. 2018).

The microturbulence velocity is assumed to be $1\,{\rm km\,s^{-1}}$ throughout the envelope, which is within the range of values $0.65{-}1.5\,{\rm km\,s^{-1}}$, derived in the literature for the C-rich envelope IRC +10216 (Skinner et al. 1999; De Beck et al. 2012); however, this parameter has a limited impact when modeling the SiC_2 lines because it is well below the terminal expansion velocity of the wind for all sources.

We also consider the dusty component of the envelope, although, as will be discussed below, in our models dust plays a minor role in the excitation of the rotational lines of SiC_2 observed. We consider spherical grains of amorphous carbon with a radius of 0.1 μm, a mass density of 2 g cm^{-3}, and optical properties from Suh (2000). Dust grains are assumed to be

present from the dust condensation radius r_c with a constant gas-to-dust mass ratio Ψ. The radial structure of the dust temperature T_d is assumed to be given by the power-law expression

$$T_d = T_d(r_c)\left(\frac{r}{r_c}\right)^{-\delta_d}, \quad (3)$$

where we assume $\delta_d = 0.4$ based on theoretical expectations for carbonaceous grains (e.g., Kerschbaum et al. 2007). This value is also close to that derived for IRC +10216 (Agúndez et al. 2012). The values of Ψ, r_c, $T_d(r_c)$ were taken from the literature where they are typically derived by modeling the SED using photometric data, such as IRAS and 2MASS fluxes and in some cases submillimeter data (Schöier et al. 2006, 2013; Ramstedt & Olofsson 2014; Danilovich et al. 2015). In cases where those parameters were not available in the literature, we assumed a typical value of 5 $R_\star$ for r_c, 1200 K for $T_d(r_c)$, and 300 for the gas-to-dust mass ratio Ψ.

The adopted distances to the AGB stars were taken from the literature (see references in Table 1). The data include measurements from HIPPARCOS parallaxes and estimations based on bolometric magnitudes using the period-luminosity relation for Mira variables. When nothing else was available, the distances were estimated assuming $L_* = 10^4\ L_\odot$.

4.2. Excitation and radiative transfer calculations

We performed excitation and radiative transfer calculations to model the line emission of SiC_2 based on the multi-shell large velocity gradient (LVG) method. The circumstellar envelope is divided into a number of concentric shells, each of which has a characteristic set of physical properties and SiC_2 abundance, and statistical equilibrium equations are solved in each of them. In each shell, the contribution of the background radiation field (cosmic microwave background, stellar radiation, and thermal emission from surrounding dust) is included (see Agúndez et al. 2012, for further details). For the current study, the LVG method provides a good compromise between the assumption of local thermal equilibrium (LTE) and more computationally expensive nonlocal methods. Rate coefficients for the rotational excitation of SiC_2 through collisions have been computed theoretically (Chandra & Kegel 2000), which makes it worth using more advanced methods than LTE. Our calculations indicate that the emission from the SiC_2 lines observed here arises from intermediate regions in the envelope where the rotational levels are not fully thermalized (see Sect. 5). Moreover, the observed lines of SiC_2 are optically thin in most sources, which implies that the LVG method should be accurate enough.

In the excitation calculations, we consider rotational levels up to $J = 39$ and $K_a = 20$ within the ground vibrational state of SiC_2 (i.e., a total number of 620 energy levels). Level energies and transition frequencies were calculated from the rotational constants reported by Müller et al. (2012), and line strengths for rotational transitions were computed from the dipole moment, 2.393 ± 0.006 D, measured by Suenram et al. (1989). The rate coefficients for excitation through inelastic collisions with H_2 and He were taken from Chandra & Kegel (2000), who calculated rate coefficients for transitions between the first 40 rotational levels in the temperature range 25−125 K. At temperatures higher than 125 K, we adopted the theoretical rate coefficients calculated at 125 K and did not perform an extrapolation in temperature. This could introduce uncertainties in the excitation calculations. To evaluate the impact of this assumption, we carried out calculations in which we implemented a linear extrapolation in temperature of the rate coefficients at $T_k > 125$ K and verified that the calculated line profiles of the SiC_2 transitions observed were not sensitive to the particular choice of the collision rate coefficients at temperatures higher than 125 K. The reason is that, as is discussed in Sect. 5, most of the SiC_2 emission detected with the IRAM 30 m telescope arise from intermediate regions of the envelope, where gas kinetic temperatures are in the range ∼50−300 K, i.e., not excessively far from the 25−125 K temperature range. Since the calculations of Chandra & Kegel (2000) only include the first 40 rotational levels, for transitions involving higher levels, the de-excitation rate coefficients were approximated using the expression

$$\log\gamma = -10 - 0.25\,(J' - J'') - 0.45\,|K'_a - K''_a|, \quad (4)$$

where γ is the rate coefficient in units of $cm^3\ s^{-1}$, and $'$ and $''$ denote the upper and lower level, respectively. Equation (4) provides a first-order approximation for asymmetric rotors, based on theoretical calculations carried out for the molecules SiC_2 (Chandra & Kegel 2000), SO_2 (Green 1995), and HCO_2^+ (Hammami et al. 2007).

4.3. The SiC_2 radial abundance profile

We consider that SiC_2 is formed close to the star with a given fractional abundance that remains constant throughout the envelope up to the outer regions of the envelope, where it is photodissociated by the ambient ultraviolet radiation field of the local interstellar medium. To compute the falloff of abundance due to photodissociation, we assume that the photodissociation rate of SiC_2 is given by the expression $\alpha\exp(-\beta A_V)$, where A_V is the visual extinction. We adopt an unattenuated rate of $\alpha = 10^{-10}\ s^{-1}$ and a dust shielding factor of $\beta = 1.7$, values which are merely educated guesses (MacKay & Charnley 1999) because the photodissociation cross section of SiC_2 is not well known. The radial variation of the SiC_2 abundance in the expanding envelope is then given by the differential equation (Jura & Morris 1981; Huggins & Glassgold 1982)

$$\frac{df}{dr} = -\frac{\alpha}{V_{exp}}\exp\left[-\left(\frac{r_d}{r}\right)\right] f, \quad (5)$$

where f is the fractional abundance of SiC_2 relative to H_2 and r_d is a parameter that can be considered as a photodissociation radius and which is given by

$$r_d = \frac{\beta\,\dot{M}}{4\pi\,V_{exp}\,\overline{m}_g\,1.87\times10^{21}}, \quad (6)$$

where the numerical value is the canonical N_H/A_V ratio given by Bohlin et al. (1978) for the local interstellar medium. The solution to Eq. (5) can be expressed as

$$\ln\frac{f}{f_0} = -\frac{\alpha}{V_{exp}}\left\{\left[r_d\,E_i\left(-\frac{r_d}{r}\right) + r\,e^{(-r_d/r)}\right] - \left[r_d\,E_i\left(-\frac{r_d}{R_*}\right) + R_*\,e^{(-r_d/R_*)}\right]\right\}, \quad (7)$$

where E_i is the exponential integral. This approach provides a simple and accurate way to take into account the abundance falloff due to photodissociation. Once the physical structure of the envelope is set and a given initial abundance f_0 is chosen, the abundance profile $f(r)$ becomes fully described by Eq. (7). We note that it is likely that SiC_2 can experience an abundance decline around the dust formation zone. The adopted abundance

profile, however, does not include such a feature since we are tracing a specific region of the envelope, more specifically the intermediate one (see Sect. 5), and thus it is not possible to accurately derive the radial abundance profile from the very inner regions out to the outer envelope. In this work we thus determine the mean abundance of SiC_2 in the intermediate regions of the envelope of the studied sources.

In summary, to model the emission lines of SiC_2 and determine its abundance in the observed sources we constructed a model of the envelope for each source, as described in Sect. 4.1, with the parameters given in Table 1. We then performed excitation and radiative transfer calculations, as explained in Sect. 4.2, using the abundance profile described in Sect. 4.3. We varied the initial fractional abundance of SiC_2 relative to H_2, f_0 in Eq. (7), until the calculated line profiles matched the observed ones. We choose as the best-fit model the one that results in the best overall agreement between calculated and observed line profiles for the entire set of SiC_2 lines observed. In those cases where no lines of SiC_2 are detected, we derive upper limits to the abundance of SiC_2 by choosing the maximum abundance that results in line intensities compatible with the noise level of the observations.

5. Results from SiC_2 radiative transfer modeling

In most sources (see Fig. 1), the shapes of the SiC_2 lines observed are nearly flat-topped, which is indicative of optically thin emission not resolved by the 15.0−17.5″ beam of the IRAM 30 m telescope. One notable exception is IRC +10216, whose close proximity (130 pc) means that the emission is spatially resolved by the telescope beam, and the line profiles show a marked double-peaked character. The calculated line profiles resulting from our best-fit LVG model for each of the sources are shown in blue in Fig. 1, where they are compared with the observed line profiles. The agreement between calculated and observed line shapes is good in most sources, except in IRC +10216, for which the LVG model produces a less marked U-shape than observed, and a few sources like LP And, for which the calculated lines are more curved than flat-topped; in other words, in some sources the LVG model seems to result in lines that are more optically thick than indicated by the observed line shapes. To investigate this, we also ran models where we assumed LTE excitation for SiC_2. These models tend to produce line shapes that are in better agreement with the observed ones in sources like IRC +10216, where calculated line profiles have a clearer U-shaped character, and LP And, where line shapes are more flat-topped (see red lines in Fig. 1). This suggests that the LVG model lacks sufficient excitation for the levels involved in the observed SiC_2 transitions. There are various possible causes of the suspected lack of excitation, which we discuss below.

According to the LVG model, the excitation of the rotational levels of SiC_2 in the envelopes studied is dominated by inelastic collisions with H_2 and He. Even though thermal emission from dust is included in the model, it has little impact on the excitation of the observed SiC_2 rotational lines. The five lines of SiC_2 observed here involve upper levels with relatively low energies (31−55 K), and thus are preferentially excited in intermediate layers of the envelope where gas kinetic temperatures are of this order. In Fig. 4 we show the contribution to the velocity-integrated intensity of the five SiC_2 lines observed as a function of the impact parameter relative to the position of the star for two sources in our sample, U Cam and IRC +30374. These two envelopes are representative of very different mass-loss rates. While U Cam lies in the lower range, with $\dot{M} = 2{\times}10^{-7}\ M_\odot\ \mathrm{yr}^{-1}$, IRC +30374 lies at the higher end, with $\dot{M} = 10^{-5}\ M_\odot\ \mathrm{yr}^{-1}$. In

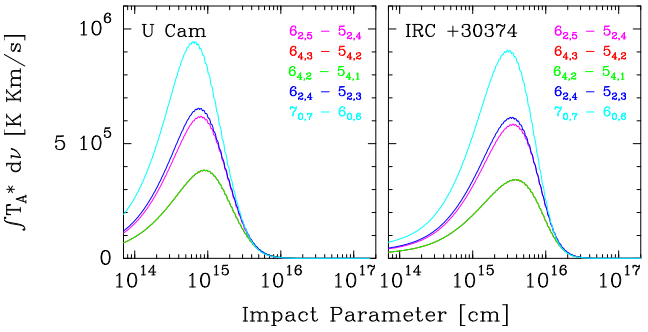

Fig. 4. Velocity-integrated intensity plotted as a function of impact parameter for the five observed SiC_2 lines in U Cam and IRC +30374. The transitions $6_{4,3}-5_{4,2}$ and $6_{4,2}-5_{4,1}$ have overlapping curves. For visualization reasons, the intensities of U Cam are multipled by a factor of 2.75.

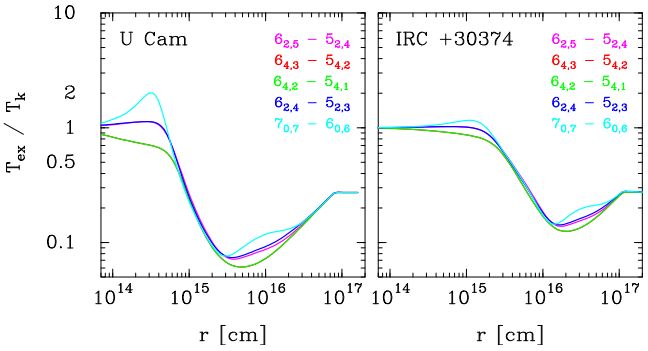

Fig. 5. Calculated ratio of excitation temperature to kinetic temperature (T_{ex}/T_k) as a function of radius for the five observed rotational transitions of SiC_2 in U Cam and IRC +30374. The transitions $6_{4,3}-5_{4,2}$ and $6_{4,2}-5_{4,1}$ have overlapping curves.

U Cam, the maximum contribution to the line emission comes from regions at $\sim 10^{15}$ cm, while in the case of IRC +30374 the regions around $\sim 10^{16}$ cm contribute the most to the observed emission; i.e., in envelopes with low mass-loss rates the SiC_2 rotational levels involved in the five observed transitions are only efficiently excited by collisions in the inner regions (and thus most of the emission detected in these lines comes from such regions), while in envelopes with high mass-loss rates the densities are still high enough in the outer regions to excite the SiC_2 rotational levels and thus most emission comes from these outer regions. Among the studied sources, the LVG models indicate that emission from the five SiC_2 observed lines arises typically from intermediate regions of the envelope, at radial distances in the range $10^{15}-10^{16}$ cm.

It is interesting to have a look at the excitation of SiC_2 predicted by the LVG model in the studied envelopes, in particular to the extent to which the rotational levels involved in the five observed transitions are close to or far from thermalization. In Fig. 5 we show the calculated ratio of excitation to gas kinetic temperature (T_{ex}/T_k) for the five SiC_2 transitions as a function of radius for the envelopes U Cam and IRC +30374, which lie at low and high ranges, respectively, of mass-loss rates. We see that for most transitions $T_{ex}/T_k = 1$, i.e., rotational levels are thermalized, in the hot and dense inner regions, and that as the radius increases and the gas density decreases, the rotational levels become increasingly subthermally excited, as indicated by the fact that the ratio T_{ex}/T_k falls below unity. The much lower mass-loss rate of U Cam compared to IRC +30374 implies substantially

lower densities in the envelope and thus in U Cam rotational populations start to deviate from thermalization at shorter radii than in IRC +30374. We note that in the intermediate region of the envelope from where most emission comes from, $\sim 10^{15}$ cm in U Cam and $\sim 10^{16}$ cm in IRC +30374 (see Fig. 4), the SiC_2 rotational levels are mostly subthermally excited.

As commented above, for some of the sources, the LVG model could lack sufficient excitation for the levels involved in the observed transitions of SiC_2. One possible missing source of excitation could be related to the existence of shells with an enhanced density with respect to the surrounding media (Mauron & Huggins 2000; Cordiner & Millar 2009; Cernicharo et al. 2015a; Agúndez et al. 2017; Guélin et al. 2018). From models of IRC +10216 and LP And we notice that density enhancements above a factor of 10 are needed to start to reproduce adequately the observed line shapes. In IRC +10216, the shell-intershell density contrast is just 3 (Guélin et al. 2018). It is currently unknown whether episodic mass loss in other stars could be abrupt enough to result in shell-intershell density contrasts above 10. We also note that uncertainties in the rate coefficients of SiC_2 excitation through inelastic collisions may also be at the origin of the suspected lack of excitation of SiC_2 in IRC +10216. In this sense, it would be interesting to revisit the collisional rate coefficients calculated by Chandra & Kegel (2000). Another possible missing source of excitation in the LVG model could be infrared (IR) pumping, i.e., absorption of IR photons and pumping to excited vibrational states followed by spontaneous radiative decay to rotational levels in the ground vibrational state. This effect is not included in the model for SiC_2 (mainly because there is a complete lack of information about infrared intensities), although it is an important excitation mechanism of some molecules in IRC +10216 (e.g., Agúndez & Cernicharo 2006) where the infrared flux is large (Cernicharo et al. 1999). However, vibrationally excited SiC_2 seems to be restricted to the inner layers, as indicated by the narrow lines from the vibrational states $v_3 = 1, 2$ detected with ALMA (Cernicharo et al. 2013). Moreover, if IR pumping was playing an important role for SiC_2 we could expect to see the time variation of the line intensities found by Cernicharo et al. (2014) for other molecules, but the lines of SiC_2 show a rather constant intensity along the stellar period of CW Leo, which suggests that IR pumping is not important for this molecule (Cernicharo et al. 2014).

The differences between calculated and observed line shapes for some of the sources suggests that the LVG model may lack excitation for SiC_2, and that this could happen for other sources as well. We have thus run models assuming LTE excitation for all sources. The calculated line profiles are shown in red in Fig. 1. Assuming LTE excitation throughout the whole envelope increases the excitation to outer radii, which leads to an increase in the emission size. Therefore, in general, the line opacities and fractional abundance of SiC_2 required to reproduce the observed intensities are lower when assuming LTE than when using the LVG method. Since it is unlikely that the rotational levels of SiC_2 are populated in LTE out to the outermost low-density regions of the envelope, the abundance of SiC_2 in the envelope of the observed sources is most likely between the values given by the LVG and the LTE models, which typically differ by a factor of ~3 (see Table 3).

6. Discussion

The fractional abundances of SiC_2 derived in the 25 studied envelopes are given in Table 3. We give the abundances derived using the LVG method, while those obtained assuming LTE excitation are given in the last column. The fractional abundances obtained using the LVG method range between 3.7×10^{-7} and 3.7×10^{-5} relative to H_2. Assuming that silicon has a solar elemental abundance in AGB stars (Asplund et al. 2009), the maximum possible abundance of SiC_2 relative to H_2 is 6.5×10^{-5}. Therefore, the high fractional abundances of SiC_2 of a few times 10^{-5} derived in some of the envelopes imply that gaseous SiC_2 locks an important fraction of the available silicon, possibly making it a major reservoir of this element. We note, however, that if the abundances are closer to the values derived under LTE, the maximum abundances derived for SiC_2 are $\sim 7 \times 10^{-6}$ relative to H_2, which would imply that SiC_2 locks at most ~10% of the available silicon.

Table 3. Derived fractional abundances of SiC_2.

Name	$\dot{M}$ ($M_\odot$ yr^{-1})	V_{exp} (km s^{-1})	$f_0(SiC_2)_{LVG}$	$f_0(SiC_2)_{LTE}$
IRC +10216	2.0×10^{-5}	14.5	3.7×10^{-7}	3.7×10^{-7}
CIT 6	6.0×10^{-6}	17	1.1×10^{-5}	3.4×10^{-6}
CRL 3068	2.5×10^{-5}	14.5	1.9×10^{-6}	7.2×10^{-7}
S Cep	1.2×10^{-6}	22.5	1.0×10^{-5}	2.0×10^{-6}
IRC +30374	1.0×10^{-5}	25	9.7×10^{-6}	2.3×10^{-6}
Y CVn	1.5×10^{-7}	7	4.0×10^{-6}	1.7×10^{-6}
LP And	7.0×10^{-6}	14.5	6.8×10^{-6}	2.2×10^{-6}
V Cyg	1.6×10^{-6}	12	6.6×10^{-6}	2.3×10^{-6}
UU Aur	2.4×10^{-7}	10.6	$<1.0 \times 10^{-6}$	$<3.5 \times 10^{-7}$
V384 Per	2.3×10^{-6}	15.5	1.3×10^{-5}	3.6×10^{-6}
IRC +60144	3.7×10^{-6}	19.5	6.0×10^{-6}	1.8×10^{-6}
U Cam	2.0×10^{-7}	13	3.7×10^{-5}	6.7×10^{-6}
V636 Mon	5.8×10^{-6}	20	1.7×10^{-6}	5.1×10^{-7}
IRC +20370	3.0×10^{-6}	14	4.2×10^{-6}	1.5×10^{-6}
R Lep	8.7×10^{-7}	17.5	$<2.7 \times 10^{-6}$	$<4.1 \times 10^{-7}$
W Ori	7.0×10^{-8}	11	1.4×10^{-5}	2.4×10^{-6}
CRL 67	1.1×10^{-5}	16	1.0×10^{-5}	2.6×10^{-6}
CRL 190	6.4×10^{-5}	17	8.8×10^{-7}	2.9×10^{-7}
S Aur	4.0×10^{-7}	24.5	3.6×10^{-6}	7.3×10^{-7}
V Aql	1.4×10^{-7}	8	2.0×10^{-5}	7.3×10^{-6}
CRL 2513	2.0×10^{-5}	25.5	1.6×10^{-6}	5.3×10^{-7}
CRL 2477	1.1×10^{-4}	20	6.0×10^{-7}	1.9×10^{-7}
CRL 2494	7.5×10^{-6}	20	2.7×10^{-5}	4.9×10^{-6}
RV Aqr	2.3×10^{-6}	15	3.0×10^{-6}	1.0×10^{-6}
ST Cam	1.3×10^{-7}	8.9	$<4.0 \times 10^{-6}$	$<6.0 \times 10^{-7}$

In most of the carbon-rich AGB envelopes in our sample, SiC_2 abundances are reported for the first time in this work. The only source where SiC_2 has been previously studied in detail is IRC +10216, which in fact has the lowest fractional abundance of SiC_2 among all the sources in our sample (3.7×10^{-7} relative to H_2, see Table 3). Cernicharo et al. (2010) observed 55 rotational transitions of SiC_2 in IRC +10216 using the HIFI spectrometer on board *Herschel*. These authors derive an abundance of 2×10^{-7} relative to H_2 in the inner regions of the envelope using an LTE radiative transfer analysis. Based on mm-wave interferometric observations, Lucas et al. (1995) derive an abundance relative to H_2 of 5×10^{-7} for the inner regions, and more recently Fonfría et al. (2014) inferred an abundance relative to H_2 of 8×10^{-7} at the stellar surface decreasing down to 8×10^{-8} at 20 R_*. The SiC_2 abundance derived in this work for IRC +10216 (3.7×10^{-7}) is in good agreement with the values reported in these articles.

The fractional abundance of SiC_2 shows an interesting trend with either the mass-loss rate $\dot{M}$ or the density in the envelope, evaluated through the quantity $\dot{M}/V_{exp}$. As shown in Fig. 6, SiC_2

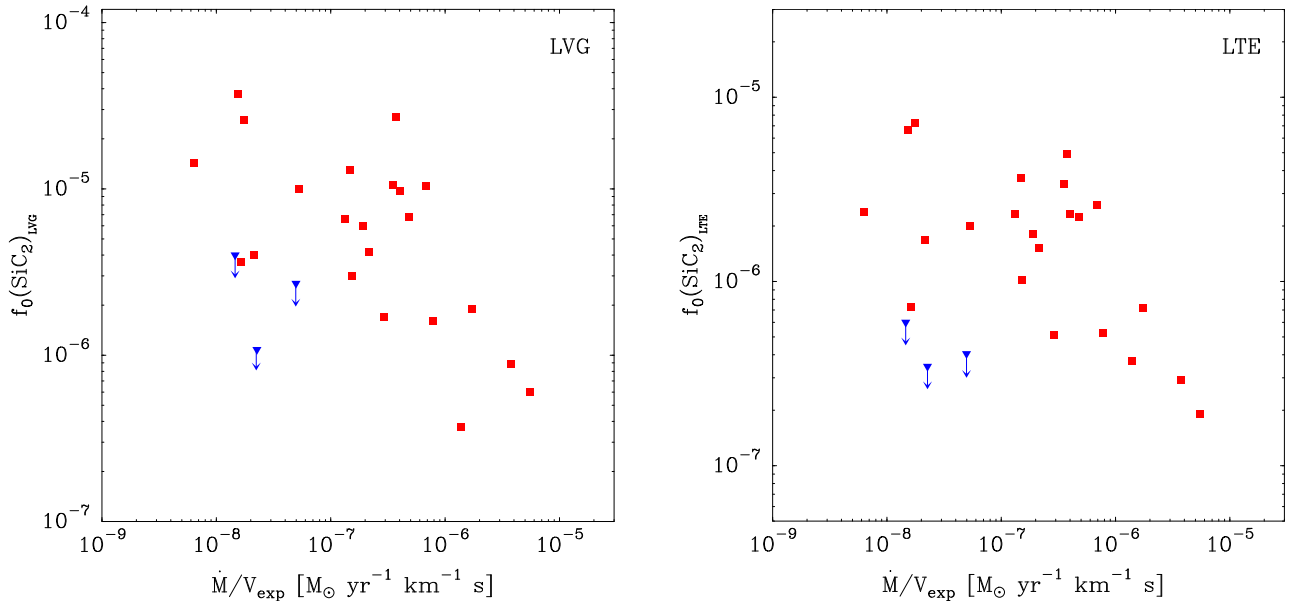

Fig. 6. Fractional abundances of SiC_2 (f_0) derived with the LVG method (*left panel*) and assuming LTE excitation (*right panel*) vs. the envelope density proxy $\dot{M}/V_{exp}$ for the 25 C-rich envelopes studied here. Blue downward triangles represent upper limits for f_0.

becomes less abundant as the density in the envelope increases. This trend is also present when the abundances derived assuming LTE are used. At this point, it is worth noting that the SiC_2 abundances derived in this work correspond to intermediate regions of the envelope. In a standard scenario describing the chemistry of an expanding envelope around an AGB star, the abundance with which a molecule is injected into the intermediate and outer envelope is set by the processes occurring in the inner regions. In this sense, the abundance of SiC_2 in the intermediate regions of the envelope is set by thermochemical equilibrium (TE) at the stellar surface and is possibly modified, i.e., driven out of thermochemical equilibrium, later on during the expansion by processes such as the formation of dust grains, shocks driven by the stellar pulsation, or even photochemical processes (e.g., Agúndez et al. 2010; Cherchneff 2012). The observational finding of a decrease in the SiC_2 abundance with increasing gas density can therefore be interpreted in different ways.

The observational trend could simply be a consequence of the way in which the TE abundance of SiC_2 depends on the density. To evaluate whether this could be a plausible explanation, we carried out thermochemical equilibrium calculations using the radial profiles of density and temperature of IRC +10216 (Agúndez et al. 2012; see downward revision on the density profile by Cernicharo et al. 2013) and scaling the density profile down or up depending on the mass-loss rate. In Fig. 7 we show the resulting TE abundance of SiC_2 within the first 10 R_* around the star for mass-loss rates between 10^{-7} and 10^{-4} $M_\odot$ yr^{-1}. In the region where SiC_2 reaches its maximum TE abundance, between 2 and 5 R_*, the abundance of SiC_2 is not very sensitive to the density. Outside this region the abundance of SiC_2 shows a marked dependence on density. At radii <2 R_*, SiC_2 becomes more abundant with increasing density (contrary to the observational trend), while beyond 5 R_* the SiC_2 abundance increases with decreasing density (as observed). At radii larger than 5 R_*, however, the TE abundance of SiC_2 experiences a drastic decline to values well below those observed, and thus it is unlikely that such regions set the abundance that is injected into the expanding envelope. Although it is difficult to precisely locate the region where molecular abundances, in general, and

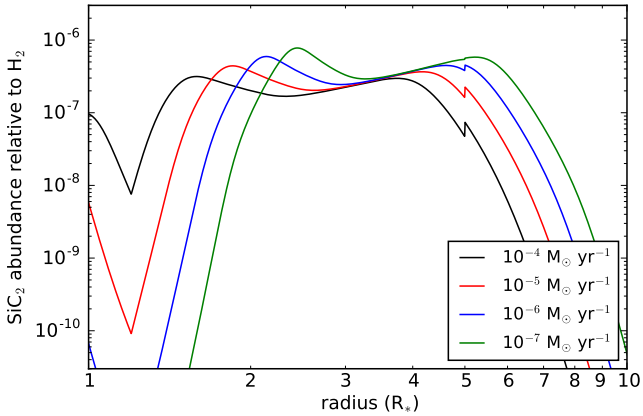

Fig. 7. Calculated fractional abundance of SiC_2 at thermochemical equilibrium as a function of distance to the star for various radial density profiles corresponding to mass-loss rates in the range 10^{-7}–10^{-4} $M_\odot$ yr^{-1}.

that of SiC_2 in particular, quench to the TE value, such a region should be located around 2–3 R_* (Agúndez & Cernicharo 2006; Agúndez et al. 2012), i.e., near the region where SiC_2 abundance is maximum and nearly insensitive to the density. We thus conclude that it is unlikely that the observational trend shown in Fig. 6 is caused by thermochemical equilibrium.

It therefore seems that the observational finding of a decline in the SiC_2 abundance with increasing density is caused by some nonequilibrium process that takes place beyond the region where thermochemical equilibrium holds. The most natural explanation is that SiC_2 molecules deplete from the gas phase to incorporate into solid dust grains, a process that is favored at higher densities owing to the higher rate at which collisions between particles occur. We stress that since the SiC_2 abundances derived here correspond to intermediate regions of the envelope where dust formation has already taken place, they have to be considered as post-condensation abundances. Further support for this scenario comes from mm-wave interferometric observations

of SiC_2 in the C-star envelope IRC +10216 (Lucas et al. 1995; Fonfría et al. 2014; Velilla Prieto et al. 2015), which shows that SiC_2 is present in regions close to the star, then experiences a marked abundance decline at 10–20 R_* (very likely due to condensation onto dust grains), and appears again in the outer envelope (probably as a result of the interaction between the UV radiation field and the envelope).

In order to further evaluate the hypothesis that the decline in the abundance of SiC_2 with increasing envelope density is caused by a more efficient incorporation of SiC_2 on silicon carbide dust, we collected information on infrared IRAS and ISO data for the sources in our sample that exhibit the SiC dust emission feature at 11.3 μm. Among the 25 sources in our sample, for 15 of them Sloan et al. (1998) have analyzed the IRAS LRS spectra and for 9 of them Yang et al. (2004) have studied the ISO SWS spectra. These authors determine the relative flux of SiC dust as the ratio of the integrated flux of the 11.3 μm emission feature (after continuum substraction) divided by the integrated flux of the continuum[4]. In Fig. 8 we plot the relative integrated flux of SiC dust vs. the fractional abundance of SiC_2 for the sources in our sample which have IRAS or ISO data. If the relative flux of SiC dust is a good proxy of the amount of silicon carbide dust, and if the hypothesis that SiC_2 is a gas-phase precursor of SiC dust is correct, one would expect to see a trend where the relative flux of SiC dust increases as the gas-phase abundance of SiC_2 decreases. This trend is not visible in Fig. 8. We note, however, that the relative flux of the 11.3 μm SiC band is an observable quantity that may not necessarily be a good proxy of the mass of silicon carbide dust in the envelope, the derivation of which requires a detailed radiative transfer analysis that includes a thorough description of the chemical composition and temperature of dust throughout the envelope. At this point, it therefore remains inconclusive whether or not there is a clear observational relation between the abundances of SiC_2 gas and SiC dust in C-rich envelopes. We plan to address this issue in a future study.

The question of identifying the main gas-phase precursors of dust grains in the ejecta of AGB stars has been, and continues to be, an exciting scientific topic. The problem has been addressed from different perspectives, mainly in the context of oxygen-rich AGB stars. For example, in a series of studies the abundance of SiO has been investigated in detail in a wide sample of envelopes around M stars (González Delgado et al. 2003), C stars (Schöier et al. 2006), and stars of S type (Ramstedt et al. 2009). Results from these studies show a clear trend of SiO becoming less abundant as the density of the envelope increases, a similar behavior to that found in this work for SiC_2 in C-rich envelopes. The observed trend for SiO has been also interpreted in terms of a more efficient adsorption of SiO onto dust grains for high envelope densities. It has been noted, however, that in the case of S stars, the trend is not as clear as in M and C stars, although this may be due to the low number of high mass-loss S stars observed (see Ramstedt et al. 2009). A similar study carried out on the abundance of SiS in envelopes around O- and C-rich stars (Schöier et al. 2007) did not find a clear correlation between the fractional abundance of SiS and the density of the envelope, suggesting that this molecule is not affected as much as SiO by freeze-out onto dust grains. The conclusions regarding SiS, however, are limited by the low number of O- and C-rich stars studied.

[4] The main difference between the two studies lies in the integration range, which is 7.67–14.03 μm for the IRAS spectra and 9–13.6 μm for the ISO data. For the sources that were observed with both telescopes, the main causes of the differences between the IRAS and ISO relative fluxes of SiC dust are the different integration ranges and the specific error in the spectra taken by each telescope.

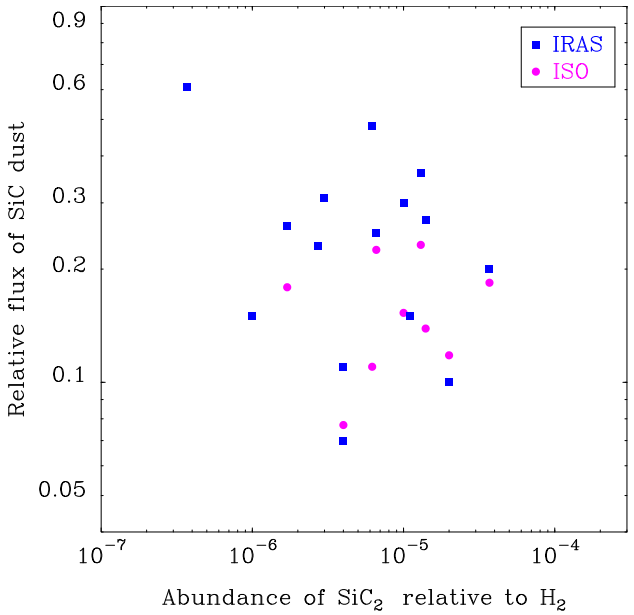

Fig. 8. Relative integrated flux of the SiC dust feature at 11.3 μm taken from the literature vs. the fractional abundance of SiC_2 derived in this work.

In a recent study, Liu & Jiang (2017) investigated the relation between the intensities of SiO maser and silicate dust emission in a sample of O-rich AGB and post-AGB stars in an attempt to relate the abundance of SiO, a highly plausible gas-phase precursor of silicates, with the amount of silicate dust. These authors find a positive correlation between the velocity-integrated intensity of SiO maser and the emission power of silicate dust, which is not against the hypothesis that SiO is a gas-phase precursor of silicate dust. It is important to note that in envelopes around O-rich AGB stars, SiO masers probe inner regions to where dust forms (Reid & Menten 1997; Danchi et al. 1994), and thus the more abundant the precursor SiO in the maser formation region is, the higher the amount of silicate dust can later be formed. In any case, given the peculiar nature of maser emission (e.g., Gray et al. 2009) and the fact that the observables are not a straightforward proxy of abundances, it is not clear whether the observed trend can be interpreted in terms of a higher fractional abundance of SiO in envelopes with a higher amount of silicate dust.

Various studies carried out in recent years have used ALMA to investigate the potential role of titanium and aluminum oxides as gas-phase precursors of inorganic dust in oxygen-rich evolved stars. In M stars, TiO_2 and Al_2O_3 are predicted to be among the first solid compounds to condense out of the gas phase (Gail & Sedlmayr 1998) and thus are ideal candidates to initiate the dust formation process. De Beck et al. (2015) and more recently Kamiński et al. (2017) have observed TiO and TiO_2 in the surroundings of the evolved stars VY Canis Majoris and Mira and found that these molecules extend out to several stellar radii from the star, and thus are unlikely to act as gas-phase precursors of TiO_2 dust. In a similar study, Kamiński et al. (2016) observed AlO around the star Mira, although they could not quantitatively assess the role of AlO as a gas-phase precursor of Al_2O_3 dust. ALMA is indeed a very promising tool for identifying gas-phase precursors of dust in evolved stars, but results are still not conclusive.

7. Conclusions

In this work we used the IRAM 30 m telescope to survey a sample of 25 C-rich circumstellar envelopes and search for rotational emission from the molecules SiC_2, SiC, and Si_2C. We detected SiC_2 in most of the sources and SiC in about half of them, while Si_2C was not detected in any of the sources with the exception of IRC +10216. We carried out excitation and radiative transfer calculations to derive SiC_2 fractional abundances. We found a clear trend in which SiC_2 becomes less abundant as the envelope density increases. We interpret this result as evidence of efficient incorporation of SiC_2 onto dust grains, a process that is more efficient at high densities because collisions between particles and coagulation processes become faster. The ring molecule SiC_2 thus emerges as a very likely gas-phase precursor in the process of formation of SiC dust in envelopes around C-rich AGB stars; therefore, SiC_2 seems to behave similarly to SiO, which has been found to deplete from the gas phase as the density in the envelope increases. The search for the gas-phase building blocks of dust grains in both carbon- and oxygen-rich AGB stars is a challenging scientific objective, in which astronomical observations still have to provide many answers. Observing other molecules containing refractory elements is necessary in order to understand which of the gas-phase molecules that are present in the atmospheres of AGB stars serve as precursor material to feed the process of dust grain formation.

Acknowledgements. We thank the IRAM 30 m staff for their help during the observations. This research has made use of the SIMBAD database, operated at CDS, Strasbourg, France. We acknowledge funding support from the European Research Council (ERC Grant 610256: NANOCOSMOS) and from Spanish MINECO through grants AYA2012-32032 and AYA2016-75066-C2-1-P. M.A. thanks Spanish MINECO for funding support through the Ramón y Cajal programme (RyC-2014-16277).

References

Agúndez, M., & Cernicharo, J. 2006, ApJ, 650, 374
Agúndez, M., Cernicharo, J., & Guélin, M. 2010, ApJ, 724, L133
Agúndez, M., Fonfría, J. P., Cernicharo, J., et al. 2012, A&A, 543, A48
Agúndez, M., Cernicharo, J., & Guélin, M. 2014, A&A, 570, A45
Agúndez, M., Cernicharo, J., Quintana-Lacaci, G., et al. 2017, A&A, 601, A4
Apponi, A. J., McCarthy, M. C., Gottlieb, C. A., & Thaddeus, P. 1999, ApJ, 516, L103
Asplund, M., Grevesse, N., Sauval, A. J., & Scott, P. 2009, ARA&A, 47, 481
Bachiller, R., Forveille, T., Huggins, P. J., & Cox, P. 1997, A&A, 324, 1123
Bohlin, R. C., Savage, B. D., & Drake, J. F. 1978, ApJ, 224, 132
Bujarrabal, V., Fuente, A., & Omont, A. 1994, A&A, 285, 247
Cernicharo, J. 1985, IRAM Internal Report, 52
Cernicharo, J., Gottlieb, C. A., Guelin, M., Thaddeus, P., & Vrtilek, J. M. 1989, ApJ, 341, L25
Cernicharo, J., Yamamura, I., González-Alfonso, E., et al. 1999, ApJ, 526, L41
Cernicharo, J., Guélin, M., & Kahane, C. 2000, A&AS, 142, 181
Cernicharo, J., Waters, L. B. F. M., Decin, L., et al. 2010, A&A, 521, L8
Cernicharo, J., Daniel, F., Castro-Carrizo, A., et al. 2013, ApJ, 778, L25
Cernicharo, J., Teyssier, D., Quintana-Lacaci, G., et al. 2014, ApJ, 796, L21
Cernicharo, J., Marcelino, N., Agúndez, M., & Guélin, M. 2015a, A&A, 575, A91
Cernicharo, J., McCarthy, M. C., Gottlieb, C. A., et al. 2015b, ApJ, 806, L3
Cernicharo, J., Agúndez, M., Velilla Prieto, L., et al. 2017, A&A, 606, L5
Chan, S. J., & Kwok, S. 1990, A&A, 237, 354
Chandra, S., & Kegel, W. H. 2000, A&AS, 142, 113
Cherchneff, I. 2012, A&A, 545, A12
Cordiner, M. A., & Millar, T. J. 2009, ApJ, 697, 68
Danchi, W., Bester, M., Degiacomi, C. G., Greenhill, L., & Townes, C. 1994, AJ, 107, 1469
Danilovich, T., Teyssier, D., Justtanont, K., et al. 2015, A&A, 581, A60
De Beck, E., Decin, L., de Koter, A., et al. 2010, A&A, 523, A18
De Beck, E., Lombaert, R., Agúndez, M., et al. 2012, A&A, 539, A108
De Beck, E., Vlemmings, W., Muller, S., et al. 2015, A&A, 580, A36
Fonfría, J. P., Fernández-López, M., Agúndez, M., et al. 2014, MNRAS, 445, 3289
Gail, H.-P., & Sedlmayr, E. 1998, Faraday Discussions, 109, 303
Gail, H.-P., Keller, R., & Sedlmayr, E. 1984, A&A, 133, 320
Gehrz, R. 1989, in Interstellar Dust, eds. L. J. Allamandola, & A. G. G. M. Tielens, IAU Symp., 135, 445
González Delgado, D., Olofsson, H., Kerschbaum, F., et al. 2003, A&A, 411, 123
Gray, M., Wittkowski, M., Scholz, M., et al. 2009, MNRAS, 394, 51
Green, S. 1995, ApJS, 100, 213
Groenewegen, M. A. T., Baas, F., de Jong, T., & Loup, C. 1996, A&A, 306, 241
Groenewegen, M. A. T., Whitelock, P. A., Smith, C. H., & Kerschbaum, F. 1998, MNRAS, 293, 18
Groenewegen, M. A. T., Sevenster, M., Spoon, H. W. W., & Pérez, I. 2002, A&A, 390, 511
Guandalini, R., & Cristallo, S. 2013, A&A, 555, A120
Guandalini, R., Busso, M., Ciprini, S., Silvestro, G., & Persi, P. 2006, A&A, 445, 1069
Guélin, M., Muller, S., Cernicharo, J., et al. 2000, A&A, 363, L9
Guélin, M., Patel, N. A., Bremer, M., et al. 2018, A&A, 610, A4
Hackwell, J. A. 1972, A&A, 21, 239
Hammami, K., Lique, F., Jaïdane, N., et al. 2007, A&A, 462, 789
Huggins, P. J., & Glassgold, A. E. 1982, ApJ, 252, 201
Jura, M., & Morris, M. 1981, ApJ, 251, 181
Kamiński, T., Wong, K. T., Schmidt, M. R., et al. 2016, A&A, 592, A42
Kamiński, T., Müller, H. S. P., Schmidt, M. R., et al. 2017, A&A, 599, A59
Kerschbaum, F., Charbonnel, C., & Wing, R. F. 2007, Why Galaxies Care About AGB Stars: Their Importance as Actors and Probes, ASP Conf. Ser., 378
Little-Marenin, I. R. 1986, ApJ, 307, L15
Liu, J., & Jiang, B. 2017, AJ, 153, 176
Loup, C., Forveille, T., Omont, A., & Paul, J. F. 1993, A&AS, 99, 291
Lucas, R., Guélin, M., Kahane, C., Audinos, P., & Cernicharo, J. 1995, Ap&SS, 224, 293
MacKay, D. D. S., & Charnley, S. B. 1999, MNRAS, 302, 793
Mauron, N., & Huggins, P. J. 2000, A&A, 359, 707
Müller, H. S. P., Cernicharo, J., Agúndez, M., et al. 2012, J. Mol. Spectr., 271, 50
Nyman, L.-A., Olofsson, H., Johansson, L. E. B., et al. 1993, A&A, 269, 377
Ohishi, M., Kaifu, N., Kawaguchi, K., et al. 1989, ApJ, 345, L83
Olofsson, H., Eriksson, K., Gustafsson, B., & Carlstrom, U. 1993, ApJS, 87, 267
Pardo, J. R., Cernicharo, J., & Serabyn, E. 2001, IEEE Transactions on Antennas and Propagation, 49, 1683
Patel, N. A., Young, K. H., Gottlieb, C. A., et al. 2011, ApJS, 193, 17
Ramstedt, S., & Olofsson, H. 2014, A&A, 566, A145
Ramstedt, S., Schöier, F. L., & Olofsson, H. 2009, A&A, 499, 515
Reid, M. J., & Menten, K. M. 1997, AJ, 476, 327
Sánchez Contreras, C., & Sahai, R. 2012, ApJS, 203, 16
Sarre, P. J., Hurst, M. E., & Lloyd Evans, T. 2000, MNRAS, 319, 103
Schöier, F. L., & Olofsson, H. 2001, A&A, 368, 969
Schöier, F. L., Lindqvist, M., & Olofsson, H. 2005, A&A, 436, 633
Schöier, F. L., Olofsson, H., & Lundgren, A. A. 2006, A&A, 454, 247
Schöier, F. L., Bast, J., Olofsson, H., & Lindqvist, M. 2007, A&A, 473, 871
Schöier, F. L., Ramstedt, S., Olofsson, H., et al. 2013, A&A, 550, A78
Skinner, C. J., Justtanont, K., Tielens, A. G. G. M., et al. 1999, MNRAS, 302, 293
Sloan, G. C., Little-Marenin, I. R., & Price, S. D. 1998, AJ, 115, 809
Speck, A. K., Corman, A. B., Wakeman, K., Wheeler, C. H., & Thompson, G. 2009, ApJ, 691, 1202
Suenram, R. D., Lovas, F. J., & Matsumura, K. 1989, ApJ, 342, L103
Suh, K.-W. 2000, MNRAS, 315, 740
Swamy, K. K. 2005, Dust in the universe: similarities and differences (World Scientific), 7
Tejero, J., & Cernicharo, J. 1991, Modelos de Equilibrio Termodinámico Aplicados a Envolturas Circunestelares de Estrellas Evolucionadas (Madrid: IGN)
Thaddeus, P., Cummins, S. E., & Linke, R. A. 1984, ApJ, 283, L45
Treffers, R., & Cohen, M. 1974, ApJ, 188, 545
Velilla Prieto, L., Cernicharo, J., Quintana-Lacaci, G., et al. 2015, ApJ, 805, L13
Wenger, M., Ochsenbein, F., Egret, D., et al. 2000, A&AS, 143, 9
Yang, X., Chen, P., & He, J. 2004, A&A, 414, 1049
Yasuda, Y., & Kozasa, T. 2012, ApJ, 745, 159
Zhang, Y., Kwok, S., & Dinh-V-Trung. 2009a, ApJ, 691, 1660
Zhang, Y., Kwok, S., & Nakashima, J.-i. 2009b, ApJ, 700, 1262

Appendix A

Table A.1. Observed line parameters of SiC_2.

Line	ν_{calc} (MHz)	ν_{obs} (MHz)	V_e (km s^{-1})	$\int T_A^* dv$ (K km s^{-1})
		IRC +10216		
$6_{2,5}-5_{2,4}$	140920.171	140920.1(1)	13.8(1)	41.2(4)
$6_{4,3}-5_{4,2}$	141751.492	141751.3(1)	13.8(1)	21.5(2)[a]
$6_{4,2}-5_{4,1}$	141755.360	141755.2(1)	13.8(1)	22.2(2)[a]
$6_{2,4}-5_{2,3}$	145325.875	145325.8(1)	14.3(1)	42.4(4)
$7_{0,7}-6_{0,6}$	158499.228	158499.1(1)	15.3(1)	58.7(5)
		CIT 6		
$6_{2,5}-5_{2,4}$	140920.171	140920.5(10)	16.2(8)	8.2(8)
$6_{4,3}-5_{4,2}$	141751.492	141751.1(2)	15.4(8)	5.4(5)[a]
$6_{4,2}-5_{4,1}$	141755.360	141754.9(3)	14.0(8)	2.7(3)[a]
$6_{2,4}-5_{2,3}$	145325.875	145325.0(10)	13.8(10)	8.0(8)
$7_{0,7}-6_{0,6}$	158499.228	158498.5(10)	15.1(8)	12.9(13)
		CRL 3068		
$6_{2,5}-5_{2,4}$	140920.171	140920.5(1)	12.8(8)	1.78(2)
$6_{4,3}-5_{4,2}$	141751.492	141751.3(1)	12.8(4)	1.07(1)[a]
$6_{4,2}-5_{4,1}$	141755.360	141755.3(1)	12.8(4)	1.02(1)[a]
$6_{2,4}-5_{2,3}$	145325.875	145325.7(1)	13.2(6)	1.84(2)
$7_{0,7}-6_{0,6}$	158499.228	158499.2(2)	14.5(8)	2.73(3)
		S Cep		
$6_{2,5}-5_{2,4}$	140920.171	140920.3(5)	20.5(4)	0.94(9)
$6_{4,3}-5_{4,2}$	141751.492	141751.3(5)	21.8(1)	0.63(6)[a]
$6_{4,2}-5_{4,1}$	141755.360	141755.9(5)	22.4(1)	0.49(5)[a]
$6_{2,4}-5_{2,3}$	145325.875	145325.5(5)	21.7(8)	1.06(10)
$7_{0,7}-6_{0,6}$	158499.228	158499.9(2)	23.0(5)	1.66(16)
		IRC +30374		
$6_{2,5}-5_{2,4}$	140920.171	140920.4(1)	23.0(8)	1.43(14)
$6_{4,3}-5_{4,2}$	141751.492	141751.8(3)	22.8(4)	0.84(8)[a]
$6_{4,2}-5_{4,1}$	141755.360	141755.5(3)	22.9(4)	0.62(6)[a]
$6_{2,4}-5_{2,3}$	145325.875	145325.9(1)	23.4(4)	1.50(4)
$7_{0,7}-6_{0,6}$	158499.228	158499.4(1)	25.5(8)	2.22(2)
		Y CVn		
$6_{2,5}-5_{2,4}$	140920.171	140921.7(10)	8.6(10)	0.23(4)
$6_{4,3}-5_{4,2}$	141751.492	141751.7(2)	7.3(8)	0.16(2)[a]
$6_{4,2}-5_{4,1}$	141755.360	141755.7(2)	7.5(6)	0.12(2)[a]
$6_{2,4}-5_{2,3}$	145325.875	145326.3(10)	7.1(10)	0.26(5)
$7_{0,7}-6_{0,6}$	158499.228	158499.1(5)	6.6(5)	0.44(9)
		LP And		
$6_{2,5}-5_{2,4}$	140920.171	140920.3(1)	13.0(8)	3.86(4)
$6_{4,3}-5_{4,2}$	141751.492	141751.6(2)	13.1(8)	1.93(2)[a]
$6_{4,2}-5_{4,1}$	141755.360	141755.4(2)	13.2(8)	2.06(2)[a]
$6_{2,4}-5_{2,3}$	145325.875	145325.9(1)	13.4(8)	3.99(4)
$7_{0,7}-6_{0,6}$	158499.228	158499.3(1)	14.6(8)	6.34(6)
		V Cyg		
$6_{2,5}-5_{2,4}$	140920.171	140920.3(1)	10.4(8)	1.87(2)
$6_{4,3}-5_{4,2}$	141751.492	141751.7(2)	10.8(4)	0.91(2)[a]
$6_{4,2}-5_{4,1}$	141755.360	141755.4(2)	10.6(4)	0.91(2)[a]
$6_{2,4}-5_{2,3}$	145325.875	145326.1(3)	11.0(8)	1.95(2)
$7_{0,7}-6_{0,6}$	158499.228	158499.4(1)	11.8(8)	3.47(3)

Notes. Numbers in parentheses are 1σ uncertainties in units of the last digits. [(a)] Blend of two lines, each of which could be fitted individually. [(b)] Blend of two lines which could not be fitted individually. Only one component was fitted. [(c)] Marginal detection.

Table A.1. continued.

Line	ν_{calc} (MHz)	ν_{obs} (MHz)	V_e (km s^{-1})	$\int T_A^* dv$ (K km s^{-1})
		V384 Per		
$6_{2,5}-5_{2,4}$	140920.171	140920.2(1)	13.5(4)	1.80(2)
$6_{4,3}-5_{4,2}$	141751.492	141751.4(1)	13.9(2)	0.80(1)[a]
$6_{4,2}-5_{4,1}$	141755.360	141755.1(1)	13.8(2)	1.04(2)[a]
$6_{2,4}-5_{2,3}$	145325.875	145326.0(1)	13.6(8)	1.88(2)
$7_{0,7}-6_{0,6}$	158499.228	158499.3(1)	15.1(1)	3.09(3)
		IRC +60144		
$6_{2,5}-5_{2,4}$	140920.171	140920.4(5)	19.1(8)	0.55(5)
$6_{4,3}-5_{4,2}$	141751.492	141751.3(1)	18.5(2)	0.37(4)[a]
$6_{4,2}-5_{4,1}$	141755.360	141755.4(4)	19.9(3)	0.25(2)[a]
$6_{2,4}-5_{2,3}$	145325.875	145325.9(2)	19.7(1)	0.25(2)
$7_{0,7}-6_{0,6}$	158499.228	158499.4(2)	21.5(4)	0.73(7)
		U Cam		
$6_{2,5}-5_{2,4}$	140920.171	140920.8(5)	11.2(5)	0.39(4)
$6_{4,3}-5_{4,2}$	141751.492	141751.9(10)	14.0(8)	0.21(2)[a]
$6_{4,2}-5_{4,1}$	141755.360	141755.5(10)	13.1(8)	0.19(2)[a]
$6_{2,4}-5_{2,3}$	145325.875	145326.3(10)	11.9(8)	0.41(4)
$7_{0,7}-6_{0,6}$	158499.228	158499.6(5)	12.6(5)	0.63(6)
		V636 Mon		
$6_{2,5}-5_{2,4}$	140920.171	140921.2(10)	21.3(10)	0.35(7)
$6_{4,3}-5_{4,2}$	141751.492	141751.8(4)	20.3(8)	0.17(3)[a]
$6_{4,2}-5_{4,1}$	141755.360	141754.4(3)	19.7(6)	0.23(5)[a]
$6_{2,4}-5_{2,3}$	145325.875	145326.5(10)	23.3(10)	0.37(1)
$7_{0,7}-6_{0,6}$	158499.228	158499.9(10)	21.8(10)	0.61(2)
		IRC +20370		
$6_{2,5}-5_{2,4}$	140920.171	140920.2(1)	13.0(2)	0.98(9)
$6_{4,3}-5_{4,2}$	141751.492	141751.6(5)	13.2(5)	0.53(5)[a]
$6_{4,2}-5_{4,1}$	141755.360	141755.3(5)	13.4(5)	0.51(5)[a]
$6_{2,4}-5_{2,3}$	145325.875	145325.9(3)	13.2(5)	1.12(11)
$7_{0,7}-6_{0,6}$	158499.228	158499.3(2)	14.6(1)	1.83(18)
		W Ori		
$6_{2,5}-5_{2,4}$	140920.171	140920.2(10)	9.4(10)	0.12(5)[c]
$6_{4,3}-5_{4,2}$	141751.492	141751.5(10)	10.5(10)	0.06(1)[c]
$6_{4,2}-5_{4,1}$	141755.360	141754.6(10)	10.9(10)	0.06(3)[c]
$6_{2,4}-5_{2,3}$	145325.875	145325.2(10)	8.2(10)	0.11(2)[c]
$7_{0,7}-6_{0,6}$	158499.228	158499.9(5)	12.1(10)	0.31(6)
		CRL 67		
$6_{2,5}-5_{2,4}$	140920.171	140920.3(1)	14.6(1)	1.57(1)
$6_{4,3}-5_{4,2}$	141751.492	141751.5(5)	15.6(5)	0.72(7)[a]
$6_{4,2}-5_{4,1}$	141755.360	141755.2(5)	14.9(5)	0.96(9)[a]
$6_{2,4}-5_{2,3}$	145325.875	145325.9(2)	14.6(4)	1.61(2)
$7_{0,7}-6_{0,6}$	158499.228	158499.3(3)	15.8(4)	2.47(2)
		CRL 190		
$6_{2,5}-5_{2,4}$	140920.171	140920.6(1)	16.4(1)	1.08(10)
$6_{4,3}-5_{4,2}$	141751.492	141751.6(3)	16.3(5)	0.29(3)[a]
$6_{4,2}-5_{4,1}$	141755.360	141755.1(2)	15.2(5)	0.37(4)[a]
$6_{2,4}-5_{2,3}$	145325.875	145325.9(1)	15.4(1)	0.12(1)
$7_{0,7}-6_{0,6}$	158499.228	158499.6(1)	16.8(4)	0.77(7)
		S Aur		
$6_{2,5}-5_{2,4}$	140920.171	140920.3(10)	23.7(10)	0.11(2)[c]
$6_{4,3}-5_{4,2}$	141751.492	141753.1(10)	22.2(14)	0.13(3)[b,c]
$6_{4,2}-5_{4,1}$	141755.360	–	–	–
$6_{2,4}-5_{2,3}$	145325.875	145324.9(10)	25.7(15)	0.15(3)[c]
$7_{0,7}-6_{0,6}$	158499.228	158499.1(5)	24.4(8)	0.28(6)

Table A.1. continued.

Line	ν_{calc} (MHz)	ν_{obs} (MHz)	V_e (km s^{-1})	$\int T_A^* dv$ (K km s^{-1})
		V Aql		
$6_{2,5}-5_{2,4}$	140920.171	140920.1(5)	6.7(4)	0.31(6)
$6_{4,3}-5_{4,2}$	141751.492	141751.7(10)	8.0(10)	0.26(5)[b]
$6_{4,2}-5_{4,1}$	141755.360	141755.3(10)	9.7(10)	0.12(2)[b]
$6_{2,4}-5_{2,3}$	145325.875	145326.1(5)	8.1(6)	0.38(7)
$7_{0,7}-6_{0,6}$	158499.228	158499.2(5)	8.0(5)	0.60(12)
		CRL 2513		
$6_{2,5}-5_{2,4}$	140920.171	140922.1(10)	20.3(10)	0.22(4)
$6_{4,3}-5_{4,2}$	141751.492	141751.7(10)	20.6(10)	0.23(4)[b]
$6_{4,2}-5_{4,1}$	141755.360	–	–	–
$6_{2,4}-5_{2,3}$	145325.875	145326.3(10)	25.6(10)	0.29(6)[c]
$7_{0,7}-6_{0,6}$	158499.228	158499.8(5)	26.9(4)	0.58(11)
		CRL 2477		
$6_{2,5}-5_{2,4}$	140920.171	140920.1(1)	18.5(10)	0.46(4)
$6_{4,3}-5_{4,2}$	141751.492	141751.5(2)	18.2(4)	0.28(6)[a]
$6_{4,2}-5_{4,1}$	141755.360	141755.2(2)	19.9(4)	0.30(6)[a]
$6_{2,4}-5_{2,3}$	145325.875	145325.7(5)	19.3(5)	0.51(1)
$7_{0,7}-6_{0,6}$	158499.228	158499.5(5)	20.0(5)	0.72(14)
		CRL 2494		
$6_{2,5}-5_{2,4}$	140920.171	140920.2(5)	17.4(8)	1.41(1)
$6_{4,3}-5_{4,2}$	141751.492	141751.8(5)	18.1(5)	0.81(1)[a]
$6_{4,2}-5_{4,1}$	141755.360	141755.3(5)	18.1(5)	0.91(1)[a]
$6_{2,4}-5_{2,3}$	145325.875	145326.7(5)	18.3(8)	1.53(1)
$7_{0,7}-6_{0,6}$	158499.228	158499.5(3)	19.5(4)	2.10(2)
		RV Aqr		
$6_{2,5}-5_{2,4}$	140920.171	140920.7(10)	14.3(10)	0.37(7)
$6_{4,3}-5_{4,2}$	141751.492	141751.4(5)	14.7(10)	0.18(3)[a]
$6_{4,2}-5_{4,1}$	141755.360	141755.3(5)	14.2(10)	0.18(3)[a]
$6_{2,4}-5_{2,3}$	145325.875	145325.9(10)	15.6(10)	0.39(8)
$7_{0,7}-6_{0,6}$	158499.228	158499.6(5)	15.5(5)	0.65(10)

Table A.2. Observed parameters of the SiC $^3\Pi_2$ $J = 4-3$ line.

Source	ν_{calc} (MHz)	ν_{obs} (MHz)	V_e (km s^{-1})	$\int T_A^* dv$ (K km s^{-1})
IRC +10216	157494.101	157494.1(1)	15.4(8)	5.86(6)
CIT 6	157494.101	157493.2(10)	15.4(8)	0.96(9)
CRL 3068	157494.101	157494.2(5)	15.7(5)	0.29(6)
IRC +30374	157494.101	157495.5(10)	25.1(10)	0.18(3)[a]
LP And	157494.101	157493.8(5)	14.4(4)	0.56(6)
V Cyg	157494.101	157496.3(10)	11.3(10)	0.11(2)[a]
V384 Per	157494.101	157493.7(10)	15.2(10)	0.17(3)[a]
IRC +60144	157494.101	157492.8(10)	20.2(10)	0.12(6)[a]
IRC +20370	157494.101	157494.3(10)	15.8(10)	0.13(2)[a]
CRL 67	157494.101	157494.8(10)	16.6(10)	0.28(6)[a]
CRL 2477	157494.101	157493.7(10)	18.7(10)	0.10(2)[a]
CRL 2494	157494.101	157493.5(10)	21.8(10)	0.23(4)[a]

Notes. Numbers in parentheses are 1σ uncertainties in units of the last digits. [(a)] Marginal detection.

A&A 628, A62 (2019)
https://doi.org/10.1051/0004-6361/201935069

Astronomy & Astrophysics

Study of CS, SiO, and SiS abundances in carbon star envelopes: assessing their role as gas-phase precursors of dust[⋆,⋆⋆]

S. Massalkhi, M. Agúndez, and J. Cernicharo

Instituto de Física Fundamental, CSIC, C/Serrano 123, 28006 Madrid, Spain
e-mail: sarah.massalkhi@csic.es

Received 16 January 2019 / Accepted 24 May 2019

ABSTRACT

Aims. We aim to determine the abundances of CS, SiO, and SiS in a large sample of carbon star envelopes covering a wide range of mass loss rates to investigate the potential role that these molecules could play in the formation of dust in the surroundings of the central AGB star.

Methods. We surveyed a sample of 25 carbon-rich AGB stars in the λ 2 mm band, more concretely in the $J = 3-2$ line of CS and SiO, and in the $J = 7-6$ and $J = 8-7$ lines of SiS, using the IRAM 30 m telescope. We performed excitation and radiative transfer calculations based on the large velocity gradient (LVG) method to model the observed lines of the molecules and to derive their fractional abundances in the observed envelopes. We also assessed the effect of infrared pumping in the excitation of the molecules.

Results. We detected CS in all 25 targeted envelopes, SiO in 24 of them, and SiS in 17 sources. Remarkably, SiS is not detected in any envelope with a mass loss rate below 10^{-6} $M_\odot$ yr^{-1} while it is detected in all envelopes with mass loss rates above that threshold. We found that CS and SiS have similar abundances in carbon star envelopes, while SiO is present with a lower abundance. We also found a strong correlation in which the denser the envelope, the less abundant are CS and SiO. The trend is however only tentatively seen for SiS in the range of high mass loss rates. Furthermore, we found a relation in which the integrated flux of the MgS dust feature at 30 μm increases as the fractional abundance of CS decreases.

Conclusions. The decline in the fractional abundance of CS with increasing density could be due to gas-phase chemistry in the inner envelope or to adsorption onto dust grains. The latter possibility is favored by a correlation between the CS fractional abundance and the 30 μm feature, which suggests that CS is efficiently incorporated onto MgS dust around C-rich AGB stars. In the case of SiO, the observed abundance depletion with increasing density is most likely caused by an efficient incorporation onto dust grains. We conclude that CS, SiO (very likely), and SiS (tentatively) are good candidates to act as gas-phase precursors of dust in C-rich AGB envelopes.

Key words. astrochemistry – molecular processes – stars: abundances – stars: AGB and post-AGB – circumstellar matter

1. Introduction

The circumstellar envelopes (CSEs) of asymptotic giant branch (AGB) stars, formed through extensive stellar mass loss, are rich in chemical diversity and have long been known to be efficient sites for molecule and grain formation. In the Galaxy, AGB stars are the main sources of interstellar dust (Gehrz 1989). It is therefore of particular interest to study their CSEs because these envelopes contain gas (mainly in the form of molecules), dust, and products of nucleosynthesis that are eventually expelled into the interstellar medium (ISM) and will contribute to its evolution and enrichment (Herwig 2005).

The type of molecules and dust grains found in CSEs is to a great extent determined by the carbon-to-oxygen (C/O) abundance ratio at the photosphere of the AGB star. At the temperatures and densities of AGB atmospheres, thermochemical equilibrium (TE) predicts that carbon monoxide (CO) molecules have a very high abundance because of their stability, which locks most of the available carbon in oxygen-rich stars (M-type, C/O < 1) or oxygen in carbon-rich stars (C-type, C/O > 1). As a consequence of this, envelopes around M-type stars contain a variety of oxygen-bearing molecules (e.g., H_2O, SiO, and TiO; see Velilla Prieto et al. 2017) and silicate dust, while CSEs around C-type stars display a variety of carbon-bearing molecules (e.g., C_2H_2, HCN, CS, and SiC_2; see Olofsson et al. 1993 and Cernicharo et al. 2000) and contain carbonaceous, silicon carbide, and magnesium sulfide dust. After some gas-phase precursors condense near the surroundings of the stellar photosphere, the condensation nuclei grow to micrometer sizes as a consequence of accretion and coagulation processes. In C-rich AGB stars, molecules such as CS (Olofsson et al. 1993), SiS (Schöier et al. 2007), and SiO (Schöier et al. 2006b) are found to be abundant and are potential precursors of dust grains, in which case their abundances in the gas phase should experience a decline as they incorporate into solid grains. Eventually, interstellar ultraviolet (UV) photons destroy the molecules remaining in the gas phase in the outer envelope owing to photodissociation. However, the picture is yet poorly constrained from an observational point of view. It is still not well understood what are the gas-phase building blocks of dust grains in CSEs.

One of the first major studies of abundances in a large sample of AGB stars was performed by González Delgado et al. (2003), who investigated SiO in ∼40 M-type stars. Later on, Schöier et al. (2006b) studied SiO in a sample of 19 C-rich AGB

⋆ Reduced spectra (FITS) are available at the CDS via anonymous ftp to cdsarc.u-strasbg.fr (130.79.128.5) or via http://cdsarc.u-strasbg.fr/viz-bin/qcat?J/A+A/628/A62

⋆⋆ Based on observations carried out with the IRAM 30 m Telescope. The Institut de Radioastronomie Millimétrique (IRAM) is supported by INSU/CNRS (France), MPG (Germany) and IGN (Spain).

Table 1. Sample of carbon stars.

Name	RA J2000.0	Dec J2000.0	V_{LSR} (km s^{-1})	D (pc)	$T_\star$ (K)	$L_\star$ ($L_\odot$)	$\dot{M}$ ($M_\odot$ yr^{-1})	V_{exp} (km s^{-1})	$T_d(r_c)$ (K)	r_c (cm)	Ψ
IRC +10216	09:47:57.45	+13:16:43.9	−26.5	130	2330	8750	2.0×10^{-5}	14.5	800	2.0×10^{14}	300
CIT 6	10:16:02.27	+30:34:18.6	−1	400	1800	10 000	6.0×10^{-6}	17	1000	2.1×10^{14}	141
CRL 3068	23:19:12.24	+17:11:33.4	−31.5	1300	1800	10 900	2.5×10^{-5}	14.5	1500	2.0×10^{14}	174
S Cep	21:35:12.83	+78:37:28.2	−15.3	380	2200	7300	1.2×10^{-6}	22.5	1400	5.8×10^{13}	360
IRC +30374	19:34:09.87	+28:04:06.3	−12.5	1200	2000	9800	1.0×10^{-5}	25	1000	2.2×10^{14}	1008
Y CVn	12:45:07.83	+45:26:24.9	+22	220	2200	4400	1.5×10^{-7}	7	1500	8.7×10^{13}	500
LP And	23:34:27.53	+43:33:01.2	−17	630	1900	9600	7.0×10^{-6}	14.5	1100	1.8×10^{14}	288
V Cyg	20:41:18.27	+48:08:28.8	+13.5	366	2300	6000	1.6×10^{-6}	12	1400	9.4×10^{13}	364
UU Aur	06:36:32.84	+38:26:43.8	+6.7	260	2800	6900	2.4×10^{-7}	10.6	1500	6.3×10^{13}	1000
V384 Per	03:26:29.51	+47:31:48.6	−16.8	560	2000	8100	2.3×10^{-6}	15.5	1300	1.0×10^{14}	584
IRC +60144	04:35:17.54	+62:16:23.8	−48.8	1030	2000	7800	3.7×10^{-6}	19.5	1200	2.0×10^{14}	1014
U Cam	03:41:48.17	+62:38:54.4	+6	430	2695	7000	2.0×10^{-7}	13	1500	4.4×10^{13}	833
V636 Mon	06:25:01.43	−09:07:15.9	+10	880	2500	8472	5.8×10^{-6}	20	1200	1.7×10^{14}	300
IRC +20370	18:41:54.39	+17:41:08.5	−0.8	600	2200	7900	3.0×10^{-6}	14	1500	8.1×10^{13}	266
R Lep	04:59:36.35	−14:48:22.5	+11.5	432	2200	5500	8.7×10^{-7}	17.5	1000	1.8×10^{14}	500
W Ori	05:05:23.72	+01:10:39.5	−1	220	2600	3500	7.0×10^{-8}	11	1500	4.3×10^{13}	333
CRL 67	00:27:41.10	+69:38:51.5	−27.5	1410	2500	9817	1.1×10^{-5}	16	1200	1.8×10^{14}	495
CRL 190	01:17:51.62	+67:13:55.4	−39.5	2790	2500	16 750	6.4×10^{-5}	17	1000	4.7×10^{14}	424
S Aur	05:27:07.45	+34:08:58.6	−17	300	3000	8900	4.0×10^{-7}	24.5	1500	7.3×10^{13}	500
V Aql	19:04:24.15	−05:41:05.4	+53.5	330	2800	6500	1.4×10^{-7}	8	1500	6.1×10^{13}	500
CRL 2513	20:09:14.25	+31:25:44.9	+17.5	1760	2500	8300	2.0×10^{-5}	25.5	1200	1.6×10^{14}	453
CRL 2477	19:56:48.43	+30:43:59.9	+5	3380	3000	13 200	1.1×10^{-4}	20	1800	2.8×10^{14}	532
CRL 2494	20:01:08.51	+40:55:40.2	+29	1480	2400	10 200	7.5×10^{-6}	20	1200	2.3×10^{14}	436
RV Aqr	21:05:51.74	−00:12:42.0	+0.5	670	2200	6800	2.3×10^{-6}	15	1300	7.6×10^{13}	200
ST Cam	04:51:13.35	+68:10:07.6	−13.6	360	2800	4400	1.3×10^{-7}	8.9	1500	5.0×10^{13}	500

Notes. The adopted parameters are discussed in Massalkhi et al. (2018). See references therein. Ψ for UU Aur and R Lep is from Schöier & Olofsson (2001) and for IRC +60144 from Groenewegen et al. (2002).

stars. Interestingly, it was found that SiO behaves similarly in both types of stars, showing a trend of decreasing abundance with increasing mass loss rate, thought to be due to an increased depletion of SiO onto dust grains. On the other hand, when Schöier et al. (2007) investigated SiS in a reduced sample of C-rich stars, they did not find a clear trend; this contrasted with the results of SiO, which could imply that SiS is less likely to be adsorbed onto dust grains than SiO in carbon-rich envelopes. Recently, we investigated SiC_2 in a sample of 25 carbon-rich AGB stars and found a similar trend as that found for SiO; that is, we discovered an abundance decline with increasing envelope density, which points to SiC_2 being efficiently incorporated into dust grains and playing an important role in the formation of silicon carbide dust (Massalkhi et al. 2018).

In this paper, we follow up on our last study to investigate the abundance of CS, SiO, and SiS in the envelopes of carbon stars and to understand their potential role as gas-phase precursors of dust grains. We present observations of SiO (J = 3−2), SiS (J = 7−6 and J = 8−7), and CS (J = 3−2) in a sample of 25 carbon stars with diverse mass loss rates. We carried out a detailed non-local thermodynamic equilibrium (non-LTE) radiative transfer analysis to derive molecular abundances in the CSEs. The sample of stars and observational details are presented in Sect. 2 and the main results obtained from the observations in Sect. 3. In Sect. 4 we describe the model and the excitation and radiative transfer calculations and discuss the most interesting features from these calculations in Sect. 5. Finally, we discuss the main implications of our study in Sect. 6 and present our conclusions in Sect. 7.

2. Observations

The observations were carried out in September 2017 with the IRAM 30 m telescope, located at Pico Veleta, Spain. The sample of 25 C-rich AGB stars observed is the same used in our previous study of SiC_2 (Massalkhi et al. 2018) and was selected according to intense molecular emission, mainly based on the intensity of the HCN J = 1−0 line (Loup et al. 1993; Bujarrabal et al. 1994; Schöier et al. 2013). The observed sources and their parameters are listed in Table 1. In this study, we focused on the emission of CS, SiO, and SiS and therefore the spectral setup used was slightly shifted from that employed in Massalkhi et al. (2018) and accommodated in a way to include the lines CS J = 3−2, SiO J = 3−2 and SiS J = 7−6 and J = 8−7 (see line parameters in Table 2).

We used the E150 receiver in dual side band, with image rejections >10 dB, and observed the frequency ranges 125.7−133.5 GHz and 141.4−149.2 GHz in the lower and upper side bands, respectively. The beam size of the telescope at these frequencies is in the range 16.7–19.3″. We used the wobbler-switching technique. This technique consists of a symmetric position switching with the OFF position (atmosphere) at 180″ in azimuth from the ON position (source + atmosphere). Spectra at the OFF and ON positions are taken by nutating the secondary mirror at a rate of 0.5 Hz, and the OFF is subtracted from the ON to remove the contribution of the atmosphere to the signal. The focus was regularly checked on Venus and the pointing of the telescope was systematically checked on a nearby quasar before observing each AGB star. The error in

Table 2. Covered rotational transitions of CS, SiO, and SiS.

Transition	Frequency (MHz)	A_{ul} (s^{-1})	E_u (K)	θ_{mb} ($''$)
CS $J = 3-2$	146 969.025	6.07×10^{-5}	14.1	16.7
SiO $J = 3-2$	130 268.665	1.06×10^{-4}	12.5	18.8
SiS $J = 7-6$	127 076.178	3.36×10^{-5}	24.4	19.3
SiS $J = 8-7$	145 227.052	5.05×10^{-5}	31.4	16.9

the pointing is estimated to be 2–3$''$. The E150 receiver was connected to a fast Fourier transform spectrometer providing a spectral resolution of 0.2 MHz. The weather was good and stable during most of the observations, with typical amounts of precipitable water vapor of 1–3 mm and average system temperatures of 115 K. The intensity scale, calibrated using two absorbers at different temperatures and the atmospheric transmission model (ATM) (Cernicharo 1985; Pardo et al. 2001), is expressed in terms of T_{mb}, the main beam brightness temperature. The error in the intensities due to calibration is estimated to be ∼20%.

The data were reduced using CLASS[1] within the package GILDAS[2]. For each source, we averaged the spectra corresponding to the horizontal and vertical polarizations and subtracted a baseline consisting of a first order polynomial. When the lines were not very strong, the spectra were smoothed to a spectral resolution of 1 MHz to increase the signal-to-noise ratio (S/N). This corresponds to a velocity resolution of 2–2.4 km s^{-1}. Typical on source integration times, after averaging horizontal and vertical polarizations, were ∼1 h for each source, resulting in T_{mb} rms noise levels per 1 MHz channel of 2–6 mK.

3. Observational results

The spectra obtained are shown in Fig. 1 (CS $J = 3-2$), Fig. 2 (SiO $J = 3-2$), and Figs. 3 and 4 (SiS $J = 7-6$ and $J = 8-7$, respectively). The observed lines exhibit profiles typical of expanding circumstellar shells, i.e., either double-peaked, flat-topped, or parabolic, which can be reasonably well fit by the `shell` method of CLASS. The method fits the function

$$f(\nu) = \frac{A}{\Delta\nu} \frac{1 + 4H[(\nu - \nu_0)/\Delta\nu]^2}{1 + H/3}, \quad (1)$$

where A is the area under the profile in K MHz, ν_0 is the middle frequency in MHz, $\Delta\nu$ is the full width at zero intensity level in MHz, and H is the horn-to-center ratio, which is dimensionless. The expansion velocity V_{exp} can then be obtained by the following expression:

$$V_{exp} = c\frac{\Delta\nu/2}{\nu_0}, \quad (2)$$

where c is the speed of light.

By performing the fit, we aim to derive for the target lines in every source the centroid frequency, expansion velocity, and line area, i.e., the velocity-integrated intensity. Most of the observed lines show profiles that match one of the types mentioned above, apart from the two sources U Cam (see line profile of CS emission in Fig. 1) and CIT 6 (see line profile of SiO in Fig. 2), which have profiles that deviate from the expected line profile of a spherical expanding shell. The CS emission of U Cam is interpreted below as having two components, which we faced no difficulty considering separately. CIT 6 shows a rather asymmetrical profile in the SiO $J = 3-2$, SiS $J = 7-6$ and $J = 8-7$ lines. In any case, the two most interesting parameters, the line area and the expansion velocity, are reasonably well fitted. The derived parameters of the observed line profiles are shown in Table A.1.

The observations resulted in the clear detection of CS $J = 3-2$ in all targeted sources. In the case of SiO, we detected the $J = 3-2$ line in all target sources with the exception of ST Cam. As previously mentioned, the case of U Cam deserves particular attention because this source exhibits emission arising from a present-day wind and from a geometrically thin detached shell surrounding the central star (Schöier et al. 2005). The detached shell is probably the result of episodic mass loss driven by helium shell flashes, i.e., thermal pulses (Olofsson et al. 1990). According to the observed line profiles, CS emission in U Cam arises from both the present-day wind and the detached envelope, while SiO emission arises exclusively from the present-day wind; compare line profiles of CS and SiO in Figs. 1 and 2, respectively, with that of CO $J = 1-0$ in Fig. 6 of Schöier et al. (2005). To disentangle the contribution from each component in the emission line of CS, we fitted the observed line with two components of different line widths; the narrow line width corresponds to the present-day wind and the wide to the detached envelope. The green line in Fig. 1 corresponds to the emission from the present-day wind, which we are ultimately interested in modeling. In the case of SiS, the $J = 7-6$ and $J = 8-7$ lines were detected in 17 out of 25 sources, that is, in all sources except U Cam, V Aql, S Aur, W Ori, Y CVn, R Lep, ST Cam, and UU Aur.

The lines profile shapes usually give information about the emission being observed. When the emission is optically thick and unresolved by the beam of the telescope, the line profiles can be described as parabolic. We see that in most sources, the observed line shapes of CS and SiO exhibit such profile. If the emission is optically thin and unresolved, a flat-topped profile is seen. This kind of profile is seen in the observed lines of SiS. One notable exception for the three molecules is IRC +10216, whose close proximity and high mass loss rate result in an extended envelope whose molecular emission is spatially resolved by the telescope beam, and the line profiles show a more or less marked double-peak character.

4. Excitation and radiative transfer modeling

We aim at deriving molecular abundances of CS, SiO, and SiS in each source of our sample to provide a global view of how abundant these molecules are in envelopes around carbon stars. For this purpose, we performed excitation and radiative transfer calculations. The rotational lines of CS, SiO, and SiS studied in this work have upper level energies in the range 12.5–31.4 K. As shown in Sect. 5, the emission from these lines does not arise from the inner parts of the envelope but from the intermediate and outer regions, where gas densities are not high enough to thermalize the rotational levels. Therefore, level populations cannot be described by local thermodynamic equilibrium (LTE), and detailed non-LTE excitation and radiative transfer calculations have to be carried out taking into account the specific parameters for each envelope (see Table 1) to derive accurate molecular abundances.

We consider an envelope model consisting of a central AGB star surrounded by a spherically symmetric envelope of gas and

[1] Continuum and Line Analysis Single-dish Software.
[2] http://www.iram.fr/IRAMFR/GILDAS

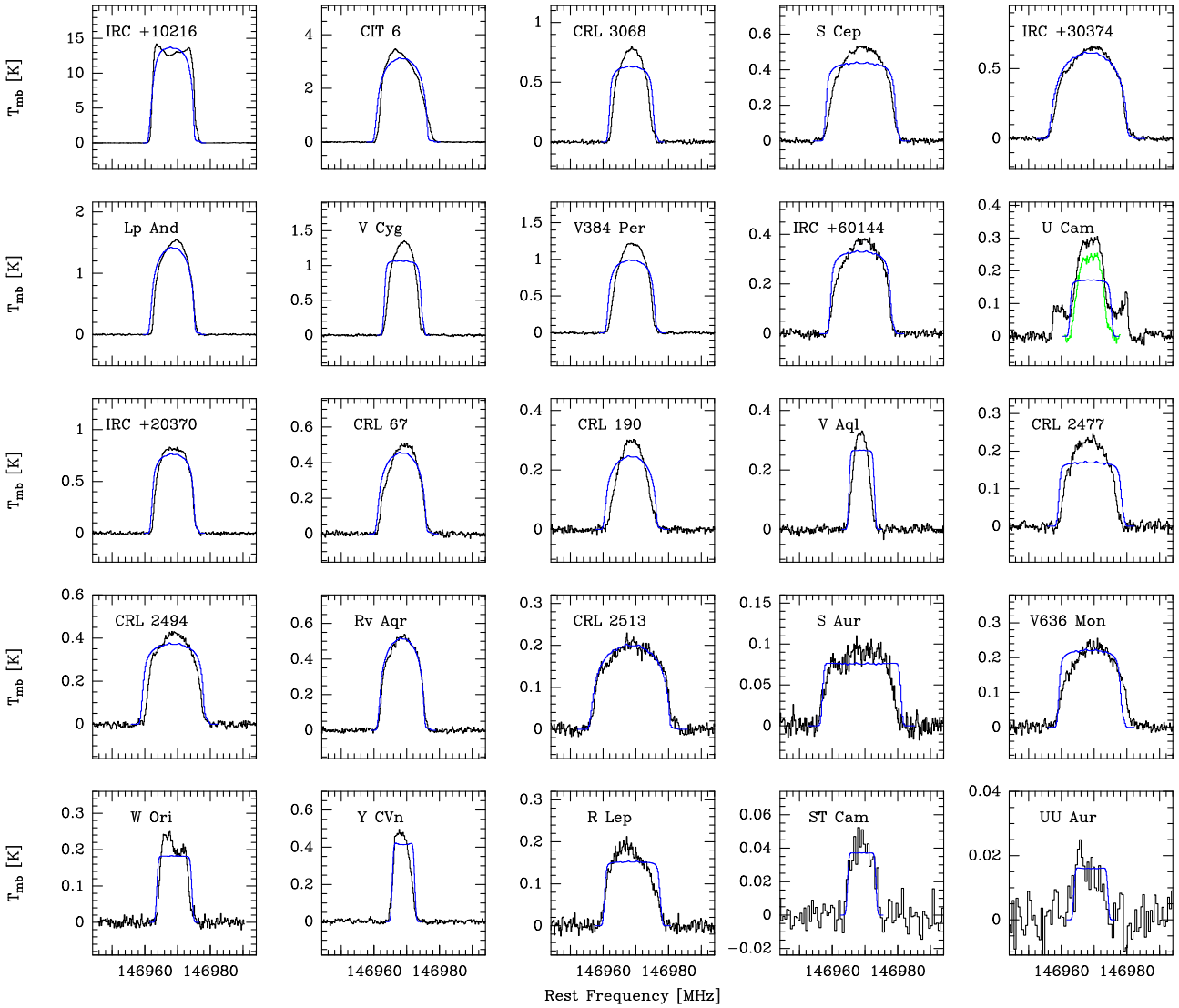

Fig. 1. CS $J = 3-2$ line observed with the IRAM 30 m telescope in the 25 carbon stars (black histograms). U Cam shows emission contribution from the present day wind and the detached envelope. The green histogram corresponds to the observed line profile in which a fit to the detached envelope contribution (the wider one) has been subtracted. The blue lines indicate the calculated line profiles from the best-fit LVG model.

dust expanding at constant velocity $V_{\rm exp}$ and with a mass loss rate $\dot{M}$, so that the radial density distribution follows an r^{-2} law. The adopted physical properties of the stars and associated CSEs are presented in Table 1. The various physical quantities describing the envelope, such as the radial profiles of the gas density, gas temperature, and dust temperature, as well as the properties of the dust grains, are described in Massalkhi et al. (2018).

We performed excitation and radiative transfer calculations to model the line emission of the studied molecules based on the multishell large velocity gradient (LVG) method. The LVG formalism is described in Sobolev (1960) and Castor (1970), whereas the implementation of the multishell method for CSEs is described in more detail in Agúndez (2009) and Agúndez et al. (2012). The LVG method deals well with optically thin lines and lines with moderate optical thickness (Castor 1970). This method is a good compromise with respect to other methodologies such as Monte Carlo, which are more computationally expensive and exhibit problems of convergence when including a high number of energy levels. Briefly, the circumstellar envelope is divided into a number of concentric shells, each of which has a characteristic set of physical properties. The excitation and radiative transfer is solved locally in each shell through statistical equilibrium equations, where collisional and radiative processes determine the level populations. In each shell, the contribution of the background radiation field is included and is composed of the cosmic microwave background, stellar radiation, and thermal emission from dust. We also include infrared (IR) pumping, that is, absorption of IR photons and pumping to excited vibrational states followed by spontaneous radiative decay to rotational levels in the ground vibrational state. This process has been found to play an important role in the excitation of some molecules in IRC +10216 (e.g., Agúndez & Cernicharo 2006). For the three molecules studied here (CS, SiO, and SiS), we only considered IR pumping to the first vibrationally excited state ($v = 1$). We did verify that adding upper vibrational states had no effect on the calculated line intensities, i.e., including up to $v = 1$ changed

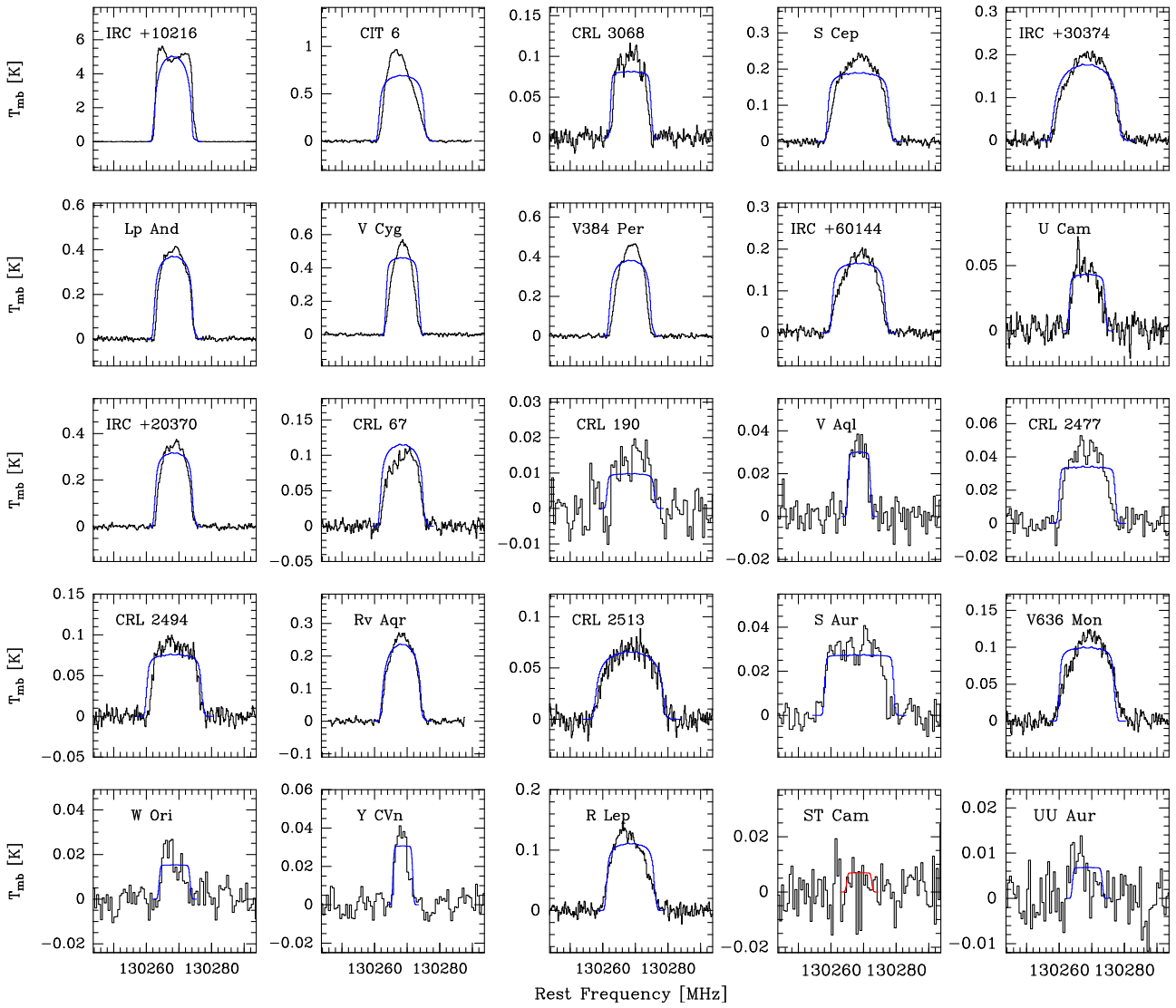

Fig. 2. SiO $J = 3-2$ line observed with the IRAM 30 m telescope in the 25 carbon stars (black histograms). The blue lines indicate the calculated line profiles from the best-fit LVG model. The SiO line is not detected in ST Cam; the red line corresponds to the calculated line profile with the maximum intensity compatible with the non-detection.

the line intensities for the three molecules in all the stars, but including up to $v = 3$ did not cause further changes.

4.1. Molecular data

A major prerequisite for a successful radiative transfer code is the availability of accurate spectroscopic and collisional excitation data. We discuss below the spectroscopic and collisional excitation data of the three molecules that were input into our calculations. We considered enough rotational states to include levels with energies higher than 2000 K to better deal with the inner hot regions of the envelopes.

In the excitation analysis of CS we considered the first 50 rotational levels within the $v = 0$ and $v = 1$ vibrational states (i.e., a total number of 100 energy levels). The level energies and transition frequencies were calculated from the Dunham coefficients given by Müller et al. (2005). The line strengths of pure rotational transitions were computed from the dipole moments for each vibrational state, $\mu_{v=0}$ =1.958 D and $\mu_{v=1}$ = 1.936 D (Winnewisser & Cook 1968), while for ro-vibrational transitions we used the Einstein coefficient of 15.8 s^{-1} given for the $v = 1 \rightarrow 0$ P(1) transition by Chandra et al. (1995). We adopted the collision rate coefficients recently calculated by Denis-Alpizar et al. (2018) for pure rotational transitions and up to temperatures of 300 K. At higher temperatures and for ro-vibrational transitions we used the rate coefficients calculated by Lique & Spielfiedel (2007) multiplying the original values computed for He as collider by the squared ratio of the reduced masses of the H_2 and He colliding systems.

In the case of SiO, we considered the first 50 rotational levels of the ground and first excited vibrational states. To calculate the line frequencies and strengths, we used the Dunham coefficients given by Sanz et al. (2003), the dipole moments for pure rotational transitions within the $v = 0$ and $v = 1$ vibrational states of 3.0982 and 3.1178 D, respectively, from Raymonda et al. (1970) and an Einstein coefficient for the ro-vibrational transition $v = 1 \rightarrow 0$ P(1) of 6.61 s^{-1} from Drira et al. (1997). As collisional rate coefficients we adopted those calculated by

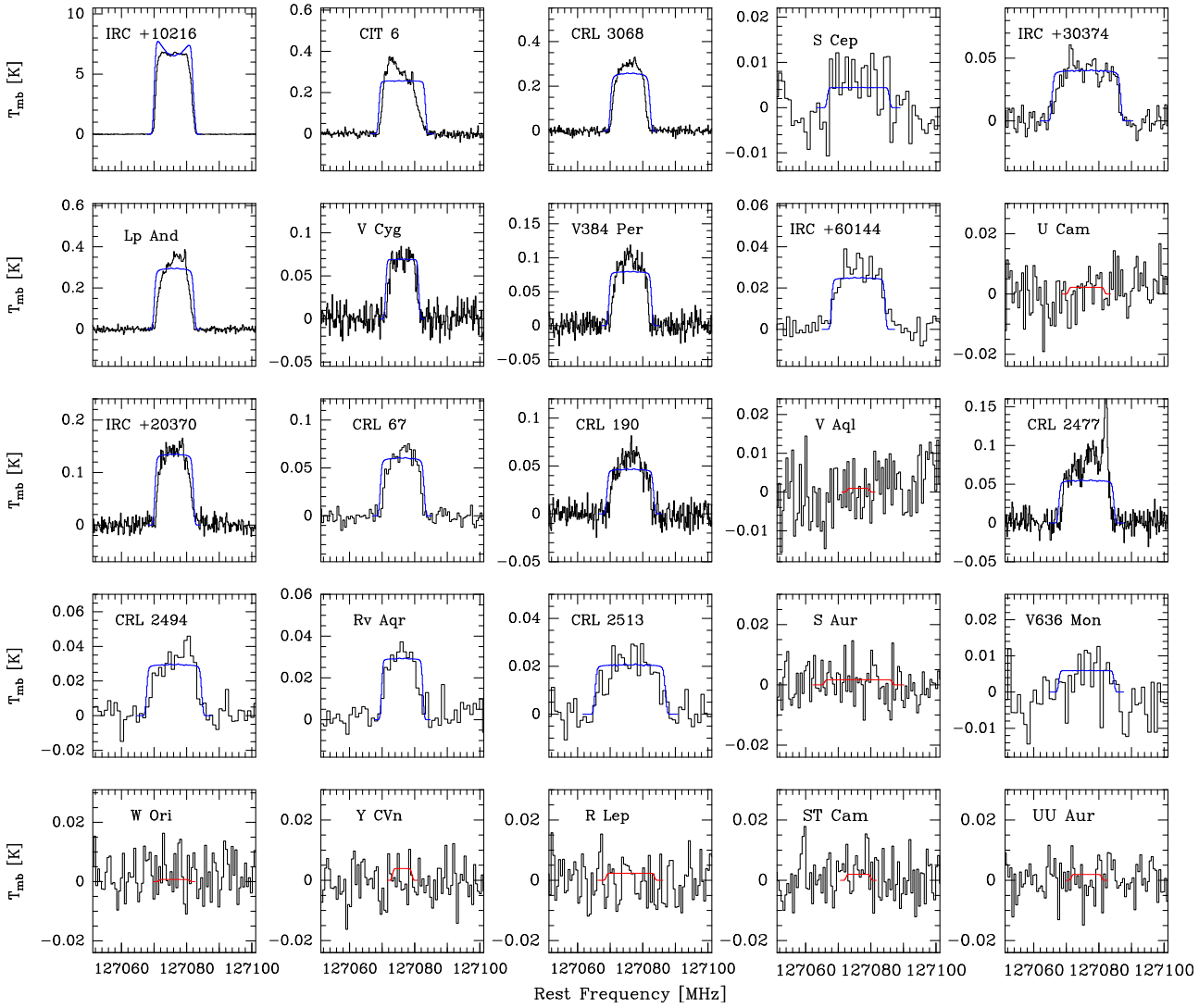

Fig. 3. SiS $J = 7-6$ line observed with the IRAM 30 m telescope in the 25 carbon stars (black histograms). The blue lines indicate the calculated line profiles from the best-fit LVG model. The SiS line is not detected in various sources, for which we plot in red the calculated line profiles with the maximum intensity compatible with the non-detection.

Dayou & Balança (2006) for pure rotational transitions and for temperatures up to 300 K, while at higher temperatures and for ro-vibrational transitions we used the values computed by Balança & Dayou (2017) scaling from He to H_2 as collider as in the case of CS.

For SiS, we include the first 70 rotational levels within the $v = 0$ and $v = 1$ vibrational states. Level energies were computed from the Dunham coefficients given by Müller et al. (2007). Line strengths were computed from the dipole moments $\mu_{v=0} = 1.735$ D, $\mu_{v=1} = 1.770$ D, and $\mu_{v=1\rightarrow0} = 0.13$ D (Müller et al. 2007; Piñeiro et al. 1987). The collisional rate coefficients have been taken from the calculations of Kłos & Lique (2008), while for temperatures higher than 300 K and for ro-vibrational transitions we adopted the collisional rate coefficients computed by Toboła et al. (2008) scaled from He to H_2 as with CS and SiO.

4.2. Abundance distributions

We consider that CS, SiO, and SiS are formed close to the star with a given fractional abundance that remains constant throughout the envelope up to some region in the envelope where the abundance drops. This abundance falloff can be driven by at least two different processes: (1) condensation onto grains around the dust formation zone, and (2) photodissociation by the ambient UV radiation field in the outer envelope. While these molecules can certainly deplete in the dust formation region owing to condensation onto dust grains, in this work we are not sensitive to such potential abundance decline since the observed lines mostly probe intermediate and outer regions of the envelopes, that is, post-condensation regions (see Sect. 5). It is interesting to note that in IRC +10216, the emission from CS, SiO, and SiS vanishes at relatively outer radii, where photodissociation takes place (Bieging & Nguyen-Quang-Rieu 1989; Lucas et al. 1992, 1995; Velilla Prieto et al. 2019). Various studies have reported on the abundance depletion in the inner regions of IRC +10216. These studies show different degrees of depletion for the molecules, and in some cases the studies even have contradictory findings (Keady & Ridgway 1993; Boyle et al. 1994; Schöier et al. 2006a; Decin et al. 2010a; Agúndez et al. 2012.) Regardless of whether these molecules may experience a first

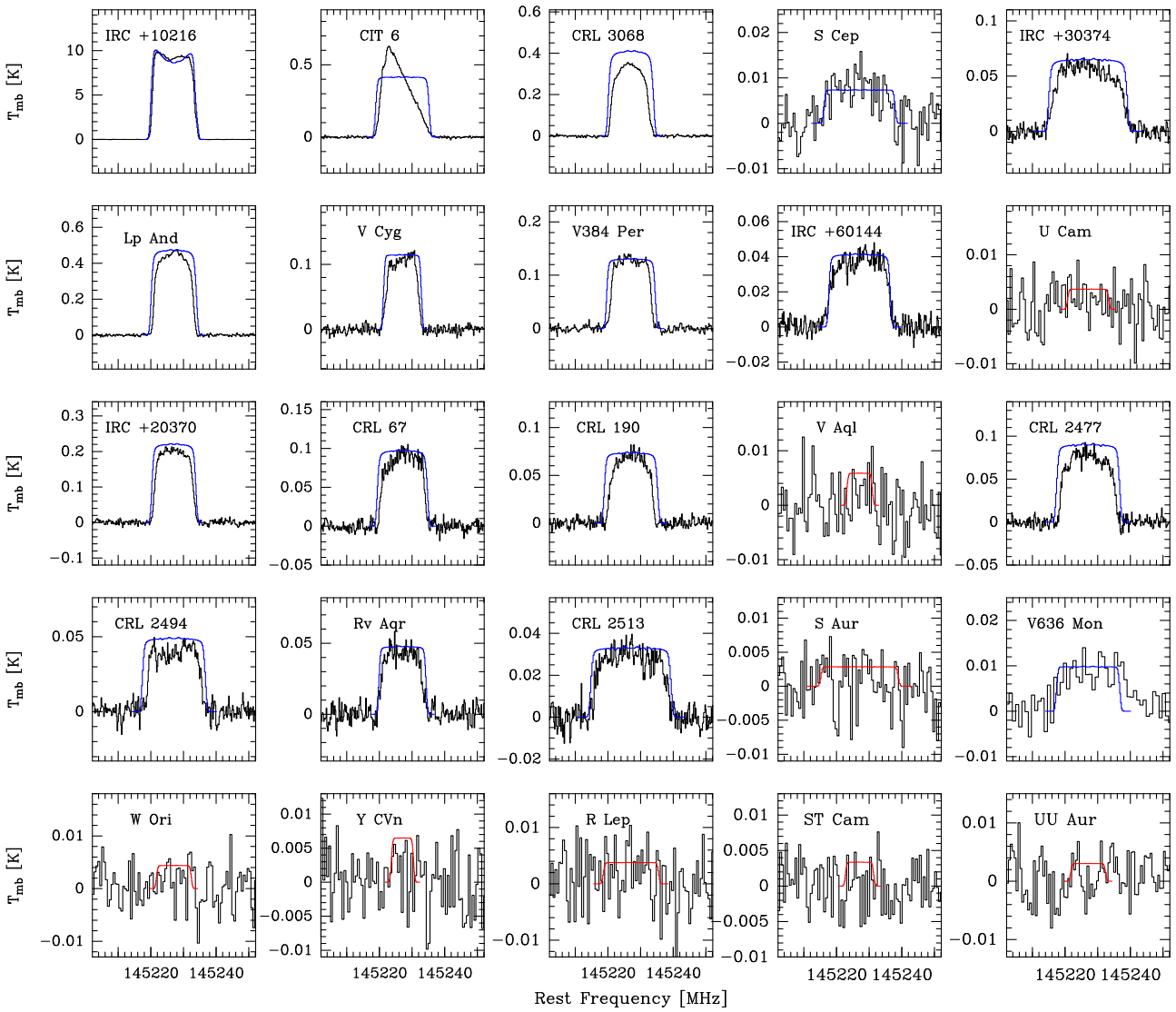

Fig. 4. Same as in Fig. 3 but for SiS $J = 8-7$.

abundance decline in the dust formation region or not, what is clear is that they maintain a significant abundance in the gas phase out to the outer envelope, where photodissociation is probably driving the disappearance of these molecules from the gas phase.

The above considerations suggest that a constant fractional abundance from the star and an abundance falloff driven by photodissociation in the outer envelope is a reasonable abundance distribution to model the lines observed in this work. In this scenario, the radial extent of each molecule would be entirely controlled by its corresponding photodissociation rate under the ambient UV radiation field and by the way in which circumstellar dust attenuates UV photons as they penetrate into the envelope. See Massalkhi et al. (2018) for more details on how the radial distributions were calculated using the photodissociation model. We however noticed that by using photodissociation rates from the literature when available (Heays et al. 2017 for SiO and Pattillo et al. 2018 for CS; see Sect. 6.4 for more details) and adopting the canonical interstellar $N_{\rm H}/A_V$ ratio for the local ISM (Bohlin et al. 1978), where $N_{\rm H}$ is the hydrogen column density in cm^{-2} and A_V is the visual extinction measured in magnitudes, the radial extent of these molecules is very likely underestimated, at least for some of the envelopes. This suspicion was based on the fact that the abundances derived for CS, SiO, and/or SiS were anomalously high in some sources, as they exceeded the elemental abundances of sulfur and/or silicon, which a priori are expected to be similar to those in the Sun (Asplund et al. 2009). Given the small number of observed lines (one for CS and SiO and two for SiS), the fact that they are sensitive to both the fractional abundance and the radial extent[3] and the fact that the radial extent is very likely not well described by a simple photodissociation model, we thus decided to fix the radial extent using an empirical correlation from the literature (see below) and leave as a free parameter the fractional abundance so that it can be derived by modeling the observed lines. Therefore, following the work by González Delgado et al. (2003) and Schöier et al. (2006b, 2007), in this study we adopted a simple abundance

[3] The emission arises from intermediate and outer regions of the envelopes and such regions are not resolved by the IRAM 30 m beam in most sources, with the notable exception of IRC +10216.

distribution given by a Gaussian

$$f(r) = f_0 \exp\left(-(r/r_e)^2\right), \quad (3)$$

where f is the fractional abundance relative to H_2, f_0 is the initial abundance, and r_e is the e-folding radius at which the abundance has dropped by a factor e. From a multiline study of SiO in M-type stars, González Delgado et al. (2003) found the following empirical correlation between the e-folding radius and the envelope density evaluated through the quantity $\dot{M}/V_{\rm exp}$,

$$\log r_e({\rm SiO}) = 19.2 + 0.48 \log\left(\frac{\dot{M}}{V_{\rm exp}}\right), \quad (4)$$

where r_e is given in cm, the mass loss rate $\dot{M}$ in $M_\odot$ yr^{-1}, and $V_{\rm exp}$ in km s^{-1}. Although the scaling law in Eq. (4) was derived for SiO in oxygen-rich stars, we adopted this law for SiO and SiS in our sample of carbon stars. Schöier et al. (2006b, 2007) made the same assumption in the lack of better constraints for C-type stars. Concerning the assumption of similar radial extents for SiO and SiS, it is worth noting that although the photodissociation rate of SiS is unknown[4], there are arguments that to a first order SiO and SiS should behave similarly with respect to photodissociation (van Dishoeck 1988; Wirsich 1994). Interferometric observations of these two molecules in IRC +10216 show that they have similar emission sizes, where the SiO emission is slightly more extended than that of SiS (Velilla Prieto et al. 2019). In the case of CS, we found it necessary to adopt a larger radial extent than for SiO and SiS because using Eq. (4) resulted in anomalously high CS abundances for some sources. We therefore adopted the following relation between e-folding radius and density in the envelope:

$$\log r_e({\rm CS}) = 19.65 + 0.48 \log\left(\frac{\dot{M}}{V_{\rm exp}}\right), \quad (5)$$

which was derived by starting from Eq. (4) and increasing the first term in small steps so that the amount of sulfur locked in CS and SiS does not exceed the solar elemental abundance of sulfur (i.e., $f_0({\rm CS}) + f_0({\rm SiS}) \leq 2.6 \times 10^{-5}$; Asplund et al. 2009) in any envelope of our sample. Such a larger radial extent for CS, compared with SiO and SiS, is consistent with the lower photodissociation rate calculated for CS compared to that computed for SiO (Heays et al. 2017; Pattillo et al. 2018; see Sect. 6.4) and with the larger emission size observed for CS with respect to SiO and SiS in IRC +10216 (Velilla Prieto et al. 2019).

In a recent study, Danilovich et al. (2018) derived empirical relations between r_e and $\dot{M}/V_{\rm exp}$ for SiS and CS from a limited sample of M-, C-, and S-type stars. We noticed that implementing their empirical relations in our model calculations resulted in anomalously high abundances for CS and SiS for some low mass loss rate envelopes, for example, for W Ori $f_0({\rm CS}) = 3.2 \times 10^{-5}$ and $f_0({\rm SiS}) = 8.8 \times 10^{-5}$, which imply a sulfur abundance well above the solar value. The main lesson from these calculations is that the empirical relations derived by Danilovich et al. (2018) cannot be safely extrapolated outside the relatively narrow range of $\dot{M}/V_{\rm exp}$ over which they were derived. We therefore decided not to adopt the CS and SiS scaling laws of these authors. It is worth noting that Danilovich et al. (2018) derived larger e-folding radii for CS than for SiS, which again points to CS being more extended than SiS in agreement with the above arguments. Meanwhile, their SiS extent is smaller than that of SiO derived by González Delgado et al. (2003), which could point to SiS being photodissociated faster than SiO.

In summary, to model the emission lines of CS, SiO, and SiS and determine their abundance in the observed sources, we constructed a model of the envelope for each source with the parameters given in Table 1 and adopting the abundance distribution given by Eq. (3), using Eqs. (4) and (5) accordingly, and performed excitation and radiative transfer calculations by varying the initial fractional abundance relative to H_2, f_0 in Eq. (3), until the calculated line profiles matched the observed profiles. We chose the model that results in the best overall agreement between calculated and observed line profiles as the best-fit model. More specifically, our criterion was to match the line area of the calculated profile and the observed profile, and so we scaled the derived abundance until the line area is reproduced. In those cases where no line is detected, we derive upper limits to the corresponding molecular abundance by choosing the maximum abundance that results in line intensities compatible with the noise level of the observations.

5. Results from line modeling

The calculated line profiles resulting from our best-fit LVG model for each of the sources are shown in blue in Fig. 1 for CS, Fig. 2 for SiO, and Figs. 3 and 4 for SiS, where they are compared with the observed line profiles (black histograms). We note that the overall agreement of the model is good given that our criterion of matching the line areas is fulfilled as described in the previous section. Concerning the line shapes, globally, the agreement is good as well.To facilitate the differentiation between line detections and non-detections, the calculated line profiles of the latter are plotted in red. In the case of CS in U Cam, the contribution from the present-day wind, which is that we are interested in modeling, is shown in green.

In Fig. 5 we show some salient features of the excitation and radiative transfer calculations for two envelopes, ST Cam and CRL 190, which are representative of very different envelope densities. While ST Cam lies in the lower range, with $\dot{M}/V_{\rm exp} = 1.5 \times 10^{-8}$ $M_\odot$ yr^{-1} km^{-1} s, CRL 190 lies at the higher end, with $\dot{M}/V_{\rm exp} = 3.7 \times 10^{-6}$ $M_\odot$ yr^{-1} km^{-1} s. The bottom panels of Fig. 5 show the calculated ratio of excitation temperature to gas kinetic temperature ($T_{\rm ex}/T_k$) for the observed lines of CS and SiO and that of the observed lines of SiS as a function of radius. We see that the rotational levels involved in the targeted transitions of the three molecules are thermalized ($T_{\rm ex}/T_k = 1$) in the hot and dense inner regions, while as the radial distance from the star increases and the gas density decreases, the rotational levels deviate from thermalization. Concretely, lines become increasingly suprathermally excited ($T_{\rm ex}/T_k > 1$) with increasing radius, an effect that is largely caused by IR pumping. Therefore, IR pumping plays an important role in the excitation of the rotational transitions of these molecules. The much lower mass loss rate of ST Cam compared to CRL 190 implies substantially lower densities in the envelope and thus in ST Cam rotational populations start to deviate from thermalization at shorter radii than in CRL 190. The fact that the observed lines are not thermalized throughout most of the envelope, especially at low mass loss rates, stresses the need for non-LTE excitation calculations. For the low-mass loss rate ST Cam, the models without IR pumping for SiO and CS display a peculiar behavior caused by the excitation temperature becoming negative from intermediate regions of the envelope. Including IR pumping makes this behavior

[4] Prasad & Huntress (1980) reported a photodissociation rate of 1.0×10^{-10} s^{-1} for SiS. Although it is difficult to trace the exact origin of this number, we suspect that it was most likely assumed to be equal to that of SiO.

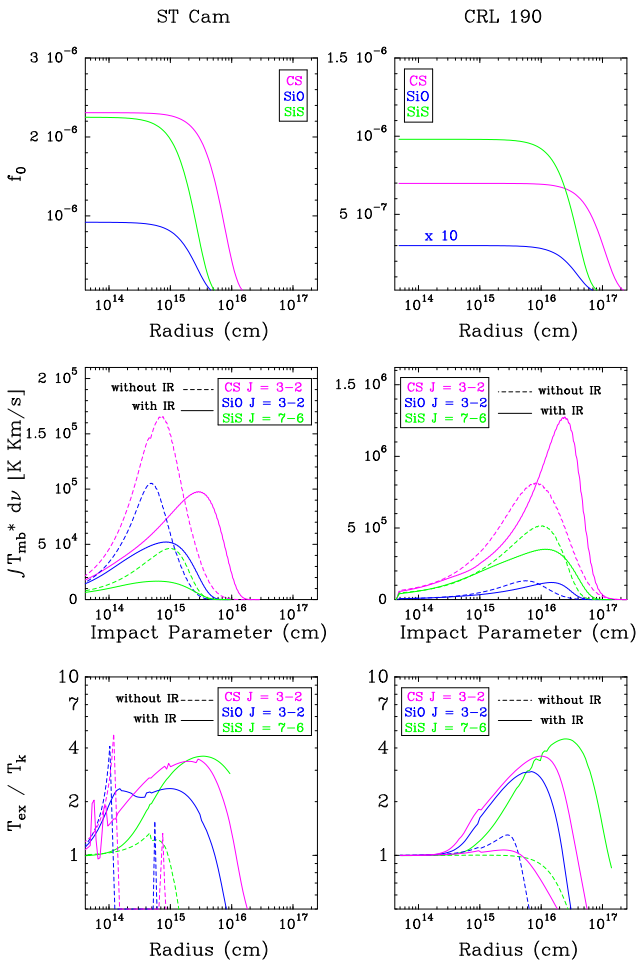

Fig. 5. Various features from the excitation and radiative transfer models for a low mass loss rate object (ST Cam) and a high mass loss rate object (CRL 190). *Top panels*: radial abundance profiles of CS, SiO, and SiS. *Middle panels*: calculated velocity-integrated intensities for the observed lines of CS, SiO, and SiS as functions of the impact parameter. *Bottom panels*: calculated ratio of excitation temperature to kinetic temperature (T_{ex}/T_k) as a function of radius for observed lines of CS, SiO, and SiS. Solid lines correspond to the model in which IR pumping is included, whereas dashed lines correspond to the model excluding IR pumping. The SiS abundance in ST Cam corresponds to an upper limit.

disappear. We note the SiS lines seem to end so abruptly because of the choice of the envelope outer edge in our model, where we chose the envelope to end at a radius at which the fractional abundance has dropped by a factor of 10^5.

The middle panels of Fig. 5 show the velocity-integrated intensity of the observed lines as a function of the impact parameter (solid lines). We see that in ST Cam the maximum contribution to the line emission comes from regions at a few 10^{15} cm from the star, while in the case of CRL 190 the regions located at radii of a few 10^{16} cm contribute the most to the observed emission. Therefore, most of the emission of the observed lines arises from intermediate and outer regions of the envelope, rather than from inner regions. Moreover, the λ 2 mm lines studied in this work probe regions where the abundance falloff has already started, which is especially marked in objects with low mass loss rates such as ST Cam (compare middle and top panels in Fig. 5). This fact explains why the observed lines are sensitive to both

Table 3. Fractional abundances of CS, SiO, and SiS derived.

Name	$\dot{M}$ ($M_\odot$ yr^{-1})	V_{exp} (km s^{-1})	f_0(CS)	f_0(SiO)	f_0(SiS)
IRC +10216	2.0×10^{-5}	14.5	1.1×10^{-6}	2.6×10^{-7}	1.3×10^{-6}
CIT 6	6.0×10^{-6}	17	6.4×10^{-6}	1.5×10^{-6}	4.8×10^{-6}
CRL 3068	2.5×10^{-5}	14.5	7.4×10^{-7}	1.4×10^{-7}	3.8×10^{-6}
S Cep	1.2×10^{-6}	22.5	9.9×10^{-6}	9.4×10^{-6}	1.9×10^{-6}
IRC +30374	1.0×10^{-5}	25	1.0×10^{-5}	5.0×10^{-6}	7.2×10^{-6}
Y CVn	1.5×10^{-7}	7	5.7×10^{-6}	8.1×10^{-7}	$<8.0\times10^{-7}$
LP And	7.0×10^{-6}	14.5	3.6×10^{-6}	1.0×10^{-6}	7.0×10^{-6}
V Cyg	1.6×10^{-6}	12	3.3×10^{-6}	2.9×10^{-6}	4.0×10^{-6}
UU Aur	2.4×10^{-7}	10.6	3.0×10^{-7}	2.5×10^{-7}	$<6.1\times10^{-7}$
V384 Per	2.3×10^{-6}	15.5	8.4×10^{-6}	6.4×10^{-6}	1.0×10^{-5}
IRC +60144	3.7×10^{-6}	19.5	7.3×10^{-6}	9.5×10^{-6}	1.0×10^{-5}
U Cam [a]	2.0×10^{-7}	13	1.9×10^{-5}	1.0×10^{-5}	$<4.1\times10^{-6}$
V636 Mon	5.8×10^{-6}	20	2.0×10^{-6}	1.7×10^{-6}	9.6×10^{-7}
IRC +20370	3.0×10^{-6}	14	4.1×10^{-6}	3.0×10^{-6}	1.1×10^{-5}
R Lep	8.7×10^{-7}	17.5	3.6×10^{-6}	5.7×10^{-6}	$<1.1\times10^{-6}$
W Ori	7.0×10^{-8}	11	2.1×10^{-5}	3.6×10^{-6}	$<4.9\times10^{-6}$
CRL 67	1.1×10^{-5}	16	3.5×10^{-6}	1.1×10^{-6}	4.6×10^{-6}
CRL 190	6.4×10^{-5}	17	7.0×10^{-7}	3.0×10^{-8}	9.8×10^{-7}
S Aur	4.0×10^{-7}	24.5	9.3×10^{-6}	6.9×10^{-6}	$<3.3\times10^{-6}$
V Aql	1.4×10^{-7}	8	1.0×10^{-5}	2.5×10^{-6}	$<2.3\times10^{-6}$
CRL 2513	2.0×10^{-5}	25.5	3.1×10^{-6}	1.3×10^{-6}	2.8×10^{-6}
CRL 2477	1.1×10^{-4}	20	2.7×10^{-7}	1.0×10^{-7}	1.7×10^{-6}
CRL 2494	7.5×10^{-6}	20	7.0×10^{-6}	2.9×10^{-6}	1.1×10^{-5}
RV Aqr	2.3×10^{-6}	15	7.7×10^{-6}	5.5×10^{-6}	4.6×10^{-6}
ST Cam	1.3×10^{-7}	8.9	2.3×10^{-6}	$<9.2\times10^{-7}$	$<2.2\times10^{-6}$

Notes. [a]U Cam has a present-day wind and a detached shell expanding away from the central star (for further details see Schöier et al. 2005). The values of f_0 given in this table correspond to the present-day wind.

the fractional abundance and the radial extent, and why adopting a more compact (extended) distribution would require a higher (lower) fractional abundance to reproduce the observed lines.

Infrared pumping not only plays an important role in regulating the excitation of the observed lines but also in determining their emission distribution. The bottom panels in Fig. 5 show that the emission is more compact if IR pumping is not included (dashed lines) than if it is taken into account (solid lines). Therefore, IR pumping results in a more extended emission distribution with an impact on the emerging line intensity. In fact, neglecting IR pumping results in a systematic decrease in the integrated line intensities of CS $J = 3-2$ and SiO $J = 3-2$ of ~60 and ~50%, respectively, on average. In the case of SiS $J = 7-6$ and $J = 8-7$ the effect of excluding IR pumping is not as systematic as with CS and SiO as it leads to a decrease of the line intensities in some sources and an increase in other sources. If higher J lines of SiS were targeted (above $J = 10-9$) the effect of excluding IR pumping would be a systematic decrease in the integrated line intensities.

6. Discussion

6.1. Fractional abundances

The abundances derived for CS, SiO, and SiS in the 25 carbon-rich envelopes studied are summarized in Table 3. For some of these sources, abundances have been previously reported. For example, in IRC +10216 the abundances of CS, SiO, and SiS were derived by Agúndez et al. (2012) from a multiline study including lines from vibrationally excited states. These authors found abundances relative to H_2 of 7×10^{-7} for CS, 1.8×10^{-7} for SiO, and 1.3×10^{-6} for SiS, which are in very good agreement with the abundances derived in this work.

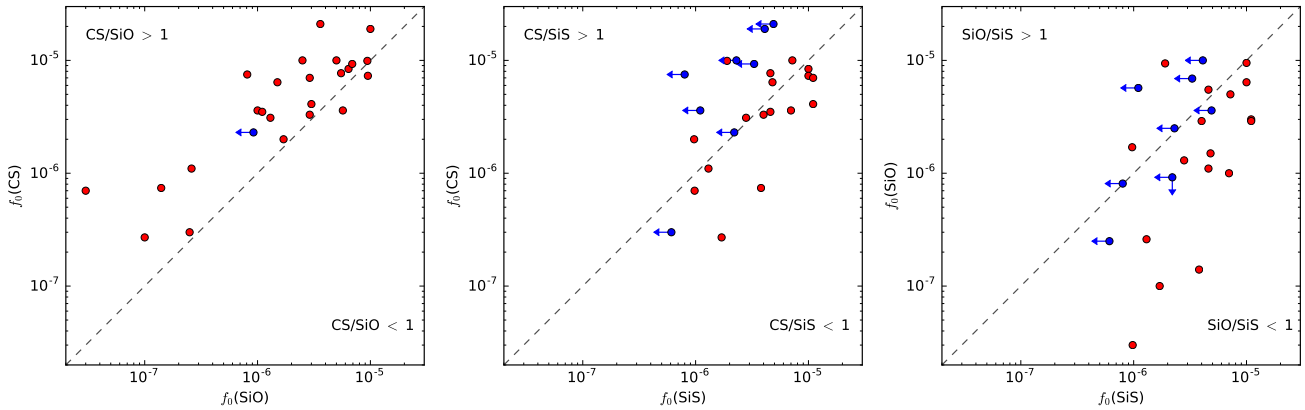

Fig. 6. Comparison of abundances between different pairs of molecules. The plots show the derived fractional abundances relative to H_2 of CS vs. SiO (*left panel*), CS vs. SiS (*middle panel*), and SiO vs. SiS (*right panel*). Those sources with non-detections are denoted with blue arrows. Diagonal dashed lines indicate where the abundances of the two molecules become equal.

Olofsson et al. (1993) looked for CS $J = 2-1$ emission in a large sample of carbon stars, 12 of which are in our sample. However, in about half of these stars the line was not detected and only loose abundance upper limits could be derived. These authors used a relatively simple method for estimating the molecular abundances, which is based on an analytical expression and where they assumed a constant excitation temperature for simplicity. In those sources where CS was detected, the abundances derived were very high, often greater than the maximum amount obtainable for solar abundance of sulfur. They suggested that these anomalously high abundances probably originate from uncertainties in the envelope model. In another study, Bujarrabal et al. (1994) surveyed a large sample of evolved stars in lines of several molecules including CS, SiO, and SiS. Their sample contains 16 C-rich AGB stars, 12 of which are also in our sample. These authors derived the abundances using an analytical expression that estimated only a lower limit if the line was optically thick. In general, their CS, SiO, and SiS abundances are lower than ours by a factor of a few and not higher than a factor of 10, apart from U Cam, where our derived CS and SiO abundances are one and two orders of magnitude, respectively, higher than theirs. Bujarrabal et al. (1994) remarked that their abundances may be underestimated owing to optical depth effects.

More recently, Schöier et al. (2006b) surveyed a sample of 19 C-rich AGB stars and detected SiO line emission in all of these objects. They performed radiative transfer calculations to derive abundances adopting, similar to us, an abundance distribution based on the scaling law established by González Delgado et al. (2003) for SiO in M-type stars. We share 13 sources with the former. Our SiO abundances are in good agreement with theirs for some sources, while for others there are significant differences. In LP And, for example, our derived SiO abundance is higher than theirs by almost a factor of ten, but on the other hand, our derived value in UU Aur is one order of magnitude lower than theirs, probably owing to differences in both the observations and the model. Later on, Schöier et al. (2007) reported on the detection of SiS line emission in 14 carbon stars, most of which are included in our sample. In general, the SiS abundances derived by us are similar to theirs, except for LP And, where we derive a SiS abundance higher than theirs by a factor of ~6.

In this work, the fractional abundances relative to H_2 derived range between 2.7×10^{-7} and 2.1×10^{-5} for CS, 3×10^{-8} and 1×10^{-5} for SiO, and $<6.1\times10^{-7}$ and 1.1×10^{-5} for SiS. Silicon monoxide is the molecule experiencing the largest variations (more than two decades) from source to source, while CS abundances span over two decades, and SiS shows the most uniform abundances across sources (with variations of less than two decades). We find that CS is systematically more abundant than SiO in most of the sources (see left panel of Fig. 6, where it is seen that most sources fall in the region of CS/SiO > 1). We also note that SiO tends to be less abundant than SiS; the right panel of Fig. 6 shows that for most sources SiO/SiS $\lesssim$ 1, while only in a few SiO/SiS is greater than one. Therefore, SiS seems to be a more efficient gas-phase reservoir of silicon than SiO in most carbon star envelopes. When comparing between CS and SiS, the two major gas-phase molecular reservoirs of sulfur in C-rich envelopes (see, Danilovich et al. 2018 and, e.g., the case of IRC +10216; Agúndez et al. 2012), we notice that in some sources such as IRC +30374 and U Cam, CS is more abundant than SiS, while in others (e.g., CRL 3068 and CRL 2494) the contrary is found. Overall, the data points in the middle panel of Fig. 6 fall along the line defined by f_0(CS) = f_0(SiS), with no clear preference for either the CS/SiS > 1 or the CS/SiS < 1 sides.

We can therefore extract as statistically meaningful conclusions that in carbon star envelopes CS and SiS have abundances of the same order, and that SiO is in general less abundant than CS and SiS. This is most likely a chemical feature related to C-rich AGB envelopes. Danilovich et al. (2018) determined the CS and SiS abundances in a sample of AGB stars, and likewise found comparable CS and SiS abundances in C-rich AGB stars, while in their O-rich sample, SiS was found to be systematically higher than CS. S stars were also found to have similar abundances. In this line, it is interesting to see what TE predicts for these molecules in C-rich AGB atmospheres. In Fig. 7 we show the calculated fractional abundances of CS, SiO, and SiS as a function of radial distance from the star for various mass loss rates. The underlying physical scenario adopted for the TE calculations is the same as adopted in Massalkhi et al. (2018), where we used the radial profiles of density and temperature of IRC +10216 (Agúndez et al. 2012; see downward revision on the density profile by Cernicharo et al. 2013) and scaled the density profile up or down depending on the mass loss rate, that is in the range of 10^{-7}–10^{-4} $M_\odot$ yr^{-1}. Therefore, the TE calculations adopt different density profiles to account for low and

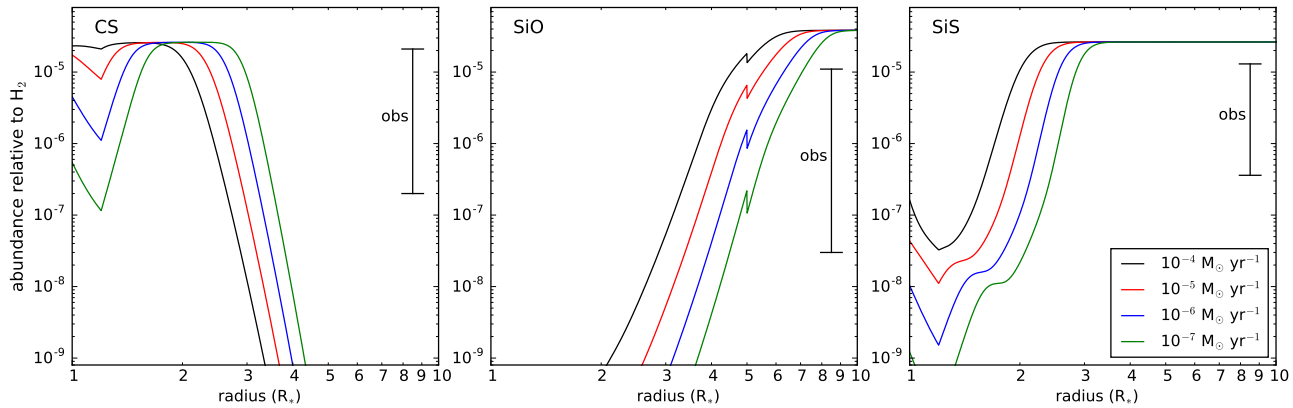

Fig. 7. Calculated fractional abundances of CS (*left panel*), SiO (*middle panel*), and SiS (*right panel*) under TE as a function of distance to the AGB star for various mass loss rates. The range of observed abundances is indicated.

high mass loss rates. We see that CS is predicted to have a high abundance (locking most of the available sulfur) in the close surroundings of the AGB star (at 1–3 R_*), while at farther distances its TE abundance vanishes to very low levels. On the other hand, SiS has almost the opposite behavior, with low abundance levels close to the star and a very high abundance beyond 2–3 R_*. The fact that CS and SiS are observed with similar abundances in our sample of envelopes is consistent with the abundances of these molecules being quenched to their TE values at radii of 2–3 R_*, which agrees with findings from the study of IRC +10216 (Agúndez & Cernicharo 2006; Agúndez et al. 2012). The process of abundance quenching is expected because as the gas expands the temperature and density drop and chemical reactions become slower and eventually too slow to proceed efficiently so that abundances are not further modified. Silicon monoxide shows a calculated radial TE abundance profile similar to that of SiS but shifted to larger radii. That is, SiO has a vanishingly small TE abundance close to the star, although calculations predict that this will reach a very high abundance (trapping most of the available silicon) beyond 5–8 R_*. The fact that the TE abundance of SiO is only high at a relatively large distance from the star is probably at the origin of the lower observed abundance of SiO compared to CS and SiS. In any case, given the range of SiO abundances derived from observations, SiO must quench its abundance to the TE value at somewhat larger radii than for CS and SiS. Predictions from a chemical kinetics model of the inner wind of AGB stars, including shocks driven by the pulsation of the star (Cherchneff 2006), indicate that for a C-rich object with a C/O elemental abundance ratio of 1.1, the abundances of CS, SiO, and SiS injected into the expanding envelope would be similar within a factor of ∼1.5, where CS is slightly more abundant than SiO and SiS. Given the scatter in the relative abundances of CS, SiO, and SiS derived by us and the very concrete physical scenario of AGB wind adopted by Cherchneff (2006), it is difficult to establish meaningful conclusions regarding whether the relative abundances we derive may be ultimately driven by shock-induced chemistry in the inner wind.

It is interesting to note that regardless of which pair of molecules is chosen, the plots in Fig. 6 show a trend in which the higher the abundance of one molecule the more abundant the other is. That is, the abundances of CS, SiO, and SiS seem to scale with each other, so that there are envelopes in which the three molecules are abundant, while in others the three molecules maintain low abundance levels. This conclusion seems robust when considering CS and SiO, although it may not be completely true concerning SiS because in some of the sources where SiS is not detected, SiS may have a low abundance while CS and SiO do not. This point is discussed in more detail below. We note that a correlation of this type was found by Danilovich et al. (2018) for CS and SiS in a sample including C-, M-, and S-type stars, although in that study the trend is considered tentative because of the small number of sources included.

In Fig. 8 we plot the fractional abundances f_0 derived for CS, SiO, and SiS as a function of the density in the envelope, evaluated through the quantity $\dot{M}/V_{\rm exp}$. In the case of CS, the data strongly suggest a negative correlation between CS abundance and envelope density. The same behavior is even more evident for SiO. That is, as the density in the envelope increases the abundances of CS and SiO decrease. This behavior was already found for SiO in both M-type stars by González Delgado et al. (2003) and carbon stars by Schöier et al. (2006b) and was interpreted as an evidence of enhanced SiO adsorption onto dust grains (and thus depletion from the gas phase) with increasing density. Using a larger sample of carbon stars, we thus confirm the result found by Schöier et al. (2006b) for SiO. The same trend of decreasing abundance with increasing density was also found recently for SiC_2, pointing to this molecule as a gas-phase precursor of silicon carbide dust around carbon stars (Massalkhi et al. 2018). We note that in the recent study by Danilovich et al. (2018), the abundances of CS derived in C-type AGB envelopes do not show the anticorrelation with envelope density found by us. The reason is that their sample of carbon stars, with just seven objects, is small and the range of $\dot{M}/V_{\rm exp}$ covered does not include high density envelopes, of which those in our sample give better evidence of the trend of decreasing abundance with increasing density.

It is worth looking at the predictions of TE to investigate whether the anticorrelation between abundance and envelope density observed for CS and SiO could be caused by an effect of the density on the TE abundance of these molecules. As shown in Fig. 7, the main effect of an increase in the mass loss rate, and thus on the envelope density, on the abundances of CS and SiO is that the curves shift slightly to inner radii. If the radius at which the CS abundance is quenched to its TE value is the same for different mass loss rates, then the quenched abundance of CS would be lower for higher mass loss rates, in agreement with the observed behavior. It is however unlikely that the radius of abundance quenching is the same for different mass loss rates because higher densities would make the region of abundance quenching occur at larger radii. The reason is that higher densities

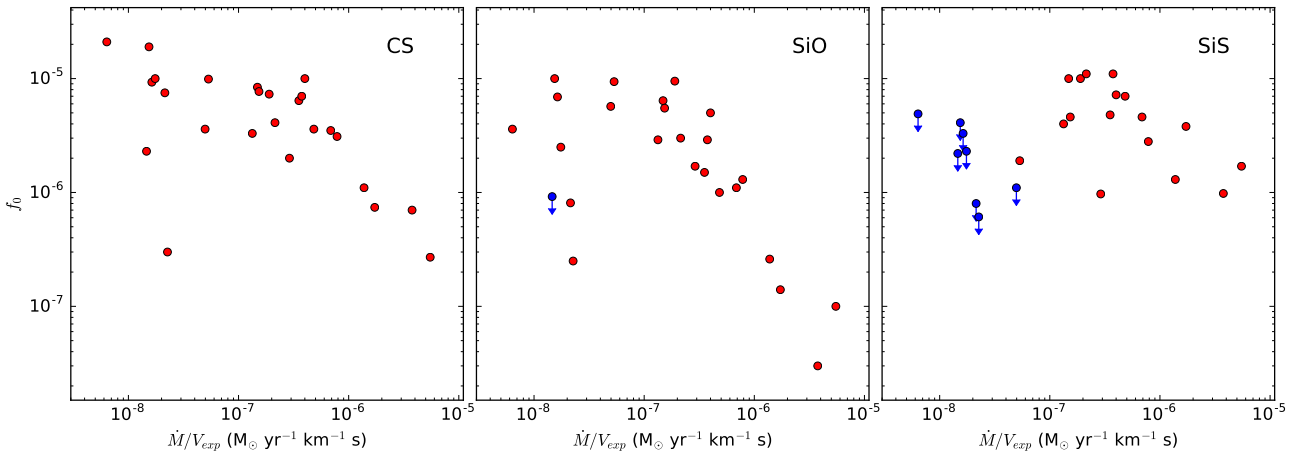

Fig. 8. Fractional abundances f_0 derived for CS (*left panel*), SiO (*middle panel*), and SiS (*right panel*) are plotted as a function of the envelope density proxy $\dot{M}/V_{\rm exp}$ for the 25 C-rich envelopes studied here. Blue downward arrows represent upper limits to f_0.

imply shorter chemical timescales and a larger region in which TE prevails. This would result in an even more pronounced decrease of the quenched CS abundance with increasing density. Although qualitatively this scenario would be in agreement with the observed trend of decreasing abundance of CS with increasing density, a detailed chemical kinetics model is needed to obtain quantitative estimates. In the case of SiO, a similar reasoning implies that the quenched abundance would be higher for higher densities (see Agúndez & Cernicharo 2006) contrary to what observations indicate. It is therefore very unlikely that the observed decrease in the abundance of SiO with increasing density is caused by gas-phase chemistry. The most likely explanation is that SiO incorporates into dust grains and depletes from the gas phase with increasing density in the envelope.

The case of SiS deserves special attention. It is remarkable that SiS is not detected in envelopes with low mass loss rates below 10^{-6} $M_\odot$ yr^{-1}, while it is detected in all sources with mass loss rates above that threshold. This fact, which has been noticed to some extent in previous observational studies (Bujarrabal et al. 1994; Schöier et al. 2007; Danilovich et al. 2018), is shown in this work in a robust way (see Table 3 and right panel of Fig. 8). The reason behind this behavior is not clear. The non-detection of SiS in these envelopes might either be due to a lack of sensitivity or a low fractional abundance of the molecule. Looking at the predictions of TE (right panel in Fig. 7), we note that for low mass loss rates the predicted abundance of SiS is indeed lower. This fact is even more marked if we take into account that the radius at which the abundance quenches to the TE value is expected to be shifted to inner radii for lower mass loss rates. A scenario of TE chemistry plus abundance quenching would be in agreement with objects with low mass loss rates having lower SiS abundances. If that is the underlying cause, it is however strange that the observed SiS abundances do not show a smooth variation with density but an abrupt differentiation between sources with and without SiS detection at 10^{-6} $M_\odot$ yr^{-1}, and show no evidence of increasing SiS abundance with increasing density for those sources where SiS is detected. We suspect that the lack of SiS detections in objects with low mass loss rates could be caused by a lack of its constituent elements, which would be largely trapped in SiO and SiC_2 (in the case of silicon) and CS (regarding sulfur). As shown in this work and in Massalkhi et al. (2018), the molecules SiO, CS, and SiC_2 (probably also Si_2C; Cernicharo et al. 2015) become very abundant in C-rich objects with low mass loss rates. This suspicion however would need to be corroborated with a detailed chemical kinetics model of the inner wind of envelopes with different mass loss rates. Apart from the upper limits to the abundance of SiS in objects with low mass loss rates, the SiS abundances derived through positive detections show hints of decreasing SiS abundance with increasing density (right panel in Fig. 8). This has to be seen as tentative, however, and in any case it is not as evident as in the cases of CS and SiO. Therefore, if the tentative decrease in the abundance of SiS with increasing envelope density is interpreted in terms of adsorption onto dust grains, we can conclude that SiS is not incorporated into dust grains to an extent as important as that of SiO.

Schöier et al. (2007) found that the SiS abundance does not show any particular correlation with the envelope density for C-rich envelopes. However, they found a slightly better fit to their observations for the case of IRC +10216 by including a compact SiS component with a fractional abundance 1.7×10^{-5} out to a radius of 5×10^{14} cm, which could imply an SiS abundance gradient in line with the results found by Agúndez et al. (2012). Introducing an inner high-abundance SiS component also produced a better fit for the oxygen-rich IK Tau implying SiS depletion. This result is similar to that found by Decin et al. (2010b) when modeling low- and high-excitation lines, however a recent study by Danilovich et al. (2019), using sensitive ALMA observations to determine the SiS distribution in the envelope of IK Tau, does not reveal a compact inner region as previously found. Regardless, we do maintain that the evidence of SiS depletion in C-rich envelopes is weak.

In any case, in this work we investigated SiS in a larger sample of carbon stars covering a broader range of envelope densities than previously studied, which permitted us to clearly see a systematic non-detection of SiS at low mass loss rates and a tentative negative correlation between SiS abundance and envelope density seen at high mass loss rates.

6.2. MgS dust: possible gas-phase precursors

A common characteristic that is seen in C-rich evolved stars is the presence of a prominent IR emission band that is centered around 30 μm. The feature was discovered by Forrest et al. (1981) in dusty carbon-rich environments; Goebel & Moseley (1985) first suggested that magnesium sulfide (MgS) dust may

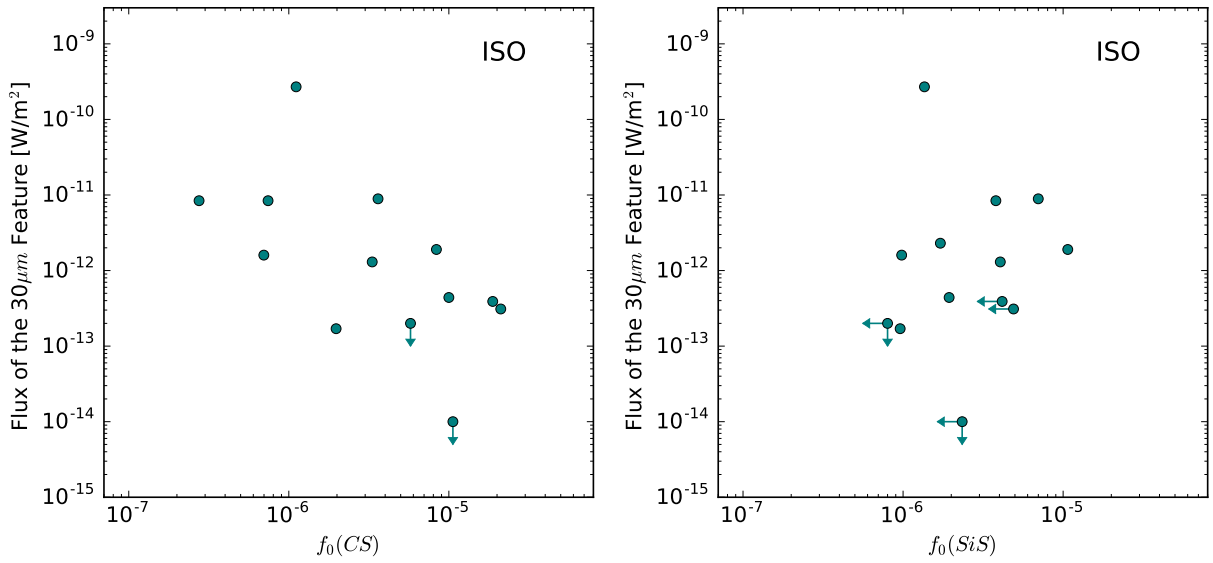

Fig. 9. Flux of the MgS dust feature at 30 μm observed by ISO (Hony et al. 2002) vs. the fractional abundance of CS (*left panel*) and SiS (*right panel*) derived in this work.

be responsible for this spectral feature and this suggestion has been widely accepted since then. However, the carrier is still argued upon. One of the major concerns is regarding the sulfur abundance that is required to explain the observed emission. Zhang et al. (2009) argued that the amount of MgS required to explain the power emitted by the 30 μm feature in the post-AGB, HD 56126, would require ten times more atomic sulfur than available in the ejected envelope. Zhukovska & Gail (2008) found the only way MgS dust can form for C-rich AGB stars is by precipitation on preexisting silicon carbide grains. Lombaert et al. (2012) then discussed that if the grains were of a heterogeneous composite nature, meaning if MgS dust forms in a layer coated around an amorphous carbon/SiC core grain, then there would not be an abundance constraint. Investigating the formation mechanism of MgS dust is out of the scope of this paper. However, we can investigate if there is a connection between the sulfur bearing molecules studied in this work and the 30 μm feature attributed to MgS dust. This way we could identify if any of these S-bearing molecules could act as precursors of MgS dust in the ejecta of AGB stars. More specifically, we aim to investigate whether there is a relation between the derived fractional abundances of CS and SiS and the strength of the 30 μm feature.

Hony et al. (2002) carried out an observational study of the 30 μm feature of a large number of C-rich sources observed with the Infrared Space Observatory (ISO). There are 13 sources in common between their sample and ours. In the left panel of Fig. 9 we plot the flux of MgS dust versus the fractional abundance of CS for these 13 sources. We clearly see a trend in which the flux of MgS dust increases as the gas-phase abundance of CS decreases. If the flux of the 30 μm feature is a good proxy of the amount of MgS dust and if the hypothesis that CS is a gas-phase precursor of dust in C-rich AGB stars is correct, then this result supports the idea that the decline in the abundance of CS with increasing envelope density is caused by a more efficient incorporation of CS on MgS dust. In the case of SiS there is no obvious correlation between the fractional abundance and the flux of the 30 μm feature (see right panel of Fig. 9). The lack of correlation suggests that SiS does likely not play a role in the formation of MgS dust in these stars, although we note that the range of SiS abundances covered is limited. Smolders et al. (2012) carried out an observational study on a large sample of S-type stars and found that many stars that show the MgS emission feature also show emission peaks at 6.6 and 13.5 μm due to molecular SiS. This fact led these authors to suggest that MgS dust could be formed as a consequence of a reaction between Mg and SiS in S-type stars in contrast with our conclusion that CS, rather than SiS, is a precursor of MgS dust in C-rich AGB stars.

6.3. SiO and SiS as possible precursors of SiC dust

Since both SiO and SiS are important Si-carriers (Olofsson et al. 1982; Lucas et al. 1995; Agúndez et al. 2012), in this section we assess if there could be a relation between these molecules and the formation of SiC dust around AGB stars. We collected information on the Infrared Astronomical Satellite (IRAS) and the ISO data for the sources in our sample that exhibit the SiC dust emission feature at 11.3 μm. Sloan et al. (1998) analyzed the IRAS spectra of carbon stars with which we share 15 sources, and Yang et al. (2004) studied the ISO spectra of C-rich AGB stars with 9 sources in common with our sample. These authors determined the relative flux of SiC dust as the ratio of the integrated flux of the 11.3 μm emission feature (after continuum substraction) divided by the integrated flux of the continuum. In Fig. 10 we plot the relative integrated flux of SiC dust versus the fractional abundance of SiO (left) and SiS (right) for the sources in our sample that have IRAS or ISO data. With the same reasoning as in the previous section, if the relative flux of SiC dust is a direct indicator of the amount of silicon carbide dust and the hypothesis that SiO and/or SiS contribute to the formation of SiC dust is correct, we would expect to see a trend in which the relative flux of SiC dust increases as the gas-phase abundance of SiO and/or SiS decreases. However, Fig. 10 does not show any clear trend indicating this; the same result was found between the gas-phase SiC_2 and SiC dust by Massalkhi et al. (2018). Regardless, it is important to note that the relative flux of the 11.3 μm SiC band is an observable quantity that may not be a direct indicator of the mass of silicon carbide dust in the envelope. The derivation of the amount of SiC dust in the envelope requires

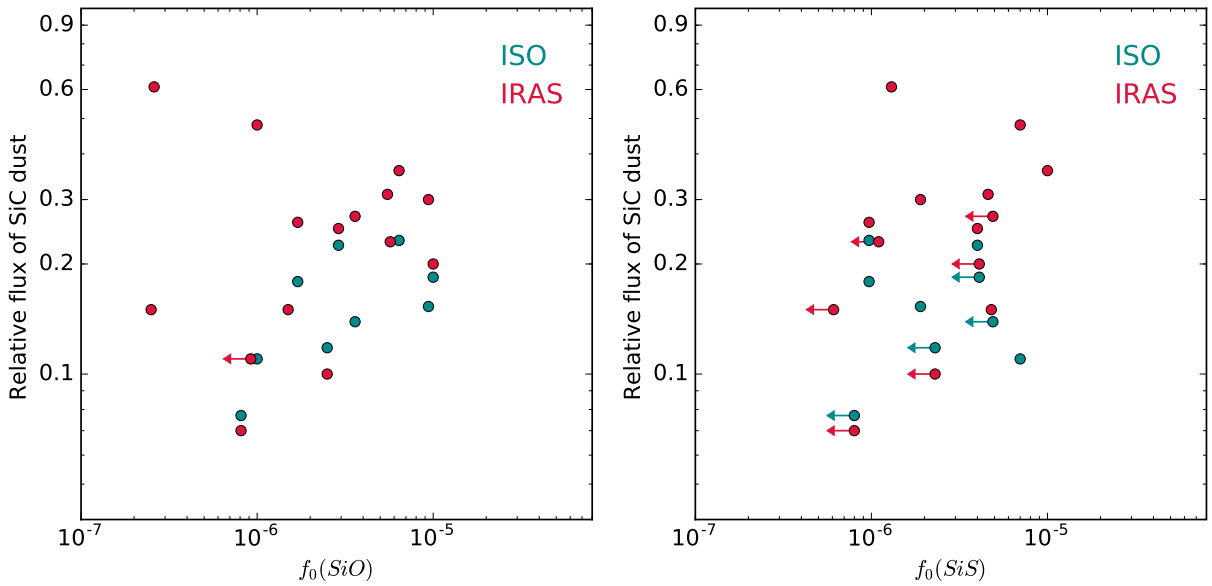

Fig. 10. Relative integrated flux of the SiC dust feature at 11.3 μm taken from Sloan et al. (1998) and Yang et al. (2004) vs. the fractional abundance of SiO and SiS derived in this work.

a radiative transfer analysis that involves a meticulous description of the chemical composition, size, and temperature of dust throughout the envelope.

6.4. Radial extent: photodissociation versus empirical relations

As discussed in Sect. 4.2, the radial extent of CS, SiO, and SiS in carbon star envelopes is probably controlled by photodissociation from the ambient interstellar UV radiation field. However, given the aforementioned difficulties to account properly for the abundance falloff using photodissociation rates from the literature (in which case the radial extent is very likely underestimated), in this work we adopted a simple radial abundance distribution given by a Gaussian function with e-folding radii derived from empirical relations between r_e and the wind density. These relations were ultimately based on a scaling law between r_e and $\dot{M}/V_{\rm exp}$ derived from a multiline study of SiO in M-type stars (González Delgado et al. 2003). In this work we adopted the same relation for SiO, based on the assumption that SiO behaves similarly in envelopes around M- and C-type stars; for SiS we adopted the same relation, based on the assumption that SiS and SiO have similar emission sizes as mentioned previously; and for CS we adopted a modified version, based on arguments to avoid requiring a sulfur abundance higher than the solar abundance. If we consider as good the adopted empirical relations and we assume that the abundance falloff is entirely controlled by photodissociation, then it is possible to extract some useful conclusions about the photodissociation of these molecules. More specifically, we aim to find the unattenuated photodissociation rates that best reproduce the abundance falloff given by the adopted empirical laws for r_e.

The photodissociation model used for this exercise is the same employed in Massalkhi et al. (2018). Briefly, the radial variation of the fractional abundance can be expressed as (Jura & Morris 1981; Huggins & Glassgold 1982)

$$\frac{{\rm d}f}{{\rm d}r} = -\frac{\alpha}{V_{\rm exp}} \exp\left[-\left(\frac{r_{\rm d}}{r}\right)\right] f, \tag{6}$$

Table 4. Photodissociation parameters.

Molecule	α	β	Ref.	α'	⟨Dev.⟩
CS	3.7×10^{-10}	2.32	a	1.5×10^{-10}	35%
SiO	1.6×10^{-9}	2.66	b	7×10^{-10}	31%
SiS	1.6×10^{-9}	2.66	c	8×10^{-10}	47%

Notes. The values of α and β are taken from the literature.
References. (a) Pattillo et al. (2018), (b) Heays et al. (2017), (c) assumed the same as SiO. The parameter α' are the values that best reproduce the empirical relations between r_e and $\dot{M}/V_{\rm exp}$ adopted in this study. The mean deviations ⟨Dev.⟩ are also given (see text).

where α is the unattenuated photodissociation rate in s^{-1} and the photodissociation radius $r_{\rm d}$ is given by

$$r_{\rm d} = \frac{\beta\,\dot{M}}{4\pi\,V_{\rm exp}\,\overline{m}_{\rm g}\,1.87\times10^{21}}, \tag{7}$$

where β is the dust shielding factor, $\overline{m}_{\rm g}$ is the average mass of gas particles in grams, and the numerical value is the canonical $N_{\rm H}/A_{\rm V}$ ratio for the local ISM (Bohlin et al. 1978). In Table 4 we list the unattenuated photodissociation rates α and dust shielding factors β collected from the literature for CS, SiO, and SiS, which were used as starting values. For each of the three molecules, we then varied the unattenuated photodissociation rate in small steps, computed the associated abundance radial profile for each envelope in the sample, and calculated the corresponding line profiles. To decide which photodissociation rate agrees best with the empirical abundance falloff, we computed for each envelope the difference between the velocity-integrated line intensity calculated with the photodissociation model and that calculated with the empirical falloff model and then estimated the mean difference.

The mean deviations found are plotted as a function of the photodissociation rate in Fig. 11. The optimal photodissociation rate α' for which the lowest mean deviation is found is given in

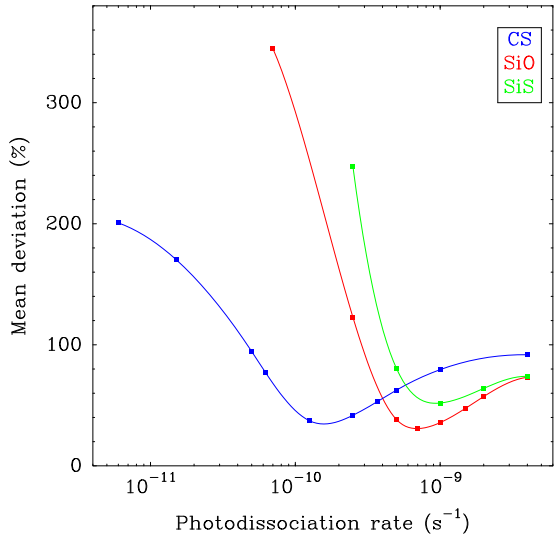

Fig. 11. The mean deviation between the calculated line areas with the photodissociation model and the model using empirical laws is plotted as a function of the unattenuated photodissociation rate adopted in the photodissociation model for CS, SiO, and SiS.

the right side of Table 4 for each of the three molecules, together with the associated mean deviation. In the case of CS, we found that the lowest mean deviation (35%) occurs for $\alpha' = 1.5 \times 10^{-10}$ s^{-1}, while for SiO and SiS the lowest deviation (31 and 47%, respectively) is found for photodissociation rates of 7×10^{-10} and 8×10^{-10} s^{-1}, respectively. There are two interesting aspects to comment on. First, the optimal photodissociation rates found for SiO and SiS are very similar, while that of CS is significantly lower. These results merely reflect the adopted empirical abundance falloffs, which were the same for SiO and SiS, while for CS we adopted an empirical scaling law implying an outer abundance falloff. And second, the optimal photodissociation rates α' are significantly lower than the literature values α. This illustrates in a different way our initial suspicion that literature photodissociation rates underestimate the radial extent of CS, SiO, and SiS. Whether, this finding implies that real photodissociation rates are indeed lower than the literature values or whether this points to a different N_H/A_V ratio than the canonical interstellar value of Bohlin et al. (1978) is not yet clear.

7. Conclusions

In this work we used the IRAM 30 m telescope to survey a sample of 25 C-rich CSEs in the $J = 3-2$ line of CS and SiO and in the $J = 7-6$ and $J = 8-7$ lines of SiS. We carried out excitation and radiative transfer calculations based on the LVG method to derive fractional abundances relative to H_2. We found that the abundances of the three molecules are positively correlated with each other (especially those of CS and SiO) and that while CS and SiS have similar abundances, SiO is present at a lower abundance level.

We also found a clear trend in which SiO and CS become less abundant as the envelope density increases. The depletion of CS with increasing density can be due to gas-phase chemistry in the inner wind or to incorporation onto dust grains. The latter scenario is favored by the fact that we find a negative correlation between the fractional abundance of CS and the 30 μm feature attributed to MgS dust, which suggests that CS is a likely precursor of MgS dust grains in C-rich AGB envelopes. In the case of SiO, the most likely explanation of the negative correlation between fractional abundance and envelope density is that SiO incorporates more efficiently onto dust grains at increasing density owing to the enhanced collision rate between particles and the acceleration of accretion and coagulation processes. Thus, both CS and SiO are probable candidates to act as gas-phase precursor of dust grains.

We find that SiS is systematically not detected in envelopes with mass loss rates below 10^{-6} $M_\odot$ yr^{-1}, probably because of the increasing importance of other molecules that lock most silicon and sulfur (SiO, SiC_2, and CS) or because of a lack of sensitivity. The SiS abundances derived in the sources in which the molecule is detected suggest a tentative trend of decreasing abundance with increasing density. This trend indicates that SiS could also be incorporated into dust grains, although the non-detections clearly undermine this tentative trend. Nevertheless, this conclusion is not as robust as that of CS and SiO.

Our conclusions on the role of CS, SiO, and SiS as gas-phase precursors of dust are based on low energy lines, which probe post-condensation regions. More observations, in particular high-J lines and interferometric observations probing the inner regions of the envelopes, are needed to affirm the conclusions obtained in this study.

Acknowledgements. We are grateful to Otoniel Denis-Alpizar, Christian Balança, and Fabrice Dayou for providing the latest collisional rate coefficients of CS and SiO. We thank the IRAM 30 m staff for their help during the observations. This research has made use of the SIMBAD database, operated at CDS, Strasbourg, France. We acknowledge funding support from the European Research Council (ERC Grant 610256: NANOCOSMOS) and from Spanish MINECO through grants AYA2012-32032 and AYA2016-75066-C2-1-P. M.A. thanks Spanish MINECO for funding support through the Ramón y Cajal programme (RyC-2014-16277).

References

Agúndez, M. 2009, PhD. Thesis, Universidad Autónoma de Madrid, Spain
Agúndez, M., & Cernicharo, J. 2006, ApJ, 650, 374
Agúndez, M., Fonfría, J. P., Cernicharo, J., et al. 2012, A&A, 543, A48
Asplund, M., Grevesse, N., Sauval, A. J., & Scott, P. 2009, ARA&A, 47, 481
Balança, C., & Dayou, F. 2017, MNRAS, 469, 1673
Bieging, J. H., & Nguyen-Quang-Rieu. 1989, ApJ, 343, L25
Bohlin, R. C., Savage, B. D., & Drake, J. F. 1978, ApJ, 224, 132
Boyle, R. J., Keady, J. J., Jennings, D. E., Hirsch, K. L., & Wiedemann, G. R. 1994, ApJ, 420, 863
Bujarrabal, V., Fuente, A., & Omont, A. 1994, A&A, 285, 247
Castor, J. I. 1970, MNRAS, 149, 111
Cernicharo, J. 1985, The Infrared and Submillimetre Sky after COBE, eds. M. Signore & C. Dupraz, IRAM Internal Rep., 52
Cernicharo, J., Guélin, M., & Kahane, C. 2000, A&AS, 142, 181
Cernicharo, J., Daniel, F., Castro-Carrizo, A., et al. 2013, ApJ, 778, L25
Cernicharo, J., McCarthy, M. C., Gottlieb, C. A., et al. 2015, ApJ, 806, L3
Chandra, S., Kegel, W. H., Le Roy, R. J., & Hertenstein, T. 1995, A&AS, 114, 175
Cherchneff, I. 2006, A&A, 456, 1001
Danilovich, T., Ramstedt, S., Gobrecht, D., et al. 2018, A&A, 617, A132
Danilovich, T., Richards, A. M. S., Karakas, A. I., et al. 2019, MNRAS, 484, 494
Dayou, F., & Balança, C. 2006, A&A, 459, 297
Decin, L., Cernicharo, J., Barlow, M. J., et al. 2010a, A&A, 518, L143
Decin, L., De Beck, E., Brünken, S., et al. 2010b, A&A, 516, A69
Denis-Alpizar, O., Stoecklin, T., Guilloteau, S., & Dutrey, A. 2018, MNRAS, 478, 1811
Drira, I., Hure, J. M., Spielfiedel, A., Feautrier, N., & Roueff, E. 1997, A&A, 319, 720
Forrest, W. J., Houck, J. R., & McCarthy, J. F. 1981, ApJ, 248, 195
Gehrz, R. 1989, in Interstellar Dust, eds. L. J. Allamandola & A. G. G. M. Tielens, IAU Symp., Vol. 135, 445

Goebel, J. H., & Moseley, S. H. 1985, ApJ, 290, L35
González Delgado, D., Olofsson, H., Kerschbaum, F., et al. 2003, A&A, 411, 123
Groenewegen, M. A. T., Sevenster, M., Spoon, H. W. W., & Pérez, I. 2002, A&A, 390, 511
Heays, A. N., Bosman, A. D., & van Dishoeck, E. F. 2017, A&A, 602, A105
Herwig, F. 2005, ARA&A, 43, 435
Hony, S., Waters, L. B. F. M., & Tielens, A. G. G. M. 2002, A&A, 390, 533
Huggins, P. J., & Glassgold, A. E. 1982, ApJ, 252, 201
Jura, M., & Morris, M. 1981, ApJ, 251, 181
Keady, J. J., & Ridgway, S. T. 1993, ApJ, 406, 199
Kłos, J., & Lique, F. 2008, MNRAS, 390, 239
Lique, F., & Spielfiedel, A. 2007, A&A, 462, 1179
Lombaert, R., de Vries, B. L., de Koter, A., et al. 2012, A&A, 544, L18
Loup, C., Forveille, T., Omont, A., & Paul, J. F. 1993, A&AS, 99, 291
Lucas, R., Bujarrabal, V., Guilloteau, S., et al. 1992, A&A, 262, 491
Lucas, R., Guélin, M., Kahane, C., Audinos, P., & Cernicharo, J. 1995, Ap&SS, 224, 293
Massalkhi, S., Agúndez, M., Cernicharo, J., et al. 2018, A&A, 611, A29
Müller, H. S., Schlöder, F., Stutzki, J., & Winnewisser, G. 2005, J. Mol. Struct., 742, 215
Müller, H., McCarthy, M., Bizzocchi, L., et al. 2007, Phys. Chem. Chem. Phys., 9, 1579
Olofsson, H., Johansson, L. E. B., Hjalmarson, A., & Nguyen-Quang-Rieu. 1982, A&A, 107, 128
Olofsson, H., Carlstrom, U., Eriksson, K., Gustafsson, B., & Willson, L. A. 1990, A&A, 230, L13
Olofsson, H., Eriksson, K., Gustafsson, B., & Carlstroem, U. 1993, ApJS, 87, 305
Pardo, J. R., Cernicharo, J., & Serabyn, E. 2001, IEEE Trans. Antennas. Propag., 49, 1683
Pattillo, R. J., Cieszewski, R., Stancil, P. C., et al. 2018, ApJ, 858, 10
Piñeiro, A. L., Tipping, R. H., & Chackerian, C. 1987, J. Mol. Spectr., 125, 184
Prasad, S. S., & Huntress, Jr. W. T. 1980, ApJS, 43, 1
Raymonda, J. W., Muenter, J. S., & Klemperer, W. A. 1970, J. Chem. Phys., 52, 3458
Sanz, M. E., McCarthy, M. C., & Thaddeus, P. 2003, J. Chem. Phys., 119, 11715
Schöier, F. L., & Olofsson, H. 2001, A&A, 368, 969
Schöier, F. L., Lindqvist, M., & Olofsson, H. 2005, A&A, 436, 633
Schöier, F. L., Fong, D., Olofsson, H., Zhang, Q., & Patel, N. 2006a, ApJ, 649, 965
Schöier, F. L., Olofsson, H., & Lundgren, A. A. 2006b, A&A, 454, 247
Schöier, F. L., Bast, J., Olofsson, H., & Lindqvist, M. 2007, A&A, 473, 871
Schöier, F. L., Ramstedt, S., Olofsson, H., et al. 2013, A&A, 550, A78
Sloan, G. C., Little-Marenin, I. R., & Price, S. D. 1998, AJ, 115, 809
Smolders, K., Neyskens, P., Blommaert, J. A. D. L., et al. 2012, A&A, 540, A72
Sobolev, V. V. 1960, Moving envelopes of stars (Cambridge, Massachusetts: Harvard University Press)
Toboła, R., Lique, F., Kłos, J., & Chałasiński, G. 2008, J. Phys. B At. Mol. Phys., 41, 155702
van Dishoeck, E. F. 1988, Astrophys. Space Sci. Lib., 146, 49
Velilla Prieto, L., Sánchez Contreras, C., Cernicharo, J., et al. 2017, A&A, 597, A25
Velilla Prieto, L., Cernicharo, J., Agúndez, M., et al. 2019, A&A, in press
Winnewisser, G., & Cook, R. L. 1968, J. Mol. Spectr., 28, 266
Wirsich, J. 1994, ApJ, 424, 370
Yang, X., Chen, P., & He, J. 2004, A&A, 414, 1049
Zhang, K., Jiang, B. W., & Li, A. 2009, ApJ, 702, 680
Zhukovska, S., & Gail, H.-P. 2008, A&A, 486, 229

Appendix A: Additional table

Table A.1. Observed line parameters of CS $J = 3-2$, SiO $J = 3-2$, and the $J = 7-6$ and $J = 8-7$ lines of SiS.

Line	ν_{calc} (MHz)	ν_{obs} (MHz)	V_{exp} (km s^{-1})	$\int T_{mb} dv$ (K km s^{-1})
		IRC +10216		
SiO $J = 3-2$	130 268.665	130 268.4(1)	13.1(1)	130.7(13)
SiS $J = 7-6$	127 076.180	127 076.0(1)	12.7(1)	162.9(16)
SiS $J = 8-7$	145 227.054	145 227.0(1)	14.7(1)	270.5(27)
CS $J = 3-2$	146 969.025	146 968.7(1)	14.7(1)	379.3(37)
		CIT 6		
SiO $J = 3-2$	130 268.665	130 267.8(5)	16.2(5)	19.8(19)
SiS $J = 7-6$	127 076.180	127 075.3(5)	16.4(5)	7.55(7)
SiS $J = 8-7$	145 227.054	145 225.4(10)	17.5(10)	12.5(19)
CS $J = 3-2$	146 969.025	146 968.6(5)	16.4(5)	89.0(89)
		CRL 3068		
SiO $J = 3-2$	130 268.665	130 268.4(1)	12.3(1)	2.18(2)
SiS $J = 7-6$	127 076.180	127 075.9(1)	12.2(1)	6.36(5)
SiS $J = 8-7$	145 227.054	145 226.7(1)	13.8(1)	9.24(9)
CS $J = 3-2$	146 969.025	146 968.6(1)	14.2(1)	17.2(10)
		S Cep		
SiO $J = 3-2$	130 268.665	130 268.6(1)	23.3(1)	7.80(7)
SiS $J = 7-6$	127 076.180	127 076.5(10)	21.0(5)	0.30(6) [a]
SiS $J = 8-7$	145 227.054	145 227.2(10)	20.8(10)	0.34(7) [a]
CS $J = 3-2$	146 969.025	146 968.9(1)	23.8(1)	19.8(2)
		IRC +30374		
SiO $J = 3-2$	130 268.665	130 268.7(1)	25.1(2)	7.07(7)
SiS $J = 7-6$	127 076.180	127 076.3(1)	22.6(4)	1.73(2)
SiS $J = 8-7$	145 227.054	145 227.2(1)	25.2(2)	2.99(3)
CS $J = 3-2$	146 969.025	146 968.6(1)	25.8(2)	26.7(26)
		LP And		
SiO $J = 3-2$	130 268.665	130 268.5(1)	12.9(2)	8.56(8)
SiS $J = 7-6$	127 076.180	127 076.1(1)	12.1(2)	7.01(7)
SiS $J = 8-7$	145 227.054	145 226.9(1)	13.8(1)	12.3(1)
CS $J = 3-2$	146 969.025	146 969.0(1)	14.7(1)	35.6(35)
		V Cyg		
SiO $J = 3-2$	130 268.665	130 268.5(1)	12.2(1)	9.03(9)
SiS $J = 7-6$	127 076.180	127 076.4(1)	12.9(1)	1.41(1)
SiS $J = 8-7$	145 227.054	145 227.2(1)	12.3(1)	2.45(2)
CS $J = 3-2$	146 969.025	146 968.8(1)	12.1(1)	25.2(25)
		V384 Per		
SiO $J = 3-2$	130 268.665	130 268.6(1)	14.8(1)	9.29(9)
SiS $J = 7-6$	127 076.180	127 076.1(1)	12.7(1)	2.15(2)
SiS $J = 8-7$	145 227.054	145 227.0(1)	14.1(1)	4.02(4)
CS $J = 3-2$	146 969.025	146 968.8(1)	15.6(1)	28.7(29)
		IRC +60144		
SiO $J = 3-2$	130 268.665	130 268.6(1)	20.8(1)	5.34(5)
SiS $J = 7-6$	127 076.180	127 076.2(10)	19.4(10)	0.9(2) [a]
SiS $J = 8-7$	145 227.054	145 226.9(1)	20.9(1)	1.65(1)
CS $J = 3-2$	146 969.025	146 968.7(1)	20.9(1)	12.5(12)

Notes. Numbers in parentheses are 1σ uncertainties in units of the last digits. [a]Marginal detection.

Table A.1. continued.

Line	ν_{calc} (MHz)	ν_{obs} (MHz)	V_{exp} (km s^{-1})	$\int T_{mb} dv$ (K km s^{-1})
		U Cam		
SiO J = 3−2	130 268.665	130 268.2(1)	11.6(1)	0.96(1)
SiS J = 7−6	127 076.180	–	–	–
SiS J = 8−7	145 227.054	–	–	–
CS J = 3−2	146 969.025	146 968.8(1)	13.5(1)	4.7(5)
		IRC +20370		
SiO J = 3−2	130 268.665	130 268.5(1)	13.1(1)	7.25(7)
SiS J = 7−6	127 076.180	127 076.1(1)	12.7(1)	3.10(2)
SiS J = 8−7	145 227.054	145 227.1(5)	13.8(4)	5.64(5)
CS J = 3−2	146 969.025	146 968.9(5)	13.2(8)	19.9(20)
		CRL 67		
SiO J = 3−2	130 268.665	130 268.6(1)	14.5(1)	2.88(3)
SiS J = 7−6	127 076.180	127 076.4(1)	13.6(1)	1.62(1)
SiS J = 8−7	145 227.054	145 226.9(1)	15.4(2)	2.83(2)
CS J = 3−2	146 969.025	146 968.9(1)	16.1(2)	12.3(12)
		CRL 190		
SiO J = 3−2	130 268.665	130 269.5(5)	16.3(5)	0.39(4)
SiS J = 7−6	127 076.180	127 076.2(1)	16.6(1)	1.45(1)
SiS J = 8−7	145 227.054	145 227.0(1)	16.2(1)	1.93(2)
CS J = 3−2	146 969.025	146 968.7(1)	16.9(2)	6.76(7)
		V Aql		
SiO J = 3−2	130 268.665	130 268.4(1)	7.2(1)	0.44(4)
SiS J = 7−6	127 076.180	–	–	–
SiS J = 8−7	145 227.054	–	–	–
CS J = 3−2	146 969.025	146 968.8(1)	9.2(1)	4.30(4)
		CRL 2477		
SiO J = 3−2	130 268.665	130 268.1(1)	16.7(1)	1.28(1)
SiS J = 7−6	127 076.180	127 076.2(1)	16.5(1)	2.64(2)
SiS J = 8−7	145 227.054	145 226.8(1)	19.2(2)	2.93(3)
CS J = 3−2	146 969.025	146 968.6(1)	20.1(1)	7.17(7)
		CRL 2494		
SiO J = 3−2	130 268.665	130 268.8(1)	16.4(2)	2.64(3)
SiS J = 7−6	127 076.180	127 077.0(10)	20.4(10)	1.04(20)
SiS J = 8−7	145 227.054	145 227.4(2)	19.0(6)	1.57(15)
CS J = 3−2	146 969.025	146 968.9(1)	19.6(1)	13.2(13)
		Rv Aqr		
SiO J = 3−2	130 268.665	130 268.3(1)	14.0(2)	5.58(5)
SiS J = 7−6	127 076.180	127 076.1(5)	13.3(5)	0.71(7)
SiS J = 8−7	145 227.054	145 226.9(1)	14.6(2)	1.34(1)
CS J = 3−2	146 969.025	146 968.6(1)	15.4(2)	13.3(13)
		CRL 2513		
SiO J = 3−2	130 268.665	130 268.5(1)	25.7(1)	2.58(2)
SiS J = 7−6	127 076.180	127 076.0(5)	24.2(6)	0.84(8)
SiS J = 8−7	145 227.054	145 226.7(5)	24.9(4)	1.66(16)
CS J = 3−2	146 969.025	146 968.7(1)	26.5(2)	8.92(9)
		S Aur		
SiO J = 3−2	130 268.665	130 267.5(1)	21.8(2)	1.25(1)
SiS J = 7−6	127 076.180	–	–	–
SiS J = 8−7	145 227.054	–	–	–
CS J = 3−2	146 969.025	146 968.1(1)	26.5(1)	4.05(4)

Table A.1. continued.

Line	ν_{calc} (MHz)	ν_{obs} (MHz)	V_{exp} (km s^{-1})	$\int T_{mb} dv$ (K km s^{-1})
		V636 Mon		
SiO J = 3−2	130 268.665	130 269.3(1)	24.3(1)	3.74(4)
SiS J = 7−6	127 076.180	127 076.2(5)	24.1(5)	0.60 [(a)]
SiS J = 8−7	145 227.054	145 227.9(5)	26.5(5)	0.50(5) [(a)]
CS J = 3−2	146 969.025	146 969.8(1)	25.8(1)	8.85(9)
		W Ori		
SiO J = 3−2	130 268.665	130 268.1(5)	8.5(4)	0.29(3)
SiS J = 7−6	127 076.180	–	–	–
SiS J = 8−7	145 227.054	–	–	–
CS J = 3−2	146 969.025	146 968.8(5)	10.5(8)	4.2(4)
		Y CVn		
SiO J = 3−2	130 268.665	130 268.3(1)	7.3(1)	0.38(4)
SiS J = 7−6	127 076.180	–	–	–
SiS J = 8−7	145 227.054	–	–	–
CS J = 3−2	146 969.025	146 968.5(1)	9.4(1)	7.58(7)
		R Lep		
SiO J = 3−2	130 268.665	130 267.9(1)	19.8(2)	3.45(3)
SiS J = 7−6	127 076.180	–	–	–
SiS J = 8−7	145 227.054	–	–	
CS J = 3−2	146 969.025	146 968.3(1)	20.9(2)	5.78(6)
		ST Cam		
SiO J = 3−2	130 268.665	–	–	–
SiS J = 7−6	127 076.180	–	–	–
SiS J = 8−7	145 227.054	–	–	–
CS J = 3−2	146 969.025	146 969.2(1)	11.5(1)	0.82(8)
		UU Aur		
SiO J = 3−2	130 268.665	130 266.2(10)	6.7(10)	0.09(2)
SiS J = 7−6	127 076.180	–	–	–
SiS J = 8−7	145 227.054	–	–	–
CS J = 3−2	146 969.025	146 968.6(10)	11.0(1)	0.30(3)

A&A 641, A57 (2020)
https://doi.org/10.1051/0004-6361/202037900

Astronomy & Astrophysics

The abundance of S- and Si-bearing molecules in O-rich circumstellar envelopes of AGB stars⋆,⋆⋆

S. Massalkhi[1], M. Agúndez[1], J. Cernicharo[1], and L. Velilla-Prieto[2]

[1] Instituto de Física Fundamental, CSIC, C/ Serrano 123, 28006, Madrid, Spain
e-mail: sarah.massalkhi@csic.es
[2] Department of Space, Earth and Environment, Chalmers University of Technology, Onsala Space Observatory, 439 92 Onsala, Sweden

Received 6 March 2020 / Accepted 22 June 2020

ABSTRACT

Aims. We aim to determine the abundances of SiO, CS, SiS, SO, and SO_2 in a large sample of oxygen-rich asymptotic giant branch (AGB) envelopes covering a wide range of mass loss rates to investigate the potential role that these molecules could play in the formation of dust in these environments.
Methods. We surveyed a sample of 30 oxygen-rich AGB stars in the λ 2 mm band using the IRAM 30m telescope. We performed excitation and radiative transfer calculations based on the large velocity gradient method to model the observed lines of the molecules and to derive their fractional abundances in the observed envelopes.
Results. We detected SiO in all 30 targeted envelopes, as well as CS, SiS, SO, and SO_2 in 18, 13, 26, and 19 sources, respectively. Remarkably, SiS is not detected in any envelope with a mass loss rate below 10^{-6} $M_\odot$ yr^{-1}, whereas it is detected in all envelopes with mass loss rates above that threshold. From a comparison with a previous, similar study on C-rich sources, it becomes evident that the fractional abundances of CS and SiS show a marked differentiation between C-rich and O-rich sources, being two orders of magnitude and one order of magnitude more abundant in C-rich sources, respectively, while the fractional abundance of SiO turns out to be insensitive to the C/O ratio. The abundance of SiO in O-rich envelopes behaves similarly to C-rich sources, that is, the denser the envelope the lower its abundance. A similar trend, albeit less clear than for SiO, is observed for SO in O-rich sources.
Conclusions. The marked dependence of CS and SiS abundances on the C/O ratio indicates that these two molecules form more efficiently in C- than O-rich envelopes. The decline in the abundance of SiO with increasing envelope density and the tentative one for SO indicate that SiO and possibly SO act as gas-phase precursors of dust in circumstellar envelopes around O-rich AGB stars.

Key words. astrochemistry – molecular processes – stars: abundances – stars: AGB and post-AGB – circumstellar matter

1. Introduction

When an evolved star with a mass lower than ∼8 $M_\odot$ is on the asymptotic giant branch (AGB), it experiences extensive mass loss up to rates of ∼10^{-4} $M_\odot$ yr^{-1} that dominates the evolution of that stage. AGB stars are considered the main providers of dust and enriched material to the interstellar medium (Gehrz 1989). The copious amount of material released gives rise to an expanding circumstellar envelope (CSE), which provides favorable thermodynamic conditions for the formation of simple molecules and dust grains. At the start of the AGB phase, the element mixture at the stellar photosphere has a carbon-to-oxygen ratio C/O < 1, making the stars oxygen-rich (O-rich). In the CSE of these stars, O-bearing molecules, such as H_2O and SiO (Engels 1979), and S-bearing species, such as SO, SO_2, and H_2S (Omont et al. 1993), are observed to be abundant. Dredge-up events experienced by the AGB star mix carbon from the interior helium-burning shell to the surface such that the C/O ratio becomes >1 and carbon-bearing molecules become abundant in the CSE. The synthesis of dust in AGB CSEs is evidenced by the identification of typical dust features in the spectral energy distribution (SED) of AGB stars, such as the 9.7 and 18 μm emission features of silicate dust in O-rich AGB stars and the 11.3 μm feature of SiC dust in carbon stars.

Despite the important role dust plays in many astrophysical phenomena, the mechanisms responsible for its formation and production are still poorly understood. In general, the main scenario for dust formation around an AGB star involves a two-step process. First, some gas-phase precursors condense to produce seed nuclei with sizes on the order of nanometers, which then grow by processes of coagulation and accretion to form a macroscopic dust particle. Yet this picture remains poorly constrained. In particular, how the transition between gas-phase molecules and solid phases occurs and which molecules act as precursors of seed nuclei are questions that have yet to be answered.

Various observational studies have provided hints as to which molecules could act as precursors of dust in the circumstellar envelopes of evolved stars. Silicon monoxide, SiO, is known to be a candidate or precursor of dust. González Delgado et al. (2003), Schöier et al. (2006a), Ramstedt et al. (2009), and Massalkhi et al. (2019) observed and modeled the SiO emission in the three chemical types of AGB stars: M-, S-, and C-type. Those studies found a trend of decreasing SiO abundance with increasing wind density, most notably for the O-rich and C-rich

⋆ The reduced spectra are only available at the CDS via anonymous ftp to cdsarc.u-strasbg.fr (130.79.128.5) or via http://cdsarc.u-strasbg.fr/viz-bin/cat/J/A+A/641/A57

⋆⋆ Based on observations carried out with the IRAM 30m Telescope. The Institut de Radioastronomie Millimétrique (IRAM) is supported by INSU/CNRS (France), MPG (Germany), and IGN (Spain).

AGB stars, which is thought to be due to an increased depletion of SiO onto dust grains. Similar studies on SiS were less conclusive as to the role of this molecule as a gas-phase precursor of dust (Schöier et al. 2007, Danilovich et al. 2018, Massalkhi et al. 2019). The molecules SiC_2 and CS were also found to show a similar behavior in C-rich CSEs as what was found for SiO, that is to say, an abundance decline with increasing envelope density, which suggests that these molecules are playing an important role in the formation of silicon carbide (SiC) and magnesium sulfide (MgS) dust in the envelopes of C-rich AGB stars, respectively (Massalkhi et al. 2018, 2019).

In this paper, we focus on potential gas-phase precursors of dust in O-rich AGB stars. Some metal oxides recently detected have been suggested to act as precursors of seed nuclei, for example, TiO and TiO_2 (Gail & Sedlmayr 1998) and AlO (Gobrecht et al. 2016). However, observational constraints are still not conclusive (Banerjee et al. 2012; Kamiński et al. 2013, 2016, 2017; Decin et al. 2017; De Beck et al. 2017). The formation of the first condensation nuclei must necessarily occur from gas-phase species present in the precondensation region, and the bulk of dust must be formed at the expense of gaseous species during the phase of grain growth. Since the gas around AGB stars is largely molecular, molecules are good candidates to serve as precursors of dust. Previous observational studies done on large samples of O-rich AGB stars to investigate potential precursors of dust are meagre. To investigate which gas-phase molecules could play a role in the formation of dust around O-rich AGB stars, in this paper we carry out a study of the abundance of five molecules, SiO, CS, SiS, SO, and SO_2, in 30 oxygen-rich AGB stars. In Sect. 2, we outline the sample. In Sect. 3 we describe the observations carried out and in Sect. 4 we present the main results from the observations. In Sect. 5, we describe the radiative transfer model, the molecular data, and the procedure adopted for the derivation of the molecular abundances. In Sect. 6 we describe the results from the radiative transfer model and comment on a few peculiar cases that stood out during the modeling. Finally, in Sect. 7 we discuss the main results of our study and present our conclusions in Sect. 8.

2. The sample

The sample contains 30 O-rich AGB stars, among which there are Mira variables (M), characterized by regular variations with a large amplitude (>2.5 mag in the V band), and semiregular variables (SR), characterized by a small amplitude (<2.5 mag in the V band). We selected sources from samples in the literature (e.g., Schöier et al. 2013; Ramstedt & Olofsson 2014; Danilovich et al. 2015) mainly based on strong line emission of molecules like CO, SiO, and SO. The sample was also chosen to cover a wide range of mass loss rates (10^{-8}–10^{-5} $M_\odot$ yr^{-1}). The list of AGB stars are presented in Tables 1 and 2 for regular and peculiar sources respectively along with their coordinates, systemic velocity with respect to the Local Standard of Rest ($V_{\rm LSR}$), distance (D), effective temperature of the star (T_*), stellar luminosity (L_*), mass loss rate ($\dot{M}$), terminal expansion velocity of the envelope ($V_{\rm exp}$), dust condensation radius ($r_{\rm c}$), dust temperature at the condensation radius ($T_{\rm d}(r_{\rm c})$), gas-to-dust mass ratio (Ψ), and the corresponding references for each parameter.

Coordinates were taken from the literature and checked using the SIMBAD astronomical database[1]. The parameters $V_{\rm LSR}$ and $V_{\rm exp}$ are determined from various strong molecular lines available in this study. These two parameters are reported in the literature mainly from CO and SiO lines with varying degrees of accuracy (e.g., Groenewegen et al. 1999; González Delgado et al. 2003; Teyssier et al. 2006). We carried out an evaluation of the values of $V_{\rm LSR}$ and $V_{\rm exp}$ derived from our data and compared with those in the literature. In cases where our lines have a well-defined shape, the values from our dataset were preferred, whereas when lines show a less clear shape, the values from literature were favored (as denoted in Table 1 where the lack of reference means that the values are derived from this work). The final values of $V_{\rm LSR}$ and $V_{\rm exp}$ adopted in this work are given in Tables 1 and 2. We adopted the values of T_* from studies where this parameter is derived by modeling the SED of each star. Stellar luminosities were adopted from the literature, where they are mostly estimated using the period-luminosity relation for Mira variables. Mass loss rates were taken from the literature, where they are determined by modeling observations of multiple CO lines. Distances were adopted from *Gaia*[2] for the stars that have available *Gaia* data. Although *Gaia* distances are known to be problematic for AGB stars due to the variability of the photocenter position (which may introduce an error of up to 20% in the parallax; Chiavassa et al. 2018), here we decided to favor distances from *Gaia* over those from HIPPARCOS or from the period-luminosity relation (see, e.g., McDonald et al. 2018; Díaz-Luis et al. 2019). Mass loss rates and luminosities are two quantities that follow the inverse-square law as $\propto D^2$, so we consistently scaled them taking into account the newly adopted *Gaia* distance and mark the new values in Table 1 with an asterisk. Note however that empirical mass loss rates derived from CO lines may scale with distance in a slightly different way according to Appendix A of Ramstedt et al. (2008), where scaling laws of the type $\propto D^{1.4-1.9}$ are found, depending on the CO line used. In any case, we evaluated the impact of adopting a scaling law $\propto D^{1.4}$ instead of $\propto D^2$ would have on the scaled mass loss rates and it is at most a factor of two.

3. The observations

The observations were carried out in the period February to October 2018 with the IRAM 30m telescope, located at Pico Veleta (Spain). Table 3 includes some basic information about the targeted lines: the rest frequency, the Einstein coefficient, $A_{\rm ul}$, the upper level energy, $E_{\rm u}$, and the beam size of the telescope, $\theta_{\rm mb}$. We used the E150 receiver in dual sideband mode, with image rejections >10 dB, and observed the frequency ranges 128.5–136.2 GHz and 144.1–151.9 GHz (in the lower and upper side bands, respectively). The beam size of the telescope at these frequencies is in the range 16.2-19.0″. The observations were done in the wobbler-switching mode with a throw of 180″ in azimuth. This technique implies that the target source is measured (ON), followed by a measurement of the sky (OFF) with similar atmospheric conditions. The OFF measurement is then subtracted from the ON measurement to obtain a spectra of the source from which the contribution of the atmosphere to the signal has been removed. The focus was regularly checked on a planet and the pointing of the telescope was systematically checked on a nearby quasar before the observation of each AGB star. The error in the pointing is estimated to be 2–3″. The E150 receiver was connected to a fast Fourier transform spectrometer providing a spectral resolution of 0.2 MHz which corresponds to velocity resolutions 0.46 km s^{-1} at 129 GHz and 0.39 km s^{-1} at 151 GHz. The weather was good and stable during most of the observations, with typical amounts of precipitable water

[1] http://simbad.u-strasbg.fr/Simbad

[2] https://gea.esac.esa.int/archive/

Table 1. Sample of oxygen stars.

Name	RA J2000.0	Dec J2000.0	V_{LSR} (km s^{-1})	D (pc)	$T_\star$ (K)	$L_\star$ ($L_\odot$)	$\dot{M}$ ($M_\odot$ yr^{-1})	V_{exp} (km s^{-1})	$T_d(r_c)$ (K)	r_c (cm)	Ψ
IK Tau	03:53:28.87	+11:24:21.7	+34.5 [e]	285 [a]	2100 [b]	9250 [b]*	2.4×10^{-5} [b]*	17.5 [e]	1000 [b]	1.8×10^{14} [b]	435 [i]
KU And	00:06:52.94	+43:05:00.0	−22	680 [c]	2000 [c]	11 800 [c]	9.4×10^{-6} [d]	19.5	1100 [c]	1.5×10^{14} [c]	200 [m]
RX Boo	14:24:11.63	+25:42:13.4	+1.5	128 [a]	1800 [c]	4550 [c]*	6.1×10^{-7} [b]*	7.5	900 [c]	1.5×10^{14} [c]	144 [x]
RT Vir	13:02:37.98	+05:11:08.4	+18.5	226 [l]	2000 [b]	4500 [b]	4.5×10^{-7} [b]	7	1000 [b]	1.6×10^{14} [b]	2000 [q]
R Leo	09:47:33.49	+11:25:43.7	+0.1	71 [a]	2000 [b]	2500 [b]	1.0×10^{-7} [b]	5	1200 [b]	1.3×10^{14} [b]	167 [m]
WX Psc	01:06:25.98	+12:35:53.1	+9.5	700 [b]	1800 [b]	10 300 [b]	4.0×10^{-5} [b]	19	800 [b]	3.2×10^{14} [b]	250 [m]
GX Mon	06:52:46.91	+08:25:19.0	−9.5	416 [a]	2600 [c]	4700 [c]*	4.9×10^{-6} [d]*	18	900 [c]	1.1×10^{14} [c]	200 [m]
NV Aur	05:11:19.44	+52:52:33.2	+3	1200 [c]	2000 [c]	9800 [c]	2.5×10^{-5} [d]	17.5	1100 [c]	1.7×10^{14} [c]	1000 [m]
V1111 Oph	18:37:19.26	+10:25:42.2	−31	357 [a]	1800 [b]	2300 [b]*	2.7×10^{-6} [d]*	15.5	800 [b]	2.7×10^{14} [b]	200 [m]
RR Aql	19:57:36.06	−01:53:11.3	+28	318 [a]	2000 [c]	2800 [c]*	8.6×10^{-7} [d]*	8.5	1500 [c]	5.9×10^{13} [c]	185 [t]
R LMi	09:45:34.28	+34:30:42.8	+0.9	330 [d]	2400 [d]	5500 [d]	2.6×10^{-7} [d]	5.5	1000 [d]	1.7×10^{14} [d]	115 [t]
BX Cam	05:46:44.10	+69:58:25.2	−1	244 [a]	2800 [c]	1800 [c]*	1.0×10^{-6} [d]*	17	1500 [c]	7.1×10^{13} [c]	300 [z]
V1300 Aql	20:10:27.87	−06:16:13.6	−17.5	620 [c]	2000 [c]	10 600 [c]	1.0×10^{-5} [d]	15	1100 [c]	1.8×10^{14} [c]	1000 [m]
R Cas	23:58:24.87	+51:23:19.7	+26.5	188 [a]	1800 [e]	10 400 [e]*	9.5×10^{-7} [e]*	7.5	1050 [e]	2.5×10^{14} [e]	91 [m]
IRC −30398	18:59:13.85	−29:50:20.4	−7.5	390 [m]	2000 [m]	8700 [m]	6.0×10^{-6} [m]	14.5	800 [b]	2.6×10^{14} [b]	200 [m]
TX Cam	05:00:50.40	+56:10:52.6	+11.5	334 [a]	2600 [c]	6600 [c]*	7.7×10^{-6} [c]*	17.5	1300 [c]	1.0×10^{14} [c]	500 [x]
S CrB	15:21:23.96	+31:22:02.6	+1.5	431 [a]	2400 [d]	6300 [d]*	2.7×10^{-7} [d]*	5	1000 [d]	1.7×10^{14} [d]	300 [z]
IRC +60169	06:34:34.88	+60:56:33.2	−22	510 [a]	2200 [c]	5900 [c]*	9.6×10^{-6} [c]*	15	1000 [c]	1.1×10^{14} [c]	300 [z]
R Hya	13:29:42.78	−23:16:52.8	−10 [o]	224 [a]	2600 [c]	17 200 [c]*	4.7×10^{-7} [c]*	5 [o]	1500 [c]	6.1×10^{13} [c]	200 [m]
R Crt	11:00:33.85	−18:19:29.6	+11.5	236 [a]	2800 [c]	7700 [c]*	1.0×10^{-6} [c]*	11	600 [c]	3.5×10^{14} [c]	333 [q]
o Ceti	02:19:20.79	−02:58:39.5	+47	107 [f]	3000 [g]	9000 [g]	2.0×10^{-7} [h]	3	1000 [z]	9.7×10^{13} [y]	195 [t]
W Hya	13:49:02.00	−28:22:03.5	+40.5	164 [a]	2600 [b]	16 800 [b]*	4.2×10^{-7} [b]*	6	1200 [b]	6.3×10^{13} [b]	500 [v]
T Cep	21:09:31.78	+68:29:27.2	−2.5	176 [a]	2400 [d]	4900 [d]*	7.8×10^{-8} [d]*	4	1000 [d]	1.8×10^{14} [d]	300 [z]
V1943 Sgr	20:06:55.24	−27:13:29.8	−14.5	666 [a]	2200 [d]	55 400 [d]*	1.0×10^{-6} [d]*	4.5	1000 [d]	1.6×10^{14} [d]	300 [z]
SW Vir	13:14:04.39	−02:48:25.2	−10.5	300 [a]	2400 [b]	17 600 [b]*	2.2×10^{-6} [b]*	7.5	800 [b]	2.9×10^{14} [b]	1000 [q]
AFGL 292	02:02:38.63	+07:40:36.5	+23.7	253 [a]	2200 [d]	6000 [d]	1.3×10^{-7} [d]*	7	1000 [d]	1.8×10^{14} [d]	300 [z]
BK Vir	12:30:21.01	+04:24:59.2	+17.5	234 [a]	3000 [n]	4500 [n]*	2.3×10^{-7} [m]*	4	1000 [z]	8.6×10^{13} [z]	2000 [q]

Notes. The coordinates of the O-rich stars are taken from the literature. An asterisk in the value of the luminosity ($L_\star$) or mass loss rate ($\dot{M}$) indicates that the value has been scaled according to the updated value of the distance. [z] Assumed value for the condensation radius r_c is 5 $R_\star$, for the dust temperature at the condensation radius $T_d(r_c)$ is 1000 K, and for the gas-to-dust mass ratio Ψ is 300.

References. [a]Gaia Collaboration (2018), [b]Ramstedt & Olofsson (2014), [c]Schöier et al. (2013), [d]Danilovich et al. (2015), [e]Maercker et al. (2016), [f]Knapp et al. (2003), [g]Woodruff et al. (2004), [h]Ryde & Schöier (2001), [i]Gobrecht et al. (2016), [k]Justtanont et al. (1996), [l]Zhang et al. (2017), [m]González Delgado et al. (2003), [n]Ohnaka et al. (2011), [o]Knapp et al. (1998), [p]De Beck et al. (2010), [q]Olofsson et al. (2002), [r]Dyck et al. (1996), [s]Winters et al. (2007), [t]Groenewegen et al. (1999), [v]Khouri et al. (2014), [x]Dharmawardena et al. (2018), [w]Gardan et al. (2006) , [y]Kamiński et al. (2016).

Table 2. Peculiar sources.

Name	RA J2000.0	Dec J2000.0	Comp.	V_{LSR} (km s^{-1})	D (pc)	$T_\star$ (K)	$L_\star$ ($L_\odot$)	$\dot{M}$ ($M_\odot$ yr^{-1})	V_{exp} (km s^{-1})	$T_d(r_c)$ (K)	r_c (cm)	Ψ
Ep Aqr	21:46:31.85	−02:12:45.9	Narrow Broad	−33.5	124 [a]	3200 [s]	4100 [s]*	1.7×10^{-8} [s]* 5.0×10^{-7} [s]*	1 [q] 9.2 [q]	1000 [z]	7.2×10^{13} [z]	860 [x]
X Her	16:02:39.17	+47:14:25.3	Narrow Broad	−73	145 [a]	3300 [r]	5100 [w]*	4.3×10^{-8} [m]* 1.6×10^{-7} [m]*	2.2 [m] 6.5 [m]	1000 [z]	6.7×10^{13} [z]	500 [q]
OH 26.5+0.6	18:37:32.51	−05:23:59.2	AGB wind Superwind	+27	1370 [k]	2200 [k]	14 000 [k]	1.0×10^{-6} [k] 5.5×10^{-4} [k]	15.4 [k]	1000 [k]	4.5×10^{14} [k]	278 [k]

Notes. References in Table 1.

vapor of 2–4 mm and average system temperatures of 115 K. The observations were calibrated by observing the sky and two absorbers at different temperatures, a hot (ambient) and a cold (liquid nitrogen) load using the atmospheric transmission model ATM (Cernicharo 1985; Pardo et al. 2001) adopted by the IRAM 30m telescope. The intensity scale of the output spectra obtained from the antenna is calibrated in antenna temperature (T_A^*). To express the latter in terms of the main beam brightness temperature (T_{mb}), we used the recommended values of B_{eff} and F_{eff} for EMIR[3] at the frequencies of the observed lines[4], where $B_{eff} = 0.863\exp[-(\nu(\mathrm{GHz})/361)^2]$ and $F_{eff} = 0.93$. The error in the intensities due to calibration is estimated to be ∼20%. Typical on source integration times, after averaging horizontal and

[3] Eight MIxer Receiver.

[4] http://www.iram.es/IRAMES/mainWiki/Iram30mEfficiencies

Table 3. Targeted molecular lines.

Transition	Frequency (MHz)	A_{ul} (s^{-1})	E_u (K)	θ_{mb} ($''$)
SiO $J = 3-2$	130 268.665	1.06×10^{-4}	12.5	18.8
CS $J = 3-2$	146 969.025	6.07×10^{-5}	14.1	16.7
SiS $J = 8-7$	145 227.052	5.05×10^{-5}	31.4	16.9
SO 3_3-2_2	129 138.983	2.21×10^{-5}	25.5	19.0
SO_2 $8_{2-6}-8_{1-7}$	134 004.811	2.50×10^{-5}	43.1	18.3
SO_2 $5_{1-5}-4_{0,4}$	135 696.016	2.21×10^{-5}	15.7	18.1
SO_2 $4_{2-2}-4_{1,3}$	146 605.519	2.47×10^{-5}	19.0	16.7
SO_2 $2_{2-0}-2_{1,1}$	151 378.662	1.88×10^{-5}	12.6	16.2

vertical polarizations, were ~1–2 h for each source, resulting in T_{mb} rms noise levels per 0.2 MHz channel of 3–7 mK.

The data were reduced using the software CLASS[5] within the package GILDAS[6]. To obtain the final spectra for each source, we followed the standard procedure of data reduction that consists of removal of bad channels and low-quality scans, averaging the spectra corresponding to the horizontal and vertical polarizations, and subtracting a baseline of a first order polynomial. In the case of weak lines, the spectra were smoothed to a spectral resolution of 0.4 MHz to increase the signal-to-noise ratio (S/N). This corresponds to a velocity resolution of 0.8–1 km s^{-1}. When a line was undetected, we smoothed the spectrum to a spectral resolution of 0.8 MHz, corresponding to 1.6–1.9 km s^{-1}.

4. Observational results

A total of 30 O-rich CSEs were observed. The spectra obtained is shown in Fig. 1. We clearly detected SiO $J = 3-2$ in all the 30 sources, CS $J = 3-2$ in 18 sources, SiS $J = 8-7$ in 13 sources, SO 3_3-2_2 in 26 sources, while SO_2 was detected in at least one of the targeted lines in 19 sources. The detection rates are therefore 100% for SiO, 60% for CS, 43% for SiS, 86% for SO, and 63% for SO_2.

The lines were fit using the `shell` method of CLASS as described in Massalkhi et al. (2019). By performing the fit, we aim to derive for each target lines in every source the centroid frequency in MHz, the expansion velocity in km s^{-1}, and the line area, that is, the velocity-integrated intensity in K km s^{-1}. These line parameters are given in Table A.1.

The shapes of the emission lines arising from spherically expanding envelopes are essentially determined by the angular size of the emitting source relative to the size of the telescope beam and the line opacity. Most of the line shapes observed here are typical of spherically expanding envelopes, that is, parabolic (optically thick spatially unresolved emission; e.g., SiO $J = 3-2$ in KU And), flat-topped (optically thin spatially unresolved emission; e.g., CS $J = 3-2$ in V1111 Oph), or double-peaked (optically thin spatially resolved emission; e.g., SO_2 lines in V1300 Aql). However, there is a number of lines that show profiles with varying kinds of asymmetries. The triangular profile shown in SiO $J = 3-2$ in R Leo and RR Aql is said to indicate that the emission is mainly originating from a region close to the star where the gas is still accelerating. Some striking lines show one side of the profile brighter than the other, sometimes in the blue-shifted side and sometimes in the red-shifted side. An example of these are the SO_2 lines in IK Tau (blue-shifted emission) and GX Mon (red-shifted emission). This indicates an asymmetry in the distribution of the gas emission. Another explanation could be due to self absorption in the line of sight, however, this effect is rather unlikely because the lines are optically thin. Regardless, the `shell` method of CLASS cannot deal with these kind of asymmetries, but we nevertheless use it on the account that the line area and the expansion velocity resulting from the fit should be trustworthy.

5. Excitation and radiative transfer modeling

We aim to derive the abundances of SiO, CS, SiS, SO, and SO_2 in each source of our sample to provide a statistically meaningful view of how abundant these molecules are in envelopes around O-rich stars. The five molecules studied here are not excited according to local thermodynamic equilibrium (LTE) in the regions of the envelope which contribute mostly to the observed emission (see Sect. 6). Determining the level populations then requires detailed knowledge of collisional excitation data. In Sect. 5.1 we describe the spectroscopic and collisional excitation data of the five molecules that were input into our calculations and in Sect. 5.2 we briefly describe the CSE model and how information on the abundances can be derived from the observed lines using non-LTE radiative transfer modeling.

5.1. Molecular data

In the excitation analysis of SiO, we considered the first 50 rotational levels within the $v = 0$ and $v = 1$ vibrational states (i.e., a total number of 100 energy levels). The level energies and transition frequencies were calculated from the Dunham coefficients given by Sanz et al. (2003). The dipole moments for pure rotational transitions within the $v = 0$ and $v = 1$ vibrational states, 3.0982 D and 3.1178 D, respectively, were taken from Raymonda et al. (1970) and the Einstein coefficient for the ro-vibrational transition $v = 1 \rightarrow 0$ P(1) of 6.61 s^{-1} from Drira et al. (1997). As collisional rate coefficients for pure rotational transitions we adopted those calculated by Balança et al. (2018) for H_2 as collider and by Dayou & Balança (2006) for He as collider, while for ro-vibrational transitions we used the values computed by Balança & Dayou (2017) scaling from He to H_2 as collider (by multiplying by the squared ratio of the reduced masses of the SiO-H_2 and SiO-He colliding systems) when needed.

For CS, we included the first 50 rotational levels within the $v = 0$ and $v = 1$ vibrational states (i.e., a total number of 100 energy levels). The level energies and transition frequencies were calculated from the Dunham coefficients given by Müller et al. (2005). The line strengths of pure rotational transitions were computed from the dipole moments for each vibrational state, $\mu_{v=0} = 1.958$ D and $\mu_{v=1} = 1.936$ D (Winnewisser & Cook 1968), while for ro-vibrational transitions we used the Einstein coefficient of 15.8 s^{-1} given for the $v = 1 \rightarrow 0$ P(1) transition by Chandra et al. (1995). We adopted the H_2 collision rate coefficients recently calculated by Denis-Alpizar et al. (2018) for pure rotational transitions and up to temperatures of 300 K. At higher temperatures and for ro-vibrational transitions we used the rate coefficients calculated by Lique & Spielfiedel (2007) scaling from He to H_2 as collider. Rate coefficients for collisions with He were taken from Lique et al. (2006a) and Lique & Spielfiedel (2007).

[5] Continuum and Line Analysis Single-dish Software.
[6] GILDAS is a software to reduce and analyze mainly (sub-)mm observations from single-dish and interferometric telescopes. See `http://www.iram.fr/IRAMFR/GILDAS`

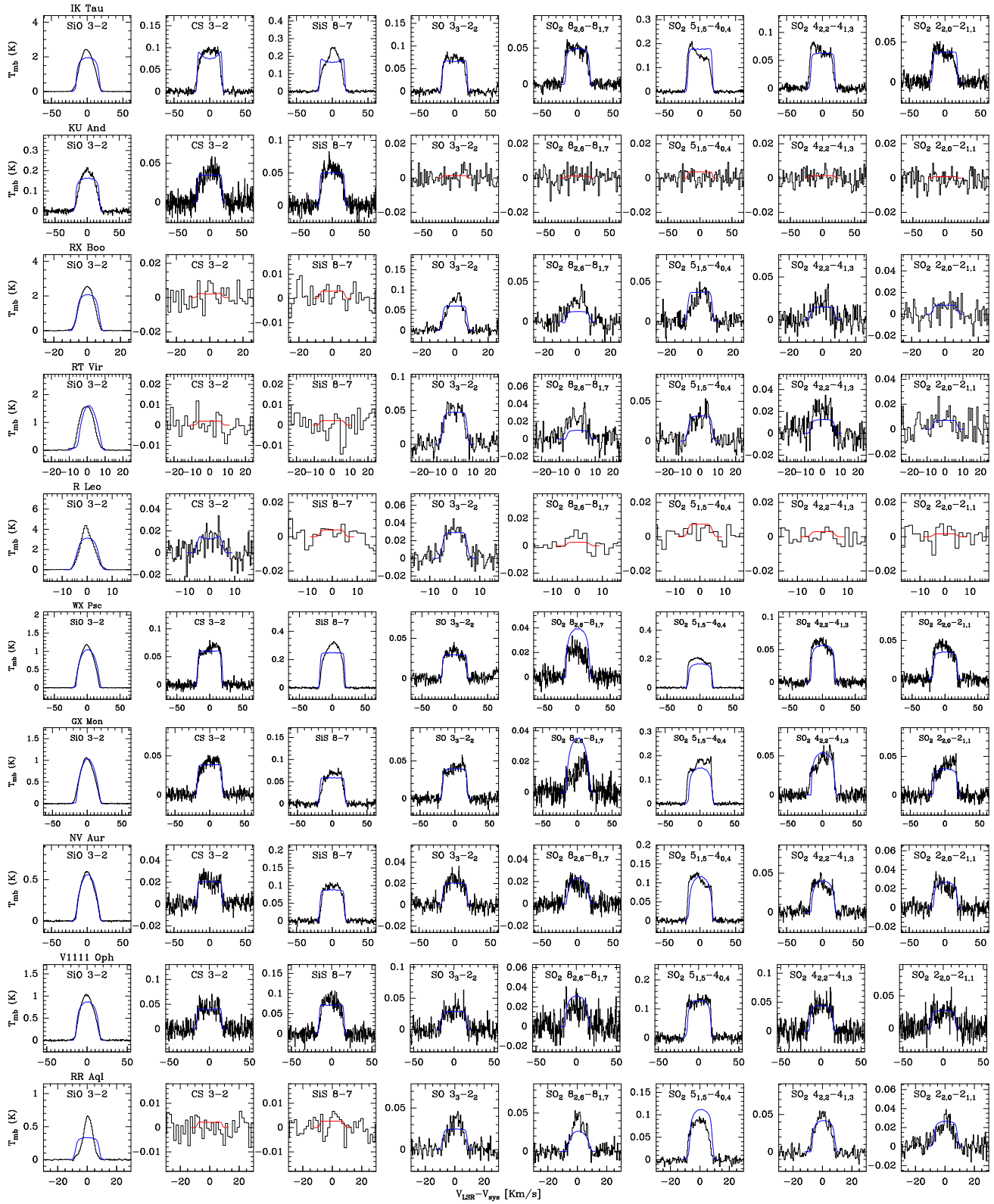

Fig. 1. Rotational lines observed with the IRAM 30m telescope in the 30 O-rich CSEs (black histograms). The blue lines indicate the calculated line profiles from the best-fit LVG model. The red lines correspond to the calculated line profiles with the maximum intensity compatible with the nondetection.

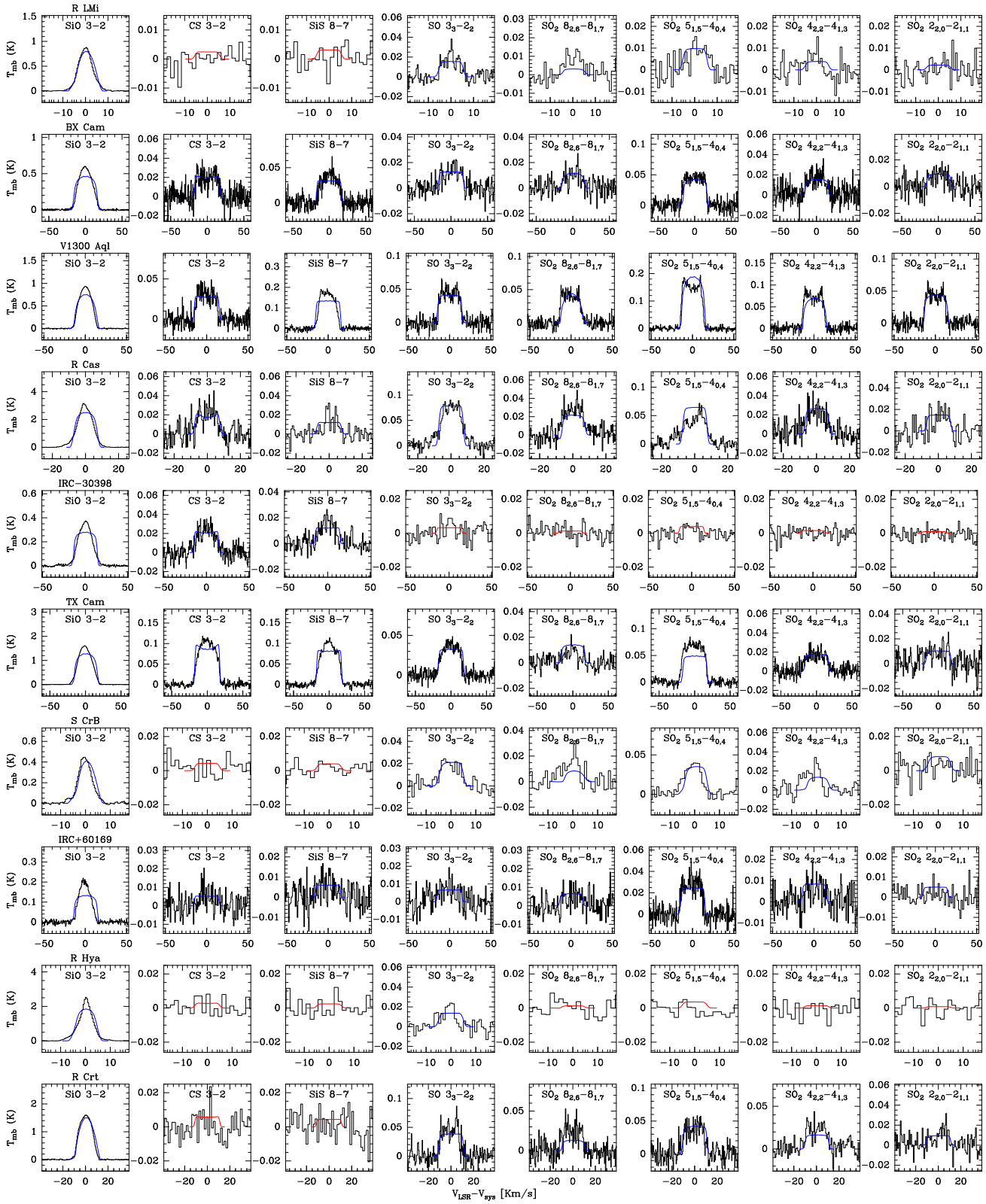

Fig. 1. continued.

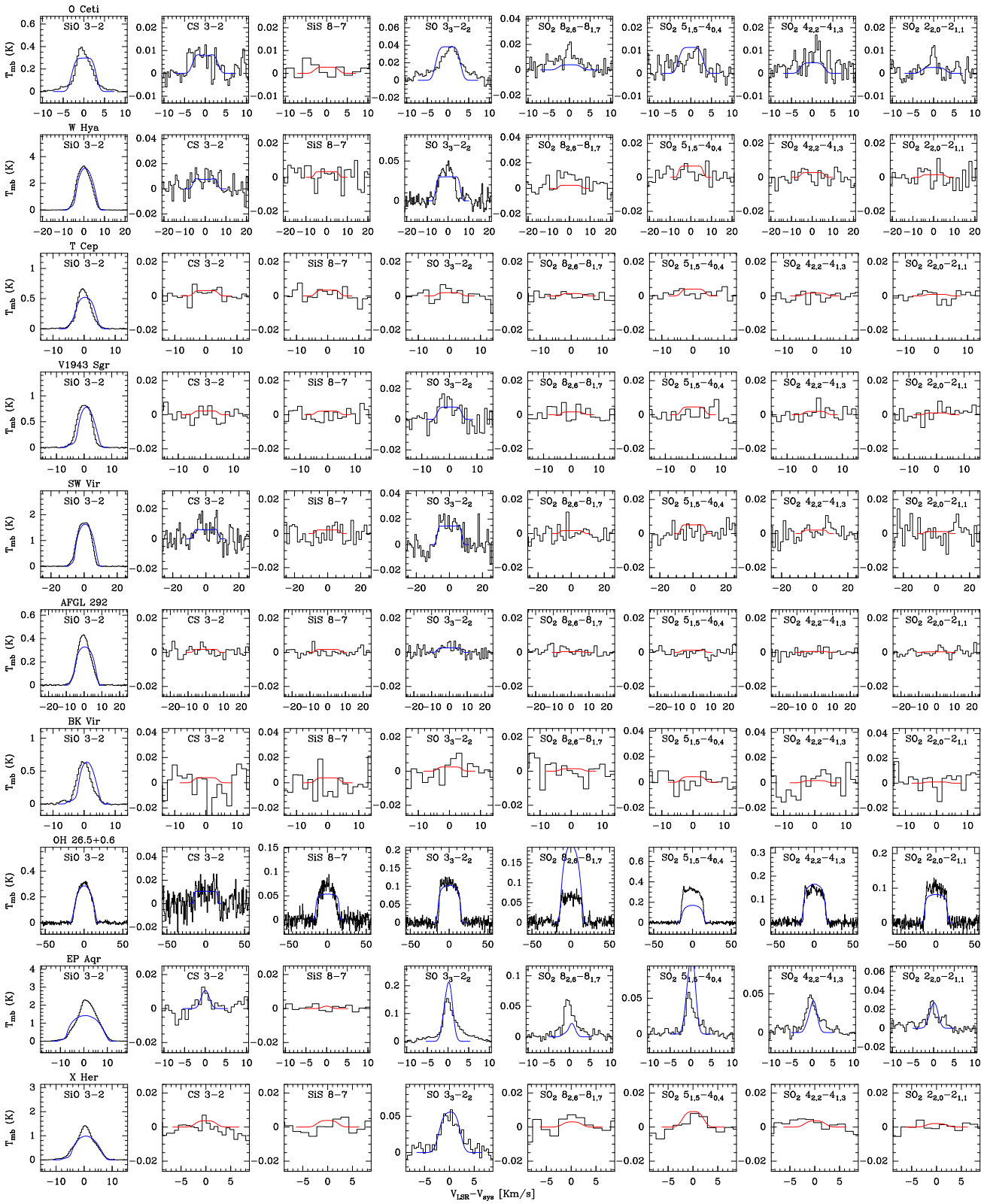

Fig. 1. continued.

For SiS, we considered the first 70 rotational levels within the $v = 0$ and $v = 1$ vibrational states (i.e., a total number of 140 energy levels). Level energies were computed from the Dunham coefficients given by Müller et al. (2007). Line strengths were computed from the dipole moments $\mu_{v=0} = 1.735$ D, $\mu_{v=1} = 1.770$ D, and $\mu_{v=1\rightarrow0} = 0.13$ D (Müller et al. 2007; Piñeiro et al. 1987). The rate coefficients for inelastic collisions with H_2 were taken from the calculations of Kłos & Lique (2008), while for temperatures higher than 300 K and for ro-vibrational transitions we adopted the rate coefficients computed by Toboła et al. (2008) scaled from He to H_2. Rate coefficients for He as collider were taken from Toboła et al. (2008).

For SO, we considered rotational levels up to $J = 30$ within the ground vibrational state $v = 0$ (i.e., a total number of 91 energy levels). Level energies and transition frequencies were calculated from the rotational constants reported by Bogey et al. (1997), and line strengths for rotational transitions were computed from the dipole moment, 1.52±0.02 D, measured by Lovas et al. (1992). The rate coefficients for excitation through inelastic collisions were taken from Lique et al. (2005) for temperatures up to 50 K and from Lique et al. (2006b) for higher temperatures, scaling from He to H_2 when needed.

For SO_2, we included the first 31 energy levels within the ground vibrational state. We used the rotational constants reported by Müller & Brünken (2005). Line strengths for rotational transitions were computed from the dipole moment measured by Patel et al. (1979). The rate coefficients for excitation through inelastic collisions with H_2 were taken from Cernicharo et al. (2011) for temperatures up to 30 K, and from Balança et al. (2016) for higher temperatures, while for collisions with He rate coefficients were taken from Green (1995).

5.2. Modeling procedure

Here, we give a brief description of the model used to perform the non-LTE excitation and radiative transfer calculations (for details see Massalkhi et al. 2018). To derive accurate molecular abundances in each object, we take into account the specific physical properties for each envelope and source presented in Tables 1 and 2.

The main assumption in the model is that the CSE that surrounds the central AGB star has a smooth and spherically symmetric geometry that is produced by an isotropic mass loss with a constant mass loss rate $\dot{M}$ and a constant expansion velocity $V_{\rm exp}$. We assume that the hydrogen in the CSE is molecular and its density structure (as a function of a distance r from the star) follows an r^{-2} law. The various physical quantities relating to the envelope such as the radial profiles of the gas density, gas temperature, and dust temperature, as well as the properties of the dust grains are described in Massalkhi et al. (2018). The only difference in this study is that we consider spherical grains of silicate with a radius of 0.1 μm, a mass density of 3.3 g cm^{-3}, and optical properties for warm silicate from Suh (1999).

We chose to model the molecular line emission using the multishell large velocity gradient (LVG) method explained in more detail in Agúndez (2009) and Agúndez et al. (2012). The LVG formalism, first developed by Sobolev (1960), has been widely used to solve the molecular excitation and radiative transfer problem in environments with large velocity gradients. This approach is valid for molecular lines in circumstellar envelopes as long as they are not too optically thick. Bujarrabal & Alcolea (2013) showed that this formalism yields quite accurate excitation conditions even when the approximations of the method are marginally satisfied. These authors investigated the validity of the LVG formalism by studying the CO molecular excitation for different conditions and conclude that although the LVG approximation still produces good behavior in cases where the velocity gradient is low, the behavior is not as accurate for the very outer regions with high opacities. The LVG method provides a good compromise with respect to other methodologies such as Monte Carlo, which are more computationally expensive and exhibit problems of convergence when including a high number of energy levels.

Briefly, the CSE is divided into several concentric shells. The statistical equilibrium equations are then solved in each shell to determine the level populations. The radiation field which is needed to solve the statistical equilibrium equations is evaluated solving the radiative transfer under the LVG approximation. We assume that the molecules are excited by collisions with H_2 molecules and He atoms and through radiation from three sources: the cosmic microwave background, the stellar radiation, and the thermal emission from dust. We also include infrared (IR) pumping to excited vibrational states for SiO, CS, and SiS. In the cases of SO and SO_2, we only consider rotational levels within the ground vibrational state for simplicity and because of the less reliable collisional rate coefficients for ro-vibrational transitions.

5.3. Adopted abundance distribution

The abundance distribution is important in the radiative transfer modeling. For parent molecules that are injected from the inner parts of the envelope, the abundance may vary with radius due to two processes: condensation onto grains and photodissociation by ultraviolet (UV) photons. In reality, the abundance is expected to decrease from the thermochemical equilibrium (TE) value at the stellar surface in the dust formation region. The molecules are further depleted by the ambient radiation field which eventually determines the size of the emission envelope. Relating to this scenario, a few studies have reported on an abundance distribution to be consisting of two components, a compact high abundance in the inner regions of the CSE, and a lower abundance in the extended outer regions of the CSE (e.g., Schöier et al. 2007, Decin et al. 2010). For example, Schöier et al. (2004) modeled the SiO emission of the $J = 6-5$, $J = 5-4$, $J = 3-2$, and $J = 2-1$ lines in the CSE of the M-type star R Dor and found the need for a two-component abundance distribution which was characterized by a high abundance of 4×10^{-5} up to 1.2×10^{15} cm and a lower abundance of 3×10^{-6} at larger radii. This initial high abundance followed by a decrease was interpreted as adsorption of SiO onto dust. However, when Van de Sande et al. (2018) modeled the SiO emission with several low- and high-J transitions (up to $J = 38-37$) in the same object, R Dor, they found no indication of a two-component abundance distribution. Similarly, in the case of SiS, Schöier et al. (2007) modeled the emission in IK Tau and found a better fit to their observations when they included an inner component out to 1×10^{15} cm with a high SiS abundance of 2×10^{-5}. However, Danilovich et al. (2019) performed sensitive ALMA observations with an angular resolution of ~150 mas that correponds to $\sim 6 \times 10^{14}$ cm and did not find evidence for such a jump in the abundance of SiS in the same source. Other studies reported on the molecular abundance distribution in CSEs as well. Agúndez et al. (2012) modeled lines of CS in the $v = 0-3$ states in addition to several transitions of the isotopologues ^{13}CS, C^{34}S, and C^{33}S in IRC +10216 and derived an abundance of 4×10^{-6} in the inner regions that decreased to 7×10^{-7} in the mid envelope at a radius of 2×10^{15} cm. Their result is in good agreement with that derived by

Velilla-Prieto et al. (2019) that modeled the $J = 2-1$ lines of CS, and ^{13}CS, C^{34}S, and C^{33}S using ALMA which also showed a decline in the abundance toward the intermediate envelope of IRC +10216 supporting a depletion scenario. However, no such abundance distribution is reported for the sulfur oxides thusfar that evidence any depletion (e.g., Danilovich et al. 2016, 2020).

Regardless whether or not these molecules experience a first abundance depletion due to dust condensation, they maintain a significant abundance in the extended outer envelope where photodissociation further removes the molecules from the gas phase. The lines observed in this study probe intermediate/outer regions of the envelope (see Sect. 6). That is, we are not sensitive to abundance gradients occurring in the inner envelope and the abundances derived are valid for the post-condensation region. We therefore adopt a simple scenario in which the fractional abundance remains constant throughout the envelope up to some region where it drops due to photodissociation. The adopted abundance radial distribution $f(r)$ is described by a Gaussian as:

$$f(r) = f_0 \exp\Big(-(r/r_e)^2 \Big), \tag{1}$$

where f is the fractional abundance of the molecule relative to H_2, f_0 is the initial abundance, and r_e is the e-folding radius at which the abundance has dropped by a factor e. Danilovich et al. (2016) observed SO and SO_2 emission in a sample of five stars O-rich CSEs, and found that SO_2 has a Gaussian abundance distribution, whereas the SO abundance distribution differs between Gaussian for high mass-loss rate envelopes, and shell-like for low mass-loss rate envelopes where the abundance peaks at a distance from the central star. In their recent study on these two molecules using ALMA in two CSEs R Dor and IK Tau, Danilovich et al. (2020) found that SO and SO_2 in R Dor have Gaussian distribution, while in IK Tau, SO and probably SO_2 have a shell-like abundance distribution. Here, we adopt a Gaussian abundance distribution for all the molecules.

In their study on M-type stars, González Delgado et al. (2003) estimated the SiO emission size by using a scaling law that correlated r_e and the envelope density evaluated through the quantity $\dot{M}/V_{\rm exp}$,

$$\log r_e({\rm SiO}) = 19.2 + 0.48 \log\left(\frac{\dot{M}}{V_{\rm exp}}\right), \tag{2}$$

where r_e is given in cm, $\dot{M}$ in $M_\odot$ yr^{-1}, and $V_{\rm exp}$ in km s^{-1}. We use Eq. (2) to determine the emission size of SiO, SiS, SO, and SO_2 in our sample. The assumption of similar radial extents for SiO and SiS is discussed in our previous study of these molecules in C-rich CSEs in Massalkhi et al. (2019). Danilovich et al. (2018) derived empirical relations between r_e and $\dot{M}/V_{\rm exp}$ for SiS and CS from a limited sample of M-, C-, and S-type stars which we noticed are unreliable outside the relatively narrow range of $\dot{M}/V_{\rm exp}$ over which they were derived (for details see Massalkhi et al. 2019). In their recent study using ALMA data, Danilovich et al. (2020) found that SO and SO_2 are colocated around the O-rich R Dor, with SO being slightly more extended than SO_2. However, statistically robust empirical relations for the emission size of SO and SO_2 have not been derived. Since the photodissociation rates of SO and SO_2 under the interstellar radiation field are of the same order of that of SiO, a few times 10^{-9} s^{-1} (Heays et al. 2017; Agúndez et al. 2018), in the lack of better constraints on the emission size, we adopt the same radial extent for SiO, SiS, SO, and SO_2. For CS, which has a significantly lower photodissociation rate than SiO, SO, and SO_2, a few times 10^{-10} s^{-1} (Pattillo et al. 2018), we use a larger emission size as suggested by Massalkhi et al. (2019) for C-rich AGB stars and described by the following empirical relation:

$$\log r_e({\rm CS}) = 19.65 + 0.48 \log\left(\frac{\dot{M}}{V_{\rm exp}}\right), \tag{3}$$

Briefly, we construct a physical model of the envelope for each source with the parameters given in Tables 1 and 2. Adopting the fractional abundance distributions given in the previous section, we perform excitation and radiative transfer calculations by varying the initial fractional abundance, f_0, until the calculated line profiles match the observed ones. The criteria we adopted to determine how well the model fits the data is by matching the area of the calculated line to the observed one. The agreement between observed and calculated line area was better than 3% for the molecules for which we have only one line, SiO, CS, SiS, and SO, and better than 30% for SO_2 because for this molecule we have four observed lines. When the line is undetected, we derive upper limits of the fractional abundance by choosing the maximum abundance that results in line intensities compatible with the noise level of the observations.

In our sample there are three sources which deserve to be considered separately, EP Aqr, X Her, and OH 26.5+0.6. We discuss the reasons and the procedure adopted for the line modeling of these sources in Sect. 5.4.

5.4. Peculiar sources

Some AGB stars are known to exhibit a double-component profile in some molecular lines like CO, with a narrow spectral feature centered on a much broader plateau, with both components having the same LSR velocity (Kahane & Jura 1996; Knapp et al. 1998; Kerschbaum & Olofsson 1999; Olofsson et al. 2002). The origin of these double-component profiles is still not clear. Knapp et al. (1998) suggested that it is an effect of episodic mass loss with highly varying gas expansion velocities that produces multiple shells where each shell has a different expansion velocity and different mass loss rate. Other studies argued that complicated geometries and kinematics play a role in the rise of the effect (Neri et al. 1998; Nakashima 2005; Castro-Carrizo et al. 2010; Kim & Taam 2012; Homan et al. 2015; Kim et al. 2019). Two of the sources that are known to exhibit this type of profile, X Her and Ep Aqr (Homan et al. 2018), are in our sample and their spectra are shown in Fig. 1. The two stars are M-type semiregular variable AGBs. From the rotational transitions observed here there is no sign of the superimposition of the narrow profile on the broader one in both sources. However, based on the observed line widths and expansion velocities it appears that the SiO line emission of X Her and EP Aqr are coming from the broad component, while the CS, SO and SO_2 line emissions arise from the narrow component. The SiS rotational line is not detected in any of the sources, but in deriving abundance upper limits we assume that it behaves as CS, SO, and SO_2 and arises from the narrow component. We then consider two different winds for the narrow and the broad component each with different values of the expansion velocity and the mass loss rate, as given in Table 2, and perform the radiative transfer and excitation analysis independently.

Another source we encountered problems modeling is the extreme OH/IR AGB star OH 26.5+0.6. This star is thought to have gone through a superwind phase characterized by a dramatic increase of the mass loss rate (by a factor of ten at least) toward the end of the AGB (Iben & Renzini 1983) which ejects most of the remaining envelope and the initial mass of the star

allowing the latter to evolve toward the planetary nebula phase. Justtanont et al. (1996) show evidence of two mass loss regimes: a higher density superwind that started recently (<200 yr), and a lower density AGB wind that started earlier. From Justtanont et al. (1996), the reported gas mass loss rate for the superwind is $\dot{M} = 5.5 \times 10^{-4}\ M_{\odot}\,\mathrm{yr}^{-1}$ at $r < 8.0 \times 10^{15}$ cm and for the outer AGB wind is $\dot{M} = 1 \times 10^{-6}\ M_{\odot}\ \mathrm{yr}^{-1}$ at greater radii. Moreover, we adopt the gas kinetic temperature profile for the object reported by the authors as well (solid line in Fig. 7b of Justtanont et al. 1996). After setting the density and temperature structure in the envelope, we model the rotational line emission of the molecules.

6. Results from line modeling

The calculated line profiles from our best-fit LVG model for each of the sources are shown in blue in Fig. 1, where they are compared with the observed line profiles (black histograms). In those cases in which the lines are not detected, the calculated line profile is plotted in red instead.

In general, the calculated line shapes agree well with the observed ones. However, there are profiles that exhibit complexities which our model is not able to reproduce, for example, the SO_2 emission in IK Tau. This is probably due to the simplicity of our approximated physical model which assumes smooth and spherically symmetric envelopes and does not take into consideration any deviations from that. In the case of the SiO $J = 3-2$ line, the observed profiles are mostly parabolic or triangular, although for some sources, such as RR Aql, the model produces flat-topped shapes. The assumption of a constant expansion velocity in our model could be playing a factor in the discrepency between the calculated and the observed line profile since as mentioned previously triangular line profiles probably indicate emission from accelerating regions close to the star. Another explanation could be related to the line opacity τ. In these cases, the line opacity is probably around one, with the modeled line having τ slightly below one and the observed line having τ slightly above one. In any case, the overall agreement between calculated and observed line profiles is good.

The excitation and radiative transfer calculations give us information about the excitation and emission region of the molecules in the envelope. In regards to the emission region, the model indicates that most of the contribution to the line emission of the five molecules is coming from regions $10^{15}-10^{16}$ cm from the star, i.e, most of the emission arises from intermediate and outer regions of the envelope, rather than from the inner regions. To evaluate the role of IR pumping to vibrationally excited states for SiO, CS, and SiS, we ran models excluding IR pumping. Our calculations indicate that in the absence of IR pumping, the emission is more compact than when IR pumping is included. The calculations also show that IR pumping has an effect on the intensities of the observed lines of SiO, CS and SiS. Neglecting IR pumping results in a systematic decrease in the integrated line intensities of ∼40% for SiO $J = 3-2$, ∼50% for CS $J = 3-2$, and ∼35% for SiS $J = 8-7$.

In regards to the excitation of the rotational levels, the model indicates that the rotational levels of the five studied molecules are thermalized in the warm and dense inner layers of the envelopes. However, as the radial distance from the star increases and the gas density decreases, the rotational levels become suprathermally populated (with the ratio of the excitation temperature, $T_{\rm ex}$, to the kinetic temperature, $T_{\rm k}$, greater than unity, $T_{\rm ex}/T_{\rm k} > 1$) for SiS, CS, SO and SO_2 in the regions where most of the emission is coming from. For SiO, the population of rotational levels vary. Mostly, they are subthermally populated ($T_{\rm ex}/T_{\rm k} < 1$), however for a few envelopes (e.g., RR Aql, NV Aur, WX PSc), the levels are suprathermally populated . The behavior for SiO, CS, and SiS, is largely caused by IR pumping. In comparison, in C-rich CSEs, IR pumping causes the rotational transitions of these molecules to be all suprathermally excited (Massalkhi et al. 2019). We can conclude that IR pumping plays an important role in the excitation of the rotational emission of SiO, CS, and SiS whether in C-rich or O-rich envelopes.

7. Discussion

The fractional abundances relative to H_2, f_0, derived for SiO, CS, SiS, SO, and SO_2 in the 30 O-rich envelopes are presented in Table 4 and are shown as a function of the envelope density proxy, $\dot{M}/V_{\rm exp}$, in blue in Fig. 2. In the panels of SiO, CS, and SiS we also include (plotted in red) the fractional abundances derived in a sample of 25 C-rich envelopes by Massalkhi et al. (2019).

7.1. Fractional abundances derived

7.1.1. SiO

The SiO fractional abundances f_0(SiO) derived in this study for the 30 O-rich AGB stars are presented in blue in the upper middle panel of Fig. 2. We overplot in red the SiO abundances derived by Massalkhi et al. (2019) for 25 C-rich AGB stars.

One of the first comprehensive studies of molecular abundances in circumstellar envelopes was done by González Delgado et al. (2003), who focused on SiO in a large sample of about 40 O-rich CSEs. They used multiline data to determine the size of the emitting region and the SiO abundance simultaneously. We share 21 objects with these authors. In general, our derived SiO abundances are very similar to theirs.

From Fig. 2, we notice from the SiO fractional abundances we are not able to distinguish the chemical type, either O-rich (in blue) or C-rich (in red). Schöier et al. (2006a) found the same result when comparing the distribution of their derived SiO abundances in C-rich stars to the distribution of SiO abundances in M-type stars derived by González Delgado et al. (2003). That is, observations indicate that the SiO abundance does not depend on the C/O ratio at the stellar surface. The mean fractional abundance of SiO we obtain is similar in both types of CSEs, with $\log f_0(\mathrm{SiO}) = -5.5 \pm 0.7$ in O-rich CSEs and $\log f_0(\mathrm{SiO}) = -5.8 \pm 0.6$ in C-rich CSEs[7].

The fact that the SiO abundance injected into the expanding wind is not sensitive to the C/O ratio is in line with theoretical expectations. Thermochemical equilibrium calculations predict that SiO maintains a uniform and high fractional abundance of several 10^{-5} from the photosphere out to 10 $R_\star$ in O-rich CSEs, while in C-rich CSEs the predicted fractional abundance from 5 $R_\star$ is also on the order of 10^{-5}. The main difference occurs in the innermost region, from the photosphere to around 5 $R_\star$, where SiO has a low abundance in C-rich conditions while it maintains a high abundance in O-rich CSEs (Agúndez & Cernicharo 2006; Agúndez et al. 2020). In a scenario of chemical equilibrium, it seems that the low SiO abundance within 5 $R_\star$ in C-rich CSEs does not have an influence on the final SiO abundance that is injected into the expanding wind, and that chemical equilibrium holds for SiO in the high abundance region located beyond 5 $R_\star$. The low SiO abundance

[7] We consider upper limits as abundances to compute mean abundances and standard deviations. The same approach is adopted for the rest of molecules: CS, SiS, SO and SO_2.

Table 4. Fractional abundances of SiO, CS, SiS, SO, and SO_2 derived.

Name	Star var.	$\dot{M}$ ($M_\odot$ yr^{-1})	V_{exp} (km s^{-1})	f_0(SiO)	f_0(CS)	f_0(SiS)	f_0(SO)	f_0(SO_2)
IK Tau	M	2.4×10^{-5}	17.5	3.1×10^{-7}	1.0×10^{-8}	1.0×10^{-7}	1.7×10^{-7}	3.2×10^{-7}
KU And	M	9.4×10^{-6}	19.5	6.2×10^{-7}	8.2×10^{-8}	9.9×10^{-7}	$<9.8 \times 10^{-8}$	$<1.8 \times 10^{-7}$
RX Boo	SRb	6.1×10^{-7}	7.5	1.7×10^{-6}	$<1.0 \times 10^{-9}$	$<1.2 \times 10^{-8}$	8.3×10^{-7}	3.5×10^{-7}
RT Vir	SRb	4.5×10^{-7}	7	4.5×10^{-5}	$<3.0 \times 10^{-9}$	$<2.5 \times 10^{-8}$	2.7×10^{-6}	1.2×10^{-6}
R Leo	M	1.0×10^{-7}	5	5.7×10^{-6}	1.2×10^{-8}	$<3.0 \times 10^{-8}$	6.6×10^{-7}	$<1.1 \times 10^{-7}$
WX Psc	M	4.0×10^{-5}	19	8.9×10^{-7}	2.7×10^{-8}	4.5×10^{-7}	2.5×10^{-7}	1.0×10^{-6}
GX Mon	M	4.8×10^{-6}	18	1.0×10^{-5}	8.9×10^{-8}	7.6×10^{-7}	2.5×10^{-6}	7.4×10^{-6}
NV Aur	M	2.5×10^{-5}	17.5	2.9×10^{-6}	2.8×10^{-8}	7.8×10^{-7}	8.5×10^{-7}	4.1×10^{-6}
V1111 Oph	M	2.7×10^{-6}	15.5	5.8×10^{-6}	7.7×10^{-8}	1.3×10^{-6}	2.0×10^{-6}	7.8×10^{-6}
RR Aql	M	8.6×10^{-7}	8.5	1.3×10^{-6}	$<4.5 \times 10^{-9}$	$<6.3 \times 10^{-8}$	1.7×10^{-6}	6.5×10^{-6}
R LMi	M	2.6×10^{-7}	5.5	2.6×10^{-5}	$<1.0 \times 10^{-8}$	$<1.5 \times 10^{-7}$	2.3×10^{-6}	9.8×10^{-7}
BX Cam	M	1.0×10^{-6}	17	5.5×10^{-6}	1.1×10^{-7}	1.9×10^{-6}	2.3×10^{-6}	5.8×10^{-6}
V1300 Aql	M	1.0×10^{-5}	15	1.5×10^{-6}	2.2×10^{-8}	9.3×10^{-7}	1.2×10^{-6}	4.5×10^{-6}
R Cas	M	9.5×10^{-7}	7.5	3.1×10^{-6}	1.2×10^{-8}	7.4×10^{-8}	1.2×10^{-6}	6.8×10^{-7}
IRC -30398	M	6.0×10^{-6}	14.5	2.9×10^{-7}	1.5×10^{-8}	6.5×10^{-8}	$<6.8 \times 10^{-8}$	$<6.0 \times 10^{-8}$
TX Cam	M	7.7×10^{-6}	17.5	1.4×10^{-6}	5.1×10^{-8}	3.9×10^{-7}	5.8×10^{-7}	6.3×10^{-7}
S CrB	M	2.7×10^{-7}	5	1.8×10^{-5}	$<2.0 \times 10^{-8}$	$<2.0 \times 10^{-7}$	4.2×10^{-6}	4.9×10^{-6}
IRC +60169	M	9.6×10^{-6}	15	1.5×10^{-7}	5.0×10^{-9}	2.6×10^{-8}	1.3×10^{-7}	3.5×10^{-7}
R Crt	SRb	1.0×10^{-6}	11	2.3×10^{-5}	$<1.0 \times 10^{-8}$	$<5.0 \times 10^{-8}$	2.3×10^{-6}	1.7×10^{-6}
R Hya	M	4.7×10^{-7}	5	3.3×10^{-6}	$<2.0 \times 10^{-9}$	$<2.0 \times 10^{-8}$	3.1×10^{-7}	$<5.2 \times 10^{-8}$
o Ceti	M	2.0×10^{-7}	3	7.0×10^{-8}	1.4×10^{-9}	$<4.0 \times 10^{-9}$	2.0×10^{-7}	4.0×10^{-8}
W Hya	SRa	4.2×10^{-7}	6	1.4×10^{-5}	5.0×10^{-9}	$<2.0 \times 10^{-8}$	6.9×10^{-7}	$<9.8 \times 10^{-8}$
T Cep	M	7.8×10^{-8}	4	4.4×10^{-6}	$<9.0 \times 10^{-9}$	$<1.0 \times 10^{-7}$	$<2.2 \times 10^{-7}$	$<3.0 \times 10^{-7}$
V1943 Sgr	SRb	1.0×10^{-6}	4.5	1.5×10^{-5}	$<3.0 \times 10^{-9}$	$<3.0 \times 10^{-8}$	4.1×10^{-7}	$<1.5 \times 10^{-7}$
SW Vir	SRb	2.2×10^{-6}	7.5	2.0×10^{-6}	2.1×10^{-9}	$<5.0 \times 10^{-9}$	1.6×10^{-7}	$<3.9 \times 10^{-8}$
AFGL 292	...	1.3×10^{-7}	7	1.2×10^{-5}	$<2.0 \times 10^{-8}$	$<2.0 \times 10^{-7}$	1.2×10^{-6}	$<3.6 \times 10^{-7}$
BK Vir	SRb	2.3×10^{-7}	4	7.0×10^{-6}	$<5.0 \times 10^{-9}$	$<3.0 \times 10^{-8}$	$<1.0 \times 10^{-7}$	$<1.2 \times 10^{-7}$
OH 26.5+0.6	M	1.0×10^{-6}	15.4	2.2×10^{-6}	3.1×10^{-8}	5.2×10^{-7}	6.0×10^{-6}	2.1×10^{-6}
Ep Aqr	SRb	1.7×10^{-8}	1	–	6.0×10^{-9}	$<6.0 \times 10^{-9}$	5.4×10^{-6}	1.9×10^{-6}
		5.0×10^{-7}	9.2	3.6×10^{-6}	–	–	–	–
X Her	SRb	4.3×10^{-8}	2.2	–	$<4.2 \times 10^{-9}$	$<3.6 \times 10^{-8}$	2.5×10^{-6}	$<2.5 \times 10^{-7}$
		1.6×10^{-7}	6.5	1.4×10^{-5}	–	–	–	–

predicted by chemical equilibrium in the innermost envelope has been inferred by modeling multiwavelength observations of the carbon star IRC +10216 by Schöier et al. (2006b). The nonequilibrium scenario of shocks induced by the stellar pulsation of Cherchneff (2006) also predicts a low sensitivity of the SiO abundance on the photospheric C/O ratio. In the model of Cherchneff (2006), for C/O < 1 shocks have a very limited effect on the SiO fractional abundance in the inner part of the wind as it stays around $\sim 10^{-5}$ from the photosphere out to 5 $R_\star$. For C/O > 1, the authors find that the low chemical equilibrium abundance of $\sim 10^{-8}$ is enhanced rapidly to values around 10^{-5} in the 1–5 $R_\star$ region. Therefore, the SiO abundances calculated at 5 $R_\star$, which are supposed to be the ones injected into the expanding wind, are of the same order in O-rich and C-rich stars. In summary, theoretical studies show that the SiO abundance has no apparent dependence on the C/O ratio in the outer wind which is in agreement with the findings from our observational study. The different behavior of the SiO abundance in the inner wind as predicted by theoretical studies probably explains why strong SiO maser emission is detected toward O-rich stars and not toward carbon stars (e.g., Pardo et al. 2004; Cotton et al. 2004). In view of the high SiO abundance observed in C-rich stars, this could suggest that the SiO molecules are formed further out in the wind in C-rich envelopes where the physical conditions are not likely to allow the pumping by IR photons, and thus the inversion of SiO level populations.

The fractional abundance of SiO in the O-rich sample varies substantially from as low as 7.0×10^{-8} up to 4.5×10^{-5}. This variation in the SiO abundance as illustrated in Fig. 2, whether C-rich or O-rich, shows a clear trend in which SiO becomes less abundant as the density in the wind, $\dot{M}/V_{exp}$, increases. Schöier et al. (2006a) and Massalkhi et al. (2019) presented analysis of circumstellar SiO abundances for carbon stars, and González Delgado et al. (2003) for M-type stars and likewise they find a similar behavior of a strong anticorrelation between the abundance and the wind density which was interpreted as an effect of increased adsorption of SiO onto dust grains at high densities. Here, we confirm the results found for O-rich stars by González Delgado et al. (2003). We found a similar trend when we investigated SiC_2 in a sample of 25 carbon-rich AGB stars (see upper left panel in Fig. 2 for comparison), which was interpreted as that SiC_2 is being efficiently incorporated into dust grains and playing an important role in the formation of silicon carbide dust in C-rich envelopes (Massalkhi et al. 2018). Adsorption of SiO onto dust grains in O-rich envelopes is predicted theoretically by chemical kinetics models (Van de Sande et al. 2019). We

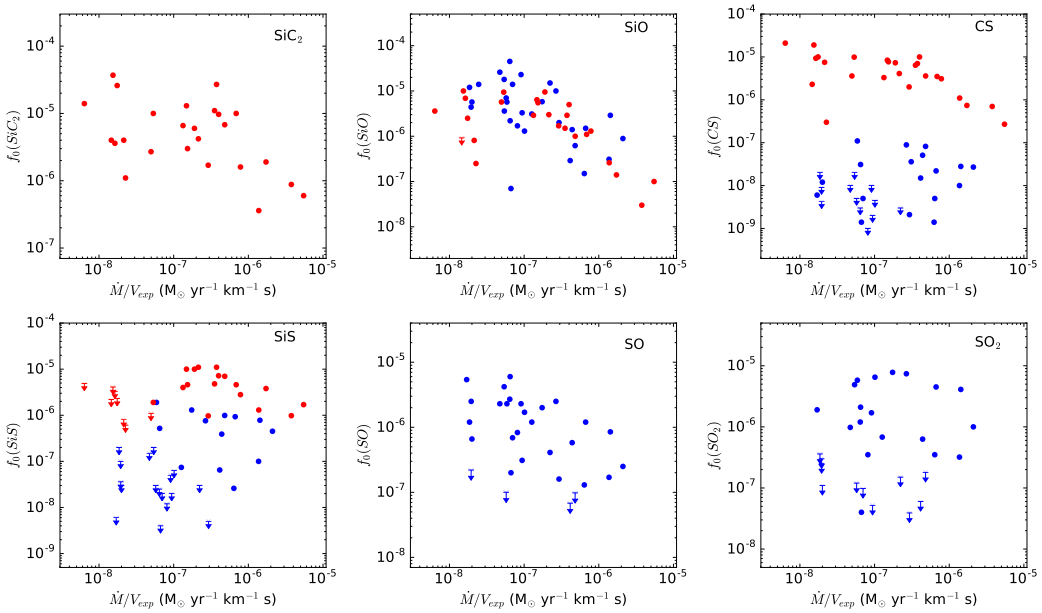

Fig. 2. Results for the radiative transfer and excitation analysis toward the sample of AGB stars. Fractional abundance f_0 derived for SiC_2 obtained by Massalkhi et al. (2018) for C-rich AGB stars (*upper left*), fractional abundance for SiO (*upper middle*), fractional abundance for CS (*upper right*), and fractional abundance for SiS (*lower left*) as a function of density measure $\dot{M}/V_{\rm exp}$ for oxygen stars (blue) and carbon stars (red; Massalkhi et al. 2019). Fractional abundance for SO (*lower middle*) and for SO_2 (*lower right*) in O-rich envelopes as a function of density measure $\dot{M}/V_{\rm exp}$. Downward arrows represent upper limits to f_0.

note that the median fractional abundance of SiO of the Mira-type variables, 2.5×10^{-6}, is lower by a factor of 6 with respect to the median value of the semiregular variables, 1.5×10^{-5}, which may be related to the mass loss rate rather than the stellar variability type. González Delgado et al. (2003) found a similar result where the high mass-loss rate Miras in their sample have a median abundance that is more than six times lower than that of the irregular and semiregular variables.

Silicates are known to be one of the most important types of dust in oxygen-rich envelopes and SiO has long been discussed to be the gas-phase precursor of silicate dust, mainly because of its high abundance in O-rich envelopes. The trend that we see here between the fractional abundance and the wind density supports this hypothesis.

7.1.2. CS

The fractional abundances derived for CS in the O-rich envelopes are shown in blue as a function of $\dot{M}/V_{\rm exp}$ in the upper right panel of Fig. 2. We also show in red the CS fractional abundances derived for the 25 C-rich AGB stars studied in Massalkhi et al. (2019).

Bujarrabal et al. (1994) searched for CS $J = 3-2$ and $J = 5-4$ transitions in a large sample of evolved stars. Their sample contains 17 O-rich stars, 10 of which are in our sample. These authors derived abundances using a simple analytical expression based on the integrated intensities of the observed lines and assumes a constant fractional abundance inside a given radius. In general, their CS abundances are higher than ours with varying degrees, for example, ranging from a factor of two for some sources, like V1300 Aql, to one order of magnitude for other sources, like IK Tau, to a highest factor of 47 for RX Boo, where our value is an upper limit. These authors remark that their approach holds for optically thin lines and estimated only a lower limit if the line was optically thick. Danilovich et al. (2018) surveyed a diverse sample of AGB stars. They detected CS in only the highest mass loss rate O-rich stars and derived CS abundances in agreement with ours for some sources, such as GX Mon and V1300 Aql, while for other sources their derived values were approximately an order of magnitude higher than ours, such as IK Tau and RR Aql, the latter being an upper limit in both studies.

Comparing the values of f_0(CS) in oxygen-rich and carbon-rich envelopes in Fig. 2, the derived abundances show substantial variations between the two chemical types where the mean fractional abundance for O-rich CSEs is $\log f_0(\mathrm{CS}) = -8.0 \pm 0.6$, more than two orders of magnitude lower than for C-rich CSEs, $\log f_0(\mathrm{CS}) = -5.4 \pm 0.5$. It is clear that the formation of CS is dependent on the photospheric C/O ratio of the star. We also notice that CS is mostly detected in O-rich CSEs with high mass-loss rates, while in C-rich CSEs, CS is detected in all the sources of the sample, regardless of the mass loss rate. Carbon monosulfide forms more readily in C-rich environments since there is available carbon, that is, not trapped by CO, to form C-bearing molecules. On the other hand, the formation of CS in O-rich CSEs is more surprising as all the available carbon is expected to be locked up in CO.

Chemical equilibrium calculations predict negligible abundances for CS in O-rich CSEs, more than 3–4 orders of magnitude below the observed values (Agúndez et al. 2020). It is clear that some nonequilibrium process is enhancing the abundance of CS in O-rich envelopes. A possible explanation for the synthesis of this molecule could be related to photochemistry in a clumpy CSE, as investigated by Agúndez et al. (2010). In this scenario, interstellar UV photons penetrate into the inner regions of the envelope, break the CO bond and induce changes in the chemical composition which ultimately allow for the formation of CS and other C-bearing molecules. Their calculations predict abundances of $\sim 10^{-9}-10^{-8}$ for mass-loss rates in the $10^{-7}-10^{-5}$ $M_\odot$ yr^{-1}, in agreement with the abundances we find

here. Similar models by Van de Sande et al. (2018) examined the effects that clumping and porosity have on the chemistry in the AGB outflow and found slightly higher peak abundances of $\sim 10^{-7}$. However, in their recently published corrigendum these authors no longer find this peak, instead the fractional abundance of CS drop to $\sim 10^{-10}$ (Van de Sande et al. 2020). Another explanation for the formation of CS in O-rich environments could be related to the variable nature of AGB stars. Periodic shock waves caused by stellar pulsations propagate through the photosphere and alter the gas chemistry where the collisional destruction of CO in the shocks could release free atomic carbon and trigger the formation of CS in O-rich environments (Duari et al. 1999; Cherchneff 2006; Gobrecht et al. 2016). The shock-induced chemistry model of Cherchneff (2006) predicts that CS reaches abundances of a few times 10^{-6} in envelopes with C/O < 1, that is to say, significantly above the mean abundance derived here from observations.

To investigate the reason for the nondetection of CS in the low mass loss rate objects, we consider the variability type (Mira variable and semiregular variable, see Table 4) of the O-rich stars. The type of variability is generally attributed to the pulsation of the star and therefore could influence the shock conditions and provide an explanation of the abundance differentiation between high- and low-mass loss rate O-rich stars. However, we see no indication of a dependence between the abundance of CS and the variability type. On one hand, the nondetection of CS in these envelopes could be due to a low fractional abundance of the molecule, on the other hand, it could be due to a lack of sensitivity.

The CS fractional abundance in the O-rich sample varies by about two orders of magnitude, ranging from as low as 1×10^{-9} to as high as 1.1×10^{-7}, yet unlike the case of SiO, this variation shows no apparent trend that the CS abundance decreases as the density in the wind ($\dot{M}/V_{\rm exp}$) increases for O-rich envelopes. Such a trend is however evident for carbon-rich envelopes. This suggests that CS molecules are more likely to adsorb onto dust grains in C-rich CSEs than in O-rich ones. While CS is thought to play a role in the formation of MgS dust in C-rich envelopes (Massalkhi et al. 2019), in the case of O-rich envelopes CS does not seem to be affected by adsorption onto dust grains and to be playing a role in the formation of dust.

7.1.3. SiS

In the lower left panel of Fig. 2 we show as a function of $\dot{M}/V_{\rm exp}$ the fractional abundances of SiS derived in the 30 O-rich envelopes studied here (in blue) and in the 25 C-rich envelopes studied by Massalkhi et al. (2019; in red).

Schöier et al. (2007) reported on the detection of SiS line emission in 8 oxygen-rich envelopes, all of which are included in our sample. They performed radiative transfer calculations to derive abundances adopting, similarly to us, an abundance distribution based on the scaling law established by González Delgado et al. (2003) for SiO in M-type stars. Our SiS abundances are in good agreement with theirs for all of the sources.

By looking to the fractional abundances f_0(SiS) derived in the O-rich sample (see Table 4) we notice that they vary considerably among different sources, between $<4.0 \times 10^{-9}$ and 1.9×10^{-6}. The mean fractional abundance in the O-rich sample is $\log f_0(\mathrm{SiS}) = -7.0 \pm 0.7$, while in C-rich AGB stars is $\log f_0(\mathrm{SiS}) = -5.5 \pm 0.4$, that is, an order of magnitude higher than in O-rich envelopes. Similarly, in their study of SiS in a small sample of oxygen- and carbon-rich envelopes, Schöier et al. (2007) found SiS abundances in carbon-rich envelopes about an order of magnitude higher than in oxygen-rich envelopes. This indicates that SiS has a marked chemical differentiation based on the photospheric C/O ratio, being more preferentially formed in C-rich environments than in O-rich ones.

According to chemical equilibrium, in C-rich envelopes SiS reaches a high fractional abundance of about 10^{-5} from 2 $R_\star$, while in O-rich envelopes the abundance of SiS is low in the very inner regions but rises to values slightly below 10^{-5} from 2 $R_\star$ beyond 5 $R_\star$ (Agúndez et al. 2020). That is, the differentiation between C-rich and O-rich is restricted to the very inner regions, but beyond 5 $R_\star$ SiS is predicted to reach high abundances, on the order of 10^{-5}, in both C- and O-rich envelopes. The low SiS abundances observed here in some O-rich envelopes are thus not expected according to chemical equilibrium. On the other hand, nonequilibrium chemical models based on shocks induced by the stellar pulsation predict a dependence of the SiS abundance on the C/O ratio, with abundances on the order of 10^{-5} and 10^{-8} at 5 $R_\star$ in the inner regions of C- and O-rich, respectively, envelopes (Cherchneff 2006). The SiS abundances derived from observations here agree with the predictions of these models in terms of differentiation based on the C/O ratio, although there is a discrepancy because some of our observed abundances are significantly above those predicted by the model. For example, Cherchneff (2006) predicts an SiS fractional abundance for TX Cam of $\sim 10^{-8}$ at 5 $R_\star$, while for this source we derive an abundance of 3.9×10^{-7}. Therefore, chemical equilibrium overestimates the SiS abundances in O-rich envelopes while nonequilibrium models underestimate them.

Strikingly, we noticed that SiS is not detected in envelopes with low mass loss rates $<10^{-6}$, while it is detected in all sources above this threshold. This fact has been reported by some previous observational studies (Bujarrabal et al. 1994; Danilovich et al. 2015, 2018; Massalkhi et al. 2019). Massalkhi et al. (2019) surveyed a sample of 25 C-rich AGB stars in SiS $J = 8-7$ and $J = 7-6$ emission and did not detect emission below the same threshold as well. They speculated that the nondetection of SiS in the low mass-loss rate C-rich envelopes could be either caused by a lack of the constituent elements, which would be trapped in other S- and Si-bearing molecules like SiO, SiC_2, and CS, or could be due to sensitivity which might be the case here as well. Danilovich et al. (2019) discussed based on previous studies that SiS does not form readily in low-mass loss rate semi-regular variables, where the molecule otherwise reaches higher abundunces in Mira variable type CSEs. However, these authors detect faint SiS $J = 19-18$ emission toward the low mass-loss rate semiregular variable, R Dor, using ALMA and derive an abundance of 1.5×10^{-8} which indicates that the nondetection of SiS in low mass loss rate semiregular variables could be due to low sensitivity. In this study, we do not detect SiS in low-mass loss rate objects of both, semiregular and Mira variables, that is to say, we do not see a dependence of the SiS fractional abundance on the variability type, similar to the case of CS.

While SiS shows a tentative trend of a decreasing abundance with increasing envelope density for C-rich CSEs (Massalkhi et al. 2019), which was interpreted in terms of adsorption onto dust grains, here we do not see any similar trend, implying that SiS is probably not an important gas-phase precursor of dust in O-rich CSEs. However, chemical kinetics models by Van de Sande et al. (2019) predict adsorption of SiS onto dust grains in O-rich outflows.

7.1.4. SO

The resulting SO fractional abundances are shown as a function of $\dot{M}/V_{\rm exp}$ in the lower middle panel of Fig. 2. Systematic studies of the abundance of SO on large samples of AGB stars

are scarce. In fact, for some of the sources in our sample, SO abundances are reported for the first time. One of those studies was made by Bujarrabal et al. (1994), who surveyed a large sample of evolved stars in several molecular lines, including SO 6_5-5_4. Their sample contains 18 O-rich objects, 11 of which are in our sample. For some sources, our derived abundances are higher than theirs, and for other sources, the opposite is found. But in general the difference is within a factor of a few. The modeling performed by these authors is based on a somewhat simple method as mentioned previously, in which an analytical expression is used to derive the abundance of the molecules. A more complex abundance derivation based on radiative transfer modeling was done by Danilovich et al. (2016) using high- and low-E_u lines of SO (and SO_2; see below) in a small sample of five M-type AGB stars, four of which are in our sample. The authors find that the spatial distribution of SO differs between the low mass loss rate objects (R Dor, and W Hya) and the high mass loss rate ones (IK Tau, R Cas, and TX Cam), where the former were best reproduced by a Gaussian disribution whereas the latter by a shell-like one. For the four sources we have in common, their derived abundances are higher than ours by a factor of a few. In their recent study of two O-rich envelopes using ALMA, Danilovich et al. (2020) confirmed their previous findings in that the SO abundance distribution in IK Tau is shell-like with a constant inner abundance of 4.1×10^{-7}, not very different from the value derived in this study (1.7×10^{-7}), that increases to 2.2×10^{-6} at 5×10^{15} cm followed by a decline at $e-$folding radius 1.3×10^{16} cm. Velilla Prieto et al. (2017) also surveyed IK Tau and derived $f_0(\mathrm{SO})\geq8\times10^{-6}$, which is significantly higher than the value derived here (1.7×10^{-7}). These authors discuss that their derived SO abundance for this source may be overestimated since it is higher than previous observational studies and higher than abundances predicted by chemical equilibrium models, and that the reason behind this discrepancy is the uncertainty in the adopted SO emitting region.

The values of $f_0(\mathrm{SO})$ range between $<6.8\times10^{-8}$ and 6×10^{-6} and have a mean fractional abundance of $\log f_0(\mathrm{SO})=-6.1\pm0.6$. Chemical equilibrium calculations predict a peak SO abundance in the 1–10 $R_\star$ region of $\sim10^{-7}$ (Agúndez et al. 2020), while nonequilibrium chemical models considering shocks induced by the pulsation of the star predict similar abundances at 5 $R_\star$ (Cherchneff 2006). Therefore, on average, our observed SO abundances are higher than theoretical predictions of the inner wind. For SO, we see no dependence of the fractional abundance on the stellar variability type.

The distribution of the fractional abundances derived in the O-rich sample show hints of decreasing SO abundance with increasing density. This is however tentative as it is not as evident as in the case of SiO. Danilovich et al. (2016) found a similar trend of SO being less abundant with wind density, although this result was based on a reduced sample of only 3 objects (TX Cam, IK Tau, and R Cas) with a limited range of mass loss rates. If the tentative decrease in the abundance of SO with increasing envelope density that we see here is interpreted in terms of adsorption onto dust grains, SO could emerge as a candidate to gas-phase precursor of dust. To date, no sulfur-containing condensate has been identified in the spectra of O-rich envelopes, although CaS and FeS are expected to be important solid carriers of sulfur in these environments (Lodders & Fegley 1999; Agúndez et al. 2020).

7.1.5. SO_2

The fractional abundances derived for SO_2 are shown as a function of $\dot{M}/V_{\mathrm{exp}}$ in the lower right panel of Fig. 2. For some of the sources in our sample, SO_2 abundances are reported for the first time.

Infrared observations, in particular, the ISO/SWS detection of the 7.3 μm ν_3 band in a few AGB stars by Yamamura et al. (1999) and observations of high energy rotational lines by, e.g., Danilovich et al. (2016) and Velilla Prieto et al. (2017) indicate that SO_2 is formed in the inner layers of the CSE. Omont et al. (1993) surveyed a diverse sample of evolved stars in sulfur-bearing molecules and derived SO_2 abundances for 7 of the objects in our sample. For some sources, the abundances derived by these authors are similar to the values derived in this work. While for other sources, the derived abundances are different, like RX Boo, their value is 50 times higher than ours. These authors used a relatively simple method for estimating the molecular abundances, which is based on an analytical expression in which they assumed a constant excitation temperature for simplicity. A study was conducted by Danilovich et al. (2016) to investigate the SO_2 rotational lines observed with *Herschel*/HIFI in addition to further archival data toward a small sample M-type AGB stars. They performed radiative transfer modeling and derived SO_2 abundance toward three of the objects that are in our sample, IK Tau, W Hya, and R Cas. They find SO_2 fractional abundance in IK Tau similar to ours assuming a Gaussian distribution. They note that their SO_2 model for IK Tau is uncertain due to the difficulty of determining an abundance distribution. In fact, in their recent study using ALMA, these authors suspect that the SO_2 abundance in IK Tau is consistent with a shell-like distribution and not a Gaussian distribution (Danilovich et al. 2020). For W Hya and R Cas, their derived abundances are higher than ours, by a factor of 50 (with ours being an upper limit) and an order of magnitude, respectively. They also note that their SO_2 model for R Cas is very uncertain due to the fact that they had only two detected lines toward that source. The mean fractional abundance of SO_2 in the 30 O-rich envelopes studied here is $\log f_0(SO_2)=-6.2\pm0.7$, that is, very similar to that of SO.

Sulfur dioxide is predicted to have low abundances ($<10^{-10}$), well below the observed values, in the inner regions of O-rich envelopes according to chemical equilibrium (Agúndez et al. 2020). There must be a nonequilibrium process that enhances the formation of SO_2 in the inner envelope. The shock-induced chemistry scenario of Cherchneff (2006) also predicts very low abundances (10^{-13}–10^{-12}) for SO_2 in the inner winds of O-rich AGB stars. Clearly, observations and theory maintain a severe discrepancy with respect to the abundance of SO_2 in the inner envelope of M-type stars. Similar to SO, we see no dependence of the SO_2 fractional abundance on the stellar variability type.

In their study on sulfur molecules in M-type AGB stars, Danilovich et al. (2016) reported that SO and SO_2 are the main reservoirs of sulfur in the inner regions of the CSE of W Hya and R Cas, with more uncertainties for the latter. For W Hya, they derived a combined fractional abundance of SO and SO_2 of $\sim10^{-5}$ within the inner layers of the wind, thus accounting for most of the sulfur. Here in this work, the combined fractional abundance of CS, SiS, SO, and SO_2 in the intermediate regions of the W Hya envelope is just $\sim8\times10^{-7}$, well below the elemental abundance of S. This could point to depletion of sulfur through dust condensation in this object. A large fraction of the sulfur could also be trapped as gaseous H_2S, which is abundant in O-rich CSEs (Danilovich et al. 2017). In any case, for SO_2 we do not see any clear trend of decreasing $f_0(SO_2)$ with increasing envelope density that could point to this molecule as a gas-phase precursor of dust in O-rich envelopes.

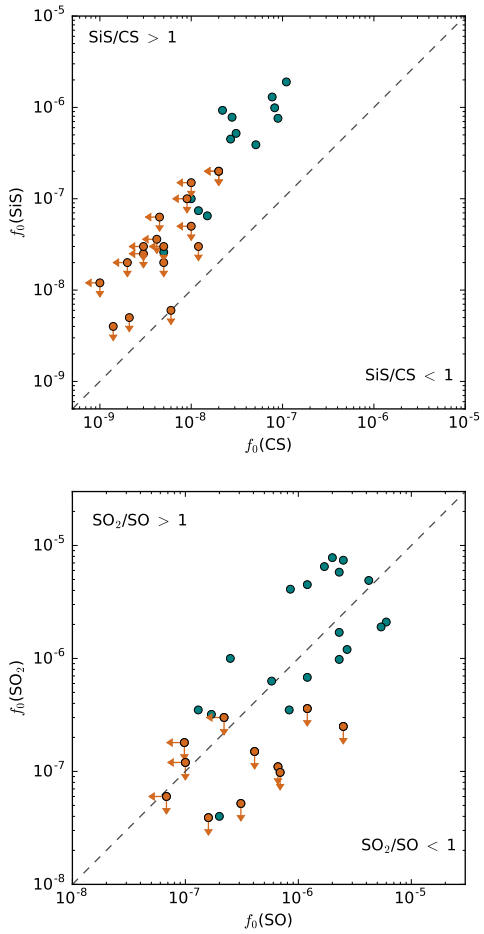

Fig. 3. Comparison of abundances between different pairs of molecules. The derived fractional abundances relative to H_2 of CS vs. SiS (*upper panel*) and SO vs. SO_2 (*lower panel*). Those sources with nondetections are denoted with arrows. The diagonal dashed lines indicate where the abundances of the two molecules become equal.The orange circles indicate fractional abundances with an upper limit.

7.2. Correlations between abundances of different molecules

In Fig. 3 we plot the derived fractional abundance of CS against that of SiS (upper panel) and the fractional abundance of SO against that of SO_2 (lower panel). We find that SiS is systematically more abundant than CS in the 30 O-rich envelopes studied, as indicated by the fact that all sources lie in the region of SiS/CS >1, apart from EP Aqr that falls on the dashed line representing equal amounts of SiS and CS. Similarly, Danilovich et al. (2018) determined the CS and SiS abundances in a sample of AGB stars, and found SiS to be systematically more abundant than CS in their O-rich sample. Therefore, SiS seems to be a more abundant gas-phase reservoir of sulfur than CS in oxygen star envelopes. The behavior is thus different to that of C-rich envelopes, where CS and SiS have comparable abundances (Massalkhi et al. 2019). Moving on to the lower panel in Fig. 3, the comparison of SO and SO_2 shows that in some sources SO is more abundant, like in R LMi and BK Vir, while in other sources SO_2 is more abundant, like in NV Aur and V1111 Oph. In general, the data points fall along the line defined by $f_0(SO) = f_0(SO_2)$ and there is no clear preference for either the $SO/SO_2 > 1$ or the $SO/SO_2 < 1$ sides. By looking to those sources where both SO and SO_2 are detected, it seems that in oxygen-rich envelopes, SO and SO_2 have abundances of the same order, carrying similar amounts of sulfur.

Regardless of which pair of molecules from those shown in Fig. 3, in both cases there is a trend in which the higher the abundance of one molecule the more abundant the other is, ie., the abundances of SO and SO_2, and of SiS and CS, seem to scale with each other which suggests a chemical connection between the members of each couple of molecules. Danilovich et al. (2018) found this type of correlation for CS and SiS in a sample including C-, M-, and S-type stars, although in that study the trend is considered tentative because of the small number of sources included. Massalkhi et al. (2019) also found a similar correlation between the three molecules CS, SiO, and SiS in their large sample of C-rich CSEs. We remark, however, that the trends in Fig. 3 become less robust given the upper limits on some of the fractional abundances in the sources where these molecules are not detected.

8. Conclusion

In this study we observed SiO, CS, SiS, SO, and SO_2 using the IRAM 30m telescope in a statistically meaningful sample of 30 O-rich AGB stars covering a wide range of mass-loss rates and circumstellar properties. We performed an extensive radiative transfer and excitation analysis based on the LVG method to derive the fractional abundance of these molecules in the circumstellar envelopes.

We found that the derived circumstellar abundances of SiS and CS have a clear dependence on the photospheric C/O ratio of the star, while SiO is not sensitive to it. Moreover, the fractional abundance of CS and SiS in carbon-rich CSEs are about two and one orders of magnitude, respectively, higher than in oxygen-rich envelopes, whereas the fractional abundance of SiO in both chemical types is of the same order of magnitude. Chemical equilibrium correctly predicts that SiO is abundant and that SiS and SO can reach high abundances in O-rich stars. However, the observed abundances of CS and SO_2 are higher than predicted by several orders of magnitude. Nonequilibrium chemical models succeed to different extents in reproducing the observed abundances. A scenario of photochemistry in a clumpy envelope accounts for the abundance enhancement of CS. On the other hand, a scenario of shocks induced by the stellar pulsation results in abundances that are 1–3 orders of magnitude too high for CS, somewhat lower than observed for SiS and SO, and well below the observed values for SO_2.

We find that the abundances of SiS and CS, on one hand, and SO and SO_2, on the other, are positively correlated which suggests a chemical connection between the members of each couple. Moreover, as already found for C-rich envelopes, we find a clear trend of decreasing SiO abundance with increasing envelope density in O-rich envelopes, which points to adsorption of SiO onto dust grains. A similar trend is observed for SO, although not as clear as for SiO. Therefore, SiO and SO are likely candidates to act as gas-phase precursors of dust in O-rich envelopes. In the cases of CS, SiS, and SO_2, abundances span over 2–3 orders of magnitude with no obvious correlation with the envelope density. These three molecules are thus less attractive candidates to be precursors of dust.

Our conclusions on the role of these molecules as gas-phase precursors of dust are based on low energy rotational lines, which probe post-condensation regions. More observations, in particular high-J lines and interferometric observations probing the inner regions of the envelopes, are needed to affirm the conclusions obtained in this study.

Acknowledgements. We thank the IRAM 30m staff for their help during the observations. This research has made use of the SIMBAD database, operated at CDS, Strasbourg, France. We acknowledge funding support from the European Research Council (ERC Grant 610256: NANOCOSMOS) and from Spanish MINECO through grant AYA2016-75066-C2-1-P. M.A. thanks Spanish MINECO for funding support through the Ramón y Cajal programme (RyC-2014-16277). L.V.P. acknowledges funding support from the Swedish Research Council and the European Research Council (ERC Consolidator Grant 614264).

References

Agúndez, M. 2009, PhD thesis, Universidad Autónoma de Madrid, Spain
Agúndez, M., & Cernicharo, J. 2006, ApJ, 650, 374
Agúndez, M., Cernicharo, J., & Guélin, M. 2010, ApJ, 724, L133
Agúndez, M., Fonfría, J. P., Cernicharo, J., et al. 2012, A&A, 543, A48
Agúndez, M., Roueff, E., Le Petit, F., & Le Bourlot, J. 2018, A&A, 616, A19
Agúndez, M., Martínez, J. I., de Andres, P. L., Cernicharo, J., & Martín-Gago, J. A. 2020, A&A, 637, A59
Balança, C., & Dayou, F. 2017, MNRAS, 469, 1673
Balança, C., Spielfiedel, A., & Feautrier, N. 2016, MNRAS, 460, 3766
Balança, C., Dayou, F., Faure, A., Wiesenfeld, L., & Feautrier, N. 2018, MNRAS, 479, 2692
Banerjee, D. P. K., Varricatt, W. P., Mathew, B., Launila, O., & Ashok, N. M. 2012, ApJ, 753, L20
Bogey, M., Civiš, S., Delcroix, B., et al. 1997, J. Mol. Spectrosc., 182, 85
Bujarrabal, V., & Alcolea, J. 2013, A&A, 552, A116
Bujarrabal, V., Fuente, A., & Omont, A. 1994, A&A, 285, 247
Castro-Carrizo, A., Quintana-Lacaci, G., Neri, R., et al. 2010, A&A, 523, A59
Cernicharo, J. 1985, IRAM Internal Rep. 52
Cernicharo, J., Spielfiedel, A., Balança, C., et al. 2011, A&A, 531, A103
Chandra, S., Kegel, W. H., Le Roy, R. J., & Hertenstein, T. 1995, A&AS, 114, 175
Cherchneff, I. 2006, A&A, 456, 1001
Chiavassa, A., Freytag, B., & Schultheis, M. 2018, A&A, 617, L1
Cotton, W. D., Mennesson, B., Diamond, P. J., et al. 2004, A&A, 414, 275
Danilovich, T., Teyssier, D., Justtanont, K., et al. 2015, A&A, 581, A60
Danilovich, T., De Beck, E., Black, J. H., Olofsson, H., & Justtanont, K. 2016, A&A, 588, A119
Danilovich, T., Van de Sande, M., De Beck, E., et al. 2017, A&A, 606, A124
Danilovich, T., Ramstedt, S., Gobrecht, D., et al. 2018, A&A, 617, A132
Danilovich, T., Richards, A. M. S., Karakas, A. I., et al. 2019, MNRAS, 484, 494
Danilovich, T., Richards, A. M. S., Decin, L., Van de Sande, M., & Gottlieb, C. A. 2020, MNRAS, 494, 1323
Dayou, F., & Balança, C. 2006, A&A, 459, 297
De Beck, E., Decin, L., de Koter, A., et al. 2010, A&A, 523, A18
De Beck, E., Decin, L., Ramstedt, S., et al. 2017, A&A, 598, A53
Decin, L., De Beck, E., Brünken, S., et al. 2010, A&A, 516, A69
Decin, L., Richards, A. M. S., Waters, L. B. F. M., et al. 2017, A&A, 608, A55
Denis-Alpizar, O., Stoecklin, T., Guilloteau, S., & Dutrey, A. 2018, MNRAS, 478, 1811
Dharmawardena, T. E., Kemper, F., Scicluna, P., et al. 2018, MNRAS, 479, 536
Díaz-Luis, J. J., Alcolea, J., Bujarrabal, V., et al. 2019, A&A, 629, A94
Drira, I., Hure, J. M., Spielfiedel, A., Feautrier, N., & Roueff, E. 1997, A&A, 319, 720
Duari, D., Cherchneff, I., & Willacy, K. 1999, A&A, 341, L47
Dyck, H. M., Benson, J. A., van Belle, G. T., & Ridgway, S. T. 1996, AJ, 111, 1705
Engels, D. 1979, A&AS, 36, 337
Gaia Collaboration (Brown, A. G. A., et al.) 2018, A&A, 616, A1
Gail, H. P., & Sedlmayr, E. 1998, Mol. Astrophys. Stars Galaxies, 4, 285
Gardan, E., Gérard, E., & Le Bertre, T. 2006, MNRAS, 365, 245
Gehrz, R. 1989, IAU Symp., 135, 445
Gobrecht, D., Cherchneff, I., Sarangi, A., Plane, J. M. C., & Bromley, S. T. 2016, A&A, 585, A6
González Delgado, D., Olofsson, H., Kerschbaum, F., et al. 2003, A&A, 411, 123
Green, S. 1995, ApJS, 100, 213
Groenewegen, M. A. T., Baas, F., Blommaert, J. A. D. L., et al. 1999, A&AS, 140, 197
Heays, A. N., Bosman, A. D., & van Dishoeck, E. F. 2017, A&A, 602, A105
Homan, W., Decin, L., de Koter, A., et al. 2015, A&A, 579, A118
Homan, W., Richards, A., Decin, L., de Koter, A., & Kervella, P. 2018, A&A, 616, A34
Iben, I. J., & Renzini, A. 1983, ARA&A, 21, 271
Justtanont, K., Skinner, C. J., Tielens, A. G. G. M., Meixner, M., & Baas, F. 1996, ApJ, 456, 337
Kahane, C., & Jura, M. 1996, A&A, 310, 952
Kamiński, T., Gottlieb, C. A., Menten, K. M., et al. 2013, A&A, 551, A113
Kamiński, T., Wong, K. T., Schmidt, M. R., et al. 2016, A&A, 592, A42
Kamiński, T., Müller, H. S. P., Schmidt, M. R., et al. 2017, A&A, 599, A59
Kerschbaum, F., & Olofsson, H. 1999, A&AS, 138, 299
Khouri, T., de Koter, A., Decin, L., et al. 2014, A&A, 561, A5
Kim, H., & Taam, R. E. 2012, ApJ, 759, 59
Kim, H., Liu, S.-Y., & Taam, R. E. 2019, ApJS, 243, 35
Kłos, J., & Lique, F. 2008, MNRAS, 390, 239
Knapp, G. R., Young, K., Lee, E., & Jorissen, A. 1998, ApJS, 117, 209
Knapp, G. R., Pourbaix, D., Platais, I., & Jorissen, A. 2003, A&A, 403, 993
Lique, F., & Spielfiedel, A. 2007, A&A, 462, 1179
Lique, F., Spielfiedel, A., Dubernet, M.-L., & Feautrier, N. 2005, J. Chem. Phys., 123, 134316
Lique, F., Spielfiedel, A., & Cernicharo, J. 2006a, A&A, 451, 1125
Lique, F., Dubernet, M.-L., Spielfiedel, A., & Feautrier, N. 2006b, A&A, 450, 399
Lodders, K., & Fegley, B., J. 1999, IAU Symp., 191, 279
Lovas, F. J., Suenram, R., Ogata, T., & Yamamoto, S. 1992, ApJ, 399, 325
Maercker, M., Danilovich, T., Olofsson, H., et al. 2016, A&A, 591, A44
Massalkhi, S., Agúndez, M., Cernicharo, J., et al. 2018, A&A, 611, A29
Massalkhi, S., Agúndez, M., & Cernicharo, J. 2019, A&A, 628, A62
McDonald, I., De Beck, E., Zijlstra, A. A., & Lagadec, E. 2018, MNRAS, 481, 4984
Müller, H. S., & Brünken, S. 2005, J. Mol. Spectros., 232, 213
Müller, H. S., Schlöder, F., Stutzki, J., & Winnewisser, G. 2005, J. Mol. Struct., 742, 215
Müller, H., McCarthy, M., Bizzocchi, L., et al. 2007, Phys. Chem. Chem. Phys., 9, 1579
Nakashima, J.-i. 2005, ApJ, 620, 943
Neri, R., Kahane, C., Lucas, R., Bujarrabal, V., & Loup, C. 1998, A&AS, 130, 1
Ohnaka, K., Weigelt, G., Millour, F., et al. 2011, A&A, 529, A163
Olofsson, H., González Delgado, D., Kerschbaum, F., & Schöier, F. L. 2002, A&A, 391, 1053
Omont, A., Lucas, R., Morris, M., & Guilloteau, S. 1993, A&A, 267, 490
Pardo, J. R., Cernicharo, J., & Serabyn, E. 2001, IEEE Trans. Antennas Propag., 49, 1683
Pardo, J. R., Alcolea, J., Bujarrabal, V., et al. 2004, A&A, 424, 145
Patel, D., Margolese, D., & Dykea, T. 1979, J. Chem. Phys., 70, 2740
Pattillo, R. J., Cieszewski, R., Stancil, P. C., et al. 2018, ApJ, 858, 10
Piñeiro, A. L., Tipping, R. H., & Chackerian, C. 1987, J. Mol. Spectrosc., 125, 184
Ramstedt, S., & Olofsson, H. 2014, A&A, 566, A145
Ramstedt, S., Schöier, F. L., Olofsson, H., & Lundgren, A. A. 2008, A&A, 487, 645
Ramstedt, S., Schöier, F. L., & Olofsson, H. 2009, A&A, 499, 515
Raymonda, J. W., Muenter, J. S., & Klemperer, W. A. 1970, J. Chem. Phys., 52, 3458
Ryde, N., & Schöier, F. L. 2001, ApJ, 547, 384
Sanz, M. E., McCarthy, M. C., & Thaddeus, P. 2003, J. Chem. Phys., 119, 11715
Schöier, F. L., Olofsson, H., Wong, T., Lindqvist, M., & Kerschbaum, F. 2004, A&A, 422, 651
Schöier, F. L., Olofsson, H., & Lundgren, A. A. 2006a, A&A, 454, 247
Schöier, F. L., Fong, D., Olofsson, H., Zhang, Q., & Patel, N. 2006b, ApJ, 649, 965
Schöier, F. L., Bast, J., Olofsson, H., & Lindqvist, M. 2007, A&A, 473, 871
Schöier, F. L., Ramstedt, S., Olofsson, H., et al. 2013, A&A, 550, A78
Sobolev, V. V. 1960, Moving Envelopes of Stars (Harvard: Harvard University Press)
Suh, K.-W. 1999, MNRAS, 304, 389
Teyssier, D., Hernandez, R., Bujarrabal, V., Yoshida, H., & Phillips, T. G. 2006, A&A, 450, 167
Toboła, R., Lique, F., Kłos, J., & Chałasiński, G. 2008, J. Phys. B At. Mol. Phys., 41, 155702
Van de Sande, M., Sundqvist, J. O., Millar, T. J., et al. 2018, A&A, 616, A106
Van de Sande, M., Walsh, C., Mangan, T. P., & Decin, L. 2019, MNRAS, 490, 2023
Van de Sande, M., Sundqvist, J. O., Millar, T. J., et al. 2020, A&A, 634, C1
van Langevelde, H. J., van der Heiden, R., & van Schooneveld, C. 1990, A&A, 239, 193
Velilla Prieto, L., Sánchez Contreras, C., Cernicharo, J., et al. 2017, A&A, 597, A25
Velilla-Prieto, L., Cernicharo, J., Agúndez, M., et al. 2019, A&A, 629, A146
Winnewisser, G., & Cook, R. L. 1968, J. Mol. Spectrosc., 28, 266
Winters, J. M., Le Bertre, T., Pety, J., & Neri, R. 2007, A&A, 475, 559
Woodruff, H. C., Eberhardt, M., Driebe, T., et al. 2004, A&A, 421, 703
Yamamura, I., de Jong, T., Onaka, T., Cami, J., & Waters, L. B. F. M. 1999, A&A, 341, L9
Zhang, B., Zheng, X., Reid, M. J., et al. 2017, ApJ, 849, 99

Appendix A: Observed lines

Table A.1. Observed line parameters.

Line		ν_{calc} (MHz)	ν_{obs} (MHz)	V_e (km s^{-1})	$\int T_{mb}\,dv$ (K km s^{-1})
			IK Tau		
SiO	3−2	130 268.665	130 268.7(1)	17.7(2)	55.6(55)
SiS	8−7	145 227.054	145 226.9(5)	19.5(5)	6.1(6)
CS	3−2	146 969.025	146 969.4(5)	17.3(8)	3.11(3)
SO	3_3-2_2	129 138.983	129 139.5(5)	16.8(6)	2.29(2)
SO_2	$8_{2-6}-8_{1-7}$	134 004.811	134 005.3(5)	16.6(5)	3.80(4)
SO_2	$5_{1-5}-4_{0,4}$	135 696.016	135 696.7(5)	16.8(8)	5.20(5)
SO_2	$4_{2-2}-4_{1,3}$	146 605.519	146 606.3(6)	16.6(6)	2.19(2)
SO_2	$2_{2-0}-2_{1,1}$	151 378.662	151 379.4(5)	17.0(6)	1.21(1)
			KU And		
SiO	3−2	130 268.665	130 268.3(1)	20.7(1)	5.62(6)
SiS	8−7	145 227.054	145 227.1(1)	19.0(1)	1.88(2)
CS	3−2	146 969.025	146 968.5(1)	19.4(1)	1.4(4)
SO	3_3-2_2	129 138.983	–	–	–
SO_2	$8_{2-6}-8_{1-7}$	134 004.811	–	–	–
SO_2	$5_{1-5}-4_{0,4}$	135 696.016	–	–	–
SO_2	$4_{2-2}-4_{1,3}$	146 605.519			
SO_2	$2_{2-0}-2_{1,1}$	151 378.662	–	–	–
			RX Boo		
SiO	3−2	130 268.665	130 268.7(1)	7.8(1)	26.0(26)
SiS	8−7	145 227.054	–	–	–
CS	3−2	146 969.025	–	–	–
SO	3_3-2_2	129 138.983	129 138.9(1)	7.8(1)	0.88(1)
SO_2	$8_{2-6}-8_{1-7}$	134 004.811	134 005.0(5)	7.9(5)	0.83(8)
SO_2	$5_{1-5}-4_{0,4}$	135 696.016	135 695.9(1)	6.5(1)	0.37(4)
SO_2	$4_{2-2}-4_{1,3}$	146 605.519	146 606.4(5)	6.3(4)	0.23(5) [a]
SO_2	$2_{2-0}-2_{1,1}$	151 378.662	151 377.8(10)	9.0(10)	0.12(2) [a]
			RT Vir		
SiO	3−2	130 268.665	130 268.7(1)	7.1(1)	6.56(6)
SiS	8−7	145 227.054	–	–	–
CS	3−2	146 969.025	–	–	–
SO	3_3-2_2	129 138.983	129 139.2(1)	6.9(1)	0.64(1)
SO_2	$8_{2-6}-8_{1-7}$	134 004.811	134 004.9(5)	6.0(4)	0.67(3)
SO_2	$5_{1-5}-4_{0,4}$	135 696.016	135 696.0(5)	5.8(6)	0.35(3)
SO_2	$4_{2-2}-4_{1,3}$	146 605.519	146 605.5(5)	5.5(6)	0.24(2)
SO_2	$2_{2-0}-2_{1,1}$	151 378.662	151 379.3(10)	4.5(10)	0.09(2) [a]
			R Leo		
SiO	3−2	130 268.665	130268.6(5)	5.1(5)	15.09(15)
SiS	8−7	145 227.054	–	–	–
CS	3 − 2	146 969.025	146 968.5(5)	4.8(5)	0.10(1) [a]
SO	3_3-2_2	129 138.983	129 138.9(1)	4.5(3)	0.27(3)
SO_2	$8_{2-6}-8_{1-7}$	134 004.811	–	–	–
SO_2	$5_{1-5}-4_{0,4}$	135 696.016	–	–	–
SO_2	$4_{2-2}-4_{1,3}$	146 605.519	–	–	–
SO_2	$2_{2-0}-2_{1,1}$	151 378.662	–	–	–
			WX Psc		
SiO	3−2	130 268.665	130 268.7(1)	18.8(4)	29.0(30)
SiS	8−7	145 227.054	145 227.0(1)	19.4(4)	26.2(26)
CS	3−2	146 969.025	146 969.0(1)	17.8(6)	2.41(2)
SO	3_3-2_2	129 138.983	129 139.2(1)	18.5(3)	1.11(1)

Notes. Numbers in parentheses are 1σ uncertainties in units of the last digits. [a]Marginal detection.

Table A.1. continued.

Line		ν_{calc} (MHz)	ν_{obs} (MHz)	V_e (km s^{-1})	$\int T_{mb}\,dv$ (K km s^{-1})
SO_2	$8_{2-6}-8_{1-7}$	134 004.811	134 005.2(5)	17.7(5)	1.7(2)
SO_2	$5_{1-5}-4_{0,4}$	135 696.016	135 696.2(1)	18.3(4)	6.81(7)
SO_2	$4_{2-2}-4_{1,3}$	146 605.519	146 605.8(1)	18.4(2)	2.02(2)
SO_2	$2_{2-0}-2_{1,1}$	151 378.662	151 378.8(1)	18.0(6)	1.40(1)
		GX Mon			
SiO	3–2	130 268.665	130 268.6(1)	18.4(1)	25.0(25)
SiS	8–7	145 227.054	145 226.8(4)	18.2(6)	2.10(20)
CS	3–2	146 969.025	146 968.9(5)	17.4(8)	1.51(1)
SO	3_3-2_2	129 138.983	129 138.9(1)	17.6(6)	1.39(1)
SO_2	$8_{2-6}-8_{1-7}$	134 004.811	134 005.2(5)	16.6(6)	1.2(1)
SO_2	$5_{1-5}-4_{0,4}$	135 696.016	135696.2(5)	18.1(5)	5.79(8)
SO_2	$4_{2-2}-4_{1,3}$	146 605.519	146 605.4(5)	18.5(6)	1.54(1)
SO_2	$2_{2-0}-2_{1,1}$	151 378.662	151 379.1(5)	18.0(4)	1.28(1)
		NV Aur			
SiO	3 – 2	130 268.665	130 268.5(1)	17.7(1)	13.7(14)
SiS	8 – 7	145 227.054	145 226.9(5)	17.1(4)	2.98(3)
CS	3 – 2	146 969.025	146 968.5(5)	16.3(4)	0.77(8)
SO	3_3-2_2	129 138.983	129 138.7(5)	16.4(4)	0.67(7)
SO_2	$8_{2-6}-8_{1-7}$	134 004.811	134 004.9(5)	17.0(4)	1.4(1)
SO_2	$5_{1-5}-4_{0,4}$	135 696.016	135 696.1(1)	17.1(1)	3.57(3)
SO_2	$4_{2-2}-4_{1,3}$	146 605.519	146 605.6(5)	17.0(8)	1.14(1)
SO_2	$2_{2-0}-2_{1,1}$	151 378.662	151 379.0(6)	17.3(5)	0.76(7)
		V1111 Oph			
SiO	3–2	130 268.665	130 268.6(6)	15.7(1)	21.0(20)
SiS	8–7	145 227.054	145 227.2(5)	14.2(7)	2.17(2)
CS	3–2	146 969.025	146 969.4(1)	14.2(1)	1.18(1)
SO	3_3-2_2	129 138.983	129 138.9(5)	15.2(3)	0.87(8)
SO_2	$8_{2-6}-8_{1-7}$	134 004.811	134 005.0(1)	14.5(1)	1.2(3)
SO_2	$5_{1-5}-4_{0,4}$	135 696.016	135 696.1(5)	15.9(5)	3.89(4)
SO_2	$4_{2-2}-4_{1,3}$	146 605.519	146 605.4(5)	15.5(6)	1.27(1)
SO_2	$2_{2-0}-2_{1,1}$	151 378.662	151 378.7(5)	15.3(5)	0.77(7)
		RR Aql			
SiO	3–2	130 268.665	130 268.4(1)	6.0(10)	4.86(5)
SiS	8–7	145 227.054	–	–	–
CS	3–2	146 969.025	–	–	–
SO	3_3-2_2	129 138.983	129 138.9(5)	8.5(6)	0.40(4)
SO_2	$8_{2-6}-8_{1-7}$	134 004.811	134 004.3(1)	7.8(1)	0.36(3)
SO_2	$5_{1-5}-4_{0,4}$	135 696.016	135 696.2(1)	8.0(1)	1.17(1)
SO_2	$4_{2-2}-4_{1,3}$	146 605.519	146 605.5(1)	8.0(1)	0.58(1)
SO_2	$2_{2-0}-2_{1,1}$	151 378.662	151 379.0(5)	7.5(4)	0.31(3)
		R LMi			
SiO	3–2	130 268.665	130 268.6(5)	5.8(5)	6.23(6)
SiS	8–7	145 227.054	–	–	–
CS	3–2	146 969.025	–	–	–
SO	3_3-2_2	129 138.983	129 139.1(5)	5.5(5)	0.18(2)
SO_2	$8_{2-6}-8_{1-7}$	134 004.811	134 004.9(5)	4.8(5)	0.21(2)
SO_2	$5_{1-5}-4_{0,4}$	135 696.016	135 694.6(10)	4.6(10)	0.09(2)[a]
SO_2	$4_{2-2}-4_{1,3}$	146 605.519	146 606.1(5)	5.2(5)	0.05(1)[a]
SO_2	$2_{2-0}-2_{1,1}$	151 378.662	–	–	–
		BX Cam			
SiO	3–2	130 268.665	130 268.6(1)	17.3(1)	13.2(13)
SiS	8–7	145 227.054	145 226.7(5)	15.4(6)	1.06(3)

Table A.1. continued.

Line		ν_{calc} (MHz)	ν_{obs} (MHz)	V_e (km s^{-1})	$\int T_{mb}\,dv$ (K km s^{-1})
CS	3–2	146 969.025	146 969.0(5)	17.6(5)	0.74(7)
SO	3_3–2_2	129 138.983	129 138.7(5)	15.4(5)	0.84(17) [a]
SO_2	8_{2-6}–8_{1-7}	134 004.811	134 004.5(5)	14.9(8)	0.72(14) [a]
SO_2	5_{1-5}–$4_{0,4}$	135 696.016	135 696.3(1)	17.0(1)	1.47(1)
SO_2	4_{2-2}–$4_{1,3}$	146 605.519	146 606.0(1)	14.9(1)	0.49(5) [a]
SO_2	2_{2-0}–$2_{1,1}$	151 378.662	151 378.9(10)	14.8(10)	0.25(5) [a]
		V1300 Aql			
SiO	3–2	130 268.665	130 268.5(1)	14.1(1)	7.51(7)
SiS	8–7	145 227.054	145 227.3(1)	14.7(5)	10.9(11)
CS	3–2	146 969.025	146 969.3(5)	14.0(5)	0.91(18)
SO	3_3–2_2	129 138.983	129 138.9(4)	13.6(4)	1.19(1)
SO_2	8_{2-6}–8_{1-7}	134 004.811	134 004.8(6)	13.0(5)	1.16(11)
SO_2	5_{1-5}–$4_{0,4}$	135 696.016	135 696.1(2)	13.7(5)	4.02(4)
SO_2	4_{2-2}–$4_{1,3}$	146 605.519	146 605.6(5)	13.1(8)	1.91(2)
SO_2	2_{2-0}–$2_{1,1}$	151 378.662	151 378.9(5)	13.2(5)	1.14(1)
		R Cas			
SiO	3–2	130 268.665	130 268.7(5)	8.3(5)	31.9(32)
SiS	8–7	145 227.054	145 226.2(10)	6.4(10)	0.18(4) [a]
CS	3–2	146 969.025	146 969.2(5)	6.8(5)	0.32(6)
SO	3_3–2_2	129 138.983	129 138.8(1)	7.0(1)	0.98(1)
SO_2	8_{2-6}–8_{1-7}	134 004.811	134 004.9(5)	6.8(5)	0.87(9)
SO_2	5_{1-5}–$4_{0,4}$	135 696.016	135 696.1(6)	8.2(8)	0.67(7)
SO_2	4_{2-2}–$4_{1,3}$	146 605.519	146 606.0(5)	7.3(5)	0.30(3)
SO_2	2_{2-0}–$2_{1,1}$	151 378.662	151 378.0(10)	6.7(10)	0.18(4) [a]
		IRC -30 398			
SiO	3–2	130 268.665	130 268.6(1)	14.8(5)	6.90(7)
SiS	8–7	145 227.054	145 227.2(5)	13.7(5)	0.34(7)
CS	3–2	146 969.025	146 969.1(5)	14.0(5)	0.59(6)
SO	3_3–2_2	129 138.983	–	–	–
SO_2	8_{2-6}–8_{1-7}	134 004.811	–	–	–
SO_2	5_{1-5}–$4_{0,4}$	135 696.016	–	–	–
SO_2	4_{2-2}–$4_{1,3}$	146 605.519	–	–	–
SO_2	2_{2-0}–$2_{1,1}$	151 378.662	–	–	–
		TX Cam			
SiO	3–2	130 268.665	130 268.8(5)	17.7(7)	36.4(36)
SiS	8–7	145 227.054	145 226.7(1)	17.1(1)	7.6(7)
CS	3–2	146 969.025	146 968.9(1)	19.4 (1)	8.8(9)
SO	3_3–2_2	129 138.983	129 139.5(1)	16.7(1)	1.09(1)
SO_2	8_{2-6}–8_{1-7}	134 004.811	134 005.5(10)	18.6(10)	0.60(12) [a]
SO_2	5_{1-5}–$4_{0,4}$	135 696.016	135 696.5(5)	17.9(5)	2.29(2)
SO_2	4_{2-2}–$4_{1,3}$	146 605.519	146 606.6(5)	19.5(5)	0.60(6)
SO_2	2_{2-0}–$2_{1,1}$	151 378.662	151 379.1(10)	19.2(10)	0.39(8) [a]
		S CrB			
SiO	3–2	130 268.665	130 268.7(1)	4.9(1)	2.74(30)
SiS	8–7	145 227.054	–	–	–
CS	3–2	146 969.025	–	–	–
SO	3_3–2_2	129 138.983	129 139.0(5)	4.5(5)	0.17(4) [a]
SO_2	8_{2-6}–8_{1-7}	134 004.811	134 005.6(5)	4.4(5)	0.30(3) [a]
SO_2	5_{1-5}–$4_{0,4}$	135 696.016	135 696.4(5)	5.4(7)	0.31(3) [a]
SO_2	4_{2-2}–$4_{1,3}$	146 605.519	146 606.7(5)	4.7(5)	0.18(2) [a]
SO_2	2_{2-0}–$2_{1,1}$	151 378.662	151 378.5(10)	4.2(10)	0.02(1) [a]

Table A.1. continued.

Line		ν_{calc} (MHz)	ν_{obs} (MHz)	V_e (km s^{-1})	$\int T_{mb}\,dv$ (K km s^{-1})
			IRC +60169		
SiO	3−2	130 268.665	130 268.8(1)	13.2(1)	3.43(3)
SiS	8−7	145 227.054	145 227.8(10)	15.6(10)	0.15(3) [a]
CS	3−2	146 969.025	146 969.5(10)	11.3(10)	0.11(2) [a]
SO	3_3-2_2	129 138.983	129 138.5(10)	15.3(10)	0.17(3) [a]
SO_2	$8_{2-6}-8_{1-7}$	134 004.811	134 004.2(10)	15.0(10)	0.10(2) [a]
SO_2	$5_{1-5}-4_{0,4}$	135 696.016	135 696.7(5)	15.1(1)	0.77(7)
SO_2	$4_{2-2}-4_{1,3}$	146 605.519	146 604.5(10)	15.0(10)	0.18(21) [a]
SO_2	$2_{2-0}-2_{1,1}$	151 378.662	151 378.5(10)	15.3(10)	0.20(4) [a]
			R Hya		
SiO	3−2	130 268.665	130 268.5(5)	4.9(5)	14.0(14)
SiS	8−7	145 227.054	–	–	–
CS	3−2	146 969.025	–	–	
SO	3_3-2_2	129 138.983	129 140.0(10)	3.9(10)	0.11(2) [a]
SO_2	$8_{2-6}-8_{1-7}$	134 004.811	–	–	–
SO_2	$5_{1-5}-4_{0,4}$	135 696.016	–	–	–
SO_2	$4_{2-2}-4_{1,3}$	146 605.519	–	–	–
SO_2	$2_{2-0}-2_{1,1}$	151 378.662	–	–	–
			R CrT		
SiO	3−2	130 268.665	130 268.5(1)	10.4(1)	22.3(20)
SiS	8−7	145 227.054	–	–	–
CS	3−2	146 969.025?	–	–	–
SO	3_3-2_2	129 138.983	129 139.5(5)	8.5(4)	0.82(1)
SO_2	$8_{2-6}-8_{1-7}$	134 004.811	134 004.5(5)	10.6(6)	1.3(1)
SO_2	$5_{1-5}-4_{0,4}$	135 696.016	135 696.4(1)	9.6(3)	0.73(7)
SO_2	$4_{2-2}-4_{1,3}$	146 605.519	146 605.2(5)	10.4(6)	0.49(9) [a]
SO_2	$2_{2-0}-2_{1,1}$	151 378.662	151 379.0(5)	10.3(5)	0.20(4) [a]
			O Ceti		
SiO	3−2	130 268.665	130 268.6(5)	3.4(10)	1.62(16)
SiS	8−7	145 227.054	–	–	–
CS	3−2	146 969.025	146 969.4(5)	5.3	0.17(3) [a]
SO	3_3-2_2	129 138.983	129 138.7(5)	5.1(4)	0.22(2)
SO_2	$8_{2-6}-8_{1-7}$	134 004.811	134 005.3(10)	4.7(10)	0.21(4) [a]
SO_2	$5_{1-5}-4_{0,4}$	135 696.016	135 696.6(5)	2.7(5)	0.04(1) [a]
SO_2	$4_{2-2}-4_{1,3}$	146 605.519	146 605.6(5)	3.7(7)	0.05(1) [a]
SO_2	$2_{2-0}-2_{1,1}$	151 378.662	151 378.7(10)	1.5(10)	0.020(4) [a]
			W Hya		
SiO	3−2	130 268.665	130 268.6(1)	6.3(1)	26.6(26)
SiS	8−7	145 227.054	–	–	–
CS	3−2	146 969.025	146 969.7(10)	6.1(10)	0.31(6) [a]
SO	3_3-2_2	129 138.983	129 139.3(5)	4.7(1)	0.33(3)
SO_2	$8_{2-6}-8_{1-7}$	134 004.811	–	–	–
SO_2	$5_{1-5}-4_{0,4}$	135 696.016	–	–	–
SO_2	$4_{2-2}-4_{1,3}$	146 605.519	–	–	–
SO_2	$2_{2-0}-2_{1,1}$	151 378.662	–	–	–
			T Cep		
SiO	3−2	130 268.665	130 268.7(1)	3.8(1)	3.20(3)
SiS	8−7	145 227.054	–	–	–
CS	3−2	146 969.025	–	–	–
SO	3_3-2_2	129 138.983	–	–	–
SO_2	$8_{2-6}-8_{1-7}$	134 004.811	–	–	–
SO_2	$5_{1-5}-4_{0,4}$	135 696.016	–	–	–

Table A.1. continued.

Line		ν_{calc} (MHz)	ν_{obs} (MHz)	V_e (km s^{-1})	$\int T_{mb}\,dv$ (K km s^{-1})
SO_2	$4_{2-2}-4_{1,3}$	146 605.519			
SO_2	$2_{2-0}-2_{1,1}$	151 378.662	–	–	–
		V1943 Sgr			
SiO	3−2	130 268.665	130 268.6(1)	4.5(5)	5.07(5)
SiS	8−7	145 227.054	–	–	–
CS	3−2	146 969.025	–	–	–
SO	3_3-2_2	129 138.983	129 138.9(10)	4.2(10)	0.20(4)
SO_2	$8_{2-6}-8_{1-7}$	134 004.811	–	–	–
SO_2	$5_{1-5}-4_{0,4}$	135 696.016	–	–	–
SO_2	$4_{2-2}-4_{1,3}$	146 605.519	–	–	
SO_2	$2_{2-0}-2_{1,1}$	151 378.662	–	–	–
		SW Vir			
SiO	3−2	130 268.665	130 268.6(1)	7.5(1)	17.4(17)
SiS	8−7	145 227.054	–	–	–
CS	3−2	146 969.025	146 969.0(10)	7.5(8)	0.33(6) [a]
SO	3_3-2_2	129 138.983	129 139.0(5)	7.1(6)	0.57(11)
SO_2	$8_{2-6}-8_{1-7}$	134 004.811	–	–	–
SO_2	$5_{1-5}-4_{0,4}$	135 696.016	–	–	–
SO_2	$4_{2-2}-4_{1,3}$	146 605.519	–	–	–
SO_2	$2_{2-0}-2_{1,1}$	151 378.662	–	–	–
		AFGL 292			
SiO	3−2	130 268.665	130 268.6(1)	6.9(6)	3.69(4)
SiS	8−7	145 227.054	–	–	–
CS	3−2	146 969.025	–	–	–
SO	3_3-2_2	129 138.983	129 138.7(10)	5.5(7)	0.09(2) [a]
SO_2	$8_{2-6}-8_{1-7}$	134 004.811	–	–	–
SO_2	$5_{1-5}-4_{0,4}$	135 696.016	–	–	–
SO_2	$4_{2-2}-4_{1,3}$	146 605.519	–	–	–
SO_2	$2_{2-0}-2_{1,1}$	151 378.662	–	–	–
		BK Vir			
SiO	3−2	130 268.665	130 268.6(1)	4.2(8)	3.3(3)
SiS	8−7	145 227.054	–	–	–
CS	3−2	146 969.025	–	–	–
SO	3_3-2_2	129 138.983	–	–	–
SO_2	$8_{2-6}-8_{1-7}$	134 004.811	–	–	–
SO_2	$5_{1-5}-4_{0,4}$	135 696.016	–	–	–
SO_2	$4_{2-2}-4_{1,3}$	146 605.519	–	–	–
SO_2	$2_{2-0}-2_{1,1}$	151 378.662	–	–	–
		OH 26.5+0.6			
SiO	3−2	130 268.665	130 268.6(1)	14.2(1)	6.55(6)
SiS	8−7	145 227.054	145 227.0(1)	12.6(1)	1.54(1)
CS	3−2	146 969.025	146 968.5(5)	15.6(5)	0.96(9)
SO	3_3-2_2	129 138.983	129 138.6(1)	13.1(3)	6.29(3)
SO_2	$8_{2-6}-8_{1-7}$	134 004.811	134 005.5(1)	14.2(1)	4.15(4)
SO_2	$5_{1-5}-4_{0,4}$	135 696.016	135 696.1(1)	14.3(4)	8.53(8)
SO_2	$4_{2-2}-4_{1,3}$	146 605.519	146 605.4(4)	14.4(7)	3.79(4)
SO_2	$2_{2-0}-2_{1,1}$	151 378.662	151 378.6(5)	14.1(4)	2.71(3)
		Ep Aqr			
SiO	3−2	130 268.665	130 268.0(5)	8.1(10)	22.5(22)
SiS	8−7	145 227.054	–	–	–
CS	3−2	146 969.025	146 969.0(10)	0.9(5)	0.030(6) [a]
SO	3_3-2_2	129 138.983	129 138.8(5)	3.0(10)	1.16(23)

Table A.1. continued.

Line		ν_{calc} (MHz)	ν_{obs} (MHz)	V_e (km s^{-1})	$\int T_{mb}\,dv$ (K km s^{-1})
SO_2	$8_{2-6}-8_{1-7}$	134 004.811	134 004.8(5)	2.2(10)	0.38(8)
SO_2	$5_{1-5}-4_{0,4}$	135 696.016	135 696.0(5)	2.3(10)	0.13(1)
SO_2	$4_{2-2}-4_{1,3}$	146 605.519	146 605.4(5)	3.2(10)	0.15(2)
SO_2	$2_{2-0}-2_{1,1}$	151 378.662	151 378.6(5)	3.7(10)	0.08(2)
			X Her		
SiO	3−2	130 268.665	130 268.4(5)	6.5(5)	10.2(10)
SiS	8−7	145 227.054	–	–	–
CS	3−2	146 969.025	–	–	–
SO	3_3-2_2	129 138.983	129 138.8(5)	2.8(5)	0.52(5)
SO_2	$8_{2-6}-8_{1-7}$	134 004.811	–	–	–
SO_2	$5_{1-5}-4_{0,4}$	135 696.016	–	–	–
SO_2	$4_{2-2}-4_{1,3}$	146 605.519	–	–	–
SO_2	$2_{2-0}-2_{1,1}$	151 378.662	–	–	–